Springer Series in Optical Sciences 186

Arun K. Majumdar

Advanced Free Space Optics (FSO)

A Systems Approach

Springer

Springer Series in Optical Sciences

Volume 186

Founded by
H.K.V. Lotsch

Editor-in-Chief
William T. Rhodes, Atlanta, USA

Editorial Board
Ali Adibi, Atlanta, USA
Toshimitsu Asakura, Sapporo, Japan
Theodor W. Hänsch, Garching, Germany
Takeshi Kamiya, Tokyo, Japan
Ferenc Krausz, Garching, Germany
Bo A.J. Monemar, Linköping, Sweden
Herbert Venghaus, Berlin, Germany
Horst Weber, Berlin, Germany
Harald Weinfurter, München, Germany

For further volumes:
www.springer.com/series/624

Springer Series in Optical Sciences

The Springer Series in Optical Sciences, under the leadership of Editor-in-Chief William T. Rhodes, Georgia Institute of Technology, USA, provides an expanding selection of research monographs in all major areas of optics: lasers and quantum optics, ultrafast phenomena, optical spectroscopy techniques, optoelectronics, quantum information, information optics, applied laser technology, industrial applications, and other topics of contemporary interest.
With this broad coverage of topics, the series is of use to all research scientists and engineers who need up-to-date reference books.
The editors encourage prospective authors to correspond with them in advance of submitting a manuscript. Submission of manuscripts should be made to the Editor-in-Chief or one of the Editors.
See also www.springer.com/series/624.

Editor-in-Chief
William T. Rhodes
School of Electrical and Computer Engineering
Georgia Institute of Technology
Atlanta, GA 30332-0250, USA
bill.rhodes@ece.gatech.edu

Editorial Board
Ali Adibi
School of Electrical and Computer Engineering
Georgia Institute of Technology
Atlanta, GA 30332-0250, USA
adibi@ee.gatech.edu

Toshimitsu Asakura
Faculty of Engineering
Hokkai-Gakuen University
1-1, Minami-26, Nishi 11, Chuo-ku
Sapporo, Hokkaido 064-0926, Japan
asakura@eli.hokkai-s-u.ac.jp

Theodor W. Hänsch
Max-Planck-Institut für Quantenoptik
Hans-Kopfermann-Straße 1
85748 Garching, Germany
t.w.haensch@physik.uni-muenchen.de

Takeshi Kamiya
National Institution for Academic Degrees
Ministry of Education, Culture, Sports
Science and Technology
3-29-1 Otsuka, Bunkyo-ku
Tokyo 112-0012, Japan
kamiyatk@niad.ac.jp

Ferenc Krausz
Ludwig-Maximilians-Universität München
Lehrstuhl für Experimentelle Physik
Am Coulombwall 1
85748 Garching, Germany

Max-Planck-Institut für Quantenoptik
Hans-Kopfermann-Straße 1
85748 Garching, Germany
ferenc.krausz@mpq.mpg.de

Bo A.J. Monemar
Department of Physics and Measurement Technology,
Materials Science Division
Linköping University
58183 Linköping, Sweden
bom@ifm.liu.se

Herbert Venghaus
Fraunhofer Institut für Nachrichtentechnik
Heinrich-Hertz-Institut
Einsteinufer 37
10587 Berlin, Germany
venghaus@hhi.de

Horst Weber
Optisches Institut
Technische Universität Berlin
Straße des 17. Juni 135
10623 Berlin, Germany
weber@physik.tu-berlin.de

Harald Weinfurter
Sektion Physik
Ludwig-Maximilians-Universität München
Schellingstraße 4/III
80799 München, Germany
harald.weinfurter@physik.uni-muenchen.de

Arun K. Majumdar

Advanced Free Space Optics (FSO)

A Systems Approach

Springer

Arun K. Majumdar
105 W. Mojave Rose Ave.
Ridgecrest, CA 93555
USA

ISSN 0342-4111
ISBN 978-1-4939-0917-9
DOI 10.1007/978-1-4939-0918-6
Springer New York Heidelberg Dordrecht London

ISSN 1556-1534 (electronic)
ISBN 978-1-4939-0918-6 (eBook)

Library of Congress Control Number: 2014940091

© Springer Science+Business Media New York 2015
This work is subject to copyright. All rights are reserved by the Publisher, whether the whole or part of the material is concerned, specifically the rights of translation, reprinting, reuse of illustrations, recitation, broadcasting, reproduction on microfilms or in any other physical way, and transmission or information storage and retrieval, electronic adaptation, computer software, or by similar or dissimilar methodology now known or hereafter developed. Exempted from this legal reservation are brief excerpts in connection with reviews or scholarly analysis or material supplied specifically for the purpose of being entered and executed on a computer system, for exclusive use by the purchaser of the work. Duplication of this publication or parts there of is permitted only under the provisions of the Copyright Law of the Publisher's location, in its current version, and permission for use must always be obtained from Springer. Permissions for use may be obtained through Rights Link at the Copyright Clearance Center. Violations are liable to prosecution under the respective Copyright Law.
The use of general descriptive names, registered names, trademarks, service marks, etc. in this publication does not imply, even in the absence of a specific statement, that such names are exempt from the relevant protective laws and regulations and therefore free for general use.
While the advice and information in this book are believed to be true and accurate at the date of publication, neither the authors nor the editors nor the publisher can accept any legal responsibility for any errors or omissions that may be made. The publisher makes no warranty, express or implied, with respect to the material contained herein.

Printed on acid-free paper

Springer is part of Springer Science+Business Media (www.springer.com)

Preface

The motivation for writing this book stemmed from two reasons: (i) recent tremendous growth of Free Space Optics (FSO) as evidenced by vast improvement in information technology (resulting in many exciting implementations and experimental demonstrations presented at major conferences and via increased number of publications), and (ii) encouragement from colleagues and researchers from industry, university, recent conferences, and the students (USA and abroad) interested in this field. Some of the conferences include SPIE's, OSA's, and MILCOM's conferences, specifically on Free Space Laser Communications. Some portions of this book are based on Short Courses offered by the author at various professional societies' conferences and aerospace industries, as well as lecture series and invited seminars at various universities and institutes of technology (USA and international, including Brno University of Technology, Czech Republic, as well as different parts within India like Kolkata, Burdwan, Karnataka, and Gujarat).

The book provides the basic materials of a comprehensive introduction to the principle and applications of the FSO communications. It is addressed principally to scientists, engineers, and physicists to be used as a text at various levels, as an instrument for the research worker in current problems, and it is hoped to be a starting point for new developments. The student, the communications systems engineer, or the research scientist approaching this field will find this book about where to start.

This book is one of the most coherent and comprehensive books available to date in the area covering advanced FSO with the state-of-the-art applications. This book could be used as both a textbook and a research text. The material presented here is complementary and a companion to the author's book, *Free-Space Laser Communications: Principles and Advances*, Arun K. Majumdar and Jennifer C. Ricklin, Springer, 2008.

Different areas of FSO communication have been published in many excellent articles during the past few years, many of those publications are scattered throughout the archival literature of scientific and technical journals. This book aims to bring together into one source much of this wealth of information. The present book offers a wide variety of topics, yet having a coherence across chapters that enables the readers to cross-reference similar topics, and hence, to develop deeper into their presentation and explanation.

FSO is becoming a mainstream technology that not only addresses access applications, but will also play a major role in core networking applications. It has the capability to address connectivity bottlenecks that have been created in high-speed networks due to the tremendous success and continued acceptance of the Internet. Future growth and success of the contemporary internet society anticipates growing global bandwidth, and the multimedia-driven society will accommodate high-bandwidth applications such as downloading movies and online bidirectional video-conferencing, all in the presence of atmosphere. The next generation of Internet connectivity will push the limits of existing infrastructure with high-bandwidth applications and network enabled portable devices. Optical capacity in the access and edge networks will therefore be needed to satisfy these demands. FSO will become a critical tool for the service providers to bridge the gap between the end user and the high-capacity fiber infrastructure already in place. This book will help to better understand the FSO technology and applications operating under various atmospheric conditions.

This book discusses the materials using a systems approach point of view so that a specific system-of-interest (SOI) to be open and dynamic to interact with and adapt to other systems. The systems are generally characterized as functional, i.e., the systems, subsystems, containing systems, etc., all performing various FSO technology functions. The systems approach is effective not only for understanding or designing physical systems, but also for abstract construction in mathematical formulations and theories needed for understanding FSO communications.

FSO is a practical solution for creating a three-dimensional global broadband communication grid, offering bandwidths far beyond possible in Radio Frequency (RF) range. However, the attributes of atmospheric turbulence and scattering impose perennial limitations on availability and reliability of FSO links. The main drivers behind the emergence of advanced FSO are: (i) high demands in bandwidth, thanks to the recent growth of Internet usage, IPTV, VoIP, and YouTube; and (ii) rapid advance of signal processing capability to achieve higher data rate with much smaller devices (for example using MEMS and nanotechnology). With the rapid growth of data-centric devices and the general deployment of broadband access networks, there has been a strong demand for pushing, for achieving higher data rate from 10 Gbps to more spectrally efficient 40 Gbps or 100 Gbps/channel, and beyond. However, numerous challenges exist today for accomplishing higher transmission rates due to degradation in the signal quality as a result of atmospheric channel impairments.

This book covers both fundamentals and the recent progress in FSO concepts and the technology. The book explains the theory to back up the systems approach with a distinctive focus on the broad range of applications. Using the systems approach, the book explains each topic with a focus on the impact of systems performance. The reader will find all the important topics of FSO system in one place with in-depth coverage. Each chapter will have a section on fundamentals (with necessary derivations of the equations), theory of operation, and the recent developments with examples. Some of the pioneers and world's experts in the field have contributed to the last two chapters. They include: L. C. Andrews, R. L. Phillips, Z.C. Bagley,

N.D. Plasson, L. B. Stotts for Chap. 9, and Ronald E. Meyers, Keith S. Deacon and Arnold D. Tunick for Chap. 10.

The book is organized as follows. There are 10 chapters, each chapter having complete entities in and of themselves.

Chapter 1 discusses the Fundamentals of FSO Communication System and the overall laser communications architecture, explaining how FSO must be included in the set of solutions for meeting the bandwidth requirements of the modern internet. FSO communication is the most practical alternative to solve the bottleneck broadband connectivity problem, and as a supplement to conventional RF/microwave links. This chapter serves as a general background for the concepts presented in subsequent chapters.

Chapter 2 provides a theoretical treatment and analysis of FSO communication signal propagation through Atmospheric Channel. The goal of a communication system is to transmit information which can be accomplished in many ways. FSO technology depends on the propagation of optical beam through various media, which interact with and affect the quality of the propagating optical signal. The understanding of the atmospheric phenomena and how they affect the propagating light is essential in designing effective, intelligent and cost-efficient FSO links and reliable networks in order to provide uninterrupted service at the expected quality.

Chapter 3 provides the different techniques of modulation, detection and coding for FSO communications. The chapter introduces and explains in details the modulation techniques used in FSO and their performance in the presence of channel impairments such as noise, interference, and channel fading/loss induced by atmospheric turbulence and scattering medium. Error detection and correction (EDAC) to achieve good communication is discussed employing various coding schemes that are particularly suitable for atmospheric channels.

Chapter 4 describes the need and techniques for atmospheric mitigation and compensation for FSO links. The chapter provides an in-depth treatment of the critical issue of limitations imposed by the atmospheric effects to establish a successful free-space optical link. There are a variety of deleterious features of the atmospheric channel that may lead to serious signal fading, and even the complete loss of signal altogether. The chapter starts with a detailed discussion of the two primary atmospheric effects relevant to FSO links: turbulence and scattering. Several mitigating strategies are discussed. All mitigating techniques are explained in detail with appropriate derivations, and performance enhancements with each technique are discussed. Various scenarios of practical importance are described with examples in order to determine the applicability of the techniques to be useful for designers in optimizing the performance of a FSO link in presence of atmospheric turbulence, Fog, Marine environment and aerosols.

Chapter 5 presents a new concept for exploiting non-line-of-sight (NLOS) ultraviolet and indoor FSO communications. NLOS configuration can be achieved using scattering, as a vehicle for a viable link, or using multipath propagation as in an indoor optical communication link. This chapter discusses the promising enabling technology of ultraviolet (UV) NLOS optical wireless communication. This chapter introduces another related NLOS FSO link for indoor inter-device connectivity

using near infrared light. Possible configurations for indoor optical wireless systems include: (i) directed beam infrared (DBIR), (ii) diffuse infrared (DFIR), and (iii) quasi-diffuse infrared (QDIR). Some of the discussions in this chapter include propagation modeling (with multi-path response), different modulation techniques suitable for different configurations, multi-access techniques, and broadband communication links for multiple sensor networks. The impact of this new technology on future FSO links and various applications is addressed.

Chapter 6 discusses the various FSO platforms including UAV and mobile. The chapter describes the emerging technology of unmanned aerial vehicle (UAV)-based FSO communication links. UAVs are a possible future application for both civil and military use. The large amount of data generated by the UAVs requires high data rate connectivity, thus making FSO communication very suitable. Detailed descriptions are provided in the following areas: alignment and tracking of a FSO link to a UAV, short-length Raptor codes for mobile UAV, and a modulating retro-reflector (MRR) FSO communication terminal on a UAV. Another section of this chapter deals with the problem associated with mobile platforms, i.e., tracking in moving vehicles and gimbals. Some basic building blocks for high-speed mobile ad-hoc networks (MANET) using FSO is described with protocols operating under high mobility.

Chapter 7 discusses two related topics. The first one is chaos-based FSO communication in which the application of chaos to communications can provide many promising new directions in areas of coding, security, and ultra-wideband communications. The chapter describes generation and synchronization of optical chaotic signal where chaotic system can be applied to the encryption/decryption blocks of a digital communication system. Some experimental results of chaotic free space laser communication over a turbulent channel are also described. With increasing demand, Terahertz (THz) frequencies are being considered for short-range, high data rate applications. THz-based FSO communications is the second main topic of this chapter. It has the potential to add new capabilities for imaging, communications, sensors, and materials research. The chapter provides information about quantum cascade laser and quantum well photo detector for THz generation and detection, modulators with terahertz bandwidth, and some recent results of THz FSO link.

In Chapter 8, the niche area of Modulating Retro-Reflector-based FSO Communications and data links which use modulating retro-reflectors, or retro-modulators, are discussed. Retro- modulators require very little power draw and offer extremely small form factors and mass. Novel photonics components and devices provide new opportunities for FSO communications for various applications offering flexibility and mobility. New sensors capable of generating large amounts of data are needed for fast information transfer. Retrocommunication, i.e., communications with retro-modulation is attractive in these cases where semi-passive optical nodes operating by retro-modulation are more suitable than conventional transceivers implementations. While conventional FSO uses similar terminals on both ends of the link, links to modulated retro-reflector (MRR) are asymmetric links. The concept also opens up the possibility of designing a point-to-multiple- point communications with the local hub comprising the laser interrogator and many distributed MRR modules.

Chapter 9 describes a new technology of Hybrid Optical RF FSO Communications. Recent developments in free-space optical communications (FSOC) technology have shown promise for developing practical FSOC systems. The primary challenge has been the ability to compensate for rapidly-changing propagation effects that induce large variations in received optical signal strength and inhibit link stability. To overcome this situation, significant progress in the development of a hybrid FSO/RF system concept has been achieved. The hybrid system couples an FSOC subsystem with a traditional directional RF system and adaptive network mechanisms to establish a stable multi-Gigabit airborne network that is highly reliable and approaches error-free. This chapter will provide background on the key physics of the link challenges and the various technologies that come together to overcome them for error-free networking. The use of hybrid free-space optical/radio-frequency links can provide robust, high-throughput communication networks for both commercial and military applications.

Chapter 10 introduces the reader to free space quantum communications by providing both fundamental foundations of quantum communications as applied to free-Space and atmosphere, and a review of representative free-space and atmospheric quantum communications experiments. The chapter shows how Quantum Mechanics provides a physical layer of quantum security beyond classical communications encryption. The subjects of quantum decoherence and quantum memory is introduced to better understand long distance quantum communications. Spontaneous parametric downconversion (SPDC) and upconversion are explained as nonlinear processes of special source generation and detection. Quantum cryptography, quantum key distribution (QKD), the protocols BB84, and B92 are reviewed as examples of QKD schemes of past interest as well as new trends. The atmosphere has a major impact on quantum communications. Consequently, photon absorption, decoherence, and phase distortions are discussed regarding their role in fidelity of quantum communications and their effect on security and disruptive attacks. The atmosphere's turbulence effects on photon count fluctuations, orbital angular momentum, entanglement, synchronization accuracy, and quantum bit error rates are reviewed. The chapter also reviews representative free-space and atmospheric quantum communications field experiments, discusses the experimental aims, and progress achieved. In particular key ground-to-ground; ground-to-aircraft and ground-to-satellite experiments are presented as a function of laser sources, wave-lengths, distances, detection schemes, quantum protocols, and environmental conditions.

I wanted to thank Dr. Jace Harker, Springer Physics Editor for initiating this book project and providing advice, comments, and inspiration. Also, I wanted to thank HoYing Fan of Springer Science + Business Media (Physics) for many helpful business details in preparing this book. I wish to express my appreciation to Dr. Amita Raval, Springer Physics Editor for her expert vision, support, and encouragement in putting together this successful book. I would like to express my sincere thanks to Dr. Thomas M. Shay, Professor of the department of Electrical & Computer Engineering for carefully reading the chapters and providing helpful comments in this field. I also wish to extend my sincere thanks and appreciation to

Dr. Timothy J. Brothers of Georgia Tech Research Institute for reviewing the book with valuable suggestions.

I thank all of the contributors named earlier for sharing their expert knowledge in this field to be included in the two chapters. Over the years, I have benefited from technical discussions and informal conversations with many colleagues in the academic, research, and applied areas of optical communications, for which I am gratefully indebted. I would like to thank Dr. Hasmukh Raval for his translation from the Bhagavad Gita. He has perfectly and succinctly captured the relationship between the greater power of knowledge, and light which this book is all about. I wish to thank my wife Gargi for her support, typing, and inserting all the equations in three chapters, and my daughter Sharmistha for her constant encouragement and inspiration throughout the preparation of this book. Finally, a constant remembrance of the memory of my feline friends, Rocky and Sasha, who always provided unconditional companionship, helped me in preparing most of the part of this book.

यद् आदित्यगतं तेजो जगद् भासयतेऽखिलम् ।
यच् चन्द्रमसि यच् चाग्नौ तत् तेजो विद्धि मामकम् ॥ १५-१२ ॥

Bhagavad-Gita
Chapter 15, verse 12

Light that makes Sun shine the world,
Light that makes Moon & Fire so bright,
That Brilliance is mine!

Arun K. Majumdar
Ridgecrest, California

Contents

Chapter 1
Fundamentals of Free-Space Optical (FSO) Communication System

Arun K. Majumdar

1.1 Introduction

Free-space optical (FSO) must be included in the set of solutions for meeting the bandwidth requirements of the modern internet. FSO communication is the most practical alternative to solve the bottleneck broadband connectivity problem, and as a supplement to conventional radio frequency (RF)/microwave links. FSO is recently very active with many exciting fundamental and technological challenges to improve its performance in a range of scenarios. The data rate provided by FSO links continue to increase in both long- and short-range applications. FSO will be one of the most unique and powerful tools to address connectivity bottlenecks that have been created in high-speed networks during the past decade due to the tremendous success and continued acceptance of the Internet. The next generation of Internet connectivity will push the limits of existing infrastructure with high-bandwidth applications such as video-conferencing, streaming multi-media content, and network-enabled portable devices. Clearing these bottlenecks is crucial for the future growth and success of the contemporary Internet society. The bandwidth of optical communications access and edge networks will be needed to satisfy these demands. Figure 1.1 shows a scheme of FSO communication technology with optical wireless and different user connectivity.

Links for FSO long range between mobile and airborne platforms (e.g., unmanned aerial vehicles, UAVs) remains an area of active research and development. One of the critical problems facing with long-range FSO communications is severe scintillation caused by atmospheric turbulence which presents significant challenges in beam pointing and leads to deep fades. An open question remains as to how much the performance of FSO links can be improved with adaptive optics, and how these improvements depend on the length of the link. The performance of free-space links can also be improved by forward error correction and packet-level correction codes. Clever transceiver implementations and the efficient modulation schemes can also improve link performance. Non-line-of sight links using solar blind ultraviolet (UV) radiation scattered from transmitter to receiver open interesting communication scenarios. Different FSO link scenarios need to satisfy different system requirements which include different propagation channel characteristics,

A. K. Majumdar, *Advanced Free Space Optics (FSO),*
Springer Series in Optical Sciences 186, DOI 10.1007/978-1-4939-0918-6_1,
© Springer Science+Business Media New York 2015

different methods of transmission, and detection techniques. The use of FSO communications in indoor spaces for secure communications and sensor networking over short ranges is attracting attention as a non-interfering alternative to RF communications. Multiple inputs and multiple outputs (MIMO) concepts open up new possibilities for FSO links under various atmospheric conditions (turbulence and scattering). Quantum communications is a very hot topic for achieving secure communications in free space.

The FSO techniques and technologies are growing at much higher rate than they are covered by any book. All these issues are addressed as a systems approach in this book to learn about the exciting potential of FSO. This chapter discusses the fundamentals and the issues of the FSO communications system.

Communication systems are concerned with the transmission of information from a source to a user. The purpose of a communication system is therefore to transfer information. The most powerful aspect of FSO communications for either analog or digital communication system is the tremendous bandwidth available at optical frequencies. A wavelength of 1 μm corresponds to 3×10^{14} Hz (=300,000 GHz), and therefore a single 16 GHz channel corresponds to only 3.3×10^{-6} μm of wavelength spread.

There are two types of communication systems, a digital communication system and an analog communication system. A digital communication system transfers information from a digital source (producing a finite set of possible messages) to the user whereas an analog communication system transfers information from an analog source (producing messages that are defined as a continuum) to the user. A very basic block diagram of any communication system (optical or RF) is shown in the Fig. 1.2.

The Fig. 1.2 shows a single point-to-point system, whereas in a multiplexed system, there may be multiple input and output message sources and users (also called destinations). The purpose of the signal processing block at the transmitter is to condition the source for more efficient transmission (e.g., in a digital system might provide redundancy reduction of the source). An efficient channel coding can also be provided by this signal-processing block so that error detection and corrections can be used at the receiver site signal processing unit in order to reduce error caused by noise in the channel. An analog signal-processing unit can be, for example, an analog low-pass filter. In a hybrid (analog and digital combined) system, the signal processor may take samples of analog input and then digitize them for transmission. The output of the transmitter signal processor block is in general a complex signal (having both magnitude and phase) and has a frequency spectrum which is concentrated about frequency, f=0 (0 Hz, direct current, DC). The signal is called a baseband signal which is then converted by the carrier circuit into a higher frequency, which is suitable for propagation over the communication channel to the user (destination). The spectrum of the carrier circuits output signal contains a band of frequency about $f=f_c$, where f_c is called the carrier frequency. The purpose of a communication system is to transfer information over the required distance (e.g., ~1 m to 350,000 km), to the required destination, securely (encryption, electrical vs. optical), quickly, cost effectively, and most importantly with minimum possible deterioration (i.e., with the highest possible quality).

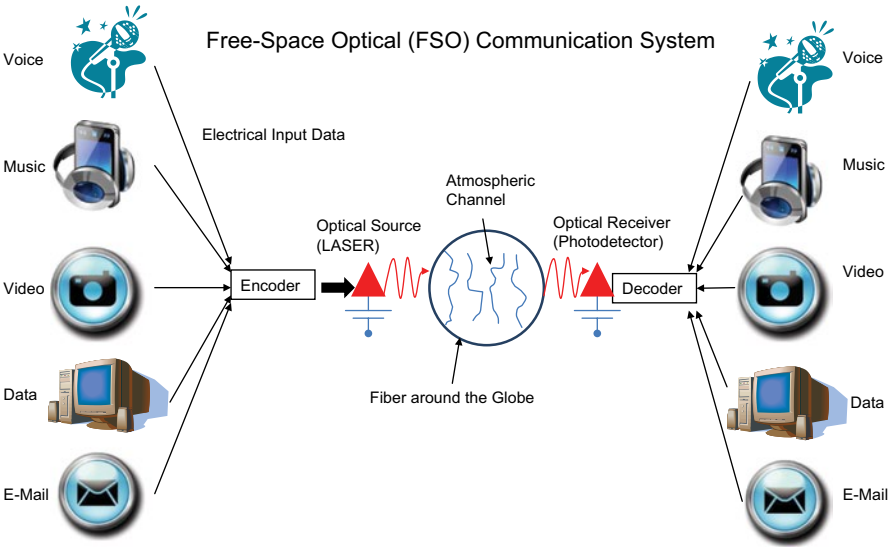

Fig. 1.1 A scheme of FSO communication technology with optical wireless and different user connectivity

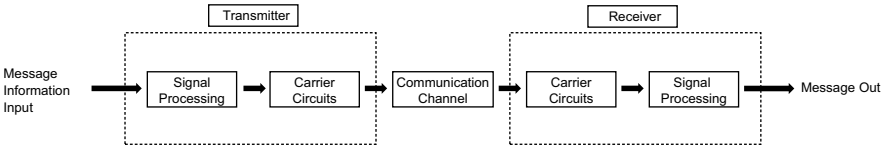

Fig. 1.2 Basic communication system

In digital systems, the measure of deterioration is usually described as the probability of bit error (the number of errors in a given group of bits divided by the number of bits, or the ratio of bits in error to the transmitted bits in some time interval). In analog systems, the performance measure may be the signal to noise ratio (SNR) at the receiver output.

1.2 What is Information and how do we Measure it?

We can define the information sent from a digital source when the jth message is transmitted as follows:

$$I_j = \log_2\left(\frac{1}{P_j}\right) \text{bits} \tag{1.1}$$

Where P_j is the probability of transmitting the jth message. A probability of an event A, denoted by $P(A)$, may be defined in terms of the relative frequency of A occurring in n trials, and is given by:

$$P(A) = \lim_{n\to\infty}\left(\frac{n_A}{n}\right) \tag{1.2}$$

Where n_A = number of times that A occurs in n trials. All probability functions have the property

$$0 \le P(A) \le 1 \tag{1.3}$$

The information measure depends on the likelihood of sending the message. The units of information are measured in bits since a base 2 logarithm is used. The average information measure for m number of messages of a digital source is given by:

$$H = \sum_{j=1}^{m} P_j I_j = \sum_{j=1}^{m} P_j \log_2\left(\frac{1}{P_j}\right) \text{bits} \tag{1.4}$$

The average information is called entropy. The rate of information is described from the source rate which is given by:

$$R = \frac{H}{T} \text{ bits/sec} \tag{1.5}$$

where T=Time it takes to send a message, and H is defined above.

The metrics for evaluating the performance of an "ideal" FSO communication system depends on many parameters such as cost involved, transmitter power availability, atmospheric channel bandwidth used, SNR of various points of the system, and probability of error for digital systems. One way to optimize a digital communication system is to minimize probability of bit error at to output subject to constraints on optical transmitted energy and atmospheric channel bandwidth. A channel capacity C (bits/sec) may be calculated from the equation:

$$\mathrm{C} = \mathrm{B}\log_2\,[1 + \mathrm{S/N}] \tag{1.6}$$

Where B is the channel bandwidth in hertz (Hz), and S/N is the signal to noise power ratio at the input to the digital receiver. For the case of signal plus white Gaussian noise, Shannon [1, 2] showed that the probability of error would approach zero, if the information R (bit/sec) was less than a channel capacity C. Note that Shannon gives us only a theoretical performance bound for a communication system. Compared to an analog system where achievable SNR at the receiver output is the communication system performance criteria, it is possible to obtain infinite SNR at the output when there is noise introduced by the cannel.

1.3 Bandwidth: Know the Data Transmission Rates and what you Need!

The delivery of information has been so critical now because of the tremendous serge in digital media and new technologies. As explained earlier, in telecommunications and FSO communications computing bit rate is defined by the number of bits that are conveyed or processed per unit of time. In other words, bit rate or data transfer rate is the average number of bits, characters, or blocks per unit time passing between equipment in a data transmission system. The bit rate is quantified using the bits per second (bit/s or bps) unit, often in conjunction with the International System of Units (SI) prefix such as Kilo- (Kbits/s or kbps), Mega- (Mbits/s. or Mbps), Giga- (Gbit/s or Gbps), or Terra- (Tbit/s or Tbps).

In reality, bandwidth rate will be determined by a number of factors including compression rates and desired quality of signal. Some typical example rates for data streams for various application may be:

Audio MP3

- 32 Kbit/s, 96 Kbit/s, 100–160 Kbit/s, 192 Kbit (highest level supported by most MP3 encoders when ripping from a compact disc)
- 224–320 Kbit/s→ to highest MP3 quality

Video

- 16 Kbit/s-videophone quality
- 128–384 Kbit/s-business-oriented video conferencing quality using video compression
- 1.5 Mbit/s max-VCD quality (using MPE G1 compression)
- 3.5 Mbit/s typical-standard-definition television quality (with bit-rate reduction from MPE G-2 compression)
- 9.8 Mbit/s max-DVD (using MPE of 2 compression)
- 8–15 Mbit/s typical-HDTV quality (with bit-rate reduction from MPEG-4 advanced video coding (AVC) compression)
- 19 Mbit/s approximate-HDTV 720 (using MPE G-2 compression)
- 25 Mbit/s approximate –HDV 1080 I (us is MPE G-2)
- 29.4 Mbit/s, HD DVD
- 40 Mbit/s-may-Blue-ray disc (using MPE G 2, AVC or video compression (VC)-1 compression)

Internet Technology

- Integrated Services for Digital Network (ISDN)-128 Kbps
- T1-1.544 Mbps
- Domain-specific language (DSL)-512 Kbps–8 Mbps
- T3-44.736 Mbps
- Gigabit ethernet-1 Gbps
- OC-256-13.271 Gbps

Cell Phones ~ 10 Gbps

Computer Technology

- Universal serial bus (USB)-12 Mbps
- Firewire (a.k.a "IEEE 1394" or "i-Link")-400 Mbps
- Ultra-3 small computer system interface (SCSI)-160 Mbps

1.4 How the Data Transmission Rates are Provided in Today's Networks

Optical Channels—The Categories In FSO optical communication, the channels can be classified in three categories:

a. Free-space channel
b. Free-space atmospheric channel
c. Free-space underwater channel

Note that the FSO channels are "unguided" or "free" channels. The fundamental difference between "guided" (e.g., fiber-optic) and "free" channels is that in the free channels, the radiation diffracts as it propagates from the source outwards, whereas in the guided channels the radiation is confined within their guiding structure (such as fiber waveguide).

In this context, communications network can be regarded as the physical infrastructure that enables the transmission and exchange of voice, video, and data among two or more individuals. Optical networking with its inherent tremendous capacity and capability to handle data/voice/video plays an important role in the global communications network to cope with the elements of next-generation Internet offering 3D graphics, real-time streaming audio and video, telemedicine, just to name a few. In order to understand the today's global communications industry and the direction for the future, it is important to understand synchronous optical NET-work for North America (SONET) and synchronous digital hierarchy (SDH; European and Japanese) which are basically multiplexing schemes. These schemes allow the communications traffic into higher and higher data rates. Some typical SONET level names and the corresponding data rates are OC-1 (52 Mbps), OC-3 (155.5 Mbps), OC-12 (622 Mbps), OC-24 (1.24 Gbps), OC-48 (2.5 Gbps) and OC-192 (~10 Gbps). A multiplexed electrical signal can then be converted into optical signal to transmit (via fiber or free space). The SONET box contains electronic hardware, and the architecture is quite complex and rigid. With all-optical network, the SONET box can be eliminated altogether to make the broadband communications network much more effective, versatile, and flexible. Some of the optoelectronic and photonic elements and devices making this possible include Optical Amplifier, dense wavelength division multiplexing (DWDM) and high-speed optical switching. Explosive demand for bandwidth drive by the Internet is clearly shown by the increase of communications traffic doubling every year. This is evident from the Fig. 1.3 which shows the count of internet hosts during 1994–2013.

The numbers of worldwide broadband subscriptions for the year 2007–2011 are shown below:

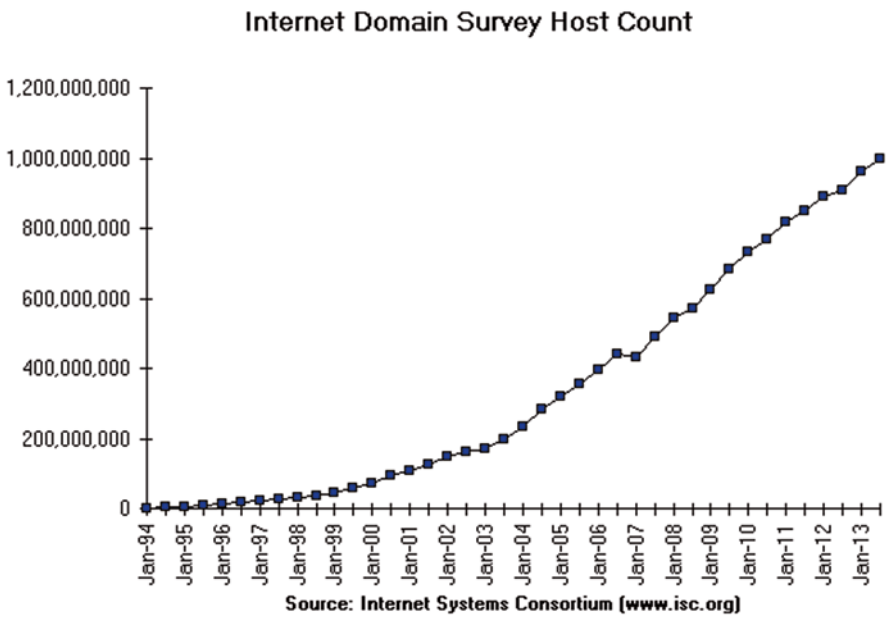

Fig. 1.3 Internet host count during 1994–2013. (*Reproduced with permission from isc.org:* Source: Internet Systems Consortium, www.isc.org)

	2007	2011
Worldwide population	6.6 billion (%)	7.0 billion (%)
Fixed broadband	5.3	8.5
Developing world	2.3	4.8
Developed world	18.3	25.7
Mobile broadband	4.0	17.0
Developing world	0.8	8.5
Developed world	18.5	56.5

Reference: Wikipedia, the free encyclopedia: website: http://en.wikipedia.org/wiki/File:Internet_host_count_1988-2012_log_scale.png

http://en.wikipedia.org/wiki/List_of_countries_by_number_of_broadband_Internet_subscriptions#Countries_by_number_of_fixed_broadband_subscriptions

At the same time, as the number of worldwide broadband subscriptions grow along with the Internet host counts, the demand for bandwidth is increasingly growing. Figure 1.4 clearly shows the tremendous demand for bandwidth for the years 1975–2015 (projected) for both core and access areas.

How does the Internet Work? A Short Description It is important to learn about how the Internet works since FSO connectivity has important role now and in future about the importance of FSO connecting with the Internet.

The Internet is a global network of interconnected computers, enabling users to share information along multiple channels.

Web refernce: http://en.wikipedia.org./wiki/Internet

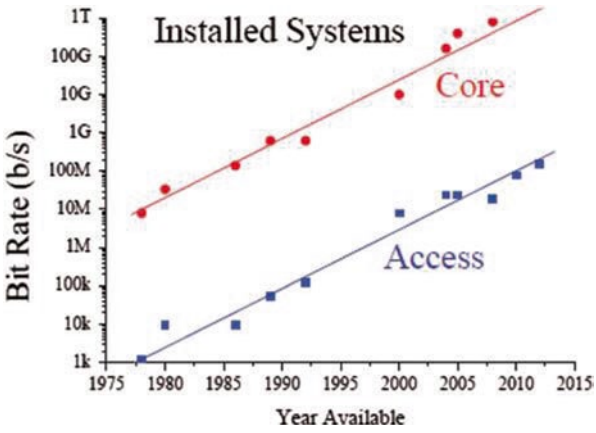

Fig. 1.4 Bit rate for the years 1975–2015 (projected) for both core and access areas

From the user perspective, suppose one has a little laptop at home in Texas and want to exchange information with a big server in California (or Europe or anywhere). Each computer must have a unique identifier (Internet protocol, IP number and IP name) and must be able to exchange data (electrons, photons). Everyone involved must speak the same language, transmission control protocol (TCP)/IP. The protocol is a mutually agreed-upon convention or standard that controls or enables the connection, communication, and data transfer between computing end points.

The fundamental means of moving data around the Internet is controlled by the protocol TCP/IP. Under TCP/IP, a file is broken into smaller parts called "packets" by the file server. Each packet is assigned an IP address of the computer it has to travel to. As the packet moves through global network, it is "switched" by a member of servers and routers along the way to destination.

http://en.wikipedia.org./wiki/protocol-computer

The communication on one Internet usually takes place between a client and a sever program/computer.

How email works:

E-mail systems work with two server programs and two protocols. Since all Internet traffic is public, the data portion of IP packets must be encrypted in order to protect the users or client.

1.5 Basics of Optical Networks Relevant to FSO Communications

FSO Networks Concept, Architectures, Protocols, and Topologies To address the bandwidth shortage and satisfy the bandwidth requirement, fiber is the most reliable means of optical communications so far. But fiber is significantly more costly (e.g., for digging, the cost to lay that fiber). Furthermore, in some areas, it is almost

impossible or impractical to lay fiber, for example, in some downtown areas or areas with hills or mountains. RF technology, even though it is mature, requires expensive investments for acquiring the spectrum licenses, and still cannot be scaled to optical capacities in terms of satisfying the tremendous bandwidth requirement. FSO technology offers the most optimal solution in terms of bandwidth scalability, speed of deployment, security flexibility, and cost-effectiveness. Note that the optical networking has the lowest cost structure for the transportation of bandwidth per unit distance which also makes optical networking extremely attractive.

FSO-based local area network (LAN), wide area network (WAN), and metropolitan area network (MAN; defined below), the three types of networks that can be established using FSO communications technology. A LAN typically is confined to a single area, such as an office building, home network, or a college campus. A WAN spans multiple geographic locations and is typically made up of multiple LANs. For example, an office in Los Angeles having 50 computers, all connected together via FSO will be considered a LAN. Let us suppose the company has another office in Austin, Texas and the network in Austin also would be considered a LAN. If the two offices want to share information with one another, the two LANs can be connected together, creating a WAN. The term MAN is not used often anymore. MAN exists within a single city or metropolitan area where two or more different buildings within a city were connected together.

The FSO for a point-to-point link such as between two outdoor buildings can provide data rates higher than 1 Gbps per link which can be increased to 10 Gbps and potentially 50 or 120 Gbps per link using wavelength division multiplexing (WDM). WDM is an optical technology where many optical channels are optically multiplexed and all are together coupled onto a single fiber. Recently, there is a field demonstration of optical networking equipment capable of transporting data at 1.7 Tbps with a WDM-based system. The system transported the data using eight channels, each with a capacity of 216.4 Gbps. The distance during the demonstration was 1,750 km using a standard single mode fiber optic cable. Another vendor conducted demonstration for next-generation WDM systems, showing the prototype system to be able to handle 400 Gbps per channel and offer a total capacity of 20 Tbps. In the real world, operators are today moving to channel speeds at 40 and 100 Gbps, in existing networks.

1.6 FSO Connectivity in Today's Networks

FSO communications refers to a line-of-sight technology transmitting modulated visible or infrared (IR) beams through the atmosphere to establish optical communications. In some cases, such as indoor communication, FSO may also use non-line-of-sight (NLOS) technology utilizing scattering or reflectivity, for the receiver within the coverage space to detect the radiation, which is modulated for data transmission. FSO communications have many advantages: typically they operate in unlicensed Tera-Hertz spectrum bands (wavelength 800–1700 nm), provides several magnitudes of improvement in signal bandwidth over RF, FSO channels are

immune to electromagnetic interference (EMI), are secure with low probability of interception and low probability of detection (LPI/LPD), and so on. Some of the other advantages of FSO systems include ease of installation, low costs per bit ratio, and protocol independent to support multiple platform and interfaces. Due to these advantages, FSO has therefore been considered as one of the most viable technologies for next generation broadband communicating and wireless networks. The greatest disadvantage of FSO is the weather. When the communication link includes part of the atmosphere, clear-air turbulence, and a possible boundary-layer turbulence (for example, one end of the communication link is on an aircraft) cause serious phase distortions and fading to the link. FSO networks may also suffer because of insufficient availability and low reliability due to weather turbulence. Weather conditions such as fog, smog, snow, rain, dust particles, etc. affect FSO communications performance. Atmospheric electricity between clouds and between cloud and earth's surface can build up lightning flashes with duration of each flash being between 20–130 msec. For FSO communications at 1 Gbps, a time delay of 100 msec flash corresponds to 10^8 bits (i.e., 12.5 Mbps) causing a substantial data loss if the flash interferes with the signal at the receiver [3]. Solar interference effects also must be considered for FSO link performance if the sunlight falls on to the photodetector (within its field-of-view, FOV).

1.7 Optical Networks: Integration of FSO

FSO system offers the most flexible networking solution for achieving the highest broadband capability. FSO provides the essential qualities required to bring the traffic to the optical fiber backbone virtually unlimited bandwidth, low cost, ease, and speed of deployment. In FSO network transmission, data can be transmitted over an encrypted connection adding to the degree of security needed for specific applications.

1.7.1 FSO Basic Architectures/Topologies

There are three basic main FSO architectures that have been used.

- *Point-to-point:* This architecture is a dedicated connection that offers higher bandwidth, but is less scalable
- *Mesh:* This architecture offers redundancy and higher reliability with easy nodes addition, but restrict distances more than other options
- *Point-to-multipoint:* Offers cheaper connections and facilitates node addition, but at the expense of lower bandwidth than the point-to-point option

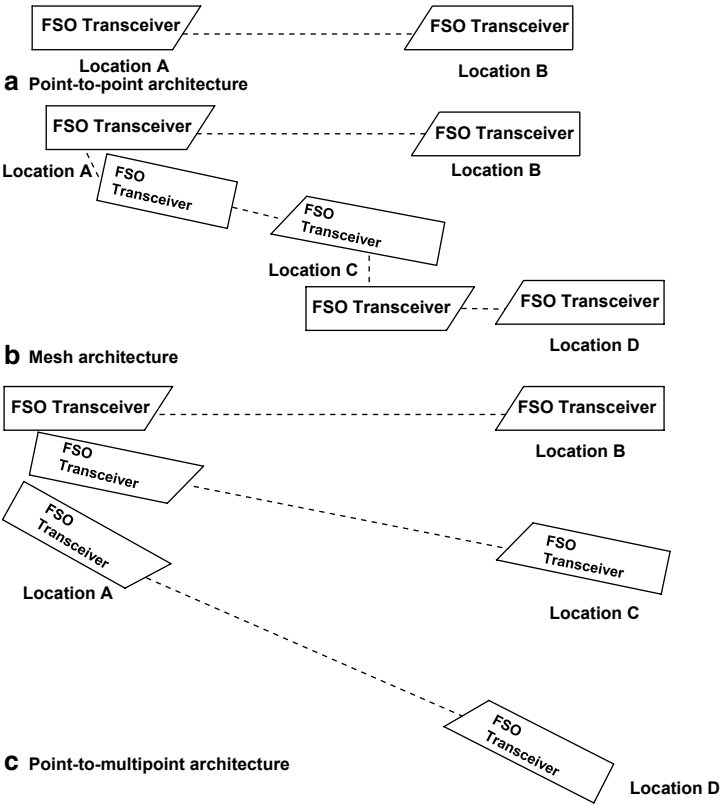

Fig. 1.5 Three basic main FSO architecture

Figure 1.5 shows three basic main FSO architectures.

Note that these FSO architectures require any two transceivers line of sight (LOS) to establish a full duplex communication link, and there cannot be any obstructions. In a given location, the FSO transceivers are connected with the electronic routers via cables, where the routers are located in cabinets within the building and are connected with the public or private network.

1.7.2 FSO Network: How to Implement?

Figure 1.6 shows an illustration of a simple FSO network.

The basic hierarchy concept for high-capacity, broadband optical network is shown in Fig. 1.6. The access network consists of a base station (BS) connected to the fiber-ring backbone infrastructure. Each base station is equipped with a number

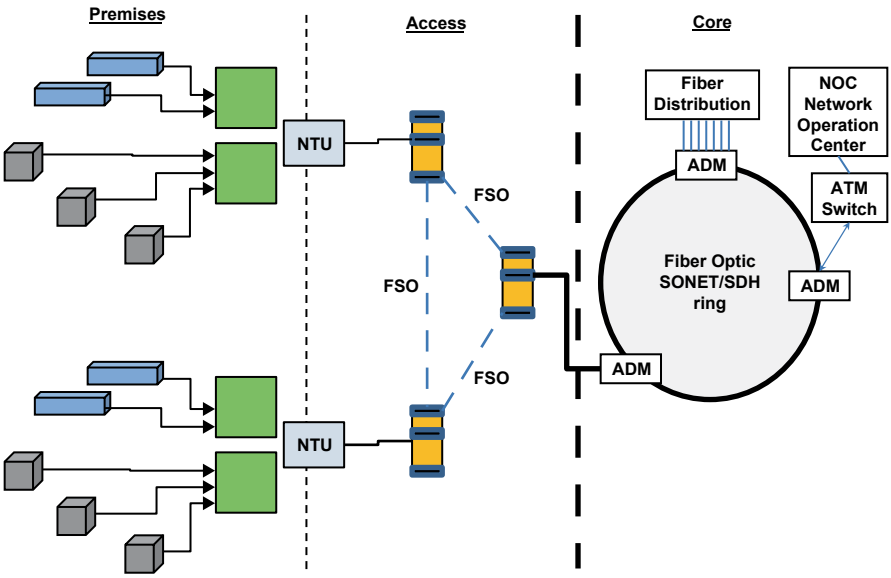

Fig. 1.6 A simplified FSO network implementation

of optical transceivers (up to, say four) that serves as either redundant access points or relay points to the next networked building. The mesh configuration eliminates the point-to-point and point-to-multipoint single-point-of-failure weakness. The customer premises equipment (CPE) nodes may be connected to Network Termination Units (NTU) via fiber. Multiple devices/users in the premises Network may share the CPE nodes. The core network consists of (1) network operation center (NOC), (2) asynchronous transfer mode (ATM) switch, (3) add-drop multiplexers (ADM), and (4) fiber-optic SONET/SDH ring that serves as the backbone infrastructure. Network management software (NMS) used by the NOC performs management and performance monitoring operations for a specified customer region. The ADM performs multiplexing and de-multiplexing of data at various network junctions. The ATM switch performs data regulation and control.

1.7.3 Integrated FSO for Satellite, Terrestrial, and Home Networks

Due to many advantages as discussed earlier, FSO has been considered a viable technology for next generation broadband communications. Various multimedia services like Audio on Demand (AOD), Video on Demand (VOD) such as the provider Net-flex, and peer-to-peer (P2P) data sharing require the necessity for higher data rate networks. The extensive range of FSO networks from home to satellite, ranging from a few meters to over thousands of kilometers, offers the potential usability of optical links for various applications. Various FSO networks involving

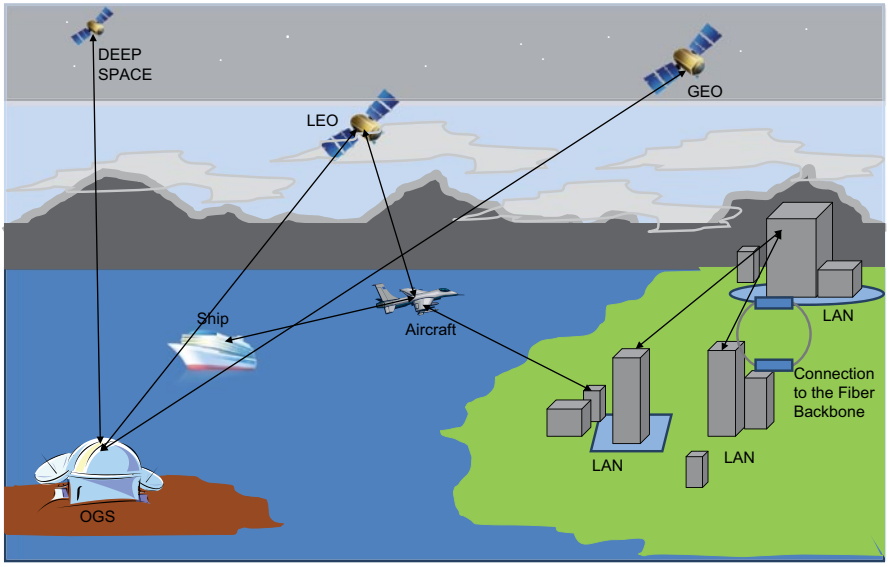

Fig. 1.7 All-optical network conceptual topology of integrated optical wireless, satellite, terrestrial, and home networks

optical wireless satellite, terrestrial, and home networks can be integrated and operated as a whole, as shown in Fig. 1.7. From the Fig. 1.7, it is clear that a global all-optical network can be potentially implemented with FSO networks and links by connecting FSO links and networks to the backbone realized with optical fibers. However, one important issue for the integrated all optical network globally is the reliability and the availability of FSO links and FSO networks. The enormous complexity of building an externally reliable global optical arises because of the two reasons: (1) The characteristics of the physical links, which is part of an integrated network with great geographic extent and large numbers of uses, must be well matched to the network architecture; (2) The propagation medium is different for each layer protocols. For example, for inter-satellite link, the medium has practically no atmosphere (i.e., like a vacuum link) and the only effect to channel will be propagation loss (due to unavoidable diffraction-limited beam spread). A terrestrial link involving atmosphere, when multiple users share the same optical medium, channel's randomness interacts with the upper layer protocol. As a result, throughput performance of the network is reduced drastically. All optical global networks therefore must be designed to account for multiple-network layers.

FSO satellite network can provide a high-bandwidth-optical-wireless-network access to the end users because the satellites can cover large areas on the earth. The optical link architecture utilizing inter-satellite, satellite-to-aircraft, aircraft-to-aircraft, or aircraft-to-ground networks (up and down) can offer very high dater rates $(\geq 10 Gbps)$. Commercially, backbone nodes can also be served by Geostationary Earth Orbit (GEO: ~40,000 km altitude), Medium Earth Orbit (MEO: ~5,000–15,000 km , and Low Earth Orbit (LEO: ~1,000–2,000 km) satellites. Some of the other important features of the FSO inter-satellite network are:

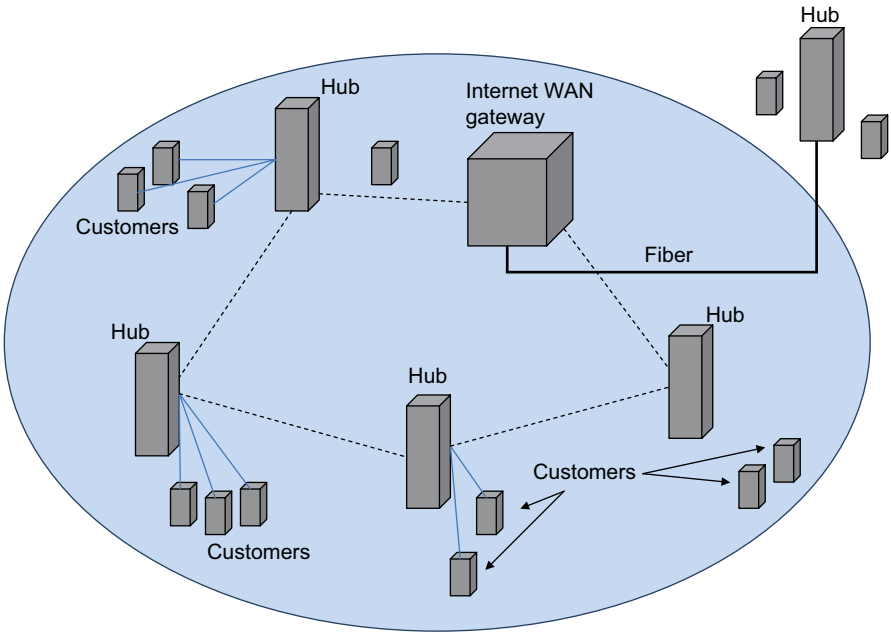

Fig. 1.8 Free-space optical (FSO) links connecting a small area

1. can be an alternative for the current wired Internet including undersea fiber communication system for over-the-ocean communications (potential FSO global broadband Internet)
2. can provide Internet services in any remote areas or for the users on a mobile platform. Figure 1.8 shows a FSO links connecting a small area.

FSO terrestrial network involves atmosphere (turbulence, scattering) as communication channel for establishing optical wireless connection between transceivers. The LOS propagation path can range from hundreds of meters up to tens of kilometers. This type of telecommunication scenario is opening up the important for broadband Internet access, with extreme flexibility. Some of the most important applications of the FSO terrestrial network are: (1) It can provide a solution for the "last" or "first" mile problem to connect the high bandwidth from the fiber optic backbone to all of the business with highbandwidth networks. Less than 5% of all buildings in the USA have direct connection to the very-high-speed (2.5–10 Gbps) fiber optic backbone, yet more than 75% of business are within 1 mile of the fiber backbone. High-speed data network such as fast Ethernet (100 Mbps) or Gigabit Ethernet (1.0 Gbps) exists within the building of these businesses. However, Internet access can be reached using much lower bandwidth technologies available through the existing copper wire infrastructure, T-1(1.5 Mbps), cable modem (5 Mbps shared), DSL (6 Mbps one way), etc. FSO link is therefore the only solution for this "last" of "first" mile bottlenecks. (2) There is no need to ditch or lay

optical fibers to establish communications for building-to-building, ship-to-ship, or community-to-community, and mobile terminals, and (3) It can be integrated with wireless radio networks to mitigate the capacity and scalability limitations of RF channels (optical/RF hybrid communication). The main problem with this terrestrial FSO link is that the reliability and availability of the optical path is mainly influenced by the local weather conditions, with fog being the most limiting factor. FSO network architecture design should involve how to handle signal deterioration caused by atmospheric turbulence and scattering in order to achieve the required level of Quality of Service (QoS). The goal of the terrestrial FSO network is to design FSO transceivers and the network to support hundreds of meters to kilometers transmission distances with data rates ranging from hundred of Mbps to multi-Gbps. Many mitigation techniques for minimizing the atmospheric effect exist, and will be discussed in later chapter of the book.

FSO home networks are used for wireless broadband communications inside houses and offices. A LAN can be constructed out of a number of cells situated in divided spaces in the building. Each cell may have a base station connecting several terminals with short-range-optical wireless connections such as IR and Light Emitting Diode (LED). Individual cells are then connected and integrated to a broadband backbone infrastructure. The indoor FSO link can be LOS or non-LOS links. Infrared Data Association (IrDA) standards are example of indoor LOS links which can support data rates varying from several Kbps to tens of Mbps. IrDA Ir Simple, a new high-speed-infrared communications protocol designed for mobile devices aims in delivering 100 Mbps data rates. Gigabyte IR communications (Giga-IR) was proposed to develop a protocol for 1Gbps data rate. Indoor FSO communications will be discussed in details in a later chapter of the book.

FSO networks have potential capability of delivering Gbps data rate per link covering a wide range from home to satellite, and FSO channels are easily deployable. Many challenging problems exist to fully utilize FSO networks to accomplish multi-Gbps global communication, anytime, anywhere.

1.8 FSO Mobile Ad-Hoc Networks (MANET)

The recent growth in FSO wireless technologies and the choices available to user applications have created tremendous wireless demand. The wireless nodes are dominating the Internet as evidenced by a sharp increase in the usages of mobile Web applications by smartphones. Innovative dynamic optical networks are therefore urgently needed in order to respond to the exploding mobile wireless traffic demand. A MANET is a set of wireless mobile nodes forming a dynamic autonomous network. MANET is a wireless network without an access point. In many real-world applications, MANETs are absolutely necessary where an access point and existing infrastructure is not available. As an example, in emergencies and battlefields no one has the time to establish access points. It is important to set up a quick network in emergency situations, for example, a building has been destroyed due to fire, earthquake, or bombs. In such an emergency operations, police

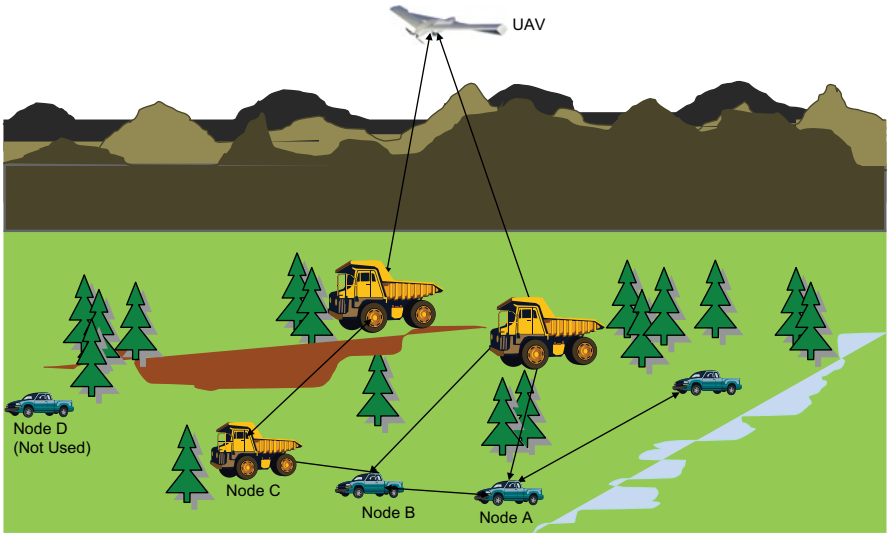

Fig. 1.9 A free-space optical (FSO) mobile ad hoc network (MANET) scenario

and firefighters can communicate through a MANET and perform their operations without adequate wireless coverage. In emerging highly-directional network, constructing and managing a dynamic FSO links where links may be fragile will result in an intermittently connected network of tremendous capacity on a per-link basis. Communication traffic's enormous growth over the next couple of decades involve communication network users which humans and a large number of manned and unmanned mobile sensors and platforms such as FSO links between a UAV and ground vehicles. This means that the point-to-point communication between two nodes or users will not be sufficient. Figure 1.9 depicts a scenario which shows the extreme difficulty involved in multi-level dynamic pointing, acquisition, and tracking with long ranges and mobility on rugged terrain. In order to maintain reliable communications, a stable FSO mobile and ad hoc network (FSO MANET) formation of high-capacity links will be required to support multiple users. Automatic protection and restoration schemes/algorithms for fiber-optic and FSO networks are needed for establishing a high-reliabile backbone MANET. FSO MANET can then be created through integration of fiber-optic and FSO communication backbones. In order to establish the MANET reliably, it must address issues of dynamic allocations and medium access control (MAC) which is common to all networks because all communication devices have to know about the access at any given time. Routing protocols for MANET and algorithms determine the optimum path between senders and receivers based on specific metrics, for example shortest time delay (see Fig. 1.10). The routing protocols should be highly adaptive, fast, and energy/bandwidth efficient.

Recently researchers have reported [5] a multi-transceiver spherical FSO structure as a basic building block for enabling optical spectrum in mobile ad hoc networking. They have proposed an omni-directional optical antenna formed of a spherical

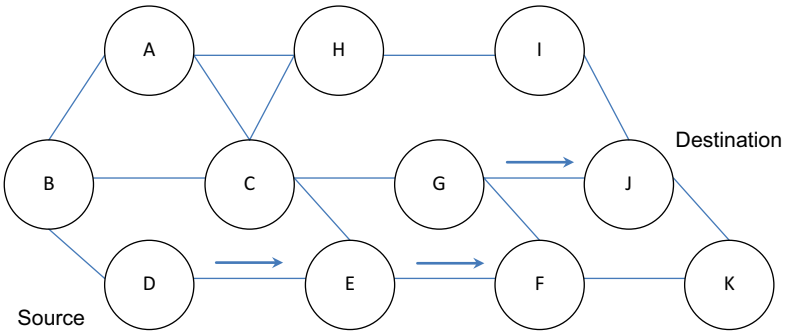

Fig. 1.10 A typical routing algorithm for MANET

structure tessellated with equally spaced hexagons of transceiver units. A 3D spherical structure covered with inexpensive FSO transceivers (for example, LED/vertical-cavity surface-emitting laser (VCSEL) and photo-detector pair) solve the problems of mobility and LOS management via availability of several transceivers per node.

In addition to some of the previously mentioned applications, FSO MANET can support other applications such as group meeting, exhibitions, conferences, presentations meetings, and lectures where the access points may not exist ahead of time. The details of FSO-based mobile ad hoc systems with some application will be discussed in a later chapter of this book.

1.9 Underwater FSO Communications Network

Underwater FSO communications is very promising in establishing underwater links for various applications like undersea explorations (detected underwater oil fields and determine routes for laying undersea fiber cables), environmental monitoring (monitoring ocean currents and winds for improved weather for tracking of fish or microorganisms), disaster prevention (measure seismic activity from remote locations to provide tsunami warnings to coaster areas), and distributed tactical surveillance (unmanned underwater vehicles, UUVs) and underwater sensors to monitor areas for surveillance, reconnaissance, targeting, and intrusion detection). Current RF wireless technologies for communications from land to submarines are extremely inefficient due to requiring large ground stations offering extremely low bandwidth compared to today's communication standards. Acoustic communication is ultimately band-limited to sub-MHz-type data rates due to the frequency-dependent attenuation and surface -induced pulse-spread from reflection. For ranges of a kilometer, data rates of acoustic communication is around tens of Mbps, and is less than a thousand Kbps for ranges up to 100 km. Furthermore, long-range acoustic communication also has problems with real-time response, synchronization, and multiple-access protocols. Thus acoustic technology is not useful for high-data-rate communication network in real time. Underwater FSO communication, on

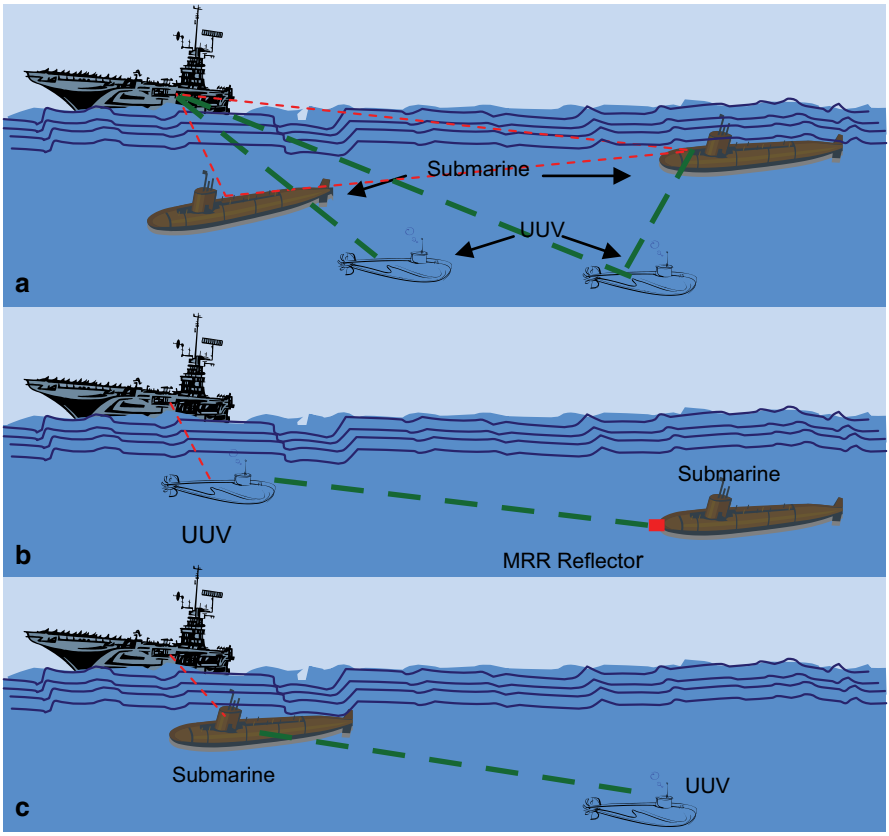

Fig 1.11 Different possible underwater FSO scenarios: **a** LOS, **b** Modulated Retroreflector equipped Communications, **c** Communication link by surface water reflection

the other hand, can offer high bandwidths with very low frequency enabling real-time networking. However, seawater absorption and scattering are the main causes of extremely high wavelength-dependent attenuation of optical signals. Spatial dispersion of photos due to scattering causes spatial spreading of the optical beam which reduces the photon density at the underwater receiver position. The limited range of optical links < 100 m can be accepted in exchange for the gain in information bandwidth. However, FSO demonstration shows from both laboratory and field studies can achieve data rates of over 1 Gbps for transmissions over ranges of tens of meters. FSO can provide broadband communication for underwater wireless sensor networks (WSN), for example, for transmitting video streams or executing downloads of large bursts of stored data in a brief time slot. This will be extremely useful for some situations where there is a need for sporadic on-demand interrogation from sensors when data is required from a specific location or within a short polling time slot. Three scenario of FSO underwater communications are depicted in Fig. 1.11., which are: (a) LOS, (b) Modulating retro-reflector (MRR) link, and (c) communications surface reflection link.

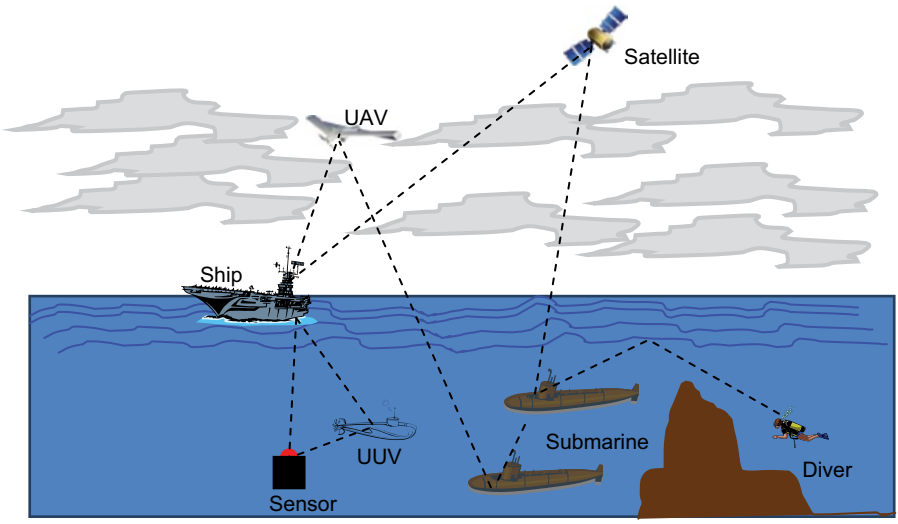

Fig. 1.12 Underwater FSO communication for global network concept

Figure 1.12 shows a global network concept using under FSO communication where UAV, satellite and ship can be part of the FSO involving underwater platforms such as UUVs, submarines, divers, and sensors. Note that every type of link in the transmission layer of a broad spectrum of optical network from LAN, MAN to ultra-long-haul can be accomplished similar to FSO in terrestrial optical communication.

The underwater FSO for higher layers of network design can also include the MANET, WDM/TDM, code division multiple access (CDMA) or, clustering and SONET/SDH ring designs. Point-to-multipoint links can be achieved in an energy efficient manner to accomplish broadband communications for video transmissions.

1.10 Indoor FSO Communications

Another type of optical communication that uses the FSO concept is indoor-wireless optical communication as shown in Fig. 1.13. The transmitter can consist of LED arrays and the communication link between the transmitter and the different receiving terminals located in different places can be achieved by either line-of-sight links or by reflection (or scattering) by walls in the room. Two rooms can also be connected by hardware. The details of the indoor communications will be discussed in a separate chapter of this book.

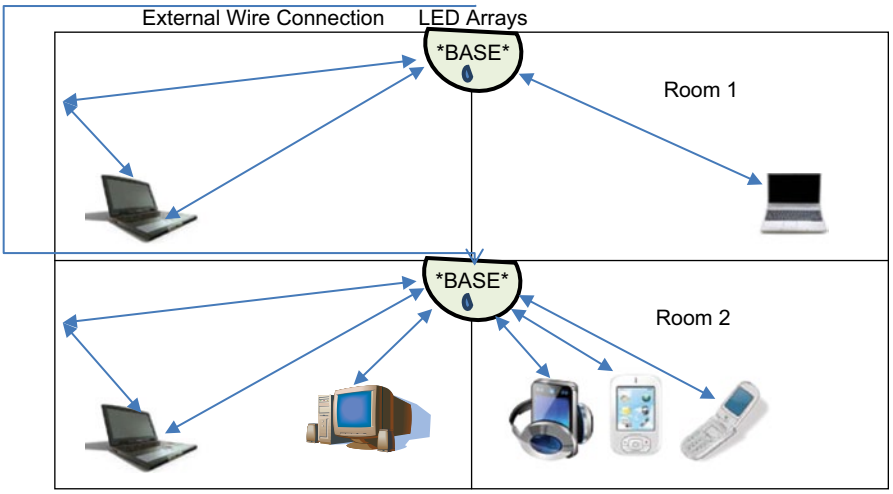

Fig. 1.13 Indoor FSO wireless optical communications

References

1. C.E. Shannon, A mathematical theory and communications. Bell Syst. Tech. J. **27**, 379–423 and 623–656 (July and October 1948)
2. C.E. Shannon, Communications in the presence of Noise. Proc. IRE **37**, 453–456, (1949)
3. S.V. Kartalopoulos, Free Space Optical Networks for Ultra-Broad Services (Wiley, New Jersey, 2011)
4. http://www.infoworld.com/print/188763
5. Multi-Transceiver Optical Wireless, IEEE 2009

Chapter 2
Theory of Free-Space Optical (FSO) Communication Signal Propagation Through Atmospheric Channel

Arun K. Majumdar

2.1 Introduction

The goal of a communication system is to transmit information which can be accomplished in many ways. Free-space optical (FSO) technology depends on the propagation of optical beam through various media, which interact with and affect the quality of the propagating optical signal. The understanding of the atmospheric phenomena and how they affect the propagating light is essential in designing effective, intelligent and cost-efficient FSO links and reliable networks in order to provide uninterrupted service at the expected quality. FSO communication has increasingly attracted attention in the past decade for a number of applications for providing high bandwidth wireless communication links. Some of these applications include satellite-to-satellite cross-links, up-and-down links between space platforms and aircraft, ships, and other ground platforms, and among mobile or stationary terminals to solve the last mile problem through the atmosphere. However, there are a variety of deleterious features of the atmospheric channel that may lead to serious signal fading, and even the complete loss of signal altogether.

The atmosphere is composed of gas molecules, water vapor, aerosols, dust, and pollutants whose sizes are comparable to the wavelength of a typical optical carrier affecting the carrier wave propagation not common to a radio frequency (RF) system. Absorption and scattering due to particulate matter may significantly attenuate the transmitted optical signal, while the wave-front quality of a signal-carrying laser beam transmitting through the atmosphere can be severely degraded, causing intensity fading, increased bit error rates, and random signal losses at the receiver. Random fluctuation in the irradiance of the received optical laser beam caused by atmospheric turbulence usually refers to an effect called scintillation. Therefore, atmosphere can be a limiting factor in reliable high-data rate wireless FSO optical communication link performance. It is therefore important to learn about the interaction of the optical wave with the atmosphere so that one can predict the FSO communication performance in presence of the atmospheric communication channel.

A. K. Majumdar, *Advanced Free Space Optics (FSO),*
Springer Series in Optical Sciences 186, DOI 10.1007/978-1-4939-0918-6_2,
© Springer Science+Business Media New York 2015

2.2 Statistical Description of Random Processes and Random Fields

In this section, a brief description of the statistical descriptions of the random processes and random fields will be provided which will be helpful in understanding the random nature of the atmospheric parameters that affect the propagation.

2.2.1 Random Variables and Random Process

In nature, there are many physical quantities, such as wind speed, ocean waves, air temperature, and seismic signal for earthquakes that show the behavior of very irregular random fluctuations of different amplitudes and frequency of occurrence. The mathematical theory of probability deals with the phenomena and observations (experiment, trials) which can be repeated many times under similar conditions. The probability theory describes the phenomena being studied with numerical characteristics so that qualities take various values depending on the result of observation. Such qualities are called random variables [1]. The fields of phenomena in nature, as mentioned earlier, are described in terms of random functions, the concept of which is a generalization of the more familiar concept of a random variable.

A random process is a process (i.e., variation in time or one-dimensional space, for example) whose behavior is not completely predictable and can be characterized by statistical laws.

Figure 2.1 depicts the concept of a random process $X(t)$ which describes the mapping of a random experiment with sample space S onto an ensemble of simple functions $\mathrm{X}(\lambda_i, \mathrm{t})$. For each point in time t_1, $X(t_1)$ describes a random variable. A random variable is thus a quantity that may assume one of many (even infinitely many) values with a certain probability. A random variable can be a discrete random variable (one that can assume only certain discrete values or a continuous random variable (one that can assume any value from a continuous interval). Note that the concept of random process is to enlarge the random variable to include time. Thus a random variable x becomes a function of the possible outcome (values) λ_1 of an experiment and time t, $x(\lambda_i, t)$ and the family of all such functions is called a random process, $\mathrm{X}\left(\lambda_i, t\right)$. Figure 2.2 illustrates the hierarchy of random processes.

2.2.2 Characterizations of a Random Process

The laws governing a random variable are given by the probability with which the variable will assume certain values [2]. For a specific t, $X(t)$ is a random variable with distribution

$$\mathrm{F}\left(\mathrm{x}, \mathrm{t}\right) = \mathrm{p}\left[\mathrm{X(t)} \leq \mathrm{x}\right] \tag{2.1}$$

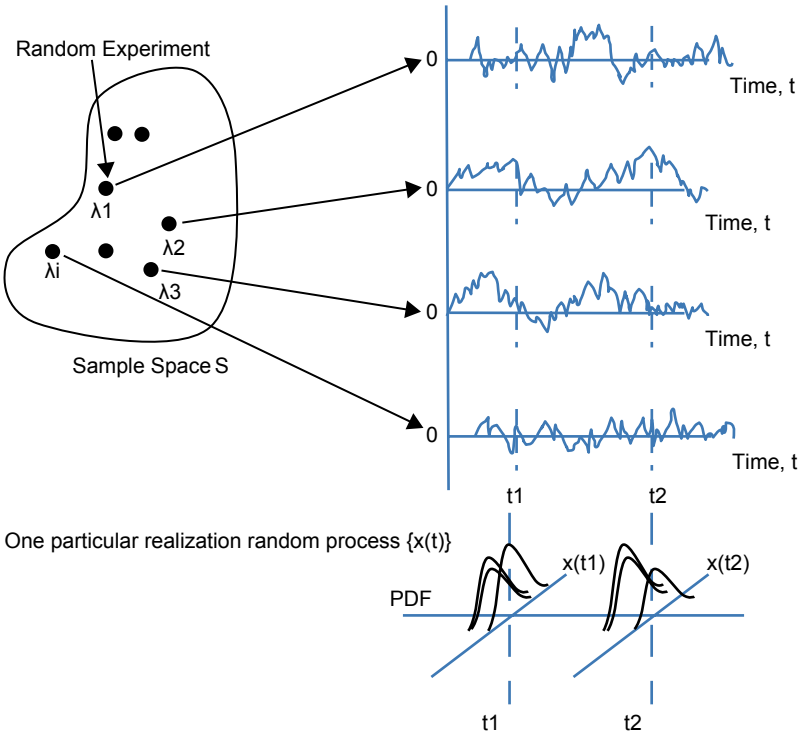

Fig. 2.1 Concept of a random process

The function $F(x, t)$ is defined as the first-order distribution of the random variable $X(t)$.

Its derivative with respect to x

$$f(x,t) = \partial F(x,t) / \partial x \tag{2.2}$$

is the first-order density of $X(t)$, called probability density function, PDF.

Mean and Variance of a Random Process The first-order density of a random process $f(x, t)$, gives the probability density function (PDF) of the random variables X(t) defined for all time. For each time instance of a random process, the average value (mean or expected value), variance etc. can be calculated from all sample functions $X(\lambda_i, t)$. The mean of a random process, $m_x(t)$, is thus a function of time specified by

$$m_x(t) = E\left[X(t)\right] = E\left[X_t\right] = \int_{-\infty}^{\infty} x_t f(x_t, t) dx_t \tag{2.3}$$

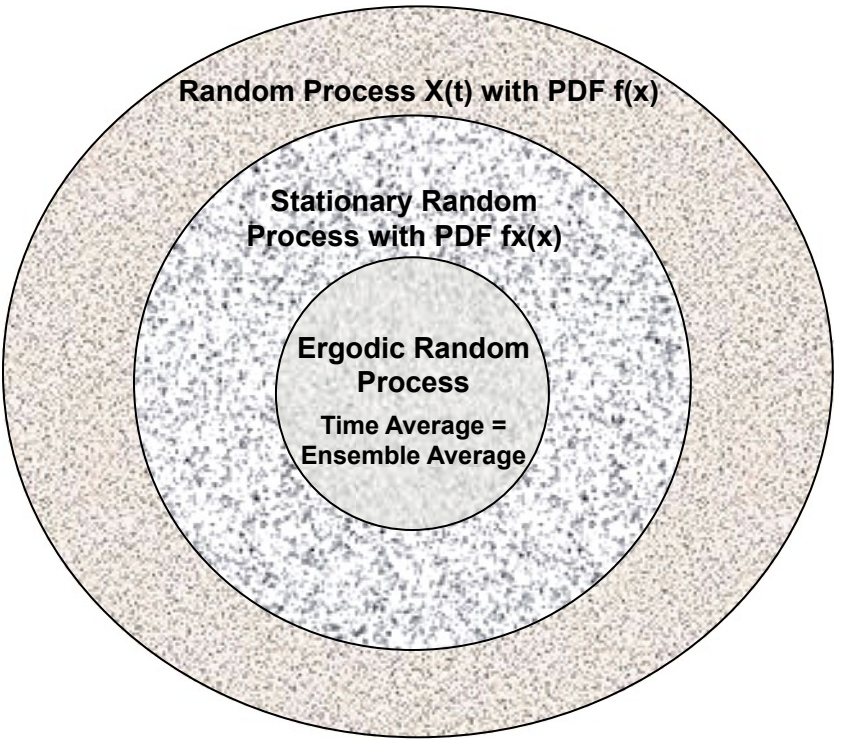

Fig. 2.2 Hierarchy of random processes

For the case where the mean of $X(t)$ does not depend on t, we have

$$m_x(t) = E\left[X(t)\right] = m_x(\text{a constant}) \tag{2.4}$$

The variance of a random process, also a function of time, is defined by

$$\begin{aligned}\sigma_x^2(t) &= E\left\{\left[X(t) - m_x(t)\right]^2\right\} \\ &= \int_{-\infty}^{\infty} \left|x - m_x(t)\right|^2 f(x_t, t)dx_t = E\left[X_t^2\right] - \left[m_x(t)\right]^2\end{aligned} \tag{2.5}$$

Second-order Densities of a Random Process If there are two random variables $X(t_1)$ and $X(t_2)$, the second-order provability densities of a random process can be defined as $f(x_1, x_2; t_1, t_2)$.

Nth-order Densities of a Random Process The nth order density functions for $X(t)$ at times $t_1, t_2, \ldots\ldots\ldots t_n$ are given by $f(x_1, x_2, \ldots x_n; t_1, t_2, \ldots t_n)$.

Time Averages and Ergodicity So far, the average value and the variance of a random process $X(t)$ were calculated based on the PDF $f(x_t, t)$. However, in practical experiments the provability density function of a random process is often unknown.

Also, in many cases, there is only one sample function $X(\lambda_i, t)$ available. Therefore, it is meaningful to average over-time instead of taking the ensemble average.

Average Value

$$m_{x_{(\lambda_i)}} = \lim_{T\to\infty} 1/T \int_{-T/2}^{T/2} X(\lambda_i, t)dt \tag{2.6}$$

Variance

$$\sigma^2{}_{X(\lambda_i)} = \lim_{T\to\infty} 1/T \int_{-T/2}^{T/2} (X(\lambda_1, t) - m_{X(\lambda_i)})^2 dt \tag{2.7}$$

Ergodicity A stationary random process $X(t)$ is called ergodic, if the time average of each sample function $X(\lambda_i, t)$ converge towards the corresponding average with probability one. In practical situations ergodicity is often assumed since just one sample function is available during the experiment and therefore the ensemble averages cannot be taken.

Auto-correction and Auto-covariance Functions:

We are interested in how the value of a random process $X(t)$ evaluated at t_2 depends on its value at time t_1. At t_1 and t_2, the random process is characterized by random variables X_1 and X_2, respectively. The relationship between X_1 and X_2, can be understood from the joint probability density function $f_{x_1x_2}(x_1, x_2)$. A linear relationship between two rand variables $X(t_1)$ and $X(t_2)$ can be specified by $E[X(t_1)X(t_2)]$, which in general a function of t_1 and t_2. The auto-correlation function of a random process $\{X(t)\}$ is defined as

$$\begin{aligned} R(t_1, t_2) &= E[X(t_1)X(t_2)] = R(t_2, t_1) \\ &= \int_{-\infty}^{\infty}\int_{-\infty}^{\infty} x_1 x_2 f_{x_1x_2}(x_1, x_2)dx_1dx_2 \end{aligned} \tag{2.8}$$

The auto-covariance function of a random process $\{X(t)\}$ is defined by

$$\begin{aligned} C(t_1, t_2) &= E\left[\left(X(t_1) - m_X(t_1)\right)\left(X(t_2) - m_X(t_2)\right)\right] \\ &= \int_{-\infty}^{\infty}\int_{-\infty}^{\infty} \left(x_1 - m_x(t_1)\right)\left(x_2 - m_X(t_2)\right) f_{X(t_1)X(t_2)}(x_1, x_2)\, dx_1dx_2 \\ &= R(t_1, t_2) - m_X(t_1)m_X(t_2) \end{aligned} \tag{2.9}$$

The normalized auto-covariance function is defined by

$$\rho(t_1, t_2) = C(t_1, t_2) \Big/ \sqrt{C(t_1, t_1)C(t_2, t_2)} \tag{2.10}$$

Stationary of Random Processes A random process $\{X(t)\}$ is called strictly stationary (SSS) if the sets of random variables $X(t_1)$, $X(t_2)$, … $X(t_n)$, and $X(t_1+\Delta)$, $X(t_2+\Delta)$, … $,X(t_n+\Delta)$

have the same probability density functions for all t_1, all n and all Δ, i.e.,

$$f(x_1,\ x_2,\ \ldots\ ,x_n;t_1,t_2,\ \ldots\ ,t_n)=f(x_1,x_2,\ \ldots\ ,x_n;t_1+\Delta,t_2+\Delta,\ \ldots\ ,t_n+\Delta) \quad (2.11)$$

A wide-sense stationarity (WSS) is a constant expected value for all t. $E[X(t)]=m$ (constant)

$$\begin{aligned} \mathrm{R}(\mathrm{t}_1,\mathrm{t}_2) &= R(|t_2-t_1|)=R(\tau) \\ \mathrm{C}(\mathrm{t}_1\ \mathrm{t}_2) &= \mathrm{C}(\mathrm{t}_2-\mathrm{t}_1)=C(\tau) \end{aligned} \quad (2.12)$$

where, $\tau=t_1-t_2$

The variance is constant and finite: $\sigma^2=C(0)=R(0)-m^2<\infty$

For example, for a second-order PDF where the joint PDF of a stationary process does not change if a constant value Δ is added to both t_1 and t_2.

$$f_{X_1X_2}(x_1,x_2)=f_{X(t_1)X(t_2)}(x_1,x_2)=f_{X(t_1+\Delta)X(t_2+\Delta)}(x_1,x_2) \quad (2.13)$$

The autocorrelation function then only depends on the difference τ between t_1 and t_2

$$\begin{aligned} R_{XX}(t_1,t_2)&=E\{X(t_1)X(t_2)\}=\int_{-\infty}^{\infty}\int_{-\infty}^{\infty}x_1x_2f_{X(t_1)X(t_2)}(x_1,x_2)dx_1dx_2 \\ &=\int_{-\infty}^{\infty}\int_{-\infty}^{\infty}x_1x_2f_{X(0)X(t_2-t_1)}(x_1,x_2)dx_1dx_2=R_{X,X}(0,t_2-t_1)=R_{XX}(\tau) \end{aligned} \quad (2.14)$$

The auto-covariance function is given by (note: the average value is a constant):

$$\begin{aligned} C_{XX}(t_1,t_2)&=E\{(X(t_1)-m_X)(X(t_2)-m_X)\} \\ &=\int_{-\infty}^{\infty}\int_{-\infty}^{\infty}(x_1-m_X)(x_2-m_X)f_{X(t_1)X(t_2)}(x_1,x_2)dx_1dx_2 \\ &=\int_{-\infty}^{\infty}\int_{-\infty}^{\infty}(x_1-m_X)(x_2-m_X)f_{X(0)X(t_2-t_1)}(x_1,x_2)dx_1dx_2 \\ &=C_{XX}(0,t_2-t_1)=C_{XX}(\tau) \end{aligned} \quad (2.15)$$

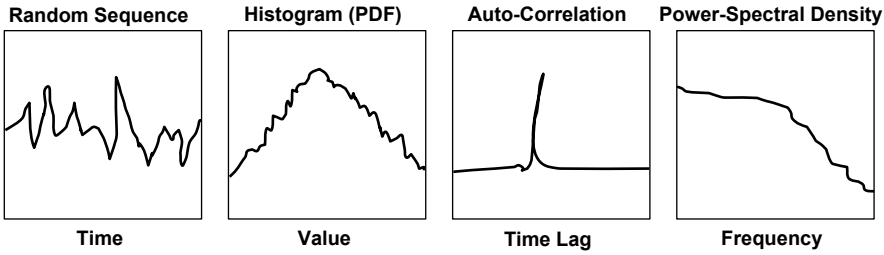

Fig. 2.3 Illustration of random sequences, histogram (PDF), auto-correlation, and power spectral density

Properties of Auto-correlation Function of a Stationary Random Process:

- Symmetry: $R_{xx}(\tau) = R_{xx}(-\tau)$
- Mean Square Average: $R_{xx}(0) = E\left\{x(t)^2\right\} \geq 0$
- Maximum: $R_{xx}(0) \geq \left|R_{xx}(\tau)\right|$
- Periodicity: if $R_{xx}(0) = R_{xx}(t_0)$,

then $R_{xx}(\tau)$ is period with period t_0.

Auto-correlation and Auto-covariance Function of an Ergodic Random Process:

$$R_{XX}(\tau) = \lim_{T\to\infty} 1/T \int_{-T/2}^{T/2} X_T(\lambda_i, t)\left(X_T\right)\left(\lambda_i, t+\tau\right)dt$$
$$C_{XX}(\tau) = \lim_{T\to\infty} 1/T \int_{-T/2}^{T/2} \left(X_T(\lambda_i, t) - m_X\right)\left(X_T(\lambda_i, t+\tau) - m_X\right)dt \tag{2.16}$$

Note: $X_T(\lambda_i, t)$ is a sample function of random process $X(t)$ windowed to be of length T (extending from $-T/2$ to $T/2$).

Figure 2.3 depicts some sketches of random sequences, histogram (PDF), its auto-correlation function, and the power-spectral density.

2.2.3 Power Spectral Density of Random Process

A random process is an ensemble of discrete time signals and a description of random processes in the frequency domain is necessary. Calculation of the Fourier Transform of the random process is not straight forward. The random process considered is at least WSS if not stationary. The auto-correlation of a WSS random process is however a deterministic function of delay. The power spectral density (psd) of a WSS random process $X(t)$ is defined as the Fourier Transform of the auto-correlation function $R_{xx}(\tau)$:

$$S_{XX}(f) = F.T\{R_{XX}(\tau)\} = \int_{-\infty}^{\infty} R_{XX}(\tau) e^{-j2\pi f\tau} d\tau \tag{2.17}$$

where $F.\mathrm{T}$ is the notation for Fourier Transform. The inverse transform,

$$R_{XX}(\tau) = \int_{-\infty}^{\infty} S_{XX}(f) e^{+j2\pi f\tau} df \tag{2.18}$$

The above equations are called Wiener-Khintchine relations.

Figure 2.3 depicts some sketches of random sequences, its auto-correlation function, histogram (PDF), and the power spectral density.

Properties of the Power Spectral Density Ergodic Random Process $x(t)$:

$$\begin{aligned} &S_{xx}(f) = S_{xx}(-f),\ S_{xx}(f) \geq 0 \\ &I_m\{S_{XX}(f)\} = 0 \end{aligned} \tag{2.19}$$

Auto-correlation Function:

$$R_{XX}(\tau) = \lim_{T\to\infty} 1/T \int_{-T/2}^{T/2} \left(x_T(\lambda_i, t) x_T(\lambda_i, t+\tau)\right) dt = \lim_{T\to\infty} 1/T \int_{-T/2}^{T/2} x_T(t) x_T(t+\tau) dt \tag{2.20}$$

Power Spectral Density:

$$\begin{aligned} S_{XX}(f) &= \int_{-\infty}^{\infty} R_{XX}(\tau) e^{-j2\pi f\tau} d\tau = \int_{-\infty}^{\infty} \lim_{T\to\infty} 1/T \int_{-T/2}^{T/2} x_T(t) x_T(t+\tau) dt e^{-j2\pi ft} d\tau \\ &= \lim_{T\to\infty} 1/T \int_{-T/2}^{T/2} x_T(t) \int_{-\infty}^{\infty} x_T(t+\tau) e^{-j2\pi f\tau} d\tau dt = X_T(f) \lim_{T\to\infty} 1/T \int_{-T/2}^{T/2} x_T(t) e^{-j2\pi ft} dt \\ &= \lim_{T\to\infty} X(f) X_T^*(f)/T = \lim_{T\to\infty} \left|X_T(f)\right|^2 / T \end{aligned} \tag{2.21}$$

2.2.4 Concepts of Random Process for the Treatment of Random Fields

A random field denoted by $x(r, t)$ can be understood from the concepts of random process (discussed earlier) which is a function of time t, and of a vector spatial variable, $r=(x, y, z)$. To describe the random field completely, it is necessary to know the joint probability distributions of all orders of the random field. Since it is not possible to derive the complete family of probability distributions, only the lower order field moments are sufficient for practical purposes. In many applications such as optical propagation through the random medium when the medium does not change appreciably during the time the random field parameters are being evaluated, the random field can be described as $x(r)$.

Spatial Covariance Function If the time-dependency factor of the random field $x(r, t)$ can be suppressed, the mean value $m(r)$ of the random field can be defined by

$$\mathrm{m}(r) = < \mathrm{x}(r) > \tag{2.22}$$

where the bracket < > denotes an ensemble average, i.e., the mean value. The spatial covariance function, $B_x(r_1, r_2)$, of the random field, $x(r)$, can then be defined as (where r_1 and r_2 are three-dimensional spatial vectors),

$$\mathrm{B_x}(\mathrm{r_1}, \mathrm{r_2}) = < \left[\mathrm{x}(\mathrm{r_1}) - \mathrm{m}(\mathrm{r_1}) \right] \quad \left[\mathrm{x}^*(\mathrm{r_2}) - \mathrm{m}^*(\mathrm{r_2}) \right] > \tag{2.23}$$

where the x^* denotes the complex conjugate of x. The spatial covariance function, $B_x(r_1, r_2)$ is sufficient to describe a stationary random process, where $m(r_i)$ is the expected value of $x(r_i)$ and <> refers to the ensemble average. Note that the mean value of the random field, $m(r)$ is dependent on the spatial position, r. In other words, the value of the field at any specific position can be thought of as a random variable. In general, any two positions in the field, say r_1 and r_2 may have different mean values which means that they are random variables with different probability descriptions. As a special case, if the mean value of the random field does not depend on the spatial position, r, the field is said to be statistically homogeneous, and its mean value is denoted by

$m = <x(r)>$. In that case, the spatial covariance function for a statistically homogenous field is reduced to

$$\mathrm{B_x}\ (\mathrm{r}) = < \mathrm{x}(\mathrm{r_1})\ \mathrm{x}^*(\mathrm{r_1} + \mathrm{r_2}) > - \left| m^2 \right| \tag{2.24}$$

where $r = r_2 - r_1$. The homogeneity is the spatial equivalent of a random process which is stationary in time. If the random field, in addition to being statistically homogenous, depends only on the scalar distance, $r = \left| r_2 - r_1 \right|$, and not on the positions r_1 and r_2, the field is then said to be statistically isotropic. The spatial covariance can then be written as $B_x(r)$.

Three-Dimensional Spatial Power Spectrum If the random field is statistically homogenous with a zero mean, the field depends on the vector $r = r_2 - r_1$, and can be represented by the Riemann-Stieltje integral given by

$$x(r) = \int_{-\infty}^{\infty} e^{ik.r}\, d\upsilon(k) \tag{2.25}$$

Where $k = (k_x, k_y, k_z)$ is the vector wave number, and $d\upsilon(k)$ denotes the random amplitude of the field, $x(r)$. The spatial covariance function can then be written as [3].

$$B_x(\mathbf{r}) = < x(\mathbf{r}_1) x^*(\mathbf{r}_2) > = \iiint \int_{-\infty}^{\infty} \exp \quad i\left(k \cdot \mathbf{r}_1 - \mathbf{k}' \cdot \mathbf{r}_2\right) \langle d\upsilon(k)\, d\upsilon^*(\mathbf{k}') \rangle \tag{2.26}$$

For statistical homogeneity condition to be satisfied it is required that

$$< d\upsilon(k)\, d\upsilon(k') >= \delta(k-k')\Phi_x(k)\, d^3k d^3k' \tag{2.27}$$

Where $\delta(x)$ is the Dirac delta function, and $\Phi_x(k)$ is the three-dimensional spatial power spectrum of the random field $x(r)$.

For statistically homogeneity condition, the Eq. (2.26) can be simplified to

$$\mathrm{B_x(r)} = \int_{-\infty}^{\infty}\int\int e^{ik.r}\Phi_x(\mathrm{k})\, d^3k \tag{2.28}$$

By taking the inverse Fourier Transform, the spatial power spectrum, $\Phi_x(k)$ can be written as

$$\Phi_x(k) = \left(\frac{1}{2\pi}\right)^3 \iiint_{-\infty}^{\infty} e^{-ik.r} B_x(r)\, d^3r \tag{2.29}$$

With further assumption of the statistically homogenous and isotropic properties of the random field, the Eqs. (2.28) and (2.29) can be further reduced to

$$\Phi_x(k) = \frac{1}{2\pi^2 k}\int_0^{\infty} B_x(r)\sin(kr)\, r dr \tag{2.30}$$

$$B_x(r) = \frac{4\pi}{r}\int_0^{\infty} \Phi_x(k)\sin(kr)\, k dk \tag{2.31}$$

where $\mathrm{k}=|k|$ is the magnitude of the wave number.

As a special case, a statistically homogenous and isotropic random field, can be represented by a Riemann-Stieltjes integral [3] of the form

$$x(r) = \int_{-\infty}^{\infty} e^{ikr}\, d\upsilon(k) \tag{2.32}$$

where $d\upsilon(k)$ is a random complex amplitude. Assuming the mean value of the random field is zero ($m=0$), the spatial covariance function can be defined as

$$B_x(r) = \int_{-\infty}^{\infty} e^{ikr} V_x(k)\, dk \tag{2.33}$$

where k denotes the spatial frequency and $V_x(k)$ is the one-dimensional spectrum of the random field $x(r)$. The one-dimensional spectrum $V_x(k)$ can then be obtained by taking the inverse Fourier Transform of Eq. (2.33):

$$V_x(k) = \frac{1}{2\pi} \int_{-\infty}^{\infty} e^{-ikr} B_x(r)\, dr \tag{2.34}$$

From Eqs. (2.34) and (2.31), the three-dimensional spatial power spectrum can be related to the one-dimensional spatial spectrum by

$$\Phi_x(k) = -\frac{1}{2\pi k} . \frac{dV_x(k)}{dk} \tag{2.35}$$

Structure Function In many applications of practical interest, the random field does not have a constant mean over large spatial distances, and one cannot generally assume that the field is strictly homogenous. The difference in the physical parameters (such as velocity fields in a turbulent medium) representing the random field at two points in the field usually can be assumed as a statistically homogenous field. A locally homogenous random field can be defined as the random field which can be expressed as the sum of a varying mean and a statistically homogenous fluctuation as follows

$$\mathrm{x}(\mathrm{r}) = \mathrm{m}(\mathrm{r}) + \mathrm{x}_1(\mathrm{r}) \tag{2.36}$$

where $m(r)$ is the varying mean, and $x_1(r)$ is the statistically homogenous fluctuations with zero mean $<x_1(r)>=0$ for all vector position, r.

If a random process $x(r)$ has a slowly varying mean, it cannot be represented by the covariance function. Accordingly three-dimensional structure function adequately describes this process and is denoted by

$$\mathrm{D_x}(\mathrm{r_1}, \mathrm{r_2}) = \mathrm{D_x}(r) = <[\mathrm{x}(\mathrm{r_1}) - \mathrm{x}(\mathrm{r_1}+\mathrm{r})]^2> \approx <[\mathrm{x_1}(\mathrm{r_1}) - \mathrm{x_1}(\mathrm{r_1}+\mathrm{r})]^2> \tag{2.37}$$

The power spectrum and the structure function are related by

$$D_x(r) = 2\iiint_{-\infty}^{\infty} \Phi_n(k)\left[1-\cos(k.r)\right] d^3k \tag{2.38}$$

If the random field locally homogenous and isotropic, the scalar separation distance, $r = |r_2 - r_1|$, the vector equation distances. For the isotopic case, the structure function is determined by

$$D_x(r) = 8\pi \int_{-\infty}^{\infty} k^2 \Phi_x(k)\left(1 - \frac{\sin kr}{kr}\right) dk \tag{2.39}$$

The inverse relationship gives the spatial power spectrum for locally homogenous and isotropic case isotropic case

$$\Phi_x(k) = \frac{1}{4\pi^2 k^2} \int_{-\infty}^{\infty} \frac{d}{dr}\left[r^2 \frac{d}{dr} D_f(r)\right] \frac{\sin kr}{kr} dr \tag{2.40}$$

2.3 FSO Communications in Presence of Atmosphere

In FSO, when a light beam propagates through the atmosphere, most of its properties are affected. The atmosphere is a mixture of gases, molecules, and particles that continuously gain or lose energy (heat). There is a constant movement of air cells causing thermal turbulence in air cells characterized by inhomogeneous and dynamically changing refractive index, density, and air consistency. Most of the properties of the FSO light beam are thus severely affected by the atmosphere which include changes in polarization refraction, absorption, scattering, and attenuation. This results in random fluctuations of the light beam at a frequency between 10 mHz and 200 Hz [4], or more. In FSO, when the laser beam interacts with atmospheric turbulence, its polarization and coherency fluctuates due to random fluctuations of the air mass along the path, and its attenuations constantly fluctuates due to non-consistent power loss throughout the air mass along the path. From communications point of view when the signal arrives at the receiver, its intensity fluctuates due to random temporal and spatial irradiance fluctuations of the light beam. The signal therefore focuses and defocuses onto the photodetector randomly. The signal fluctuation due to atmospheric turbulence is termed as scintillation. The scintillations of a laser beam are a major obstacle for gigabit data rates and long-distance optical communications [5, 6]. In FSO communication links, knowledge of the scintillation (measured by the scintillation index) is important for determining system performance. There are a variety of deleterious features of the atmospheric channel that may lead to serious signal fading, and even the complete loss of signal altogether. Atmospheric turbulence is not the only cause to affect the deterioration received signal. There are many situations where FSO communication link has to be established in presence of scattering medium such as fog, aerosol, smoke, dust, etc. Absorption and scattering due to particulate matter in the atmosphere may significantly decrease the transmitted optical signal, whereas random atmospheric distortions due to optical turbulence can severely degrade the wave-front quality of a signal-carrying laser beam, causing intensity fading and random signal losses at the receiver [6, 7].

Besides these atmospheric channels which involve turbulence and scattering media, free-space underwater optical communication channel [8, 9] is becoming a challenging field of investigation. The necessity if wireless underwater connections has dramatically increased in the last few years for a wide range of applications, from environmental monitoring to surveillance. Underwater communication channel for potential high data rate communication will be covered in a separate chapter of the book.

2.3.1 FSO Communication Scenarios

The FSO is an outdoor wireless communications technology with a potential high data rate and bandwidth per link exceeding 10 Gb/s or even 50 or 120 Gb/s per link.

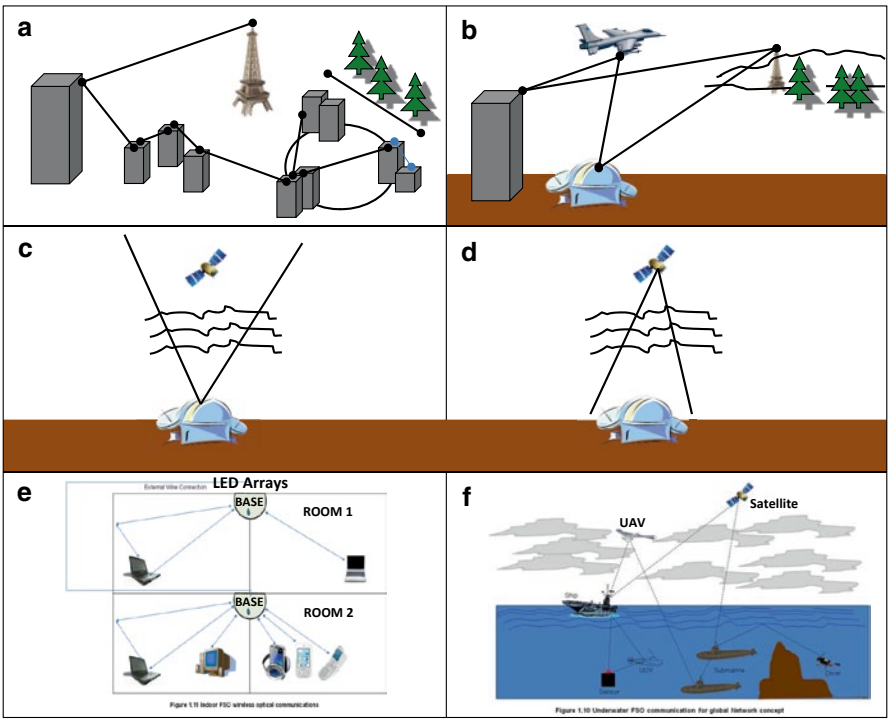

Fig. 2.4 FSO communications scenarios

Figure 2.4 depicts the different FSO communication scenarios each of which are described as follows.

- *Horizontal link,* such as from rooftop-to-rooftop of tall buildings, from window-to-rooftop or from window-to-window, and some FSO nodes may be mounted on tall poles. Some of these FSO links may include a base Transceiver station, Backhaul, and cell sites. The range of this horizontal link is typically up to a few kilometers connecting office buildings in a metro area (Fig. 2.4a). In computing the fluctuating intensity of the received signal, the strength of the turbulence is usually assumed uniform for the horizontal link. Physical obstructions, such as birds, insects, tree, limbs, or other factors can temporarily or permanently block the laser line-of-sight. Furthermore, building motion due to wind, differential heating and cooling, building sway, or ground motion over time can result in serious misalignment of fixed-position FSO communication system.
- *Slant Path FSO link*: The slant path situation can arise when the FSO path is not quite horizontal and the turbulence strength is not uniform along the propagation path, i.e., variable. Some of the examples to be treated in other chapters of the book include unmanned aerial vehicle (UAV; or airborne) or top of a mountain to a ground link (Fig. 2.4b).

- *Uplink*: Typical example for uplink scenario is ground-to-space propagation path, such as ground station to a satellite. It is necessary to consider the altitude profile of the turbulence strength parameters in order to compute the fluctuations of the signal intensity received at the receiver. (Fig. 2.4c)
- *Downlink*: From space-to-ground is an example for a downlink FSO communication, such as a satellite-to-ground link. The altitude variation of the turbulence strength must be considered to compute the received FSO signal intensity fluctuations (Fig. 2.4d).

  - *Indoor communications*:The short-range indoor wireless communication is receiving increasing attention because of its role in the emerging technologies involving portable computing and multimedia terminals at work and everyday environment. Some of the typical portable devices may include laptop, computers, phones, whereas the base stations inside the room are usually connected to a computer with other networked connections (Fig. 2.4e). Many indoor communication systems employing infrared light-emitting diode (LED) wireless links are available. Using pure diffuse links, a high-speed, power-efficient indoor wireless infrared communication using code combining has been reported [10] where a multiple transmitter link design was used with a narrow field-of-view direction diversity receiver. Indoor optical wireless communications using visible light communication (VLC) has been point out [11]. Note that the effect of signal functions and signal loss of indoor optical communications will be discussed in a separate chapter of the book.
  - *Underwater Optical Communications:*The importance of underwater wireless optical communication has grown for application of underwater observation and sea-monitoring system. Underwater optical communications system can provide the capability to communicate optically at data rates of the order of a few hundred Mb/s and can be designed for ships, submarines, unmanned underwater vehicles, and fixed data nodes (Fig. 2.4f). Underwater FSO can offer high bandwidths with very low latency and directional links, reducing multipath effects and enabling real-time networking. A detailed description underwater FSO communication will be provided in a separate chapter of the book.

2.3.2 Flowchart for FSO Communication System Performance Evaluation

A system approach provides a practical and realistic way to understand how the FSO communication performance is evaluated. Like any other system analysis, a set of requirements has to be established first. These requirements usually come from the goals of the required FSO communication system specified by the particular research or provided by the customer (who funds the project or the ultimate users). FSO communication system which has to operate under diverse atmospheric conditions such as various atmospheric turbulence is very complex because it in-

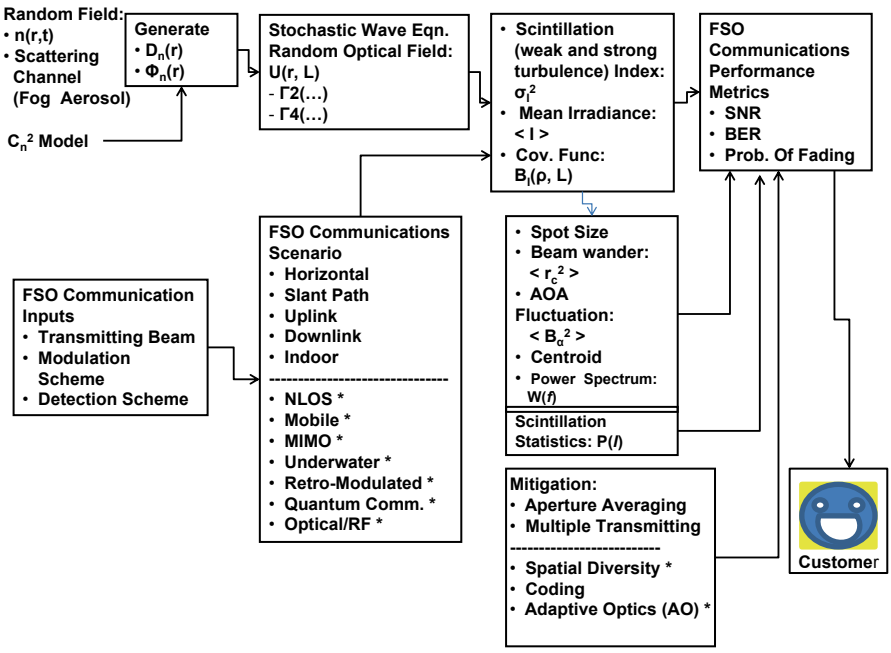

Fig. 2.5 Flowchart for FSO communications systems performance evaluation

volves tremendous number of variables. Atmospheric channel which in this case is random (stochastically dynamic) and the optical field originating from the optical transmitter undergoes various temporal and spatial changes in the communication signal before reaching the receiver. The system analysis must start with a communications scenario (same of the examples are shown in the Fig. 2.4). A communication scenario will then determine the FSO transceiver (both optical transmitter and receiver) design with the knowledge of the signal distortions due to atmospheric turbulence. Once the type of atmospheric turbulence (such as low, moderate, or strong turbulence) is assumed, the solution of optical wave equation (discussed in the next section) provides the second- and fourth-order moment of the random optical field from which mean irradiance, scintillation index, and covariance function can be deduced. FSO communication parameters such as beam wander, angle-of-arrival fluctuations, correlation width, etc. can then be determined. Combined with scintillation statistics/PDF (discussed in the subsequent section) and appropriate mitigation technique (such as aperture averaging, coding, adaptive optics, etc.), the FSO communication performance metrics such as Bit-Error-Rate (BER), signal-to-noise ratio (SNR), and probability of fading can be evaluated. This overall picture of the complete systems approach is shown in Fig. 2.5. The symbols used in the system blocks are identified and the functional relationships of the necessary parameters and how they are related to the solutions of the optical wave equation are referred to and discussed in detail in the next sections.

2.3.3 FSO Transmitting Beam Types

The propagation of laser beams through a turbulent atmosphere has many applications in FSO communications. The signal intensity fluctuations through turbulent atmosphere at the detector, determines the FSO communications system performance. This subject has been extensively studied which covers mainly the scintillations under the plane wave, the spherical wave, and the Gaussian beam wave (fundamental mode) excitations at the source, i.e., at the transmitter end. However, due to the tremendous growth into the telecommunications infrastructure using FSO communication links, there is increased need for computing the scintillation index in turbulence with different kinds of laser beams, other than plane, spherical, or Gaussian beam waves. The object to search for the best (optimum) beam at the source (transmitter) is to minimize the degrading effects of turbulence in the atmospheric FSO links. Some source excitation beam types commonly used and proposed for FSO communications today depicted in Fig. 2.6 are the following:

- *Plane Wave*

A plane wave in this FSO context is defined as the type of electromagnetic wave when generating from the source point (transmitter end) propagates through the atmosphere in which the phase fronts are parallel planes.

Mathematical description:

$$\mathrm{U_o(r,z)} = \mathrm{A_o} e^{i\varphi_0 + ikz} \tag{2.41}$$

where U_0 is the complex amplitude at distance z from the transmitter wave propagating along the positive Z-axis in free space, A_0 is a constant amplitude of the wave field, φ_0 is the phase, k is the optical wave number related to the optical wavelength λ by $k = 2\pi / \lambda$.

Note that the above formulation describes the plane wave propagation in free space. FSO communications has to be operated in a random atmospheric turbulent channel. When a plane wave propagates through this random medium, it undergoes both amplitude and phase fluctuations when the signal arrives at the detector surface. Figure 2.6a sketches qualitatively how

- *Spherical Wave*

A spherical wave is defined as one in which the phase fronts are spherical surfaces.

Mathematical description:

The complex wave amplitude is given by (at a distance, z)

$$\mathrm{U_0\ (r,z)} = \frac{A_o}{4\pi z} \exp\left(ikz + \frac{ikr^2}{2z} \right) \tag{2.42}$$

The phase $\varphi = k\left(z + \frac{r^2}{2z} \right)$ has a transverse radial dependency. Spherical wave are assumed when the source excitation for FSO communication can be considered as a

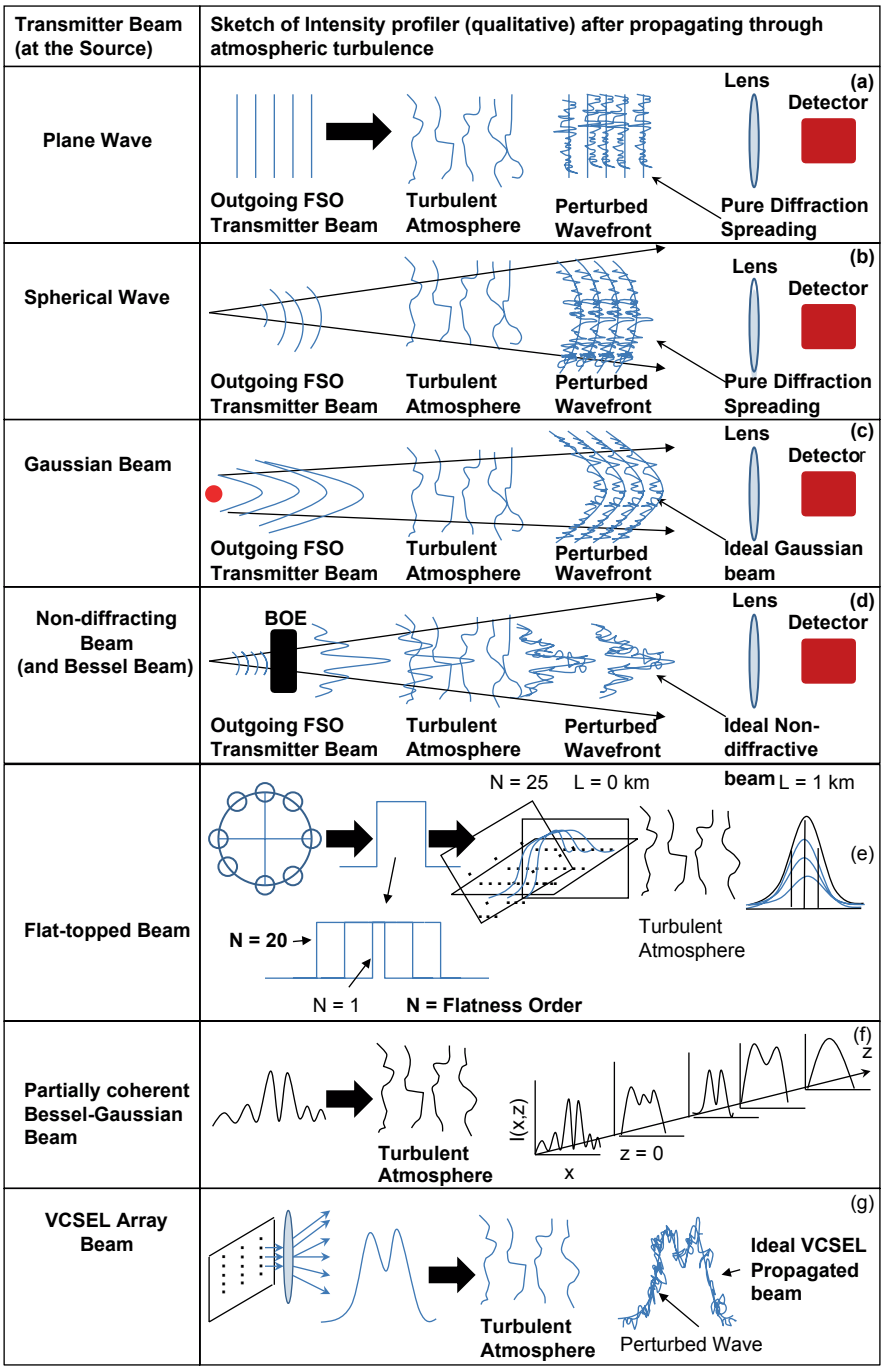

Fig. 2.6 Sketches to illustrate intensity profiles of transmitting beams propagated through atmospheric turbulence

point source. Figure 2.6b sketches the spherical waves intensity profile propagated through atmospheric turbulence.

- *Gaussian-beam wave*

A Gaussian-beam is a beam whose transverse electric field and intensity (irradiance) distributions are approximated by Gaussian functions. Many lasers operating on the fundamental transverse mode, or TEM_{00} mode of the laser's optical resonator emit an approximate Gaussian profile. The outgoing Gaussian beam passing through a lens also is transformed into another Gaussian.

Mathematical Description The complex amplitude at distance z from the source is the Gaussian wave [3] is

$$U_0\ (r,z) = \frac{1}{1+i\alpha_o z}\exp\left[ikz - \frac{1}{2}\left(\frac{\alpha_o k}{1+i\alpha_o z}\right)r^2\right] \tag{2.43}$$

where r is radial distance from the beam center line, α_0 is a complex parameter related to spot size and phase front radius of curvature as

$$\alpha_o = \frac{2}{kW_o^2} + i\frac{1}{F_o} \tag{2.44}$$

W_0 is the radius at which the field amplitude falls to $1/e$ of that on the beam axis, and the phase front is taken to be parabolic with radius of curvature F_0. $F_0 = \infty$ (collimated), $F_0 > o$ (convergent) and $F_0 < o$ (divergent). Figure 2.6c sketches the Gaussian beam intensity profile distribution after propagating through turbulent atmosphere [see also 12].

- *Non-diffracting Beam*

An ideal optical field with completely eliminated diffraction is termed non-diffractive beam and is promising for wireless optical communications (WOC). Non-diffracting beam is much less influenced by atmospheric turbulence than other beams [13]. It means that the non-diffractive beam is suitable for long-range FSO communications. In practice, however, only the approximation of ideal non-diffractive beam, called pseudo-non-diffractive (P-N) beam is realizable [14]. In this case, the beam intensity depends on the propagation coordinate but inside a propagation region of the well-defined length, the beam profile remains nearly unchanged. There are a number of ways to generate non-diffractive beams. Generation of the P-N beam using a thin annular ring placed at the front focal plane of the Fourier lens and illuminated by a spatially filtered and collimated laser beam is described in [14]. The use of an axicon to generate P-N beam is also discussed in that reference [14]. The researchers in the reference [13] presented a binary optical element (BOE) that shapes and incident place wave or divergent spherical wave into a non-diffractive beam.

Mathematical Description The intensity distribution of the non-diffracting beam at the different propagation distances for the case of a spherical wave incidence is explained in the reference [13]. The BOE is located at the (*x, y, o*) co-ordinate (z=o), and the intensity was computed on the points in the plane (x', y', z). The transformations of the two co-ordinate axes where: $x = \rho\cos\theta$, $y = \rho\sin\theta$; $x' = \sigma\cos\phi$, $y' = \sigma\sin\phi$ The intensity distribution was computed from the wave-amplitude distributions incident on the BOE and on the (x', y', z) plane. The result is shown as follows:

$$I(\sigma,\varphi,z) = \frac{A^2}{\lambda^2 z^2}$$
$$\int_{-\infty}^{\infty}\int \exp\left(j\frac{k\rho^2}{2f}\right)\times\exp\left(j\frac{\pi R^2}{\lambda(d_2-d_1)}\ln\left(\left(\frac{z_{d_2}-z_{d_1}}{R^2}\right)d_1\right.\right. \tag{2.45}$$
$$\left.\left.+\left(\frac{d_2-d_1}{R^2}\right)^2\rho^2\right)\exp\left(j\frac{k}{2z}[\rho^2+\sigma^2-2\rho\sigma\cos(\theta+\varphi)]\right)\right)\rho d\rho d\theta\Bigg|^2$$

In the above equation, A is the constant amplitude of the initial wave-amplitude, $k = 2\pi/\lambda$, the optical wave number, λ= optical wavelength, z= distance from the BOE element, f in the distance between the source point and BOE element, R= radius of the element, d_1 and $d_2$are points on optical axis, non-diffractive beam propagates between z_{d_1} and z_{d_2}. By numerical integration, one can analyze the intensity distributions of the non-diffracting beam with the propagation distance. Note that the intensity distributions referred will still be corrupted by the atmospheric turbulence. Figure 2.6d shows schematically the intensity profiles. For FSO communications applications, the intensity distributions of the non-diffractive beams perturbed by atmospheric turbulence will ultimately determine the communication performance.

- *Bessel Beam*

A Bessel beam is a field of electromagnetic wave (in the context of FSO propagation) whose electric field is explicitly described by a zeroed-order Bessel function of the first kind (J_0). A true Bessel is non-diffractive, described earlier, which means that as it propagates, it does not diffract and spread out. A Bessel beam is also self-healing, meaning that the beam if is partially obstructed at one point will re-form at a pint further down the beam axis. The properties of Bessel beams make them useful for WOC. A true Bessel beam cannot be created, as it is unbounded and would require an infinite amount of energy. Approximation to Bessel beams can be achieved by focusing a Gaussian beam with an axicon or conical lens element to generate a Bessel-Gauss beam.

Mathematical Description The mathematical function which describes a Bessel beam is a solution of Bessel's differential equation, originating from separable solutions to Laplace's equation and the Helmholtz equation in cylindrical coordinates. The intensity profile of the Gaussian-Bessel beam is [15]:

$$I(r,z) = 2k\pi\left(\tan^2\alpha\right)(n-1)^2\, zI_o e^{-2(n-1)z\tan\frac{\alpha}{\omega_0}} J_o^2\left(kr(n-1)\tan\alpha\right) \tag{2.46}$$

Where r and z are the radial and longitudinal coordinates, I_o and ω_0 are the intensity and beam waist of the incident Gaussian beam, k is the wave vector, n is the index of refraction of the axicon material, and d is the wedge and angle. Because of the similarity of the Bessel beam with the non-diffraction beams, a separate sketch in Fig. (2.6) is not shown separately.

- *Flat-topped Beam (or Top-hat Beam)*A flat-top beam (or top-hat beam) is a light beam having an intensity profile which is flat over most of the covered area. When a laser beam propagates through the atmospheric turbulence, it experiences scintillation, beam spreading, degradation of beam quality, and beam wandering induced by the atmospheric turbulence. These effects limit the application of laser beams in long-distance FSO communications. A flat-topped beam array has been recently studied for overcoming turbulence-induced degradation.

Mathematical Description Formulation of the average receiver intensity has been described in details in reference [16] and is not repeated here. Also the authors in reference [16] have formulated the scintillation index of a phase-locked radial flat-topped beam array propagating in a weekly turbulent atmosphere. These results will be useful in long-distance FSO communications. Figure 2.6e shows the basic concepts of the flat-topped beam propagation through atmospheric turbulence, and the intensity profiles.

- *Partially Coherent Bessel-Gaussian Beam*A partially coherent source (spatially) can be generated in a number of different ways. One method to generate a partially coherent beam is to place a diffuser at the laser transmitter of a quasi-monochromatic source. A Gaussian Schell model may be used to describe the coherence of the source beam [17, 18]. Propagation of laser beams through a turbulent atmosphere has many applications in a FSO communications. Recently many researchers have shown that partially coherent beams are less influenced by a turbulent atmosphere than is a completely coherent beam. The statistical properties of arbitrary coherent and partially coherent beams propagating through atmospheric turbulence have been reported [18–20]. A Bessel-Gaussian beam is constructed by introducing a Gaussian exponential as a windowing function to confine the energy of the beams [21].

Mathematical Description The intensity distribution of a partially coherent Bessel-Gaussian originating at $z = 0$ (i.e., the source plane) and propagated a distance z is given by [21] (this is the intensity distribution in the received plane)

$$I(\rho,z)=\frac{k^2}{4\pi^2 z^2}\sum_{l=-\infty}^{\infty}\iint J_n(\alpha r_1)J_n(\alpha r_2)J_1\left(\frac{kr_1\rho}{z}\right)J_1\left(\frac{kr_2\rho}{z}\right)I_{n+l}\left[2r_1r_2\left(\frac{1}{L_c^2}+\frac{1}{\rho_o^2}\right)\right]$$
$$\exp\left[-\left(\frac{1}{L_c^2}+\frac{1}{\rho_o^2}+\frac{1}{\omega_o^2}\right)\left(r_1^2+r_2^2\right)\right]\exp\left[\frac{ik}{2z}\left(r_2^2-r_1^2\right)\right]r_1r_2dr_1dr_2 \tag{2.47}$$

where r_1 and r_2 are modulus of the position vectors $r_1$and $r_2$located in the transverse plane, L_c is the transverse coherence length, J_n is the Bessel function, $\alpha$and ω_0 are the width parameters, $k=2\pi/\lambda$ is the wave number, ρ_0 is the coherence length of a spherical wave propagations in the turbulent medium.

- *Vertical-Cavity Surface-Emitting Laser (VCSEL) Array Beam*Recently the concept of a compact free-space laser communications terminal has been proposed using a Vertical-Cavity Surface-Emitting Laser (VCSEL) array. The optical system has no mechanically moving parts and the compact terminal can transmit multiple optical communications beams to the counter terminals as well as receive optical communications signals simultaneously from multiple platforms. High power VCSEL devices with 4, 9, and 16 simultaneously driven spots operating at 850 nm have been developed [22] to produce a single-cone-shaped far-field pattern. For FSO communications application, these light sources are useful because of their high-speed modulation (capable of 2.5 Gb/s data rate) and high reliability under high optical power operation. Some of the characteristics of the VCSELs regarding beam profile involve for field patterns of each single device are a multiple cone shape where the amount of the dip at the center between 20 and 40%, for example of the far-field pattern is different. For FSO application, the dip at the center is an important parameter when a VCSEL with a multi-cone shape far-field pattern is used. The far-field pattern of 4×4 VCSEL array were shown in [22] to have single cone-like pattern. Further research is needed to over the dip at the center of the far-field pattern to obtain higher power to make useful for long range FSO communication. Figure 2.6f shows a qualitative sketch of VCSEL array and the intensity profile at the far field. Note that the intensity profile will include the intensity fluctuation induced by the atmospheric scintillation effect.

2.3.4 Random Nature of Atmospheric Turbulence

Study of turbulence in earlier research involved investigating the concept of velocity fluctuations in a viscous fluid. The velocity field may in a turbulent state be considered to develop random subfields known as turbulent eddies, and can be used to qualitatively describe be turbulent atmosphere. These turbulent eddies exist in a continuum of spatial dimensions. The larger eddies bread-up into continuously smaller eddies and energy is transferred between these eddies in the form of velocity. During this breaking-up process eddies of all sizes are created: there exists

a largest eddy size L_o, known as the outer scale of turbulence, and a smallest eddy size, l_o, known as the inner scale *of* turbulence. The so-called inertial sub-range covers and inner scale. Scale sizes smaller than the inner scale belong to the dissipation range where energy is dissipated in the form of heat. The transition from laminar to turbulent flow is usually characterized by the Reynolds number, $R_e = Vl/\upsilon$ where V is the characteristic velocity, l is the characteristic dimension of the flow, and V is the kinematic viscosity. A typical value of $R_e \approx 10^5$ for ground level wind velocity is considered to be highly turbulent flow. The fluid flows in the atmosphere are highly unstable because random movement of the eddies of scale sizes on the order of flow dimensions, giving rise to eddies of smaller scale sizes and lower velocities. Ultimately, eddies become small enough that viscosity forces overcome initial forces and eddies no longer decay. The turbulent energy redistribution can be considered to have an initial energy input region, inertial sub- range, and energy dissipation region [23, 24]. Energy begins to cascade when the characteristic length reaches a specific outer scale length, L_o. The energies of the eddies start to be redistributed into eddies of smaller eddies, until caddies reach a size equal to the inner scale length, l_o. Kolmogorov proposed that in the inertial sub-range where $L_o > l > l_o$, the turbulence can be considered as isotropic. After reaching the dimension l_o, the energy of the eddy is dissipated as heat energy through viscosity process [23].

Statistical descriptions of the atmospheric wind velocity field are related to the index of refraction fluctuation. The atmospheric index of refraction can be treated as a random field the index of refraction at any spatial point in the atmosphere at any given time can be considered a random variable. Specifically, the index of refraction is a random function of both space and time. The time dependency of the index of refraction is usually suppressed in optical studies assuming the wave maintains a single frequency as it propagates. The index of refraction fluctuations caused by atmospheric turbulence can be written as (see also Eq. 2.36)

$$n(\vec{r}) = \mathrm{n}_o + \mathrm{n}_1(\vec{r}) \tag{2.48}$$

Where $\vec{r}$ is a point in space, $\mathrm{n}_0 = <\mathrm{n}(\vec{r})> \cong 1$ is the mean value of the index of refraction of air at atmospheric pressure and $\mathrm{n}_1(\vec{r})$ represents the random deviation of $\mathrm{n}_1(\vec{r})$ from its mean value, with a zero average, i.e., $<\mathrm{n}_1(\vec{r})> = 0$. The refractive index if air at optical frequencies is,

$$n(\vec{r}) = 1 + 79 \times 10^{-6} \frac{P(\vec{r})}{T(\vec{r})} \tag{2.49}$$

where P is the pressure in millibars, and T is the temperature in degree Kelvin. The index of refraction fluctuations within the visible and near-IR region of the spectrum are primarily due to random temperature fluctuations.

The covariance function of $\mathrm{n}_1(\vec{r})$ can be written as (see also Eq. 2.23)

$$B_n(\vec{r_1}, \vec{r_2}) = B_n(\vec{r_1}, \vec{r_1} + r) = \langle n_1(\vec{r_1}) n_1(\vec{r_1} + \vec{r}) \rangle + n_0^2 \tag{2.50}$$

where $\vec{r}_1$ and $\vec{r}_2$ are two points in space, and $\vec{r} = \vec{r}_2 - \vec{r}_1$. If the media is assumed to be homogeneous and isotropic turbulent, the covariance function reduces to a function of one scalar distance $r = \left|\vec{r}_2 - r_1\right|$.

A locally homogeneous field [3] is usually not characterized by the covariance function, but by the structure function given by

$$D_n(r) = <\left[n(r_1 + r) - n(r_1)\right]^2> = 2\left[B_n(o) - B_n(r)\right] \tag{2.51}$$

From Eqs. (2.50) and (2.51), the structure function of refractive index fluctuations can be determined and Kolmogorov-Obhukov two-thirds power law can be derived as [3]

$$D_n(r) = C_n^{\ 2}\ r^{2/3} \qquad l_o << r << L_o \tag{2.52}$$

where l_o(inner scale size) and L_o(outer scale size) are discussed earlier, and $C_n^2$is the index of refractions structure parameter. For FSO communications for horizontal links, $C_n^2$is essentially constant; however for uplink, downlink and slant path FSO scenarios, $C_n^2$is a function of height. Typical values of C_n^2range form 10^{-17} $m^{-2/3}$ (weak turbulence) and 10^{-12} $m^{-2/3}$ (strong/very strong turbulence). Similar concept of determining various frequency component in a time-varying electrical signal by Fourier Transform method, the ability of different eddy sizes contributing to the refractive index of random medium can be applied. The three-dimensional spatial power spectrum of the random field $\Phi_n(\vec{k})$ form a Fourier Transform pair with the covariance function (see Eqs. 2.28 and 2.29)

$$B_n(\vec{r}) = \int\int\int_{-\infty}^{\infty} e^{i\vec{k}.\vec{r}}\,\Phi_n(\vec{k})\,d^3k \tag{2.53}$$

$$\Phi_n(\vec{k}) = \left(\frac{1}{2\pi}\right)^3 \int\int\int_{-\infty}^{\infty} e^{-i\vec{k}.r}\,B_n(\vec{r})\,d^3r \tag{2.54}$$

where $\vec{k}$ is the wave number vector. The above Fourier Transform relations for homogeneous and isotropic medium reduce to (see Eqs. 2.30 and 2.31)

$$\Phi_n(\vec{k}) = \left(\frac{1}{2\pi^2 k}\right)\int_0^{\infty} B_n(r)\sin(kr)\,r\,dr \tag{2.55}$$

$$B_n(r) = \left(\frac{4\pi}{r}\right)\int_0^{\infty} \Phi_n(\vec{k})\sin(kr)\,k\,dk \tag{2.56}$$

A one-dimensional spectrum $V_n(k)$ is related to the three-dimensional spectrum $\Phi_n(\vec{k})$ (see Eq. 2.35)

$$\Phi_n(k) = -\frac{1}{2\pi k}.\frac{dV_n(k)}{dk} \tag{2.57}$$

The relation between the structure function and the power spectrum are (see also Eqs. 2.39 and 2.40)

$$D_n(r) = 8\pi \int_0^{\infty} k^2 \Phi_n(k) \left(1 - \frac{\sin(kr)}{kr}\right) dk \tag{2.58}$$

$$\Phi_n(\mathrm{k}) = \left(\frac{1}{4\pi^2 k^2}\right) \int_0^{\infty} \frac{\sin(kr)}{kr} \frac{d}{dr}\left[r^2 \frac{d}{dr} D_n(r)\right] dr \tag{2.59}$$

Using $D_n(\mathrm{r}) = C_n^{\ 2}\ r^{2/3}$, the wave number spectrum is (within the inertial range)

$$\Phi_n(k) = 0.033 C_n^2 k^{-11/3} \qquad 1/L_o \le k \le 1/l_o \tag{2.60}$$

To evaluate FSO communications performance, it is necessary to compute characteristics of the received signal on the detector such as intensity fluctuations, mean intensity, temporal power spectrum, etc. The evaluation of these parameters will require a knowledge of the refractive index spectrum valid for the intended applications. Some of the commonly used spectrum, are discussed below.

Tatarskii Spectrum To include the inner or outer scale effects, the modified Kolmogorov power law spectrum is given by Tatarskii spectrum which uses a Gaussian function to extend coverage to the dissipation range ($k > 1/l_o$) where small eddies are influential:

$$\Phi_n(k) = 0.033 C_n^2 k^{-11/3} \exp\left(-k^2/k_m^2\right) \tag{2.61}$$

where $k_m = 5.92/l_o$.

Von Karman Spectrum This modified spectrum is valid over both the inner- and outer-scale parameters,

$$\Phi_n(k) = 0.033 C_n^2 \frac{\exp\left(-k^2/k_m^2\right)}{\left(k^2 + k_o^2\right)^{11/6}} \tag{2.62}$$

where $k_o = 1/L_o \quad \left(\text{or } k_o = 2\pi/L_o\right), \qquad o \le k < \infty$

Hill Spectrum (Modified Atmospheric Spectrum) [25, 5] This spectrum includes a "bump" at high wave numbers near $1/l_o$

$$\Phi_n(k) = 0.033 C_n^2 \ [1 + 1.802(k/k_l) - 0.254(k/k_l)^{\frac{7}{6}}] \ \frac{\exp\left(-k^2/k_L^2\right)}{\left(k^2 + k_o^2\right)^{11/6}}$$
$$o \le k < \infty \tag{2.63}$$

Where $k_l = 3.3/l_o$

2.4 Theory of Optical Propagation Through Atmospheric Turbulence Relevant to FSO Communications:

For WOC or FSO communication links, atmosphere is not an ideal communication channel. Atmospheric turbulence can cause fluctuations in the received signal level as a result of a number of effects, which increase the bit errors in a digital communication link. In order to quantify the FSO performance limitations, a better understanding of these effects are needed. Known effects of atmospheric turbulence include:

A. *Beam scintillation*—Fluctuations in the spatial power density at the receiver plane. The scintillation process is low compared to the large data rates typical of FSO transmission.
B. *Beam steering*—Angular deviation of the beam from its original line-of-sight (LOS) causing beam to miss the receiver.
C. *Image dancing*—The received beam focus moves in the image plane due to variations in the beam's angle of arrival (AOA); the AOA of the phase fronts at a receiver fluctuates.
D. *Beam spread*—Increased beam divergence due to scattering causing a reduction in received power density.
E. *Other deterioration* include (i) deviations of the beam shape (from circularly symmetric Gaussian beam, for example) from that are time dependent(ii) wander off the centric of the beam(iii) break-up of the beam into distinct patches of illumination whose shapes and locations fluctuate with time
F. *Spatial coherence degradatio*n—Turbulence also induces losses in coherence across the beam phase fronts—can be deleterious for photo-mixing as incoherent receiver.

The random variations on the amplitude and phase of the propagating wave can be addressed theoretically, by solving the wave equation for the electric field and its respective statistical moments. The electric field for a propagating electromagnetic wave is derived from the wave equation

$$\nabla^2 E + k^2 n^2(r) E + 2\nabla\left[E \bullet \nabla \log n(r)\right] = 0 \tag{2.64a}$$

Where $k = \frac{2\pi}{\lambda}$ is the wave number of the electromagnetic wave, λ is the wavelength, $n(r)$ is the index of refraction whose time variations have been suppressed, and

$$\nabla^2 = \frac{\partial^2}{\partial x^2} + \frac{\partial^2}{\partial y^2} + \frac{\partial^2}{\partial z^2}$$

is the Laplacian operation. The time variations in the refractive index are sufficiently slow that a quasi steady approach can be used where $n(r)$ is a function of position only. The third term on the left-hand side of the Eq. (2.64) is a depolarization term and can be neglected so that the Eq. (2.64) can be written as

$$\nabla^2 E + k^2 n^2 E = 0 \tag{2.64b}$$

The above equation for the vector E can be decomposed into three scalar equations one of which can be denoted by a scalar component $U(r)$. This scalar component $U(r)$ is transverse to the direction of propagation along the positive Z-axis. The scalar stochastic Helmholtz equation for $U(r)$ can then be written as

$$\nabla^2 U + k^2 n^2(r) U = 0 \tag{2.65a}$$

From the Eq. (2.48)

$n(r) = n_o + n_1(r)$ with $n_o = \langle n(r) \rangle = 1$, $\langle n_1(r) \rangle = 0$.

In order to solve the Eq. (2.65b) above for weak turbulence case, Rytov approximation was used which allows to write the field of the electromagnetic wave as

$$\mathrm{U(r,L)} = \mathrm{U_o(r,L)} \exp\left[\varphi(\mathrm{r,L})\right] \tag{2.65b}$$

Where $U_o(r)$ represents the unperturbed field, i.e; an optical wave travelling through free-space at the receiver, φ is a complex phase perturbation due to turbulence and can be written as

$$\varphi(r,L) = \varphi_1(r,L) + \varphi_2(r,L) + \quad \ldots \tag{2.65c}$$

Where $\varphi_1(r,L)$ and $\varphi_2(r,L)$ are first-and second-order perturbations, respectively.

For FSO communication applications, what matters is the amount and quality of the received signal on the detector. The received signal in the form of optical field $U(r, L)$ on the detector located at a distance L from the transmitter end which is then converted to electrical signal by the photo-detector for further communications related processing, r is a vector in the receiver plane transverse to the propagation axis. The coherent portion of the field is represented by the first moment $\langle U(r, L) \rangle$, where $\langle\ \rangle$ denotes an ensemble average. The mutual coherence function (MCF) of the wave defined by the second moment is given by

$$\mathrm{MCF} \equiv \Gamma_2(r_1, r_2, L) = \langle U(r_1, L) U^*(r_2, L) \rangle \tag{2.66}$$

where r_1 and r_2 are two points in the receiver plane $U^*(r, L)$ is the complex conjugate of $U(r_1, L)$. When the optical field in the receiver plan is detected at the same point, the mean irradiance is determined from the second moment. The fourth-order moment or the cross-coherence function of the field can be represented by

$$\Gamma_4(\mathrm{r_1, r_2, r_3, r_4, L}) = \langle \mathrm{U(r_1, L)\, U^*(r_2, L)} U(\mathrm{r_3, L}) U^*(\mathrm{r_4, L}) \rangle \tag{2.67}$$

From the fourth moment, the second moment of irradiance can be determined. The scintillation index σ_I^2 can then be evaluated from the second moment of irradiance and the mean irradiance. By setting $r_1 = r_2 = r_3 = r_4 = r$ for the same point in the receiver plane,

$$\langle \mathrm{I^2(r, L)} \rangle = \Gamma_4(\mathrm{r, r, r, r, L}) \qquad \langle \mathrm{I(r, L)} \rangle = \Gamma_2(\mathrm{r, r, L}) \tag{2.68}$$

From which a theoretical expression for the scintillation index can be obtained as follows

$$\sigma_I^2(r,L)=\frac{<I^2(r,L)>}{<I(r,L)>^2}-1 \tag{2.69}$$

Weak and strong regimes of turbulence Sect. 2.2.4 discussed various refractive index spectrum relevant to FSO communications. Weak or strong fluctuation theories are generally classified based on the values of Rytov variance, denoted by $\sigma_R^2\left(or\ \sigma_I^2\right)$

$$\sigma_R^2=1.23C_n^2\mathrm{k}^{7/6}\mathrm{L}^{11/6} \tag{2.70}$$

Where C_n^2 is the refractive-index structure parameter. The different range of the values of σ_R^2 specify the various turbulence conditions as follows

$$\begin{aligned}
&\sigma_R^2<1 \quad (\text{weak fluctuations})\\
&\sigma_R^2\approx 1 \quad (\text{moderate fluctuation})\\
&\sigma_R^2>1 \quad (\text{strong fluctuations})\\
&\sigma_R^2>>1,\ \sigma_R^2\to\infty \quad (\text{saturation regime})
\end{aligned} \tag{2.71}$$

For a Gaussian-beam the above criteria based on σ_R^2 is not adequate the conditions for a Gaussian-beam are

$\sigma_R^2<1$ and $\sigma_R^2\Lambda^{5/6}<1$ (weak fluctuations)

Where $\Lambda=\dfrac{2L}{kW^2}$, W= free-space beam radius at the receiver.

If either of these conditions fails, the fluctuations are classified as moderate to strong.

Historically there are two approaches to solve the scalar stochastic Helmholtz Eq. (2.66): Born approximation and Rytov approximation. In the Born approximation, the solution of the Eq. (2.66) is assumed to be a sum of terms of the form

$$\mathrm{U(r)=U_o(r)+U_1(r)+U_2(r)+\ldots} \tag{2.72}$$

$U_o(r)$ represents the unperturbed field, i.e, an optical wave travelling through free-space, $U_1(r)$ and $U_2(r)$ denote first-order, and so on, perturbations caused by inhomogeneities due to the random term $n_1(r)$ in the refractive index. The Rytov approximation, on the other hand, assumes a solution for Eq. (2.66) formed by the unperturbed field $U_o(r)$ modified by complex phase-perturbation, terms, represented by

$$\mathrm{U(r)=U_o(r)\exp\left[\varphi_1(r)+\varphi_2(r)+\ldots\right]} \tag{2.73}$$

Where $\varphi_1(r)$ and $\varphi_2(r)$ are first and second-order phase perturbations terms. These perturbations are defined by

$$\begin{aligned}\varphi_1(r) &= \Phi_1(r)\\ \varphi_2(r) &= \Phi_2(r) - \frac{1}{2}\Phi_1^2(r)\end{aligned} \tag{2.74}$$

where the new function $\Phi_m(r)$ in Eq. (2.74) is related to the Born-perturbation terms by

$$\Phi_m(r) = \frac{U_m(r)}{U_o(r)} \tag{2.75}$$

Under weak fluctuation theory, the second-order moment, or MCF as defined in Eq. (2.26), can be expressed as (see Eq. 36 of Andrews and Phillips, 2005 [26]).

$$\Gamma_2(r_1, r_2, L) = \Gamma_2^o(r_1, r_2, L)\exp[\sigma_r^2(r_1, L) + \sigma_r^2(r, L) - \mathrm{T}].\ \exp[-1/2\Delta(r_1, r_2, L] \tag{2.76}$$

$$\text{where, } \Gamma_2^o(r_1, r_2, L) = \mathrm{U}_o(r_1, L)\mathrm{U}_o^*(r_2, L) < \exp[\varphi(r_1, L) + \varphi^*(r_2, L)] > \tag{2.77}$$

$$\sigma_r^2(r, L) = 2\pi^2 k^2 L \int_o^1 \int_o^\infty k\Phi_n(k)\exp\left(\frac{-\Lambda L k^2 \xi^2}{k}\right)[I_o(2\Lambda r\xi k) - 1]dkd\xi \tag{2.78}$$

$$\mathrm{T} = 4\pi^2 k^2 L \int_0^1 \int_0^\infty k\Phi_n(k)\left[1 - \exp\left(\frac{-\Lambda L k^2 \xi^2}{k}\right)\right]dkd\xi \tag{2.79}$$

and $I_o(x) = J_o(i\,x)$ is the modified Bessel function. The Gaussian-beam parameters can be characterized by

$$\theta_o = 1 - \frac{L}{F_o}$$

and by the output parameter in the receivers plane at $z = L$,

$$\Theta = 1 + \frac{L}{F} = \frac{\theta_o}{\theta_o^2 + \Lambda_o^2} \tag{2.80}$$

$$\Lambda = \frac{2L}{kW^2} = \frac{\Lambda_0}{\theta_o^2 + \Lambda_o^2} \tag{2.81}$$

where W and F are the beam radius and phase front radius at the receiver plane, respectively.

Mean Irradiance and Beam Spreading Due to Turbulence

The mean from the Eq. (2.68) gives

$$\left\langle \mathrm{I}(\mathrm{r},\mathrm{L})\right\rangle = \Gamma_2(r,r,L) = \frac{W_o^2}{W^2}\exp\left(-\frac{2r^2}{W^2}\right)\exp[2\sigma_r^2(r,L)-T] \tag{2.82}$$

For a Kolmogorov spectrum (Eq. 2.60)

$$\Phi_n(k) = 0.033C_n^2 k^{-11/3}$$

the quantity $\sigma_r^2(r,L)$ from Eq. (2.78) can be evaluated and is given by [26]

$$\begin{aligned}\sigma_r^2(r,L) &= 0.066\sigma_R^2\Lambda^{5/6}\left[1-{}_1F_1\left(-\frac{5}{6};1;\frac{2r^2}{W^2}\right)\right]\\ &\cong 1.11\sigma_R^2\Lambda^{5/6}\frac{r^2}{W^2}, \qquad r < W\end{aligned} \tag{2.83}$$

Where $\sigma_R^2 = 1.23\,C_n^2\mathrm{k}^{7/6}\mathrm{L}^{11/6}$ is the Rytov variance, and ${}_1F_1(a;\,c;\,x)$ is the confluent hyper-geometric function.

The Eq. (2.82) can then be approximated by the Gaussian function as follows

$$\left\langle \mathrm{I}(\mathrm{r},\mathrm{L})\right\rangle \cong \frac{W_o^2}{W_{LT}^2}\exp\left(-\frac{2r^2}{W_{LT}^2}\right)\left[W/m^2\right] \tag{2.84}$$

where W_{LT} is a measure of the effective or, long-term beam spot size given by,

$$\mathrm{W_{LT}} = W\sqrt{1+T} = W\sqrt{1+1.33\sigma_R^2\Lambda^{5/6}} \tag{2.85}$$

Mean Irradiance and Beam Spread for Strong Fluctuations **[26]** The Rytov variance criterion for strong fluctuation condition is

$\sigma_R^2 >> 1$, or $\sigma_R^2\ \Lambda^{5/6} >> 1$

$\Lambda = \dfrac{2L}{kw^2}$ where w is the spot size of the Gaussian beam parameter at the receiver. The mean irradiance in this case is given by

$$\left\langle \mathrm{I}(\mathrm{r},\mathrm{L})\right\rangle = \frac{W_o^2}{W_{LT}^2}\exp\left(-\frac{2r^2}{W_{LT}^2}\right) \tag{2.86}$$

Where W_{LT} is the effective or long-term spot radius

$$\begin{aligned} \mathrm{W_{LT}} &\cong W\sqrt{1+1.63\sigma_R^{12/5}\Lambda} = W\sqrt{1+4q\Lambda/3} \\ L &<< z_i = \left(C_n^2 k^2 l_o^{5/3}\right)^{-1} \quad q = 1.22\,\sigma_R^{12/5} \end{aligned} \tag{2.87}$$

This is valid for the propagation length $L<<z_i$, which is valid under most practical situation.

Scintillation Index Atmospheric turbulence can ultimately limit the FSO communications performance. Scintillation index is therefore very critical in determining the communications system performance when data with high bandwidth is transferred through atmospheric turbulence. The notation and the development of the mathematical formulations used in this section are taken from Andrews and Phillips, 2005 [26]. Results are provided for both weak and strong turbulence regimes.

The fourth-order cross-coherence function:

From the Eqs. (2.67) and (2.65b), the fourth-order cross-coherence function for a beam wave can be expressed in a general form.

$$\begin{aligned} &\Gamma_4\left(r_1, r_2, r_3, r_4, L\right) = U_{o(r_1, L)}\, U^*_{o(r_2, L)} U^*_{o(r_3, L)} U^*_{o(r_4, L)} \\ &\left\langle \exp\left[\phi(r_1, L) + \phi^*(r_2, L) + \phi(r_3, L) + \phi^*(r_4, L)\right]\right\rangle \end{aligned} \tag{2.88}$$

Note that the scintillation index $\sigma_I^2(r, L)$ is given by Eq. (2.69) which can be written as

$$\sigma_I^2(r, L) = \frac{\Gamma_4(r, L)}{\left[\Gamma_2(r, L)\right]^2} - 1 = \frac{< I^2(r, L) >}{< I(r, L) >^2} - 1 \tag{2.89}$$

A general expression for the scintillation index for the special case of a Kolmogorov spectrum is given by Andrews and Phillips, 2005 [26] as follows

$$\begin{aligned} &\sigma_I^2(r, L) = \\ &3.86\sigma_R^2 R_e\left[i^{5/6}\,{}_2F_1\left(-\frac{5}{6}, \frac{11}{6}; \frac{17}{6}; \bar{\Theta} + i\Lambda\right)\right] - 2.64\sigma_R^2\Lambda^{5/6}\,{}_1F_1\left(-\frac{5}{6}; 1; \frac{2r^2}{W^2}\right) \end{aligned} \tag{2.90}$$

Where ${}_2F_1(a; b; c; x)$ is the hyper-geometric function of Guass and ${}_1F_1(a; b; x)$ is the confluent hyper-geometric function of the first kind.

An approximate simple algebraic form for the scintillation index is [26]

$$\begin{aligned} &\sigma_I^2(r, L) \cong 4.42\sigma_R^2\Lambda^{5/6}\frac{r^2}{W^2} + 3.86\sigma_R^2 \\ &\left\{0.40\left[(1+2\Theta)^2 + 4\Lambda^2\right]^{5/12}\cos\left[\frac{5}{6}\tan^{-1}\left(\frac{1+2\Theta}{2\Lambda}\right)\right] - \frac{11}{16}\Lambda^{5/6}\right\} \ldots\ldots \mathrm{r<w} \end{aligned} \tag{2.91}$$

where σ_R^2 is the Rytov variance for a plane wave. Note that for a plane wave $(\Theta = 1, \Lambda = 0)$ and a spherical wave $(\Theta = \Lambda = 0)$, the scintillation index for a Kolmogorov spectrum can simplified as

$$\begin{aligned} \sigma_I^2(L) &= \sigma_R^2 = 1.23 C_n^2 k^{7/6} L^{11/6} \quad (\text{plane wave}) \\ \sigma_I^2(L) &= 0.5 C_n^2 k^{7/6} L^{11/6} \quad (\text{spherical wave}) \end{aligned} \tag{2.92}$$

Scintillation index including inner scale effects:

The von *K′arma′n* spectrum can be used for computing scintillation index, which includes the effects of inner scale size l_o and outer scale size, L_o:

$$\Phi_n(k) = 0.033 C_n^2 \frac{\exp\left(-k^2/k_m^2\right)}{\left(k^2 + k_o^2\right)^{11/6}}, \quad \mathrm{k_m} = 5.92/\mathrm{l_o} \quad \mathrm{k_o} = 2\pi/\mathrm{L_o} \tag{2.93}$$

The scintillation index for plane wave and spherical wave including inner scale effects, 2005 [26]

$$\sigma_I^2(L) = 3.86\,\sigma_R^2 \left[\left(1 + \frac{1}{Q_m^2}\right)^{11/12} \sin\left(\frac{11}{6}\tan^{-1} Q_m\right) - \frac{11}{6} Q_m^{-5/6} \right]$$

$$\sigma_I^2(L) = 9.65\,\beta_o^2 \left[0.40 \left(1 + \frac{9}{Q_m^2}\right)^{11/12} \sin\left(\frac{11}{6}\tan^{-1}\frac{Q_m}{3}\right) - \frac{11}{6} Q_m^{-5/6} \right]$$

where

$$Q_m = \frac{Lk_m^2}{k} = \frac{35.04L}{kl_0^2}, \quad \beta_o^2 = 0.5 C_n^2 \mathrm{k}^{7/6} \mathrm{L}^{11/6} \ (\text{Spherical wave}) \tag{2.94}$$

$$(\text{Spherical wave Rytov variance})$$

Case of Strong Turbulence The scintillation results described earlier were limited to weak fluctuations as defined by $\sigma_R^2 < 1$. Strong fluctuations situation can be attained when the, strength of the turbulence parameter C_n^2 is high and for long-range communication link (e.g., ≈ 5 km or longer). The scintillation index for strong turbulence regime is typically $\sigma_R^2 \approx 1$ to $\sigma_R^2 > 1$. The saturation regime is defined when $\sigma_R^2 \to \infty$. The extended Rytov theory has been recently applied to explain the irradiance fluctuations applicable for moderate-to-strong turbulence regimes. The extended theory assumes an "effective" random part of the refractive index term as follows:

$$\mathrm{n_{1,e}}(\mathrm{r}) = \mathrm{n_x}(\mathrm{r}) + \mathrm{n_y}(\mathrm{r}) \tag{2.95}$$

where $n_x(r)$ and $n_y(r)$ are large-scale and small-scale in homogeneities, respectively. The received irradiance of an optical wave is the resultant of the small-scale (diffractive) fluctuations multiplicatively modulated by random large-scale (refractive) fluctuations.

The perturbed optical wave can be written in this case as

$$\begin{aligned} &\mathrm{U}(\mathrm{r}) = U_o(\mathrm{r},\mathrm{L}) \exp\left[\phi_x(r,L)+\phi_y(r,L)\right] = U_o(\mathrm{r},\mathrm{L}) \\ &\exp\ \varphi_x(r,L).\exp\varphi_y(r,L) \end{aligned} \tag{2.96}$$

The extended Rytov theory also assumes the form of the atmospheric, spectrum as an "effective" spectrum given by

$$\Phi_{n,e}(k) = \Phi_n(k)\mathrm{G}(\mathrm{k},\mathrm{l_o},\mathrm{L_o}) = 0.033C_n^2\mathrm{k}^{-11/3}\mathrm{G}(\mathrm{k},\mathrm{l_o},\mathrm{L_o}); \tag{2.97}$$

where $G(k, l_o, L_o)$ is an amplitude spatial filter.

With the assumptions of "effective" random refractive index term and "effective" spectrum, Andrew and Phillips, 2005 [26] have derived the scintillation index for moderate-to-strong-to saturation regimes. A detailed explanation on the derivation of the scintillation index equations can be found in Andrews and Phillips, 2005 [14].

2.5 FSO Communication Signal Temporal Frequency Spectrum

For FSO communications, the irradiance fluctuations resulting from the propagation of optical beam through the atmospheric turbulence is one of the main noise. It is therefore necessary to formulate the temporal power spectrum of irradiance fluctuations, both on the optical axis and in points located at a certain distance from it. Quantitative analysis of the temporal behavior of the irradiance provides significant merit figures in the optical link. Without the detailed temporal information, the overall performance of a FSO communication link is essentially incomplete. The mean value of the SNR or the mean BER (to be discussed in other later chapter) are not the relevant parameters, but the instaneous values are important. In order to evaluate the burst error rate and the overall availability of the FSO communication system, a knowledge of the statistics of the instantaneous values is necessary [27]. Also, the temporal characteristics of the FSO system is necessary to develop and design optimal schemes for detection and coding.

Tatarskii [28] and Ishimaru [29] defined the temporal spectrum of irradiance fluctuations, or power spectral density (PSD) $S(w)$ by the Fourier Transform of the temporal covariance function as follows:

$$S(\omega) = 2\int_{-\infty}^{\infty} B_I(\tau,L)e^{-j\omega\tau}d\tau = 4\int_{-\infty}^{\infty} B_I(\tau,L)\cos(\omega\tau)d\tau \tag{2.98}$$

Where $B_I(\tau, L)$ is the temporal covariance function. The general fourth-order cross-coherence function was defined earlier by Eq. (2.67) and the mutual coherence function (MCF) by (2.66). The covariance function of irradiance is a two-point statistic defined by the normalized quantity.

$$\mathrm{B_I}\left(\mathrm{r_{l,}r_2}, L\right) = \frac{\Gamma_4(r_1, r_1, r_2, r_2, L) - \Gamma_2(r_1, r_1, L)\Gamma_2(r_2, r_2, L)}{\Gamma_2(r_1, r_1, L)\Gamma_2(r_2, r_2, L)} = \frac{\Gamma_4(r_1, r_1, r_2, r_2, L)}{\Gamma_2(r_1, r_1, L)\Gamma_2(r_2, r_2, L)} - 1 \tag{2.99}$$

For $r_1 = r_2 = r$,

$$\mathrm{B_I}(\mathrm{r,L}) = \frac{\Gamma_4(r, L)}{\left[\Gamma_2(r, L)\right]^2} - 1 \tag{2.100}$$

Andrew and Phillips [26] have worked out the detailed formulations of the temporal spectrum of irradiance. A summary of their results [26] are shown in the Table 2.1.

The temporal spectrum of irradiance for strong turbulence for a plane wave is outlined and calculated in the reference [26] by Andrews and Phillips, and is not repeated here.

2.6 PDF Models for Intensity Fluctuations Relevant to FSO Communication Systems

FSO communication systems have recently attracted considerable attention for a variety of applications because of the high bandwidths and the ability to transfer high data-rate of information. The performance of a laser-com system operating in the atmosphere is reduced by irradiance scintillations and phase fluctuations due to optical turbulence effects at the optical wavelength. Fading or scintillation impair and degrade FSO system performance particularly for link ranges of 1 km and above even in clear sky conditions. The reliability of FSO communication system depends on the probability of detection, miss and false alarm, and the probability of fade, all of which requires an accurate knowledge of the PDF for the received optical power. An accurate mathematical model for the exact PDF of the received signal under all intensity fluctuation regimes is difficult. From the probability theory random variable (discussed earlier in this chapter) is a function whose integral over an interval determines the probability that the random variable attains a certain value in that interval.

In a FSO communication system, the PDF of the received power at the photo detector is assumed to come from the same family as the PDF of irradiance at a point in the pupil plane of the receiver [26]. Over the last decades, various statistical models for irradiance PDF have been proposed for different degrees of turbulence regimes. Depending on weak or strong irradiance fluctuations and the propagation distances, these proposed PDFs have different forms.

Table 2.1 Temporal spectrum of irradiance

	Mathematical form
Plane wave (Kolmogorov spectrum, weak turbulence)	$S(\omega)=\frac{6.95}{\omega_t}\sigma_R^2\mathrm{Re}\left\{\left(\frac{\omega}{\omega_t}\right)^{-8/3}\left[1-{}_1F_1\left(-\frac{5}{6};-\frac{1}{3};-\frac{i\omega^2}{2\omega_t^2}\right)\right]-0.72\,\mathrm{i}^{4/3}{}_1F_1\left(\frac{1}{2};\frac{7}{3};-\frac{i\omega^2}{2\omega_t^2}\right)\right\}$ $\sigma_R^2=1.23\,C_n^2\mathrm{k}^{7/6}\mathrm{L}^{11/6}$ $\omega_t=\mathrm{V}_\perp/\sqrt{\frac{L}{k}}$, the characteristic frequency, where $\mathrm{V}_\perp$ = means transverse wind velocity, ${}_1F_1(a;c;x)$ is the confluent hyper-geometric function
Spherical wave (weak turbulence)	$S(\omega)=\frac{5.47}{\omega_t}\sigma_R^2\mathrm{Re}\left\{\left(\frac{\omega}{\omega_t}\right)^{-8/3}\left[1-{}_1F_1\left(-\frac{5}{6};-\frac{1}{3};-\frac{2i\omega^2}{9\omega_t^2}\right)\right]-0.24\mathrm{i}^{4/3}{}_1F_1\left(\frac{1}{2};\frac{7}{3};-\frac{2i\omega^2}{9\omega_t^2}\right)\right\}$ σ_R^2,ω_t defined above $\mathrm{S}(\omega)=\mathrm{S}_l(\omega,r)+\mathrm{S}_\mathrm{r}(\omega,r)$

Table 2.1 (continued)

Gaussian-beam wave (weak turbulence)	$S_l(\omega, r)$ = longitudinal component of power spectrum $= \frac{3.90}{\omega_t d_t^{5/6}} \sigma_R^2 \mathrm{Re}\left\{\left(\frac{\omega}{\omega_t}\right)^{-8/3}\left[{}_1F_1\left(-\frac{5}{6};-\frac{1}{3};-\frac{\omega^2}{4a_2\omega_t^2}\right)-{}_1F_1\left(-\frac{5}{6};-\frac{1}{3};-\frac{\omega^2}{4a_1\omega_t^2}\right)\right]\right.$ $\left. +0.29i^{4/3}\left[\frac{1}{a_2^{4/3}}\,{}_1F_1\left(\frac{1}{2};\frac{7}{3};-\frac{\omega^2}{4a_2\omega_t^2}\right)-\frac{1}{a_1^{4/3}}\,{}_1F_1\left(\frac{1}{2};\frac{7}{3};-\frac{\omega^2}{4a_1\omega_t^2}\right)\right]\right\}$ Where $a_1 = \frac{1}{4id_t\left[1-(\bar{\Theta}+i\Lambda)dt\right]}$ $a_2 = \frac{1}{4\Lambda d_t^2}$ $d_t = 0.67\text{-}0.17\,\Theta$ The Gaussian-beam parameters are defined elsewhere in the section

A closed form expression, theoretical or heuristic derivation, valid regimes of turbulence, number of PDF parameters, and relationships of parameters to physical quantities are discussed in this section for several commonly used PDF models that describe irradiance fluctuations. Some of the early studies in irradiance statistics focused on single family distributions. In many cases under real atmospheric conditions, due to the non-stationary nature of the turbulence along the propagation path, a single family distribution can not accurately describe irradiance statistics. In that case the technique used to develop PDF models treated the first-order PDF as a function of random parameters. The second-order PDF containing a single random parameter described the fluctuations of the mean of the first-order PDF. The unconditional PDF of irradiance fluctuations was then derived using conditional statistics: In addition experimental data of received irradiance fluctuations can generate higher-order moments which can then be inverted to reconstruct an unknown PDF (to be discussed later in this section). Alternatively, parameters of the theoretical distribution could be inferred by comparing higher-order moments of the theoretical distribution to calculated higher-order moments of experimental data [30]. The accuracy of a PDF could be judged by comparing higher-order moments. A heuristic model based on physical parameters has the advantage that it does not require parameters of the distribution to be inferred from observed moments [31].To derive a single distribution valid in weak fluctuations all the way through saturation is difficult. There is currently no closed-form PDF to completely describe the irradiance statistics in all regions of optical turbulence in the presence of aperture averaging. The Table 2.2 shows the functional forms of the commonly considered distributions and the applicability of the distributions for different turbulence regimes.

2.7 Reconstruction of PDF of Intensity Fluctuations Relevant FSO Communications Through Atmospheric Turbulence

The performance of FSO communication system can be significantly degraded by turbulence-induced scintillation resulting from beam propagation through the atmosphere. For example, scintillation can lead to power losses at the receiver and eventually to fading of the received signal below a prescribed threshold causing an increased BER (to be discussed later in other chapter). The reliability and the performance of the FSO communication system operating in such an environment can be derived from a mathematical description for the PDF of the randomly fading irradiance (intensity) signal. This section provides a methodology for computing a tractable PDF function of the laser irradiance fluctuations which is valid for various atmospheric conditions, such as weak, moderate, and strong turbulence regimes. The PDF is dependent on the FSO communications scenario, such as horizontal (terrestrial), ground/airborne-to-space (uplink), or space-to-ground/airborne data links as well as on the different atmospheric environments because of the different

Table 2.2 Proposed probability density functions (PDFs) of irradiance fluctuations as a function of normalized irradiance (< I > = 1):

PDF	Mathematical form, P(I)=….I > 0, < I > =1	Parameters
Nakami m-distribution	$\frac{1}{2\sigma_5^2}\exp\left(-\frac{I+A_o^2}{2\sigma_5^2}\right)I_o\left(\frac{A_o\sqrt{I}}{\sigma_5^2}\right)$ $I_0(.)$ is the zero-order modified Bessel function of the first kind	σ_5^2 = variance A_o = constant
Lognormal-distribution	$\frac{1}{I\sqrt{2\pi\,\sigma_{\ln I}^2}}\exp-\left\{\frac{\left[\ln(I)+\frac{1}{2}\,\sigma_{\ln I}^2\right]^2}{2\sigma_{\ln I}^2}\right\}=\frac{1}{I\sqrt{2\pi\,\sigma_I^2}}\exp-\left\{-\frac{\left[\ln(I)+\frac{1}{2}\,\sigma_I^2\right]}{2\sigma_I^2}\right\}$	$\sigma_{\ln I}^2$ =log-irradiancevariance σ_I^2 = scintillation index
K-distribution	$\frac{2\alpha}{\Gamma(\alpha)}(\alpha I)^{\frac{(\alpha-1)}{2}}K_{\alpha-1}(2\sqrt{\alpha I}),\quad I>0\,,\ \alpha>0$ Kn (.) is nth order modified Bessel function of the second kind	α = effective number of discrete scatterers
Universal-distribution [32]	$\frac{m\Gamma(m)}{b\Gamma(M)}e^{-mI/b}\sum_{k=o}^{\infty}\frac{(-1)^k}{k!}L_k(mI/b)$ $\sum_{j=o}^{k}\left[\begin{matrix}k\\j\end{matrix}\right]^2\frac{\Gamma(M+j)(rm/M)^j}{\Gamma(m-k+j)}$ Ln (…) is the nth order Laguerre polynomial, $\left[\begin{matrix}k\\j\end{matrix}\right]$ is the binomial coefficient,	b= mean intensity of diffuse component of scattered field c= mean intensity of specular component of scattered field r=c/b M= parameter related to the reciprocal of the variance of amplitude of specular component m=parameter related to the reciprocal of the variance of different component

Table 2.2 (continued)

PDF	Mathematical form, P(I)=….I>0, < I >=1	Parameters
I-K-distribution [33]	$\{2\alpha\,(1+\rho)[\frac{(1+\rho)I}{\rho}]^{\frac{(\alpha-1)}{2}}\,K_{\alpha-1}[2\sqrt{\alpha\rho}]I_{\alpha-1}[2\sqrt{\alpha(1+\rho)I}],\quad \ldots\quad I<\frac{\rho}{1+\rho}$ $2\,\alpha(1+\rho)[\frac{(1+\rho)I}{\rho}]^{\frac{(\alpha-1)}{2}}\,I_{\alpha-1}[2\sqrt{\alpha\rho}]\mathrm{K}_{\alpha-1}[2\sqrt{\alpha(1+\rho)}I],\quad \ldots I>\frac{\rho}{1+\rho}$	
	Kn (…) is the nth order modified Bessel function of the second kind I_p (x) is the modified Bessel function of the first kind and order p	α = effective number of scatterers ρ = coherence parameter
Generalized K-distribution [34]	$\frac{1}{2}I_o(\frac{\upsilon I^{1/2}}{\alpha})\int_o^\infty\{1+\frac{<N>}{\alpha}[1-\frac{J_o(\alpha\omega)}{I_o(\upsilon)}]\}^{-\alpha}J_o(I^{1/2}\omega)\omega d\,\omega$	N =discrete number of scaterers υ = departure from uniform phase of the complex scattered field α = deterministic amplitude
	J_0 (…) is the Bessel function of the first kind I_0(…) is a Modified Bessel function of the first kind	
Log normally modulated exponential (LNME)-distribution [35]	$\frac{1}{\sqrt{2\pi\sigma_z^2}}\int_o^\infty\frac{dz}{z^2}\exp[-\frac{I}{z}-\frac{(\ln(z)+\frac{1}{2}\sigma_z^2)^2}{2\sigma_z^2}]$	σ_z^2 = variance of the lognormal modulation factor,z=e2x
Log normally modulated Rician (LNMR)-distribution [31]	$\frac{(1+\rho)e^{-\rho}}{\sqrt{2\pi}\sigma_z}\int_o^\infty\frac{dz}{z^2}I_o[2\sqrt{\frac{(1+\rho)\rho I}{z}}]\exp[-\frac{(1+\rho)I}{z}-\frac{(\ln(z)+\frac{1}{2}\sigma_z^2)^2}{2\sigma_z^2}]$	ρ = coherence parameter σ_z^2 = variance of the lognormal modulation factor, z=e2x
Inverse-Gaussian (IG)-distribution [36]	$\sqrt{\frac{1}{2\pi\sigma_I^2 I^3}\exp\left(-\frac{(I-1)^2}{2\sigma_I^2 I}\right)}$	σ_I^2 = irradiance scintillation index

Table 2.2 (continued)

PDF	Mathematical form, P(I)=….I>0, < I >=1	Parameters
Gamma-Gamma distribution [26]	$p(I) = \frac{2}{\Gamma(\alpha)T(\beta)I}(\alpha\beta I)^{\frac{\alpha+\beta}{2}} K_{\alpha-\beta}\left(2\sqrt{\alpha\beta I}\right)$, I>0	α = effective number of large scale eddies β = effective number of small scale eddies
Exponential Weibull (EW)-distribution [37]	$\frac{\alpha\beta}{\eta}(\frac{1}{\eta})^{\beta-1}\exp[-(\frac{1}{\eta})^{\beta}]\{1-\exp[(\frac{I}{\eta})^{\beta}]\}^{\alpha-1}$	α = shape parameter that gives more versatility to the EW distribution in the shape of the tails, strongly depend as the receiver aperture size, α >o $\beta \cong (\alpha\sigma_I^2)^{-6/11}$ (shape-parameter) η (scale parameter) = $\frac{1}{\alpha\Gamma(1+1/\beta)g(\alpha,\beta)}$ $g(\alpha,\beta)\overset{\Delta}{=}\sum\frac{(-1)^i(i+1)^{-\frac{(1+\beta)}{\beta}}\Gamma(\alpha)}{i!\Gamma(\alpha-i)}$
Double-Weibull (DW)-distribution	$\frac{\beta_2 k(kl)^{1/2}}{(2\pi)^{\frac{l+k}{2}-1}} I^{-1}G_{k+l,o}^{o,k+l}\left[(\frac{\Omega_2}{I^{\beta_2}})^k k^k l^l \Omega_1^l \middle\vert \Delta(l;0),\underline{\Delta}(k;0)\right]$ $G_{p,q}^{m,n}$ [ ] is the Meijer's G-function (50, Eq. 9.301)	β_1,Ω_1 = parameters of a Weibull distribution for large scale turbulent eddies, β_2,Ω_2 = parameters of a Weibull distribution for small scale turbulent eddies $\Delta(j;x)\overset{\Delta}{=}\frac{x}{j};\ldots;\frac{x+j-1}{j}$

Table 2.2 (continued)

PDF	Mathematical form, P(I)=….I>0, < I >=1	Parameters
		l and k are positive integers that satisfy $\frac{l}{k}=\frac{\beta_2}{\beta_1}$ $\Omega_i=\left(\frac{1}{\Gamma\left(1+\frac{1}{\beta_i}\right)}\right)^{\beta_i}$ i=1, 2
Ma'laga (M)-distribution	$A\sum_{k=1}^{\beta} a_k I^{\frac{\alpha+k}{2}-1} K_{\alpha-k}\left(2\sqrt{\frac{\alpha\beta I}{\nu\beta+\Omega'}}\right)$ Where $A\overset{\Delta}{=}\frac{2\alpha^{\alpha/2}}{\nu^{1+\alpha/2}\Gamma(\alpha)}\left(\frac{\nu\beta}{\nu\beta+\Omega'}\right)^{\beta+\alpha/2}$ $a_k\overset{\Delta}{=}\binom{\beta-1}{k-1}\frac{(\nu\beta+\Omega')^{1-k/2}}{(k-1)!}\left(\frac{\Omega'}{\nu}\right)^{k-1}\left(\frac{\alpha}{\beta}\right)^{k/2}$ $K_\upsilon(\bullet)$ is the modified Besssel function of the second kind and order υ,	β = amount of fadingParameter $\nu=2b_o(1-\rho)$ $\Omega'=\Omega+\rho 2b_o$ $+2\sqrt{2b_o\Omega\rho}$ · $\mathrm{Cos}(\phi_A-\phi_B)$ $2b_o$ = Average value of the intensity of quasi-forward scattered field and field scattered to the receiver by off-axis eddies, ϕ_A and ϕ_B are the deterministic phases of the line-of-sight and coupled-to-line-of -sight scatter terms, Ω = average power of the Line-of-sight term of optical field. α = effective number of large-scale cells of the scattering process $_{\mathrm{O}}\leq\rho\leq 1=$ factor expressing the amount of scattering power coupled to the line-of-sight component of optical field

optical wave propagation effects. Since the characteristic function of the random variable (e.g., laser intensity fluctuations) contains a series of moment terms of higher orders, the information about the probability distribution can be obtained from these moments. The higher-order moments give more information concerning the contributions from the tails of the PDF [38, 39]. Even- and odd-order moments give information generally about the width and the lack of symmetry of the distribution, respectively. In many practical cases, such as laser beam propagation through atmospheric turbulence, one deals with random processes where the probability distribution is in general non-Gaussian. The analysis of a non-Gaussian statistics of the received intensity fluctuations may require higher-order correlation study. In many cases, it is necessary to consider beyond the fourth-order moments. For practical purposes, moments up to eighth order are usually sufficient for the statistical characterization of the non-Gaussian random process, although the moments for some statistical distributions do not define the process always uniquely [40].

Fundamental Limitations in Reconstructing the PDF Based on Higher-order Moments An experiment of irradiance fluctuations through atmospheric turbulence measures the instantaneous intensity as a function of time from which a histogram of irradiance (i.e., number of occurrences versus bins of values that the random variables can assume) is constructed. The reconstructed PDF is then obtained by fitting the experimental data to a prescribed parametric function. There are several different PDF's that can be used to fit this histogram; therefore, a unique PDF cannot be derived from the histogram and an exact model of the random process is not available. If we incorrectly "smooth" the histogram by a well-behaved line so that an incorrect PDF can be matched to the resulting line, most of the times information about the random process is lost. The method based on higher-order moments can solve this problem and can reconstruct accurately the unknown PDF describing the random process. The method of moments (see the moment problem [41]) can provide, in principle, a complete knowledge of phenomenon when infinitely many moments are known whose implementation is not often practical due to measurement uncertainties and computational limitations. One needs a very large amount of samples to derive accurate higher-order moments, but must record all data while experimental conditions remain the same. Thus the samples must be kept statistically independent.

There are basically two methods available for obtaining a PDF from experimental data: (1) Construct a histogram from the data and compare it to known PDF's. One then selects the PDF that in some way best matches the histogram and uses that PDF to model the random process, (2) Calculate the moments of the data and compare them to moments of known PDF's. Again the PDF whose moments best match the data moments is used to describe the random process. The proposed method provides a methodology for computing the PDF function in terms of physics based functions a weighted set of finite number of moments from observed experimental data.

Analytical Techniques to Reconstruct PDF from Higher-order Moments The method described here is based on generalized Laguerre Polynomial expansion and is outlined in details elsewhere [42].

In this method, the PDF is expressed in terms of the corresponding lower-order moments, whether measured or derived theoretically. The sought-for PDF is given by a gamma PDF modulated by a series of generalized Laguerre polynomials; the expansion coefficients are expressed in terms of the intensity moments with the nth coefficient containing only the first n moments. The Laguerre PDF is not a statistical fit to the data; there are no free parameters in this expansion, and the answer depends directly on the first n moments. This proposed method is a scheme for solving this reduced moment problem with use of either measured moments or theoretically derived moments and is based on generalized Laguerre polynomials expansion.

The proposed intensity PDF is given by (denoting x = intensity)

$$f(x) = f_g(x)\sum_{n=0}^{\infty} W_n L_n^{(\beta-1)}\left(\frac{\beta x}{\mu}\right) \tag{2.101}$$

where x is the random intensity $(0 \le x \le \infty)$. Here $f_g(x)$ is the gamma PDF

$$f_g(x) = \frac{1}{\Gamma(\beta)}\left(\frac{\beta}{\mu}\right)^{\beta} x^{\beta-1}\exp(-\beta x/\mu) \tag{2.102}$$

where $\mu = < x >$, the mean value of x

and $\beta = \dfrac{< x >^2}{< x^2 > - < x >^2}$

The generalized Laguerre polynomials are defined by

$$L_n^{(\beta-1)}(x) = \sum_{l=0}^{n}\binom{n+\beta-1}{n-l}\frac{(-x)^l}{l!} \tag{2.103}$$

They are orthogonal with respect to $f_g(x)$.

Using the orthogonality condition we can show that the W_n expansion coefficients are given by

$$W_n = n!\Gamma(\beta)\sum_{l=0}^{n}\frac{(-\beta/\mu)^l < x^l >}{l!(n-l)!\Gamma(\beta+l)} \tag{2.104}$$

where $< x^l >$ is the intensity moment of order l.

Furthermore,

$$W_0 = 1$$

$$W_1 = W_2 = 0$$

so that

$$f(x) = f_g(x)\left[1 + \sum_{n=3}^{\infty} W_n L_n^{(\beta-1)}(\beta I)\right] \tag{2.105}$$

Let us denote the normalized intensity, $I = \frac{x}{< x >}$

$$\text{Then } f(I) = f_g(I)\left[1 + \sum_{n=3}^{\infty} W_n L_n{}^{(\beta-1)}(\beta I)\right] \tag{2.106}$$

$$\text{Where } f_g(I) = \frac{1}{\Gamma(\beta)}\beta^{\beta} I^{\beta-1}\exp(-\beta I) \tag{2.107}$$

$$\text{and, } W_n = n!\Gamma(\beta)\sum_{l=0}^{n}\frac{(-\beta)^l < I^l >}{l!(n-l)!\Gamma(\beta+l)} \tag{2.108}$$

where $< I^l >$ is the normalized intensity moment of order *l*.

Also note that

$$L_n{}^{(\beta-1)}(x) = \frac{(\beta)n}{n!} 1F_1(-n;\beta;x) \tag{2.109}$$

where ${}_1F_1$ is confluent hypergeometric function, and the notation $(\beta)n = (\beta)(\beta+1))\beta+2)\ldots\ldots(\beta+n-1)$ is used.

Using Eqs. (2.107), (2.108), and (2.109), we can thus reconstruct the PDF defined by the Eq. (2.106).

Test of the reconstruction method of PDFs: With the analytical expressions for the three-test probability density functions as defined below (Log-Normal, Rice-Nakagami, and Gamma-Gamma), the ideal PDF and the PDF fit with the generalized Laguerre polynomials, after the reconstruction from the higher-order moments are compared.

Log-normal PDF (parameters μ and σ):

(Notation: I= intensity of laser fluctuations)

$$p(I) = \frac{1}{\sqrt{2\pi}\cdot\sigma\cdot I} e^{-\frac{(\log I-\mu)^2}{2\sigma^2}} \tag{2.110}$$

Higher-order moments: $\mu_k = e^{\frac{1}{2}k^2\varpi^2 + k\mu}$

Rice-Nakagami PDF (parameters β and):

$$\text{PDF}:(I) = \frac{(1+\beta)}{< I >}\exp(-\frac{(1+\beta)}{< I >}\cdot I)\cdot\exp(-\beta)\cdot I_0\left[2\sqrt{\frac{\beta(1+\beta)}{< I >}\cdot I}\right] \tag{2.111}$$

I_0 = Modified Bessel function of order zero.

Higher-order Moments:

$$m_k = (\frac{< I >}{(\beta+1)})^k\cdot\exp(-\beta)\cdot\left[\Gamma(k+1)/\Gamma(1)\right]\cdot{}_1F_1(k+1;1;\beta) \tag{2.112}$$

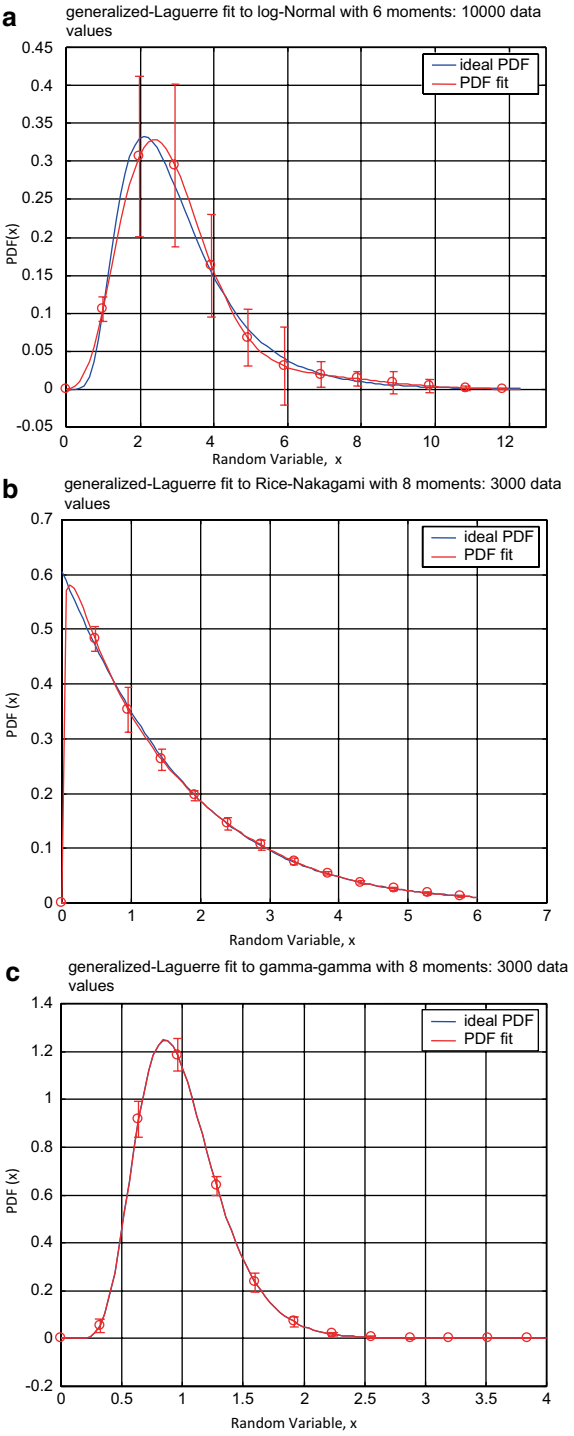

Fig. 2.7 **a** Generalized Laguerre PDF fit: 10,000 data points: Log-Normal distribution, Moment Order = 6, parameters, mean = 1.0, sigma = 0.5; **b** Generalized Laguerre PDF fit: 3,000 data points: Rice Nakagami distribution, Moment Order = 8, parameters, mean = 1.5, beta = 0.5; **c** Generalized Laguerre PDF fit: 3,000 data points: Gamma-Gamma distribution, Moment Order = 8, parameters, alpha = 17.13, beta = 16.04(*Reprinted with permission from SPIE, 2007*)

where $\Gamma(x)$ is a Gamma function, and ${}_1F_1(a;b;z)$ is a Confluent Hypergeometric function or Kummar function.

Gamma-Gamma distribution PDF (parameters α and β):

$$PDF: p(I) = \frac{2(\alpha\beta)^{(\alpha+\beta)/2}}{\Gamma(\alpha)\Gamma(\beta)} \cdot I^{(\alpha+\beta)/2-1} \cdot K_{\alpha-\beta}(2\sqrt{\alpha\beta I}), \qquad I > 0 \tag{2.113}$$

where $K_p(x)$ is a Modified Bessel function of the second kind.

Higher-order moments:

$$m_k = \frac{1}{(\alpha\beta)^k} \cdot \frac{\Gamma(k+\alpha)\cdot\Gamma(k+\beta)}{\Gamma(\alpha)\cdot\Gamma(\beta)} \tag{2.114}$$

Γ(x) is a Gamma function.

Figure 2.7 shows the analytical Log normal, Rice Nakagami, and Gamma-Gamma PDFs, and the generalized Laguerre polynomial expansion fit for moment orders as shown for each curves. The error bars are also shown in the figures. In the Fig. 2.7, the random variable, *x* is the "intensity" and the PDF of intensity is shown in the Y-axis. Results show excellent agreement of the PDF fit was obtained by the method developed. The accuracy of the reconstructed PDF is also evaluated. Reconstructing the unknown PDF by the method outlined here, we should be able to determine design parameters needed for the FSO communication system to operate under various atmospheric conditions.

References

1. A.M. Yaglom, *An Introduction To The Theory Of Stationar Random Functions* (Dover Publications Inc., New York, 1962). (Translated and Edited by Richard A. Silverman)
2. P. Beckman, *Probability in Communication Engineering* (Harcourt, Brace & World, Inc., New York, 1967)
3. L.C. Andrews, R.L. Phillips, *Laser Beam Propagation Through Random Media* (SPIE Engineering, Bellingham, 1998)
4. S.V. Kartalopoulos, Free Space Optical Networks For Ultra-Broad Band Services (IEEE/Wiley, Hoboken, 2011)
5. L.C. Andrews, R.L. Phillips, C.Y. Hopen, *Laser Beam Scintillation With Application* (SPIE, Bellingham, 2011).
6. J.C. Ricklin, S.M. Hammel, F.D. Eaton, S.L. Lachinova, Atmospheric channel effects on free-space laser communication, in Arun K. Majumdar and Jennifer C. Ricklin "Free-Space Laser Communications: Principles and Advances". 9–56, Springer, New York (2008).
7. D. Kedar, S. Arnon, Evaluation of coherence interference in optical wireless communication through multi-scattering channels, Appl Opt. **45**(14), 3263–3269 (2006).
8. S. Jaruwatanadilok, Underwater wireless optical communication channel modeling and performance evaluation using vector radiative transfer theory, Selected Areas in communications, IEEE J. **26**(9), 1620–1627 (2008).
9. D. Kedar, Underwater sensor network using optical wireless communication, SPIE. Newsroom—The International Society for Optical Engineering (2007)

10. K. Akhavan, M. Kavehrad, S. Jivkova, High-speed-power-efficient indoor wireless infrared communication using code combining—part 1, IEEE Trans. Commun. **50**(7), 1098–1109 (2002)
11. D. O' Brien, Indoor optical wireless communications: Recent developments and future challenges, Proc. SPIE. **7464**, 7464B (2009)
12. W. Dta, Laser beam attenuation determine by the method of available applied power in turbulent atmosphere, J Telecommun Inf Technol, (2009)
13. K. Wang, L. Zeng, C. Yin, Influence of the incident wave-front on intensity distribution of the non-diffracting beam used in large-scale measurement, Opt Commun. **216**, 99–103 (2003)
14. V. Kollárová, T. Med ik, R. $\bar{C}$ elechovsk y', Z. Bouchal, O. Wilfert, Z. Kolka, Application of non-diffracting beams to wireless optical communications "Application of nondiffracting beams to wireless optical communications", Proc. SPIE 6736, Unmanned/Unattended Sensors and Sensor Networks IV, 67361C (October 05, 2007); doi:10.1117/12.737361.
15. M. Duocastella, A.B. Craig, Bessel and annular beams for materials processing, Laser Photonics Rev. **6**, No.5, 607–621 (2012)
16. H.T. Eyyuboglu, C. Arpali, Y. Baykal, Flat topped beams and their characteristics in turbulent media, Opt. Express. **14**(10), 4196 (2006)
17. A.C. Schell, The multiple plate antenna, Ph.D Dissertation, Massachusetts Institute of Technology, Cambridge; MA 1961
18. J. Wu, A.D. Boardman, Coherence length of a Gaussian-Schell beam and atmosphere turbulence, J. Mod. Opt. **38**, 1355–1363 (1991)
19. G. Gbur, E. Wolf, Spreading of partially coherent beams in random media, J. Opt. Soc. Am. A. **19**, 1592–1598 (2002)
20. G. Gbur, O. Korotkova, Angular spectrum representation for the propagation of arbitrary coherent and partially coherent beams through atmospheric turbulence, J. Opt. Soc. Am A. **24**, 745–752 (2007)
21. B. Chen, Z. Chen, J. Pu, Propagation of partially coherent Bessel-Gaussian beams in turbulent atmosphere, Opt Laser Technol. **40**, 820–827 (2008)
22. M. Yoshikawa, A. Murakami, J. Sakurai, H. Nakayama, T. Nakamura, High power VCSEL devices for free space optical communications, IEEE Electron Compon Technol Conf, **2**, 1353–1358 (2005)
23. A.D. Wheelon, *Electromagnetic Scintillation, Vol.1*, *Geometrical Optics* (Cambridge University, Cambridge, 2001)
24. N.K. Vinnichenko, et al. *Turbulence in the Free Atmosphere* (Consultants Bureau, New York, 1980)
25. R. Hill, Models of scalar spectrum for turbulent advection, J. Fluid Mech. **88**, 541–662 (1978)
26. L.C. Andrews, R.L. Phillips, Laser Beam Propagation Through Random Media, (SPIE, Bellingham, 2005)
27. H.R. Anderson, *Fixed Broadband Wireless System Design* (Wiley, West Sussex, 2003)
28. V.I. Tatrskii, *The effects of the turbulent atmosphere on wave propagation, A*vailable from U.S. Department of Commerce, Springfield, VA 22151, Translated by IPST Satf, 1971
29. A. Ishimaru, Wave Propagation And Scattering In Random Media (IEEE, Piscataway, 1997)
30. A.K.Majumdar, H. Gamo, Statistical measurements of irradiance fluctuations of a multipass laser beam propagated through laboratory-simulated atmospheric turbulence, Appl. Opt. 21 (12), 2229-2235 (1982).
31. J.H. Churnside, S.F. Clifford, Log—normal Rician probability—density function of optical scintillations in the turbulent atmosphere, J. Opt. Soc. Am. A, **4**, 1923–1930 (1987)
32. R.L. Phillips, L.C. Andrews, Universal statistical model for irradiance fluctuations in a turbulent medium, J. Opt. Soc. Am. **72**, 864–870 (1982)
33. L.C. Andrews, R.L. Phillips, I-K distribution as a universal propagation model of laser beams in atmospheric turbulence, J. Opt. Soc. Am. A. **2**, 160–163 (1985)
34. R. Barakat, Weak—scatterer generalization of the K—density function with application to laser scattering in atmospheric, J. Opt. Soc. Am. A. **3**, 401–409 (1986)

35. J.H. Churnside, R.J. Hill, Probability density of irradiance scintillations for strong path-integrated refractive turbulence, J. Opt. Soc. Am. A. **4**, 727–733 (1987)
36. N.D. Chatzidiamantis, H.G. Sandalidis, G.K. Karagiannidis, M. Matthaiou, Inverse Gaussian modeling of turbulence-induced fading in Free-Space Optical Systems, J. Lightwave Technol. **29**(10) (2011)
37. R. Barrios, F. Dios, Exponential Weibull distribution family under aperture averaging for Gaussian beam waves, Opt Express. **20**(12), 13055–13064 (2012)
38. A.K. Majumdar, Higher-order statistics of laser-irradiance fluctuations due to turbulence, J.Opt. Soc. Am. A. **1**, 1067–1074 (1984)
39. A.K. Majumdar, Higher-order skewness and excess coefficients of some probability distributions applicable to optical propagation phenomena, J. Opt. Soc. Am. **69**(1), 199–202 (1979)
40. A.K. Majumdar, Uniqueness of statistics derived from moments of irradiance fluctuations in atmospheric optical propagation, Opt. Commun. **50**(1), 1–7 (1984)
41. J.A. Shehat, J.D. Tamarkin, *The Problem Of Moments* (American Mathematical Society, New York, 1943)
42. A.K. Majumdar, C.E. Luna, P.S. Idell, Reconstruction of Probability Density Function of intensity fluctuations relevant to Free-Space Laser communications through atmospheric turbulence, Proc. SPIE. **6709**, 67090 M-1-67090 M—15, (2007)

Chapter 3
Modulation, Detection, and Coding for Free-space Optical (FSO) Communications

Arun K. Majumdar

3.1 Introduction

The process of modulation consists of mapping the information onto magnetic medium (a carrier). There are mainly three parameters of the carrier which can be varied to perform the modulation process for mapping the information into changes in either the amplitude, phase, or frequency of the carrier. The result of this modulation process is amplitude, phase, and frequency modulations, respectively. Demodulation is the reverse process of removing the carrier signal to obtain the original signal waveform (and thus the message/information) back.

The source of information can be analog or digital. In digital communication, the signal produced by this source is converted into digital signal consists of 1s and 0s. The object will be to use as few binary digits as possible to represent the signal in such a way this efficient representation of the source output result in little or no redundancy. The sequence of binary digits is called information sequence. The process of efficiently converting the output of either analog or digital source into a sequence of binary digits is known as source encoding. This is accomplished by a source encoder as shown in the Fig. 3.1 which is a typical system configuration. The information sequence is passed through the channel encoder in order to introduce, in a controlled manner, some redundancy in the binary information sequence that can be used at the receiver to overcome the effects of noise and interference encountered in the transmission on the signal through the channel. A block of information bits k is mapped via encoding to codeword n, and by modulation to a channel symbol vector x which is transmitted over an optical channel. The communication channel is the physical medium that is used for transmitting signals from transmitters to receiver. For free-space optical (FSO) communications, the optical channel consists of atmosphere. The optical detector output is quantized and synchronized providing either slot counts or symbol estimates y to the channel decoder. The receiver maps detector outputs to a quantized signal. The decoder using the channel output information performs the process of demodulation and generates estimates $\hat{k}$ of the transmitted user data. The original information sequence is thus reconstructed from the knowledge of the code used by the channel encoder and the redundancy contained in the

A. K. Majumdar, *Advanced Free Space Optics (FSO),*
Springer Series in Optical Sciences 186, DOI 10.1007/978-1-4939-0918-6_3,
© Springer Science+Business Media New York 2015

received data. The performance of the FSO communication system operating in the atmospheric channel is measured in terms of the bit error rate (BER; to be discussed later in this chapter) which is typically of the order of 10^{-6}. When a codeword error is detected, the entire codeword is discarded. A real system configuration is however much more complicated. When a multiuser system is needed, a multiplexing stage is inserted before the modulator. For multi-station system, a multiple access control stage before the transmitter will be required to be inserted. In some complex system, frequency spread and encryption can also be added to the system.

3.2 Digital Communications System: Modulation and Demodulation

The modulation and demodulation techniques introduced in one block diagram of digital communication system (Fig. 3.1) can be described by Fig. 3.2. This is a simplified system model for understanding and analyzing the performance of modulation and demodulation. The system model excludes irrelevant blocks with regard to modulation so that relevant blocks stand out [1]. As mentioned in the reference [1], recently [5] developed techniques combine modulation and channel coding together where the channel encoder is also a part of the modulator with the channel decoder being a part of the demodulator.

The communication signal $s(t)$ from the modulator must pass the transmitter, the communication channel (transmission medium), and the receiver (not shown) before it can reach the demodulator. The received signal at the input of the demodulator can be described as

$$r(t) = A(t)[s(t) * h(t)] + n(t) \tag{3.1}$$

where $h(t)$ is the impulse response of the channel filter, * denotes convolution, $A(t)$ is the multiplicative contribution due to the fading (temporally varying) channel, and $n(t)$ is the additive noise and interference. The channel transfer function can be lumped together with the transmitter, channel, and the receiver transfer functions as follows:

$$H(f) = H_T(f)\, H_C(f)\, H_R(f) \tag{3.2}$$

$H_T(f)$, $H_C(f)$, and $H_R(f)$ are the transfer functions of the transmitter, channel, and receiver, respectively. The impulse response of the channel filter, is therefore (by taking the inverse of Eq. (3.2)).

$$h(t) = h_T(t) * h_C(t) * h_R(t) \tag{3.3}$$

where $h_T(t)$, $h_C(t)$, and $h_R(t)$ are the impulse responses of the transmitter, the channel, and the receiver, respectively. The term $A(t)$ in the Eq. (3.1) represent the fading

Fig. 3.1 Block diagram of a typical digital communication system

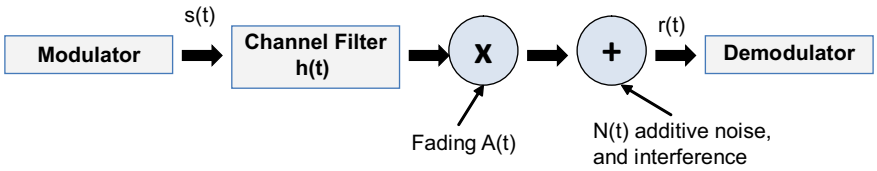

Fig. 3.2 Digital communication system model for modulation and demodulation

from the atmospheric channel. $A(t)$ is a random signal characterized by the random intensity fluctuations of optical wave when propagated through atmospheric turbulence. The exact form of the random signal $A(t)$ is not deterministic, but the statistical distributions can be estimated from the recent propagation models.

3.3 FSO Communication Channel Models

In order to design and optimize the performance of a FSO communication system, a knowledge of channel characteristics is important so that the right modulation scheme can be used to accomplish the communications system's requirements. Different modulation schemes are studied for different channels to optimize communication system performance. In this section, some of the important channel models relevant to atmospheric optical communications are discussed.

3.3.1 Additive White Gaussian Noise (AWGN) Channel

Additive white Gaussian noise (AWGN) channel is a universal channel model for analyzing modulation schemes. When the signal propagates through the channel, this model adds a white Gaussian noise to the signal. In the frequency domain, the channel's amplitude frequency response is flat (~ infinite bandwidth) and phase frequency response is linear for all frequencies [1]. The channel-propagated signal thus suffers only distortions introduced by the AWGN. From Eq. (3.1), the received signal (without fading) is simplified to

$$r(t) = s(t) + n(t) \tag{3.4}$$

where $n(t)$ is the additive Gaussian noise. The probability density function (PDF) of n can be written as

$$p(n) = \frac{1}{\sqrt{2\pi\sigma_n^2}} e^{\frac{-n^2}{2\sigma_n^2}} \tag{3.5}$$

where σ_n^2 is the noise variance. In strict sense, the AWGN channel does not exist since no channel can have an infinite bandwidth. In real practical situations, the FSO channel will include both AWGN and fading channel. The AWGN performance can still provide an upper bound on the performance for a modulation scheme.

Comparison of AWGN with Poisson Channel The statistics of photon arrivals for a coherent state, e.g., a laser source far above threshold, are Poisson [2, 3]. The Poisson distribution defined by the probability of detecting η photons in a time interval T given the average number of photons arrivals per interval is $<n>=N_{\text{avg}}$ can be written as [5].

$$P\left[\frac{n}{\mathrm{N_{avg}}}\right] = \frac{\left(\mathrm{N_{avg}}\right)^{\eta} e^{-\mathrm{N_{avg}}}}{\mathrm{n!}} \underset{N\to l\arg e}{=} \frac{e^{-\frac{(n-\mathrm{N_{avg}})^2}{2\mathrm{N_{avg}}}}}{\sqrt{2\pi\mathrm{N_{avg}}}} \tag{3.6}$$

The right-hand expression in Eq. (3.6) is a discrete Gaussians approximation of the Poisson distribution. The average number of photons over observation interval T can be written as

$$\mathrm{N_{avg}} = \frac{\eta P}{h\upsilon} T = \eta PPB \tag{3.7}$$

where η = detection efficiency, P = incident optical power, $h\upsilon$ = energy/bit and T = bit period. The mean number of photon arrivals, m is equal to the variance σ^2, are given by [5]

$$m = < n > = \sum_{0}^{\infty} \mathrm{nP}\left[\frac{\mathrm{n}}{\mathrm{N_{avg}}}\right] = \sum_{0}^{\infty} \frac{n(\mathrm{N_{avg}})^{\mathrm{n}} e^{-\mathrm{N_{avg}}}}{(n)!} = \mathrm{N_{avg}} \tag{3.8}$$

$$\sigma_{sn}^2 = \left\langle (n - \langle n \rangle)^2 \right\rangle = \sum n^2 \frac{(\mathrm{N_{avg}})^{\mathrm{n}} e^{-\mathrm{N_{avg}}}}{\mathrm{n!}} - \mathrm{N_{avg}}^2 = \mathrm{N_{avg}} \tag{3.9}$$

The signal to noise ratio (SNR) is thus given by (in terms of power)

$$\mathrm{SNR} = \frac{\langle n \rangle^2}{\langle \Delta n^2 \rangle} = \frac{m^2}{\sigma_{sn}^2} = \mathrm{N_{avg}} = \eta \mathrm{PPB} \tag{3.10}$$

As the mean number increases, the Poisson distribution becomes more symmetric and converges towards a Gaussian (with equal mean and variance). The continuous time photocurrent $i(t)$ for an ideal noiseless photodetector generated by detecting a discrete photon stream has mean (signal) and variance (noise) given by [5]:

$$i_{avg} = \frac{\eta q P}{h\upsilon} \text{ and } \sigma^2_{sn=2q}\, i_{avg} \mathrm{B_e} \tag{3.11}$$

where B_e is the noise equivalent power band width of the electrical response over which the noise is observed, q is the electronic change.

3.3.2 Band-limited Channel

When the channel bandwidth is smaller than the signal bandwidth, the channel is band limited. Some examples of band-limited channel include multiple scattering media such as fog, turbid medium, cloud, haze, dust, smoke, and rain. The greatest degradations are scintillation which causes temporal fluctuations of the signal count at the receiver, pulse stretching of the initially transmitted short pulse and random propagation time delays. Severe turbulence and multiple scattering in the communication channel may lead to an acceptable symbol error probabilities. Severe bandwidth limitation causes inter-symbol interference (ISI). This means that initially transmitted digital pulses will be stretched (temporally) when received at the detector and thus will extend beyond their transmission duration (symbol) period (T_s) and interfere with the next symbol or even more symbols. The ISI causes an increase in the bit error probability. The impulse response function in the case of multiple scattering and its effect on calculating the BER (to be explained later in this chapter) is explained in the reference [6]. Theory and formulation of BER with stretched pulses in multiple scattering media is described in reference [7]. Channel equalization techniques can be used for combating ISI.

3.3.3 Fading and Randomly Varying Optical Channel

FSO links suffer from random change of refractive index caused by the variation of air temperature and pressure. FSO communication performance can be severely degraded due to atmospheric turbulence, which causes the temporal and spatial fluctuation of light intensity called scintillation of optical signals. Optical wireless communication (OWC) also suffer another degrading effect called fading which is a phenomena occurring when the amplitude and phase of a signal change rapidly over a short period of time or travel distance. Fading is caused by interference between two or more versions of the transmitted signal which arrive at the receiver at slightly different times [1]. The resultant signal is the combination of all the multipath waves arriving at the receiver can vary widely in amplitude and phase.

In mobile communication channels, such as between moving vehicles or between a moving vehicle and a fixed terminal, or in a satellite mobile channel, the multipath interference and hence fading are caused by reflections from surrounding buildings and terrains. Also, the relative motion between moving terminals (transmitter and receiver) can cause Doppler shifts on each multipath components resulting in random frequency modulation in the signal. Scintillation effects can also contribute in the multipath interference phenomena of fading. ISI caused by multipath and carrier frequency drift and signal bandwidth spread caused by Doppler shift can be significant in affecting FSO communication performance. It is therefore important to learn the modulation performances of FSO system in fading and randomly varying optical channel.

3.4 Modulation Schemes in FSO Communications

In FSO communication systems, the intensity of an optical source is modulated to transmit signals. For digital data transmission, digital modulation provides source coding (data compression), channel coding (error detection/correction), and easy multiplexing of multiple information streams. Either a bit-by-bit basis (binary encoding) or a bit-word basis (block encoding) can be performed to transmit the digital data. The optical carrier can be modulated in its amplitude, frequency, phase, and polarization. The modulation of FSO is different from the radio frequency (RF). Currently the most viable modulation is intensity modulation (IM) where the desired waveform is modulated onto the instaneous power of the carrier. At the receive side, the most practical method is direct detection (DD) where a photon detector produces a current proportional to the received instaneous power. The reliance on IM/DD will have a significant impact on the design of a pixilated optical system [8]. Note that the transmitted signal can never be negative. The intensity of the transmitted signal which bears the information can never be negative. Therefore, the modulation coefficients must be set such that the signal satisfies a non-negativity constraint. This is different from RF modulation scheme where the coefficients, for example, for a quadrature amplitude modulation (QAM) are complex, representing the amplitude and phase of the signal. There are severed different types of modulation schemes that are suitable for FSO communication systems. Since the average emitted optical power is limited, the different modulation techniques are usually compared in terms of the average received optical power required to achieve a desired BER at a given data rate. A power-efficient modulation scheme is desirable in order to maximize the ratio of peak to average power. The intensity modulation and direct detection (IM/DD) is the most practical modulation technique in OWC systems; currently, most popular schemes are binary-level for the reasons of simple and in expensive implementations. Other complex schemes can provide higher bandwidth efficient with the trade-off power efficiency and robustness. Different modulation techniques and schemes have been proposed and analyzed for FSO communication systems. Each modulation scheme has its own attractive features and applicability for any

specific OWC scenario under different channel and environmental conditions. A proper design of day FSO communication system requires a right decision for selecting any particular modulation technique. The essential metrics to be compared among various modulation schemes are the following:

1. *Power Efficiency*

Perhaps this is the most important consideration since the available optical power for transmission is limited due to eye and skin safety and cost. The modulation schemes are usually compared in terms of the required average optical power (or SNR) to achieve a desired error performance at given data rate.

2. *Bandwidth Efficiency*

An FSO communication system is ultimately limited by the bandwidth of the subsystems, such as the photodetector and of the multipath channel (which arises, for example, in a turbid media like fog, aerosols, etc. and diffuse/non-line-of-sight links). Bandwidth efficiency is therefore an important design consideration for selecting modulation type.

3. *Simplicity and cost for implementing*

The FSO communication system are also important in considering a modulation scheme. In some situations channel-induced dispersion and various external noise sources under which the FSO has to be operated are to be considered. As mentioned earlier, the intensity of an optical source is modulated to transmit signal. Digital data transmission include source coding (data compression), channel coding (error detection correction), and easy multiplexing of multiple information streams digital data can be transmitted on a bit-by-bit basis (binary encoding), or on a bit-word basis (block encoding).

Some of the modulation schemes which are commonly used for FSO communication systems are discussed below.

3.4.1 On-Off Keying (OOK)

The on-off keying (OOK) modulation format is the dominant modulation scheme employed in FSO communication system. Because of its simplicity and resilience to laser nonlinearity, OOK is widely used for OWC in an FSO system. OOK can use either non-return-to-zero (NRZ) or return-to-zero (RZ) pulse formats. In NRZ-OOK, an optical pulse of peak power $\alpha_e \mathrm{P_T}$ ($\alpha_e =$ optical source extinction ration, $0 \le \alpha_e \le 1$) represents a digital symbol "0" while the transmission of an optical pulse of peak power P_T represents a digital symbol "1." The finite duration of the optical pulse is the same as symbol duration T.

Basics of OOK Relevant to FSO Communication The transmitter and the receiver hardware relatively simple for OOK. Known as binary amplitude-shift keying (ASK), OOK is a form of IM in which binary information is represented by the

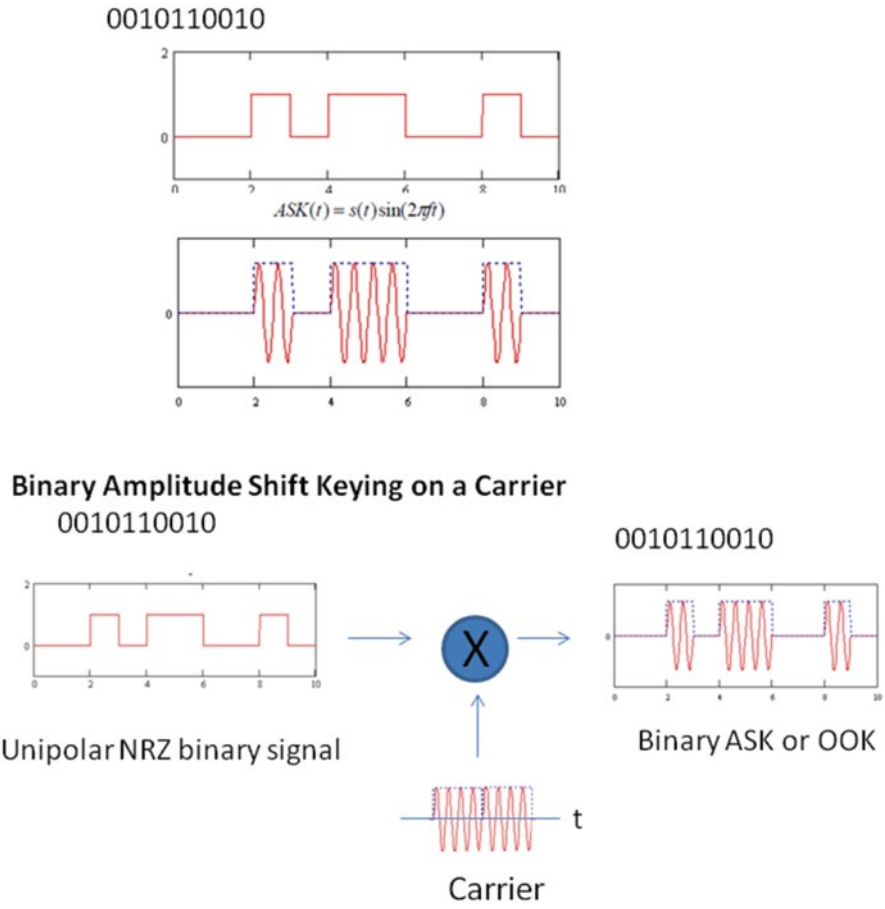

Fig. 3.3 Binary ASK (OOK) Signal

presence or absence of optical signal energy within the symbol. At the receiver, the "1" or "0" decision is determined by the received symbol energy being above or below a threshold (predetermined). The bit rate is denoted by $R_b = 1/T_b$ where T_b is the bit duration and is directly related to the rate at which the transmitter optical source is switched on and off. The normalized transmit pulse shape for OOK is given by

$$\mathrm{P(t)} = \begin{cases} 1, \text{ for t } \in [0, \mathrm{T_b}] \\ 0 \end{cases}, \text{ elsewhere} \tag{3.12}$$

OOK is also known as binary ASK. In ASK, the amplitude of the carrier is changed in response to information and all else is kept fixed. Bit "1" is transmitted by a carrier of one particular amplitude. To transmit "0," we change the amplitude keeping the frequency constant. OOK is a special form of ASK where one of the amplitudes is zero as shown below (Fig. 3.3).

BER in FSO Links Using OOK Modulation The goal of a FSO communication system for digital communication is to transmit the maximum number of bits per second over the maximum possible range with the fewest errors [6]. Electrical data signals are converted to optical signals via a modulator. A "1" is transmitted as a pulse of light while a "0"has no light output. The number of "1s" and "0s" transmitted per second determines the speed of the FSO link (data rate). At the receiving end of the link, the optical signal is detected by an optical-to-electrical converter (e.g., a photodetector). A decision circuit then identifies the "1s" and "0s" in the signal, and thus recovers the information sent. For digital communication system, information is sent over the optical link as digital symbols. This is accompanied by encoding the source information into binary symbols (bits), and transmitting the bits as some type of coded optical field, for example, by encoding on a bit-by-bit basis (binary encoding). Each bit is then sent individually by transmitting one of two optical fields to represent each bit. This section will consider only direct detection (DD) system in which the standard binary procedure is to pulse an optical source (e.g., a laser or and LED) "on" or "off" depending on data bit. This encoding referred to as OOK is considered here. At the receiver, OOK decoding is based on a decision as to whether the pulse slot time has high enough field energy or not. The selected threshold determines the best performance in decoding the correct signal with the lowest probability of making a bit decision error and thus the BER can be obtained. The other modulation formats will also be discussed.

The appropriate channel model for FSO communication system using IM will depend on the background light. For low background light, the received signal can be modeled as a Poisson process and will depend on both instantaneous optical power of the received signal and the power of the background light. When the background light is assumed to be zero, the channel is quantum limited. Otherwise, in presence of large background noise, the wideband photodetector shot noise is accurately modeled as an AWGN plus a DC offset.

BER in AWGN Channel (No Turbulence) As mentioned earlier, normalized transmit pulse shape for OOK was given by Eq. (3.12). In the demodulator, the received pulse is integrated over one bit period, then sampled and compared to a threshold to decide a "1" or "0" bit. This is called the maximum likelihood receiver, which minimizes the BER. In determining the actual symbols transmitted, errors may be made because of detector noise as well as due to the random noise (this can be approximated as Gaussian distribution). Without any loss of generality in analyzing the received signal current probability distribution, the receiver area may be normalized to unity. Then the optical power may be represented by the optical intensity, I. The received signal, i.e, photocurrent in an OOK system is therefore given by [9]:

$$\mathrm{i(t)} = \mathrm{R\,I}\left[1 + \sum_{j=-\infty}^{\infty} d_j g(t - jT)\right] + \mathrm{n(t)} \tag{3.13}$$

where R is the responsibility of the positive-intrinsic-negative (PIN) photodetector, $n(t) \sim N(0,\ \sigma^2)$ is the additive Gaussian noise, $g\,(t - jT)$ is the pulse shape function,

and $d_j=[-1,1]$. At the receiver, the received signal is fed into a threshold detector which compares the received signal with a predetermined threshold level. In digital communications, the performance measure is provided not directly by the SNR, but rather by the probability of error, also called BER.

In the absence of turbulence, the BER can be calculated by assuming the errors result from receiver noise which can be determined from the shot and Johnson noise. Thus, errors may be made at the receiver in determining the actual symbols transmitted. A "0" may be mistaken for a "1" can be denoted by $\mathrm{p_r}(0|1)$. Similarly, let $\mathrm{p_r}(1|0)$ denotes when a "1" may be mistaken for a "0." The overall probability of error is

$$\mathrm{BER} = \mathrm{p}_0\,\mathrm{p_r}(\mathrm{I}1|0) + \mathrm{p}_1\mathrm{p_r}(0|1\mathrm{I}) \tag{3.14}$$

where p_0 and p_1 are transmission probabilities of a binary "0" and binary "1," respectively, and $\mathrm{p_r}(1|0)$, $\mathrm{p_r}(0|1)$ are the conditional probabilities explained earlier. Note the $p_0+p_1=1$. If either symbol is equally likely to be transmitted with equal probability, $p_0=p_1=1/2$. At the receiver, the received signal is fed into a threshold detector which compares the received signal with a predetermined threshold level. A digital symbol "1" is assumed to have been received if the received signal is above the threshold level, and "0" otherwise.

As mentioned earlier for OOK transmission, the probability distributions of both noise alone and of signal-plus noise are assumed to be Gaussian. For a set threshold level of the probability of errors are thus given by,

$$\mathrm{P_r}(\mathrm{I}1|0) = \frac{1}{\sqrt{2\pi}\sigma_n}\int_{i_T}^{\infty} e^{\frac{-i^2}{2\sigma_n^2}}\,di = 1/2\,erfc\left(\frac{i_T}{\sqrt{2}\sigma_n}\right) \tag{3.15}$$

$$\mathrm{p_r}(0|1\mathrm{I}) = \frac{1}{\sqrt{2\pi}\sigma_n}\int_{0}^{i_T} e^{\frac{(i-i_s)^2}{2\sigma_n^2}}\,di = 1/2\,erfc\left(\frac{i_s-i_T}{\sqrt{2}\sigma_n}\right) \tag{3.16}$$

where the total detector output current $i=+i_n$ with i_s is from the signal current, and i_n is the detector (receiver) noise current with variance σ_n^2. The signal current i_s can be expressed as (see Eq. (3.13)) $i_s=R\,I$ where I is the optical intensity I=power/receiver area=P_s if receive area is normalized to unity.

Thus $i_s=R\,p_s$, p_s being the signal power of the pulse. For equiprobable symbols, $p(0)=p(1)=0.5$ (see Eq. (3.14)). Thus, the optimum threshold point is at i_T=½ is =½ $R\,I$. Then the overall probability of error can be written as (from Eqs. (3.14), (3.16)):

$$P_r(e)_{OOK} = BER_{OOK} = 1/2\,erfc\left(\frac{i_s}{2\sqrt{2}\sigma_n}\right) = 1/2\,erfc\left(\frac{SNR_0}{2\sqrt{2}}\right) \tag{3.17}$$

where *erfc*(*x*) is the complementary error function defined by

$$\text{erfc(x)}=\frac{2}{\sqrt{\pi}}\int_{x}^{\infty} e^{-u^2}\,du \tag{3.18}$$

and

$$\text{SNR}_0=\frac{i_s}{\sigma_n}=\text{R}\frac{P_s}{\sigma_n} \tag{3.19}$$

Equation (3.17) is the BER for OOK. Modulation in AWGN FSO communication channel (no turbulence or fading).

BER for OOK Keying in Turbulent Atmosphere In the presence of atmospheric turbulence, the threshold level, i_T is no longer fixed midway between the signal levels representing symbols "1" an "0." It was shown in Eq. (3.14) that the BER of an OOK signal requires the knowledge of P_r (I 1|0) and p_r (0|1I) which are the conditional probabilities of data "0" and "1." As the transmitted signal corresponding to bit "0" is zero. The received signal for this bit will have only AWGN. Since scintillation is a multiplicative effect, it mainly affects data "1," i.e., both turbulence noise and AWGN are both present for bit "1." In other words, the conditional error probabilities need to be modified to include the turbulence as (from Eq. (3.13) with normalized responsivity R and representing the optical intensity as a function of time, *I[t]*).

$$\text{r(t)=I(t)}\left[1+\sum_{j=-\infty}^{\infty}\text{I(t)d}_\text{j}g(t-jT)\right]+n(t) \tag{3.20}$$

The signal currents for bit "0" and "1" can then be written as

$$\begin{aligned}\text{r(t)}=\{&\text{n(t)} && \text{d}_\text{j}=-1\\ &2\,\text{I(t)}+\text{n(t)} && \text{d}_\text{j}=1\}\end{aligned} \tag{3.21}$$

Let the variances of $n(t)$ and $I(t)$ be σ_n^2 and σ_I^2, respectively. The PDF of the converted electrical signal when bit "0" or "1" is sent is given by

$$p(r|0)=\frac{1}{\sqrt{2\pi}\sigma_n}e^{-r^2}\Big/2\sigma_n^2 \tag{3.22}$$

$$p(r|1)=\int_0^{\infty}p(rl1,x)\,p(x)dx \tag{3.23}$$

In Eq. (3.23), the marginal probability $p(rl1)$ is modified by averaging the conditional PDF of $r(t)$ over the scintillation statistics which is then given by see Eq. (3.25), note that for d_j=+1, $r(t)$=2$I(t)$+$n(t)$. Replacing now I with variable x, $p(r|1, x)$ can be written as:

$$\mathrm{p(rl1,x)} = \frac{1}{\sqrt{2\pi}\sigma_n} e^{-\frac{(r-2x)^2}{2\sigma_n^2}} \tag{3.24}$$

and p(i) is the PDF of the irradiance I in presence of turbulence. Note that the variable I is changed to x in Eq. (3.23) with same PDF. Several atmospheric channel models have been proposed to describe scintillation. The log-normal (LN) distribution is widely used to describe scintillation under weak atmospheric turbulence conditions. For moderate to strong turbulence, Gamma-Gamma (GG) distribution is commonly used. The PDF if irradiance (intensity) for the GG distribution in the previous chapter and can be expressed as [10].

$$\mathrm{p(I)} = \frac{2}{\Gamma(\alpha)T(\beta)I}(\alpha\beta I)^{\frac{\alpha+\beta}{2}} K_{\alpha-\beta}\left(2\sqrt{\alpha\beta I}\right), \mathrm{I}>0 \tag{3.25}$$

where I is the normalized irradiance, α and β are parameters of the PDF, $\Gamma(\bullet)$ is the gamma function, $K_{\alpha-\beta}$. The parameters α and β are defined by Rytov variance σ_R^2, which are given by

$$\alpha = \left\{\exp\left[\frac{0.49\sigma_R^2}{(1+1.11\sigma_R^{12/5})^{7/6}}\right]-1\right\}^{-1} \tag{3.26}$$

$$\beta = \left\{\exp\left[\frac{0.51\sigma_R^2}{(1+0.69\sigma_R^{12/5})^{5/6}}\right]-1\right\}^{-1} \tag{3.27}$$

From Eqs. (3.23), (3.24), and (3.25), $p(r|1)$ can be written as [11]

$$p\left(\mathrm{r}|1\right) = \int_0^\infty \frac{1}{\sqrt{2\pi}\sigma_n} e^{-\frac{(r-2x)^2}{2\sigma_n^2}} \frac{2(\alpha\beta x)^{\frac{\alpha+\beta}{2}}}{\Gamma(\alpha)\Gamma(\beta)x} K_{\alpha-\beta}(2\sqrt{\alpha\beta x})dx$$

$$= \frac{1}{\sqrt{2\pi}\sigma_n} \frac{2(\alpha\beta)^{\frac{\alpha+\beta}{2}}}{\Gamma(\alpha)\Gamma(\beta)} \int_0^\infty x^{\frac{\alpha+\beta}{2}-1} K_{\alpha-\beta}(2\sqrt{\alpha\beta I}) e^{-\frac{(r-2x)^2}{2\sigma_n^2}} dx \tag{3.28}$$

Let the threshold $T>0$, the BER is given by

$$\mathrm{P_r(e)_{ook}} = \mathrm{BER_{ook}} = \mathrm{p(0)}\int_T^\infty p(r|o)dr + p(1) - \int_\infty^T p(r|1)dr =$$

$$\frac{1}{2}p(0)erfc(\frac{T}{\sqrt{2}\sigma_n}) + \frac{p(1)(\alpha\beta)^{\frac{\alpha+\beta}{2}}}{\Gamma(\alpha)\Gamma(\beta)} \int_0^\infty x^{\frac{\alpha+\beta}{2}-1}$$

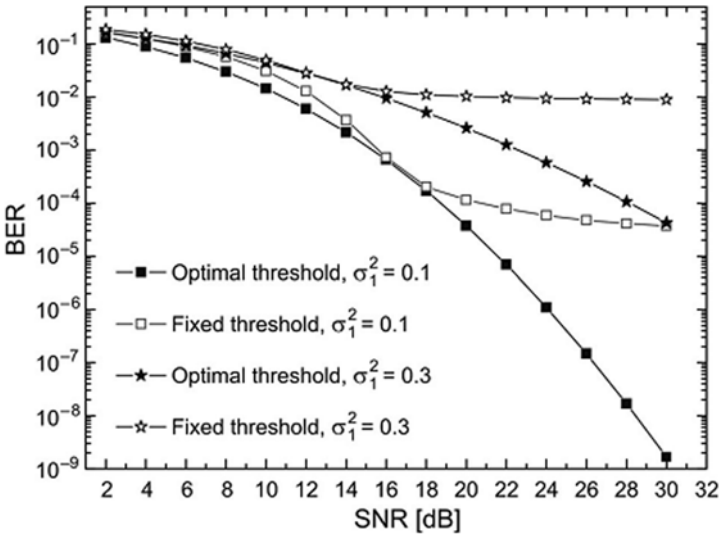

Fig. 3.4 The BER is plotted as a function of the SNR for OOK modulation format for Gamma-Gamma turbulence model: comparison of a fixed and optimal threshold for various turbulence strengths (*Reprinted with permission from Optica Applicata, 2009* [11]). *BER* bit error rate, *SNR* signal to noise ratio, *OOK* on-off keying

$$.K_{\alpha-\beta}\left(2\sqrt{\alpha\beta x}\right)erfc\left[\frac{2x-T}{\sqrt{2}\sigma_n}\right]dx \tag{3.29}$$

The likelihood function for the optimal maximum a posteriori (MAP) symbol-by-symbol detection with equiprobable OOK data is given by

$$\Lambda(r)=\frac{p(r|1)}{p(r|0)}=\frac{2(\alpha\beta)^{\frac{\alpha+\beta}{2}}}{\Gamma(\alpha)\Gamma(\beta)}\int_0^{\infty}x^{\frac{\alpha+\beta}{2}-1}K_{\alpha-\beta}\left(2\sqrt{\alpha\beta x}\right)e^{-\left[\frac{4x(x-r)}{2\sigma_n^2}\right]}dx \tag{3.30}$$

The optimal threshold T can be obtained from the equation satisfying $\Lambda(r)=1$, for different Rytov variances σ_R^2 and noise variances σ_n^2 (note the parameters α and β are related to σ_R^2 via Eqs. 3.26 and 3.27. The receiver thus must be able to select the threshold point adaptively for the optimal performance provided σ_R^2 values are known or sensed independently.

Note that in an FSO communication system when a fixed threshold is used (which is chosen as half of the mean of received signal corresponding to bit 1), it will not optimize the performance of the communication systems over changing atmospheric turbulent conditions. The optimal threshold can optimize the performance of the communication systems. For fixed threshold, $T=0.5$ and the optimal threshold is obtained by Eq. (3.30). Figure 3.4 shows the significant improvement of performance of communication system for OOK modulation format by using optimal threshold which reduces the BER significantly.

3.4.2 Pulse position Modulation (PPM)

Pulse position modulation (PPM) is a modulation technique mainly to increase transmission efficiency in the FSO systems. PPM is an orthogonal baseband modulation technique and has been studied extensively in optical communications for its superior power efficiency compared to any other baseband modulation techniques. The technique can improve on the power efficiency of OOK, but at the expense of an increased bandwidth requirement and greater complexity. The factor of superior power efficiency makes it well suited for handheld devices which requires low consumption. Point-to-point optical communications using laptops and palmtops use this modulation technique widely.

Basics of PPM Relevant to FSO Communications In this scheme, an L-PPM symbol consists of a single pulse of one slot duration within L ($=2^M$ where $M>0$ is an integer) possible time slots with the remaining slots being empty. Information is sent by transmitting a non-zero optical intensity in a single time slot, while other slots remain dark. Each block of $\log_2 M$ data bits is mapped to one of M possible symbols. The notation M-PPM is commonly used to indicate the order. Each symbol consists of a pulse of constant power P occupying one slot, with the rest of the M-1 slots empty. The position of the pulse corresponds to the decimal value of the $\log_2 M$ data bits. The information is thus encoded by the position of the pulse within the symbol.

PPM can be continuous or quantized PPM where time delay of initiation of a short-duration carrier pulse is set proportional to information sample amplitude. The carrier field representation of a PPM wave of duration τ is given by [32]

$$\mathrm{E_M(t)} = A_c \cos\omega_0 \mathrm{t} \quad \text{for} \quad \mathrm{t_n} + \tau_d \le \mathrm{t} \le \mathrm{t_n} + \tau_d + \tau \tag{3.31}$$

where the time delay, τ_d of the leading edge of the carrier pulse with respect to the same time t_n, is

$$\tau_d = \frac{\tau_p}{2}[1 + M(t_n)] \tag{3.32}$$

In analog modulation system, an analog information signal $M(t)$, continuously varies. In most pulse-modulation systems the information signal is time-sampled. Figure 3.5 illustrates PPM of analog signal.

To understand the digital signal in a PPM scheme, note that the position of the pulse location conveys the information. The average power can be written as $P_{PPM} = \frac{A^2}{L}$ where A is the pulse amplitude, $L=2^M$, M is the input data bit resolution. Let R_b be the input data rate so that the PPM slot duration, $T_s = \log_2 L/LR_b$. For example, if $L=4=2^{2,}$ so that $M=2$. Then $T_s = \log_2 4/4R_b = 2/4R_b = 1/2R_b$. Figure 3.6 shows an example of a pictorial representation of mapping to transmitter (laser) power for 4-PPM format.

The figure depicts the assignment of bit patterns to pulse pattern for 4-PPM format. At the receiver side, the receiver detects the encoded PPM symbols by

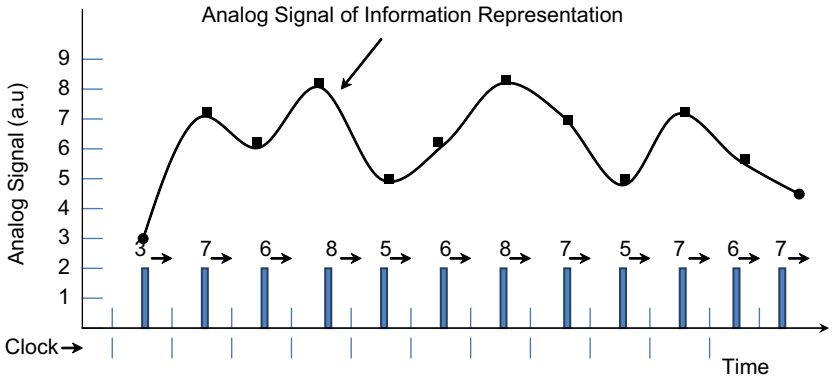

Fig. 3.5 An illustration of pulse position modulation of analog signal *a.u.* arbitrary unit

Fig. 3.6 Example of assignment of bit patterns to pulse patterns for a 4-PPM format (mapping of source data to transmitted symbols). *PPM* pulse position modulation

Source Data	4-PPM
00	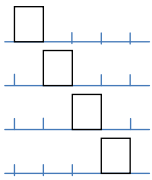
01	
10	
11	

determining which of the M-slots contains the laser pulse, and performs the inverse mapping operation to recover the bits stream. An example of the representation of an information bit 10110001 for 4-PPM is shown in Fig. 3.7.

A PPM signal can be expressed by

$$x(t) = LP\sum_{R=0}^{L-1} c_k\, p(t - kT / L) \tag{3.33}$$

where $[c_0, c_1, \ldots c_{L-1}]$ is the PPM codeword, and $p(t)$ is a rectangular pulse of duration T/L and unity height. $x(t)$ represents optical power for FSO communication application, and therefore it must satisfy

$$\mathrm{x(t)} \geq 0 \quad \text{and} \quad \langle \mathrm{x(t)} \rangle \leq \mathrm{P} \tag{3.34}$$

where P is the average optical power constraint of the transmitter.

BER for PPM in Turbulent Atmosphere In FSO link, M-ary PPM scheme has the advantage that no thresholds are require for detection. In many power-limited FSO systems including handheld devices, average transmitted power requirement using M-ary PPM decreases with increasing modulation level M in the absence of

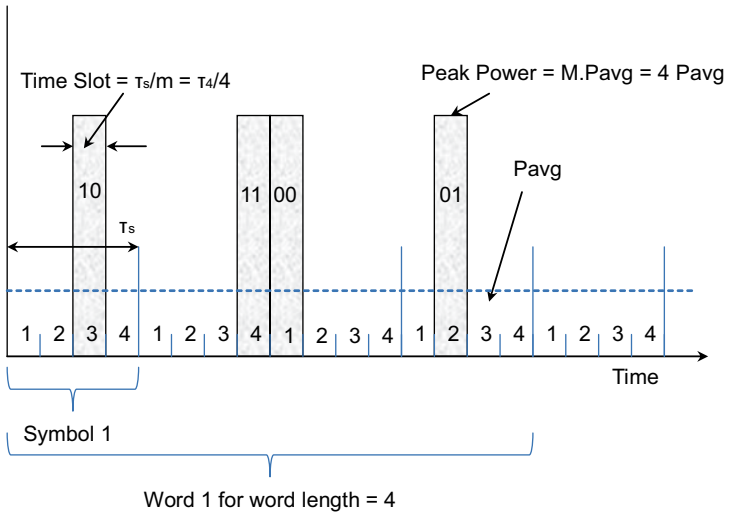

Fig. 3.7 Representation of an information bit 10110001 for a 4-PPM format. *PPM* pulse position modulation

atmospheric turbulence. However, in presence of atmospheric turbulent channel, the increasing modulation level cannot significantly reduce the transmitted power requirement to achieve a desired BER for *M*-ary PPM. The average BER in presence of moderate to strong atmospheric turbulence is determined in this section in order to evaluate the performance of FSO communication system using the *M*-ary PPM scheme.

The IM/DD FSO system can be modeled to have an optical source transmitting data which are modulated onto instantaneous optical intensity, transmitted through the turbulent atmosphere and received by a receiver using a photodiode. Assuming the shot and thermal noise to follow Gaussian noise statistics with zero-mean, the received electrical signal, *y* (output of the photodetector) can be written as

$$y = RP_R\, x + n \tag{3.35}$$

where $x \geq 0$ is the transmitted signal with an average optical power $\langle x \rangle \leq P$, R is the photodiode responsitivity for optical intensity to an electrical signal, and *n* is a signals-independent zero mean white Gaussian noise with variance, σ_n^2. For *M*-ary PPM, one data symbol consists of *M* time slots, *x* equals "1" during one of these slots, and "0" during the remaining *M*-1 slots, encoding $\log_2 M$ bits in a symbol. In presence of atmospheric turbulence, the received optical power P_R fluctuates following a PDF of distribution model, appropriate for the atmospheric turbulence scenario. For FSO communication with an atmospheric turbulence channel, the average optical signal power received at the photodiode can be expressed by a link range equation as follows:

$$\mathrm{P_R(h)} = P_T \eta_T \eta_R G_T G_R \left(\frac{\lambda}{4\pi L}\right)^2 h \tag{3.36}$$

where P_T is the average transmitted power, η_T and η_R are the transmitter and receiver optics efficiencies, G_T and G_R are the transmitter and receiver telescope gains, λ is the transmitting wavelength, L is the range or distance between the transmitter and the receiver, and h is the channel state due to atmospheric turbulence. For simplicity, the same telescope for the transmitter and the receiver may be assumed with same gain:

$$G_T = G_R = (\pi D / \lambda)^2 \tag{3.37}$$

where D is the telescope diameter. From Eqs. (3.36) and (3.37) assuming $\eta_T = \eta_R = \eta$,

$$P_R(h) = P_T \left(\frac{\eta A}{\lambda L}\right)^2 h \tag{3.38}$$

where $\mathrm{A} = \pi D^2 / 4$ is the transceiver telescope area. The random channel state h is assumed to follow the GG distribution [4] given by

$$f(h) = \frac{2(\alpha\beta)^{\frac{(\alpha+\beta)}{2}}}{\Gamma(\alpha)\Gamma(\beta)} h^{\frac{(\alpha+\beta)}{2}-1} K_{\alpha-\beta}\left(2\sqrt{\alpha\beta h}\right) \tag{3.39}$$

where, $K_{\alpha-\beta}(\bullet)$ is the modified Bessel function of the second kind, and order $(\alpha-\beta)$, $\Gamma(\bullet)$ is the gamma function. Assuming plane wave propagation, the parameters α and β can be directly related to atmospheric conditions as follows:

$$\alpha = \left\{\exp\left[\frac{0.49\sigma_R^2}{(1+0.18d^2+0.56\sigma_R^{12/5})^{7/6}}\right]-1\right\}^{-1} \tag{3.40}$$

$$\beta = \left\{\exp\left[\frac{0.51\sigma_R^2(1+0.69\sigma_R^{12/5}}{(1+0.9d^2+0.62d^2\sigma_R^{12/5})^{5/6}}\right]-1\right\}^{-1} \tag{3.41}$$

In the above Eqs. (3.43) and (3.44), $d = \sqrt{\frac{kD^2}{4L}}$, $k = \frac{2\pi}{\lambda}$ is the optical wave number, and λ were defined before, D is the receiver aperture diameter. σ_R^2 is the Rytov variance and for a plane wave is given by,

$$\sigma_R^2 = 1.23 c_n^2 k^{7/6} L^{11/6} \tag{3.42}$$

where C_n^2 is the strength of the atmospheric turbulence which varies from 10^{-17} $m^{-2/3}$) (weak turbulence) to 10^{-12} $m^{-2/3}$ (strong turbulence).

The conditional BER of *M*-ary PPM taking into account of the channel state *h* due to atmospheric turbulence is given by [12]

$$BER(h) \approx \frac{M}{4} erfc\left[\mathrm{R}\, P_R(h) \frac{\sqrt{M \log_2 M}}{2\sigma_n} \right] \tag{3.43}$$

where *M* is modulation level for *M*-ary PPM scheme, and erfc(·) us complementary error function. From Eqs. (3.36) and (3.43), BER(*h*) is given by

$$BER(h) \approx \frac{M}{4} erfc\left\{ \mathrm{R}\, P_T \left(\frac{\eta A}{\lambda L} \right)^2 \frac{\sqrt{M \log_2 M}}{2\sigma_n} h \right\} \tag{3.44}$$

Note that BER(*h*)is a conditional BER and depends on the characteristics of the channel state *h* due to atmospheric turbulence. The channel state *h* follows certain statistical distribution which in this case is assumed to be the GG distribution *f*(*h*) defined by Eq. (3.39). Therefore, the average BER is more meaningful parameter to evaluate the performance of the FSO communication system. This also makes sense since the bit duration is much less than the fading coherence time of the atmospheric turbulence so that a slow fading environment is considered. Eq. (3.44) can be averaged over the *f*(*h*) to obtain the average BER and is given by

$$\langle BER \rangle = \int_0^\infty BER(h) f(h) dh \tag{3.45}$$

Using Eqs. (3.39) and (3.44), < BER > is obtained as follows [13]

$$< BER >= \frac{M(\alpha\beta)^{\frac{(\alpha+\beta)}{2}}}{2\Gamma(\alpha)\Gamma(\beta)} \int_0^\infty h^{\frac{(\alpha+\beta)}{2}-1} K_{\alpha-\beta}(2\sqrt{\alpha\beta h}$$

$$\mathrm{erfc}\left\{ \mathrm{R}\, P_T \left(\frac{\eta A}{\lambda L} \right)^2 \frac{\sqrt{M \log_2 M}}{2\sigma_n} h \right\} \mathrm{dh} \tag{3.46}$$

The Eq. (3.49) can be numerically evaluated using the turbulence parameters α and β, *M* and other quantities already defined earlier. In order to reduce the Eq. (3.46) to a closed form, the $K_\upsilon(\bullet)$ and the erfc $(\bullet)$ functions can be expressed as [14]

$$K_\upsilon\left(\sqrt{z}\right) = \frac{1}{2} G_{0,2}^{2,0}\left\{ \frac{z}{4}\Big|_{\frac{\upsilon}{2},-\frac{\upsilon}{2}}^{-} \right\} \tag{3.47}$$

$$erfc(z) = \frac{1}{\sqrt{\pi}} G_{1,2}^{2,0}\left\{ z^2 \Big|_{0,\frac{1}{2}}^{1} \right\} \tag{3.48}$$

$G_{0,2}^{2,0}$ and $G_{1,2}^{2,0}$ are Meijer G-functions [14]. Substituting Eqs. (3.47) and (3.48) in Eq. (3.46)

$$< BER >= \frac{M(\alpha\beta)^{\frac{(\alpha+\beta)}{2}}}{4\sqrt{\pi}\Gamma(\alpha)\Gamma(\beta)} \int_0^{\infty} h^{\frac{(\alpha+\beta)}{2}-1} G_{0,2}^{2,0}\left\{ \left| \begin{matrix} - \\ \frac{\alpha-\beta}{2}, \frac{\beta-\alpha}{2} \end{matrix} \right. \right\}$$

$$G_{1,2}^{2,0}\left\{ \mathrm{R}^2 \frac{P_T^2 M \log_2 M}{4\left(\frac{\lambda L}{\eta A}\right)^4 \sigma_n^2} h^2 \Big|_{0,\frac{1}{2}}^{1} \right\} \mathrm{dh} \tag{3.49}$$

Meijer G-function is standard built-in function available in mathematical software packages such as Maple, Mathematica.

The above Eq. (3.49) can then be finally expressed in closed form given by [13]

$$< BER >= \frac{M(2^{\alpha+\beta-4})}{\pi^{\frac{3}{2}}\Gamma(\alpha)\Gamma(\beta)} G_{5,2}^{2,4}$$

$$\left\{ 4\,\mathrm{R}^2 \frac{P_T^2 M \log_2 M}{\left(\frac{\alpha L}{\eta A}\right)^4 \sigma_n^2 (\alpha\beta)^2} \left| \begin{matrix} \frac{1-\beta}{2}, \frac{2-\beta}{2}, \frac{1-\alpha}{2}, \frac{2-\alpha}{2}, 1 \\ \frac{0,1}{2} \end{matrix} \right. \right\} \tag{3.50}$$

The Fig. 3.8 shows the plot of the average BER as a function of the transmitted power, P_T for this example of the FSO, communication system for two modulation levels, 2 PPM and 4 PPM. For moderate turbulence strength, the modulation level M has more effect on the average BER, and as the turbulence strength become strong, the increase of M does not improve the BER performance and therefore is not significant. The BER curves are useful in designing a practical FSO communication system to operate under different atmospheric turbulence conditions.

3.4.3 Binary Phase-Shift Keying (BPSK) Modulation

Phase-shift keying is the modulation technique that alters the phase of the carrier. In a binary phase-shift keying (BPSK) where number of bits (number of output

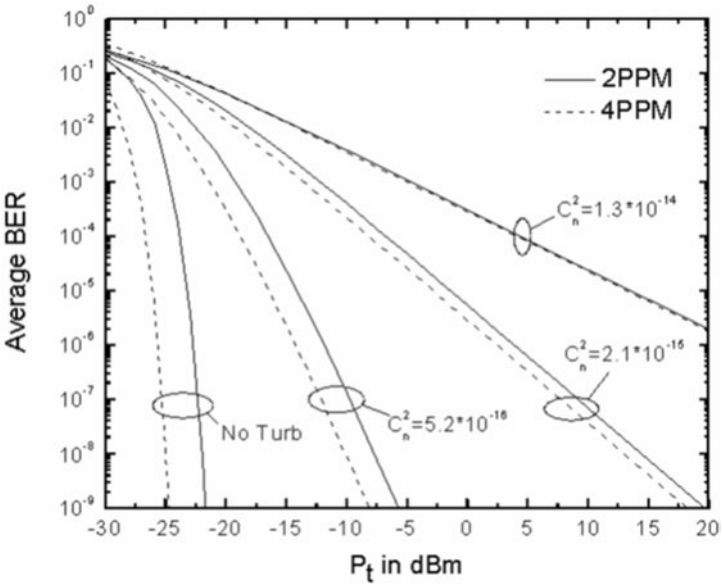

Fig. 3.8 Average BER vs. the average transmitted power for different turbulent strengths, assuming a Gamma-Gamma distributed channel fading model and for 2-PPM and 4-PPM (*Reprinted with permission from IEEE, 2010* [13]). *BER* bit error rate, *PPM* pulse position modulation

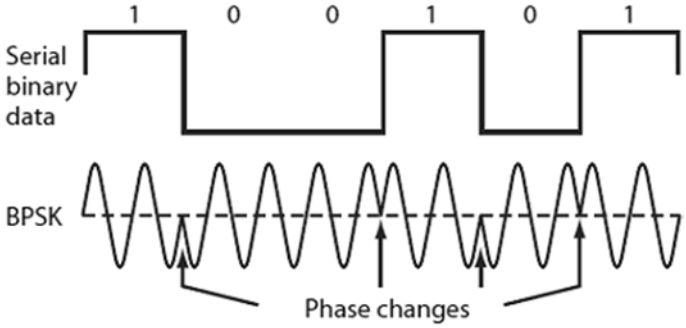

Fig. 3.9 Concept of BPSK modulation. *BPSK* binary phase-shift keying

phases) = 2, one phase represents a logic "1" and another phase represents a logic "0." As the input digital signal changes state (i.e., from "1" to "0" or "0" to "1"), the phase of the output carrier shifts between two angles that are separated by 180^0 (or, π). Figure 3.9 illustrates the concept of BPSK.

For a FSO communication system employing subcarrier phase-shift keying (PSK) intensity modulation, the data sequence is first modulated with PSK, which can be implemented with existing microchips readily available at low cost. The PSK signal is up converted to an intermediate frequency (IF) which can be imple-

mented in the electrical circuit of the transmitter using any of the currently used RF modulation formats. The modulated electrical signal then controls the optical irradiance of the transmitting optical beam. At the receiver end, the photodetector converts the optical signal to an electrical signal which is then demodulated by RF devices like selective filters and stable oscillators. For FSO communication system employing IM through atmospheric turbulence, the received optical intensity $P(t)$ can be written as

$$\mathrm{P(t)=I(t)P_0(t)+\eta(t)} \tag{3.51}$$

where $P_0(t)$ is the received optical intensity without turbulence, and $\eta(\mathrm{t}) \approx \mathrm{N}(0,\sigma_n^2)$ is the AWGN, $I(t)$ is a stationary random process representing the intensity gain induced by atmospheric turbulence. The PDF of $I(t)$ is assumed to be a GG distribution given by Eq. (3.25) discussed earlier with the parameters α and β Eqs. (3.26) and (3.27).

The output electrical signal for subcarrier BPSK IM scheme can be written as [15]

$$\begin{aligned}\mathrm{r(t)=I(t)+m\,I(t)[s_i(t)\cos(2\pi f_c t)-s_q(t)\sin(2\pi f_c t)]}\\ \mathrm{+\eta_i(t)\cos(2\pi f_c t)-\eta q(t)\sin(2\pi f_c t)}\end{aligned} \tag{3.52}$$

where $s_i(t)$ and $s_q(t)$ are the in-phase and quadrature components of the signal, respectively, m is the modulation index $m\,\varepsilon(0,1)$, and f_c is the intermediate carrier frequency. $\eta_i(t)$ and $\eta_q(t)$ are the narrow band white Gaussian processes with the variance σ_n^2. For subcarrier BPSK modulation format, the threshold is chosen at 0, i.e., $T=0$. The condition PDF $p(r|x)$ of the received signal can be written as [11]

$$\begin{aligned}p\left(r\middle|x\right)&=\frac{2}{\sqrt{2\pi}\sigma_n\Gamma(\alpha)\Gamma(\beta)}\left(\frac{\alpha\beta}{m}\right)^{\frac{\alpha+\beta}{2}}\int_0^\infty t^{\frac{(\alpha+\beta)}{2}-1}K_{\alpha-\beta}\left(2\sqrt{\frac{\alpha\beta t}{m}}\right)e^{-\frac{(r-t)^2}{2\sigma_n^2}}dt,\ x=+1\\ &\frac{2}{\sqrt{2\pi}\sigma_n\Gamma(\alpha)\Gamma(\beta)}\left(\frac{\alpha\beta}{m}\right)^{\frac{\alpha+\beta}{2}}\int_0^\infty t^{\frac{(\alpha+\beta)}{2}-1}K_{\alpha-\beta}\left(2\sqrt{\frac{\alpha\beta t}{m}}\right)e^{-\frac{(r+t)^2}{2\sigma_n^2}}dt,\ x=-1\end{aligned} \tag{3.53}$$

BER in presence of atmospheric turbulence with GG turbulent model is then given by [11]

$$\mathrm{BER}=\frac{(\alpha\beta)^{\frac{\alpha+\beta}{2}}}{\Gamma(\alpha)\Gamma(\beta)}\int_0^\infty x^{\frac{(\alpha+\beta)}{2}-1}K_{\alpha-\beta}\left(2\sqrt{\alpha\beta x}\right)erfc\left[\frac{mx}{\sqrt{2}\sigma_n}\right]dx \tag{3.54}$$

When there is no fading (without turbulence) and in presence of AWGN only, the BER is given by [15]

$$\mathrm{BER}_{\mathrm{AWGN}} = \frac{1}{2} erfc\left(\sqrt{\frac{m^2}{2\sigma_n^2}}\right) \tag{3.55}$$

Without loss of generality, the modulation index $m = 1$ is assumed.

Under all the turbulence conditions, the BER performance of subcarrier BPSK is always better than that of OOK, especially in the higher strength of turbulence regions.

Implementing Modulation and Demodulation In the past unique circuit implemented modulation and demodulation. Today, functions like modulation and demodulation are handled in software. DSP algorithms performed the operation previously assigned to modulator and demodulator circuits. The DSP circuitry may be a conventional programmable DSP chip or may be implemented by fixed digital logic implementing the algorithm. Fixed logic circuits are smaller and faster, and are preferred for their low latency in the modulation and demodulation process. For BPSK, an efficient nonlinear amplifier is needed to faithfully reproduce the amplitude and phase information.

BPSK Subcarrier Intensity Modulation This section describes the performance of BPSK subcarrier IM relevant to FSO communication. In optical subcarrier intensity modulation (SIM) links, an RF subcarrier signal pre-modulated with the source data $d(t)$ is used to modulate the intensity of the optical carrier—a continuous wave (CW) laser diode. A very popular phase shift keying shifts the carrier sine wave 180° for each change in binary state as shown earlier in the Fig. 3.9. In BPSK where the number of bits is equal to 2, One phase represents a logic 1 and another phase represents a logic 0. As the input digital signal changes state (i.e., from 1 to 0, or 0 to 1), the phase of the output carrier shifts between two angles that are separated by 180°. BPSK is coherent as the phase transitions occur at the zero crossing points. This means that a proper demodulation of BPSK requires the signal to be compared to a sine carrier of the same phase. This involves carrier recovery and other complex circuitry.

Source data, say $d(t)$, which carries the information pre-modulate first an RF subcarrier signal, which then modulates the intensity of the optical carrier—a CW laser diode. $d(t)$ is modulated onto the RF subcarrier signal using BPSK in which bits "1" and "0" are represented by two different phases 180° apart. The subcarrier signal $m(t)$ being sinusoidal with both positive and negative values, a DC level b_0 is added to $m(t)$ before it is used to drive the laser diode so that the bias current is always equal to or greater than the threshold current required for the laser diode to turn ON. The transmitted optical signal is thus proportional to $m(t)$ and propagates through the atmospheric turbulence to be detected by the receiver. An optical band-pass filter is placed just before the photodetector to eliminate background radiation which the photodetector otherwise detects as noise. The input optical power is converted to electrical signal by the photodetector which is the instantaneous photocurrent, $i_r(t)$:

$$\mathrm{i_r} = \mathrm{RI}\,(1 + \alpha\,\mathrm{m(t)}) + \mathrm{n(t)} \tag{3.56}$$

where R is the photodetector responsivity, I is the received irradiance, $I=0.5\ I_{\text{peak}}$, I_{peak} being the peak received irradiance, α is the modulation index which satisfies $\leq$ condition $|\alpha m(t)| \leq 1$, and $n(t) \approx \mathrm{N}(0, \sigma^2)$ is AWGN. The noise is due to both the thermal noise and the background noise, i.e., $\sigma^2 = \sigma^2_{Thermal} + \sigma^2_{B_g}$. A single symbol duration is considered so that $m(t) = A(t)g(t)\cos(\omega_c t + \theta)$, where $A(t)$ is the subcarrier amplitude, $g(t)$ is the rectangular pulse shaping function, and ω_c is the intermediate carrier angular frequency and θ is the phase.

For the atmospheric turbulence, a GG model [4, 16] can be used, which is reasonably valid for all turbulence scenarios for weak, moderate, and strong atmospheric turbulence regimes. The GG model for the PDF of received irradiance fluctuation is given by [16]

$$p(I) = \frac{2(\alpha\beta)^{\frac{\alpha+\beta}{2}}}{\Gamma(\alpha)\Gamma(\beta)} I^{\frac{(\alpha+\beta)}{2}-1} K_{\alpha-\beta}\left(2\sqrt{\alpha\beta I}\right), \mathrm{I}>0 \tag{3.57}$$

where the parameters α and β defined for a plane wave are:

$$\alpha = \left[\exp\left(\frac{0.49\sigma_R^2}{(1+1.11\sigma_R^{12/5})^{7/6}}\right) - 1\right]^{-1}$$

$$\beta = \left[\exp\left(\frac{0.51\sigma_R^2}{(1+0.69\sigma_R^{12/5})^{5/6}}\right) - 1\right]^{-1} \tag{3.58}$$

where σ_R^2 is the Rytov variance and $K_{\alpha-\beta}(\cdot)$ is the modified Bessel function of the 2nd kind of order ($\alpha-\beta$); note: the PDF, $p(I)$ and the parameters were discussed earlier in this chapter.

BER analysis for BPSK subcarrier intensity modulated FSO link

The received signal at the photodetector output is (DC component filtered out and over a symbol duration, T) [17]

$$\mathrm{i_r}(\mathrm{t}) = \mathrm{d}_j RI\alpha A g(t)\cos(\omega_c t) + n(t) \tag{3.59}$$

where $d_j \in \{1, -1\}$ is the signal level for the jth data symbol corresponding to the data symbols "1" and "0," and A is the fixed subcarrier amplitude. The threshold level is then fixed at zero mark. The electrical SNR ($\mathrm{SNR_e}$) at the input of the BPSK demodulator is given by [19]

$$SNR_e = \frac{(RI\alpha)^2 P_m}{2B_{el}(qRI_{B_g} + 2kT_e / R_L)} \tag{3.60}$$

where $P_m = \left(\frac{1}{T}\right)\int_T m^2(t)dt$ is the subcarrier signal power, B_{el} is the electrical filter bandwidth required to pass $m(t)$ without distortion, q and k are the electronic change

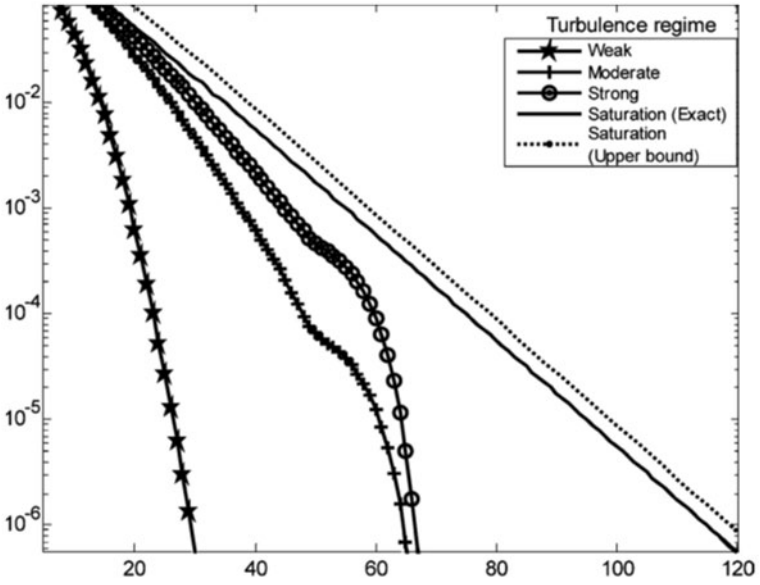

Fig. 3.10 BER as a function of normalized SNR employing BPSK subcarrier intensity modulation in the Gamma-Gamma atmospheric turbulence (*Reprinted with permission from IEEE, 2009* [17]). *BER* bit error rate, *SNR* signal to noise ratio, *BPSK* binary phase-shift keying

and the Boltzmann's constant, respectively. I_{B_g} is the background radiation irradiance, T_e and R_L are the temperature and the receiver circuit load resistance, respectively. With BPSK coherent detection, the baseband signal

$\mathrm{i_d}(\mathrm{t}) = \mathrm{d}_j RI\alpha(A/2)\cos(\omega_c t) + n_d(t)$, where $n_d(t) \approx N\left(0, \frac{\sigma^2}{2}\right)$. For an equiprobable data symbols, the BER is given by the probability of $i_d(t) > 0$ when a data symbol "0" was transmitted. The unconditional BER is [16]:

$$BER = \int_0^\infty \int_0^\infty \frac{1}{\sqrt{\pi}\sigma} \exp\left[-\frac{(i_d + 0.5RI\alpha A)^2}{\sigma^2}\right] p(I) di_d dI = \int_0^\infty Q\left(\frac{IRA\alpha}{\sqrt{2\sigma^2}}\right) p(I) dI \quad (3.61)$$

The noise variance in the above equation is $\sigma^2 = 2B_{el}(qRI_{B_g} + 2kT_e / R_L)$. The function, $Q(.)$ is the Q function.

The PDF of irradiance, $p(I)$ given by Eq. (3.57) is substituted in the above equation to obtain

$$BER = \int_0^\infty Q\left(\frac{IRA\alpha}{\sqrt{2\sigma^2}}\right) \frac{2(\alpha\beta)^{\frac{\alpha+\beta}{2}}}{\Gamma(\alpha)\Gamma(\beta)} I^{\frac{(\alpha+\beta)}{2}-1} K_{\alpha-\beta}\left(2\sqrt{\alpha\beta I}\right) dI \quad (3.62)$$

Note that the electrical SNR at the input of the subcarrier demodulator with modulation index normalized to unity can be written as [18]

$$SNR_e = \frac{R^2 A^2 I^2}{2\sigma^2} \tag{3.63}$$

so that BER can be written as [18]

$$BER = \int_0^\infty Q\left(\sqrt{SNR_e}\right) \frac{2(\alpha\beta)^{\frac{\alpha+\beta}{2}}}{\Gamma(\alpha)\Gamma(\beta)} I^{\frac{(\alpha+\beta)}{2}-1} K_{\alpha-\beta}\left(2\sqrt{\alpha\beta I}\right) dI \tag{3.64}$$

The above equation has no closed form solution and has to be solved numerically. Figure 3.10 shows BER plot as a function of normalized SNR for weak, moderate, and strong turbulence regimes. The normalized $SNR_e=(R.E[I])^2/2\sigma^2$ for all turbulence regimes was used where $E(I)$ is the expected value (averaged received) of irradiance.

Differential Phase Shift Keying (DPSK) Modulation for FSO Communication Link The differential phase-shift keying (DPSK) can be viewed as the noncoherent version of the phase shift keying (PSK). It eliminates the need for a coherent reference signal at the receiver by combining two basic operations at the transmitter:

(1) differential encoding of the input binary wave, and (2) PSK. DPSK has gained considerable interest for FSO communications due to a ~3 dB sensitivity improvement over the popular OOK, and reduced peak power [5]. Two orthogonal symbols represented by the relative phase between two differentially encoded bits carry the binary information: a "0" represented by no-phase change and a "1" by a π phase difference (or vice-versa). The receiver is equipped with a storage capability, so that it can measure the relative phase difference between the waveforms received during two successive bit intervals. The phase difference between waveforms received in two successive bit intervals will be independent of the unknown phase θ, if θ contained in the received wave varies slowly (slow enough for it to be considered essentially constant over two bit intervals). DPSK is another example of noncoherent orthogonal modulation when it is considered over two bit intervals. The average probability of error or BER for DPSK is given by [5,19]

$$BER = 1/2 \exp\left(-\frac{E_b}{N_0}\right) \quad or, \quad = 1/2 \exp(-N_{avg}) \tag{3.65}$$

where E_b and N_0 are the signal and noise energy per bit, respectively and N_{avg} is the SNR, equal to the average number of photons per bit (PPB), i.e, $N_{avg}=SNR_{DPSK}$

In case of atmospheric scintillation, the unconditional BER is obtained by averaging the above equation over the irradiance fluctuations statistics given by $P(I)$. The BER result in presence of atmospheric turbulence is given by

$$BER_{Turbulence} = \int_0^\infty 1/2 e^{-SNR_{DPSK}} P(I) dI \tag{3.66}$$

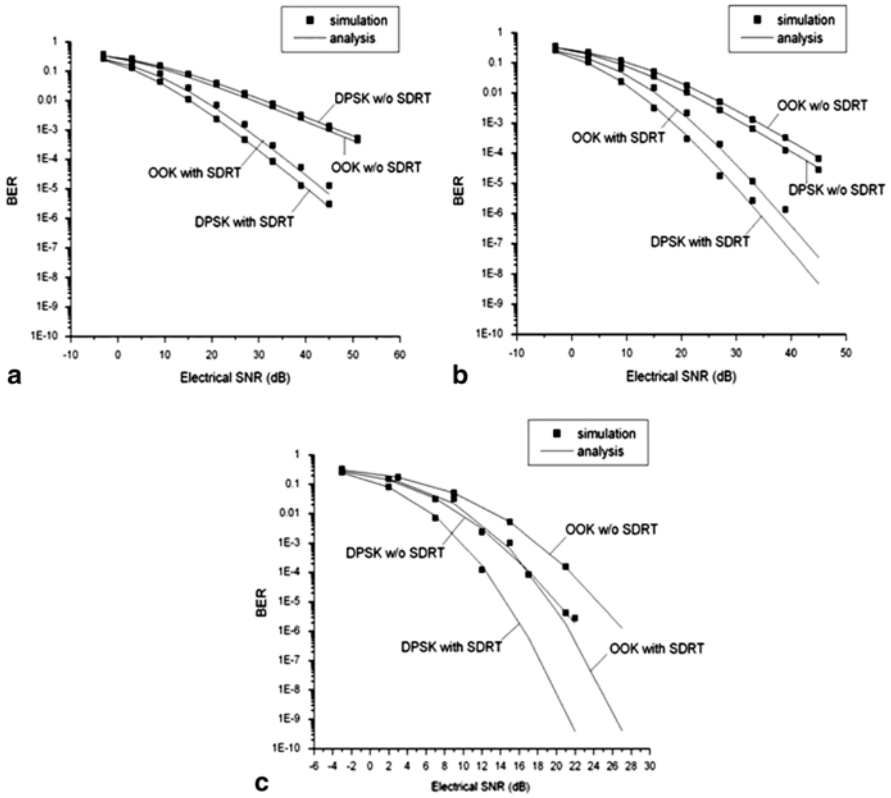

Fig. 3.11 BER performance of FSO communications using DPSK formats in **a** the strong turbulent channel, **b** the moderate turbulent channel, and **c** the weak turbulent channel. OOK modulation is also shown for comparison. The Gamma-Gamma distributed atmospheric channel model was used. Note: space diversity reception technique (SDRT) notation in the figure. In this case, the figures of interest applicable to the description here are without space diversity reception (without SDRT; *Reprinted with permission from IEEE, 2009* [30]). *BER* bit error rate, *FSO* free-space optical, *DPSK* differential phase-shift keying, *OOK* on-off keying

where $P(I)$ can be assumed as GG distribution discussed earlier in this chapter. The BER can be computed from the above equation by numerical solution. Figure 3.11 shows the BER performance of DPSK and OOK formats in different turbulence regimes. In the Fig. 3.11, the cases of without the space diversity reception technique, i.e., without SDRT are applicable for our discussion.

Some Other Modulation Formats Relevant to FSO Communications The most common modulation formats relevant to FSO links have been discussed. However, there are many modulation possibilities besides OOK, PPM, BPSK, and DPSK described in the previous sections. Some of the formats include *M*-ary frequency-shift keying (M-FSK) and polarization-shift keying (polSK), which are briefly described below.

M-ary Frequency-shift keying (M-FSK) There are M frequencies in the FSK symbol with $k=\log_2 M$ bits of information per symbol (like PPM). For M-FSK, the

bandwidth expansion directly impacts the modulation bandwidth and associated transmit/receive electronic bandwidth [13]

$$B_{E(M-FSK)} = \frac{R_{Data}}{\log_2 M} = R_{sym(M-FSK)} \tag{3.67}$$

This electronic bandwidth requirements are actually less than or equal to the data rate, R_{Data}. A spread of M-frequencies is used in the expansion of the M-FSK bandwidth expansion. This requires a parallel M-channel receiver design adding some complexity. FSK waveforms can have a 100 % duty cycle, which is thus well suited for use with average or peak power-limited transmitters. For parallel TX and RX designs, the duty-cycle per channel is approximately $1/M$ assuming all symbols to be equally likely. The general analytic expression for FSK modulation is [20]

$$S_i(t) = \sqrt{\frac{2E}{T}} \cos(\omega_{it} + \phi),\ 0 \le t \le T \quad \text{i} = 1, 2, \ldots..\text{M} \tag{3.68}$$

where $S_i(t)$ is the transmitted signal. The transmitted signals are of equal duration T, and have equal energy E. Over a symbol duration T, the frequency term, ω_i, will have M-discrete values, and the phase term, ϕ is arbitrary constant. M is usually a non-zero power of 2 (2, 4, 8, 16, …). The signal set is characterized by Cartesian coordinates, such that each of the mutually perpendicular axes represents a sinusoid with a different frequency. An upper bound for the probability of symbol error is given by [19]

$$P_e \le \frac{1}{2}(M-1) erfc\left(\sqrt{\frac{E}{2N_0}}\right) \tag{3.69}$$

The probability of symbol error for the noncoherent detection of M-ary FSK is given by [19]

$$P_e = \sum_{k=1}^{M-1} \frac{(-1)^{k+1}}{k+1} \binom{M-1}{k} \exp\left(-\frac{kE}{(k+1)N_0}\right) \tag{3.70}$$

where $\binom{M-1}{k}$ is a binomial coefficient, i.e.,

$$\binom{M-1}{k} = \frac{(M-1)!}{(M-1-k)!k!} \tag{3.71}$$

The leading term of the series in the equation for P_e provides an upper bound on the probability of symbol error for the noncoherent detection of M-ary FSK

$$P_e \le \frac{M-1}{2} \exp\left(-\frac{E}{2N_0}\right) \tag{3.72}$$

Polarization Shift Keying (PolSK) The symbol set in the *M*-ary orthogonal formats can be extended using the binary polarization shift keying (2-PolSK) by a bit (1 bit per symbol [21,34]), i.e., $M \rightarrow 2M$ and $k \rightarrow k+1$ without increasing peak power or electrical bandwidth requirements per channel. A binary information is encoded in two orthogonal polarization bases, such as left- and right-hand circular polarization or, "s" and "p" linear polarizations. These can be implemented by using phase modulator and parallel intensity modulators.

Note that the final choice of modulation format for FSO communication link will depend on both power and spectral efficiency as well as the complexity and the cost involved.

3.5 Channel Capacity and Coding for FSO Communications

In any real-world FSO communication system which has to operate in presence of noise (due to atmospheric turbulence, detector, etc.) is always susceptible to errors in the transmission of information. The fundamental resources available for designing communication systems are signal power, time, and bandwidth. These three resources can be traded against each other such that errors which occur in transmission can be reduced to arbitrarily small probability. The object is often to achieve maximum data transfer, in a minimum bandwidth while maintaining an acceptable quality of transmission. For digital communications, the quality of transmission is essentially expressed in terms of probability of bit error, i.e., BER defined earlier in this chapter. Different coding techniques are used to reduce BER and accomplish reliable communication.

3.5.1 Channel Capacity and Spectral Efficiency of FSO Channel

The capacity is defined as a maximum rate of information data stream within the communication channel, and the spectral efficiency is defined as a ratio of the capacity and the bandwidth of the communication channel. The capacity of a noise channel relates the SNR of the received signal to the average rate of symbols per channel use that can be recovered with an arbitrary small BER. For a binary alphabet, the maximum rate of 1 bit per channel use can be achieved, but only when SNR is infinite. If the frequency response of the channel is known, the spectral bandwidth efficiency (bits/Hz) can be defined to understand channel capacity.

The Shannon-Hartley formula can be used to calculate the capacity of the channel with AWGN:

$$C = B_{\omega} \log_2[1 + SNR] \qquad \text{bits/s} \tag{3.73}$$

where B_ω is the bandwidth. The spectral efficiency can then be expressed as:

$$\tilde{C} = \frac{C}{B_w} = \log_2[1 + SNR] \tag{3.74}$$

The capacity of the channel gives a theoretical limit for the transmission rate of (reliable, i.e., error-free) data from a transmitter of given power, over channel with a given bandwidth, operating in a given noise environment. In order to realize this theoretical limit, however, an appropriate coding scheme must be found. The SNR can be written as $SNR = \frac{E[I]^2}{N_0}$ where E [.] is the expectation operation, and I is the received intensity, and N_0 is the electrical noise power. The procedure for determining the channel capacity of the FSO channel for turbulent condition is the following:

The statistical channel is modeled by

$$\mathrm{Y} = \mathrm{I}\,\mathrm{X} + \mathrm{N}, \qquad \mathrm{I} > 0 \tag{3.75}$$

where Y is the received signal, I is a random variable representing the intensity gain, X is the transmitted binary signal, and N is the noise at the receiver. The PDF of the intensity fluctuation is assumed to follow a GG distribution, already described in this chapter. Without a loss of generality, the responsivity factor of the detector may be assumed to be equal to 1. If a "0" is transmitted, the received signal is given by noise alone. If a "1" is transmitted, the channel will randomly scale the input signal by a random factor whose PDF is GG distribution. Channel capacity is for a binary-input continuous-output channel and is defined as the maximum of the mutual information between X and Y over all input distributions [20]. The input follows a binomial distribution. The mutual information for this channel is given by [22]

$$I(Y;X) = \int_0^\infty \sum_{x=0}^{1} f_Y(y|x) P_X(x) \log_2 \frac{f_Y(y|x)}{\sum_{z=0}^{1} f_Y(y|z) P_X(z)} dy \tag{3.76}$$

where $f_Y(y|x)$ is the conditional distribution of the output Y given the input X, and $P_X(x)$ is the probability of $X=x$. Note that the conditional distribution and $f_Y(y|x=0)$ is a zero-mean Gaussian distribution and $f_Y(y|x=1)$ is the distribution of $I+N$, which can be evaluated numerically using the fact the PDF of the sum of two random variables (I and N in this case) is the convolution of their PDFs [36]. Figure 3.12 shows the channel capacity for plane waves using OOK modulation and a point receiver as a function of SNR. The capacity of an OOK/AWGN channel is also shown for comparison. The curves represent the maximum possible coding rate at which the probability of error can be made arbitrarily small for a given SNR and turbulence strength. Under weak turbulence, the capacity approaches that of abinary AWGN channel. With increased σ_R, the capacity decreases resulting in worse performance of the communication link. The capacity curves approach a limit asymptotically for very strong turbulence.

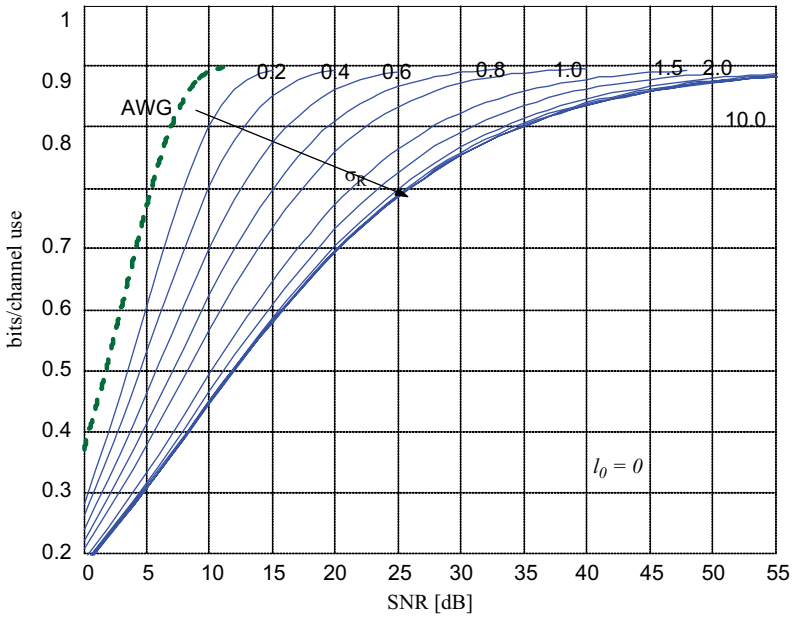

Fig. 3.12 The channel capacity for plane waves using OOK modulation as a function of SNR for various values of σ_R (where σ_R is the Rytov variance), i.e., different atmospheric conditions (Reprinted with permission from The Optical Society of America, OSA, 2005 [22]). *OOK* on-off keying, *SNR* signal to noise ratio

3.5.2 Coding Techniques as a FSO Link Aid

For a reliable FSO communication system design, coding techniques are needed to reduce the probability of error to an arbitrary small probability. Coding usually involves adding extra bits of information that, when processed at the receiver, aid in correcting errors that were made during transmission. For a fixed SNR, the only practical option available for changing data quality to be acceptable is to use error-control coding. The use of coding can be also to reduce the required SNR for a fixed BER. This reduction in SNR may reduce the required transmitted power or reduce the hardware costs. The use of error-control coding, however, adds complexity to the system, especially for the implementation of decoding operations in the receiver. Therefore, the design trade-offs in the use of error-control coding to achieve acceptable error performance include considerations of bandwidth and system complexity. The design goal of channel coding or error-control coding is to increase the resistance of a digital communication system to a channel noise. Error-control coding is used to detect and often correct symbols which are received in error. The most frequent use of coding on a communications link is to reduce the required signal at the receiver. Coding gain measures this reduced signal requirement and is defined as

$$\Gamma_{code} = 10\log_{10}\left[\frac{P_{req}(uncoded)}{P_{req}(coded)}\right] \tag{3.77}$$

Review of channel coding techniques is relevant to FSO communication. In this section, a few channel coding techniques are presented.

Convolution Codes (CC) and Linear Block Codes Convolution codes (CC) are powerful error-correcting codes usually used in digital communication systems and are extensively used for real-time error correction. Convolution coding is done by combining the fixed numbers of input bits which are stored in fixed-length shift register and are combined with the help of mod-2 adders. An input sequence and contents of shift registers performs mod-2 addition after information sequence is sent to shift registers so that an output sequence is obtained. The code rate, R is defined by $R=k/n$ for a convolution code where k is the number of parallel input bits and n is the number of parallel decoded output bits. The state information of convolution encoder is stored in shift registers and contstraint length (k) relates the number of bits upon which the output depends. CC are generally more complicated than linear block codes. The linear block codes are the types of codes where each code word in the set is a linear combination of a set of generator code words. If the messages are k bits long and the code words are n bits long (where $n>k$), there are k linearly independent code words of length n that form a generator matrix. In the linear block code scheme, the message vector u is simply multiplied by the generator matrix to produce a code word vector v that is n bits long. The convolution codes are popular in satellite and deep space communications where bandwidth is essentially unlimited, but the BER is much higher.

Viterbi Decoding of CC The Viterbi decoding algorithm is applied to convolutional encoder using maximum likelihood decoding. This device has been implemented on a chip. The decoded error rate to symbol error rate can be approximately written as [23]

$$p_e \approx (0.757/2)erfc\left[\sqrt{(-\ln 2P_{be})10^{\beta/10}}\right] \tag{3.78}$$

where $erfc(.)$ is the complementary error function, $\beta = 0$ for soft-decision decoding, $\beta = 0.2$ for hard-decision decoding, P_{be} is the probability of bit error.

Reed-Solomon Codes (RS) The Reed-Solomon (RS) code proposed in 1960 [24] is one of the linear block codes. It is vulnerable to the random error but strong to burst errors, and therefore has good performance in fading channel which have more burst errors. The RS code describes a systematic way of building codes that could detect and correct multiple random symbol errors. By adding t check symbols to the data, an RS code can detect any correct data stream up to $[t/2]$ symbols. As an erasure code, it can correct up to t known erasures, or it can detect and correct combinations or errors and erasures. These codes are suitable as multiple-burst bit-error

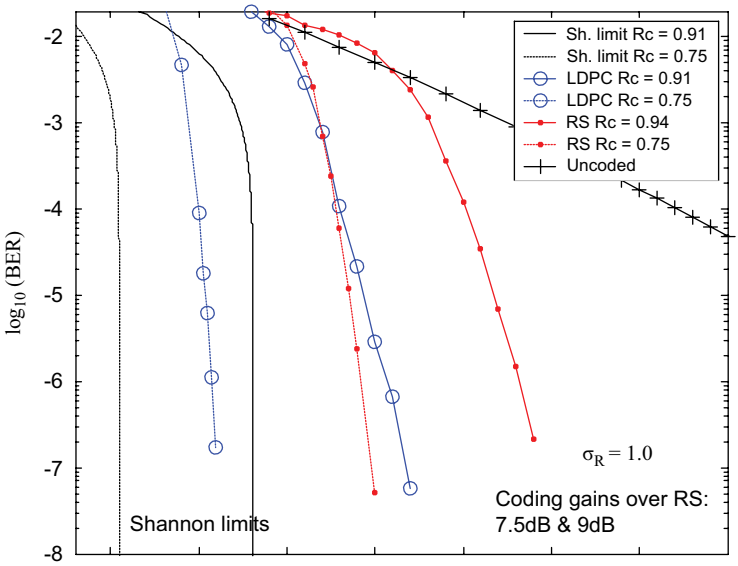

Fig. 3.13 The BER performance curves using LDPC and RS coding schemes as a function of SNR for various turbulence conditions: ($\sigma_R = 1$ where σ_R is the Rytov variance. Also plotted are the BER of the uncoded system and the Shannon limits representing the achievable best performance (Reprinted with permission from The Optical Society of America, OSA, 2005 [24]). *BER* bit error rate, *LDPC* low-density parity-check, *RS* Reed-Solomon, *SNR* signal to noise ratio

correcting codes, since a sequence of $b+1$ consecutive bit errors can affect at most two symbols of size b. The RS family of codes is block codes and as such are M-ary rather than binary-based codes and thus they act upon blocks or segments of data as opposed to each data element. The decoded probability of bit error is given by [23]

$$P_{be} = \frac{n+1}{2n^2}\left[(2t+1)\sum_{i=t+1}^{2t+1}\binom{n}{i}p_s^i q_s^{n-i} + \sum_{j=2t+2}^{n} j\binom{n}{j}p_s^j q_s^{n-j}\right] \tag{3.79}$$

where n is the code length, $2t+1$ the number of correctable bits. A number of RS (n, k, t) codes where the code rate is given by k/n, are given in the reference [20] with the corresponding p_s values.

Low-density Parity-check (LDPC) Low-density parity-check (LDPC) codes are a class of highly efficient linear block codes which can provide performance very close to the channel capacity (the theoretical maximum) using an iterated soft-decision decoding approach at linear time complexity in terms of their block length. In the LDPC code, the parity-check matrix of a linear block code has a low density of 1s and the number of 1s per row and per column is constants. Decoding of LDPC codes is based on sum-product algorithm (SPA) [25]. This is an iterative decoding algorithm where extrinsic probabilities are iterated forward and back between variable

and check nodes of bipartite (Tanner) graph representation of a parity-check matrix H. The LDPC error-correction codes for the FSO channel can give efficient performance in all turbulence regimes (weak, moderate, and strong) [22]. Figure 3.13 shows the BER performance as a function of SNR for different turbulence regimes using LDPC and RS coding schemes. For comparison, the BER of the uncoded system and the Shannon limits representing the best available performance are also shown. The details of the results are described in [22]. These codes have low encoding and decoding complexity, suitable for implementing actual FSO communication system. The details of an LDPC chip architecture is described elsewhere [26].

Turbo Codes Turbo coding is an iterated soft-decoding scheme that combines two or more relatively simple convolution codes and an inter-leaver to produce a block code that can perform to within a fraction of a decibel of the Shannon limit [27]. The parallel concatenation of two identical recursive systematic convolution (RSC) codes is considered here. For each information bit b_k at the encoder output one gets the systematic bit C_{1k} as well as two parity bits C_{2k} and C_{3k} provided by the two RSC encoders [28].

There is an excellent paper describing several communication techniques and coding for atmospheric turbulence channels for the interested readers [29]. The techniques are based on the statistical properties of fading, and are applicable in the regime in which the receiver aperture is smaller than the correlation length of the fading, and the observational interval is shorter than the correlation time of the fading.

Performance Bounds for Coded FSO Communications through Atmospheric Turbulence Zhu and Kahn [29] discussed analytical performance bounds to study the error performance of communication systems. An expression for the pair-wise codeword-error probability and upper-bound codeword-error probability P_{block} is given by [29]

$$\mathrm{P_{block}} \leq \sum_{j, C_j \in S_c} P(C_j) \left[\sum_{\mathrm{k,\, j \neq k.}\ C_k \in S_c} P_e(C_j, C_k) \right] \quad j \neq k \tag{3.80}$$

where S_c is the set of all code words and PC_j is the probability that code word C_j is transmitted. The pair-wise error probability $P(C_j, C_k)$ is the probability that when code word C_j is transmitted, the decoder favors selection of an incorrect code word C_k over C_j. The above equation can be simplified with the knowledge of the weight enumerating function (WEF), and can be extended to accurately estimate the error bounds of constituent codes where the number of code words is infinite, such as convolutional codes and turbo codes. The authors have derived error-probability bounds for various coding schemes such as block codes, convolutional codes, and turbo codes with numerical simulation results.

The BER derivations in atmospheric turbulence for various coding techniques described earlier in this section are beyond the scope of this book.

References

1. X. Fuquin, *Digital Modulation Techniques* (Artech House, Boston, 2000)
2. B.E.A. Saleh, M.C. Teich, *Fundamentals of Photonics* (Wiley, New York, 1991)
3. H.A. Haus, *Electromagnetic Noise and Quantum Optical Measurements* (Springer-Verlag, Berlin, 2000)
4. M.A. Al-Habash, L.C. Andrews, R.L. Phillips, Mathematical model for the irradiance probability density function of a laser beam propagating through turbulent media. Opt. Eng. **40**, 1544–1562 (2001)
5. D.O. Caplan, Laser communication transmitter and receiver design, in *Free-space Laser Communications: Principles and Advances*, ed. by A.K. Majumdar, J.C. Ricklin (Springer, New York, 2008), pp. 109–246
6. A.K. Majumdar, Free-space laser communication performance in the atmospheric channel, in *Free-Space Laser Communication: Principles and Advances*, ed. by A.K. Majumdar, J. C. Ricklin (Springer, New York, 2008)
7. A.K. Majumdar, W.C. Brown, Atmospheric turbulence effects on the performance of multi-gigabit downlink ppm laser communications. Proc. SPIE **1218**, 568–584. (1990) (Free-space laser communication technologies II)
8. T. Ohtsuki, Multiple-subcarrier modulation in optical wireless communications, IEEE Commun. Mag. **3**, 74–79 (2003)
9. O.P. Wasiu, Thesis Ph.D, University of Northumbria at Newcastle, September 2009
10. L.C. Andrews, R.L. Phillips, *Laser Beam Propagation through Random Media* (SPIE Optical Engineering, Bellingham, 2005)
11. W. Hanling, Y. Haixing, L. Xinyang, Performance analysis a bit error rate for free space optical communication with tip-tilt compensation based on gamma-gamma distribution. Opt Appl. **39**(3), 533–545 (2009)
12. A.A. Farid, S. Hranilovic, Link reliability range and rate optimization for free-space optical channels, conTEL 2009. 10th International conference on Telecommunications Zagreb, Croatia, 2009, pp. 19–23
13. Y.I. Xiang, L.I.R. Zengji, Y.U.E. Peng, S. Tao, BER Performance Analysis for M-ary PPM over Gamma-Gamma atmospheric turbulence channels, in Wireless Communications Networking and Mobile Computing (WiCOM), ISBN: 978-1-4244-3709, IEEE Conference, 23–25 Sept 2010
14. The Wolfram function site, 1998-2014 Wolfram Research, Inc. http://functions.Wolfram.com
15. J. Li, J.Q. Liu, D.P. Taylor, Optical communication using subcarrier PSK intensity modulation through atmospheric turbulence channels. IEEE Trans. Commun. **55**(8), 1598–1606 (2007)
16. L.C. Andrews, R.L. Phillips, Y.C. Hopen, *Laser Beam Scintillation with Application* (SPIE, Bellingham, 2001)
17. W.O. Popoola, Z. Ghassemlooy, BPSK Subcarrier Intensity Modulated Free-Space Optical Communications in Atmospheric Turbulence. J. Lightwave Technol. **27**(8), 967–973 (2009)
18. W.O. Popoola, Z. Ghassemlooy, E. Leitgeb, Free-space optical communication using subcarrier modulation in gamma-gamma atmospheric turbulence, in 9th International conference on Transparent optical Networks (ICTON'07), Rome. Italy 3, 2007, pp. 156–160
19. H. Simon, *Digital Communications* (Wiley, New York, 1988)
20. S.Klar Bernard, *Digital Communications: Fundamentals and Applications* (PTR Prentice Hall, New Jersey, 1988)
21. S. Bendetto, R. Gaudino, P. Poggiolini, Direct detection of optical digital transmission based on polarization shift keying modulation. IEEE Sel. Areas Commun. **13**, 531–542 (1995)
22. J.A. Anguita, I.B. Djordjevic, M.A. Neifeld, B.V. Vasic, Shannon capacities and error-correction codes for optical atmospheric turbulent channels. J Opt. Netw. **4**(9), 586–601 (2005)
23. S.G. Lambert, W.L. Casey, *Laser Communications in Space* (Artech House, Boston, 1995)

24. I.S. Reed, G. Solomon, Polynomial codes over certain finite fields. J Soc. Ind. Appl. Math. **8**, 300–304 (1960)
25. I.B. Djordjevic, W. Ryan, B. Vasic, *Coding for Optical Channels* (Springer-Verlag, New York, 2010)
26. M. Mansour, Implementation of LDPC decoders, presented at the IEEE communication Theory Workshop, Park City, Utah, 13–15 June 2005
27. C. Berrou, A. Glavieux, Near optimum error connecting coding and decoding: Turbo-codes. IEEE Trans. Commun. **44**, 1261–1271, (1996)
28. X. Fang, K. Ali, C. Patrice, B. Salah, Channel coding and time-diversity for optical wireless links. Opt. Express. **17**(2), 872–887 (2009)
29. Z. Xiaoming, M.Kahn Joseph, Communication techniques and coding for atmospheric turbulence channels, in *Free-Space Laser Communications: Principles and Advances*, ed. by A.K. Majumdar, J.C. Ricklin (Springer, Berlin, 2008), pp. 303–345
30. Z. Wang, W.-D. Zhong, S. Fu, C. Lin, Performance comparison of different modulation formats over free-space optical (FSO) turbulence links with space diversity reception technique, IEEE Photonics J. **1**(6), 277–285 (2009)
31. E. Hu, K. Wong, M. Marhic, L.G. Kazovsky, K. Shimizu, N. Nikuchi, 4-level Direct-Detection Polarization Shift-Keying (DD-PolSK) system with Phase Modulators, in optical Fiber Conference (OFC), 2003
32. T.M. cover, J.A. Thomas, *Elements of Information Theory* (Wiley-Interscience, New Jersey, 1991)
33. A. Papoulis, *Probability Random Variables, Chapter 6 Two Random Variables and Stotachastic Processes* (WCB/McGraw Hill, 1991)

Chapter 4
Mitigation Techniques for Improved Free-space Optical (FSO) Communications

Arun K. Majumdar

4.1 Introduction

Modern free-space optical (FSO) communications need to be robust and seamless, providing high bandwidth at the right quality of service to both communication terminals in presence of various atmospheric conditions. This means that FSO communications need to have improved reliability when operating in adverse atmospheric conditions. Atmospheric conditions ultimately determines the FSO communications system performance not only for terrestrial applications but also for uplink-downlink (e.g., between ground and satellite, aircraft or unmanned-aerial-vehicle, UAV, terminals), because a portion of the atmospheric path always includes turbulence and scattering media (due to fog, aerosols, etc.) [1]. Chapter 4 provides an in-depth treatment of the critical issues of limitations imposed by the atmospheric effects to establish a successful FSO link. There are a variety of deleterious features of the atmospheric channel that may lead to serious signal fading, and even the complete loss of signal altogether. The performance of FSO communication systems is highly susceptible to degradation caused by atmospheric absorption, atmospheric scattering ,and atmospheric turbulence. For example, intensity fluctuations called scintillation can result in a considerable degradation of the system performance which is normally quantified by the bit error rate (BER). The variations in the received optical signal caused by atmospheric turbulence experiences loss of signal due to the effects such as beam wander and scintillations determine the received fluctuating signal to noise ratio (SNR). The system performance characterized by the BER is therefore affected by the random loss of SNR. Channel fading also determines another metric for quantifying the performance of communications systems, namely outage probability (OP). Fading can be important for long-distance transmissions as well as communication with a moving platform. Ultimately, the system reliability is reduced because of the atmospheric effects. It is therefore very important to develop effective mitigating techniques in order to design a reliable FSO communication system. The chapter starts with a detailed discussion of the two primary atmospheric effects relevant to FSO links: turbulence and scattering. Random atmospheric distortions due to optical turbulence can severely degrade the wave-front quality of a signal-carrying laser (optical) beam, causing intensity fading and random signal

A. K. Majumdar, *Advanced Free Space Optics (FSO),*
Springer Series in Optical Sciences 186, DOI 10.1007/978-1-4939-0918-6_4,
© Springer Science+Business Media New York 2015

losses at the receiver. Absorption and scattering due to particulate matters in the atmosphere may significantly decrease the transmitted optical signal.

Figure 4.1 depicts how the mitigation can help in reducing intensity variations of the received signal. The corresponding probability density/distribution function (PDF) of intensity fluctuations for no turbulence, turbulence without mitigation, and turbulence with mitigation are also shown. All mitigating techniques are explained in details with appropriate derivations, and performance enhancements with each technique are discussed. Various scenarios of practical importance are described with examples in order to determine the applicability of the techniques to be useful for designers in optimizing the performance of a FSO link in presence of atmospheric turbulence, fog, marine environment, and aerosols. Several mitigating strategies are discussed and are shown in the tree diagram, Fig. 4.2.

The PDF of intensity fluctuations of the signal intensity with no turbulence, turbulence without mitigation, and turbulence with mitigation are also depicted

Growing bandwidth demands of various applications require reliable FSO communication, and FSO communication terminals need to address variable link conditions in order to maximize both system availability and throughput. In order to optimize overall system performance in presence of various atmospheric conditions, the FSO communication terminals must dynamically react to changing atmospheric conditions. The free-space communication system should therefore be properly designed to dynamically optimize performance under varying atmospheric conditions. Understanding communication impacts caused by the atmospheric channel are essential to implement advanced mitigation techniques to improve overall performance.

4.2 Aperture Averaging

4.2.1 Aperture Averaging Technique

Increasing the effective receive aperture can be very useful and is one of the simplest methods for mitigating turbulence. The basic concept behind this technique is that if the receiving aperture is larger than a spatial scale size (originating from turbulence) producing the irradiance fluctuations, the receiver will average out the fluctuations over the aperture. The irradiance fluctuations or the scintillation in this case will be less than the scintillation measured with a point receiver. There is also a shift of the frequency content of the irradiance spectrum toward lower frequencies caused by aperture averaging since the fastest fluctuations due to turbulence small-scale sizes average out [2]. The measured scintillation by a receiving aperture is therefore produced by scale sizes larger than the aperture. The optimum size of the receiver will of course have to be determined by the communication link configuration and system requirements. In strong turbulence case, there is a sharp decrease in the scintillation with increasing aperture size up to the coherence

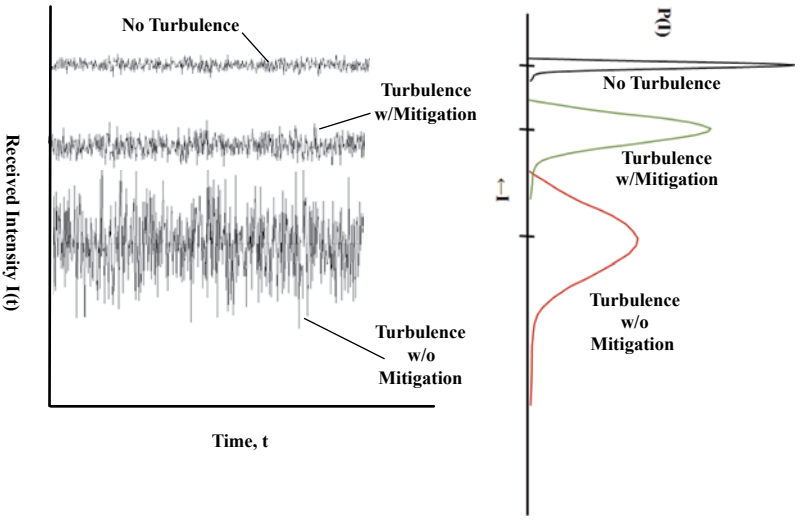

Fig. 4.1 The reduction of intensity variations of the received signal with mitigation

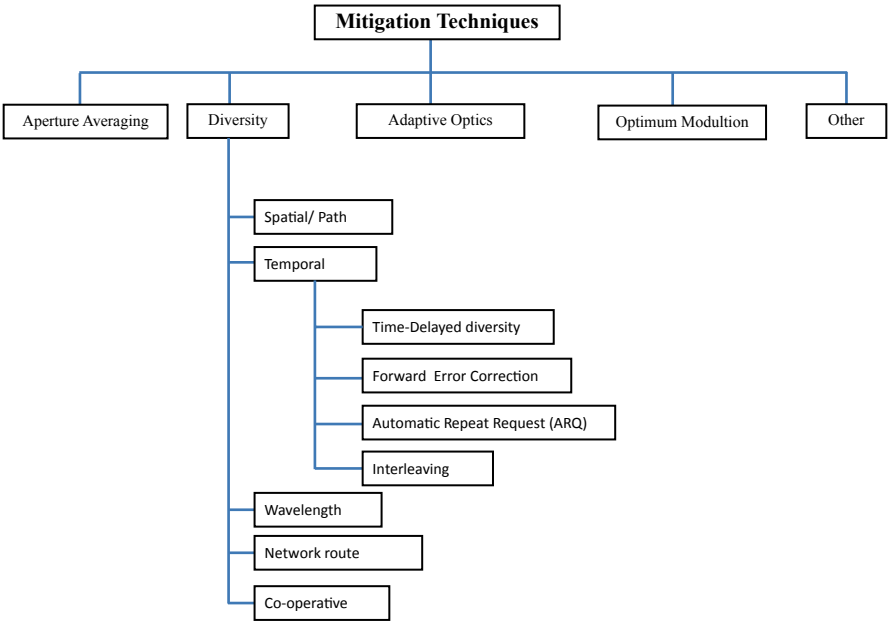

Fig. 4.2 Tree diagram showing the various atmospheric mitigation techniques

scale, $\rho_0 = (1.46C_n^2 k^2 L)^{-3/5}$ (Plane Wave). The scintillation is shown to level out followed by a second decrease in the irradiance flux variance when the aperture exceeds the scattering disk $L/k\rho_0$ where L is the link length, k is the wave number, i.e., $k = 2\pi/\lambda$, λ being the wavelength [2, 3]. In strong turbulence, the small-scale

scintillation is mostly averaged out when the aperture size is larger than ρ_0. The aperture averaging factor will therefore depend on the correct model of the PDF used for the link to operate in presence of specific atmospheric turbulence cases.

Intensity fluctuations caused by atmospheric turbulence which would be measured with a point detector is given as (for a weak turbulence and plane wave case) [4]:

$$\sigma_I^2 = 1.23\, C_n^2 k^{7/6} L^{11/6} \tag{4.1}$$

In practice, the receiving aperture has a finite diameter and the intensity fluctuations measured will not be, σ_I^2 but will have a value which is an average of the fluctuations over the whole aperture. The physics behind this effect was already discussed earlier. The parameter that is usually used to quantify the fading reduction by aperture averaging is called the aperture averaging factor, defined as [4]:

$$A = \frac{\sigma_I^2(D)}{\sigma_I^2(D=0)} \tag{4.2}$$

This parameter describes the reduction A in the scintillation index for a receiver of diameter D compared to a point receiver, and does not depend on the exact shape of the aperture but depends primarily on the receiver aperture area.

The factor A can be calculated from the correlation function of the normalized intensity derived by Tatarski as follows [5]:

$$A = \frac{16}{\pi D^2}\int_0^D b_I(\rho)\left[\cos^{-1}\left(\frac{\rho}{D}\right) - \frac{\rho}{D}\left(1-\frac{\rho^2}{D^2}\right)^{\frac{1}{2}}\right]\rho d\rho \tag{4.3}$$

where ρ is the separation distance between two points and $b_I(\rho)$ is the normalized covariance function.

For a plane wave with small inner scale, $l_0 << \sqrt{L/k}$, the aperture averaging factor can be approximated by,

$$A \approx \left[1 + 1.07\left(\frac{kD^2}{4L}\right)^{7/6}\right]^{-1} \tag{4.4}$$

For small apertures, $A = 1$ as expected, and as aperture size D increases the factor A, and thus the variance decreases.

To aperture averaging effect contributes in mitigating atmospheric turbulence in a FSO communication system in the following way:

- Increasing the aperture diameter D reduces the scintillation variance, $\sigma_I^2(D)$
- Reduced scintillation variance increases average power SNR at the receiver
- Increased average SNR improves FSO systems performance in presence of atmospheric turbulence by decreasing BER to an acceptable level

This section will discuss the above issues to determine the effectiveness of the aperture averaging as a mitigating technique for communications.

For FSO communication systems the effect of aperture depends on the propagation conditions which also include transmitting beam type. Ricklin et al. [6, 7] has given an expression for aperture averaging factor A for a Gaussian beam wave which is typical for a laser communication system. The factor A is given by [6, 7]:

$$A = \frac{16}{\pi}\int_0^1 x dx \; exp\left\{-\frac{D^2x^2}{\rho_0^2}\left[2+\frac{\rho_0^2}{w_0^2\hat{z}^2}-\frac{\rho_0^2\varphi^2}{w^2(z)}\right]\right\} \cdot\left[\arccos(x)-x\sqrt{1-x^2}\right] \tag{4.5}$$

The notations used in the above equation are:

$x=\rho/D$, where D is the receiver aperture diameter, ρ is the transversal distance from the beam optical axis in the receiver plane; z is the propagating distance of the optical field from the transmitter, w_0 is the transmitter beam radius (beam size), R_0 is the radius of curvature of the phase front, $\hat{z} = z/(kw_0^2/2)$ is diffractive distance, and $k = 2\pi/\lambda$ is the optical wave number.

$\rho_0(z) = \left(0.55C_n^2k^2z\right)^{-3/5}$ is the coherence length of a spherical wave propagating in optical turbulence. The parameter, $\hat{r}\ (z)$ characterizes focusing properties of the beam in terms of deviation of the wave-front curvature from the condition of optimal focusing, and $\varphi \equiv \frac{\hat{r}}{\hat{z}} - \hat{z}\frac{w_0^2}{\rho_0^2}$. Other beam parameters not used in the above equation are discussed [6, 7].

The beam size (radius) after propagating a distance z in optical turbulence, $w(z) = w_0(\hat{r}^2 + \zeta\hat{z}^2)^{1/2}$, ζ = the global coherence parameter, ζ_S = spatial coherence of the signal-carrying laser beam as it exits the transmitter ($\zeta_S = 1$ for a coherent beam, $\zeta_S > 1$) for a partially coherent beam.

An example of how to calculate aperture-averaging factor A and aperture-averaged scintillation index using Math Cadis given in Appendix C of Reference [1], Page 50. Figure 4.3 shows aperture-averaging factor as a function of the receiver lens diameter for wavelength, $\lambda = 1.55$ μm, a collimated ($\hat{r} = 1$), partially coherent ($\zeta_S = 100$), transmitter beam size (radius), $w_0 = 2.5$cm , path length, $z = 2$ km. Note that more aperture averaging occurs (for a fixed lens diameter) when turbulence is stronger (5 times stronger for C_n^2 value). This is because for stronger turbulence the coherence length ρ_0 decreases relative to the size of the receiver aperture resulting in additional aperture averaging.

Effect of Aperture-Averaging Mitigation Technique on FSO Communications Performance The parameters to quantify a FSO communication system performance are BER and average <SNR>. The average SNR depends on the PDF of the irradiance fluctuations statistics which contains the intensity variance parameter. Aperture-averaging improves both the amount of received power and the scintillation. The BER depends on average received power, the intensity variance over

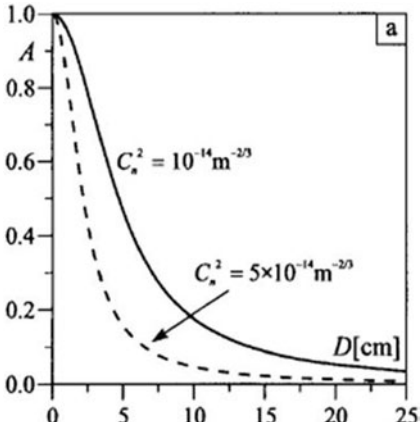

Fig. 4.3 Aperture averaging factor as a function of the receiver lens diameter for $\lambda = 1.55\ \mu m (\hat{r} = 1,\ \zeta s = 100,$ $w_0 = 2.5\ \text{cm},\ z = 2000\text{m}$ (*Reprinted with kind permission from Springer Science+Business Media B.V., Fig. 14 [a], page 38,* [1])

the aperture, the receiver noise (e.g., Johnson and shot noise), and the modulating scheme. Therefore, to understand the aperture-averaging effect on the FSO communication system, it is important to evaluate the following parameters: (i) BER under statistically varying atmospheric turbulence condition (different intensity variances), and (ii) gain in effective SNR because of the increased aperture diameter. Yuksel et al. [8] have given expressions to analyze the aperture-averaging effects in presence of atmospheric turbulence and are discussed below.

1. *BER improvement by aperture averaging*

BER is constantly changing in presence of atmospheric turbulence. The noise in the BER calculation has two factors, namely, receiver noise (Johnson and shot) and intensity fluctuations caused by turbulence. To calculate BER in an on-off keying (OOK) optical wireless system, the intensity fluctuations are only apparent for a received "1," since a received "0" implies no received signal. Therefore the probability of making an error in detecting a "1" can be evaluated by averaging over the appropriate PDF for different intensity variances [9]. The average BER is computed from the product of the probability of a "1" error and the PDF integrated over all possible intensity values and is given by [8, 9]:

$$< BER > = \frac{1}{2}\left(< p_{one} > + p_{zero}\right) \tag{4.6}$$

where the probability of a "0" error can be written as [8, 9]:

$$p_{zero} = \frac{1}{2}\, erfc\left(\frac{1}{2\sqrt{2}}\sqrt{\frac{S}{N}}\right) \tag{4.7}$$

$$< p_{one} > = \int_0^{\infty} \frac{1}{2}\, erfc\left(i - \frac{1}{2}\right)\frac{1}{\sqrt{2}}\sqrt{\frac{S}{N}}\,\frac{1}{\sqrt{2\pi\sigma_I^2}}\,\frac{1}{i}\exp\left\{\frac{-1}{2\sigma_I^2}\left(\ln i + \left(\frac{1}{2}\right)\sigma_I^2\right)^2\right\} di \tag{4.8}$$

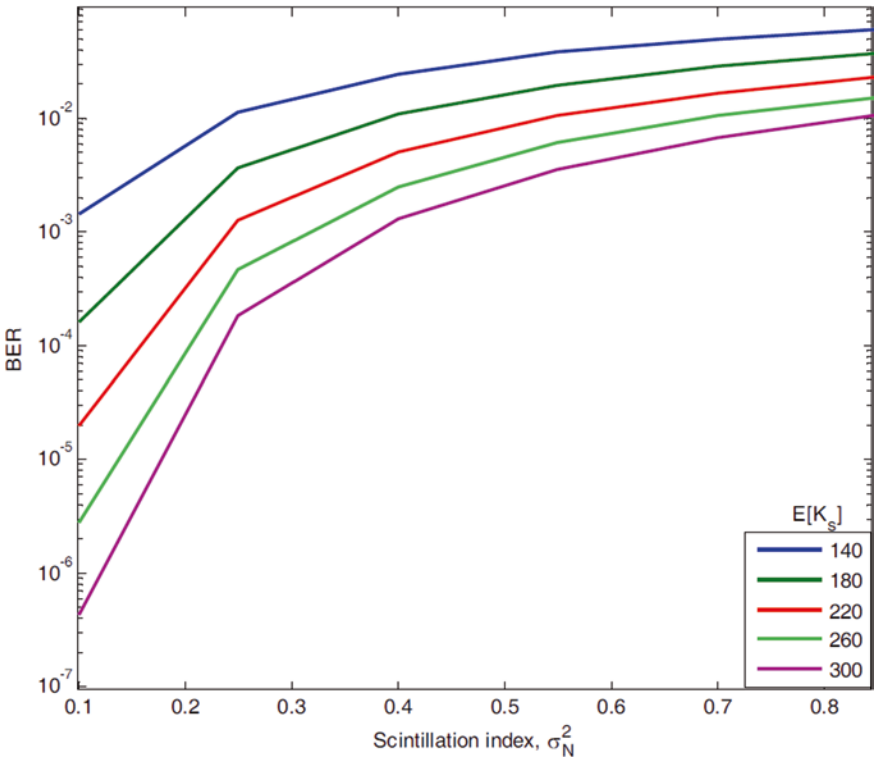

Fig. 4.4 Reduction of BER with decreasing value of variance (scintillation index). The figure shows different signal levels (denoted by Ks) (*Reprinted with permission by Wasiu Popoola, Intechopen, Fig. 15, page 385, 2010, doi:10.5772/7698*). *BER* bit error rate

In the above equation, *erfc* is the complimentary error function, the SNR in absence of turbulence is $\frac{S}{N} = \frac{< I >^2}{\sigma^2}$ (note that the received detector signal in absence of turbulence has a steady value $< I >$, and the normalized received signal is 1; errors result from receiver noise is assumed to have Gaussian distribution with zero mean and variance σ^2).

The quantity σ_I^2 is the variance of log-intensity fluctuations in presence of turbulence (same as intensity variance under weak turbulence condition), and is: $\sigma_I^2 = 1.23 C_n^2 k^{7/6} L^{11/6}$.

Expected reduction in BER as the variance is decreased is shown in the Fig. 4.4. Figure 4.5 shows the decrease of BER as the values of variance is decreased (for a given SNR). The figures imply that a better FSO communications system performance is achieved when the variance is low.

2. *Effects of aperture averaging on mean SNR in presence of atmospheric turbulence*

The SNR is determined by the noise contributions from all possible sources which include signal shot noise, dark current noise, thermal/Johnson noise in the

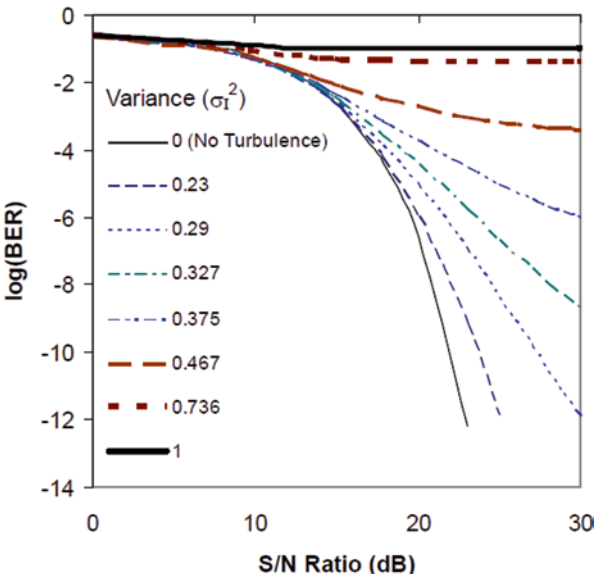

Fig. 4.5 Decrease of BER as intensity variance is decreased for a given SNR (*Reprinted with permission from The Optical Society of America, OSA, 2005* [8]). *BER* bit error rate, *SNR* signal to noise ratio

electronics following the photodetector, and the background noise. Assuming a Gaussian distribution of noise, the SNR at the output of the photodetector in the absence of turbulence is given by [1, 10]

$$SNR_0 = \frac{P_S}{\sqrt{\left(\frac{2hvB}{\eta}\right)(P_S + P_B) + \left(\frac{hv}{\eta e}\right)^2 \left(\frac{4kT_N B}{R}\right)}} \tag{4.9}$$

where P_S is the signal power of the optical transmitter and P_B is the background noise, both in watts, η is the detector quantum efficiency, e is the electronic charge, in coulombs, h is the Planck's constant, v is the optical frequency in hertz, k is the Boltzmann constant, B is the bandwidth of the (detector) filter, T_N is the effective noise temperature, and R is the effective input resistance to the amplifier of the detector. For shot-noise-limited operation, the background noise and the thermal noise can be ignored.

In presence of turbulence, the SNR is a statistically fluctuating term (i.e., an instantaneous value) and therefore the average value is to be taken. The mean SNR can be expressed as [1, 10]

$$< SNR > = \frac{SNR_0}{\sqrt{\frac{P_{S0}}{< P_S >} + \sigma_I^2(D) SNR_0^2}} \tag{4.10}$$

where SNR_0 is the SNR in absence of turbulence defined earlier, P_{S0} is the signal power in the absence of atmospheric effects, the mean input signal power $< P_S >$

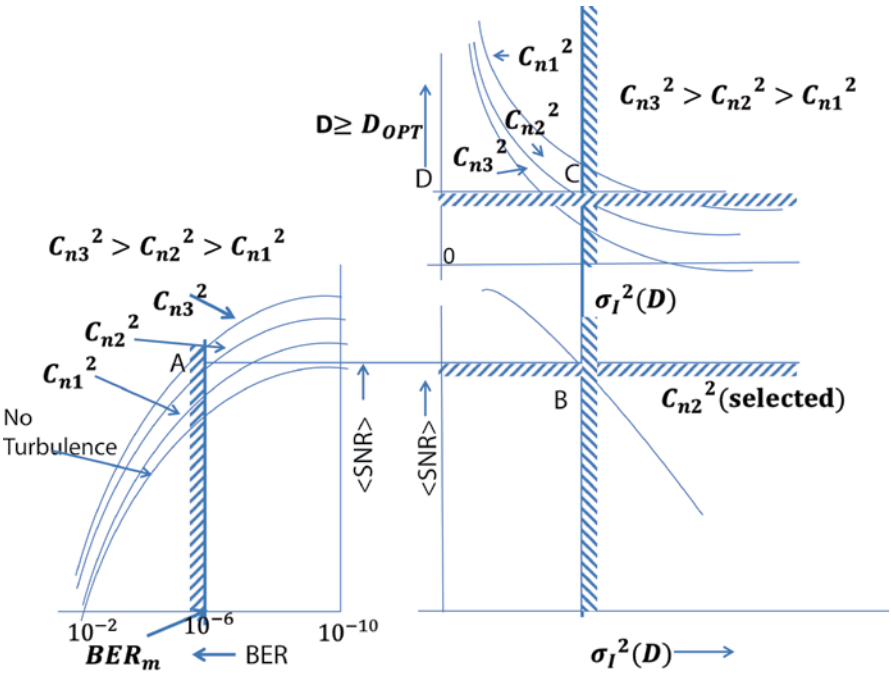

Fig. 4.6 The significant parametric relationships between various FSO system parameters. **a** Estimated average <SNR> from the required BER. **b** Estimated aperture- averaged scintillation variation needed for the required average <SNR>. **c** optimum aperture size satisfying the BER, <SNR>, and scintillation variance requirements. *FSO* free-space optical, *SNR* signal to noise ratio, *BER* bit error rate

(i.e., the mean of the instantaneous input signal power P_S), and $\sigma_I^2(D)$ is the aperture-averaged scintillation index previously discussed. As seen from the above equation, the mean <SNR> decreases with increasing aperture-averaged variance.

Example of Parametric Design Analysis To clarify parametric analysis discussed above, we apply this procedure to the optimum design of a receiver aperture in a FSO communication system. Figure 4.6 illustrates the significant parametric relationships between various FSO systems parameters. Figure 4.6a shows the required BER for the FSO system to be designed as a function of mean SNR for various strengths of turbulence, for example, C_{n1}^2 (low), C_{n2}^2 (moderate), and C_{n3}^2 (strong) where $C_{n3}^2 > C_{n2}^2 > C_{n1}^2$. The FSO system performance requires a minimum BER to be achieved which is denoted as $\text{BER}_\text{m} = 10^{-6}$, as an example only. When a desired strength of turbulence, C_n^2 is specified, Fig. 4.6a indicates the dependency of the BER on the mean SNR for different values of C_n^2. The maximum acceptable BER is usually determined by the value of BER above which the required system performance starts to degrade. Note that the maximum BER is a system requirement, and is to be specified from the mission or the object of the FSO communications which also depends on the communications link scenario. The line of $\text{BER}_\text{m} = 10^{-6}$ in Fig. 4.6a gives the lower bound of BER versus mean SNR for different values of C_n^2.

Figure 4.6b illustrates the relationship between aperture-averaged scintillation variance and the corresponding average SNR values for the specific strength of turbulence chosen (C_{n2}^2 in this example, for illustration purpose only). This curve indicates the trade-off which can be made between mean SNR and aperture-averaged variance. Increasing the variance will reduce the mean SNR requirement which might decrease the FSO communication performance BER, not an acceptable choice. Only a trade-off analysis between system costs and performance sensitivity can determine the optimum choice between these two parameters. The initial choice usually results from several iteration processes. The line AB in Figs. 4.6 (a) and (b) indicates the usual starting point of the iteration processes which ultimately chooses the minimum mean SNR and maximum aperture-averaged variance. Figure 4.6 (c) indicates the aperture size in the receiver design as a function of aperture-averaged variance for various strengths of turbulence as specified earlier. Note that the minimum average SNR has already been selected from Fig. 4.6 (a). The optimum receiver size can now be chosen as the point at which the aperture size needs to be at least double the desired SNR in order to achieve an additional 3 dB reduction in the intensity fluctuations. The line BC in Figs. 4.6 (b) and (c) indicates the usual starting point of this stage of iteration process.

An upper limit of aperture-averaged variance can determine the optimum receiver aperture size: Further reduction in the intensity fluctuations requires an impractical and costly increase in the aperture size. The optimum receiver size is indicated by D_{opt} which satisfies both the system requirements of BER and the average SNR. To achieve an acceptable (minimum) mean SNR, the required minimum laser power needs to be determined. The required laser power for the transmitter determines the system costs and complexity. The link margin analysis for a typical FSO communication scenario for a specific communication range using the transmitting and receiving optics, data modulation technique, enables to determine the laser power needed to accomplish the desired communication performance in order to attain the acceptable minimum BER, and probability of fades and occurrence.

The above procedure determines a set of basic design parameters and trade-off curves which relate functional FSO communication parameters to mission requirements. An optimum design is usually obtained from iteration processes using these curves.

4.3 Diversity Technique

There are two types of diversity technique applicable for mitigating atmospheric turbulence and scattering for FSO communications, namely spatial diversity and temporal diversity. This section discusses the mitigation capabilities of both the diversity techniques in terms of reducing scintillation and improving the link performance.

FSO communication provides a cost-effective, license-free, and wide-bandwidth access technique for high data rate applications. The performance of single-input

single-output (SISO) FSO links is severely affected by the turbulence-induced fading causing performance degradation in terms of BER and OP.

4.3.1 Spatial Diversity

FSO systems using diversity reception can achieve significant performance improvements by mitigating the atmospheric channel turbulence, and was proposed for FSO systems by Ibrahim and Ibrahim [11]. Diversity techniques use multiple identical transmissions from sources to receivers. Multiple transmitters/receivers are used for the multiple transmissions with uncorrelated paths so that the effective level of scintillation and probability of fade can be reduced. This method of turbulence mitigation makes use of spatial transmit and/or receive diversity to create at least two paths between the transmitter and receiver. For good diversity, the separation between the transmitter/receiver should be spaced further apart than the lateral correlation distance on the link. Basically if these diverse paths are uncorrelated, then each path experiences independent fading, improving the overall system performance since the probability of all paths simultaneously experiencing a deep fade is quite small. The system will be complicated to implement, however, if a large spatial separation is needed, because every source and sink must be aligned. For n independent apertures when the received signals are logically combined, the probability of a fade of a given depth is reduced to $Prob(P \le P_{min})^n$ where P_{min} is the minimum power at each receiver aperture [12]. To compare the diversity approaches, the probability should be evaluated for the same total power transmitted and the fade reduction is then $frac\left(\frac{P_{Total}}{n} \le P_{min}\right)^n$ where *frac(x)* denotes the fractional part of x [12].

Understanding Array Receivers in Direct Detection An array of receivers in direct detection systems can reduce the deleterious effects caused by scintillation through aperture averaging. Instead, it is possible to achieve the spatial diversity of a large aperture collecting lens by the use of several smaller apertures separated sufficiently far apart so that each received signal are uncorrelated. The summed output from such an array of smaller receivers will then behave like aperture averaging from one large aperture.

If we have an array of M direct detection receivers, the summed output of M statistically independent detectors is given by [13]:

$$i = \sum_{j=1}^{M} \left(i_{s,\,j} + i_{N,\,j}\right) \tag{4.11}$$

where i_S is the a random signal and i_N is a zero-mean noise current in each of the detector array. Assuming each signal and noise current in each detector has the same mean and variance, the mean amplitude SNR is then [13]

$$< SNR_M > = \frac{M < i_{S,1} >}{\sqrt{M}\,\sigma_{SN,1}} = \sqrt{M} < SNR_1 > \tag{4.12}$$

where $< SNR_1 > = < i_{S,1} > / \sigma_{SN,1}$ is the mean SNR of a single detector. If we want to compare the performance of an array of single detectors whose total area is the same as the area of a large detector, then $D^2 = M D_1^2$ where D is the diameter of a large aperture and D_1 is the diameter of each detector. The aperture averaging factor of the summed output is then

$$A_M = \frac{\sigma_I^2\left(\frac{D}{\sqrt{M}}\right)}{M\sigma_I^2(0)} \tag{4.13}$$

Since the mean SNR is increased as the square root of the aperture number, $\sqrt{M}$, the mean BER is also expected to decrease and thus the system performance is improved.

To mitigate the turbulence fading by exploiting the advantage of spatial diversity, multiple transmitters/receivers can be placed at the both ends of the FSO communication link. There are three possible architectures that can be implemented to achieve spatial diversity which depend on how many of the transmitters or receivers are placed in the FSO system: (i) multiple-input multiple-output (MIMO; multiple transmitters/receivers), (ii) multiple-input single-output (MISO; multiple transmitters and single receiver), and (iii) single-input multiple-out (SIMO; single transmitter and multiple receivers). SISO system will serve as a benchmark for the performance analysis. The spatial diversity is particularly critical for strong turbulence fading where SISO performance is poor.

There are two important FSO communications systems performance metrics: BER and the OP. The OP is defined as the probability that the SNR of the signal at the output of a receiver falls below a threshold, specified by the system's acceptable requirement. To understand the utility of the spatial diversity, both these metrics will be investigated and compared for various FSO systems' spatial diversity architecture with the benchmark SISO system. This is critical in successfully designing an FSO communication system.

FSO System Model for Spatial Diversity Multiple transmit/receive apertures is a well-known diversity technique in radio frequency (RF) systems and can be used in FSO communication systems where the inherent redundancy of spatial diversity has the potential to significantly improve the performance. The possible temporal blockage of the transmitting laser beams by obstructions in the communication path can be reduced, and thus a longer FSO communication range can be achieved. This section discusses the performance of various inputs and outputs configurations for FSO links over independent but not necessarily identical distributed turbulence channel. The performance metrics such as the average BER and OP expressions are derived for a turbulence channel model.

For a MIMO (FSO) system under consideration, the information signal is transmitted via M apertures and received by N apertures over a discrete time ergodic channel with additive white Gaussian noise (AWGN). Assuming a binary input and continuous output and intensity modulation with direct detection (IM/DD) with OOK modulation, the received signal at the *n-th* receiver aperture is given by [14]

$$r_n = \eta s \sum_{m=1}^{M} I_{mn} + v_n, n = 1, \ldots \ldots N \tag{4.14}$$

where $s \in \{0,1\}$ represents the information bits and v_n is the AWGN with zero mean and variance $\sigma_v^2 = \frac{N_0}{2}$, where N_0 is the noise power spectral density (Watts/Hz). The I_{mn}'s are independent random variables which follow Gamma-Gamma probability distribution functions. For link distances of the order of kilometers and for aperture separation distances of the order of centimeters, this independence is reasonably valid [15].

There are basically three combining schemes employed at the receiver side: (i) Optimal Combining, (ii) Equal gain Combining (EGC), and (iii) Selection Combining (SC). Expressions for the average BER at the output of the receivers will be discussed for different FSO systems architecture.

Case 1. SISO FSO Links The case of SISO is introduced for benchmark purpose so that the spatial diversity can be appreciated when using multiple transmitters and/or receivers in the FSO communication link. Two performance metrics need to be evaluated: the average BER and the OP.

a. Average BER

Since I_{mn} is random, the SNR at the receiver is also random that depends on the specific turbulence-induced model statistics, $f_{I_{mn}}(I_{mn})$ used. The calculation of the average BER requires the computation of average SNR. The instantaneous SNR can be defined as

$$\mu_{mn} = (\eta I_{mn})^2 / N_0 \tag{4.15}$$

The average SNR is then obtained from the first moment of the instantaneous SNR, which is given by

$$< \mu_{mn} > = < \frac{(\eta I_{mn})^2}{N_0} > = (\eta < I_{mn} >)^2 / N_0 \tag{4.16}$$

where $< >$ denotes an average.

If we use IM/DD with OOK modulation in the presence of AWGN and under perfect channel state information (CSI) at the receiver side, the BER is given by

$$P_r(E) = P_r(1)\, P_r(E \mid 1) + P_r(0) P_r(E \mid 0) \tag{4.17}$$

where $P_r(1)$ and $P_r(0)$ are the probabilities of sending 1 and 0, respectively, and $P_r(E \mid 1)$ and $P_r(E \mid 0)$ are the conditional bit-error probabilities when the transmitted bit is 1 and 0. The following assumptions can be made: $P_r(1) = P_r(0) = 0.5$, and $P_r(E \mid 1) = P_r(E \mid 0)$. The conditional probability is given by [16]

$$P_r\left(E \mid I_{mn}\right) = P_r\left(E \mid 1, I_{mn}\right) = P_r\left(E \mid 0, I_{mn}\right) = Q\left(\frac{\eta I_{mn}}{\sqrt{2N_0}}\right) \tag{4.18}$$

where $Q(.)$ is the Gaussian Q-function, $Q(x) = \left(\frac{1}{\sqrt{2\pi}}\right)\int_x^\infty \exp\left(-\frac{t^2}{2}\right)dt$.

The average BER can then be obtained by averaging $P_r(E \mid I_{mn})$ over the probability density function $f_{I_{mn}}$ of the intensity fluctuations of I_{mn} as follows (omitting the indexes *m, n* for irradiance *I*):

$$P_r(E) = < BER > = \int_0^\infty P_r(E \mid I) f_I(I) dI \tag{4.19}$$

The term $P_r(E \mid I)$ in the above equation can be expressed in terms of the electrical SNR:

$$Q\left(\frac{\eta I}{\sqrt{2N_0}}\right) = Q\left(\sqrt{\frac{\mu}{2}}\right) = 0.5 erfc\left(\frac{\sqrt{\mu}}{2}\right) \tag{4.20}$$

where *erfc* is a complementary error function.

The PDF of irradiance fluctuations which follow a Gama-Gamma distribution is given by [17]

$$f_I(I) = \frac{2(km)^{(k+m)/2}}{\Gamma(k)\Gamma(m)\bar{I}}(I/\bar{I})^{(k+m)/2-1} K_{k-m}\left[2\sqrt{km(I/\bar{I})}\right] \tag{4.21}$$

where $K_\alpha(\cdot)$ is the modified Bessel function of the second kind and order α, $\Gamma(\cdot)$ is the gamma function and $\bar{I}$ is the expectation of irradiance *I*. The parameters $k>0$ and $m>0$ in the above equation can be selected to match the experimental data with theoretical model of Gamma-Gamma distribution. The parameters are related to the atmospheric turbulence conditions and the aperture sizes [15].

By changing the variables *I* and μ, and performing the integration, the average BER can be obtained.

From the earlier equations, the average BER can be evaluated after performing the integration by changing the variables *I* and μ and assuming the PDF of the irradiance distribution function $f_I(I)$ (in this case Gamma-Gamma distribution). A closed form expression is given by [14]:

$$P_r(E) = < BER > = 0.5F\left(k, m, < \mu >, \frac{1}{2}\right) \tag{4.22}$$

where $F(k, m, < \mu >, s)$ is given by [14]:

$$F(k, m, < \mu >, s) = \frac{\Xi^{k+m} s^{-(k+m)/2}}{4\pi^{3/2}\Gamma(k)\mathrm{T}(m)} G_{2,5}^{4,2}\left[\frac{k^2 m^2}{16 < \mu > s^2}\Big|_{b_p}^{a_p}\right] \tag{4.23}$$

In the above equation, $G_{p,q}^{m,n}[\bullet]$ is the Meijer-G function [18] and is a standard built-in function available in the mathematical software packages, such as Maple or Mathematica.

The parameters in the above equation are defined as

$$a_p = \left\{1 - \frac{k+m}{4}, \frac{1}{2} - \frac{k+m}{4}\right\}$$

$$b_p = \left\{\frac{1}{2} + \frac{k-m}{4}, \frac{k-m}{4}, \frac{1}{2} + \frac{m-k}{4}, \frac{m-k}{4}, -\frac{k+m}{4}\right\} \text{ and } \Xi = \sqrt{\frac{km}{\sqrt{<\mu>}}}$$

b. OP

The other FSO performance metric is the OP. In order to determine if the received signal contains a signal, a threshold value, μ_{th} had to be decided below which the SNR of the signal at the output of the receiver is not considered as a signal. OP is defined as that probability for which $\mu < \mu_{th}$ which represents a protection value of the SNR above which the quality of the channel is satisfactory. Obviously, this is an important design parameter for FSO link to be operated as a part of a data network and is critical in the design of both transport and network layer [19].

To calculate the OP, it is necessary to compute the cumulative distribution function (CDF) of the random irradiance, *I*. The CDF is used to predict probabilities of detection and fade in an FSO communication system. The CDF associated with a probability distribution $f_I(I)$ is in general given by

$$\mathrm{P}(I \le I_T) = \int_0^{I_T} f_I(I)dI \tag{4.24}$$

The CDF using the PDF of irradiance fluctuations described by a Gamma-Gamma distribution, Eq. (4.21) is given by [19]

$$F_I(I) = \frac{1}{\Gamma(k)\Gamma(m)} G_{1,3}^{2,1}\left[\frac{km}{\bar{I}} I\Big|_{k,m,0}^{1}\right] \tag{4.25}$$

With $\bar{I} = 1$ and note that (from Eq. (4.15), omitting the parameters *m, n*) $\mu = (\eta I)^2/N_0$.

The OP is obtained as [14]:

$$P_{out} = \Pr\{\mu < \mu_{th}\} = \Pr\left\{\frac{I^2\eta^2}{N_0} < \mu_{th}\right\}$$

$$= \Pr\left\{I < \sqrt{\frac{\mu_{th}}{<\mu>}}\right\} = F_I\left(\sqrt{\frac{\mu_{th}}{<\mu>}}\right) \tag{4.26}$$

Figure 4.7a shows the average <BER> as a function of the received average electrical SNR, $<\mu>$. The FSO communication system considered here uses intensity modulation and direct detection scheme in presence of Gamma-Gamma turbulence

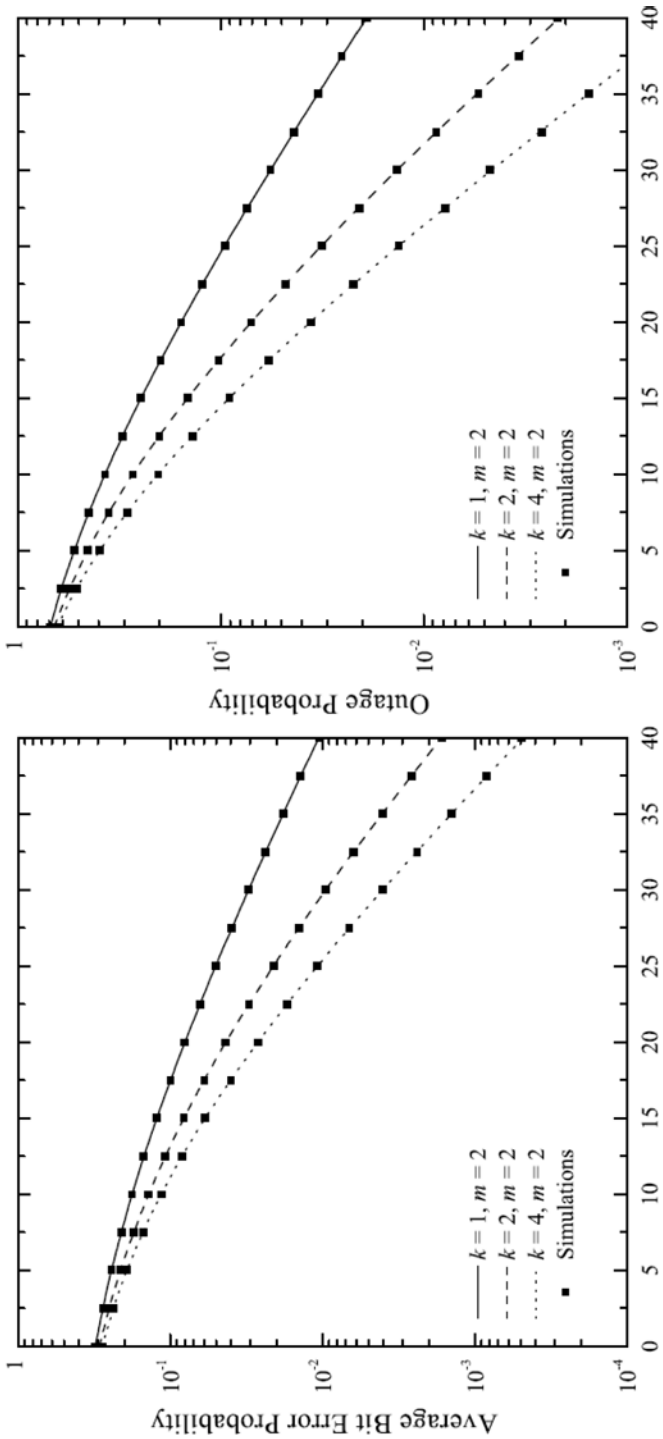

Fig. 4.7 **a** Average bit-error-probability <BER> as a function of the received average electrical signal to noise ratio, $< \mu >$ for different values of the probability distribution parameters, k and m. **b** Outage probability as a function of the inverse normalized outage threshold $< \mu > / \mu_{th}$ *(Reprinted with permission © 2012 Kostas Peppas, Hector E. Nistazakis, Vasiliki D. Assimakopoulos and George S. Tombras. Originally published in* [14] *under CC BY 3.0 license)*

channel, which is characterized by different values of the distribution parameters k and m. Figure 4.7b shows OP as a function of the inverse normalized outage threshold, $< \mu > / \mu_{th}$ under the same modulation, detection, and channel conditions. From the Figs. 4.7a and b, it is clearly shown that for a SISO (FSO) communication system, even with SNR in the range of 30–40 dB, the performance is poor (higher than 10^{-3}). The improvement of the performance using the MIMO (FSO) communication system is described in the following section.

Case 2. MIMO FSO Links: Equal gain combining (EGC) Since the performance for a SISO FSO link is very poor within the SNR range of 30–40 dB under strong turbulence (characterized by the values of the distribution parameters, k and m), a spatial diversity technique must be employed. MIMO (FSO) link provides a scheme with multiple transmitters and multiple receivers at both ends of the link. The optimum decision metric for OOK is given by [20]:

$$P(r \mid on, I_{mn}) \lesseqgtr_{n}^{m} P(r \mid off, I_{mn}) \tag{4.27}$$

where $r=(r_{1,} r_{2,} \ldots r_{n})$ is the received signal vector. Assuming a perfect CSI, <BER> of the FSO communication system for M transmitters and N receivers is given by [20]:

$$< BER >= \frac{1}{2}\int_0^\infty \ldots \int_0^\infty f_I(\mathbf{I}) Q\left(\frac{\eta}{NM\sqrt{2N_0}} \sum_{n=1}^{N} I_n\right) dI \tag{4.28}$$

The Eq. (4.28) can be expressed as [19]:

$$< BER >= \frac{1}{2}\int_0^\infty f_I(I) erfc\left(\frac{\eta}{2MN\sqrt{N_0}} I\right) dI \tag{4.29}$$

where $I = \sum_{n=1}^{N} I_n$. When I_n's are independent and ideally distributed (i.i.d) Gamma-Gamma random variables, the distribution of I can be approximated by the so-called $\alpha - \mu$ distribution [21]. The PDF $f_I(I)$ and CDF $F_I(I)$ can be accurately approximated with the $\alpha - \mu$ PDF and CDF as follows [21]:

$$f_I(I) = \frac{\alpha \mu^{\mu} I^{\alpha\mu - 1}}{\hat{I}^{\alpha\mu}\Gamma(\mu)} exp\left(-\mu \frac{I^{\alpha}}{\hat{I}^{\alpha}}\right) \tag{4.30}$$

$$F_I(I) = 1 - \frac{\Gamma(\mu, \mu I^{\alpha}/\hat{I}^{\alpha})}{\Gamma(\mu)} \tag{4.31}$$

The distribution parameters, in Eqs. (4.30) and (4.31), $\alpha, \mu > 0$, and $\hat{I} = \mathbf{E}\{\hat{I}^{\alpha}\}^{1/\alpha}$ is a scale parameter, E is denoted as an expectation value, and $\Gamma(\bullet,\bullet)$ is the incomplete gamma function [22].

a. Average BER

To calculate average <BER>, the PDF of irradiance fluctuations I (at the combined output of the receiver) which is defined by Eq. (4.30) needs to be approximated by a

single channel where the parameters α and μ can be estimated as functions of the Gamma-Gamma distribution parameters k and m. Estimated parameters can then be used to determine the PDF $f_I(I)$ in Eq. (4.30). The average <BER> can then be evaluated by substituting Eq. (4.30) into Eq. (4.29) and then performing symbolic or numerical integration. Figure 4.8a shows the average BER of MIMO FSO systems employing equal gain control (EGC) operating over Gamma-Gamma fading channel. Figure 4.8a shows that using MIMO FSO system, a substantial improvement in FSO performance can be achieved compared to SISO system. The FSO communication links $L = 2$ km and $L = 4$ km transmitting wavelength $\lambda = 1,550$nm, the strength of turbulence $C_n^2 = 1.7 \times 10^{-14}$ m$^{-2/3}$ and D (aperture diameter)/L (link range) to approach 0 (i.e., point receiver) were used in the Fig. 4.8a. The BER improvement is illustrated by the fact that much lower BER is obtained within the same range of average electrical signals (for example within 30–50 dB range).

b. OP

The OP can be evaluated from the Eq. (4.31). The parameter $\hat{I}$ can be estimated as [14]:

$$\hat{I} = \frac{\mu^{\frac{1}{\alpha}} \Gamma(\mu) \mathbf{E}\{I\}}{\Gamma\left(\mu + \frac{1}{\alpha}\right)} \tag{4.32}$$

The OP for the MIMO FSO system employing EGC as a function of the inverse normalized outage threshold $< \mu > / \mu_{th}$ is shown in Fig. 4.8b. Compared to SISO FSO system the OP curves also show substantial performance improvement using MIMO configuration.

Case 3. MISO FSO Links A few years ago, researchers reported [23] for the first time scintillation reduction for uplink scenario for a laser communication between a satellite and the ground, using multiple transmitters. It was shown that fluctuations on the uplink beacon and communications lasers can be minimized by transmitting multiple independent lasers from separate apertures which then sum incoherently at the satellite. The object of the experiment was to determine the number and spacing required for separate transmitters to reduce fluctuations in the received power due to atmospheric scintillation to acceptable levels. Experimental results for horizontal laser links were established between a laser-transmitting platform and a receive telescope assembly separated by distances of 1.2 and 10.4 km to mimic the expected atmospheric effects of an uplink slant path to a satellite. For all laser separations and ranges, a reduction in received intensity fluctuations due to scintillation was observed as the number of laser transmitters increased from 1 to 16. Figure 4.9 shows recorded intensity vs. time for 1, 2, 4, 8, and 16 laser transmitters located on an 18-inch diameter circle at a horizontal path range of 10.4 km using a 2 in. receive aperture. Figure 4.10 shows histograms of probability of intensity vs. intensity for their sets of data normalized so that the integrated probability is 1 and the mean intensity is 1. The reduction in

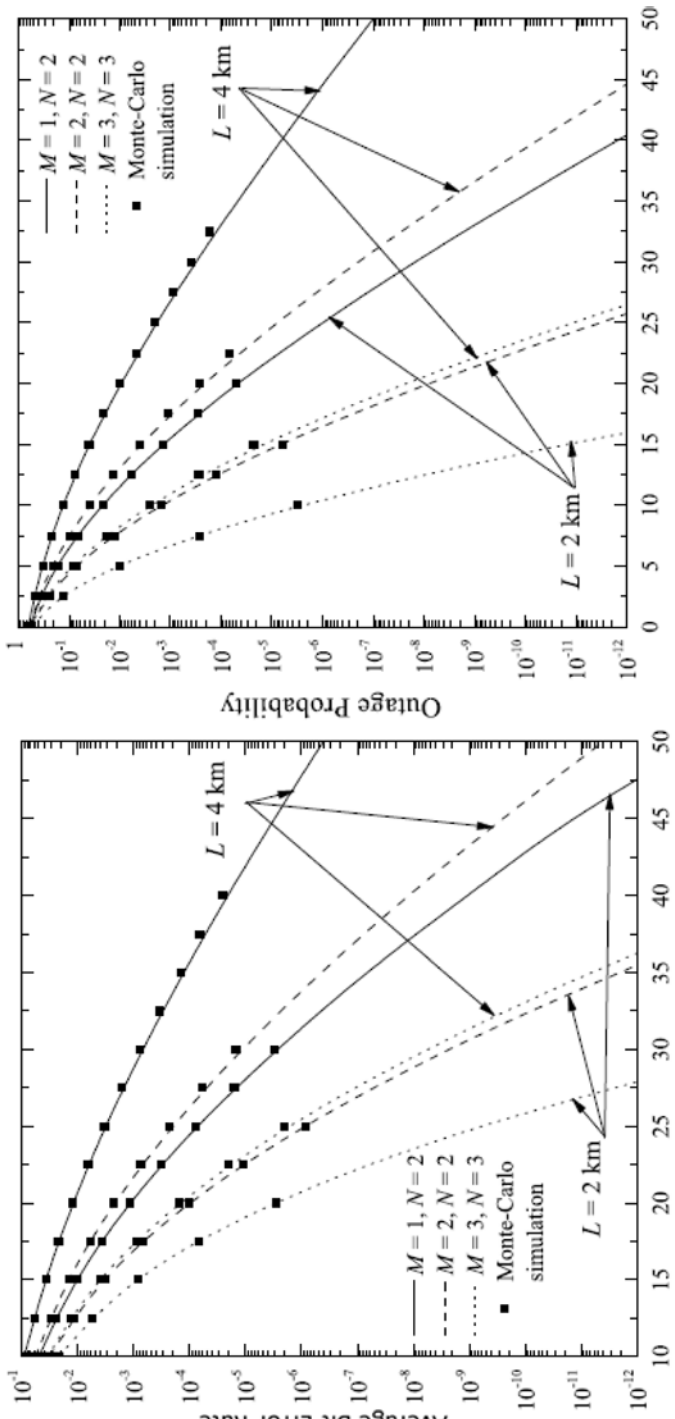

Fig. 4.8 **a** Average bit-error-rate <BER> of a MIMO FSO System employing EGC operating over gamma-gamma fading channel (Reprinted with permission R> of a MIMO FSO System employing EGC operating over gamma-gamma fading channel of average electrical signals (for example within 30a50 dB rcense). **b** Outage probability as a function of inverse normalized outage threshold $< \mu > / \mu_{th}$ employing EGC for MIMO FSO System. (Reprinted with permission © 2012 Kostas Peppas, Hector E. Nistazakis, Vasiliki D. Assimakopoulos and George S. Tombras. Originally published in [14] under CC BY 3.0 license). *MIMO* multiple-input multiple-output, *FSO* free-space optical, *EGC* equal gain control

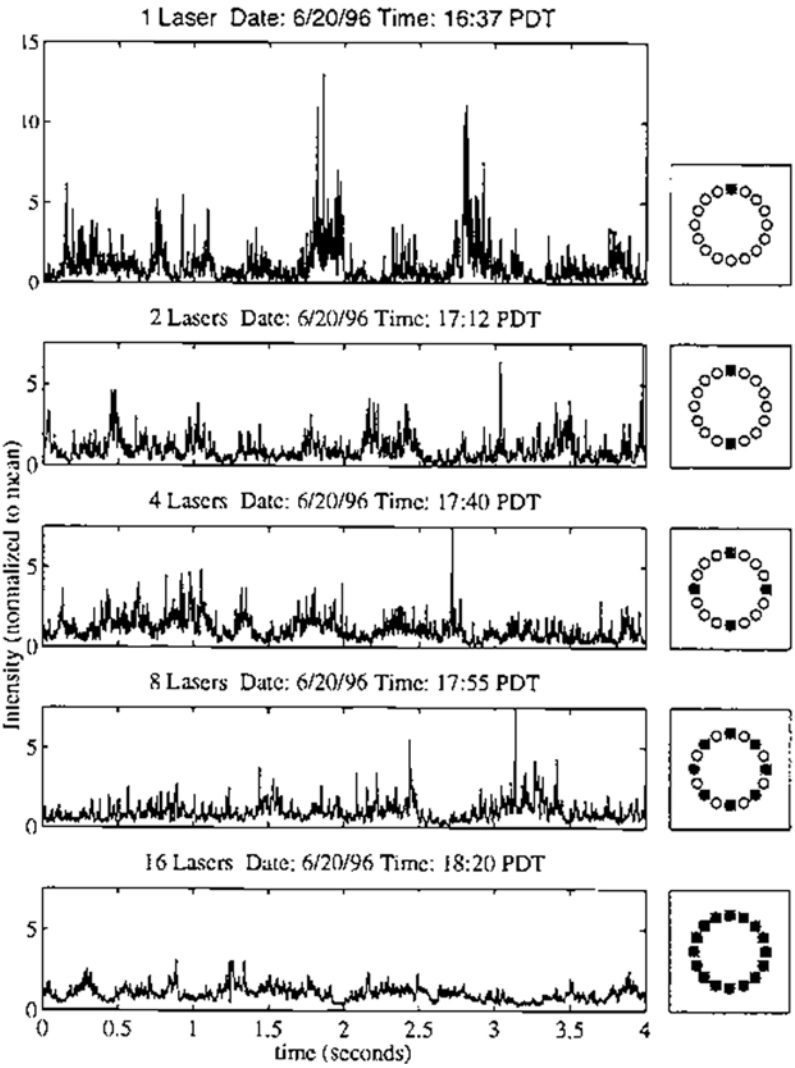

Fig. 4.9 Recorded signal intensity vs. time for 1, 2, 4, 8, and 16 laser transmitters for 10.4 km horizontal path. (*Reprinted with permission from SPIE, 1997* [23])

fluctuations as more laser transmitters are used can easily be seen from the time series data. The reduction of scintillation by the use of multiple uplink beams, each incoherent with the rest, was demonstrated by a group of researchers [24]. The objective of the experiment was to establish a 1-Mbps optical communication link between a satellite and a ground terminal. The link was established by first transmitting a beacon from the ground station to the satellite and the scintillation effects were investigated by launching multiple beams during uplink. Figure 4.11 shows the expected PDF when the total laser power was equally distributed in 1, 2, 4, 8, or 16 beams. With increasing number of beams, the mean varied a little, but the variance drops significantly with additional beams. The method of divid-

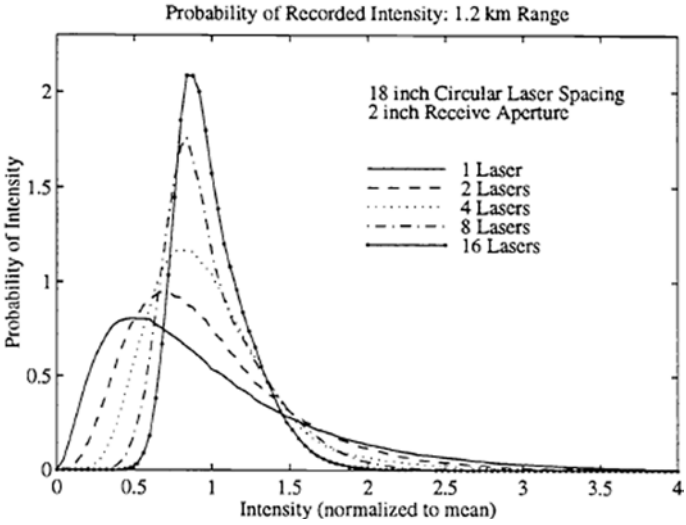

Fig. 4.10 Histograms of probability of intensity vs. intensity for 1, 2, 4, 8, and 16 laser transmitters. (*Reprinted with permission from SPIE, 1997* [23])

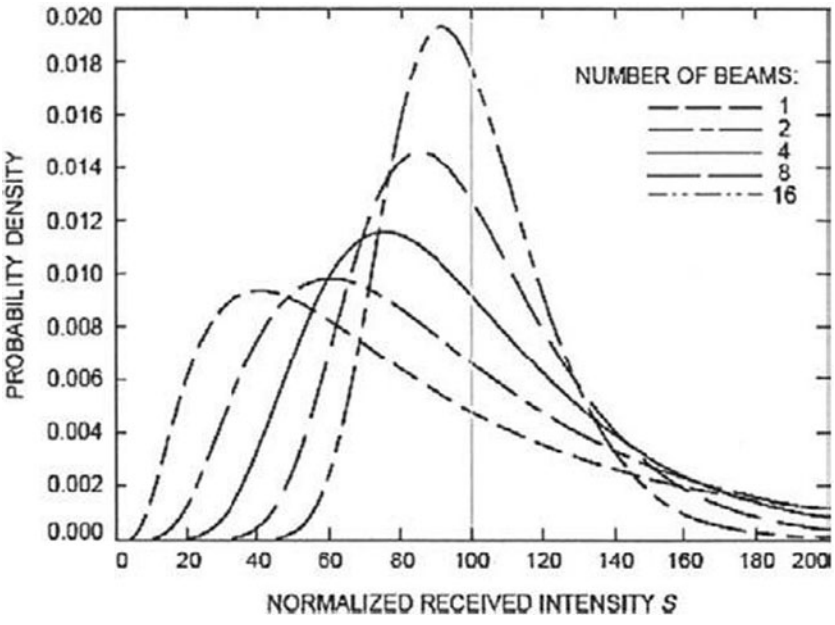

Fig. 4.11 Expected probability density function of intensity as a function of normalized received signal intensity for 1, 2, 4, 8, and 16 laser beams. (*Reprinted with kind permission from Springer Science+Business Media B.V. [Fig. 24, page 04,* [1])

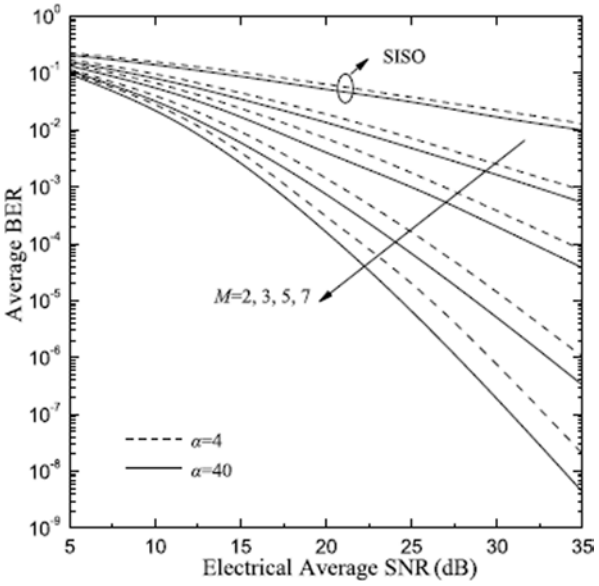

Fig. 4.12 The average BER as a function of electrical average SNR for MISO FSO links with M=2, 3, 5, and 7 transmitters. (*Reprinted with permission from IEEE, Copyright © 2009 IEEE* [16])

ing the laser beam into a number of beams will help in the presence of strong scintillation to avoid deep fades and to improve BER statistics.

The average <BER> for transmit diversity with M transmitters and one receiver is given by [16]:

$$< BER >= \int f_I(\mathbf{I}) Q\left(\frac{\eta}{M\sqrt{2N_0}} \sum_{m=1}^{M} I_m \right) d\mathbf{I} \tag{4.33}$$

where $f_I(\mathbf{I})$ is the PDF of vector $\boldsymbol{I}$ of length M. An M-dimensional integration is required to evaluate the above average BER. The multidimensional Gaussian quadrature rule (GQR) can be applied which involves multiple averaging of a Gaussian Q-function over the PDF vector $f_I(\mathbf{I})$. The procedure involves the calculation of GQR providing a set of weights and abscissas [25] to make use of the equation:

$$\int_a^b G(x)W(x)dx \approx \sum_{j=1}^{K} w_j G(x_j) \tag{4.34}$$

With $G(X)$ is a polynomial of degree up to $2K$-1. If $W(x)$ is the joint PDF of the random variables I_m, the K-point GQR can be computed using the first $2K$-1 moments of I_m. Figure 4.12 shows the average BER as a function of electrical average SNR for MISO FSO links with multiple transmitters, M=2, 3, 5, and 7 transmit apertures over i.i.d atmospheric turbulence channels. The BER is significantly improved as the transmitter number is increased compared to the SISO system. Figure 4.12 shows the performance comparisons for various parameters of the scintillation index (i.e., for various atmospheric channel parameters denoted by α, assuming a K-distribution of turbulence-induced fading statistics [16]). A comparison with SISO FSO link is also shown in the Fig. 4.12. This figure is applicable to strong atmo-

spheric turbulence channel so that the valid scintillation index is between 1 and 4. The BER increases with increasing scintillation index, i.e., decreasing values of the channel parameter, α, as expected. The spatial diversity approach for MISO thus improves the FSO performance.

Case 4. SIMO FSO Links: Selection Diversity (SD) This is a situation where multiple receivers are used for mitigating atmospheric turbulence in order to improve FSO performance. Many years ago, the advantage of using multiple receivers was already pointed out [26] to demonstrate the optical communication concept between aircraft. The advantage of using a number of detectors, each having small field of view (FOV) with very narrowband optical filters, effectively reduce the overall background noise as compared to using a single large FOV with a single detector. The multiple detectors can increase the received SNR and therefore improving the FSO performance in presence of atmospheric turbulence.

The SD is the least complicated among the combining schemes. In this combining scheme, only one of the diversity apertures with the maximum received irradiance (or electrical [SNR] is processed. Among all the N received irradiances I_1, I_2... I_N, the irradiance I_{SDS} is selected based on the criteria:

$$I_{SD} = \max\{I_1, I_2 \ldots I_N\} \tag{4.35}$$

The average BER at the output of SD receiver is given by [16]:

$$< BER >= \int_0^\infty f_{I_{SD}}(I_{SD}) Q\left(\frac{\eta I_{SD}}{\sqrt{2NN_0}}\right) dI_{SD} \tag{4.36}$$

where $f_{I_{SD}}(I_{SD})$ is the PDF of the output which can be evaluated as

$$\begin{aligned} f_{I_{SD}}(I_{SD}) &= \frac{d}{dI_{SD}} F_{I_{SD}}(I_{SD}) = \frac{d}{dI_{SD}} \prod\nolimits_{j=1}^{N} F_{I_j}(I_{SD}) \\ &= \sum_{i=1}^{N} \prod\nolimits_{j=1,\ j\neq i}^{N} f_{I_i}(I_{SD}) F_{I_j}(I_{SD}) \end{aligned} \tag{4.37}$$

where $F_{I_{SD}}(I_{SD})$ is the CDF of I_{SD}.

Using Eqs. (4.36) and (4.37), the average BER can be evaluated in terms of a sum N semi-infinite integrals:

$$< BER >= \sum_{i=1}^{N} \prod\nolimits_{j=1,\ j\neq i}^{N} f_{I_i}(I_{SD}) F_{I_j}(I_{SD}) Q\left(\frac{\eta I_{SD}}{\sqrt{2NN_0}}\right) dI_{SD} \tag{4.38}$$

Assuming I_n are i.i.d random variables, following the similar earlier steps, the OP of the SD receivers can be obtained as follows [14]:

$$P_{out} = \left[F_I\left(\sqrt{\frac{\mu_{th}}{<\mu>}}\right)\right]^N \tag{4.39}$$

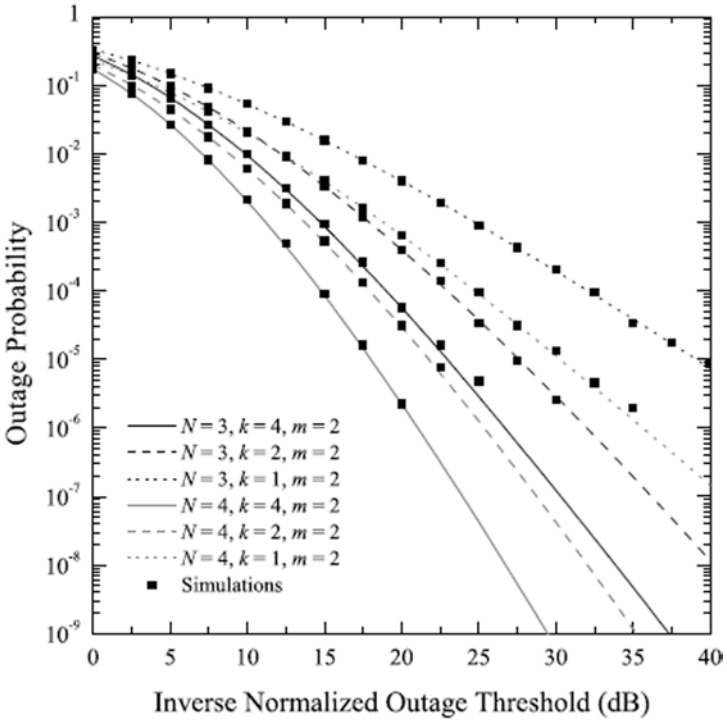

Fig. 4.13 The outage probability vs. inverse normalized outage threshold, $< \mu > / \mu_{th}$, of SIMO FSO links employing selection diversity combining scheme over exponentially correlated Gamma-Gamma turbulence channel. The different values of the parameter k and m describe a Gamma-Gamma PDF. *(Reprinted with permission © 2012 Kostas Peppas, Hector E. Nistazakis, Vasiliki D. Assimakopoulos and George S. Tombras. Originally published in* [14] *under CC BY 3.0 license*). *SIMO* single-input multiple-out, *FSO* free-space optical, *PDF* probability density/distribution function

where F_I is the CDF of I_n. Figure 4.13 shows the OP of triple and quadruple branch SIMO receivers employing intensity modulation and direct detection with SD combining scheme operating over exponentially correlated Gamma-Gamma turbulence channel for a power correlation coefficient of 0.25. The different values of the parameters *k* and *m* describe a Gamma-Gamma PDF. The OP is shown as a function of the inverse normalized outage threshold, $< \mu > / \mu_{th}$. The figure clearly shows the significant improvement of the OP using spatial diversity.

4.3.2 Time diversity

An alternate approach to spatial diversity is to use time diversity where identical messages are transmitted in different time slots separated by time periods on the order of coherence time. A general description of this technique with applications

in fading channels can be found in [27]. Transmissions of the same data take place between a single transmitter and a single receiver. For FSO communication system operated in atmosphere signal received at the receiver undergoes fluctuations due to scintillation resulting in signal fading at the receiver in IM/DD system. The probability of fade is an estimate to determine how likely the receiver output is to drop below a prescribed threshold. The incoming signal will be randomly fading depending on the probability distributions of the turbulence channel. An accurate PDF is therefore needed to predict the probability of fade for an FSO communication system. In the previous section, spatial diversity techniques were used to improve the reliability of fading channel. Under the Taylor frozen turbulence hypothesis, turbulent eddies are treated as frozen in space and are moved across the observation path by the mean wind speed component V. This hypothesis permits converting spatial statistics into temporal statistics by knowledge of the average wind speed transverse to the direction of observation. Therefore, time diversity can also improve performance of FSO communication system.

Temporal Covariance and Coherence Time of the Atmospheric Channel Since we are interested in FSO communications performance in the time domain, the temporal covariance function of the turbulence channel is important. The temporal covariance is useful in determining the correlation time τ_c which is defined as the e^{-1} point of the normalized temporal covariance function and can be obtained by substituting $\rho \to V\tau$ where ρ is the spatial coordinate in the spatial intensity covariance function. The temporal covariance function of the intensity fluctuations for an unbounded plane wave incident on the collecting lens is given by [10]:

$$B_I(\tau, D) = 8\pi^2 k^2 L \int_0^1 \int_0^\infty k\Phi_n(\kappa) J_0(\kappa V\tau) \times exp\left(-\frac{D^2\kappa^2}{16}\right)\left(1 - \cos\frac{L\kappa^2\xi}{k}\right) d\kappa d\xi \tag{4.40}$$

where τ is the time lag, D is the receiver aperture diameter, $\Phi_n(k)$ is the spatial power spectrum of refractive index, J_0 is the Bessel function of the first kind, L is the propagation path, $k = 2\pi/\lambda$ is the optical wave number, κ is the spatial wave number, and ξ is the transformation variable. The normalized covariance function $b_I(\tau, D)$ is defined as

$$b_I(\tau, D) = \frac{B_I(\tau, D)}{B_I(0, D)} \tag{4.41}$$

Figure 4.14 shows two normalized covariance functions for two different weak turbulence conditions by the researchers [28] along with theoretically predicted function defined by Eq. (4.41) using a 785 nm laser for a propagation path length of approximately 1 km The correlation times for two turbulence conditions are approximately 15 and 3 ms for variances of 0.03 and 0.73, respectively. For time diversity scheme for FSO communication, delays longer than a few ms should be sufficient in weak turbulence ranges to improve systems performance.

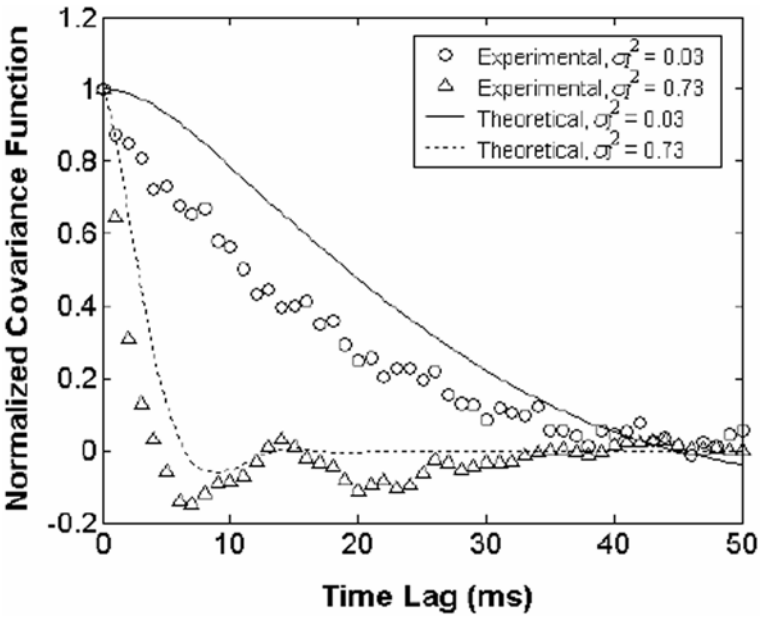

Fig. 4.14 Normalized temporal covariance function for two different weak turbulence conditions. (*Reprinted with permission from SPIE, 2005* [28])

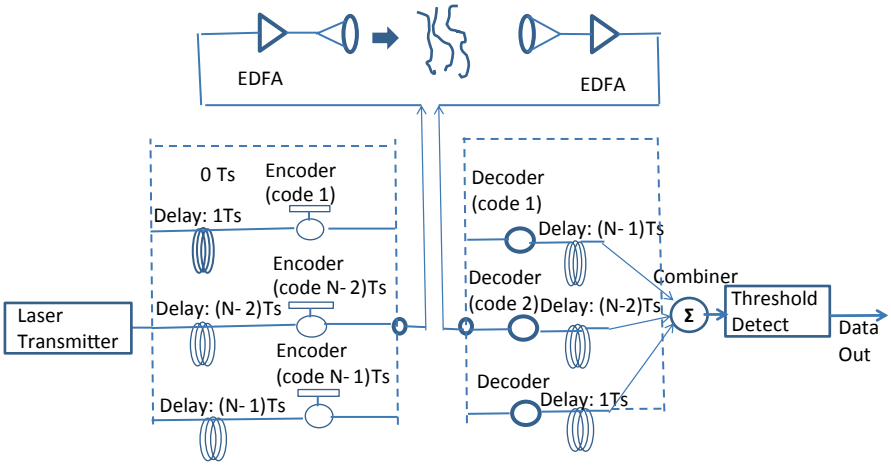

Fig. 4.15 Block diagrams of time-diversity-based FSO communication system: N channels. (*Reproduced with permission from Peng LIU, Ph.D Thesis, Waseda University, February 2012.*). *FSO* free-space optical

Time Diversity System Model and Performance: N-channels Figure 4.15 shows a block diagram of time-diversity-based FSO communication system. The transmitter sends the signal N times separated by source coding so that each data stream is first delayed or separated by fixed time periods, T_{sep} (accomplished by encoders). The

receiver now receives N independently faded copies of the signal. The copies are decoded and delayed with the corresponding code before sending. The N recovered copies are then combined and determine whether a "0" or "1" was sent using a threshold detector. The time diversity is done entirely in the optical domain. The N times transmitted laser intensities each delayed by T_{sep} can be expressed as

$$I_1 = I(t), I_2 = I(t - T_{sep}), \ldots, I_N = I(t - NT_{sep} + T_{sep}) \tag{4.42}$$

where $I(t)$ is the laser transmitter intensity. At the receiver, the fading signal in each path can be written as RP_i where R is a constant (such as responsively) of the receiver and $P_i$is the received optical power at the *i-th* path. It is assumed that the intensity fluctuations statistics (PDF) of each fading signal is identical.

A log-normal distributed normalized irradiance (<I>= 1) is assumed in this analysis and is described by:

$$P_I(I) = \frac{1}{I\sqrt{2\pi\sigma_{\ln I}^2}} \exp\left[-\frac{\left[\ln(I) + \frac{1}{2}\sigma_{\ln I}^2 \right]^2}{2\sigma_{\ln I}^2} \right], \qquad \text{I>0} \tag{4.43}$$

where $\sigma_{\ln I}^2$ is the log-irradiance variance, $\sigma_{\ln I}^2 \approx \sigma_I^2$ under weak turbulence condition.

Performance of time diversity can be understood from a description of the joint probability distribution of the fading at different delay time at a single receiver. Assuming that the log-amplitude at receiver can be described by a joint Gaussian distribution [29], the auto-covariance matrix of the log-amplitude at different time is given by [30]:

$$B = \sigma_I^2 \begin{bmatrix} 1 & b(T_{sep}) \cdots & b(NT_{sep} - T_{sep}) \\ b(T_{sep}) & 1 \quad \cdots & b(NT_{sep} - 2T_{sep}) \\ \cdots & \cdots & \cdots \\ b(NT_{sep} - T_{sep}) & b(NT_{sep} - 2T_{sep}) \cdots & 1 \end{bmatrix} \tag{4.44}$$

where σ_I^2 is the irradiance variance quantifying the strength of atmospheric turbulence. The joint probability density function of I is given by [30]:

$$f_{I_1, I_2, \ldots, I_N}(i_1, i_2, .., i_N) = \frac{1}{(2\pi)^{N/2} |B|^{1/2} \prod_{k=1}^{N} i_k} \times \left[-\frac{1}{2}(\mathbf{A} - a)B^{-1}(a - \mathbf{A})^T \right] \tag{4.45}$$

where $\mathbf{A} = \ln i_1, \ln i_2, .., \ln i_N$ and $a = \left(\ln < I > -\frac{\sigma_I^2}{2} \right) I_{1\times N}$.

Probability of Fade The probability of fade is a useful metric to describe performance of an FSO communication system. This quantity gives an estimate of how

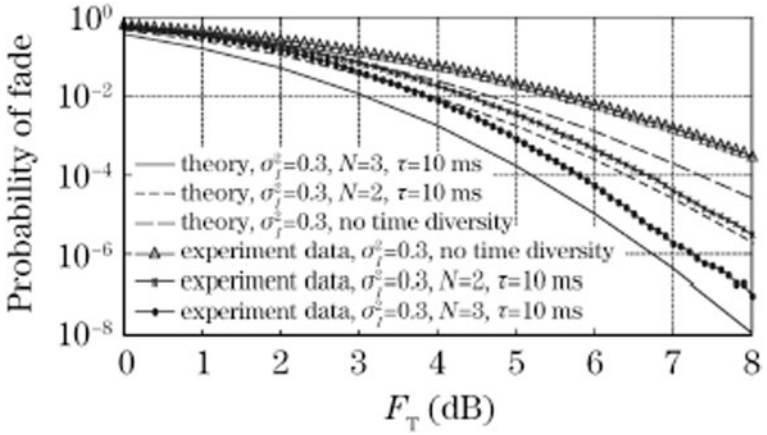

Fig. 4.16 Probability of fade with time diversity. (*Reprinted with permission from The Optical Society of America, OSA, 2008* [30])

likely the detector output is to drop below a prescribed threshold determined from the system requirement. The probability of fade with PDF of irradiance fluctuations, *P(I)* can be expressed as:

$$\text{Probability of fade:} \qquad P(I < I_t) = \int_0^{I_t} (I)dI \tag{4.46}$$

where I_t is the threshold irradiance. I_t can also be expressed in terms of the fade threshold parameter, F_T, which is the number of decibels below the mean. F_T can be written as

$$F_T = 10\log\left(\frac{< I >}{I_t}\right).$$

The probability of fade for the time diversity scheme is then obtained by integrating Eq. (4.46) over the joint density function in Eq. (4.45) and is given by [30]:

$$\text{Probability of fade:} \quad P = \int_0^{I_t} \ldots \int_0^{I_t} f_{I_1, I_2, \ldots, I_N}(i_1, i_2, .., i_N) di_1 di_2, \ldots di_N \tag{4.47}$$

Figure 4.16 shows probability of fade with time diversity as a function of F_T for different values of N=1, 2, 3. The time diversity can improve the performance and can provide a gain of 1.5–2.7 at a probability of fade of 10^{-6}.

Special Case: Dual Branch Time Diversity System (N = 2) We discuss here the simplest case of time diversity when only two channels are used: one transmitting directly and the other with delayed transmission. The FSO system can be modeled as a dual branch diversity system over two correlated identically distributed log-normal fading channels. The normalized covariance is determined by the delay period and thus the delay between two transmissions can be adjusted to reduce the dependency between the two channels. The two transmitted laser intensities separated by a delay period T_{sep} can be defined as $I_1 = I(t) and\, I_2 = I(t - T_{sep})$. The joint probability density function of I_1 and I_2 is [28]:

$$P_{I_1 I_2}(i_1, i_2, T_{sep}) = \frac{1}{2\pi \left|\sum(T_{sep})\right|^{1/2} i_1 i_2} exp\left[-\frac{1}{2}(ln\mathbf{i} - \boldsymbol{\mu})^T \sum^{-1}(T_{sep})(ln\mathbf{i} - \boldsymbol{\mu})\right] \quad (4.48)$$

where $lni = [lni\_1, lni\_2]^T$ and $\boldsymbol{\mu} = \left(\ln < I > -\frac{\sigma_I^2}{2}\right)\mathbf{I}_{2\times 2}$. The mean received intensity <I> given by [4]:

$$< I > \cong I_0 w_0^2 / w_L^2 [1 + 1.33\sigma_I^2 (2L/kw_L^2)^{5/6}]$$

The temporal covariance matrix $\sum(T_{sep})$ can be written as [28]:

$$\sum(T_{sep}) = \sigma_I^2 \begin{bmatrix} 1 & b(T_{sep}) \\ b(T_{sep}) & 1 \end{bmatrix} \quad (4.49)$$

BER Computation for Time Diversity Scheme Considering the conditional probability in each branch conditioned upon random intensity fluctuations I_1 and I_2, the conditional BER at the receiver can be written as [28]:

$$BER_{conditional} = \frac{1}{2} erfc\left(\frac{S_1 + S_2}{2\sqrt{2}\sigma_z}\right) = \frac{1}{2} erfc\left(\frac{< SNR > (i_1 + i_2)}{4\sqrt{2 < I >}}\right) di_1 di_2 \quad (4.50)$$

where *erfc* is the complementary error function, $S_1 and S_2$ are received signals at channel 1 and channel 2, respectively (assuming identical means) and σ_z is the noise associated with the receiver system, and SNR is the instantaneous SNR. The average <BER> is now obtained by integrating the Eq. (4.50) over the joint probability density function, Eq. (4.48) of i_1 and i_2.

This is given by [28]:

$$< BER >= \frac{1}{2}\int_0^\infty \int_0^\infty P_{I_1 I_2}(i_1, i_2, T_{sep}) erfc\left(\frac{(SNR)(i_1 + i_2)}{4\sqrt{2 < I >}}\right) di_1 di_2 \quad (4.51)$$

Figure 4.17 shows the average BER plots for two-channel time diversity scheme for two turbulence variances of 0.03 and 0.73 reported by the researchers [28]. At the BER probability of 10^{-9}, a SNR gain of about 4.1 dB and 5.4 dB for the turbulence variances of 0.03 and 0.73 were obtained showing the usefulness of the time diversity technique for mitigating turbulence-induced fading in the FSO communication system.

4.3.3 Temporal-Domain Detection Techniques

Time domain techniques are different than time diversity technique discussed in the previous section. Various detection schemes are applied at a single receiver in time domain in order to mitigate atmospheric turbulence for FSO communication system performance improvement. Atmospheric turbulence-induced intensity fluc-

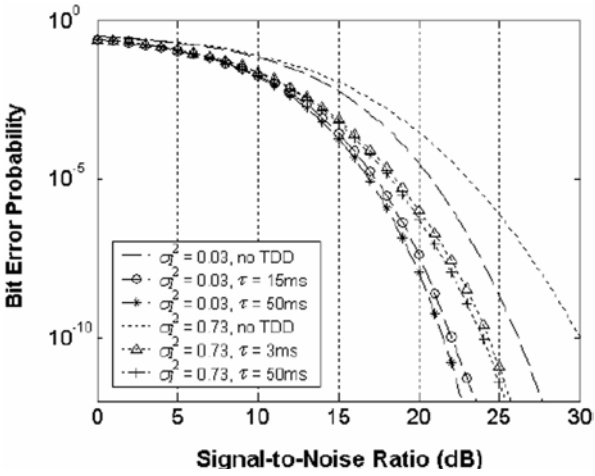

Fig. 4.17 Average bit-error-rate probability for two-channel time diversity scheme for two turbulence variances of 0.03 and 0.73. (*Reprinted with permission from SPIE, 2005* [28])

tuations (signal fading) degrade systems performance by increasing the BER of the received information signal. In the previous sections of aperture averaging, spatial, or time diversity, the receiver aperture D_0 was assumed larger than the correlation length d_0 (typically of the order of 1–10 cm) and the receiver observation interval T_0 during each bit interval was larger than the correlation time τ_0 (typically of the order of 1–10 ms). However, in many practical FSO communications scenarios, these requirements cannot be met. In this section, various time domain techniques for mitigating atmospheric turbulence are discussed where $D_0 < d_0$ and $T_0 < \tau_0$. This is important when we consider the bit rates of gigabit or multi-gigabit per second data rate. Three types of temporal-domain techniques are reported [27]: maximum likelihood (ML) symbol-by-symbol detection, maximum likelihood sequence detection (MLSD), and pilot-symbol assisted detection (PSAD). BER curves for each technique demonstrate the effectiveness of each of these methods in mitigating atmospheric turbulence for analyzing systems performance. The techniques are summarized below with the corresponding expressions for BER.

An IM/DD using OOK is assumed throughout the discussion here. For propagation distances of less than a few kilometers, variations of log-amplitude of the signal are much smaller than variations of the phase. When light is propagating through a large number of turbulent blobs of the atmosphere, each of which causing an independent and identically distributed phase delay and scattering of the optical wave. The marginal distribution of the log-amplitude X is therefore Gaussian by the Central Limit Theorem and is given by [27]:

$$f_X(X) = \frac{1}{(2\pi\sigma_X^2)^{1/2}} exp\left\{-\frac{(X - E(X))^2}{2\sigma_X^2}\right\} \tag{4.52}$$

where σ_X^2 is the log-amplitude variance of the incidence light wave, and $E(X)$ is the ensemble average of log-amplitude X. Relating intensity I of light to the

log-amplitude X by $I = I_0 \exp(2X - 2E(X))$, the average light intensity of log-amplitude fluctuations given by Eq. (4.52) is given by:

$$E(I) = E[I_0 \exp(2X - 2E(X))] = I_0 \exp(2\sigma_X^2) \tag{4.53}$$

In terms of the intensity, I, the marginal distribution of light intensity fading due to turbulence is log-normal [27]:

$$f_I(I) = \frac{1}{2I} \frac{1}{(2\pi\sigma_X^2)^{1/2}} exp\left\{ -\frac{\left[\ln(I) - \ln(I_0)\right]^2}{8\sigma_X^2} \right\} \tag{4.54}$$

a. *ML symbol-by-symbol detection*

For the system model, the receiver SNR is assumed to be limited by system shot noise caused by ambient light and/or thermal noise. The noise is AWGN and is statistically independent of the received signal. The bit duration T and the interval T_0 needed for the receiver to integrate the received photocurrent is such that $T_0 \le T$. The receiver integration interval is also assumed to be much less than the correlation time of the atmospheric turbulence, i.e., $T_0 << \tau_0$ so that the light intensity is constant during each integration interval. The electrical signal at the receiver for a received signal light intensity I_s and ambient light intensity I_B is given by:

$$s_e = \eta(I_s + I_B) + n \tag{4.55}$$

η is the optical-to-electrical conversion efficiency, and n is the additive white Gaussian noise with zero mean and covariance *N/2,* independent of whether received is Off or On. The receiver is assumed to have knowledge of the marginal distribution of the fading statistics, but has no knowledge of the channel's instantaneous fading. When the ambient light level ηI_B is subtracted from the electrical signal, the electrical signal $s = \eta I_s + n$ can be described by the conditional densities depending on when the transmitted bit is Off or On:

$$P(\text{sig}|\text{Off}) = \frac{1}{\sqrt{\pi N}} \exp\left(-\frac{sig^2}{N} \right) \tag{4.56}$$

$$\begin{aligned} P(\text{sig}|\text{On}) &= \int_{-\infty}^{\infty} P(\text{sig}|On, X) f_X(X) dX \\ &= \int_{-\infty}^{\infty} \frac{1}{\sqrt{\pi N}} f_X(X) \cdot exp\left[-\frac{(\text{sig} - \eta I_0 e^{2X - 2E[X]})^2}{N} \right] dX \end{aligned} \tag{4.57}$$

where $I_0 = \dfrac{E(I)}{\exp(2\sigma_X^2)}$ (see Eq. 4.53, *E(I)* being the average light intensity).

The ML symbol-by-symbol detector chooses the symbol $\hat{s}$ using the rule [27]

$$\hat{s} = \text{argmax}_s P(sig \mid s) \tag{4.58}$$

where $P(\text{sig}|\text{s})$ is the conditional distribution that if a bit s (On or Off) is transmitted, a signal level "sig" will be received, i.e., PDF of the signal "sig" given $\text{s} \in \{\text{off}, \text{on}\}$. The Eq. (4.58) is applicable if On and Off bits are equally probable. "sig" is compared to a fixed threshold that depends on X (log-amplitude), σ_X^2 (log-amplitude variance), and N (additive Gauss noise covariance).

The likelihood function $\lambda(\text{sig})$ is the ratio of the two conditional probabilities for On and Off conditions [27]:

$$\lambda(\text{sig}) = \frac{P(\text{sig}|\text{On})}{P(\text{sig}|\text{Off})} = \int_{-\infty}^{\infty} f_X(X) \cdot exp\left[-\frac{(\text{sig} - \eta I_0 e^{2X - 2E[X]})^2 - \text{sig}^2}{N} \right] dX \quad (4.59)$$

The BER of OOK can be computed as follows.

$$BER = P(\text{Off}) P(\text{BitError}|\text{Off}) + P(\text{On}) P(\text{BitError}|\text{On}) \quad (4.60)$$

The conditional probabilities $P(\text{BitError}|\text{Off})$ and $P(\text{BitError}|\text{On})$ are the bit error probabilities when the transmitted bit is Off and On, respectively. Assuming there is no intersymbol interference (ISI), the conditional bit-error probabilities are

$$P(\text{BitError}|\text{Off}) = \int_{\lambda(\text{sig})>1} P(\text{sig}|\text{Off}) d(\text{sig}) \quad (4.61)$$

$$P(\text{BitError}|\text{On}) = \int_{\lambda(\text{sig})<1} P(\text{sig}|\text{On}) d(\text{sig}) \quad (4.62)$$

b. *Maximum-Likelihood Sequence Detection (MLSD)*

When we take into account of the temporal correlation of turbulence-induced fading, MLSD can offer a temporal-domain technique to accomplish better FSO communication performance. For the received signal in n consecutive bits, $\overline{\text{sig}} = [\text{sig}_1, \text{sig}_2, \ldots, \text{sig}_n]$, the likelihood ratio of each of the possible 2^n possible bit sequences $\bar{s} = [\text{s}_1, \text{s}_2, \ldots, \text{s}_n]$ where $s_i \in \{\text{off}, \text{on}\}$ is computed according to the rule [31]:

$$\begin{aligned} \bar{s} &= \text{argmax}_{\overline{\text{sig}}} P(\overline{\text{sig}}|\bar{s}) \\ \bar{s} &= \text{argmax}_{\overline{\text{sig}}} \int_{\bar{\text{x}}} f_{\bar{\text{x}}}(\bar{\text{X}}) \\ &\cdot exp\left[-\sum_{i=1}^{n} \frac{(\text{sig}_i - \eta s_i I_0 e^{2X_i - 2E[X_i]})^2}{N_i} \right] d\bar{X} \end{aligned} \quad (4.63)$$

The joint distribution of intensity for a sequence of transmitted bits is modeled by the distribution $f_{\bar{\text{x}}}(\bar{\text{X}})$ as follows [31] when each s_i can take Off or On, so that $s_i \in \{0,1\}$:

$$f_{\bar{X}}(\bar{X}) = \frac{1}{(2\pi)^{n/2}\left|C_X^{T}\right|^{1/2}} \exp\{-\frac{1}{2}(X_1 - E[X_1])\ldots(X_n - E[X_n])]$$
$$\mathrm{x}\,(C_X^T)^{-1}\begin{bmatrix}(X_1 - E[X_1])\\ \ldots \\ (X_n - E[X_n])\end{bmatrix}\} \tag{4.64}$$

where the covariance matrix of a string of n bits is given by [31]:

$$C_X^T = \begin{bmatrix} \sigma_X^2 & \sigma_X^2 b_X\left(\frac{T}{\tau_0}d_0\right) & \ldots\sigma_X^2 b_X[\frac{(n-1)T}{\tau_0}d_0] \\ b_X(\frac{T}{\tau_0}d_0) & \sigma_X^2 & \ldots\sigma_X^2 b_X\left[\frac{(n-2)T}{\tau_0}d_0\right] \\ \sigma_X^2 b_X[\frac{(n-1)T}{\tau_0}d_0] & \sigma_X^2 b_X\left[\frac{(n-2)T}{\tau_0}d_0\right] & \ldots\sigma_X^2 \end{bmatrix}_{nxn} \tag{4.65}$$

In the above Eq. (4.64), b_X is the normalized log-amplitude covariance function for two positions in a receiving plane and the spatial coordinate can be transformed to temporal coordinate by Tailor's frozen turbulence theory. Here T is the bit interval and τ_0 is coherence time: $\tau_0 = \frac{d_0}{\mathrm{v}}$, d_0 is the coherence diameter of the turbulence-induced fading, and v is the perpendicular component of the wind velocity.

The MLSD technique has the disadvantage of high computational complexity which is proportional to $n \cdot 2^n$.

The performance of the FSO communications using the three time-domain techniques, namely ML symbol-by-symbol, MLSD, and pilot-symbol assisted detection (PSAD) is reported in [27, 32].

PSAD This time-domain technique can be applied in a situation when the temporal coherence of fading is known, but the instantaneous fading state is not known. When communicating at high data rate through atmospheric turbulence, the bit interval, T in many FSO links is much shorter than the turbulence-induced intensity correlation time, τ_0, i.e., $\mathrm{T} \ll \tau_0$. Therefore, the instantaneous state of the intensity fluctuations remains constant for many consecutive bit intervals. The receiver integrates the received photocurrent for an interval $T_0 \ll T$ and therefore for $T_0 \ll \tau_0$, and thus the light intensity is constant for each interval. In the PSAD [33] scheme, an On-state pilot symbol is periodically inserted by the transmitter prior to a block of *M-1* information bits to form an *M*-bit block, *M* being the frame length. This inserted known symbol contains a reference for the receiver to derive the correlated channel fading information. The receiver detects *M-1* information bits by using the received intensity of the pilot symbols preceding and following each block.

Temporal Joint PDF of Turbulence-induced Fading Considering IM/DD links using OOK for the FSO communication system where SNR is limited by shot noise caused by ambient light, the received electrical signal at the end of the integration interval is given by Eq. (4.55). Assuming no ISI, the *i*-th On-state symbol intensity can be expressed as [33]:

$$I_i = I_0 \exp(2X_i - 2\chi) \tag{4.66}$$

where X_i is the log-amplitude of optical signal which is assumed to be Gaussian random variable with a mean of χ and variance σ_X^2. The temporal joint PDF of log-amplitude sequences $\vec{X} = \left[X_{n1} - \chi, X_{n2} - \chi, \ldots, X_{n_m} - \chi\right]$ is jointly Gaussian and is given by [33]:

$$f_{\vec{X}}(\vec{X}) = \frac{1}{(2\pi)^{m-2}\left|C_X^{\mathrm{On}}\right|^{1/2}} \exp\left[-\frac{1}{2}\vec{X}\cdot(C_X^{On})^{-1}\cdot\vec{X}^T\right] \tag{4.67}$$

where C_X^{On} is the covariance matrix of On-state bits sequence and can be expressed as [33]:

$$C_X^{On} = \begin{bmatrix} \sigma_X^2 & \sigma_X^2 \exp\left[-\left(\frac{|n_1 - n_2|T}{\tau_0}\right)^{\frac{5}{3}}\right] \ldots & \sigma_X^2 \exp\left[-\left(\frac{|n_1 - n_m|T}{\tau_0}\right)^{\frac{5}{3}}\right] \\ \sigma_X^2 \exp\left[-\left(\frac{|n_2 - n_1|T}{\tau_0}\right)^{\frac{5}{3}}\right] & \sigma_X^2 & \sigma_X^2 \exp\left[-\left(\frac{|n_2 - m|T}{\tau_0}\right)^{\frac{5}{3}}\right] \\ \sigma_X^2 \exp\left[-\left(\frac{|n_m - n_1|T}{\tau_0}\right)^{\frac{5}{3}}\right] & \sigma_X^2 \exp\left[-\left(\frac{|n_m - n_2|T}{\tau_0}\right)^{\frac{5}{3}}\right] & \sigma_X^2 \end{bmatrix}_{nxn} \tag{4.68}$$

Here T is the bit interval and τ_0 is coherence time: $\tau_0 = \frac{d_0}{\mathrm{v}}$, d_0 is the coherence diameter of the turbulence-induced fading, and v is the perpendicular component of the wind velocity. Note that this is based on Taylor's frozen turbulence theory.

Based on the above covariance matrix, the joint distribution of the signal intensity of *m* On-state symbols which is a joint log-normal and is given by [33]:

$$f_I(I_{n1}, I_{n2}, \ldots, I_{nm}) = \frac{1}{2^m \prod_{i=1}^m I_{ni} (2\pi)^{m/2} \left|C_X^{on}\right|^{1/2}} exp\left\{-\frac{1}{8}\left[\ln\left(\frac{I_{n1}}{I_o}\right)\ldots\ln\left(\frac{I_{nm}}{I_o}\right)\right](C_X^{on})^{-1}\begin{bmatrix} \ln\left(\frac{I_{n1}}{I_o}\right) \\ \ldots \\ \ln\left(\frac{I_{nm}}{I_o}\right) \end{bmatrix}\right\} \tag{4.69}$$

c. *Pilot-Assisted Maximum-Likelihood Detection (PSA-ML)*

Like ML symbol-by-symbol detection discussed earlier, the receiver decodes the symbol ŝ (see Eq. (4.58)):

$$\hat{s} = \text{argmax}_s P(\text{sig}|\text{s})$$

After periodically inserting On-state symbols to the information bit string, the composite symbols (as mentioned earlier) are transmitted over the atmospheric channel. Let sig_i be the received photocurrent signal of the *i*-th information bit in the frame, sig_0 and sig_M are the received signal of the pilot symbol of the current frame and the next frame. The joint probabilitydistribution of $\overline{\text{sig}} = [\text{sig}_0, \text{sig}_i, \text{sig}_M]$ conditioned on the *i*-th $(1 \le i \le \text{M})$ information bit s_i are given by [27]:

$$P(\text{sig} \mid s_i = 0) = \frac{1}{(\pi N)^{3/2}} \exp\left[-\frac{sig_i^2}{N}\right] \iint_{-\infty}^{\infty} f\text{x}(X_0, X_M)$$

$$\text{x exp}[-\sum\nolimits_{j=0,M} \frac{(\text{sig}_i - \eta I_0 e^{2X_j - 2E[X_j]})^2}{N}] dX_0 dX_M$$

$$P(\mathbf{sig}|s_i = 1) = \frac{1}{(\pi N)^{3/2}} \iiint_{-\infty}^{\infty} f_X(X_0, X_i, X_M) \tag{4.70}$$

$$\text{x exp}\,[-\sum\nolimits_{j=0,1,M} \frac{(\text{sig}_i - \eta I_0 e^{2X_j - 2E[X_j]})^2}{N}] dX_0 dX_i dX_M \tag{4.71}$$

$$\iint_{-\infty}^{\infty} \quad f_X(X_0, X_M)$$

$f_X(X_0, X_M)$, and $f_X(X_0, X_i, X_M)$ are log-amplitude PDFs and are already shown in Eq. (4.64) in the MLSD section.

The likelihood ratio $(\text{sig}) = \frac{P(\text{sig} \mid s_i = 1)}{P(\text{sigs}_i = 0)}$. The similar decision rule like MLSD can be applied: $\lambda(\text{sig}) \underset{<\text{Off}}{\overset{>\text{On}}{}} 1$, assuming that the receiver has a knowledge of the fading correlation but not the instantaneous fading state.

The BER of the *i*-th information bit in the *M*-bit frame is expressed as:

$$P(\text{Bit Error}|s_i = 0) = \int_{\lambda(\text{sig})>1} P(\mathbf{sig}|s_i = 0)\, \text{d}\mathbf{sig} \tag{4.72}$$

$$P(\text{Bit Error}|s_i = 1) = \int_{\lambda(\text{sig})>1} P(\mathbf{sig}|s_i = 1)\, \text{d}\mathbf{sig} \tag{4.73}$$

Figure 4.18 [27] shows the BER for On-state bits as a function of average received electrical SNR for three temporal-domain techniques for mitigating atmospheric turbulence. The theoretically calculated curves are shown by dashed (symbol-by-symbol ML), solid (MLSD), and dot-dashed (PSAD) techniques along with the measured points. For a BER of 10^{-3}, compared to symbol-by-symbol detection, PSAD offers an SNR gain of about 1.9 dB and MLSD gives an SNR gain of 2.4 dB. For detailed description of their results, the reader is urged to read [27, 32].

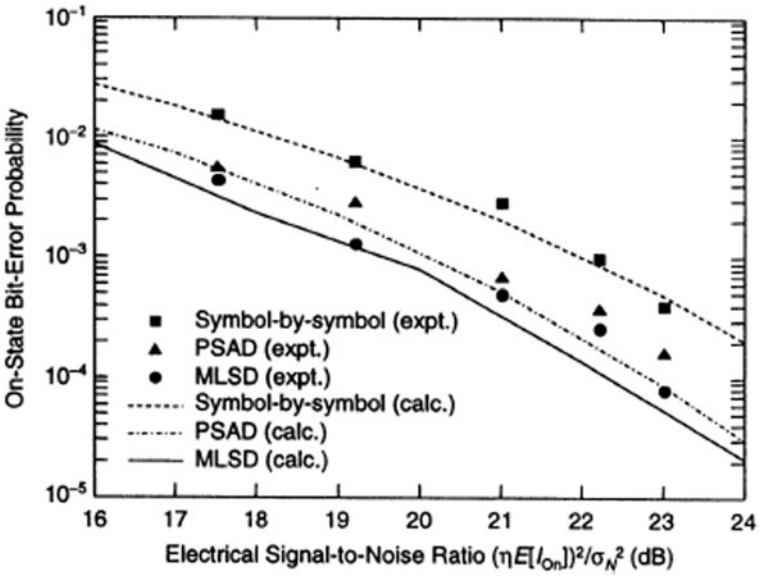

Fig. 4.18 BER for On-state bits as a function of average received elected SNR for symbol-by-symbol *ML*, *MLSD*, and *PSAD* techniques. (*Reprinted with kind permission from Springer Science+Business Media B.V. [Fig. 13, page 332,* [27]). *BER* bit error rate, *ML* maximum likelihood, *MLSD* maximum likelihood sequence detection, *PSAD* pilot-symbol assisted detection

4.3.4 Coding Techniques

It is also possible to improve the reliability of FSO communications system and to achieve the predetermined BER by utilizing coding schemes used in RF communication technology which can be applied to optical communications. In terrestrial FSO communications system, coding techniques can be applied for either a SISO or MIMO configuration. However, in a communication scenario such as airborne terminals, it is not practical to use diversity technique to allow multiple transmissions because of the practical limitations such as power, weight, and size of the system. Error correction is a simple way of mitigating atmospheric turbulence suitable for a SISO system. Many researchers have been and are being done in this subject. Excellent references on the research in coding theory and schemes for mitigating atmospheric turbulence are available. Detailed derivations of the equations of probability of errors in various atmospheric conditions are not presented in this section since they are out of the scope of this text book. The interested readers are referred to the references for detailed derivations. This section describes and discusses the basics of the coding techniques most commonly used for mitigating atmospheric turbulence for FSO communications. This section goes on to explain the FSO communications performance improvement using these coding techniques. Specifically, the improvement of the BER performance over an uncoded system is discussed.

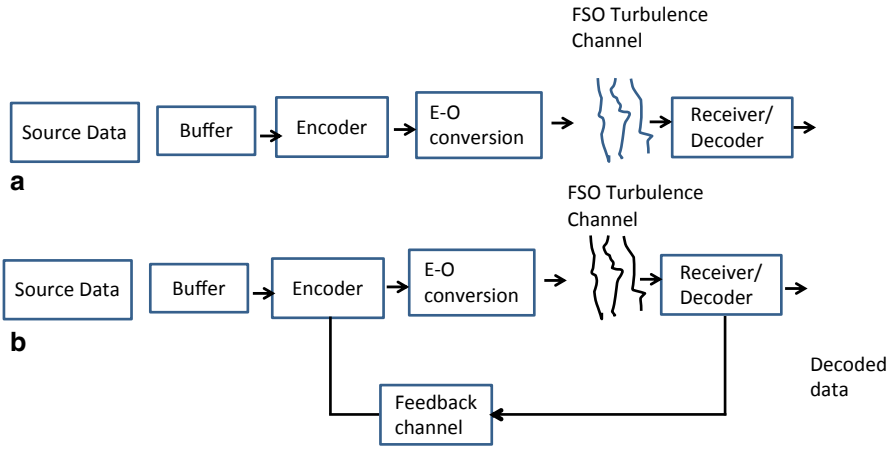

Fig. 4.19 **a** Block diagram of an FSO communication system using a direct coding scheme. **b** FSO coding system with feedback channel

Every coded FSO communications adds new parameters in the design, and comes at a price in terms of system complexity, cost, and applicability to typical scenario and turbulence strength. For example, Forward Error Correction (FEC) codes insert check bits into the data stream which contribute an additional power and bandwidth overhead on the FSO system. In many cases, the decision for selecting the appropriate coding scheme depends on the communications scenario which includes range, propagation characteristics such as levels of turbulence strength, diversity schemes if applicable, suitable modulation techniques, and available laser transmitter power and detector sensitivity. An optimum decision of coding scheme can then only be decided. The objective of this section is to provide the basic information on coding to be familiarizing with the techniques so that researchers can evaluate the different types of coding for improving the FSO communications systems performance.

Figure 4.19a shows the block diagram of an FSO communications system through the atmosphere using a direct coding scheme where the data uses the selected coding scheme to the encoder. The receiver decodes the received data to obtain information data originally sent by the laser transmitter. Figure 4.19b shows a FSO coding system with feedback channel. This system model is suitable for study of some specific code (e.g., raptor code, to be discussed later in this section) for use in temporally correlated FSO channels. The CSI, for example, can be determined which is feedback to the laser transmitter that can be adapted according to the FSO channel conditions.

A block code is linear if any linear combination of two codes is also a code word. If *v* and *w* are code words, then $v \oplus w$ is also a code word. The symbol $\oplus$ denotes bit-wise modulo-2 addition. At the receiver end, the decoder has to recover the message block *u* of *k-tuple* from the code word *v* of *n-tuple*. In mathematics and computer science, a *tuple* is an ordered list of elements and in set theory an (ordered) *n-tuple* is a sequence (or ordered list) of *n* elements, where *n* is a non-

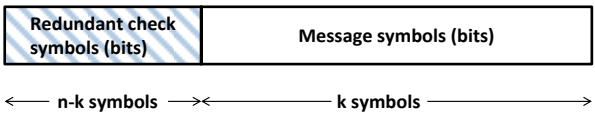

Fig. 4.20 Basic format of a code word

negative integer. The receiver then recovers the message block after decoding the received word r to the most likely transmitted code word v. Figure 4.20 shows the basic format of a code word.

a. *Basics of Coding Relevant to FSO Communications*

Error-correcting codes have been successfully implemented in wireless communication (including RF) to provide error-free transmission. Increased transmission capacity in fiber-optic links has drawn the attention of coding experts to implement FEC for optical communication systems for the past many years. FEC adds additional patterns to each coded packet being transmitted, which allows all transmitted bits to be recovered even if some lost due to atmospheric turbulence-induced fading effect.

From the Shannon's theory, the basic limitation that noise causes in a communication channel is not on the reliability of communication, but on the speed of communication [34, 35]. The capacity of a communication channel with AWGN is given by

$$C = W\ log\left[1+\frac{P}{N_0 W}\right] bits/\sec \tag{4.74}$$

where W=the channel bandwidth, P=signal power in watts, and N_0 is the noise power spectral density in watts/Hz. In the limiting case when the channel capacity is infinity, the channel capacity is given by

$$\underset{W\to\infty}{Lim}\, C = 1.44\frac{P}{N_0} \tag{4.75}$$

The Eq. (4.75) imposes a fundamental limitation on the maximum achievable channel capacity (even if by increasing W). Error-control codes (ECC) exist such that information can be transmitted across the channel at the transmission rate R below the channel capacity C with error probability close to zero [34, 35]. ECC is a signal processing technique where controlled redundancy is added to the transmitted symbols to improve the reliability of communication over a given noisy (or fading) channels to achieve transmission rate R close to the theoretical upper limit of the channel capacity C. The channel impairments limit the practically feasible transmission rates. Distance-capacity is a metric sometimes used to compare different optical communication systems. Improving either distance or capacity will result in a reduction of the other so that the distance-capacity product remains constant.

The optical communication system model is depicted in Fig. 4.21, where the information source generates a sequence of binary bits. For the Reed-Solomon (RS; to be described later in this section) encoder, these binary bits are grouped to form a q-ary symbols from Galois field (GF, to be discussed later; $q = 2^m$).These symbols (bits) are then grouped into blocks of k symbols denoted by $u=(u_1, u_2, \ldots, u_k)$ the

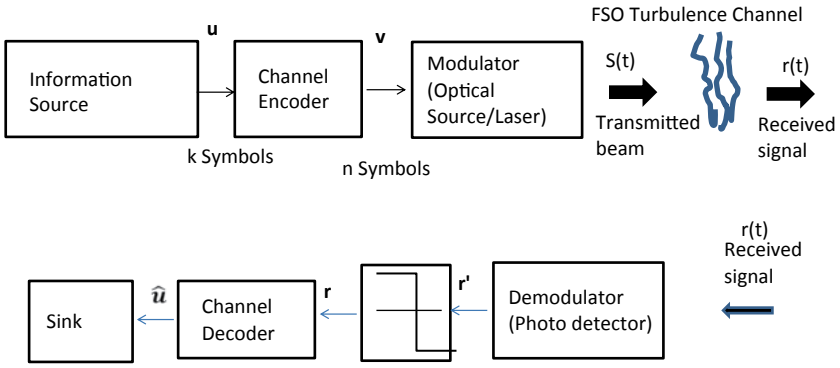

Fig. 4.21 FSO communication system with coding

message block. Controlled amount of redundant symbols are added by the channel encoder to each of the k symbol message blocks to form *code word* blocks of n symbols denoted by $v=(v_1, v_2, \ldots, v_n)$. The electrical bit stream then modulates the intensity of the optical carrier (laser transmitter) to generate modulated signals. In our discussion, IM/DD or OOK is used. For RS encoder, the q-ary symbols have to be translated into a sequence of $log_2(q)$ binary bits before driving the laser transmitter. Thus, the modulator output is an optical pulse of duration T for a bit 1, and no pulse for bit 0. In addition, AWGN channel model is also used for the noise statistics. For decoding, ML criteria will be used.

Error correction is a fade mitigation technique to improve communication system performance in a fading channel. Since redundancy is introduced in the transmitted data stream, this imposes a requirement on increased rate which accounts for increase in bandwidth requirement. Also at data rates of 10 Gbits/s and above the computational complexity and power consumption involved in implementing FEC plays an important role in the design of a FSO system design. In implementing FEC, there is a trade-off in power efficiency and spectral efficiency which needs to be accounted for.

b. *Error Correcting Codes in FSO Communication Systems*

ECC are classified in two categories: (i) block codes, and (ii) convolution codes. For block codes, the encoder takes a message block of k information symbols represented by *k-tuple* $u=(u_1, u_2, \ldots, u_k)$ transforming each message u independently into an *n-tuple* $v=(v_1, v_2, \ldots, v_n)$ of discrete symbols called a code word ($k<n$). Generally, a field is a set of elements in which we can perform addition, subtraction, multiplication, and division without leaving the set. A field with finite number of elements is called a Finite field or GF. For the binary case, the field consists of two elements {0, 1} and is called the binary field. Thus, GF $[q]=\{0, 1, 2, \ldots, q\text{-}1\}=\{0, 1\}$ has a finite number of elements, specifically 2. For the code word, in general for q finite elements, there are a total of q^k different possible messages and thus the encoder generates q^k possible code words where k is the number of symbols. For

binary case $q=2$ and the set of the encoder generates 2^k possible code words. The set of q^k code words of length n is called a $C(n, k)$ block code. But in case of convolution codes, the encoder accepts *k-tuple* of information symbols u and generates *n-tuple* code word v which depends not only on the current k symbol message, but also on m previous message blocks. In block coding, a finite length of output code word is generated for all input message words of finite length, whereas in convolution coding, input and output symbol sequences are infinite with introduction of memory elements.

Some of the relevant coding and decoding techniques in FSO communications are presented below.

1. *Convolutional Codes*

Convolutional codes are powerful ECCs used in digital communication systems. The information bits are unchanged during the encoding process in a systematic (n, k) linear block code. Only n-k parity-check bits related to the information bits. With the statistically independent information bits, the redundant bits will be dependent on the information block of current code word, so that the code words are statistically independent. In an (n, k, M) convolutional code with M memory elements, the parity bits are functions of both the current information *k-tuple* and previous m information *k-tuples*. The statistical dependence is introduced in a window of $K=n(M+1)$ symbols. In a convolutional code architecture, the k information bits taken during the encoding process from a serial to parallel converter follows an information buffer as the input of the encoder memory of size k- by -M [36]. The n-outputs are determined based on current *k-tuple* and previous Mk bits. The logic outputs are written in parallel to the output shift register which allows the code word to be transmitted in a serial fashion over the FSO channel.

The free distance of convolutional codes can be calculated from the generating function of a convolutional code [37, 38]. The state diagram can be used as an effective tool to determine the generating function of the code. Using a modified state diagram [36] BER for a convolutional code can be estimated. For an AWGN channel model, assuming that the all-zero code word is transmitted then an error event to occur if a non-zero code word survives at state 0 eliminating the correct path (all-zero code word). The bounds on the bit error ratio of convolutional codes can be found from the probability that the first error event E of weight d occurring and is given by [36]:

$$P(E,d) = \begin{cases} \sum_{i=(d+1)/2}^{d} \binom{d}{i} p^i (1-p)^{d-i} & ,d \text{ is odd} \\ \frac{1}{2}\binom{d}{d/2} p^{d/2}(1-p)^{d/2} + \sum_{i=(d/2)+1}^{d} \binom{d}{i} p^i (1-p)^{d-i} & ,d \text{ is even} \end{cases} < 2^d p^{d/2}(1-p)^{d/2} \tag{4.76}$$

where p is the crossover probability of binary symmetric channel. The event error probability upper bound can be determined from [38]:

$$P_E < \sum_{d=d_{free}}^{\infty} T_d \, p(E,d) \tag{4.77}$$

where d_{free} is the free distance of the convolution code defined as the minimum Hamming distance between any two code words in the code, and T_d denotes the number of code words of weight d.

From the Eqs. (4.76) and (4.77), the error probability upper bound is given by [36]:

$$P_E < T_d \left[4p(1-p)\right]^{d/2} = T(D,I)\big|_{I=1,D=\sqrt{4p(1-p)}} \tag{4.78}$$

The BER for a convolutional code is given by [36, 38]:

$$BER \le \frac{1}{k}\sum_{d=d_{free}}^{\infty} \beta_d D^d \approx \frac{1}{k}\sum_{d=d_{free}}^{d} 1.06^d \beta_d \exp\left(-\frac{dR\dfrac{E_b}{}}{2N_0}\right) \tag{4.79}$$

where β_d denotes the number of non-zero data bits carried by all T_d paths of weight d, and E_b / N_0 is electrical energy power spectral density ratio and R is the code rate (e.g., the code rate of an $[n, k]$ block code is defined as $R=k/n$). For high SNR, the only the first term in the above summation series dominates. Therefore, for large SNR,

$$BER \approx \frac{1}{k} 1.06^{d_{free}} \beta_d \exp\left(-\frac{d_{free} R E_b}{2N_0}\right) \tag{4.80}$$

Uncoded BER for large SNR is given by [36]:

$$BER_{uncoded} \approx 0.282 \exp\left(-\frac{E_b}{N_0}\right) \tag{4.81}$$

Comparing the coded and uncoded BER from the above Eqs. (4.80) and (4.81), the argument in the coded case is $\dfrac{d_{free} R}{2}$ times larger achieving a hard decision asymptotic coding gain of $10 \log_{10}\left(\dfrac{d_{free} R}{2}\right)$ [dB].

2. *RS and Bose-Chaudhuri-Hocqueaghem Codes (BCH)*

In optical communication systems operating at very high data rate, the challenge is to find the low overhead codes that are capable of correcting random errors due to noise (e.g., from channel fading) and burst errors with special emphasis on complexity and cost. It may be difficult to implement convolution codes that operate at high data rates required for FSO communications systems. Algebraic block codes, such as *Bose-Chaudhuri-Hocqueaghem (BCH)* and *RS* codes are capable of correcting multiple bit-errors with low overhead constraints. When redundancies of (n-k)

symbols are introduced, the bandwidth requirement of the system is also increased. The time required to transmit one symbol is T/k where T is the time duration required to transmit k symbols without coding. The k symbols are encoded into a code word of n symbols which are then transmitted in time duration T. The symbol period is thus T/n and is less than T/k. The width of each symbol after encoding is thus reduced by a factor k/n, whereas the bandwidth required to transmit them is increased by a factor $1/(k/n)=n/k$. This factor is called the bandwidth expansion ratio and the ratio k/n is called the code rate R_c. Overhead requirement is therefore an important parameter in selecting FEC for FSO communication design criterion. The BCH codes are binary and form a class of multiple random error correcting cyclic codes and were discovered by Hocqueaghem and Bose-Chaudhuri [38, 39]. The most important decoding algorithms include Massey-Berlekamp algorithm and Chien's search algorithm. The RS codes are nonbinary cyclic codes with code word symbols from GF(q^m) and are very powerful block codes capable of correcting random as well as burst errors. Both BCH and RS codes can be implemented using high speed shift-register-based encoder/decoder.

The channel models used in the performance analysis of BCH and RS codes are the AWGN channel model. For soft decision decoding the detector experiences an AWGN with received word unquantized while for hard decision, a binary symmetric channel (BSC) becomes applicable with received word quantized by the threshold detector to binary output.

BCH Code Error Detection Performance The probability of undetected word error for a *C (n, k)* code is bounded by the probability of occurrence of an error pattern of weight d_{min} or greater is given by [40]:

$$P_u(e) \le \sum_{i=d\,min}^{n} \binom{n}{i} p^i (1-p)^{n-i} \tag{4.82}$$

where $P_u(e)$ is the probability of undetected word error, and p is the transition probability of BSC. The detected word error, $P_d(e)$ is bounded by the probability that one or more bit-errors occur and is given by [40]:

$$P_d(e) \le \sum_{i=1}^{n} \binom{n}{i} p^i (1-p)^{n-i} = 1-(1-p)^n \tag{4.83}$$

The weight distribution of a block code can be expressed as the Hamming weight of a code word v_i which is the number of non-zero components of the code word. If Ai is the number of code words of weight I in a $C(n, k)$ code, then $A_0, A_1, ., A_n$ is called the weight distribution of $C(n, k)$. The weight distribution of $C(n, k)$, for example, can be expressed in polynomial form called the weight enumerating function (WEF). If the WEF of the code is known, then the exact expression for the probability of undetected word can be written as follows [40]:

$$P_{u(exact)}(e) = \sum_{i=d\,min}^{n} A_i p^i (1-p)^{n-i} \tag{4.84}$$

where A_i is the WEF of the code as described earlier.

BCH Code Error Correction Performance All codes are assumed to be equally likely to be transmitted and the best decision rule at the receiver would be always to decode a received word ***r*** into a transmitted code word ***v*** that differs from the received word ***r*** in the fewest positions (bits). This is called ML decoding which minimizes the Hamming distance between ***r*** and ***v, d(v, r)***. This is called bounded-distance decoder. Thus, the decoder selects the most likely code word $\hat{\mathrm{v}}$ if the received word *r* is within Hamming distance $t = \left[\frac{d_{\min} - 1}{2}\right]$ of $\hat{\mathrm{v}}$. The decoded error occurs when $\hat{\mathrm{v}} \neq \mathbf{v}$ and the decoder failure occurs when there is no $\hat{\mathrm{v}}$ within the Hamming distance *t* of ***r.*** The probability that the decoder performs an erroneous decoding is upper-bounded given by [40]: 1068

$$P(e) \leq \sum_{i=t+1}^{n} \binom{n}{i} p^i (1-p)^{n-i} = 1 - \sum_{i=0}^{t} \binom{n}{i} p^i (1-p)^{n-i} \tag{4.85}$$

The probability of the decoder failure, *P(F)* has the same as the bound on *P(e)*:

$$P(F) \leq 1 - \sum_{i=0}^{t} \binom{n}{i} p^i (1-p)^{n-i} \tag{4.86}$$

When the WEF of the code is known, the exact probability of code error is given by [40]:

$$P_{exact}(e) = \sum_{i=d\,min}^{n} A_i \sum_{k=0}^{t} P_k^i \tag{4.87}$$

where P_k^i is the probability that *r* is exactly Hamming distance *k* from a weight code *I* code word and can be written as:

$$P_k^i = \sum_{r=0}^{k} \binom{i}{k-r} \binom{n-i}{r} p^{i-k+2r} (1-p)^{n-i+k-2r} \tag{4.88}$$

The exact probability of decoder failure can be written as [40]:

$$P_{exact}(F) = 1 - \sum_{i=0}^{t} \binom{n}{i} p^i (1-p)^{n-i} - P_{exact}(e) \tag{4.89}$$

The probability of information bit-error is given by:

$$P_{exact}(e) \geq P_{b(inf)}(e) \geq \frac{1}{k} P_{exact}(e) \tag{4.90}$$

RS Code Error Correction Performance The probability that the decoder performs an erroneous decoding is upper-bounded by [40]:

$$P(e) \leq \sum_{i=t+1}^{n} \binom{n}{i} (1-s)^i s^{n-i} = 1 - \sum_{i=0}^{t} \binom{n}{i} (1-s)^i s^{n-i} \tag{4.91}$$

The upper-bound on the probability of decoder failure in this case is the same as Eq. (4.89). When the WEF of the code is known, the exact expression for decoder word error and failure are given by [40]:

$$P_{exact}(e) = \sum_{i=d\,min}^{n} A_i \sum_{k=0}^{t} P_k^i \tag{4.92}$$

where P_k^i is the probability that r is exactly Hamming distance k from a weight I code word v_i:

$$P_k^i = \sum_{r=0}^{k} \binom{i}{k-r}\binom{n-i}{r} p_e^{i-k+r}\left(1-p_e\right)^{k-r} s^{n-i-r}\left(1-s\right)^{r} \tag{4.93}$$

$$A_i = \binom{n}{i}(q-1)^{i-d_{min}} \sum_{j=0}(-1)^j \binom{i-1}{j} q^{i-j-d_{min}} \tag{4.94}$$

The probability of decoder failure:

$$P_{exact}(F) = 1 - \sum_{i=0}^{t} \binom{n}{i}(1-s)^i s^{n-i} - P_{exact}(e) \tag{4.95}$$

The probability of code word symbol error at the input of the decoder is

$$P_{se} = 1-(1-p)^{\frac{m}{b}} \tag{4.96}$$

Note that b= 1 (binary phase shift keying, BPSK). p is given by $p = \mathrm{Q}\left\{\sqrt{\frac{2 * R_c * E_b}{N_0}}\right\}$ where R_c is the code rate of the code. The probability of uncorrected error is given by:

$$P_u(e) \approx \sum_{i=t+1}^{n} \binom{n}{i} p_{se}{}^{i}\left(1-p_{se}\right)^{n-i}, \quad \text{where n=q}^{\text{m}}\text{-1} \tag{4.97}$$

The information BER at the output of the decoder is given by:

$$P_{b(output)} \approx 1-(1-P_u(e))^{\frac{1}{m}} \tag{4.98}$$

RS Code Error Detection Performance For RS codes the code word symbols are elements of GF (2^m). When the code words symbols are transmitted over BSC using BPSK a 2^m-ary uniform discrete symmetric channel can be considered. The code word symbols are from GF(2^m) and the channel symbols are from GF(2). The probability of channel symbol error is the transition probability p of the BSC and the probability of code word symbol error is given by:

$$P_{se}(e) = 1-(1-p)^{m/b} \quad \text{note that b=1(BPSK)} \tag{4.99}$$

If s denotes the probability that a code word symbol is correctly received, then

$$s = (1-p)^{m/b} \tag{4.100}$$

The probability that a particular incorrect word symbol other than the transmitted one is received is the probability of receiving any one of the q^m-*1* symbols and is given by:

$$P_e = \frac{P_{se}}{q^m - 1} \quad \text{note that b} = 1(\text{BPSK}), \text{and q} = 2 \tag{4.101}$$

The upper-bound for the undetected and detected word error is given by [40]:

$$P_u(e) \le 1 - \sum_{i=0}^{d\,min-1} \binom{n}{i} (1-s)^i s^{n-i} \tag{4.102}$$

$$P_d(e) \le 1 - s^n \tag{4.103}$$

The exact expressions for the two word error probability can be obtained from the WEF of the RS code are known and are given by [40]:

$$P_{u(exact)}(e) = \sum_{i=d\,min}^{n} A_i P_e^i s^{n-i} \tag{4.104}$$

$$P_{d(exact)}(e) = 1 - s^n - P_u(e) \tag{4.105}$$

3. *Concatenated Codes*

It is possible to improve and construct powerful error correcting codes by concatenating two or more codes called component codes separated by an interleaver. The resultant code is then decoded component-wise. Interleaving performs the process of rearranging the ordering of a symbol sequence in a one-to-one deterministic format, whereas deinterleaving is an inverse process which restores the received sequence to its original order. The performance of the concatenation scheme depends upon the interleaver size and its structure and the type of component code used. For example, a hard decision decoding for the concatenated codes with RS codes as component codes and hard decision as well as soft decision decoding for the concatenated codes with BCH codes as component codes are used. The hard decision decoder for the RS and BCH component codes is the bounded-distance algebraic decoder based on the Berlekamp-Massey algorithm and Berlekamp algorithm, respectively. The soft-input/soft-output decoder for the soft decision decoding of the concatenated code with BCH component codes is based on Chase algorithm using the algebraic decoder. Convolution codes are efficient especially when errors caused by the communication channels are statistically independent. For the FSO communication channel burst errors occur due to channel fading. An efficient concatenation scheme consists of a cascade of an outer code (e.g., the RS code) and inner code (e.g., convolution code) as shown in the Fig. 4.22. The interleaver is used to randomize the errors due to the inner decoder. As shown in the Fig. 4.22, encoded data by the outer (RS) code are first interleaved by an outer interleaver before passing to the inner (convolution) encoder. The resulting bits are then permuted by the inner interleaver before being mapped to symbols. At the receiver end soft-input/

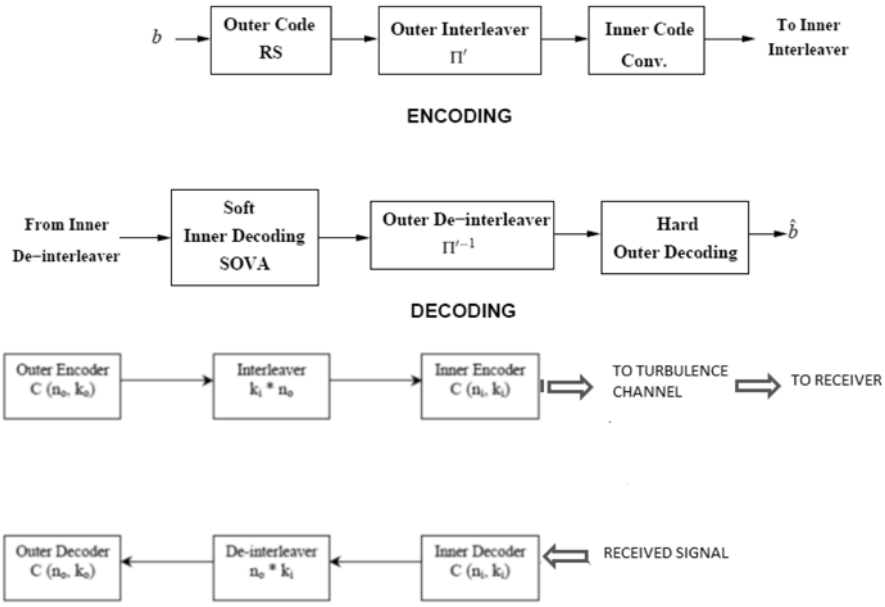

Fig. 4.22 Connection of RS and convolution codes. *RS* Reed-Solomon,

soft-output decoding of the inner (convolutional) code is performed after the operation of symbol detection and inner deinterleaving. Finally, hard decoding of the outer (RS) code is accomplished after outer-interleaving as shown in the Fig. 4.22.

4. *Turbo Codes (TCs)*

Turbo codes (TCs) can provide communications performance close to the Shannon limit. Parallel concatenation is another strategy based on concatenation of the component codes in parallel through an interleaver where the interleaver is a part of the resultant code. When the component codes are block codes in the parallel scheme, it is called TC or parallel concatenated convolution code. The low overhead constraint is the prime criterion for selecting ECCs for optical communication systems so that the selected code should have high code rate. The reader is referred to [36] for a detailed description of convolutional TCs. An estimate of the BER probability of a ML decoder for TCs on the binary-input AWGN channel with power spectral density $N_0/2$ is given by [36]:

$$P_b \cong \sum_{w=1}^{K} \sum_{v=1}^{\binom{K}{w}} \frac{w}{K} \mathrm{Q}\left(\sqrt{\frac{2Rd_{wv}E_b}{N_0}}\right) \tag{4.106}$$

Where the first sum is over the weight w inputs, the second sum is over the $\binom{K}{w}$ different weight w inputs, and d_{wv} is the weight of the v-th code word produced by a weight-w input. The function of the interleaver is to take each incoming block of bits and rearrange them in a pseudorandom fashion prior to encoding by the encoder. For

the parallel concatenated convolution code (which is also parallel TC) the interleaver permutes K bits, and R is the code rate in the above equation. For parallel concatenated convolution code d_{wv} is the smallest for w small (say w = 1, 2, and 3) and the above equation can be approximated by keeping the first few terms [36]:

$$P_b \cong \sum_{w=1}^{3} \frac{wn_w}{K} \mathrm{Q}\left(\sqrt{\frac{2Rd_{w,min}E_b}{N_0}}\right) \tag{4.107}$$

where $d_{w,\min}$ the minimum weight of code words is produced by weight w inputs and n_w is the number of each code words.

5. *Low Density Parity Check Codes (LDPC)*

– *Understanding LDPC Coding: Basics*

Low-density parity-check (LDPC) codes are a class of linear block codes which involve parity-check matrix containing only a few 1s in comparison to the amount of 0s and are capacity-approaching codes allowing the performance to the theoretical maximum (the Shannon limit). The codes were invented by Robert Gallager in his 1960 MIT Ph. D. dissertation [41] and were long-time ignored due to the computational effort in implementing coder and encoder for such codes. The codes were rediscovered by MacKay (1999) and Richardson/Urbanke (1998) [42]. Detailed introductions and tutorials of LDPC codes can be found in [43, 44].

– *Matrix and Graphical Representations for LLDPC Codes*

An example for a low-density parity-check matrix with dimension $n \times$ m for a (8, 4) code is given by [43]:

$$H = \begin{bmatrix} 01011001 \\ 11100100 \\ 00100111 \\ 10011010 \end{bmatrix} \tag{4.108}$$

If we define w_r and w_c to represent the number of 1s in each row and each column, respectively, for a low-density matrix $\mathrm{w_r} \ll \mathrm{m}$ and $\mathrm{w_c} \ll \mathrm{n}$. Figure 4.23 shows a graphical representation introduced by Tanner of the matrix H where the nodes of the graph separated into two distinctive sets and edges are only connecting nodes of two different types, namely, variable nodes (v-nodes) and check nodes (c-nodes).

– *LDPC Encoding*

ECC attach extra bits (or in general symbols) which can be thought of as redundancy to the transmitted data. The extra bits can then be used to detect and correct errors on the received data. The transmitted data is segmented into blocks of fixed length of K bits and the encoder transforms the input segment into an output block of length N where $N>K$ providing the redundancy needed for error correction and detection at a rate of code $R = \frac{K}{N}$. The property of the code for the modulo-2 sum

Fig. 4.23 Graphical representation of Tanner graph of Matrix *H*

$$\mathbf{H} = \begin{bmatrix} 0 & 1 & 0 & 1 & 1 & 0 & 0 & 1 \\ 1 & 1 & 1 & 0 & 0 & 1 & 0 & 0 \\ 0 & 0 & 1 & 0 & 0 & 1 & 1 & 1 \\ 1 & 0 & 0 & 1 & 1 & 0 & 1 & 0 \end{bmatrix}$$

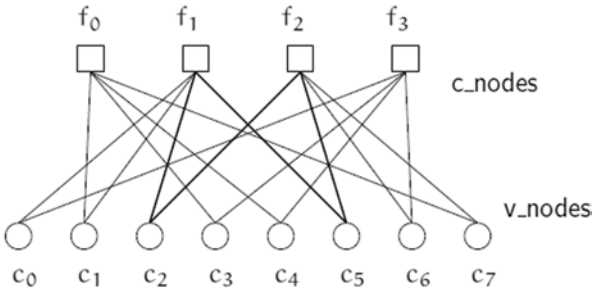

of two code words to be is also a code word. The encoder then find a generator matrix (G) defining the code which is made up of K linearly independent row vectors of size N denoted by $g_1, g_2, \ldots, g_K$. The matrix (G) can be expressed as:

$$G = \begin{bmatrix} g_1 \\ : \\ g_K \end{bmatrix} \tag{4.109}$$

Next, the encoder generates a code word, c, by multiplying the input vector of bits, u, with the generator matrix G so that $c = uG$. A parity-check matrix H can be derived from the generator matrix G is such a way that $GH^T=0$. Using the parity-check matrix H, a decoder now checks if a received word, y, is indeed a code word by satisfying the equation:

$$vH^T = 0 \tag{4.110}$$

To derive H, first the G matrix is expressed as

$$G = \left[I_K \mid P \right] \tag{4.111}$$

and then obtain

$$H = \left[-P^T \mid I_{N-K} \right] \tag{4.112}$$

where P is an $(N\text{-K}) \times K$ sub-matrix, P^T is the transpose matrix of P, and I_{N-K} is the (N-K) identity matrix. For binary code words, $-P^T = P^T$.

Data $u = u_1 \ldots u_N$ is encoded by multiplying it with the generator matrix, $c = uG$ where u is the string of information bits and the matrix G is already explained earlier. An efficient coding technique has been developed to reduce encoding complexity to $O(N)$ by rearranging the parity-check matrix before encoding.

– *LDPC Decoding*

The decoding process reconstructs the transmitted code word, *c*, from the possibly corrupted received word, *y,* by using the parity-check matrix, *H.* The condition to be satisfied is $cH^T=0$ which imposes the set of parity-check constraints for the received code word in order to be the same as the transmitted code word. Referring to the Fig. 4.23 and the matrix Eq. (4.108), an error-free received code word would be, for example, *c*=[1 0 0 1 0 1 0 1]. The next step is to write the equations with the parity-check constraints. If the values assigned to the set of variable nodes represent a valid code then each constraint equations is equal to zero. The equations in general can be written as [45]:

$$f_a = \oplus H_{ab=1} c_b \qquad a = 1.....\text{M}, \text{b}=1....\text{N} \tag{4.113}$$

where f_a is the a^{th} row of *H* and c_b is the *b*-th column. The parity check equations are formed from each row of the matrix. The interested readers are suggested to refer to the references, for example, [44, 45] for a detailed decoding algorithm description including the concept of Message Passing Algorithm (MAP), which is beyond the scope of this chapter.

– *LDPC Performance and Error Rate*

There are many ways to improve the decoding performance of a LDPC code which include minimum distance and improving girth. Although BER and other parameters could be used to predict the performance of a code in determining how good a code is in correcting errors. The Hamming distance between any two code words is the number of bits with which the words differ from each other. The minimum distance is the smallest Hamming distance between two code words and is a measure for code performance. The larger is the distance; the better is the performance of the code. The average girth is the sum of smallest cycles passing through nodes divided by the number of nodes. BER simulations show that large girths codes perform better than those with small with lower girths [46]. LDPC performance codes are evaluated using BER performance over a specified channel and type of modulation scheme. An AWGN channel is normally used in the performance evaluation. The channel bits can be described as $y_i = u_i + n_i$ where *i* is the position of a bit in the signal, noise, and received bit vectors. The Gaussian random noise *n* has a one-sided power spectral density N_0 with a variance σ^2 where $N_0 = 2\sigma^2$. The BER at a given SNR measures the number of errors $(y_i \neq c_i)$ found per iteration code over the code length and is given by

$$BER = \frac{number\ of\ errors (i.e., the\ bits\ that\ are\ not\ equal\ to\ the\ sent\ bits\ of\ the\ transmitted\ data)}{number\ of\ bits} \tag{4.114}$$

The SNR is defined as $SNR = 10\log\frac{E_s}{N_0}$ where E_s is the signal energy. The BER thus represents the probability that a bit, after decoding, will be in error at a particular SNR. Other performance measure is frame error rate (FER) or word error rate

(WER). The FER is the number of decoded words (length of code) that contains errors as a fraction of the total number of words decoded.

In most applications, LDPC coding and decoding can be done in hardware. Large codes require more complex hardware in terms of memory communication network and processing nodes. LDPC decoder memory required depends on the structure of the code and implementation architecture. The main difficulty in the hardware decoder implementation lies in the interconnection complexity between nodes and large memory. LDPC implementation thus requires careful design of the hardware to reduce the complexity.

In summary, for an FSO communication link under different turbulence conditions, the performance of some different channel coding techniques is discussed. RS coding technique alone is not robust against even if weak channel turbulence condition. Convolution and TCs can provide nearly same performances and some performance improvements in weak turbulence channel. Applying some types of time diversity, these codes are efficient under moderate to strong turbulence. Concatenated convolutional and RS codes scheme requires more decoding complexity and the performance can be very close to that of a convolutional code alone. Considering the decoding complexity and its performance, a convolutional code may be suitable for many practical applications. Channel coding should also be done with symbol interleaving for evaluating performance under various coding techniques. The TC can provide better performance than a convolutional code under the same coding rate.

c. *FSO Communications Systems Performance with Coding Techniques: Some Examples*

From the above discussions, it is clear that communications performance can be greatly improved using coding techniques and therefore improved coding and interleaving techniques are being investigated by for application in higher date rate FSO communications systems. This subsection will discuss applications of some of the coding techniques already discussed earlier. The selection of a specific coding technique will depend on many factors including the required data rate, acceptable BER, communication channel's fading characteristics, and the communication scenario defining the FSO system. In addition, efficient modulation technique and the system's power, size, weight, and cost need to be determined before performing simulations studies. Finally, a system's approach should consider the available technology devices such as laser, detector, and appropriate optics for a successful FSO communications design. We describe below some of the examples of research reported for different coding techniques under different atmospheric conditions and test scenarios.

– *RS Coding Example for FSO Communications*

Channel coding using the RS code can improve the FSO communication system performance and communication distance. In this example, the information source for the RS-coded FSO communication through the atmospheric turbulence channel generates an independent and identically distributed {0, 1} binary sequence

with $P(0)=P(1)=1/2$. The RS code encoder encodes the information sequence into code words. OOK modulation is assumed so that the optical modulator modulates the laser according to the encoded code words and the modulated laser is transmitted through the transmitter optics into the FSO channel. An avalanche photodiode detector (APD) photodetector converts the received optical signal into electronic signal. The demodulator makes binary decisions using optimal thresholds and a decoding algorithm (e.g., the Berlekamp-Massey algorithm) is used to decode the code words to obtain the transmitted original information sequence. The channel state, i.e., the realization of instantaneous channel fading is assumed to be unknown to the transmitter, but is known to the receiver, and is used for optimal data demodulation. The receiver demodulates the *t*-th bit using a hard-threshold *T(h[t])* using the decision rule

$$\hat{x}(t)=\begin{cases}0, \text{if } y(t)\le T(h(t))\\ 1, \text{if } y(t)\ge T(h(t))\end{cases} \tag{4.115}$$

where *y(t)* is the APD output electrons during the *t*-th OOK pulse period and *h(t)* is the channel state for any given realization and the channel is free of ISI. The probability of making a demodulation error of the *t*-th bit is given by [47]:

$$\begin{aligned}P_e(h(t)) &= P(\hat{x}(t)=1 \mid x(t)=0)/2 \\ &+ P(\hat{x}(t)=0 \mid x(t)=1)/2\end{aligned} \tag{4.116}$$

The optimal threshold is chosen for each pulse according to the channel state *h(t)* known to the receiver such that the probability $P_e(h(t))$ is minimized. The average BER is obtained from the ensemble average of $P_e(h(t))$ over the distribution of *h,* (i.e., the channel fading PDF *p[h]*), and is given by [47]:

$$< BER >= \overline{P}_e = \int_{h=0}^{\infty} p(h) P_e(h(t)) dh \tag{4.117}$$

Figure 4.24 shows the BER curves [47] are presented for a laser wavelength $\lambda = 1.54\mu m, C_n^2 = 5\times 10^{-15} m^{-2/3}$, the propagation distance $L=5$ km and the aperture diameter, $D=10$ cm. The channel code used is RS (255, 191, 65) code with and without using eraser. At BER $=10^{-6}$, the BER curve of the RS code with erasure has a coding gain of about 17 dB and is about only 2.5 dB from the ideal fading-free coded BER curve. The channel coding using the RS codes can thus improve the FSO communication performance.

The performance of FSO system with *M*-ary pulse position modulation (PPM) based on RS codes scheme has been analyzed for both weak and strong turbulence-–induced fading channels [48]. *M*-ary PPM achieves high power efficiency at the expense of reduced bandwidth efficiency. A high order PPM modulates creates the higher power peak power needed to overcome the weak average power. Upper bounds on the BER of *M*-ary PPM over weak (log-normal) and strong (exponential) turbulence-induced fading channels without coding and with RS (255, 207) coding show the improvement in the FSO system performance [48]. The BER of an *M*-ary PPM in log-normal channel is given by [49]:

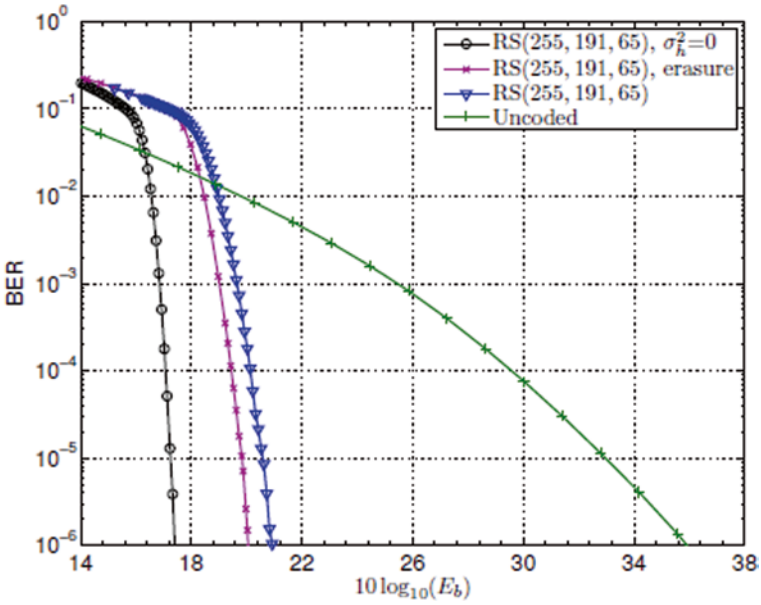

Fig. 4.24 BER curves for Reed-Solomon coding FSO communication through turbulence atmosphere. (*Reprinted with permission from IEEE, Copyright © 2010 IEEE* [47].). *BER* bit error rate, *FSO* free-space optical

$$P_b^M \le \frac{M}{2\sqrt{\pi}} \sum_{i=-N, i\neq 0}^{N} w_i \mathrm{Q}\left[\sqrt{\frac{e^{2\left(\sqrt{2}\sigma_k x_i + m_k\right)}}{Fe^{\sqrt{2}\sigma_k x_i + m_k} + K_n}}\right] \tag{4.118}$$

where M is the modulation level, w_i and x_i are the weight factors and the zeros of the Hermite polynomials, respectively. The variance of the log-normal channel ${\sigma_k}^2$ and the scintillation index ${\sigma_{SI}}^2$ are related by ${\sigma_{SI}}^2 = e^{{\sigma_k}^2} - 1$. The total noise photons per PPM slot denoted by K_n come from background noise and thermal noise, and is given by [49]:

$$K_n = \frac{2{\sigma_n}^2}{\left(E\{g\}q\right)^2} + 2FK_b \tag{4.119}$$

where K_b is the average background noise photons per PPM slot, $E\{g\}$ is the average gain of the APD and q is the electron charge. The noise factor, F, of the APD is defined by

$$F = 2 + \varsigma E\{g\} \tag{4.120}$$

where ς is the ionization factor. In a PPM slot, the variance of the thermal noise, ${\sigma_n}^2$, is defined by [49]:

$${\sigma_n}^2 = \left(\frac{2\mathrm{k}TT_{slot}}{R_L}\right) \tag{4.121}$$

where T is the effective absolute temperature of the receiver, k is the Boltzmann constant, R_L is the APD load resistance.

The PPM slot duration T_{slot} is related to the data rate, R_b by [49]:

$$T_{slot} = \frac{\log_2(M)}{MR_b} \tag{4.122}$$

The symbol error rate P_{symbol} can be calculated from the BER using the following equation [50]:

$$P_{symbol} = P_b\left(\frac{2(M-1)}{M}\right) \tag{4.123}$$

The probability of the uncorrectable symbol error is given by [51]:

$$P_{ues} \le \frac{1}{n}\sum_{i=t+1}^{n} i\binom{n}{k}P_q^i\left(1-P_q\right)^{n-i} \tag{4.124}$$

where t=([n − k]/2) is the symbol error correcting capability, P_q is the q-bit RS symbol error probability. The BER after coding is given by [51]:

$$P_{bc} = P_{ues}\left(\frac{n+1}{2n}\right) \tag{4.125}$$

The BER discussed above is valid for the weak turbulence channel which obeys log-normal distribution. For strong turbulence case, the scintillation index can be greater than 1 and a negative exponential model is valid for propagation distances more than 100 m or several kilometers [49]. The BER of an M-ary PPM in negative exponential channel is given by [49]:

$$P_b^M \le \frac{M}{2}\sum_{i=-N,i\neq 0}^{N} w_i\left|x_i\right|\mathrm{Q}\left(\frac{E\{K_s\}x_i^2}{\sqrt{2FE\{K_s\}x_i^2+K_n}}\right) \tag{4.126}$$

where K_s is the photons per PPM slot. The BER after coding (P_{bc}) due to negative exponential channel using RS (255, 207) can be calculated using the same approach as for log-normal channel.

Figure 4.25 shows a comparison of BER without and with RS (255, 207) coding for both weak and strong turbulence for 8-PPM [48]. The data rate is 2.4 Gbps, K_b (average background noise photons per PPM slot) = 10 photons, R_L (APD load resistance) = 50 Ω, ς (the ionization factor) = 0.028, T=300 °K, $E\{g\}$=150, n=255, k=207, t=24 symbols. For strong turbulence at a BER of 10^{-9}, the value of average photons per PPM bit is 728 without coding and 141 with coding which gives the system performance improvement of 11.61 dB. For weak turbulence, the value of average photons per PPM bit is 543 without coding and 32 with coding giving an improvement of 16.6 dB. The RS coding scheme therefore improves the performance for both weak and strong turbulence.

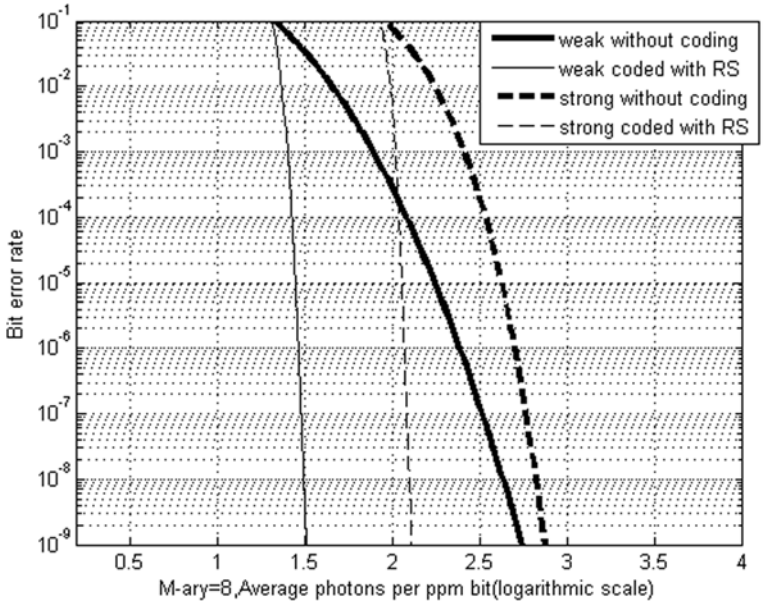

Fig. 4.25 Comparison of BER without and with RS (255, 207) coding for both weak and strong turbulence for 8-PPM. (*Reprinted with permission from IJSER* [48]). *BER* bit error rate, *RS* Reed-Solomon, *PPM* pulse position modulation

– *Comparison of Different Coding Schemes Examples for FSO Communications*

Sometime, it is of interest to compare various channel coding techniques for different time-diversity orders and turbulence conditions. However, this is also complex since a fair comparison involves a number of parameters such as FSO communications scenario, modulation scheme, power efficiency, hardware and software complexity, and cost. Comparative studies of the performances of different channel coding techniques, employed under the presence or not of time diversity, are presented [52]. For making a fair comparison, the channel coding rate R_c is set to ½ for all coding schemes. Channel coding techniques presented are convolutional (in particular recursive systematic convolutional, RSC codes), RS, concatenated convolution and RS (CCRS) codes, and TC. RSC code (1, 15/17) of constraint length $K=4$ where the numbers 15 and 17 represent the code polynomial generators in octal. RS code RS (255/127) is considered so that the code rate R_c is $127/255 \approx 0.5$. For which an RS encoder takes k data symbols of t bits each at input, and provides $n=2^t-1$ output symbols, by adding n-k parity symbols to them ($t=8$). For the CCRS coding, the RSC code (1, 133/171) of $K=7$ as the inner code and RS (255, 239) as the outer code is used. Figure 4.26 shows the BER versus E_b/N_0 for different coding schemes for weak turbulence conditions for a data rate $R=1$ Gbps corresponding to the symbol duration $T_s=1$ ns. The channel coherence time of $\tau c=1$ ms so that the channel varies over blocks of $N_c=\frac{\tau_c}{T_s}=10^6$ symbols, and frames of length $N_F=4{,}080$.

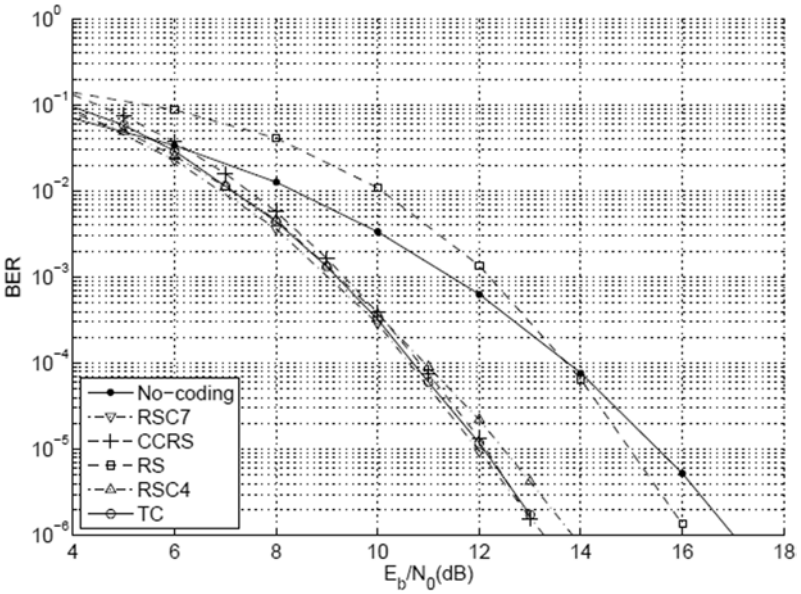

Fig. 4.26 Comparison of BER vs. E_b/N_0 for different coding schemes for a weak turbulence condition (*Reprinted with permission from The Optical Society of America, OSA, 2009* [52]). *BER* bit error rate

From the Fig. 4.26, it is seen that the RS code is not really efficient, whereas the three other codes provides better and very similar performance improvements. For example at BER = 10^{-5}, with coding, a gain of 0.6 and 3 dB in SNR is obtained for RS and RSC4, respectively and a gain of 3.4 dB for CCRS and TC. For relatively weak turbulence condition, the RSC4 provides a good performance improvement. The details of the BER curves for other turbulence conditions can be found in the reference [52].

– *LDPC Codes Example for FSO Communications*

There have been a number of researchers that have shown where LDPC codes for the FSO channel can efficiently improve the performance [53–57]. LDPC error-correction codes proposed for bursty channels, such as fiber-optics channel operating at 40 Gbit/s or higher can outperform turbo product codes of comparable code rates. These codes can also be used for the atmospheric FSO channel which also shows bursty-error-prone behavior. For practical implementation in a real FSO communication system, these codes are useful because of low encoding and decoding complexity. Figure 4.27 shows the BER performance of both LDPC and RS codes for a turbulence strength of $\sigma_R = 1.0$. The BER of the uncoded system is also shown in the figure. The Shannon limits for rates of 0.91 and 0.75 represent the best performance one can achieve with an infinitely long FEC code. The turbulence strength shows here is applicable to a medium turbulent strength. The coding gains are 7.5 and 9.0 dB, respectively over the RS codes. For the turbulent strength of

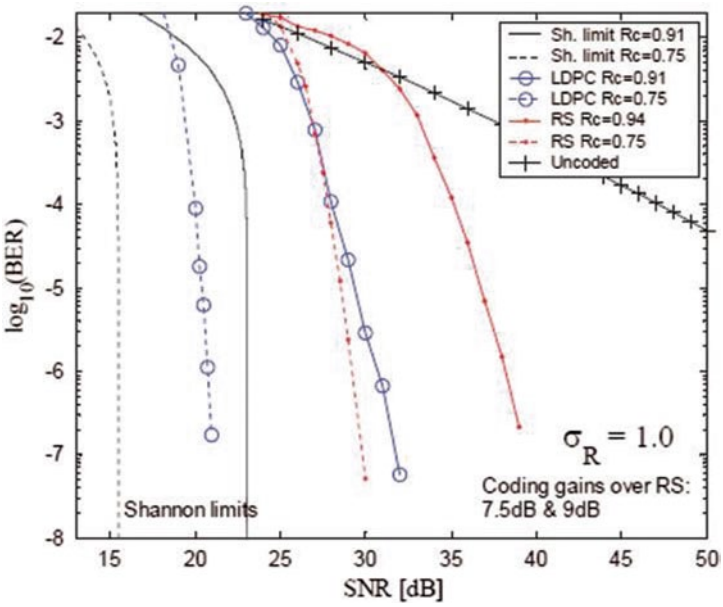

Fig. 4.27 BER curves for medium turbulence $(\sigma_R = 1.0)$ of different codes (LDPC and RS; *Reprinted with permission from The Optical Society of America, OSA* [53].). *BER* bit error rate, *LDPC* low density parity check codes

$\sigma_R = 1.0$, the performance of the uncoded system is very poor and a practical FSO communication system cannot operate without coding, since a SNR of 50 dB is almost impossible to achieve under this type of atmospheric turbulence condition.

Using LDPC codes, there is thus a significant performance improvement of providing very large SNR gains over RS codes of similar rate for a wide range of turbulence conditions for designing a practical FSO communication system. A number of LDPC coded FSO system to operate under different atmospheric turbulence conditions employing various modulation techniques is reported. Some of them includes: (i) LDPC-coded MIMO concept with space-time block codes [58], (ii) Adaptive LDPC-coded modulation [55, 56], (iii) LDPC-coded orthogonal frequency division multiplexing (OFDM) [59], and (iv) Bit-interleaved LDPC-coded pulse amplitude modulation (PAM) and PPM [57]. The interested readers are referred to these papers for detailed descriptions and analysis.

4.3.5 Adaptive Optics (AO) Techniques

This section discusses the adaptive optics (AO) concepts and technology as another potential mitigation technique for FSO communications.

– *AO for Free Space Laser Communications*

Data rates of long-range FSO communication systems are deteriorated by atmospheric turbulence which causes power in the bucket fluctuations due to the following effects: Beam broadening beyond natural diffraction effects as the beam propagates from the transmitter to the receiver, spot blurring and broadening at the receiving aperture with increased turbulence, and signal fading due to scintillation as a result of the aberrated beam wave front. From FSO communications point of view, these effects directly cause a decrease in SNR resulting in a higher BER, and increase in the OP due to fading. Intensity fluctuations can seriously increase BER of optical communication system, thus limiting the practical distance and throughput of FSO communications system. Thus, the performance of the communication system is decreased. Although the short-term data losses can be partially recovered using various coding techniques discussed earlier, long-term (up to tens of milliseconds) random breaks in the received data due to turbulence-induced deep signal fading cannot be solved by the conventional coding techniques. The situation gets worst as the data rate requirement become higher such as Gbps or multi-Gbps. AO can be useful for FSO communications system by providing additional wave-front compensation to increase SNR and decrease long-term data losses. AO technology was initially developed for atmospheric compensation in astronomical observations to mitigate wave-front distortions caused by atmospheric turbulence. The same technology can be applied to free-space laser communications for mitigating wave-front distortions by applying real-time wave-front control to reduce the likeliness of signal fading.

– *Principle of Adaptive Optics in Laser Communication System*

AO is the technology for correcting random optical wave-front distortions in real time. Conventional adaptive optics system measures the distortions with a wave-front sensor (WFS) and adapts a wave-front corrector to reduce the phase distortion so that the original signal is reconstructed. Adaptive optics is designed to measure wave-front errors continuously and correct them automatically. A special computer-controlled deformable mirror that can change its shape to correct the wave-front errors which are measured by a highly accurate system called a WFS that provides correction signal to the mirror. An AO system thus consists of a wave-front sensor, deformable mirror, computer, control hardware, and software. In a typical AO laser communication system, the laser transmitter is connected from one fiber system to the other and wave-front conjugation principle is used to compensate for turbulence-induced distortions in real time. A WFS and wave-front corrector measure and correct the distorted wave front. The wave-front corrector has a tip-tilt mirror to correct wave-fronts tip-tilt and a deformable mirror (DM) to correct higher-order phase aberrations. The input light for the WFS can generally come from a beacon, but not signal laser.

– *Laser Communications Parameters Relevant to AO*

In a FSO communications system, the laser transmitter sends the data signal which propagates through atmospheric turbulence and is collected by the receiver aperture to focus onto a detector. The wave-front at the receiver plane is distorted so that

the power in the bucket is decreased causing a reduced SNR and increased BER. Scintillation effects are characterized by the log-amplitude variance or the scintillation index. The value of the residual wave-front variance can be expressed as a function of the number of corrected Zernike modes [60]. Zernike polynomials are a set of orthonormal basis functions with modes related to various aberrations such as spherical aberration, astigmatism, coma, and so forth. Strehl ratio is defined as the ratio of the intensity on the optical axis of an aberrated or corrected point spread function (PSF) to the on-axis intensity of the diffraction-limited PSF. The residual wave-front variance, σ^2 can be computed from the measured Strehl ratio, S by the following equation:

$$S = e^{-\sigma^2} \tag{4.127}$$

The mean square of the wave-front error can be expressed as:

$$\sigma^2 = C_{Zern}\left(\frac{D}{r_0}\right)^{5/3} \tag{4.128}$$

where D is the aperture diameter, and r_0 is the atmospheric turbulence path coherence length. The coefficients C_{Zern} are related to the Zernike modes that have been compensated and are related to the fully corrected Zernike modes [60].

The BER is one communication systems performance metric and depends on the modulation format. BER for OOK modulation is an average overall possible signal levels s of a given probability distribution $p_I(s)$ and is given by [10]:

$$BER(OOK) = \frac{1}{2}\int_0^\infty p_I(s)\, erfc\left(\frac{< SNR >_s}{2\sqrt{2} < i_s >}\right) ds \tag{4.129}$$

where $< i_s >$ is the mean signal current, SNR is the electronic SNR, and *erfc* is the complementary error function. The probability distribution function $p_I(s)$ can be assumed to follow a Gamma-Gamma distribution [10] which is valid for wide range of atmospheric turbulence range. The function $p_I(s)$ contains the parameters α and β, for example, for the Gamma-Gamma distribution which also depends on the scintillation index, σ_1^2 for the turbulence propagation. The adaptive-optics corrected Rytov parameter is then given by [61]:

$$\sigma_1^2 = \frac{2.606}{2\pi} k^2 C_n^2 \int_0^{2\pi}\int_0^\infty \left[L - \frac{k}{\kappa^2}\sin\left(\frac{L\kappa^2}{k}\right)\right]\kappa^{-8/3} \times \left[1 - \sum_{i=1}^{N} F_i(\kappa, D, \phi)\right] d\kappa d\varphi \tag{4.130}$$

The above equation is valid for a horizontal path of length L, and C_n^2 is constant. We assume a plane wave propagation.

The adaptive optics filter $\left[1 - \sum_{i=1}^{N} F_i(\kappa, D, \phi)\right]$ operates on the transverse spatial spectrum (depends on κ) and represents the removal of spatial modes by adaptive

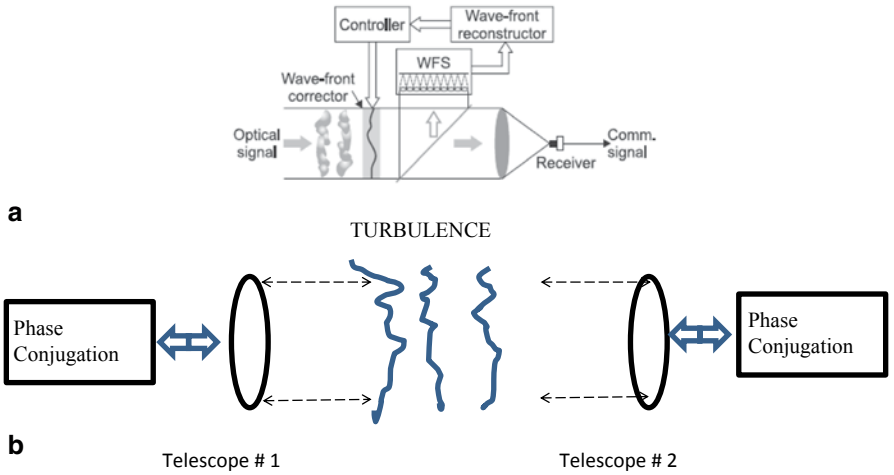

Fig. 4.28 **a** Basic concept of adaptive-optics approach for FSO communications. (*Reprinted with kind permission from Springer Science+Business Media B.V. [Fig. 13, page 332,* [27]). **b** Schematic of AO-based FSO communications for a symmetrical communication system (*Reprinted with permission from SPIE, 2009, Fig. 1, page 72000 J-2, Vol. 7200_Proc. SPIE, January 2009)*. *FSO* free-space optical, *AO* adaptive optics

optics phase conjugation. The filter functions are given by [62]. If we remove an increasing number of Zernike modes, the scintillation index, σ_I^2 values are reduced so that a potential increase in FSO communication link performance can be achieved (i.e., the decreased BER values).

– *AO System Architecture for FSO communication Systems*

The conventional adaptive optics approach is based on wave-front sensing of the received distorted wave-front and reconstructing the undistorted wave front. For FSO communication systems, a part of the received beam is directed toward a WFS, and then the wave front is reconstructed from the measured data which is then used to calculate the control signals for the actuators of the wave-front corrector. The signal with corrected wave front is received by the receiver to obtain the communication signal. Figure 4.28a shows this basic concept. Another AO system for FSO communication is a symmetrical communication system based on an approach that enables an increase in mean power in the bucket and a decrease in intensity fluctuations. This type of correction is applicable to a symmetrical system where both emitter and receiver is identical (Fig. 4.28b).

The control is based on an amplitude and phase iterative correction. The optical beam is propagated back and forth through the same turbulent volume. At the level of each telescope a pseudo-phase conjugation is performed. Both emitted amplitude and emitted phase are controlled in this approach. An algorithm utilizes an iterative between the two telescopes of the communication link. After each propagation, normalization by the nominal beam intensity is performed to take into account of initial laser beam power. This strategy for optimal correction is based on iterative phase conjugation pre-compensation.

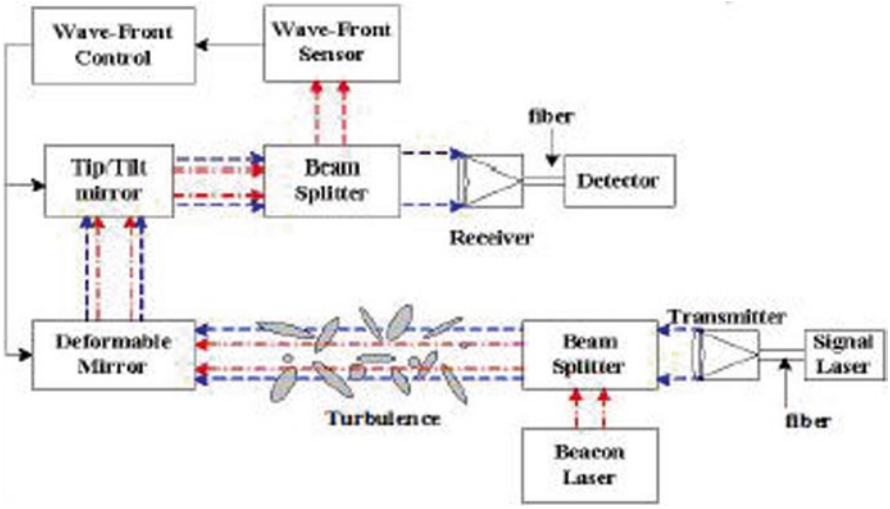

Fig. 4.29 An adaptive optics-based FSO laser communication system with a separate beacon laser. (*Reprinted with permission from AJETR, 2011* [68]). *FSO* free-space optical

Another AO architecture is shown in Fig. 4.29 where wave front is measured and corrected by WFS and wave-front corrector, respectively. There can be two types of wave-front correctors, for example, tip-tilt mirror for correcting tip-tilt and a deformable mirror (DM) for correcting higher-order phase aberrations. A beacon laser (generally of different wavelength than the signal laser transmitter wavelength) provides the light to probe the atmospheric turbulence used for WFS.

For laser communication, applications a distributed turbulence affect the beam along the entire propagation path which results in corruption of both phase and intensity. For strong intensity scintillations, phase reconstruction is extremely difficult from the wave-front measurements because of the occurrence of branch points. Therefore, wave-front sensorless adaptive optics can be appropriate for free-space laser communications to operate under all levels of turbulence strengths. This way, wave-front measurements can be avoided. Control of the wave-front correctors in AO systems can be performed by blind (model-free) optimization of a system performance metric, e.g., the Strehl ratio. Because of the new development of several technologies and new efficient control algorithms such as stochastic parallel gradient descent (SPGD) and their implementation using parallel processing hardware based on very-large-scale integration (VLSI) micro-electronics and the high-bandwidth wave-front phase controllers such as micro-mechanical systems (MEMS)-based deformable mirrors, it is feasible now to develop AO FSO communication system without a WFS. Figure 4.30 shows a scheme of free-space laser communication based on wave-front sensorless adaptive optics system [63]. Thus, there is an advantage of using wave-front control by optimization of a performance metric. Information about the received power level available in a communication terminal which may be used as a metric for the AO controller. The interested reader can get

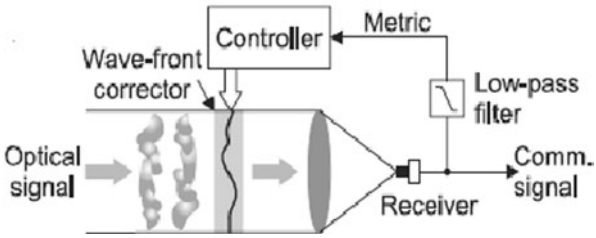

Fig. 4.30 Schematic of FSO laser communication system based on wave-front sensor less AO concept. (*Reprinted with kind permission from Springer Science+Business Media B.V. [Fig. 1(b), page 249, 2008* [63]). *FSO* free-space optical, *AO* adaptive optics

detailed information about the techniques and different design schemes from the references [63].

– *AO-based FSO Communications Systems: Some Examples, Applications, and Technology Development*

AO-based Laser Communication Performance A laboratory-based free-space optical communications system using adaptive optics with an APD is reported [64]. The results for BER as a function of received power are shown in Fig. 4.31a-c for a simulated turbulence corresponded to r_0 = 9 mm and a 70 mm (D) optical beam. Compared to the uncoded BER, gain in the received signal power is shown when AO correction is applied in the presence of background and turbulence.

Results of improvement with AO correction in a laboratory test bed under simulated atmospheric conditions are shown in the Fig. 4.32 using 100 Mbps data stream and OOK and PPM modulation formats. Gains of up to 6 dB with AO were verified in the laboratory experimental tests as well as the dependence of AO gains on modulation format. The interested reader can find more details in the reference [65].

A low-order adaptive optics laser communications system consisting of a two-axis tip-tilt corrector is described and results of a closed-loop experiment show bit-error improvement up to a factor of 42 of an OOK-modulated communications laser for a data rate of 200 Kbps [66]. Similar experiment with a high-order adaptive laser communications system characterizing a 19-channel adaptive optics system show a reduction of the BER by a factor of 41.5 under specific laboratory conditions [67]. In another report, a numerical simulation model and an experiment of AO in 2.5 Gbps laser communication system show the signal fading mitigation of turbulence [68]. The average BER without and with AO corrections were reported to be 6×10^{-3} and 1×10^{-4}, respectively. With AO higher-order correction, there was no bit-error in 120 s. In FSO communication systems, Strehl ratios are critical for developing link budgets analysis and evaluating different levels of compensation needed for specific applications. Results are presented for simulating Strehl ratio of compensated systems with both low-order (tip-tilt) and higher-order (AO) compensation under general turbulence conditions including strong turbulence [69]. Strehl ratio model for predicting better performance specifically for strong turbulence are reported.

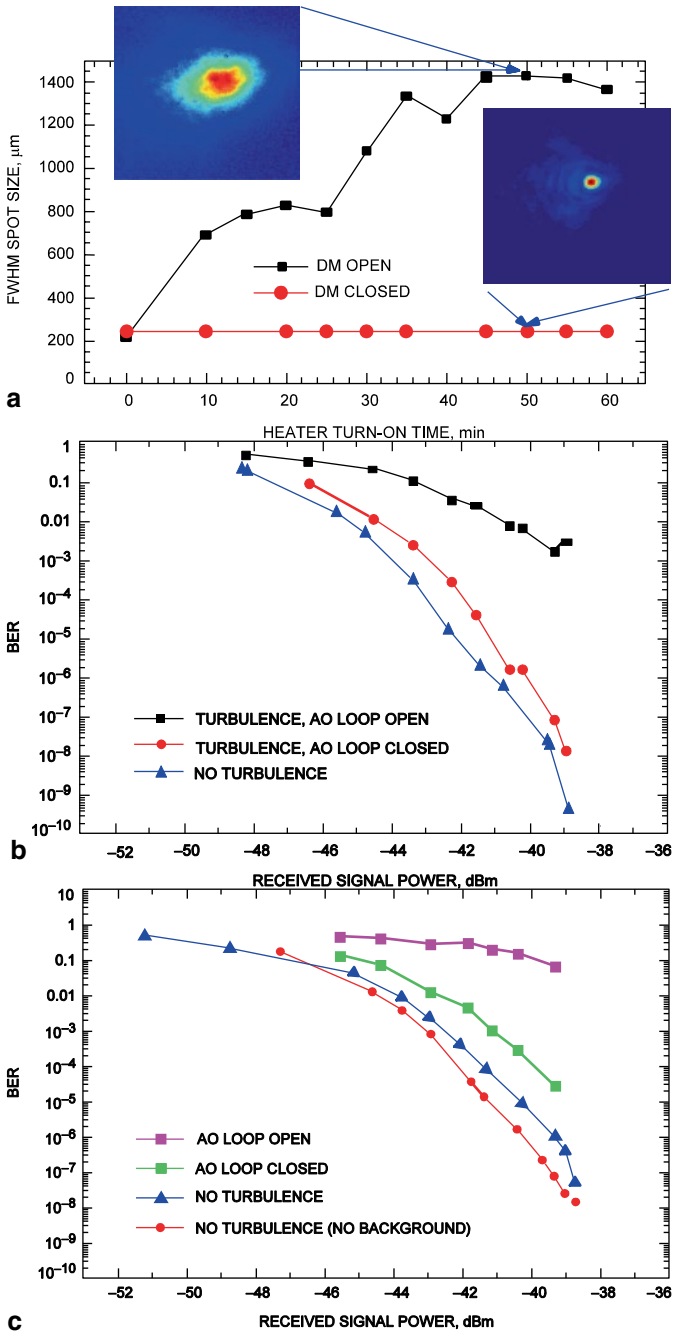

Fig. 4.31 **a** Spot size as a function of turbulence determined by heater turn-on time. **b** The BER as a function of received signal with no background signal. **c** BER as a function of received signal with turbulence (*AO loop open*), turbulence (*AO loop closed*), no turbulence, and no turbulence (*no background*). (*Reprinted with permission JPL/CalTech, JPL IPN Progress Report, 2005,* [64]). *BER* bit error rate, *AO* adaptive optics

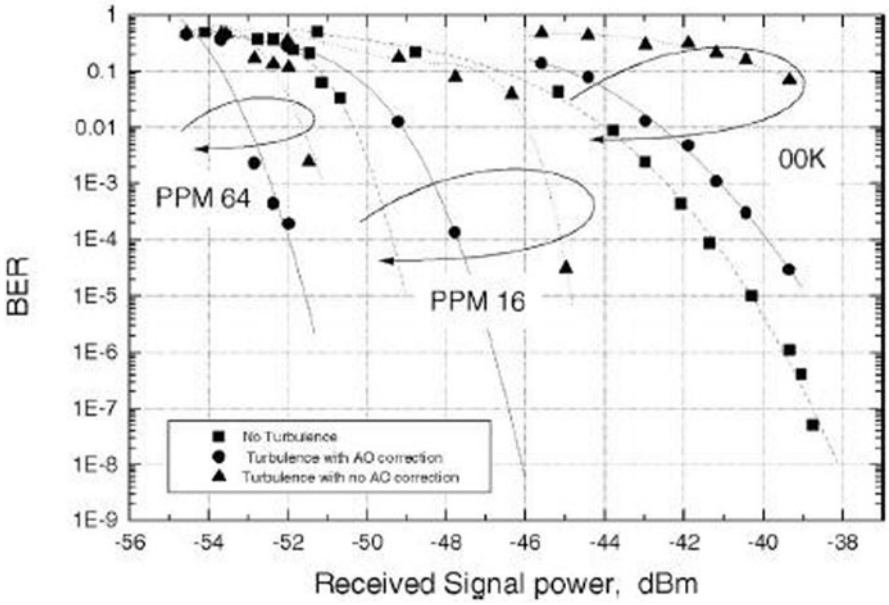

Fig. 4.32 BER improvement with AO correction in a laboratory, test-bed for *PPM* and *OOK* modulations. (*Reprinted with permission, SPIE, 2008* [65]). *BER* bit error rate, *PPM* pulse position modulation, *AO* adaptive optics

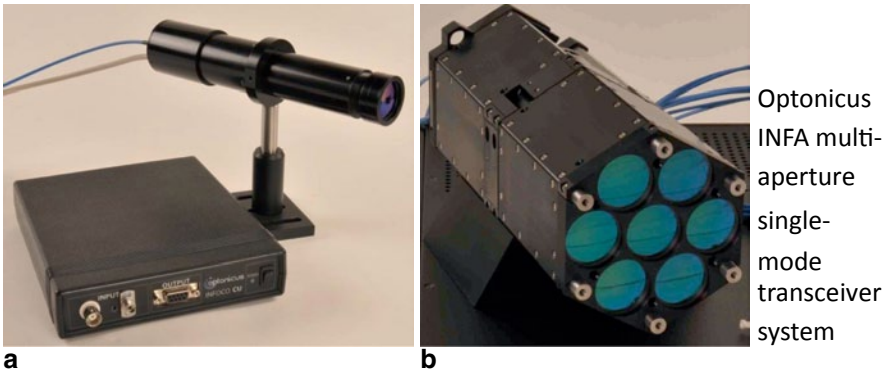

Fig. 4.33 **a** Optonicus's INFOCO lasercom system. **b** Optonicus's multiple aperture single-mode transceiver. (*Courtesy of, and permission from Dr. Mikhail A. Vorontsov, 2013, Optonicus:* www.optonicus.com)

Recently Optonicus has developed compact laser communication transceiver with an efficient control algorithm such as stochastic parallel gradient descent (SPGD) using MEM deformable mirrors [63]. Figure 4.33a shows Optonicus' INFOCO Lasercom system. Figure 4.34 shows an AO laser communication system based on cooperative information sharing.

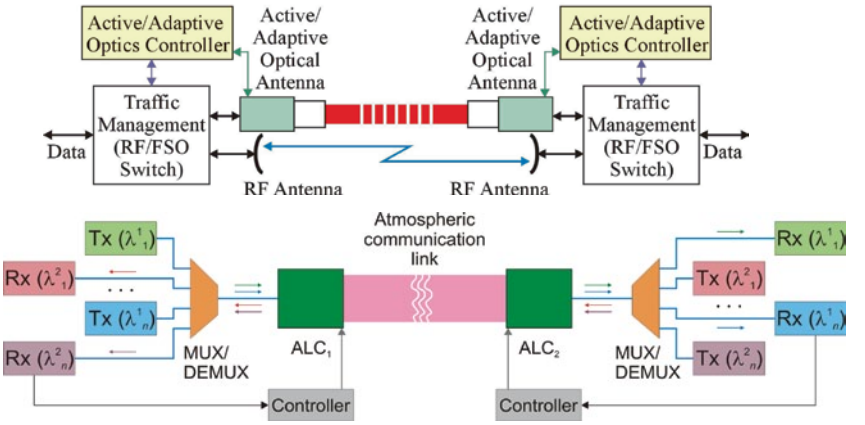

One of the WDM wavelengths performs continuous **monitoring and sharing** information about **received signal power level.** Shared information is used by **AO controllers** for independent control of **beam pointing, divergence,** and **atmospheric phase distortion compensation** using SPGD AO.

M. Vorontsov, G. Carhart, J. Gowens, & J. Ricklin "Adaptive Correction of Wave-front Phase Distortions in a Free-space Laser Communication Systems and Method" US Patent # US 7197248, March 27, (2007).

Fig. 4.34 AO laser communication system based on cooperative information sharing. (*Courtesy of, and permission from Dr. Mikhail A. Vorontsov, 2013, Optonicus*:) www.optonicus.com. *AO* adaptive optics

4.3.6 Other Techniques

There are other mitigation techniques and schemes for applications in FSO communications operating in presence of fading atmospheric channel. Some of them include: (i) wavelength diversity, (ii) modifying outgoing transmitter beam, (iii) advanced signal processing, and (iv) multiple-sites/relay-assisted communication links scheme.

1. *Wavelength Diversity*

There are a number of ways to use wavelength diversity technique. Recently a technique is described where the same signal could be transmitted at different wavelengths. Since the effects of turbulence due to random refractive index variations are different for different wavelengths, the fading characteristics such as intensity fluctuations at the receiver are different for the different wavelengths. Using SD in which the signal with the largest SNR can be selected by the receiver to reduce OP. The results are reported [70] for three different lasers at 850, 1,330, and 1,550 nm using three different detectors at the receiver. The same signal is used using the different lasers transmitting at the three wavelengths. At the receiver, the signals are combined by equal gain or a selective combiner, resulting in improved overall combined signal intensity. SD is used in their work in which the signal with the

largest SNR is selected by the receiver. For a given threshold SNR (normalized with average SNR), the OP is shown to decrease with the number of transmitter/receiver elements. By using more number of communications the OP can be further reduced but at the expense of systems complexity and cost.

Long-range scenario at high altitude with wavelength diversity technique using two lasers transmitter signal sources operating at 1550 nm and 840 nm wavelengths were investigated [71] with varying path lengths (from 4.3 to 41 km). Communications quality improvements using wavelength diversity and EGC receiver were shown by estimating long-term BER.

Wavelength diversity scheme for fog mitigation in a ground-to- UAV communication link were reported [72]. Fog can be one of the major limiting factors in FSO link performance. The researchers demonstrated the implementation of wavelength scheme on aslant path for a ground-to-UAV FSO link to be established in a foggy atmosphere. The FSO link was configured to operate using the simultaneous transmission of three wavelengths, 0.85, 1.55, and 10 μm which establishes the link between a ground station and an UAV at either 4- or 8-km altitude. An equal-gain diversity scheme and a selective diversity scheme were analyzed by combining the multiple carrier wavelengths. Their detailed simulation analysis showed that a selective diversity scheme exhibited a received power level that was 300% higher than the use of equal-gain diversity scheme. The 10 μm wavelength for ground-to-UAV FSO communications link served as a method to mitigate the effects of fog on the FSO signal.

Two closely separated near-infrared (IR) channels (1556.5 and 1558.1 nm) were exploited to remove the effects of atmospheric scintillation for ranges up to a few km [73]. Their technique was based upon the dual wavelength output of a He-Xe laser with a high level of noise coherence.

2. *Modified outgoing transmitting beam characteristics*

a. Non-diffracting beams

In FSO communications and most optical applications, the standard laser beams with a transverse intensity distribution described by a Gaussian function are utilized. As the beam propagates in the free atmosphere, the initial beam spreads and the angular divergence is determined by the wavelength and the initial waist radius of the beam. Because of diffraction effects, the beam propagation range is shortened if the spot size of the Gaussian beam is reduced. Non-diffracting beam can be used to remove this restriction. This can be thought of as an interference field created by plane waves with constant longitudinal component of the wave vector. The transverse intensity distribution of the interference field is given by the Bessel function of the first kind and zero-order, and remains exactly propagation invariant. Non-diffracting beam is thus an ideal optical field with completely eliminated diffraction. In real experimental situation, an approximation of this ideal non-diffracting beam is used, called pseudo-non-diffracting (P-N) beam. Based on the non-diffracting propagation of light, the geometrical parameters and physical properties of non-diffracting beams show promise for FSO communication [74].

b. Partially Coherent Transmitter Beam

If the spatial coherence of the transmitted beam can be controlled, the statistics of the received power can be improved in long-range FSO communications system. The long-term dropouts in the received power were reported in an experiment for a partially coherent transmitted beam propagated through a turbulent path [75]. A partially spatial coherent beam can decrease the scintillation index by ~50% and the mean intensity in the simulation by ~90% regardless of turbulence strength when compared to the intensity of a fully coherent source in turbulence. A model for partially coherent beam as a thin (complex) phase screen with Gaussian spectrum (Rytov theory applied) was presented [76]. A diffuser was used modeled as a thin random phase screen that indices a complex phase perturbation (i.e., both amplitude and phase) on the transmitted wave at the source. The model was applied to calculate the SNR and (BER in OOK modulation. The on-axis scintillation index is reduced due to partial coherence of the source. Partially coherent beams have greater divergence than coherent beams and the received power depends on the degree of coherence of the wave as well. More power is required for less coherent beams to sustain the same SNR as the perfectly coherent beams (of the same size and phase front radius of curvature). The partially coherent beam can improve the BER up to several order of magnitude over the distances under 1 km and values of C_n^2 of the order of 10^{-14} $m^{-2/3}$ (i.e., for Rytov variance $\sigma_1^2 < 1$).

Another interesting approach of a free-space, high-speed (Gbps) optical communication system based on spectral encoding of radiation from a broadband pulsed laser is presented [77]. Scintillations can be suppressed by orders of magnitude for distances more than 10 km using partially coherent laser beams, a relatively slow photosensor. The spectral coding of radiation from a light-emitting diode (LED) as gigabit rate solution was also considered of the "last mile" problem in FSO communication.

Gaussian-Schell model of partial coherence is a method to mitigate atmospheric turbulence by controlling the statistics of the source to reduce the intensity variance of the received signal while maintaining the SNR [78]. This is an alternate solution to conventional expensive AO to compensate for atmospheric turbulence.

c. Flat-Topped Beams

The flat-top beams are derived from the fundamental Gaussian beam by introducing an order of flatness and propagate with less spreading. A model based on flattened Gaussian beam was developed [79]. When propagating through atmospheric turbulence, the flat-top beam first forms a circular ring in the center. With increasing propagation length, the circumference of this ring becomes narrower, giving rise to a downward peal emerging from the center of the beam, eventually turning the intensity profile into a pure Gaussian shape. Also when the source beam is made highly asymmetric, the conversion of receiver intensity profile into an airy function becomes more visible. The flatter beams will thus be subjected to less spreading during propagation in turbulence. With rising flatness order, less power is captured for a fixed receiver aperture radius.

d. Modified Bessel-Gaussian beams

The numerical calculations for the scintillation index for the higher than zero order modified Bessel-Gaussian beams propagating in weakly turbulent media are shown to be less than the Gaussian beams at large input beam sizes and the low beam orders with the increasing width parameter initially contributing positively to less scintillation [80]. The lowest scintillation at small input beam sizes is obtained for the modified Bessel-Gaussian beam of order zero, and with propagation length continues to offer less scintillation than those of order zero. In some FSO scenario, the modified Bessel-Gaussian beams can be used to mitigate the atmospheric turbulence by providing less scintillation effects.

3. *Advanced Real-time Signal Processing*

In order to correct the signal degradation due to atmospheric turbulence, advanced real-time signal processing can be used. Wavelet-based signal processing scheme to reduce beam-wandering-related variance has been demonstrated to reduce BER by a factor of 138 compared to the original signal in an experiment with free space optical link [81]. Wavelets transforms (WT) convert a signal into a series of orthonormal base functions known as wavelets and provide a way to analyze waveforms that are bounded in both frequency and time domains. WT allow signals to be represented more accurately compared to conventional Fourier transform method. In order to utilize wavelet-based signal processing for compensating turbulence-induced effects, the optimization of the level of approximation is needed. The optimum level N_{opt} of approximation required for mitigating turbulence effects depend on the sampling rate of the received signal. For "n" samples per bit interval at the receiver, an approximation is needed such that optimum compensating level N_{opt} is satisfied $2^{N_{opt}-2} \le n \le 2^{N_{opt}-1}$. At least one sample is needed for evaluating the atmospheric gain offered for that bit interval. Data at 10 samples/bit are sampled and optimum compensation of the turbulent effects is demonstrated with level 5 approximation [81]. Daubechies wavelet analysis is used for calculating the approximation at level N_{opt}. Fluctuations due to scintillations arising from multiplicative noise can be reduced by dividing the received signal by this approximation component, and the compensated signal with relatively low multiplicative noise can be obtained [81]. This technique showed the reduction of average BER of 8.9×10^{-3} for original data to 6.43×10^{-5} for compensated data, thus improving the FSO system performance.

An adaptive Kalman filter can be sued to mitigate the turbulence-induced scintillation noise in the received signal by predicting the value of received signal and turbulence statistics. The method based on the Kalman filter provides adaptive decision threshold for detection which can reduce detection error and improve communication link performance. Kalman filter is an effective tool to mitigate turbulence for FSO systems. The results show the error between optimum decision threshold and adaptive decision threshold is smaller than 0.48% [82].

Another signal-processing technique for mitigating multi-scattering channel such as heavy rain, snow, heavy fog, hail, haze, etc. is described using Fuzzy logic

concept. A train of optical pulses is transmitted and the coherent detection scheme is used in the receiver. The receiver is adapted based on the received power and SNR levels by changing the sensitivity using Fuzzy logic concept. The nonlinear noises incorporated in the received optical signal were cancelled up to −40 dB SNR level and up to −50 dBm of received power [83]. The BER achieved under heavy turbulence condition is in the order of 10^{-1} at −40 dB SNR level (which is about the same as near to the ground), whereas the BER was much improved after applying Fuzzy logic algorithm.

For some applications of Earth-based optical receivers operating in near-space and deep-space communication links, especially during the daytime are severely affected by both atmospheric turbulence and background noise looking directly toward the sky. A concept of a pre-processor for optical communication receivers employing 2-D adaptive Wiener-filter-based practical algorithms for mitigation of turbulence and background noise effects is presented [84]. Conceptual diagram of focal plane array and space time adaptive processor for an optical communication receiver which uses a 2D-adaptive Wiener filter in the pre-processor is presented. A transmitter was used in the analysis employing a *M-ary* PPM) technique and the digital data is decoded by the position of a pulse slot within a frame of *M*-possible slots. Simulation results show that 4–7 dB performance improvement under moderate to high background and turbulence conditions. Compared to the complex and expensive AO system, this approach is simple and cost-effective.

4. *Relay-assisted Technique*

Another powerful fading mitigation tool can be relay-assisted transmission through atmospheric turbulence. Both serial (i.e., multi-hop transmission) and parallel (i.e., cooperative diversity) relaying with amplify-and-forward and decode-and-forward modes are presented [85]. Turbulence-induced fading variance depends on propagation distance in a FSO system. Relay-assisted transmission can take advantage of the resulting shorter hops to improve significant performance. From the results of OP of FSO serial and parallel amplify-and-forward scheme, a performance improvement of 18.5 dB is reported using a single relay at a target OP of 10^{-6}.

5. *Atmospheric Clouds Mitigation*

Transmission of optical communications is severely affected by the presence of clouds along the line-of-sight of the communication link. To mitigate the effects of clouds and achieve reliable communications, a geographically diverse set of ground receiver stations is needed. A redundant site is desirable so that if one site is cloudy another can be used as backup. Atmospheric fades exceeding 10 dB can occur due to clouds which are composed of liquid water and/or ice crystals and have various thicknesses. Cloud fades for a thin, ice-crystal-based cirrus clouds can be as low as 1 or 2 dB where the impacts of FSO communication collectors may be limited. To predict the clouds impact on FSO communications, researchers have developed a high resolution cloud climatology based on National Oceanic and Atmospheric Administration (NOAA) Geostationary Environmental Operational Satellite (GOES) imager data. The imager includes multi-spectral channels, one visible and four IR,

at 44-km spectral resolution and 15-minute time resolution [86]. By objectively combining the cloud data from the individual channels, a composite cloud decision is formed from high spatial and temporal resolution climatology to derive accurate Cloud Free Line of Sight (CFLOS) statistics to derive the atmospheric effects on optical communication systems. The Lasercom Network Optimization Tool (LNOT) along with cloud database can be used to find configuration of geographically diverse ground sites to provide high availability FSO communication systems.

References

1. A.K. Majumdar, J.C. Ricklin, *Free-Space Laser Communications: Principles and Advances* (Springer, New York, 2008)
2. L.C. Andrews, R.L. Phillips, C.Y. Hopen, Aperture averaging of optical scintillations: Power fluctuations and temporal spectrum. Waves Random Media **10**, 53–70 (2000)
3. J.H. Churnside, Aperture averaging of optical scintillation in the turbulent atmosphere. Appl. Opt. **30**, 1982–1994 (1991)
4. L.C. Andrews, R.L. Phillips, *Laser Beam Propagation through Random Media* (SPIE, Bellingham, 1998)
5. V.I. Tatarski, *Wave Propagation in a Turbulent Medium* (McGraw-Hill, New York, 1961) (reprinted Dover, 1967)
6. J.C. Ricklin, F.M. Davidson, Atmospheric turbulence effects on a partially coherent Gaussian beam: implication for free-space laser communication. J. Opt. Soc. Am. A, **19**(9), 1794–1803 (2002)
7. J.C. Ricklin, S. Bucaille, F.M. Davidson, Performance loss factors for optical communication through clear air turbulence. Proc. SPIE, **5160**, 1–12 (2004)
8. H. Yukesl, S. Milner, C.C. Davis, Aperture averaging for optimizing receiver design and performance on free-space optical communication links. J. Opt. Netw. **4**, 462–475 (2005)
9. C.C. Davis, I.I. Smolyaninov, The effect of atmospheric turbulence on bit-error-rate in an on-off-keyed optical wireless system. Proc. SPIE **44489**, 126–137 (2002)
10. L.C. Andrews, R.L. Phillips, C.Y. Hopen, *Laser Beam Scintillation with Applications* (SPIE, Bellingham, 2001)
11. M.M. Ibrahim, A.M. Ibrahim, Performance analysis of optical receivers with space diversity reception. IEE Proc. Commun. **143**(6), 369–372 (1996)
12. D.K. Borah, A.C. Boucouvalas, C.C. Davis, S. Hranilovic, K. Yiannopoulos, A review of communication-oriented optical wireless systems. EURASIP J. Wirel. Commun. Netw. **91**, 1–28 (2012)
13. L.C. Andrews, R.L. Phillips, Impact of scintillation on laser communication systems: Recent advances in modeling. Proc. SPIE **4489**, 23–34 (2002)
14. K. Peppas, H.E. Nistazakis, V.D. Assimakopoulos, Performance analysis of SISO and MIMO FSO communication systems over turbulent channels. Chap. 17, Optical Communication (INTECH, 2012), pp. 415–438
15. E. Bayaki, R. Schober, R. Mallik, Performance analysis of MIMO free-space optical systems in gamma-gamma fading. IEEE Trans. Commun. **57**(11), 3415–3424 (2009)
16. T.A. Tsiftis, H.G. Sandalidis, G.K. Karagiannidis, M. Uysal, Optical wireless links with spatial diversity over strong atmospheric turbulence channels. IEEE Trans. Wirel. Commun. **8**(2), 951–957 (2009)
17. A.K. Majumdar, Free laser communication performance in the atmospheric channel. J. Opt. Fiber Commun. Rep. **2**, 345–396 (2005)

18. A.P. Prudnikov, Y.A. Brychkov, O.I. Marichev, *Integrals and Series Volume 3: More Special Functions*, 1st edn. (Gordon and Breach Science Publishers, New York, 1986)
19. N. Chtazidiamantis, G. Karagiannidis, On the distribution of the sum of gamma-gamma variates and applications in RF and optical wireless communications. IEEE. Trans. Commun. **59**(5), 1298–1308 (2011)
20. S.M. Navidpour, M. Uysal, M. Kavehrad, BER performance of free-space optical transmission with spatial diversity. IEEE Trans. Wirel. Commun. **6**(8), 2813–2819 (2007)
21. M.D. Yacoub, The α–μ distribution: A physical fading model for the Stacy distribution. IEEE Trans. Veh. Technol. **56**(1), 27–34 (2007)
22. I. Gradshteyn, I.M. Ryzhik, *Tables of Integrals, Series, and Products,* 6th edn. (Academic, New York, 2000)
23 I.I. Kim, H. Hakakha, P. Adhikari, E. Korevaar, A.K. Majumdar, Scintillation reduction using multiple transmitters. SPIE. Proc. **2990**, 102–113 (1997)
24. M. Jeganathan, K.E. Wilson, J.R. Lesh, Preliminary analysis of fluctuations in the received Uplink-Beacon-Power data obtained from the GOLD experiments. JPL's TDA Progress Report 42–124, (1996), pp. 20–32
25. M. Abramovitz, I.A. Stegun, *Handbook of Mathematical Functions with Formula, Graphs, and Mathematical Tables*, 9th edn. (Dover, New York, 1972)
26. A.K. Majumdar, G.H. Fortescue, Wide beam atmospheric optical communication for aircraft application using semiconductor diodes. Appl. Opt. **22**(16), 2495–2504 (1983)
27. X. Zhu, J.M. Kahn, in *Free-Space Laser Communications: Principles and Advances*, ed. by A.K. Majumdar, J.C. Ricklin. Communication techniques and coding for atmospheric turbulence channels (Springer, New York, 2008), pp. 303–345
28. S. Trisno, I.I. Smolyanionov, S.D. Milner, C.C. Davis, Characterization of time delayed diversity to mitigate fading in atmospheric turbulence channels. Proc. SPIE. **5892, 589215–1 –589215–10** (2005)
29. S.M. Haas, J.H. Shapiro, IEEE J. Select. Areas Commun. **21**, 1346 (2003)
30. J. Chen, Y. Ai, Y. Tan, Improved free space optical communications performance by using time diversity. Chi. Opt. Lett. **6**(11), 797–799, (2008)
31. X. Zhu, J.M. Kahn, Free-space optical communication through atmospheric turbulence channels. Trans. Commun. **50**(8), 1293–1300 (2002)
32. X. Zhu, J.M. Kahn, J. Wang, Mitigation of turbulence-induced scintillation noise in free-space optical links using temporal-domain detection techniques. IEEE. Photon. Technol. Lett. **15**(4), 623–625 (2003)
33. X. Zhu, J.M. Kahn, Pilot-symbol assisted modulation for correlated turbulent free-space optical channels. Proc. SPIE. **4489**, 138–145 (2002)
34. C.E. Shannon, A mathematical theory of communication. Bell Syst. Tech. J. **27**, 379–423 (1948a)
35. C.E. Shannon, A mathematical theory of communication. Bell Syst. Tech. J. **27**, 623–656 (1948b)
36. I. Djordjevic, W. Ryan, B. Vasic, *Coding for Optical Channels* (Springer, New York, 2010)
37. S. Haykin, *Communication Systems* (Wiley, New York, 2004)
38. J.B. Anderson, S. Mohan, *Source and Channel Coding: An Algorithmic Approach* (Kluwer Academic, Boston, 1991)
39. F.J. MacWilliams, N.J.A. Sloane, *The Theory of Error-Correcting Codes* (North Holland, Amsterdam, 1977)
40. S.B. Wicker, *Error Control Systems for Digital Communication and Storage* (Prentice Hall Inc., Upper Saddle River, 1995)
41. R. Gallager, Low-density parity-check codes. IRE. Trans., 21 (1962)
42. T. Richardson, M. Shokrollahi, R. Urbanke, Design of capacity-approaching irregular low-density parity-check codes. IEEE. Trans. Inform. Theory **47**, 638–656 (2001)
43. B.M.J. Leiner, LDPC Codes- a brief Tutorial (April 8, 2005)
44. D.J.C MacKay, *Information Theory, Inference, and Learning Algorithms* (Cambridge University Press, Cambridge, 2003)

45. G.A. Malema, Low-density parity-check codes : Construction and implementation, PhD Thesis, The University of Adelaide, Australia, November 2007
46. M. O'Sullivan, Algebraic construction of sparse matrices with large girth. IEEE Trans. Inform. Theory **52**(2), 719–727 (2006)
47. Z. Zhao, R. Liao, S.D. Lyke, M.C. Roggemann, Reed-Solomon Coding for free-space optical communications through turbulent atmosphere. IEEEAC Paper #1273, 978-1-4244-3888-410, 2010
48. N.A. Mohammed, M.R. Abaza, M.H. Aly, Improved performance of M-ary PPM in different free-space optical channels due to Reed-Solomon code using APD. Int. J. Sci. Eng. Res. **2**(4), 1– 4, (2011)
49. K. Kiasaleh, Performance of APD-based, PPM free-space optical communication systems in the atmospheric turbulence. IEEE Trans. Commun. **53**, 1455–1461 (2005)
50. J. Singh, V.K. Jain, Performance analysis of BPPM and M-ary PPM optical communication system in atmospheric turbulence. IETE Tech. Rev. **25**(4), 145–152 (2008)
51. J.G. Proakis, *Digital Communications* (McGraw-Hill, New York, 1983)
52. F. Xu, A. Khalight, P. Causse, S. Bouennane, Channel coding and time-diversity for optical wireless links. Opt. Express **17**(2), 872–887 (2009)
53. J.A. Anguita, I.B. Djorjevic, M.A. Neifeld, B.V. Vasic, Shannon capacities and error-correcting codes for optical atmospheric turbulent channels. J. Opt. Netwo. **4**(9), 586–601 (2005)
54. I.B. Djordjevic, LDPC-Coded optical communication over the atmospheric turbulence channel. 978-1-4244-2110=7/08 IEEE, 2007
55. I.B. Djordjevic, G.T. Djordjevic, On the communication over strong atmospheric turbulence channels by adaptive modulation and coding. Opt. Express **17**(20), 18250–18262 (2009)
56. I.B. Djordjevic, Adaptive modulation and coding for free-space optical channels. J. Opt. Commun. Netw. **2**(5), 221–229 (2010)
57. I.B. Djordjevic, in *Coded modulation techniques for optical wireless channels*, Advanced optical wireless communication systems, Chap. 2 (Cambridge University Press, Cambridge, 2012)
58. I.B. Djordjevic, W. Ryan, B. Vasic, *Coding for Optical Channels* (Springer, New York, 2010)
59. I.B. Djordjevic, B. Vasic, M.A. Neifeld, LDPC coded OFDM over the atmospheric turbulence channel. Opt. Express **15**(10), 6336–6350 (2007)
60. R.J. Noll, Zernike polynomials and atmospheric turbulence. J. Opt. Soc. Am. **66**(3), 207–211 (1976)
61. R.K. Tyson, D.E. Canning, Indirect measurement of a laser communications bit-error-reduction with low-order adaptive optics. App. Opt. **42**(21), 4239–4243 (2003)
62. R.J. Sasiela, Wave-front correction by one or more synthetic beacons. J. Opt. Soc. Am. **A 11**, 379–393 (1994)
63. T. Weyrauch, M.A. Vorontsov, in *Free-space laser communications: Principles and advances*, ed. by A.K. Majumdar, J.C. Ricklin. Free-space laser communications with adaptive-optics: Atmospheric compensation experiments (Springer, New York, 2008), pp. 247–271
64. M.W. Wright, M. Srinivasan, K. Wilson, Improved optical communications performance using adaptive optics with an avalanche photodiode detector. JPL IPN Progress Report, 42–161, May 2005
65. M.W. Wright, J. Roberts, W. Farr, K. Wilson, Improved optical communications performance combining adaptive optics and pulse position modulation. Opt. Eng. **47**(1), 016003–1 –016003–8, (2008)
66. R.K. Tyson, D.E. Canning, J.S. Tharp, Measurement of the bit-error rate of an adaptive optics, free-space laser communications system, Part 1: Tip-tilt configuration, diagnostics, and closed-loop results. Opt. Eng. **44**(9), 096002 (2005)
67. R.K. Tyson, J.S. Tharp, D.E. Canning, Measurement of the bit-error rate of an adaptive optics, free-space laser communications system, part 2: Multichannel configuration, aberration characterization, and closed-loop results. Opt. Eng. **44**(9), 096003 (2005)

68. W. Yunyun, C. Erhu, Z. Yu, Y. Hongwei, L. Min, L. Xinyang, X. Zhun, C. Jin, A. Yong, Z. Heng, Y. Zhi, Simulation and experiment of adaptive optics in 2.5 Gbps atmospheric laser communication. Am. J. Eng. Technol. Res. **11**(12), 3399–3403, (2011)
69. J.C. Juarez, D.M. Brown, D.W. Young, Strehl ratio simulation results under strong turbulence conditions for actively compensated free-space optical communication systems. Proc. SPIE **8732**, 873207 (2013)
70. A.J. Kshatriya, Y.B. Acharya, A.K. Aggarwal, A.K. Majumdar, Performance of free space optical link using wavelength and spatial diversity in atmospheric turbulence. Proceedings of National Conference on Emerging Areas of Photonics and Electronics, EAPE 2013 (to be published)
71. D. Giggenbach, B.L. Wilkerson, H. Henniger, N. Perlot, Wavelength-diversity transmission for fading mitigation in the atmospheric optical communications channel. Proc. SPIE **6304** 63041H–1–63041H–12, (2006)
72. A. Harris, J.J. Sluss Jr., H.H. Refai, Free-space optical wavelength diversity scheme for fog mitigation in a ground-to-unmanned-aerial-vehicle communications link. Opt. Eng. **45**(8), 086001 (2006)
73. J.E. Davies, B.D. Nener, K.J. Grant, K.Corbett, B. Clare, Numerical experiments in atmospheric scintillation correlation for applications in dual channel optical communications. Proc. SPIE **5793**, doi:10.1117/12.604750, (2005)
74. V. Kollarova, T. Medrik, R. Celechovsky, Z. Bouchal, O. Wilfert, Z. Kolka, Application of non-diffracting beams to wireless optical communications. Proc. SPIE **6736**, 67361C, (2007)
75. K. Drexler, M. Roggermann, D. Voelz, Use of partially coherent transmitter beam to improve the statistics of received power in a free-space optical communication system: Theory and experimental results. Opt. Eng. **50**, 025002 (2011)
76. O. Korotkova, L.C. Andrews, R.L. Phillips, Model for a partially coherent Gaussian beam in atmospheric turbulence with application in lasercom. Opt. Eng. **43**(2) 330–341 (2004)
77. G.P. Berman, A.R. Bishop, B.M. Chernbrod, D.C. Nguyen, V.N. Gorchakov, Suppression of intensity fluctuations in free space high-speed optical communication based on spectral encoding of a partially coherent beam. Opt. Commun. **280**, 247–270 (2007)
78. K.R. Drexler, Utilizing Gaussian-Schell model beams to mitigate atmospheric turbulence in free space optical communications. Dissertation for Doctor of Philosophy, Michigan Technological University, 2012
79. H.T. Eyyuboglu, C. Arpali, Y. Baykal, Flat topped beams and their characteristics. Opt. Exp. **14**(10), 4196–4207 (2006)
80. H. Tanyer, Y. Baykal, E. Sermutlu, O. Korotkova, Y. Cai, Scintillation index of modified Bessel-Gaussian beams propagating in turbulent media. JOSA A **26**(2), 387–394 (2009)
81. L.B. Pedireddi, B. Srinivasan, Characterization of atmospheric turbulence effects and their mitigation using wavelet-based signal processing. IEEE Trans. Commun. **58**(6), 1795–1802 (2010)
82. Chunyi Chen, Humin Yang, Huilin Jiang, Jingtao Fan, Cheng Han, and Ying Ding, Mitigation of turbulence-induced scintillation noise in free-space optical communication links using Kalman Filter. IEEE Congress on Image and Signal Processing, 2008, pp. 470–473
83. L.R.D. Suresh, S. Sundaravadivelu, Real time adaptive nonlinear noise cancellation using fuzzy logic for optical wireless communication system with multiscttering channel. Eng. Lett. 13:3, EL_13_3_8, 4 November 2006
84. A. Hashmi, A.A. Eftekhar, A. Adibi, F. Amoozegar, A novel 2-D adaptive wiener filter based algorithm for mitigation of atmospheric turbulence effects in deep-space optical communications. Proc. SPIE **7442**, 744202 (2009)
85. M. Safari, M. Uysal, Relay-assisted free-space optical communications. IEEE Trans. Wirel. Commun. **7**(12), 5441–5449 (2008)
86. R.J. Alliss, B. Felton, The mitigation of cloud impacts on free-space optical communications. Proc. SPIE **8380**, 83800S (2012)

Chapter 5
Non-Line-Of-Sight (NLOS) Ultraviolet And Indoor Free-Space Optical (FSO) Communications

Arun K. Majumdar

5.1 Introduction

This chapter presents a new concept for exploiting non-line-of-sight (NLOS) free-space optical (FSO) communication. NLOS configuration can be achieved using scattering as a vehicle for a viable link, or using multipath propagation as in an indoor optical communication link. The chapter discusses the promising enabling technology of ultraviolet (UV) NLOS optical wireless communication. The chapter describes a stochastic NLOS UV communication channel model using a Monte Carlo simulation method based on photon tracing starting with key system components. An overview of the state-of-the-art devices such as deep UV light-emitting diodes (LEDs) and solid state solar-blind deep UV avalanche photodiodes (APDs), solar blind photomultiplier tubes (PMTs), filters which are well-suited for NLOS UV FSO communication is given. Most recent experimental results with various modulation formats described in this chapter supports the potential promise of this technology for NLOS operation. Extending this enabling technology to design NLOS FSO-based distributed sensor network in multi-scattering channel is also discussed. The possibility of NLOS quantum communication using UV photons is also pointed out. This chapter introduces another related NLOS FSO link for indoor inter-device connectivity using near infrared light. Possible configurations for indoor optical wireless systems include: (i) directed beam infrared (DBIR), (ii) diffuse infrared (DFIR), and (iii) quasi-diffuse infrared (QDIR). Some of the discussions in this chapter include propagation modeling (with multipath response), different modulation techniques suitable for different configurations, multi-access techniques, and broadband communication links for multiple sensor networks. The impact of this new technology on future FSO links and various applications is addressed.

It is possible to establish short-range optical data connections without a direct line-of-sight (LOS). When UV light is used, this is strongly scattered by the molecules, aerosols, haze, fog, and other particulates in the atmosphere. Some of the transmitted light, which is scattered in the direction of the receiver will be detected and a communication channel will be established. Recent developments in the arena of semiconductor emitters and detectors operating in the UV solar blind region have

A. K. Majumdar, *Advanced Free Space Optics (FSO),*
Springer Series in Optical Sciences 186, DOI 10.1007/978-1-4939-0918-6_5,
© Springer Science+Business Media New York 2015

opened the door for efficient NLOS optical communication links. The UV NLOS technology takes advantage of atmospheric interactions with UV radiation to develop an outdoor FSO channel characterized by its ability to work around local area obstruction. The simplest communication topology is addressed first—a unidirectional half-duplex link from one transmitter to one receiver. The candidate applications for UV NLOS technology include exchanging information between electronics system that requires low power and robust local area communications links.

5.2 Ultraviolet Communications

The UV communication technology has a potential solution of establishing a link which is otherwise vulnerable to blockage because of no alternative paths or a LOS link is not practically feasible. The unique characteristics of UV waves and their interactions with practical environmental conditions can be exploited to design a NLOS FSO communication system [1]. In FSO communication system, radiation wavelengths that are highly absorbed by atmospheric particles are avoided in order to minimize beam attenuation and power requirement. Background radiation at the transmitted wavelength, particularly due to solar radiance during daytime operation, adds noise to the communication systems. This contaminates the desired signal. A narrow receiver field-of-view (FOV) is therefore needed to obtain the necessary signal to noise ratio (SNR). The spectrum of solar radiation reaching the ground is far from uniform and almost all the solar radiation in the spectral region around 200–280 nm is absorbed by ozone in the upper atmosphere. Thus, a FSO communication system transmitting at this wavelength region will encounter practically no background noise in this region, which is known as "solar-blind ultraviolet." A large FOV can be used to accept more signals without increasing the receiver background noise. Operating in this region will allow a ground-based photodetector to exploit the background radiation to approach quantum-limited photon-counting detection. Because of short wavelength of UV, high degree of relatively angle-independent scattering occurs (note that the scattering effect is proportional to the inverse forth power of the wavelength, $\propto \lambda^{-4}$) which create tremendous number of communication paths from a transmitter to a receiver. NLOS communication can thus be easily established relaxing the stringent pointing, acquisition, and tracking requirements at the receiver end. However, transmission range will still be restricted according to the transmission characteristics of the radiation in this region due to absorption by aerosols and molecules. Furthermore, due to high attenuation by the atmosphere, signal beyond the extinction range can be hardly intercepted which can be desirable for tactical applications. The NLOS communications in UV have many applications including data communication, surveillance sensor networks, unattended ground sensor networks, small unit communications in urban terrain environments, and between unmanned aerial vehicles (UAVs) and attended terminals.

Turbulence effects can degrade the FSO communication system performance at UV than at longer wavelengths. This is because of the fact that the turbulence-

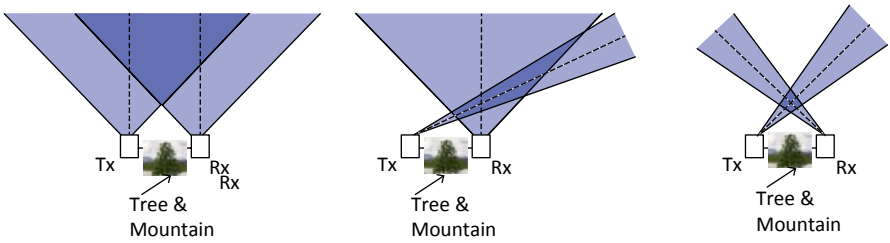

Fig. 5.1 An illustration of NLOS communication system configurations

induced log-amplitude variance of intensity fluctuations follow a −7/6 power relation variation with wavelength which means that the scintillation is higher at UV wavelengths than at longer wavelength. Depending on the transmission ranges, the effects of turbulence should be taken into account in the received SNR computation.

For eye and skin safety, which are major health-related concerns at UV, the International Commission on Non-Ionizing Radiation Protection (ICNIRP) and the International Electrotechnical Commission (IEC) enforce UV exposure power limits. The minimum allowable continuous exposure occurs at 270 nm at a level of as low as 3 mJ per cm^3 per second while increasing to 100 mJ at 200 nm and 3.4 mJ at 280 nm [2, 3].

5.3 NLOS FSO Communications Configurations and UV Source and Detector Technologies

Figure 5.1 illustrates, schematically, three typical system configurations. Case (a) requires minimum transmitter and receiver positioning in a fully NLOS mode, whereas case (b) requires medium bandwidth, and case (c) requires large bandwidth.

To design an effective UV communication transceiver that can operate under exposure to solar background radiation, UV optical source, solar-blind UV detectors with high sensitivity gain, and out-of-band rejection with a narrow band optical filters are essential. Semiconductor-based UV optical source technologies offer a potential for low cost, small size, low power, high reliability, and high bandwidth sources. State-of-the-art commercially available deep UV LEDs have been recently available at peak wavelengths 247 ~ 365 nm and with a spectral width of less than 20 nm. A single UV LED typically consumes 150 mW of electrical power emitting an average optical power of 1 mW. For detectors, PMTs and APDs are available from Hamamatsu and PerkinElmer for PMTs as off-the-shelf commercial products exhibiting high multiplication gains of $10^5 \sim 10^7$, high responsitivity of 62 A/W, large detectors area of few cm^2, reasonable quantum efficiency of $\eta = 15\%$, low dark count rate of few hertz, and low dark current of 0.1 nA/cm^2 [4]. Using a narrowband solar-blind filter, because of its enhanced out-of-band rejection ratio of

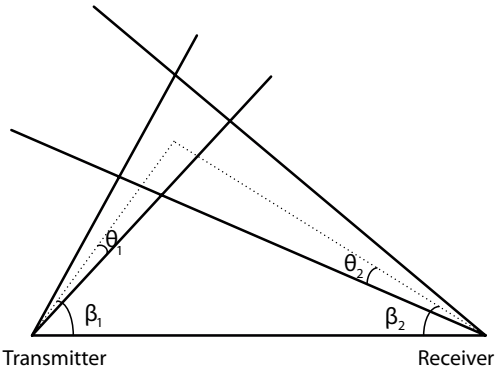

Fig. 5.2 Geometry of a NLOS FSO communication system (*Reprinted with permission from SPIE, 2008 [6]*). *NLOS* non-line-of-sight, *FSO* free-space optical

about 10^8, this type of PMT can detect very weak signal even in presence of background radiation, down to single-photon-counting resolution [4]. Deep UV solar-blind APD which is based on GaN, APD can have a responsivity of 0.15 A/W, gain of 10^4, and dark current of 100 nA/cm^2. Based on SiC, other type of APD can have a gain of 10^3, dark current of 64 nA/cm^2, quantum efficiency of 45 %, and single photon sensitivity. Some other recent deep UV APDs are being researched to demonstrate APD arrays operating in the UV band centered at 280 nm, with effective Geiger mode gain of 10^6, an effective aperture up to 1 cm^{2,} wide FOV up to 60 degrees, dark count rate below 10 kHz, and a solar rejection ratio exceeding 10^6 [4].

5.3.1 NLOS UV Scattering Channel Model

To design a UV NLOS communication system, the scattering channel needs to be characterized. According to the classical Mie scattering theory, the single-scattering and the multiple-scattering atmospheric channel can be built. Generally speaking, if the photon's path length is short, the single-scattering is suitable; if the path length is long, the multiple-scattering model should be used.

Analytical and Parametric Single-scattering Models The single-scattering model for a NLOS configuration [5] is applicable to a short-range communication channel. This model assumes that the UV is scattered by the particle only once. The geometry of a NLOS system with transmitter and receiver arrangement is shown in Fig. 5.2. To describe the single-scattering model, a prolate spheroidal coordinate system as shown in Fig. 5.3 is used. A point in space is defined by three coordinates: a radial coordinate ξ, an angular coordinate η, and an azimuthal coordinate Φ. The sum of the distances between the foci and any point on a given surface ξ is a constant. Let us define the parameters as follows:

Ω_t= solid angle of the transmitter (*Tx*) cone
R = separation between transmitter (Tx) and receiver (Rx)
r_1, r_2 = distances of the common volume to the Tx and Rx, respectively

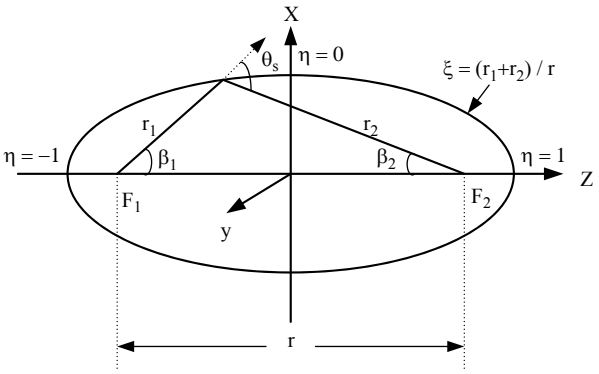

Fig. 5.3 A prolate spheroidal coordinate system geometry to describe the single-scattering model. (*Reprinted with permission from SPIE, 2008 [6]*)

θ_1, θ_2 = Tx half transmitting beam angle and receiver half FOV, respectively
β_1, β_2 = Tx and Rx focal angles between each axis and the horizontal axis
k_e, k_s, k_a = extinction coefficient, scattering coefficient, and absorption coefficient of the medium, respectively so that $k_e = k_s + k_a$
θ_s = scattering angle
A_r = area of receiving area
$p(\theta)$ = single-scattering phase function

If an impulse of energy Q_t emitted at time $t=0$ over the transmitter cone angle into a homogeneous scattering and absorbing medium, the received single scattered power at a later time t can be written as [6, 7]:

$$h(t) = \frac{Q_t A_r T_{of} c k_s \exp(-k_e ct)}{2\pi \Omega_t r^2} \mathrm{X} \int_{\eta_1(\frac{ct}{r})}^{\eta_2(\frac{ct}{r})} \frac{2G\left[\Phi\left(\frac{ct}{r}, \eta\right)\right] p(\theta_s)}{\left(\frac{ct}{r}\right)^2 - \eta^2} d\eta \tag{5.1}$$

where $h(t)$ is the impulse response of the scattering channel, $Q_t = 4\pi \sin^2\left(\frac{\theta_t}{2}\right)$ is transmitter solid cone angle, c is the velocity of light, T_{of} is transmissivity of the optical filter, $\eta_1\left(\frac{ct}{r}\right), \eta_2\left(\frac{ct}{r}\right), G\left[\Phi\left(\frac{ct}{r}, \eta\right)\right]$ are all related to the boundary of integration over the scattering volume that depends on the geometry of optical scattering channel. The function $G[.]$ is defined in the reference [5]. The received energy by a detector can be found by integrating the Eq. (5.1) over time limits, and the path loss is obtained from the ratio of received energy to the emitted energy. The total energy received at the receiver can be calculated by:

$$E_r = \int_{t_{min}}^{t_{max}} h(t) dt \tag{5.2}$$

with the limits for integration for time.

For parametric modeling, the gamma function and its modified version are selected as the matching function for the impulse response. Following the procedure [8], the two fitting models are given by [6]:

$$h_g(t) = \lambda \frac{\beta^{-\alpha}}{\Gamma(\alpha)} t^{\alpha-1} e^{-t/\beta} \tag{5.3}$$

$$h_{gl}(t) = \lambda \frac{\beta^{-\alpha}}{\Gamma(\alpha)} t^{\alpha-1} e^{-t/\beta} \sum\nolimits_0^N c_n L_n(t), L_n(t) = \frac{e^t}{n!} \frac{d^n}{dt^n}(e^{-t} t^n) \tag{5.4}$$

where $\Gamma(\alpha)$ is a gamma function, $L_n(t)$ is the *n*-order Laguerre polynomial, λ and c_n are scalar components. The two parametric models are applied to fit the theoretical impulse response function, *h(t)*.

Multiple Scattering Model A multiple scattering model using a Monte Carlo simulation method based on photon tracing is presented in terms of impulse response, path loss, and bandwidth [9]. Multiple scattering interactions of photons with the atmospheric constituents result in pulse broadening, i.e., increased channel delay spread. This limits the channel bandwidth available for communications. When multiple scattering effects are taken into account, accurate prediction of path loss is possible. It has been shown that the path loss is reduced when multiple scattering is accounted for. To evaluate NLOS UV FSO communications system performance, it is therefore crucial to include the multiple scattering effects for a longer propagation path in order to determine the maximum communication range attainable under the specific channel condition. Both the Rayleigh and Mie scattering are taken into account. The Monte Carlo simulation model is applied to track the photon's movement with the right probability model and random parameter. A large number of source photons are generated according to the source intensity distribution. The migration path for each photon is determined recursively by employing a random model and each step involves finding a scattering direction and step size from the current photon location. Only the photons within the geometric boundary defined by the system optics are considered. If the survival probability of the photon becomes too small or the photon moves out of the confined space so that it does not reach the field of view of the receiver, the recursion is terminated. Only the traversed path length contributes to the propagation delay. Repeating this process for many photons, and their aggregated arrival probabilities, all of which are function of time can then determine the expected received signal intensity, corresponding to the channel impulse response, i.e., multiple scattering *h(t)*. The inverse of the impulse response provides the information regarding the achievable bandwidth of the NLOS communication system. For a given communication range, elevation angles, transmitter bandwidth, and receiver FOV, the temporal impulse response for a multiply scattered channel can be used to design the communication system accurately.

An emitted source photon moves a distance Δs to a new location where it may be either scattered or absorbed with a certain probability. With an initial survival probability, each photon repetitively migrates until it either reaches the receiver

or creates a pulse, or die because of stop condition when its survival probability is smaller than a threshold. When applied to a large number of photons, only the surviving photons reaching the receiver will generate an average pulse (received intensity). The probability that the photon arrives at the receiver within its FOV after n scattering steps is given by [9]:

$$p_{1n} = \int_{\Omega n} P(cos\theta)\delta\Omega \tag{5.5}$$

where Ω_n is the solid angle along the scattered direction that can be seen by the receiver aperture of area S_r and $P(.)$ is the scattering phase function. The complementary probability $(1 - p_{1n})$ is therefore is the probability that the photon is out of the receiver's FOV. Next, the energy loss modeling of the photon is considered. If r_{n-1} is the $(n\text{-}1)$-th scatter center location, then the photon changes to the next n-th scatter center location r_n. The propagation distance $|r_n - r_{n-1}|$ is given by the random variable $\Delta s = -\dfrac{\ln \xi^{(s)}}{k_s}$ ($\xi^{(s)}$ is a uniform random variable between zero and one, and k_s is the total scattering coefficient arising from both Rayleigh and Mie scattering). Because of the channel absorption, the photon suffers an energy loss of $e^{-k_a|r_n - r_{n-1}|}$ *where* k_a is the absorption coefficient of the medium. When the photon is at the n-th scattering center, the photon's survival probability is reduced due to this energy loss and is updated as [9]:

$$w_n = (1 - p_{1n})e^{-k_a|r_n - r_{n-1}|}w_{n-1} \tag{5.6}$$

The probability that the photon successfully arrives at the receiver is given by [9]:

$$P_n = w_n p_{1n} p_{2n} \tag{5.7}$$

where p_{2n} represents the propagation loss of the photon from the n-th scattering center to the receiver

$$p_{2n} = e^{-k_e|r_n - r'|} \tag{5.8}$$

r' is the location vector of the receiver, and k_e denotes the total path loss which includes both scattering and absorption. The channel impulse response now can be found from the photon migration path, and is given by d_n / c, *where* d_n is the accumulated propagation distance, and c is the speed of light. If a photon undergoes N scattering interactions, then there are a set of probabilities $(P_{1,..,}P_N)$ and a corresponding set of propagation times between each scatter. The probabilities are superimposed to display the average impulse response. The probabilities versus time then represent the channel response due to all photons. When normalized by the total energy of all photons, the impulse response to a transmitted pulse is obtained. The average path loss is obtained from the ratio of the transmitted photons energy to the received photons' energy which is an important parameter to evaluate the SNR

at the receiver and then to predict the bit error rate (BER) for a communication system. The total arrival probability of one photon represents the percentage of photon energy that can be detected by the receiver

$$P = \sum_{n=1}^{N} P_n = \sum_{n=1}^{N} w_n p_{1n} p_{2n} \tag{5.9}$$

The path loss can be writen as $1/P$.

Turbulence Modeling for NLOS UV Scattering Channels In all of the discussions, the effect of turbulence in the scattering model is not included. When the communication range increases, the effect of turbulence becomes pronounced and inevitably indices additional impairments to system performance. Results are presented for average <SNR> and BER for a turbulence channel with a log-normal probability density function for NLOS UV scattering channel. The interested reader is referred to the reference [10] for a detail description.

5.3.2 Scattering-based NLOS Communication Performance Analysis

Received Optic Power and Noise Variances The NLOS optical scattering channel shown in Fig. 5.2 can be regarded as a linear and time-invariant system. Assume that a signal pulse is emitted at $t=0$ uniformly over the transmitter solid cone angle, and let $P_t(t)$ denote the power of the transmitted optical signal. The signal photons undergo the scattering and absorption through the medium, and some of them reach the receiver according to the scattering model described earlier. The received signal power can be expressed as

$$P_t = \int_{-\infty}^{\infty} P_t(\tau) h(t-\tau) d\tau \tag{5.10}$$

where *h(t)* is the impulse response of the channel given by Eq. (5.1) when the axes of the transmission and reception cone lie in a common plane. The received background radiation can be calculated as [11]

$$P_{bg} = H_{bg} A_r \Omega_r T_{of} B_{of} \tag{5.11}$$

where H_{bg} is the background spectral radiance, Ω_r is the FOV of the receiver, and B_{of} is the bandwidth of the optical filter.

The photocurrents for received optical pulse P_r at ON and OFF signals can be written as:

$$\text{ON: } I_1 = RG(P_r + P_{bg}) + I_{dc} \tag{5.12}$$

$$\text{OFF: } I_0 = RGP_{bg} + I_{dc} \tag{5.13}$$

where R is the cathode response of the PMT, G is the gain, and I_{dc} is the dark current. The shot-noise variance in the detector is [12]

$$\sigma_s^2 = 2qG^2FRP_rB \tag{5.14}$$

where q is the electron charge, F is the excess noise factor of the PMT, and B is the electrical bandwidth. The background noise variance is

$$\sigma_{bg}^2 = 2qG^2FRP_{bg}B \tag{5.15}$$

The dark current noise variance is given by

$$\sigma_{dc}^2 = 2qI_{dc}B \tag{5.16}$$

Also, the thermal noise variance can be written as

$$\sigma_{th}^2 = \frac{4K_bT_0F_iB}{R_L} \tag{5.17}$$

where K_b is the Boltzmann's constant, T_0 is the absolute temperature, F_i is the noise figure, and R_L is the load resistance. The total variance for receiving an optical signal pulse is given by

$$\sigma_1^2 = \sigma_s^2 + \sigma_{bg}^2 + \sigma_{dc}^2 + \sigma_{th}^2 \tag{5.18}$$

The total variance of current fluctuations without any pulse is given by

$$\sigma_0^2 = \sigma_{bg}^2 + \sigma_{dc}^2 + \sigma_{th}^2 \tag{5.19}$$

BER of the System Both on-off keying (OOK) and pulse position modulation (PPM) schemes are considered to predict the BER of the system.

The BER of an OOK system with a matched filter and using an optimal threshold can be calculated as [12]:

$$BER_{OOK} = \frac{1}{2}\operatorname{erfc}\left(\frac{1}{\sqrt{2}}\frac{RGP_r}{\left(\left[qG^2FR\left(P_r+P_{bg}\right)R_b + qI_{dc}R_b + \frac{2K_bT_0F_iR_b}{R_L}\right]^{\frac{1}{2}} + \left[q\left(G^2FRP_{bg}+I_{dc}\right)R_b + \frac{2K_bT_0F_iR_b}{R_L}\right]^{\frac{1}{2}}\right)}\right) \tag{5.20}$$

where *erfc* is the complementary error function and R_b is the bit rate, $R_b = 1/T_b$ *and* T_b is the bit duration. The pulse shape can be chosen to be rectangular for simplicity.

For PPM, an input word consisting of several bits is represented by the position of the pulse within a frame with frame duration T_f. The frame is divided into *L* slots with duration T_s and only one of these slots contains an optical pulse. The bit rate for *L*-PPM is, $R_b = \log_2 L / T_f$. Maximum likelihood PPM demodulator is used to assign the pulse position in each frame to the highest-energy filter output.

The BER of a PPM modulation system for Gaussian noise is given by [12]:

$$BER_{PPM} = \frac{L}{4}\operatorname{erfc}\left(\sqrt{\frac{\log_2 L}{2L}}\frac{RGP_r}{\left(\left[qG^2FR\left(P_r + 2P_{bg}\right)R_b + 2qI_{dc}R_b + \frac{4K_bT_0F_iR_b}{R_L}\right]^{\frac{1}{2}}\right)}\right) \tag{5.21}$$

BER for NLOS Scattering Communication in Presence of Turbulence NLOS UV scintillation model is used to predict the BER in presence of atmospheric turbulence. The SNR at the receiver depends on signal variance and path loss due to scattering medium as well as due to atmospheric turbulence. This fact has been mentioned earlier in the section. For NLOS UV geometry in Fig. 5.1, if atmospheric turbulence is also a contributing factor in the received signal, we can assume that the *Tx* beam is small enough so that the common volume can be analytically approximated, and scintillation among the common volume is constant. Adding the atmospheric turbulence, the arrival power at common volume has a log-normal probability density/distribution function (PDF) given by

$$f_x(x) = \frac{1}{x\sigma_x\sqrt{2\pi}}\exp\left(-\frac{\left(\frac{lnx}{E[x]} + \frac{1}{2}\sigma_x^2\right)^2}{2\sigma_x^2}\right) \tag{5.22}$$

where *x* represents the power level in the common volume, σ_x^2 is the scintillation index. The conditional arrival power level (*y*) at the *Rx* is given by [10]:

$$f_y(y\,|\,x) = \frac{1}{y\sigma_y\sqrt{2\pi}}\exp\left(-\frac{\left(\frac{\ln y}{E[y\,|\,x]} + \frac{1}{2}\sigma_y^2\right)^2}{2\sigma_y^2}\right) \tag{5.23}$$

where $E[y\,|\,x] = x \cdot \frac{A_r e^{-k_s r_2}}{r_2^2}$ for a fixed NLOS geometry, A_r is the area of the receiver, and σ_y^2 is the scintillation index. The joint PDF of *x* and *y* can be derived from the relation

$$f_{x,y}(x,y) = f_y(y\,|\,x) f_x(x) \tag{5.24}$$

so that we can represent the PDF of y as

$$f_y(y) = \int f_{x,y}(x,y)dx \tag{5.25}$$

The received signal at the receiver *Rx* has a noise contribution due to turbulence effects from the common volume. The BER for a NLOS UV system depends on several parameters, including modulation format, detector type, transmitter power, path loss, scintillation data rate, and noise. We assume OOK modulation scheme and direct detection to analyze BER performance of the NLOS UV system in atmospheric turbulence conditions. The average SNR is given by [13]:

$$\left\langle SNR_{T,NLOS} \right\rangle = \frac{SNR_{0,NLOS}}{\sqrt{\left(\frac{P_{r0}}{< P_r >}\right) + \sigma_y^2 SNR_{0,NLOS}}} \tag{5.26}$$

where P_{r0} is the received power in the absence of turbulence, $\left\langle P_r \right\rangle$ is the mean received power with turbulence, and $SNR_{0,NLOS}$ is the SNR in a NLOS communication link considering no turbulence. We can assume $P_{r0} \cong \left\langle P_r \right\rangle$ and therefore

$SNR_{0,NLOS} = \sqrt{\frac{y_0}{\frac{2Rhc}{\lambda}}}$ *where* y_0, is the received power with no turbulence, R is the link data rate, h denotes the Planck constant, c is the speed of light, and λ is the wavelength. The BER in presence of atmospheric turbulence is given by [13]:

$$BER_{T,NLOS} = \frac{1}{2}\int_0^\infty f_y(y)\,\mathrm{erfc}\left(\frac{< SNR_{T,NLOS} > y}{2\sqrt{2}}\right)dy \tag{5.27}$$

where *erfc* is the complementary error function.

Some Results: Simulation and Experiment

Some of the simulation and experimental results for NLOS UV communications are discussed. Figure 5.4 shows the simulated impulse response under single and multiple scattering models using Monte Carlo method. Comparing the two models, the single scattering assumption shows reduced delay spread and intensity [9]. The numerical simulation results are based on a LED source operating at wavelength 260 nm, and the geometric and model simulation parameters are: $(\Phi_1, \Phi_2, \theta_1, \theta_2) = (17°, 30°, 90°, 90°)$, r = 100$m$, the model parameters λ, g, and f of the phase function for Rayleigh and Mie scattering which follow a generalized Rayleigh model and a generalized Henyey-Greenstein function (see reference [9]) are $\gamma = 0.017$, $g = 0.72$, $f = 0.5$, and the receiver area is 1.77 cm^2. The multiple scattering model shows both higher intensity and longer duration.

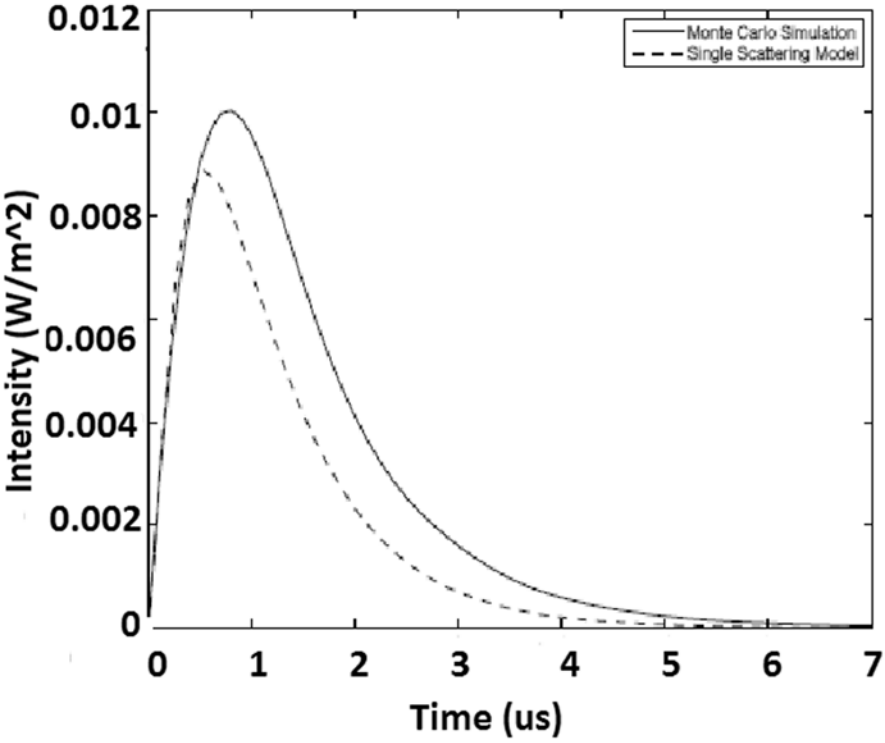

Fig. 5.4 Simulated impulse response under single and multiple-scattering models using Monte Carlo method. (*Reprinted with permission from IEEE, 2009* [9])

BER bit error rate, LED light-emitting diode Figure 5.5 shows measured and predicted BER where the prediction is based on the SNR and the Gaussian noise using a LED source with nominal center wavelength of 250 nm [4]. At SNR=10 dB, a BER of 10^{-2} is achievable, and with increased SNR to 15 dB, a BER below 10^{-4} is achievable. The impact of *Rx* elevation angles on BER is presented for fixed *Tx* elevation angles at $30°, 40°, 50°, 60°$ at a communication distance of 35 m. Figure 5.6 illustrates that the BER with *Tx* angle fixed at $30°$ can drop from from 10^{-1} to about 10^{-6} when the *Rx* angle decreases from $40°$ to $20°$.

There has been a study of BER performance for NLOS UV channel in atmospheric turbulence [10]. The turbulence NLOS UV link uses a data rate of R= 5 kbps, the angles $\theta_1 = \theta_2 = 30°$ and the strength of turbulence, $C_n^2 = 1e\text{-}14\text{m}^{-2/3}$. Figure 5.7 illustrates the BER versus baseline range and shows that the BER degrades greatly with increased LOS base baseline range, varying from 2.84×10^{-4} to 0.2466 when the baseline range changes from 100 meters to 1,000 meters. The effects of turbulence for NLOS UV communication link needs to be considered for longer propagation range. Calculations in reference [10] shows that the BER is very sensitive to the atmospheric turbulence structure parameter, for example, for atmosphere and geometry parameters $(\theta_1, \theta_2) = (30°, 30°)$, r = 100m, $C_n^2 = 1e\text{-}16\text{m}^{-2/3}$, the turbulence may influence little for the NLOS UV link.

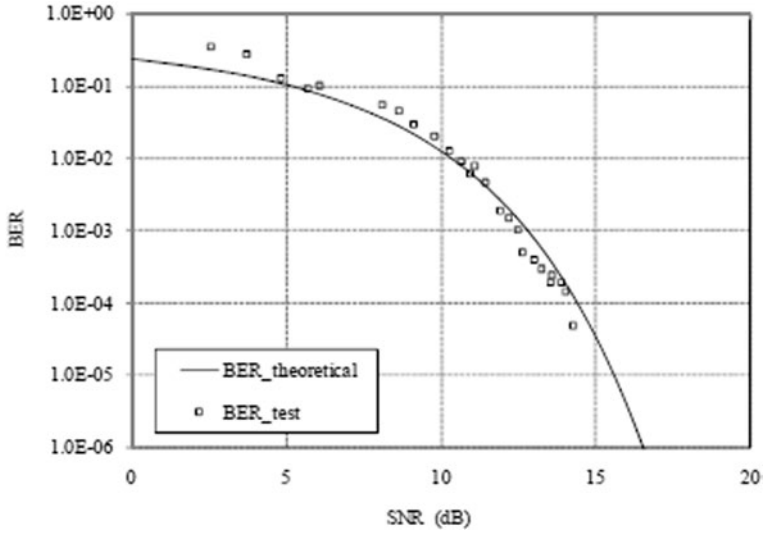

Fig. 5.5 Measured and predicted BER using LED source at 250 nm. (*Reprinted with permission from The Optical Society of America, OSA, 2008 [4])*

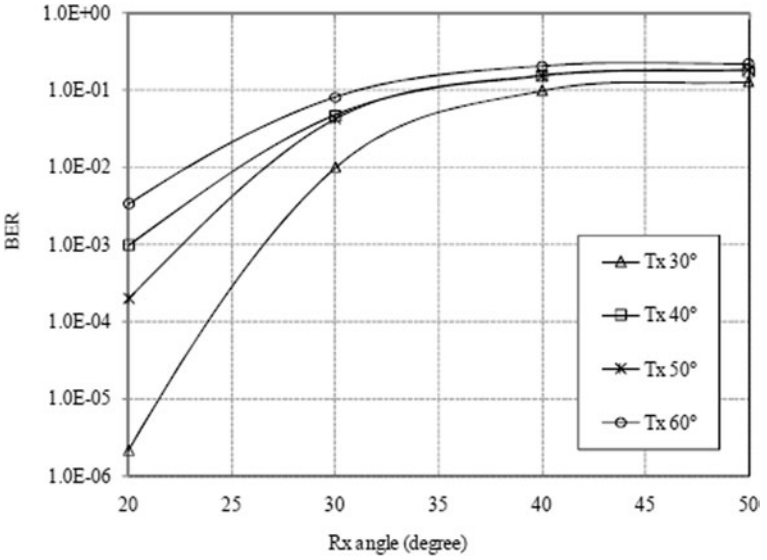

Fig. 5.6 BER verses *Rx* angle for fixed values of *Tx* angles (*Reprinted with permission from The Optical Society of America. OSA, 2008 [4]). BER* bit error rate

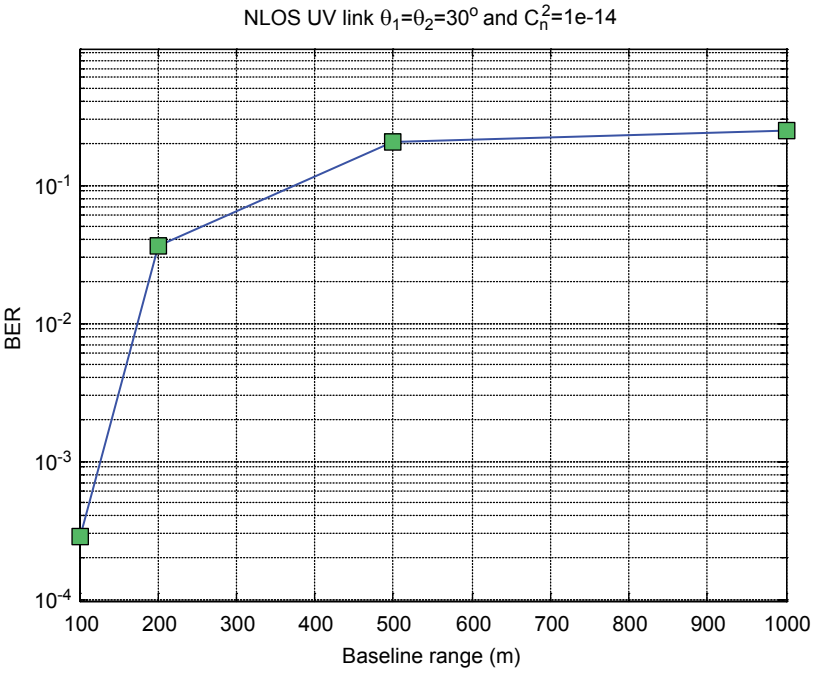

Fig. 5.7 BER verses baseline range in turbulence channel, $C_n^2 = 1e^{-14}\mathrm{m}^{-2/3}$ (*Reprinted with permission from SPIE, 2011 [10]) BER* bit error rate

5.4 Indoor FSO Communications

The design and performance factors of long-distance FSO communications systems apply equally to short-distance systems such as indoor optical communication but with one obvious exception: Atmospheric loss has no effect for all indoor systems. The communication power link budget is therefore determined almost entirely by the transmitter launch power, free space loss, and receiver sensitivity.

5.4.1 Short Distance Systems

Indoor point-to-point systems do not differ from the outdoor systems in their operating principles. But there are some practical issues in the designs of indoor point-to-point systems. They must be Class 1 eye safe such as an LED which generally limits the data rate capacity to a few Mbps. The indoor systems do not require any weather-proofing that outdoor systems require and only operate over short distances to be produced cost-effectively. Such systems could be used to extend a local area network (LAN) port to a different part of an office where no convenient port exists, or to link two separate offices via a link corridor.

Optical Telepoint systems utilize wide diverging beams rather than the narrow beams of point-to-point systems and have a number of attractive features. One important feature is for each "cell" created by an optical Telepoint base station can be shared by as many users as can be accommodated within the cell. Telepoint systems with large cells (diameter ~ 10 m or so) can be used for open offices and public areas such as libraries, waiting rooms, and hospital wards. LOS paths are required between the base station and all the user terminals for more than a few Mbps reliable data transfer. The smaller cell systems (~ 1 m or less) are suitable to applications where a cell is dedicated to a single user, for example, a desktop.

Diffuse systems use the beams as well as radiating over a wide angle are also reflected off surfaces and objects in the vicinity such as walls, ceiling, floor, and furniture in the room. The FOV in the base and user stations is widened to accept both the LOS as well as reflected light can be detected. However, the capacity or achievable transferring data rate is much reduced in a diffuse transmission compared with LOS systems. This is because of multiple signal paths reaching the receiver causing pulse spreading and intersymbol interference. The theoretical capacity of a diffuse system depends on many factors such as room size and geometry, the placements and orientation of the base and user stations, and the fabric and distribution of furnishings. Because of wide FOV of the receivers, interference from ambient light with communication signal limits the data transmission capacity of diffuse systems.

5.4.2 Indoor Link Configurations

Infrared transmission techniques may be classified as LOS or NLOS depending on whether they rely on the existence of a directed path between the transmitter and the receiver as well as the degree of directionality, i.e., source beam-angle and detector FOV. The two most common configurations are directed-LOS and non-directed NLOS systems. Non-directed NLOS systems are generally referred to as diffuse systems. Figures 5.8 (a) and (b) show some common indoor link configurations. In Fig. 5.8 (a), the transmitter (*Tx*) and the receiver (*Rx*) are in transmit-LOS mode so that the beam can travel from the transmitter to the receiver, without reflection. In Fig. 5.8 (b), there is no direct path and before reaching the receiver, the signal is reflected by the ceiling and walls. This configuration can be considered as NLOS, non-directed, and diffuse type. Figure 5.9 shows an example of NLOS and diffuse configuration where optical wireless FSO LAN can be established between various receiver devices which can leverage the existing imaging capabilities of devices. The directed-LOS links, in general, minimize path loss and maximize power efficiency, and they can achieve higher transmission rates. Since directed-LOS systems require careful aiming and are therefore not capable of supporting one-to-many and many-to-one connections. Non-directed NLOS (diffuse) systems have increased robustness against shadowing and allow higher user mobility, but at the expense of lower transmission rates.

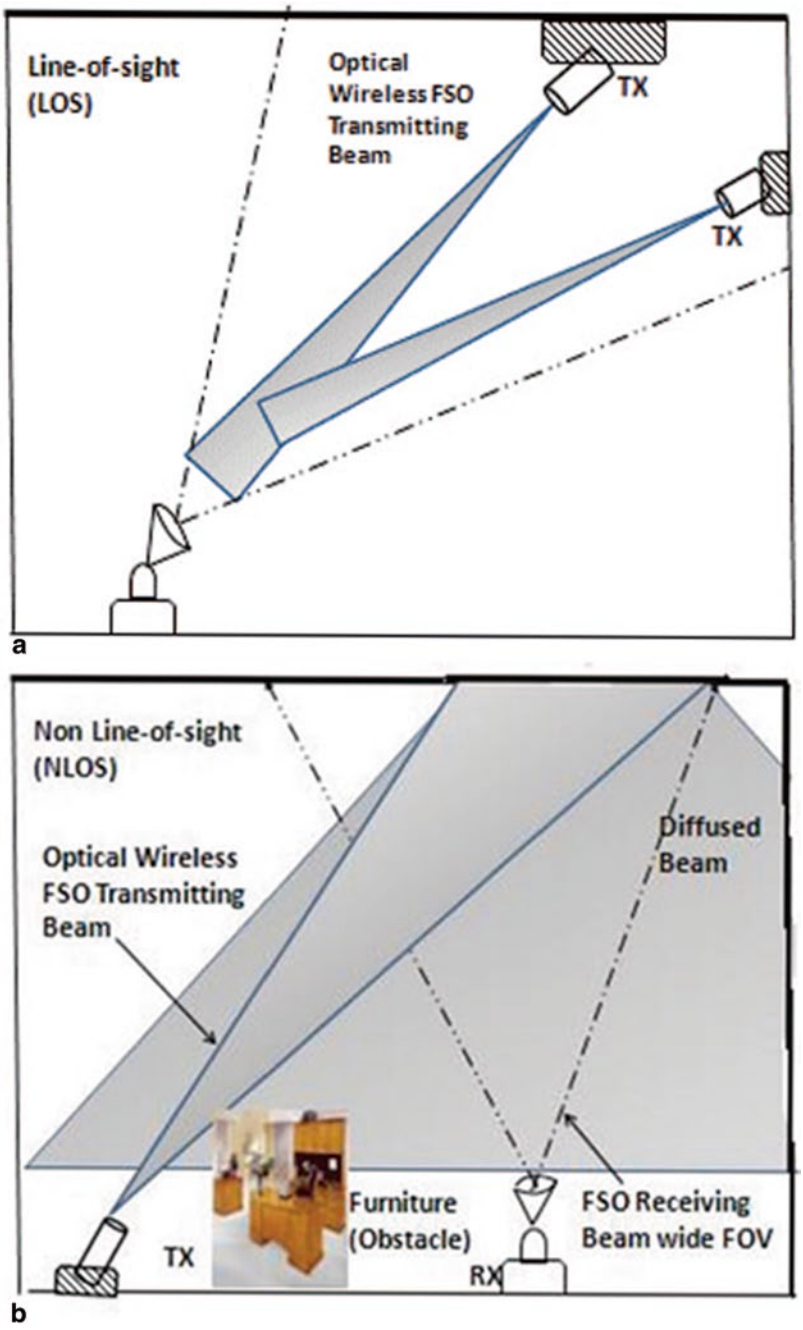

Fig. 5.8 **a** An illustration of a LOS indoor link configuration. **b** NLOS, non-directed, and diffuse configuration. *LOS* line-of-sight, *NLOS* non-line-of-sight

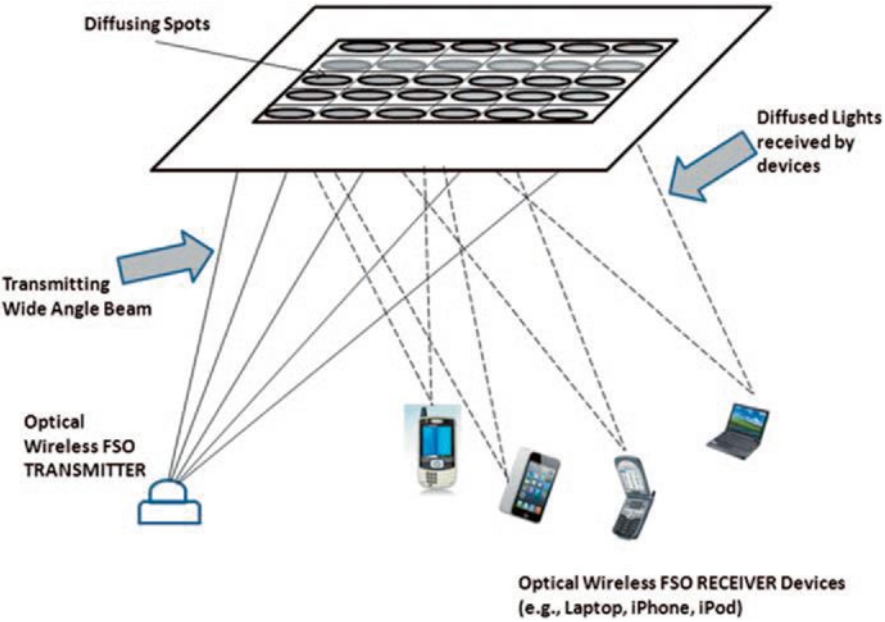

Fig. 5.9 Possible indoor configurations for directed LOS and non-directed NLOS links *LOS* line-of-sight, *NLOS* non-line-of-sight

Figure 5.9 shows an example of NLOS and diffuse configuration for an optical wireless FSO LAN using multi-spot diffusing architecture.

5.4.3 Indoor Optical Wireless System

A block diagram of an indoor optical wireless system is illustrated in Fig. 5.10. A basic indoor communication system consists of a light source (transmitter) either an LED or Laser Diode (LD), free space as the propagation medium, and a detector (using APD or PIN (an intrinsic layer, the "*i* region," is sandwiched between a *p* layer and an *n* layer of in a semiconductor device) diodes). Information, typically in the form of digital or analog signals, is input to electronic circuitry that modulates the transmitting light source (LEDs/laser diodes, LDs). The output passes through an optical system (typically has telescope and other optics) into the free space propagation medium. The received signal is collected by an optical system (an optical filter to reject optical noise, a lens or concentrator) that focuses light on the optical signal detectors (PIN diodes/APDs) and thereafter to signal processing electronics. The wavelength band from 780 to 950 nm is the best choice for indoor optical wireless system. Low cost LEDs and LDs are readily available that can be used. LEDs can be more favorable because of relaxed safety regulations for eye

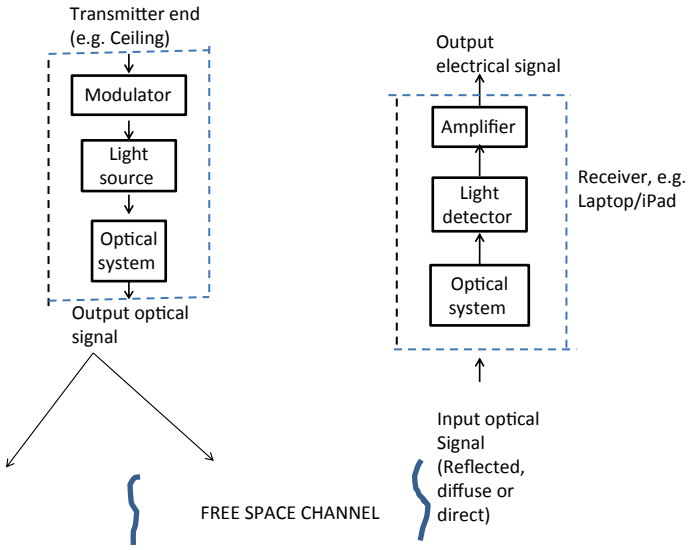

Fig. 5.10 Block diagram of an indoor optical wireless system

safety, low cost, and high reliability compared to LDs. An array of LEDs can be used to design higher power transmitter than a single LED transmitter. LEDs cannot be used beyond 100 Mbps due to limitations imposed by the mechanism by which they emit light, whereas LDs can be used for transmission at bit rates of a few Gbps. For detectors, PIN photo diodes are commonly used due to their lower cost, low-bias voltage requirement to operate (compared to APDs), and can operate in wider temperature fluctuations. The system usually uses intensity modulation with direct detection (IM/DD) scheme for modulation and detection. DD is performed by PIN photo-diodes or APDs which produces an electric current proportional to the incident optical power.

Propagation Medium The propagation medium for indoor optical wireless communication is the free space, free of environmental degradation due to turbulence, aerosol scattering, mist, clouds, etc. Indoor optical wireless communication systems encounter only free space loss and signal fading. FSO is that part of the transmitted power which is lost or not captured by the receiver's aperture (due to diffraction property of the initial beam). For a point-to-point system with a slightly divergent beam, the free space loss would be about 20 dB, whereas an indoor system using wide-angle beam could have a free loss of about 40 dB or more [14].

The signal fading can be observed in both indoor and outdoor optical wireless systems. The fading is due to the reception of signals via different paths by the receiver. Some of these interfere destructively (out of phase) so that the received signal power effectively decreases. This type of degradation is also known as multipath signal fading [15].

Transmission Techniques Depending on the applications and system requirement, there are several possible transmission techniques available by appropriately choosing the transmitter, the receiver, and the optics to direct the beams: (a) Directed radiation, (b) Diffuse radiation, and (c) Quasi-diffuse radiation.

In direct beam indoor system, the optical beams travel directly without any reflection from the transmitter to the receiver. Two fixed data terminals with highly directional transmitter and receiver at both ends of the link can be used. This technique of infrared transmission offers the minimum path loss and maximum power efficiency to achieve higher transmission rates. The main drawback of this technique is the fact that since the transmitter and receiver are fixed, there is lack of mobility and the beams can be intercepted by personnel and other objects in the room. In diffuse system, the transmitter emits a wide-angle beam to the ceiling and after one or several reflections the signals arrive at the receiver. There is no direct beam from transmitter to receiver. There is no alignment requirement for the receiver and is the most convenient for the users. However, compared to the direct transmission, this diffuse technique requires higher transmitter power, large FOV for the receiver, and suffers multipath dispersion. Due to this multipath dispersion effect, the original transmitted pulses are broadened when they reach at the receiver which causes inter-symbol interference (ISI) at higher data rates or in larger cell system [14]. In quasi-diffuse technique, a base station (BS) with a relatively broad coverage and made of either passive or active reflector is mounted on the ceiling. A quasi-diffuse link based on multisport diffusing (MSD) can also be established. Multiple narrow-beam transmitters and an angle diversity receiver with several narrow FOV detectors aimed in different directions can be used. This system is exposed to fewer multipaths and achieves lower path losses requiring lower power transmitter than wide-beam diffuse system at the expense of increased complexity.

Other Design Considerations There are other design considerations that have to be taken into account for designing an indoor optical wireless system. Some of them are discussed below.

Eye Safety The eye safety standards set by the International Electro-technical Commission (IEC) classifies LDs as Class 1, 2, 3A, and 3B depending on their total emitted power. For indoor systems, all transmitters (LEDs and LDs) must be Class 1 eye safe under all conditions, and launch power not to exceed 0.5 mW for the systems employing laser sources. Computer-generated holograms can generate arbitrary radiation patterns and can be used as diffuser which diffuses the image of the laser spot on the retina of the eye to an eye-safe level.

Interference from ambient lights The ambient light from fluorescent light, sunlight, and incandescent light are the dominant source of noise in the indoor system receiver. The ambient light contributes to the shot noise due to the random nature of the photo-detection process and degrades the performance of the optical wireless system. It is therefore important to design the indoor system to minimize the shot noise from the ambient light.

Modulation Techniques Among several techniques, the most common modulation schemes for indoor systems which have been considered in the past are: OOK and PPM. The single carrier pulse modulation techniques can provide high average power efficiency. OOK is one of the simplest in terms of hardware implementation and integration. In PPM scheme, an optical pulse is transmitted in one of L slots per symbol time and the occupied slot position denotes the bit combination conveyed by the symbol. The PPM imposes more system complexity than OOK in indoor systems design since both slot- and symbol-level synchronizations are required at the receiver. The interested readers are referred to [16] for detailed evaluations of these techniques. Multiple-subcarrier modulation technique [17] is another modulation for optical wireless communications. Orthogonal frequency division multiplexing (OFDM) can be used for multiple-subcarrier modulation scheme. In OFDM applied to parallel data transmission, high data rate can be achieved by transmitting orthogonal subcarriers. The time-varying channel can be easily estimated using frequency-domain channel estimation so that adaptive modulation technique can be applied. Combining OFDM with any multiple access scheme makes it a powerful tool for indoor optical wireless applications. For OFDM IM/DD optical systems applications, two schemes have been recently used: Direct current (DC) biased OFDM (DCO-OFDM) [18] and asymmetrically clipped optical OFDM (ACO-OFDM) [19].

Multiple Access Techniques Multiple access techniques define the way several users get access simultaneously to the available network services. This way, the different user's signals can occupy the same time slot, code, or carrier frequency. A single-cell topology using a single optical access point (OAP) per user or per room and a cellular topology with spatial reuse using multiple OAPs are examples of topologies which can be used for indoor systems. Electrical multiplexing (such as time domain multiple access, TDMA; frequency domain multiple access, FDMA; or code-division multiple access, CDMA) is also possible to realize multiple access in a single cell per room or cellular topology. For optical multiplexing techniques wavelength-division multiple access (WDMA) and space-division multiple access (SDMA) can be used.

Multiple-input multiple-output (MIMO) can be used for achieving high data rate indoor communication system. MIMO configurations can be realized by various schemes which include: MIMO using parallel single-input single-output (SISO) links, MIMO using spatial multiplexing, and MIMO using spatial modulation [20].

5.4.4 Propagation Modeling for Indoor Optical Wireless Communications

Accurate characterization of indoor channel is essential to predict the performance limits and design issues for indoor optical wireless links. This can be done by estimating the impulse response of the indoor channel which is an important param-

eter. In order to estimate the performance of indoor communications system, the received optical power and noise variances are calculated for a given transmitted optical power. The indoor channel can be regarded as a linear and time-invariant system. Assume that a signal pulse is emitted at $t=0$ uniformly over the transmitter solid cone angle, and let $P_t(t)$ denote the power of the transmitted optical signal. The signal photons undergo free-space loss through the indoor medium and some of them reach the receiver. The received signal power can be expressed as

$$P_r = \int_{-\infty}^{\infty} P_t(\tau)h(t-\tau)d\tau \tag{5.28}$$

where $h(t)$ is the impulse response of the indoor channel. Both the detector noise and the ambient noise contribute to the total receiver noise. The SNR can therefore be evaluated if we know the input transmitted power and the impulse response of the indoor channel. A short description of estimating the channel impulse response using an iterative site-based method is given below.

Simultaneous evaluation of channels for many transmitter and receiver locations can be performed using the method. In order to accurately evaluate shadowing effects, geometrical model of indoor environments may include people, furniture, and partitions. One or more transmitters and receivers are assumed to be placed inside a reflective environment with obstructions. At optical frequencies, most building surfaces are opaque limiting the propagation of light to the transmitter's room and the reflected light wave from various surfaces is diffusely reflected rather than specularly reflected (like a mirror). Figure 5.11a shows a geometry where a transmitter and receiver placed inside a reflective environment with a transmitter and a receiver placed inside a room. Figure 5.11b shows the environment with site modeled as a set of rectangular boxes containing all sources and receivers. This site model can represent a single room or an entire building. Consider a geometry with a transmitter and a receiver placed inside a room. The transmitter or source S_j can be an LED or LD transmitting a signal $X_j(t)$ using IM. Consider a collection of receivers with a photodiode with responsivity r and using DD.

The signal received by receiver R_i when source S_j is transmitting is $Y_{ij}(t)$. The photodiode current is then given by:

$$Y_{ij}(t) = rX_j(t) * h_{ij}(t) + N_i(t) \tag{5.29}$$

where $*$ denotes convolution, $h_{ij}(t)$ is the channel impulse response between source S_j and receiver R_i, and $N_i(t)$ is the noise at the receiver. Since the impulse response is a function of the source and receiver properties and the environment property, we denote the function in a general way as $h_E(t; S_j; R_i)$.

If multi-element transmitters are used, the signal received by receiver R_i can be written as [21]:

$$Y_{ij}(t) = \sum_{j=1}^{J} (rX_j(t) * h_{ij}(t)) + N_i(t) \tag{5.30}$$

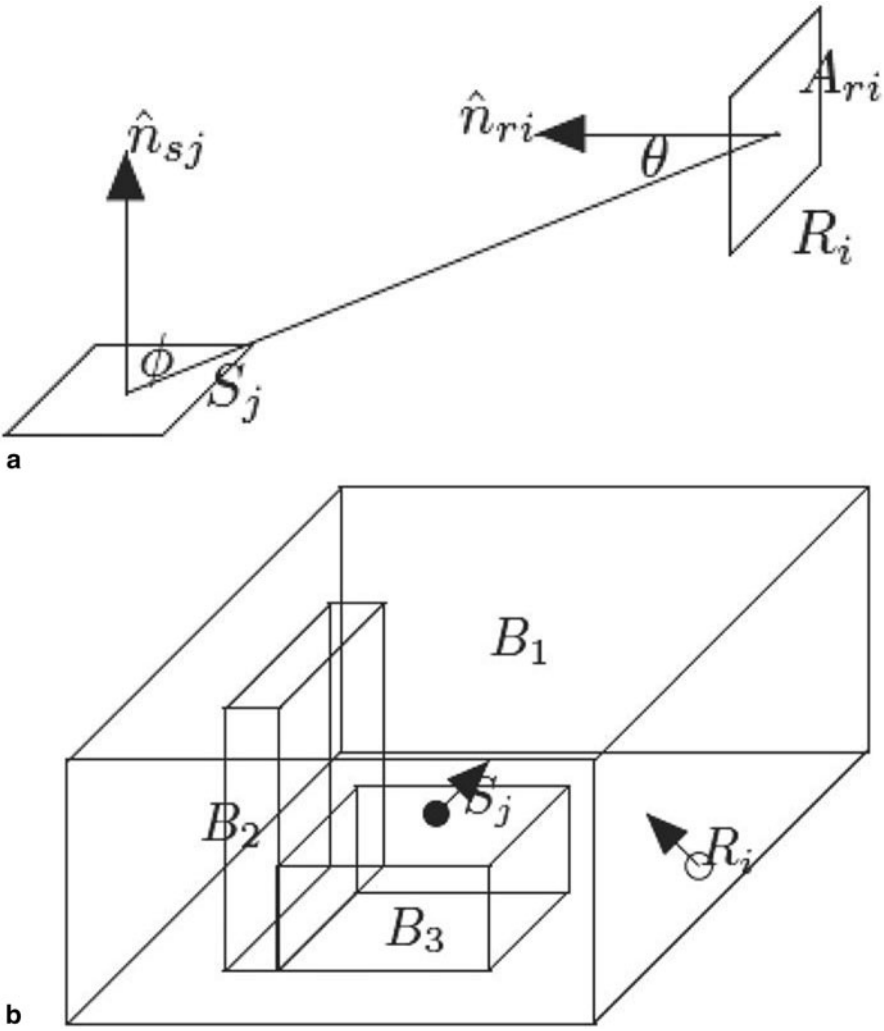

Fig. 5.11 **a** A geometry with a source and receiver link inside a room. **b** Site model for the environment where all the sources and receivers are contained. (*Reprinted with permission from the journal, IEE Proceedings-Optoelectronics (the journal of IET Optoelectronics, previously known as IEE Proceedings-Optoelectronics), 11/2003 [21])*

The transmitted signal may carry the same or different information sequences. The signal received by a multi-element receiver is given by [21]:

$$Y(t) = \sum_{i=1}^{I} \alpha_i Y_{ij}(t - \tau_i) \tag{5.31}$$

where α_i is some constant factors for each *i*. The source S_j can be described in terms of a position vector $\overrightarrow{r_{si}}$, an orientation vector $\widehat{\eta_{si}}$, and a radiant Lambertian intensity pattern $T(\Phi)$. The radiation pattern of order *n* is given by:

$$T(\Phi) = \frac{n+1}{2\pi} cos^n(\Phi) \tag{5.32}$$

The receiver R_i can be characterized by a position vector $\overrightarrow{r_{ri}}$, an orientation vec tor $\widehat{\eta_{ri}}$, an optical collection area A_{ri}, and an effective area at incident angles θ of $A_i(\theta) = A_{ri} g_i(\theta)$ where the receiver gain function $g_i(\theta)$ depends on θ. For a bare photodiode, a typical model is

$$g_i(\theta) = \cos(\theta).$$

The environment *E* can be modeled in such a way that each faces F_i in the room as a diffusive reflective surface (Lambertian) of reflectivity ρ_{F_i}.

The impulse response calculation follows the basic method described in [22]. The impulse response $h_E(t; S_j; R_i)$ can be decomposed into a number of reflections or bounces as follows [21]:

$$h_E(t; S_j; R_i) = \sum_{k=0}^{\infty} h_E^{(k)}(t; S_j; R_i) \tag{5.33}$$

where $h_E^{(k)}(t; S_j; R_i)$ is the impulse response due to signal light undergoing *k* reflections or bounces during its path from the source S_j to the receiver R_i. The LOS impulse response (i.e., for $k = 0$, no reflection) $h_E^{(0)}(t; S_j; R_i)$ is then given by [21]:

$$h_E^{(0)}(t; S_j; R_i) = V(\overrightarrow{r_{sj}}, \overrightarrow{r_{ri}}, E) T(\Phi_{ij}) \left(\frac{A_{ri} g(\theta_{ij})}{D_{ij}^2} \right) \delta(t - D_{ij}/c) \tag{5.34}$$

where the distance $D_{ij} = \left| \overrightarrow{r_{sj}} - \overrightarrow{r_{ri}} \right|$ is the distance between the source and the receiver. The visibility function $V(\overrightarrow{r_{sj}}, \overrightarrow{r_{ri}}, E)$ is 1 when there is no obstruction along the LOS path between S_j *and* R_i. Otherwise its value is zero.

If we consider the first *M* reflections, the impulse response is

$$h_E(t; S_j; R_i) \approx \sum_{k=0}^{M} h_E^{(k)}(t; S_j; R_i) \tag{5.35}$$

The impulse response $h_E^{(k)}(t; S_j; R_i)$ above can be approximated by

$$h_E^{(k)}(t; S_j; R_i) \approx \sum_{n=1}^{N} \rho_{\varepsilon_n^r} h_E^{(k-1)}(t; S_j; \varepsilon_n^r) * h_E^{(0)}(t; \varepsilon_n^s, R_i) \tag{5.36}$$

Where ρ is the surface reflectivity function, and ε_n^r and ε_n^s represent element *n* acting as a receiver and a source, respectively. An estimate of the overall impulse response function can be obtained by combining the *k*-reflections impulse response

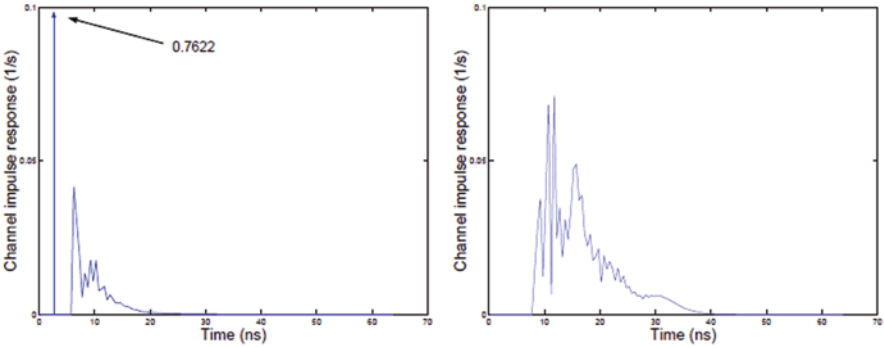

Fig. 5.12 Impulse responses for an indoor channel with an LOS path (**a**) and NLOS path (**b**) (*Reprinted with permission from the journal, IEE Proceedings-Optoelectronics. (the journal of IET Optoelectronics, previously known as IEE Proceedings-Optoelectronics), 11/2003 [21]) LOS* line-of-sight, *NLOS* non-line-of-sight

$h_E^{(k)}(t; S_j; R_i)$ from Eq. (5.36) into the Eq. (5.33). The detailed derivations of the impulse response can be found in [21]. Figure 5.12 shows typical impulse responses for an indoor channel with a LOS path and an indoor channel with no LOS path. The stretching of the pulse for NLOS case is clearly shown. For an empty room, a reasonable accurate impulse response can be calculated. For example, consider up to two bounces which include the following: LOS, first reflection off of all surfaces, and second reflections off all surfaces. To characterize and model diffuse optical wireless indoor FSO channels, channel gain (i.e., the ratio of the received power and the transmitted power) and root-mean-square (RMS) delay spread due to the channel can be sufficient. Figure 5.11 shows a qualitatively a comparison of optical wireless responses for a LOS path and NLOS paths. For example, it is reported that the average RMS delay spreads increasing with distance and ranging from 4 ns to 7 ns for NLOS channels and up to 3 ns for LOS channels [21].

Once the impulse response function is estimated, the received power can be evaluated from the Eq. (5.28) and the SNR of the indoor communication system can be estimated. The BER for the IM/DD scheme can then be calculated from the BER equations assuming Gaussian noise and ambient noise for the receiver noises.

5.4.5 *Recent Research in Indoor Optical Wireless Communications*

Infrared MSD configuration communications are reported [23] with preliminary experiments on fabrication of beam-shaping optical elements for the transmitter and receiver optical front-end. Use of holographic optical elements at both transmitter and receiver increases the SNR by at least 11 dB and significantly improves the power budget of the system by reducing path loss by more than 6 dB.

One of the recent indoor deployment scenarios which make use of new technology development is in the area of sources. For example, recently visible light communications (VLC) technology using white LEDs (WLEDs) driven by progress in WLED technology for solid state lighting. There is tremendous potential for using this type of LEDs for optical wireless data transmission. WLEDS are classified into two types: trichromatic and blue-chip LEDs. Simulation results using trichromatic LEDs for data rates up to 400 Mbps are reported [24]. Some of the challenges and possibilities with WLED for indoor communications are presented [25]. Using a modified version of the classical OFDM modulation scheme, a measured data rates higher than 500 Mbps is reported for a VLC system using blue-chip LEDs [26]. Room illumination meeting minimum levels according to the standards result in a high SNR (>60 dB through the entire room) and therefore VLC does not require full light intensity. Thus, indoor system BER can be achievable with VLC. Bit-error performance of a PPM scheme for NLOS indoor optical links employing channel equalization based on the artificial neural network (ANN) is reported [27]. Channel equalization is achieved by training a multilayer perceptions ANN. Their research shows that for a highly diffuse channel, the SNR requirement to achieve a BER of 10^{-5} for the ANN-based equalizer is ~ 10 dB lower compared with the unequilazied "soft" decoding for 16-PPM at a data rate of 155 Mbps. Neural network equalization is shown to be an effective tool for mitigating the inter-symbol interference. Indoor high-bandwidth optical wireless links for sensor network is presented [28] and demonstrates the capability of indoor optical wireless links of delivering 1 Gbps and beyond without inter-symbol interference. A broadband infrastructure can thus be deployed allowing high-quality audio-visual data communication among sensor nodes.

Reference

1. D. M. Riley, D. T. Moriarty, J. A. Maynard, Unique properties of solar blind ultraviolet communication systems for unattended ground sensor networks, Proc. SPIE, **5611**, pp. 244–254 (2004)
2. International Electrotechnical Commission (IEC), IEC 60825−12: Safety of Laser Products-Part 12: Safety of Free Space Optical Communication Systems Used for Transmission of Information, (2005)
3. International Commission on Non-Ionizing Radiation Protection (ICNIRP): Guidance on Limits of Exposure to Ultraviolet Radiation of Wavelengths between 180 nm and 400 nm (Incoherent Optical Radiation), initially published in Health Physics 49:331–340, 1985; amended in Health Physics 56:971–972, 1989; reconfirmed by ICNIRP in Health Physics 71:978, 1996; republished in Health Physics **87**(2): 171–186 (2004)
4. G. Chen, F. Abou-Gelala, Z. Xu, B. M. Sadler, Experimental evaluation of LED-based solar blind NLOS communication links, Optics Express, **16**(19), 15059–15068 (2008)
5. M. R. Luettgen, J.H. Shapiro, D. M. Riley, Non-line-of-sight single-scatter propagation model, J. Opt. Soc. Am A, **8**(12), 1964–1972 (1991)
6. H. Ding, G. Chen, A. K. Majumdar, Z. Xu, A parametric single scattering channel model for non-line-of-sight ultraviolet communications, Proc. SPIE, **7091**, (2008)
7. T. Feng, F. Xiong, G. Chen, Z. Fang, Effects of atmospheric visibility in performances of non-line-sight ultraviolet communication systems, Optik **119**, pp. 612–617, (2008)

8. A.K. Majumdar, C.E. Luna, P.S. Idell, Reconstruction of probability density function of intensity fluctuations relevant to free-space laser communications through atmospheric turbulence, Proc. SPIE, **6709**, pp. 1–15, (2007)
9. H. Ding, G. Chen, A.K. Majumdar, B.M. Sadler, Z. Xu, Modeling of Non-Line-of-Sight Ultraviolet Scattering Channels for Communication, IEEE Journal on Selected Areas in Communications, **27**(9), 1535–1544, (2009)
10. H. Ding, G. Chen, A.K. Majumdar, B.M. Sadler, Z. Xu, Turbulence modeling for non-line-of sight ultraviolet scattering channels, Proc. SPIE, **8038**, 8038OJ, (2011)
11. N. S. Kopeika, J. Bordogna, Background noise in optical communication systems, Proc. IEEE, **58**, pp. 1571–1577, (1970)
12. J. H. Franz, V. K. Jain, Optical communication components and systems. (Narosa, India, 2002)
13. L. C. Andrews, R. L. Phillips, Laser Beam Propagation through Random Media, SPIE Press Monogr., **PM152**, (2005)
14. D.J.T. Heatley, D.R. Wisely, I. Neild, P. Cochrane, Optical Wireless: The Story So Far, IEEE Commun. Mag., pp. 72–82, (1998)
15. J. R. Barry, J. M. Kahn, W. J. Krause, E. A. Lee, D. G. Messerschmitt, Simulation of multipath impulse response for wireless optical channels, IEEE J. Sel. Areas in Commun., **11**(3), pp. 367–379, (1993)
16. J.M. Kahn, J. R. Barry, Wireless infrared communications, Proc. IEEE, **85**(2), pp. 265–298, (1997)
17. T. Ohtsuki, Multiple-subcarrier modulation in optical wireless Communications, IEEE Commun. Mag., **41**(3), pp. 74–79, (2003)
18. H. Elgala, R. Mesleh, H. Haas, Indoor broadcasting via white LEDs and OFDM, IEEE Trans. Consumer Electron., **55**(3), pp. 1127–1134, (2009)
19. J. Armstrong, A. Lowery, Power efficient optical OFDM, Electron. Lett., **42**(6), pp. 370–372, (2006)
20. H. Elgala, R. Mesleh, H. Haas, Indoor optical wireless communication: Potential and state-of-the-art, IEEE Commun Mag., **49**(9), pp. 56–62, (2011)
21. J.B. Carruthers, S.M. Carroll, P. Kannan, Propagation modeling for indoor optical wireless communications using fast multireceiver channel estimation, IEE Proc.—Optoelectron. (2003). doi:10.1049/ip-opt:20030527, http://iss.bu.edu/jbc/Publications/jbc-j7.pdf
22. J.B. Curruthers, P. Kannan, Iterative site-based modeling for wireless infrared channels, IEEE Trans. Antennas Propag., **50**, pp. 759–765, (2002)
23. M. Kavehrad, S. Jivkova, Indoor broadband optical wireless communications: Optical subsytems desigbns and their impact on channel characteristics, IEEE Wireless Commun., pp. 30–35, (2003)
24. Y. Tanaka et al., Indoor visible light data transmission system utilizing white LED lights, IECE Trans. Commun., **E86-B**(8), 2420–2454, (2003)
25. D. O'brien, L. Zeng, H. Le-Minh, G. Faulkner, J.W. Walewski, S. Randel, Visible light communications: challenges and possibilities, IEEE 19th international symposium on personal, indoor, and mobile radio communications, PIMRC (2008).
26. J. Vucic et al., 513 Mbit/s visible light communications link based on DMT-modulation of a white LED, J. Lightwave Tech., **28**(24), pp. 3512–3518, (2010)
27. S. Rajbhandari, Z. Ghassemlooy, M. Angelova, Bit error performance of diffuse indoor optical wireless channel pulse position modulation system employing artificial neural networks for channel equalization, IET Optolectron., **3**(4), 169–179, (2009)
28. J. Fadlullah, M. Kavehrad, Indoor high-bandwidth optical wireless links for sensor networks, J Lightwave Techn, **28**(21), 3086–3094, (2010)

Chapter 6
Free-space Optical (FSO) Platforms: Unmanned Aerial Vehicle (UAV) and Mobile

Arun K. Majumdar

6.1 Introduction

This chapter discusses the emerging technology of unmanned aerial vehicle (UAV)-based free-space optical (FSO) communication links. UAVs are a possible future application for both civil and military use. The large amount of data generated by the UAVs requires high data rate connectivity, thus making FSO communication very suitable. This chapter discusses some important issues using FSO links such as the FSO unit alignment and the beam attenuation/fluctuation due to the atmosphere. The technical challenges for the alignment in tracking and acquisition are addressed. Detailed descriptions are provided in the following areas: alignment and tracking of a FSO link to a UAV, short-length Raptor codes for mobile UAV, and a modulating retroreflector (MRR) FSO communication terminal on a UAV. A new methodology of using multiple UAVs in a cooperative swarm mode is also described. Specific areas for UAV swarms are discussed, such as large and adaptive beam divergence for inter-UAV FSO communication, networking architectures, reliability, and appropriate modulation scheme (pulse position modulation, PPM/on-off keying, OOK; incoherent detection). Another section of this chapter deals with the problem associated with mobile platforms, i.e., tracking in moving vehicles and gimbals. The challenges addressed are: variation in receiver beam profile of the FSO link and variation in received optical power due to constantly changing transmitter/receiver separation. Some basic building blocks for high-speed mobile ad hoc networks (MANET) using FSO is described with protocols operating under high mobility. An FSO structure is described which can achieve angular diversity, spatial reuse, and are multielement. The link performance of mobile optical links in the presence of atmospheric turbulence is provided for a FSO-based mobile sensor network. Mobile communication challenges and potential solutions are discussed.

A. K. Majumdar, *Advanced Free Space Optics (FSO),*
Springer Series in Optical Sciences 186, DOI 10.1007/978-1-4939-0918-6_6,
© Springer Science+Business Media New York 2015

6.2 UAV FSO Communications

Research in the area of FSO communications is usually based on point-to-point link or long-range link for space applications. Mobility, i.e., relative movement of either the transmitting or receiving terminal (or both) is the greatest challenge in the family radio service (FRS) communication technology. By including UAV to provide a communication terminal, a number of flexible and practical applications can be developed. There is increasing interest in UAV for many applications, especially in the area of surveillance, due to zero risk of human casualty. With improved high-resolution imaging sensors that are much higher date rate than radio frequency (RF) technology can support, it is that communication links that transmit more information between UAV and ground terminal, or between UAVs. In order to meet the increasing demand, efficient ways to communicate with UAVs with FSO optics are needed since the UAVs are moving platforms.

Many commercial FSO links operate at 1–2 Gbps over ranges of 1–3 km. Most FSO links are stationary but they have been considered for mobile applications. Some of the applications include ship-to-ship [1], ground-to-air, and air-to-air [2, 3] communication systems and even deep-space communications [4].

6.2.1 UAV Scenarios for FSO Communications Link

There are three basic FSO communications link scenarios with UAV platform. These are (i) ground-to-UAV, (ii) UAV-to-ground, and (iii) UAV-to-UAV or between UAVs (UAV swarm).

Ground-to-UAV Mobile FSO Channel Figure 6.1 shows the ground-to-UAV mobile FSO link where the speed of the UAV can reach several hundred meters per second. Tracking in this scenario is typically accomplished by mechanical components such as a 2-D rotating gimbal which is oriented based on global positing system (GPS) data from the UAV. Small divergent angle of the transmitting beam makes the tracking task difficult. The received signal to noise ratio (SNR) variation can be caused by misalignment of the transmitted beam and the detector due to mechanical pointing uncertainty error and GPS positioning error which limits the data rates of such link [5]. An efficient tracking method is therefore necessary to improve the data rate.

UAV-to- ground FSO Communication Link Figure 6.2 illustrates this concept of a bidirectional daytime and nighttime optical communication link from a UAV to a stationary ground station. One of the tasks the UAV might have is to take science images over desired targets and then download the images via the optical communication channel.

An optical communication terminal receives a command from ground via RF links which also receives continuous updates of the GPS information collected by the UAV GPS receiver. Simultaneously, the UAV provides the optical communication

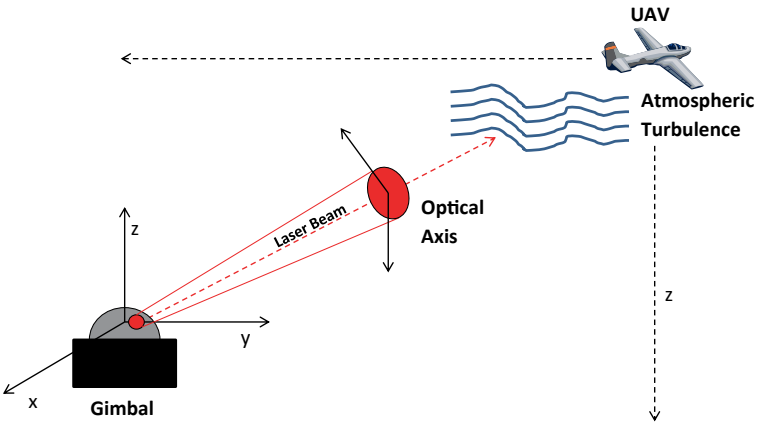

Fig. 6.1 Ground-to-UAV mobile FSO communication. *UAV* unmanned aerial vehicle, *FSO* free-space optical

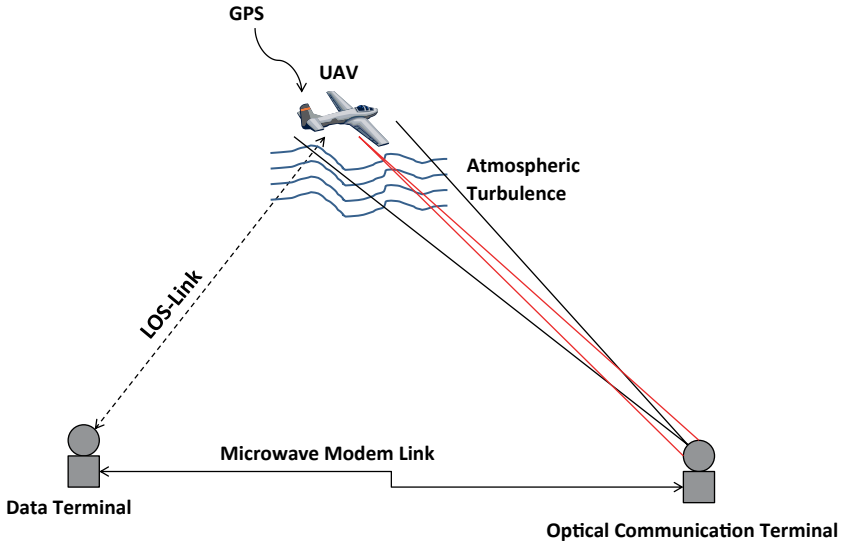

Fig. 6.2 UAV-to-stationary ground station FSO communication. *UAV* unmanned aerial vehicle, *FSO* free-space optical

terminal with its GPS information. The optical communication terminal uses updated information from both the UAV GPS receiver and the ground location to blind point the gumball by sending a beacon signal to initiate the communication signal. Data communication starts when the signal terminal tracks on the beacon signal. A demonstration of the FSO communication link at 2.5 Gbps is presented [6] for a UAV altitude of 15.8–18.3 km using a 200 mW downlink laser at 1,550 nm. They reported bit error rate (BER) of 10^{-9} which needed the pointing requirement on the flight terminal of 19.5 μrad and a bias error of 14.5 μrad with a probability

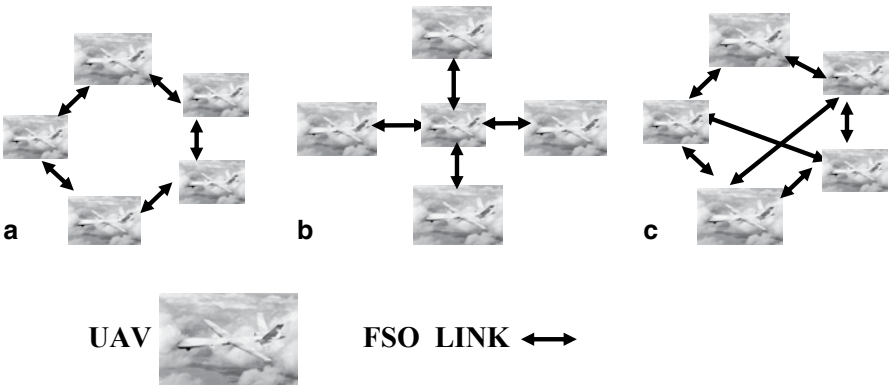

Fig. 6.3 *FSO* network for swarm *UAV*s using three different architecture. **a** Ring Architecture. **b** Star Architecture. **c** Meshed Architecture

of pointing-induced fades (due to turbulence) of 0.1 %. Vibration uncertainties also need to be eliminated for establishing a high data rate communication link.

UAV Swarms; Links Between UAVs The use of UAVs for transferring high date rate information is very rapidly attracting attention. In some situations, it may be necessary to collect data for a defined area with a variety of sensors. When these UAVs are operating in swarm formation, the observation area can be increased and an occasional loss of a UAV will not completely stop the data transfer process using the highly efficient optical communication links. FSO communications offering high bandwidth can therefore provide high data rate connectivity required by the large volume of data in UAV swarms. Figure 6.3 illustrates FSO network for swarm UAVs using three different architectures: *Ring Architecture, Star Architecture, and Meshed Architecture.*

The key point here is to develop the UAVs capabilities to handle multiple sensor information in real-time and in parallel so that a large amount of data can be transferred in real-time with a goal to achieve a rate of 2.5 Gbps or higher.

In the ring architecture mode, all FSO links are bidirectional and in case of a broken (or failure) link between any two UAVs, an indirect link may be used but the information is sent in the other direction where there is still link [7]. In a star architecture, there is one UAV in the middle of the formation which acts as an optical multipoint unit (OMU) [7] and is used as a repeater. All other UAVs equipped with transceivers are permanently connected with this OMU. A failure of the OMU can cause the breakdown of the whole configuration and a redundant OMU might be necessary. A meshed network can provide high reliability by combining the advantages of both the star and the ring architecture. Information flow from one UAV to another can be realized in different forms and can also be sent in the other direction of the ring network.

Atmospheric and Turbulence Effects For different UAV scenarios, the atmosphere plays different roles. Optical signals propagating in the Earth's atmosphere experience degradation due to absorption, scattering, and turbulence. Absorption and

scattering are caused by the interactions of optical waves with atmospheric gases and particulates, such as aerosols and fog, and result mainly in the attenuation of the signal. Turbulence is caused by the random variations of the refractive index at optical wavelength, and when an optical beam propagates through a turbulent medium atmospheric turbulence causes irradiance fluctuations, beam wandering, and loss of spatial coherence of the optical wave. Three possible propagation configurations are related to the UAV FSO communication links: *uplink, downlink, and horizontal.* Uplink configuration is the propagation of a ground-based terminal to another terminal in space in general via a slant path. Downlink is when the communication link is established from the terminal in space to a ground terminal via a slant path. Horizontal link is defined when both of the communication terminals communicate via horizontal path (either on the ground or in space). Obviously, the three links cause different effects on the received signals in a UAV receiver since the atmospheric models for these three links follow different distributions of atmospheric properties.

Atmospheric Models Related to UAV FSO Communication Links Based upon the measurements, empirical and parametric models of turbulence strength parameter, C_n^2 have been derived and several different models are commonly used to represent the effects of atmospheric turbulence, and are described below; h is altitude (meter) [8]:

i) Hufnagel-Valley (HV) model:

$$C_n^2(h) = 0.00594\left(\frac{v}{27}\right)^2 (10^{-5}h)^{10}\exp\left(-\frac{h}{1000}\right) + 2.7\times10^{-16}\exp\left(-\frac{h}{1500}\right) + A\exp\left(-\frac{h}{100}\right) \quad (6.1)$$

where v is the rms wind speed. Typical value of the parameter, $A = 1.7\times10^{-14}\ \mathrm{m}^{-2/3}$.

ii) ModifiedHufnagel-Valley (MHV) model:

$$C_n^2(h) = 8.16\times10^{-54}h^{10}\exp\left(-\frac{h}{1000}\right) + 3.02\times10^{-17}\exp\left(-\frac{h}{1500}\right) + 1.90\times10^{-15}\exp\left(-\frac{h}{100}\right) \quad (6.2)$$

(iii) Submarine Laser Communication (SLC)-Day model:

$$\begin{aligned} C_n^2 &= 0 && 0\,\mathrm{m} < \mathrm{h} < 19\,\mathrm{m} \\ &= 4.008\times10^{-13}\,\mathrm{h}^{-1.054} && 19\,\mathrm{m} < \mathrm{h} < 230\,\mathrm{m} \\ &= 1.300\times10^{-15} && 230\,\mathrm{m} < \mathrm{h} < 850\,\mathrm{m} \\ &= 6.352\times10^{-7}\,\mathrm{h}^{-2.966} && 850\,\mathrm{m} < \mathrm{h} < 7000\,\mathrm{m} \\ &= 6.209\times10^{-16}\,\mathrm{h}^{-0.6229} && 7000\,\mathrm{m} < \mathrm{h} < 20{,}000\,\mathrm{m} \end{aligned} \quad (6.3)$$

(iv) CLEAR1 model:

Note: Here h is altitude in kilometer above mean sea level (MSL)

$$
\begin{aligned}
&1.23 < \mathrm{h} \le 2.13 \\
&\log 10\left(C_n^2\right) = A + Bh + Ch^2 \\
&\text{where A} = -10.7025, \mathrm{B} = -4.3507, \mathrm{C} = +0.8141 \\
&2.13 < \mathrm{h} \le 10.34 \\
&\log_{10}\left(C_n^2\right) = A + Bh + Ch^2 \\
&\text{where A} = -16.2897, \mathrm{B} = +0.0335, \mathrm{C} = -0.0134 \\
&10.34 < \mathrm{h} \le 30 \\
&\log_{10}\left(C_n^2\right) = A + Bh + Ch^2 + D\, exp\{-0.5\left[(h-E)/F\right]^2\} \\
&\text{where A} = -17.0577, \mathrm{B} = -0.0449, \mathrm{C} = -0.0005 \\
&\mathrm{D} = 0.6181, \quad \mathrm{E} = 15.5617, \mathrm{F} = 3.4666
\end{aligned}
\tag{6.4}
$$

For an uplink laser communication link, i.e., from a ground-based terminal transmitting to a UAV, the atmospheric turbulence begins just outside the transmitter aperture, and we can assume a spherical wave for propagation. HV model turbulence profile is used. For a specific modulation scheme such as OOK modulation, and knowing the parameters such as wavelength, UAV height, transmitter divergence angle, and a data rate, the UAV communication performance BER can be computed [8]. The BER calculation is based on a Gamma-Gamma probability density function for the intensity fluctuations of the outgoing beam.

For a downlink path from a UAV to a ground terminal, the ground-level scintillation near the center of the received wave can be accurately modeled by a plane wave. The Rytov variance (i.e., intensity variance of a plane wave) in this case depends mostly on high-altitude turbulence, and is consistent with weak-fluctuation theory except the case of very large zenith angle of the UAV. The system performance denoting BER can be calculated using OOK modulation. The same HV model (as was used in uplink model) can be used. Probability of fade variation is similar to the uplink case [8].

For the horizontal case the value of C_n^2 remains constant along the propagation path. The value of C_n^2 at the altitude of the UAVs needs to be accounted for when estimating intensity fluctuations or beam wander.

When the UAVs have to operate under atmospheric scattering conditions, scattering of optical wave by aerosol particulates and fog can be important. The proposed model for short distance link is the Kruse model [7] which relates the attenuation to visibility V (in km) for a given wavelength (in nm). In visible and near infrared (IR) wavelength up to about 2.5 μm, the attenuation is given by [7]:

$$
\gamma(\lambda) \approx \beta_a(\lambda) = \frac{\ln(\tau_{TH})}{V}\left(\frac{\lambda}{550nm}\right)^{-q} = \frac{3.912}{V}\left(\frac{\lambda}{550nm}\right)^{-q} \tag{6.5}
$$

where τ_{TH} is the transmission.

The attenuation a_{dB} over the link path distance d_{link} can be calculated from the measured transmission τ or the extinction coefficient $\gamma(\lambda)$ (in km^{-1}) using the following relation:

$$a_{dB} = 10\log\left(\frac{1}{\tau}\right) = \frac{10}{\ln(10)}\gamma(\lambda)d_{link} \tag{6.6}$$

Results are presented using simulation, [9], for 1 km distance between two UAVs and a divergence angle of 50 mrad giving a system power of 11 mW for clear sky conditions. Results show that 113 mW of transmitter power is needed for moderate fog conditions. For a 2 km distance, the required powers are increased: 44 mW for clear sky and 4.6 W for foggy weather conditions needed.

6.2.2 *Alignment and Tracking of a FSO Communications Link to a UAV*

For establishing a successful FSO communication link between a ground station and a UAV, the most important criteria to start with is to make sure that the mechanical gimbal can accurately track the moving UAV in presence of atmospheric turbulence. From UAV side, it is important that the minimum transmitting beam divergence is such that the probability of fading of the signal reaching the receiver due to beam wandering caused by atmospheric turbulence is below a required threshold. The repeatability and the accuracy of the gimbal to align and track a ground-to-UAV FSO link needs to be verified. Divergence of the transmitting beam is one technique to help with alignment and tracking of FSO link.

Tracking Algorithm Example for a UAV and a Moving Station (Both Moving Vehicles) Two scenarios are considered to discuss about tracking algorithm: The first scenario is a UAV communicating with a moving vehicle station, and the second scenario is a manned aerial surveillance vehicle with an UAV.

UAV and moving vehicle station: The tracking algorithm sends steering commands to the gimbals so that laser alignment is maintained. The gimbals' angular positions and velocities are specified by the tracking algorithm. The angular position and velocity of the gimbals can be determined by the following equations [10]:

$$\theta = \arctan\left(\frac{z + z_P + z_R + z_Y}{y + y_Y}\right) \tag{6.7}$$

and

$$\alpha = \arctan\left(\frac{y + y_Y}{x + x_Y}\right) \tag{6.8}$$

$$\theta' = \frac{(\theta_2 - \theta_1)}{t}$$

$$= \frac{\left(\arctan\left(\frac{z_{t1} + z_{Pt1} + z_{Rt1} + z_{Yt1}}{y_{t1} + y_{Yt1}}\right) - \arctan\left(\frac{z_{t0} + z_{Pt0} + z_{Rt0} + z_{Yt0}}{y_{t0} + y_{Yt0}}\right)\right)}{t} \quad (6.9)$$

and

$$\alpha' = \frac{(\alpha_2 - \alpha_1)}{t}$$

$$= \frac{\left(arctan\left(\frac{y_{t1} + y_{Yt1}}{x_{t1} + x_{Yt1}}\right) - arctan\left(\frac{y_{t0} + y_{Yt0}}{x_{t0} + x_{Yt0}}\right)\right)}{t} \quad (6.10)$$

where x and y are the distance between the two vehicles on the x-axis and y-axis, respectively at a given time, α is the angular position of the gimbals in the x-y plane, i.e., the yaw, θ is the angular position of the gimbals in the z-y plane, i.e., the pitch, and z is the position of the vehicles on the z-axis. The other variables containing z also denote the z-axis position, but affected by various forces, Z_P is the z-axis position of the vehicle affected by the change in pitch of the vehicle, Z_R by the change in roll of the vehicle, and, Z_Y by the change in yaw of the vehicle. y_Y is the y-axis position of the vehicle affected by the change in yaw of the vehicle. t_0 and t_1 are the times for the vehicles at positions one and two, respectively. x_Y is the x-axis position of the vehicle affected by the yaw of the vehicle. The parameters are determined by the GPS, an inter-vehicular information system (IVIS), and an inertial navigation system (INS). The divergence of the laser source increases proportionately with the increase in distance between the vehicles so that the spread of the light can determine the update rates of the system. As opposed to stationary terminals in the conventions FSO system, when the UAV and another vehicle are moving the mobility causes the most challenge in aligning the two terminals for a successful FSO communication. If we know the various positioning systems as outlined here, an efficient tracking is achievable. This tracking method can be used for transferring real-time video between UAV and a ground vehicle using high bandwidth FSO communications.

Link Margin Analysis for Ground-to-UAV FSO Communications Link Link margin analysis requires calculating the geometric loss for a given transmitter, the transmitter initial beam shape, beam width, and the propagation path length. The transmitter input beam profile $2W_0$ is related to the complex amplitude of the amplitude wave, $U_0(r, 0)$ as follows:

$$U_0(r,0) = A_0 \exp\left(-\frac{r^2}{W_0^2} - \frac{ikr^2}{2F_0}\right) \quad (6.10)$$

where α_0 is the amplitude of the wave at the optical axis, F_0 is the radius of curvature of an assumed parabolic distribution of the phase, r is the distance from the beam center line in the transverse direction, and k is the optical wave number. Another parameter is α related to spot size and phase front radius of curvature by the following relation:

$$\alpha = \frac{2}{kW_0^2} + i\frac{1}{F_0} \tag{6.11}$$

For link margin analysis based on atmospheric loss only (i.e., no turbulence is considered for this analysis), we need to evaluate geometric loss in FSO communication which is the ratio between the receiving optics and the beam spot size in the receiver plane of the FSO link. Using the Eq. (6.10) for the transmitting lowest-order transverse electromagnetic Gaussian beam wave, with W_0 as the effective beam radius, the beam radius at the receiver plane is given by [11]:

$$W(t) = W_0\left[\left(1 - \frac{\{[x_u(t)-x_g]^2 + [y_u(t)-y_g]^2 + [h_u(t)-h_g]^2\}^{1/2}}{F_0}\right) + \left(\frac{2\{[x_u(t)-x_g]^2 + [y_u(t)-y_g]^2 + [h_u(t)-h_g]^2\}}{kW_0}\right)\right]^{1/2} \tag{6.12}$$

where (x_g, y_g, h_g) are the coordinates of the ground station and $[x_u(t), y_u(t), h_u(t)]$ are time-varying coordinates of the UAV. The Gaussian beam at the receiver plane of the link can be expressed as:

$$U_0(r, L) = A_0(\Theta - i\Lambda)\exp\left(ikL - i\frac{r^2}{W^2}\frac{kr^2}{2F}\right) \tag{6.13}$$

$$\text{where } \Theta = 1 + \frac{L}{F}, \Lambda = \frac{2L}{kW^2} \tag{6.14}$$

Their simulated results show that at 1.55 μm wavelength, for a 4-km UAV altitude, an effective beam spot size of 3.03 m, and for a 8-km UAV altitude, an effective spot size of 4.79 m which resulted in expected geometric loss values of −14.8 and −16.8 dB for the 4-km and 8-km altitudes, respectively [12]. Using a receiver threshold sensitivity value of −43 dBm, and factoring in the geometric loss, the pointing loss and optical loss, the FSO receiver threshold sensitivity to only atmospheric loss was found to be −11.3 dBm [11].

6.2.3 FSO Communication Links Using UAV(s): Practical Issues and Recent Development

To establish a UAV FSO link for communication, there are two important factors to be considered: first, to verify that that a UAV FSO link for a ground-to-UAV,

UAV-to-ground, or between UAVs be aligned and then tracked in presence of atmospheric turbulence. Both repeatability and accuracy of the gimbal need to be measured. Also how the beam divergence affects the gimbal's steering tolerance for expected geometrical losses from the configuration should be evaluated. Some of the characteristics of the gimbal's ability are investigated [3]. Their experiment simulated a scenario where a UAV follows a circular flight path of radius 4 km at an altitude of 4 km for a gimbal elevation of 45° from horizontal and a transmitter-receiver separation of 5.66 km Their experimental results show the following:

- *X-Y* scatter plot of the gimbal repeatability (fell in an area of 0.5 mm^2) and accuracy data (gimbal error ranges between 0 and 0.2 mm).
- Distribution of azimuth and elevation repeatability in meters and in degrees: azimuth repeatability mean of 1.24 m (226.89 μrad) with a standard deviation of 0.2 m (52.36 μrad); gimbal elevation repeatability of 0.41 m (69.81 μrad); and standard deviation of 0.22 m (39.91 μrad).
- The gimbal pointing error has a mean of 0.3 m (55.85 μrad) with a standard deviation of 0.2 m (34.91 μrad).
- Based on the total variance of intensity versus pointing error, the signal level is shown to drop below a threshold of 30 dB to be 3.69×10^{-29} (a very small number!).

Their results concluded that the beam divergence present in the FSO link is sufficient to offset any error introduced into the alignment and tracking algorithm by the gimbal with a very low probability of signal fade for a ground-to-UAV FSO link.

A custom designed and manufactured gimbal with a wide field-of-view (FOV) and fast response time is presented [12]. This gimbal system is a 24 V system, with integrated motor controllers and drivers which offers a full 180° FOV in both azimuth and elevation. Thus, it provides a more continuous tracking capability as well as increased velocities of up to 479 per second, as well as active and passive vibration isolation systems. Their design will improve the accuracy and stability of the precision laser pointing system required for UAV FSO communication link.

Adaptive Beam Divergence Technique:

New technique based on adaptive beam divergence is presented [13] for inter-UAV FSO under varying distance conditions. A single beam divergence employed in the link of optical communications may limit the transmission distance between UAVs. An adaptive beam divergence can improve the free space communication link performance and provides advantages over a fixed beam divergence in the inter-UAV FSO. The general link equation can be written as:

$$P_{rx} = P_{tx} \cdot L_{rx} \cdot G_{tx} \cdot L_p \cdot L_R \cdot L_{atm} \cdot G_{rx} \cdot L_{rx} \tag{6.15}$$

where P_{rx} is the received power, P_{tx} = transmit power, G_{tx} = transmit optics efficiency, L_P = transmit gain, L_R = pointing loss, L_{atm} = atmospheric loss, G_{rx} = receiver gain, and L_{rx} = receiver optics loss. If we combine the transmit gain, range loss, and receiver gain into a single term, geometrical loss, L_{geo}, the Eq. (6.15) can be re-written as:

$$P_{rx} = P_{tx} \cdot L_{geo} \cdot L_p \cdot L_R \cdot L_{atm} \cdot L_{rx} \tag{6.16}$$

$$L_{geo} = [a_{rx} / (\theta_{div} \cdot R)]^2 \tag{6.17}$$

$$L_p = \exp[-8 \cdot (\theta_{err} / \theta_{div})^2] \tag{6.18}$$

where α_{rx} = receiver aperture diameter, θ_{div} = beam divergence, R = communication range, and θ_{err} = pointing error.

When two UAVs are trying to establish a communication link, knowledge of each other's location is required provided either by a ground control relay or through the swarm control channel. An exact instantaneous position for each UAV is difficult because of its inaccuracy in its on-board positioning system and an uncertainty area is developed in which the measured UAV position and the actual UAV position can be anywhere. The size of the uncertainty area is described by its diameter d_{uca}. Platform jitter, θ_{jitter} can be neglected if it is very small compared to the uncertainty area angular size, i.e.,

$$\theta_{div} \geq \theta_{uca} + \theta_{jitter} \tag{6.19}$$

An optimum beam divergence is to be determined now in order to deliver more beam power to the edge of the uncertainty area so that UAV at that location will receive sufficient beam power to continue communications. From Eqs. (6.17) and (6.18), a larger beam divergence will increase the geometrical loss and the pointing loss will be reduced for a fixed pointing error. From the Eqs. (6.17) and (6.18), we can find the optimum beam divergence to send the most beam power to the edge of the uncertainty area while satisfying the condition, Eq. (6.19). The distance between the two communicating UAVs is continuously changing which affects the maximum angular pointing error, which is the maximum mispointing of beam when the UAV is the edge of the uncertainty area defined by [13]:

$$\theta_{\max-err} = 0.5 \cdot (d_{uca} / R + \theta_{jitter}) \tag{6.20}$$

Instead of increasing the receiver aperture size or transmit power, a more efficient method is to adopt an adaptive beam divergence to mitigate the loss due to the distance under the constraint of Eq. (6.19). Thus, the loss due to the geometrical and pointing loss can be reduced by constantly changing the beam divergence according to the distance. The amount of loss at the edge of the uncertainty area is given by [13]:

$$EdgeLoss = 0.36 \cdot \{a_{rx} / [1.4 \cdot (d_{uca} + \theta_{jitter} \cdot R)]\}^2 \tag{6.21}$$

For a Gaussian beam, collimated beam diameter is given by [14]:

$$\theta_{div} = (4 \cdot \lambda) / (\pi \cdot d_{out}) \tag{6.22}$$

where λ is the transmitter wavelength, and d_{out} is the collimated output beam diameter. The collimated beam output can therefore be altered to provide adaptive beam divergence adjustment in order to improve the FSO communication performance under varying distance conditions.

Short-length Raptor Codes for Ground-UAV Optical Channels Recently short-length Raptor codes, independent of channel misalignment caused by tracking error and atmospheric scintillation are presented for a ground-to-UAV mobile FSO channel [5]. A UAV FSO channel can suffer severe instantaneous misalignment which is not known to the transmitter causing data packet corruption and erasure. Traditional fixed-rate erasure coding technique is not suitable. Applications of rateless Raptor codes for such mobile FSO system is presented where short-length (16–1024) Raptor codes are designed to apply to a severe jitter FSO channel. For a 1 Gbps transmitter, the designed Raptor code with $k = 64$ message packets can deliver 560 Mbps data rate for a decoding cost of 4.11 operations per packet with transmitting power of 20 dB. A traditional automatic repeat-request (ARQ) algorithm technique for the same jitter channel can deliver only 60 Mbps. Thus the short-length Raptor code is useful for a ground-to-UAV FSO link performance improvement.

Modulating Retroreflector (MRR)-based UAV FSO Communications Original research on multiple quantum well (MQW) modulating retroreflector started more than 10 years ago at Naval Research Laboratory (NRL) [15]. Modulating retroreflector systems couple an optical corner cube retroreflector and an electro-optic shutter to provide a 2-way optical communications using a laser source and a pointer-tracker on only one platform. The MRR at that time at NRL used a semiconductor-based MQW shutter capable of modulation rates greater than 10 Mbps. Many years ago, they demonstrated an IR data link between a small rotary-wing UAV and a ground-based interrogator using the MQW device designed and fabricated at NRL. Optical link to an UAV in flight at that demonstration covered a range of only 100–200 ft. An airborne reconnaissance concept using a UAV was presented with MQW MRR [15]. When using an array, the MQW MRR concept reduced the payload requirements for the onboard communication system. The laser communication to small UAVs can have the loose pointing requirements of MRR. Small, lightweight, and low-cost gimbals can therefore be used for pointing. For small UAV, low precision hardware can be used which also decreases size, weight, power, and cost. The MRR transmitter can be much smaller, lighter, and uses less power than a traditional laser transmitter. NRL demonstrated an initial flight test using a small UAV. For a small UAV system, MRR transmitters and photodetectors (PDs) are installed in low-cost, lightweight gimbals. Two wingpods, each contains an MRR gimbal, a photoreceiver gimbal, a stabilized camera, and electronics. Flight tests are reported where live video is transmitted to the ground using the lasercom downlink, whereas pointing and zoom comments are sent to the camera via the lasercom link. A frame captured from a 15 frame/s video stream is shown [16].

A micro-electro-mechanical systems (MEMS)-based modulating retroreflector is proposed as a communication terminal onboard a UAV allowing both the laser

transmitter and acquisition, tracking, and pointing (ATP) subsystems to be eliminated. The ATP in the ground station is based on a GPS-aided two-axis gimbal for tracking and course pointing, and a fast steering mirror for fine pointing. The system designed is a beacon-based, taking advantage of the retroreflector optical principle to determine the UAV position in real-time. A modulating retroreflector has been proposed as the communications remote terminal where the retroreflector sends the incoming beam back to the ground station via the same path of the interrogator laser on the ground. Both liquid-crystal-based and MEMS-based MRR are considered. With MEMS device, a data rate of >1 Mbps is the goal while keeping the power consumption to remain below 100 mW with the starting laser beam-width of 0.2 cm and initial range of 10–1,000 m [17]. An air-to-ground FSO communication system design is presented with an emphasis to achieve the minimum payload power, size, and weight using a MEMS modulating retroreflector [18]. A new technique for fine pointing based on a liquid-crystal device is chosen at the ground station.

Swarm UAVs FSO Communication One of the future applications for UAV flying in swarm carrying a variety of sensors is for monitoring and surveillance a large area. Data rates of 100 Mbps to 1 Gbps are needed to handle multiple sensor information in real time and parallel. For swarm UAVs, a reliable and high-performance wireless communication link among UAVs are essential. There are two communication systems needed for the swarm UAVs: Air-to-air UAV communication system enables the sharing of sensor and map information among the UAVs, and air-to-ground system provides mission information to the ground station for mission control and display. Actions of each UAV can reduce the risk in the environment for all other UAVs. Different types of networks for swarm UAVs were mentioned earlier in this chapter: Ring, Star, and Meshed Architectures. Links between UAVs are considered [7] for short links because of high costs. The effects of turbulence on the propagation path is negligible compared to foggy environments. For short links, an omnidirectional beam arrangement and the beam broadening are interesting alternate solution to expensive and heavy tracking system. Omnidirectional multi-beam systems installed on swarm UAVs offer potential enhanced reliability and availability. Due to continuous motion and changing relative speeds of all its members, for the swarm UAV scenario to maintain a line-of-sight (LOS) FSO link is challenging [19].

6.3 Mobile FSO Communications

Originally, the FSO communication was meant for stationary terminals for providing high bandwidth solution. Introducing mobility to FSO technology will open more applications. Mobility will also have its own challenges including the LOS maintenance for continuous data flow. One of the goals is therefore to develop technology that enables a mobile terminal to be tracked.

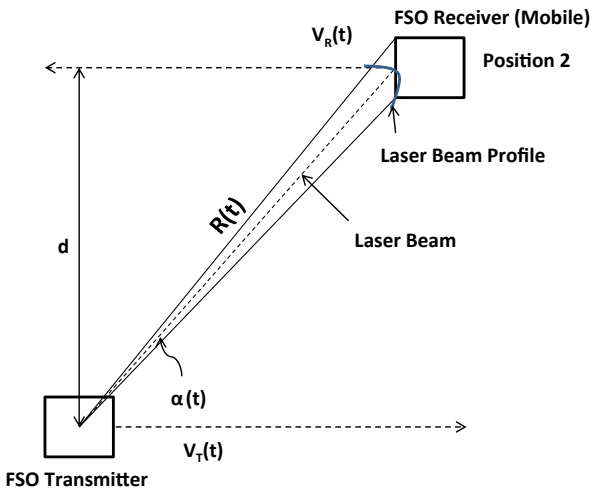

Fig. 6.4 *FSO* link configuration for a transmitter and a receiver mounted on mobile platforms. *FSO* free space optical

6.3.1 Beam Divergence and Power Levels Variations in Mobile FSO Communications

As the transmitter-receiver separation continuously changes in a mobile FSO link, the received beam profile and the received power levels also change. Beam divergence is used to simplify alignment of transmitter and receiver in FSO link. For a mobile operation using FSO link, the propagation range is continuously changing with time, and therefore the received beam profile on the receiver plane is changing. Consequently the beam divergence is changing with the propagation distance and the received power is also varying. From a communications point of view, the variations in received power cause the SNR to change constantly which results in changes in BER of the systems performance. This simply means that in mobile FSO link, it is difficult to maintain a constant high data rate that is required by the system. The system requires that the received power level should be within the maximum and minimum allowable power levels even if the distance between the transmitter and the receiver terminals changes.

Mobile FSO Link Analysis Figure 6.4 shows a FSO link configuration for a transmitter and a receiver mounted on mobile platforms. The transmitter *Tx* is travelling up with a velocity $v_{Tx(t)}$ and the receiver *Rx* is traveling down with a velocity $v_{Rx}(t)$, the range *R(t)* between the transmitter and the receiver is varying with time while keeping the horizontal separation *d* constant while both terminals move. The resulting beam profile on at the receiver plane is *W(t)*. At any time *t*, the separation between *Tx* and *Rx* is given by:

$$R(t) = \frac{d}{\sin \alpha(t)} \tag{6.23}$$

where $\alpha(t)$ the angle between *Tx* and *Rx* is also varying with time. If we assume the lowest order transverse Gaussian beam, $U_0(\bar{r},0)$ for the transmitting beam, then we can write [20]:

$$U_0(\bar{r},0) = A_0 e^{\left(-\frac{r^2}{W_0^2} - j\frac{kr^2}{2F_0}\right)} \tag{6.24}$$

where A_0 is the amplitude of the wave, r is the distance from the center line in the transverse direction, $j^2 = -1$, W_0 is the effective beam radius at the transmitter, F_0 is the parabolic radius of curvature of the phase distribution, and k is the optical wave number. If we substitute α_0 as follows:

$$\alpha_0 = \frac{2}{kW_0^2} + j\frac{1}{F_0} \tag{6.25}$$

then Eq. (6.24) can be written as:

$$U_0(\bar{r},R(t)) = A_0 e^{\left(-\frac{1}{2}\alpha_0 kr^2\right)} \tag{6.26}$$

The optical field at the distance *R(t)* can be written as Huygens-Fresnel integral [20]:

$$U_0(\bar{r},R(\mathrm{t})) = -2\,\mathrm{jk}\int\int_{-\infty}^{\infty} G(\bar{s},\bar{r};\ R(t))U_0(\bar{s},0)d^2s \tag{6.27}$$

where $U_0(\bar{s},0)$ is the optical wave at the source plane, i.e., at the ground station transmitter plane and $(\bar{s},\bar{r};\ R(t))$ is a Green's function. In general, Green's function is a spherical wave which, under the paraxial approximation, can be expressed as [20, 21]:

$$G(\bar{s},\bar{r};\ R(t)) = \frac{1}{4\pi R(t)} e^{\left[jkR + \frac{jk}{2R(t)}|\bar{s}-\bar{r}|^2\right]} \tag{6.28}$$

Evaluating the integrals, a Gaussian-beam wave with complex amplitude $\frac{A_0}{1+j\alpha_0 R(t)}$ can be obtained as

$$U_0(\bar{r},R(t)) = \frac{A_0}{1+j\alpha_0 R(t)} e^{\left[jkR(t) - \frac{1}{2}\left(\frac{\alpha_0 kr^2}{1+j\alpha_0 R(t)}\right)\right]} \tag{6.29}$$

where $\left[1+j\alpha_0 R(t)\right]$ is the propagation parameter [21]. In terms of the input plane beam parameters, such as beam radius, the following parameters are defined:

$$\Theta_0 = \mathrm{Re}(1+j\alpha_0 R) = 1 - \frac{R(t)}{F_0} \tag{6.30}$$

$$\Lambda_0 = \mathrm{Im}(1 + j\alpha_0 R) = \frac{2R(t)}{kW_0^2} \tag{6.31}$$

The parameter Θ_0 describes the amplitude change in the wave due to focusing, and Λ_0 describes the amplitude change due to diffraction. The receiver parameters can be expressed in terms of the source parameters:

$$\text{and} \quad \Theta = \frac{\Theta_0}{{\Theta_0}^2 + {\Lambda_0}^2} \quad \text{and} \quad \Lambda = \frac{\Lambda_0}{{\Theta_0}^2 + {\Lambda_0}^2} \tag{6.32}$$

where Θ and Λ are the receiver beam parameters. The beam radius W and the phase front curvature F at the receiver are given by [21]:

$$\Theta = 1 + \frac{R(t)}{F}, \ \Lambda = \frac{2R(t)}{kW^2(t)} \tag{6.33}$$

The beam radius at the receiver *Rx* can be written as:

$$W(t) = W_0({\Theta_0}^2 + {\Lambda_0}^2)^{1/2} = \frac{W_0}{(\Theta^2 + \Lambda^2)} \tag{6.34}$$

The distance between *TX* and *Rx R(t)* is related to the angle $\alpha(t)$ between them as shown in the Eq. (6.23). Thus, the beam radius can be written as:

$$W(t) = W_0 \left[\left(1 - \frac{\frac{d}{\sin\alpha(t)}}{F_0} \right) + \left(2\frac{\frac{d}{\sin\alpha(t)}}{kW_0} \right) \right]^{1/2} \tag{6.35}$$

The Gaussian-beam wave at the receiver is:

$$U_0(\bar{r}, R) = A_0(\Theta - \Lambda) e^{\left(jkR - \frac{r^2}{W^2(t)} - j\frac{krt^2}{2F} \right)} \tag{6.36}$$

The irradiance or intensity of the optical wave is the squared magnitude of the field. Thus at the receiver, the irradiance is given by [20]

$$I^0(r, R) = \left| U_0(r, R) \right|^2 \tag{6.37}$$

The total power at the receiver can be calculated from [20]

$$P = \int\int_{-\infty}^{\infty} I^0(r, R) d^2 r \tag{6.38}$$

Therefore, for mobile terminals (*Tx* and *Rx*), the divergence of the beam and the power can be computed so that the gimbals be rotated by proper aligning in order to improve the performance of the mobile FSO communication link.

Simulation results are presented [22] for a mobile FSO link using the following parameters: a 20 mW laser transmitter operating at a wavelength of 1.55 μm for a constant distance, d of 1,000 m, varying angle $\alpha(t)$ from $+15°$ to $-15°$, and the effective beam radius of the transmitter of 2 cm with a half angle divergence of 100 μrad. The simulation results reported are: The Gaussian beam profile at minimum and maximum transmitter-receiver separation is spread upto 0.67 and 0.18 radial distance, the receiver beam radius for alignment varies from 24.1 to 88.0 cm (this variation on receiver beam profile requires the implantation of a tracking algorithm to take account of this variations), and the received power varies from a maximum of 19.9 mW to a minimum of 16.9 mW for the 20 mW laser transmitter at 1.55 μm.

A tracking control method for an active FSO communication system is presented in [23] that enables a mobile terminal to be tracked in a user network area with short-range coverage. The active FSO system consists of paired terminals of a transmitter with a laser diode (LD) and a receiver with a PD. Each terminal controls the path of the laser beam to align it with the optical axis of the PD regardless of the positional changes between the terminals. An extended Kalman filter method proposed in their work in order to estimate the relative position and orientation between the terminals which is required by the axis alignment control.

For a successful PAT for a FSO links between ground and aerial vehicles is presented [24] with the capability of a high precision, agile, digitally controlled two-degree-of-freedom electromechanical system for positioning of optical instruments, cameras, telescopes, and communication laser.

6.3.2 MANET FSO Communication Links

The recent proliferation of wireless technologies for various user applications have prompted a tremendous wireless demand. Wireless nodes are essential to provide the full ranges of connectivity for gathering and exchanging information anytime, anywhere and are expected to dominate the Internet soon. Smartphones via WiFi and mobile Web allow users to get information anywhere and anytime. There is thus the exploding mobile wireless traffic demand which can only be met by leveraging the enabled optical wireless spectrum with high bandwidth capacity. Ultra-high-speed MANETs with cooperative multiple-input-multiple-output (MIMO) can satisfy today's tremendous wireless demand. This subsection will discuss the basics of FSO MANETs with conceptual node designs.

Mobile FSO Communications and MANETS FSO and MANETs are two areas in telecommunications research that have been shown rapid development over the last several years. A MANET enhanced with FSO communication units would provide improved solutions for telecommunication services where infrastructure is unavail-

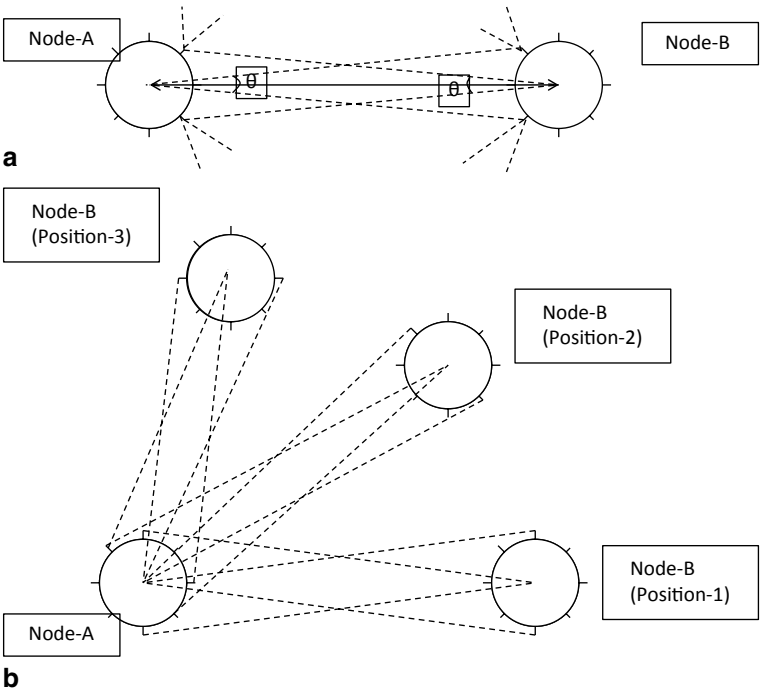

Fig. 6.5 **a** Multielement optical antenna with an interface having an alignment table on Node A to determine which interfaces of Node B can be aligned. **b** Conceptual scenario for alignment of two nodes (*Reprinted with permission [25])*

able, such as emergency response, disaster recovery, environmental monitoring, etc. The key limitation of FSO for mobile communication is that the LOS alignment has to be maintained all the time during successful communication. The transmitter and receiver pair should be aligned with respect to the focused optical beam with the capability to compensate for any sway or mobility.

For MANET to operate successfully, accurate alignment is essential. A timer-based alignment implementation is presented [25] in auto-alignment circuitry where interface alignment procedure is implemented periodically instead of sending a packet every. A timer is introduced which goes off with a predetermined (roughly 0.5 s) frequency and calculates the alignments in the network. Every transceiver determines its neighbor and keeps a table that has an entry for each aligned transceiver. A basic multielement antenna is shown in Fig. 6.5 (a) where an interface on Node A has an alignment table to determine which interfaces of Node B are to be aligned (those who are within the FOV of Node A). Every transceiver in the network keeps a table for keeping track of its neighboring transceivers which is used for alignment. Only when the interfaces are aligned, the channel delivers the packet to the transceiver. Figure 6.5 (b) shows a mobile scenario with two nodes: Node A (stationary) and Node B (moving). The two nodes lose their alignment when Node B is in an intermediate state, i.e., between position 1 and 2, or between position 2 and 3. In order to maintain the connection between the two nodes, choosing the

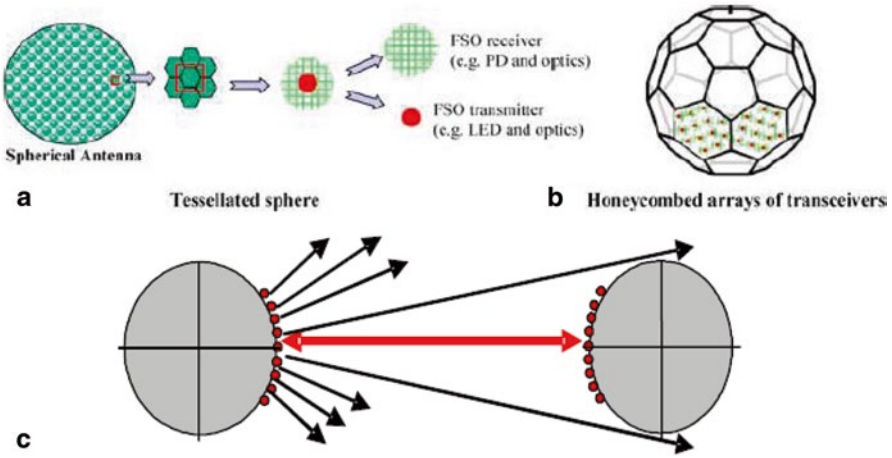

Fig. 6.6 3-D spherical FSO systems with optical transceivers. **a** Translated sphere. **b** Honeycombed arrays of transceivers. **c** 3-D spherical FSO mode showing a line-of-sight (LOS) maintenance(*Reprinted with kind permission from Springer Science+Business Media B.V., 2007, Figs. 1(a), 1(b), and (3)* [26]). *FSO* free-space optical

divergence angle and increasing the number of transceivers may be helpful. An auto-alignment circuitry has been designed [26] to remedy the problem of hand-off. When the two nodes are mobile, the alignment between them is lost and is to be regained, and the two transceivers should be changed in both nodes to accommodate these changes. Auto-alignment circuitry delivers quick response and auto hand-off of logical flows among different transceivers. In the Fig. 6.5 (b), an auto-alignment circuitry in Node A, e.g., will switch from one interface to another interface and finally to an interface in Node B position 1 as Node B changes its position from position 1 to position 2 and position 3, thus handing off the logical stream to a different physical channel. Thus to ensure uninterrupted data flow, auto-aligning transmitter and receiver modules are necessary.

Practical Issues for MANET Alignment and Recent Development MANET design with multi-transceiver optical wireless spherical structures: A concept of spherical FSO node is presented [26, 27]. The spherical FSO node provides the needed angular diversity and LOS in all directions. Figure 6.6 (a) shows the general concept of spherical surfaces where 3-D arrays of FSO transceivers are installed. Each transceiver on the sphere has a transmitter (e.g., Light Emitting Diode, LED) and optical receiver e.g. PD). To minimize the geometric loss due to beam divergence, the transmitter size should be as small as possible, and the receiver as large as possible within one slot of the 3-D array. This arrangement not only improves the range characteristics (availability of light source in every direction) but also enables multichannel simultaneous communication through multiple transceivers. One of the optimum designs includes constructing the nodes in honeycombed arrays of transceivers as shown in Fig. 6.6 (b). An auto-alignment circuitry is also incorporated which selects which transceiver to use for data communication. Figure 6.6 (c) depicts the 3-D spherical FSO node showing a LOS maintenance.

Communication Coverage Propagation Model and Optimal Coverage Higher packaging density can improve communication performance by providing higher aggregate coverage, but also introduces interference of the neighboring transceivers. The coverage area may be defined [27] as the area, points of which are within the LOS of the FSO node. Let r equal the radius of the circular 2-D FSO node (for the purpose of analysis, a 2-D FSO is considered and then a 3-D FSO is analyzed), ρ = the radius of a transceiver, θ = the divergence angle of a transceiver, and τ = the length of the arc in between two neighboring transceivers on the 2-D circular FSO node. For n transceivers placed at equal distance gaps on the circular FSO node, and the diameter of a transceiver 2ρ, τ is then given by [27]:

$$\tau = \frac{2\pi r - n2\rho}{n} = 2\left(\frac{\pi r}{n} - \rho\right) \tag{6.39}$$

The angular difference φ between two neighboring transceivers is given by [27]:

$$\varphi = 360^\circ \frac{\tau}{2\pi r} \tag{6.40}$$

The FSO transceiver's convergence (the vertical projection of a lobe) is approximated as the combination of a triangle and a half circle [27]. Let R be the height of the triangle so that the radius of the half circle is $R\tan\theta$. The coverage area of a single transceiver L can be derived from:

$$L = R^2 \tan\theta + \frac{1}{2}\pi(R\tan\theta)^2 \tag{6.41}$$

The coverage area C of a single transceiver can be found for two cases, (i) coverage areas of the neighbor transceivers do not overlap, and (ii) coverage areas of the neighbor transceivers overlap. The coverage areas of the neighbor transceivers do not overlap when $\tan\theta \le (\mathrm{R} + \mathrm{r})\tan\left(\frac{\varphi}{2}\right)$, and the coverage area is the same as the coverage area, i.e., $C = L$. When the coverage area of the neighbor transceivers overlap, i.e., $\tan\theta \ge (\mathrm{R} + \mathrm{r})\tan\left(\frac{\varphi}{2}\right)$, the coverage area is the coverage area excluding the area that interferes with the neighbor transceiver, i.e., $C = L - I$, where I is the interference area that overlaps with the neighbor transceiver's coverage. A prescription and geometry is given in [26] to find the interference area.

The Maximum Range $\mathbf{R}_{\max}$ The maximum range R_{max} that can be reached by the 2-D FSO node depends on the transmitter's and receiver's optical and electro-optical characteristics, geometry, the atmospheric attenuation, and geometrical spread of the FSO node. The geometric attenuation A_G is a function of the transmitter radius, γ, the radius of the receiver (on the other receiving FSO node) ζ cm, divergence angle of the transmitter θ, and the distance between the transmitting node and receiving node R and is given by [26]:

$$A_G = 10\log\left(\frac{\zeta}{\gamma + 200\,R\theta}\right)^2 \tag{6.42}$$

The atmospheric attenuation A_L depends on the absorption and scattering of the optical transmitting wave by the atmospheric molecules and aerosols and is given by:

$$A_L = 10\log(e^{-\sigma R}) \tag{6.43}$$

where σ is the attenuation coefficient due to both absorption and scattering coefficients. For FSO communications, Mie scattering dominates the other losses and σ (Km) can be written as (in terms of the visibility), V (Km) for a transmitting wavelength λ [28]:

$$\sigma = \frac{3.91}{V}(\lambda/550)^{-q} \tag{6.44}$$

where q is the size distribution of the scattering particles and depends on the visibility V: $q = 1.6$ (for $V \geq 50$ Km, 1.3 (for 6 km $50 \leq V < 50$ Km), and 0.585 $V^{1/3}$ (for V < 6 km).

For a transmitter source power of P dBm and receiver sensitivity $S = -43$ dBm, the following inequality needs to be satisfied for detecting optical signal:

$$S - P < A_L + A_G - (P + 43) < A_L + A_G \tag{6.45}$$

From the inequality, the maximum solution of which is R_{max}:

$$-(P + 43) < 10\,log(e^{-\sigma R}) + 10\,log\left(\frac{\zeta}{\gamma + 200R\,\theta}\right)^2 \tag{6.46}$$

R can be solved from the above equation to determine the maximum range for a given FSO transmitter and receiver parameters and atmospheric condition. The optimal number of transceivers that should be placed on the 2-D circular FSO node is obtained by optimizing the total effective coverage area of n transceivers, i.e., nC. Note that C depends on P, θ, V, and n. For a given r and ρ, the optimization problem can be written as [27]:

$$\max_{\theta, \mathrm{P}, \mathrm{V}, \mathrm{n}} \{nC(\theta, P, V, n)\} \tag{6.47}$$

As an example, a task can be to optimize the parameters such that 0.1 mRad $\leq \theta$, P ≤ 32 mW, and $V \leq 20$, 200 m.

Development of MANET technology is extremely important for satisfying the high demands for telecommunication for today and for the future.

References

1. V. Gadwal, S. Hammel, Free-space optical communication links in a marine environment. Proc. SPIE. **6304**, 1–11 (2006)
2. T. I. Kin, H. Refai, J.J. Sluss Jr., Y. Lee, Control system analysis for ground/air-to-air laser communications using simulation. Proc. IEEE 24th Digital Avionics Syst. Conf. 1.C.3-1–1.C.3-7 (2005)
3. A. Harris, J.J. Suss Jr., H.H. Refai, Alignment and tracking of a free-space optical communication link to a UAV. Proc. IEEE 24th Digital Avionics Syst. Conf., IEEE Conf. 0-7803-9307-4/05/, 1.C.2-1–1.C.2-9 (2005)
4. A. Biswas, S. Pazzola, Deep-space optical communications downlink budget from mars: System parameters. Interplanetary Network Progress Report, Jet Propulsion Laboratory (2003)
5. W. Zhang, S. Hranilovic, Short-length raptor codes for mobile free-space optical channels. 978-1-4244-3435-009/IEEE ICC Proc. (2009)
6. G.G. Ortiz, S. Lee, S. Monacos, M. Wright, A. Biswas, Design and development of a robust ATP subsystem for the Altair UAV-to-Ground Laesrcom 2.5 Gbps Demonstration. SPIE Proc. **4975**, 103–114 (2003)
7. Ch. Chlestil, E. Leitgeb, S.S. Muhammad, A. Friedl, K. Zettl, N.P. Schmitt, W. Rehm, N. Perlot, Optical wireless on swarm UAVs for high bit rate applications. Proc. IEEE Conf. CSNDSP 19th–21st July, Patras, Greece (2006)
8. A.K. Majumdar, F.D. Eaton, M.L. Jensen, D.T. Kyrazis, B. Schumm, M.P. Dierking, M.A. Shoemake, D. Dexheimer, J.C. Ricklin, Atmoepheric turbulence measurements over desert site using ground-based instruments, kite/tetherd-blimp platform and aircraft relevant to optical communications and imaging systems: Preliminary results. Proc. SPIE **6304**, 63040X-1–63040X-12 (2006)
9. E. Leitgeb, Ch. Chlestil, A. Friedl, K. Zettl, S.S. Muhammad, Feasibility study: UAVs. TU-Graz/EADS, Study (2005)
10. M. Al-Akkoumi, R. Huck, J. Sluss Free-space optics technology improves situational awareness on the battlefield. SPIE Newsroom, 1–3 (2007). 10.1117/2, 1200709.0858
11. A. Harris, J.J. Sluss, H.H. Refai, Free-space optical wavelength diversity scheme for fog mitigation in a ground-to-unmanned-aerial-vehicle communications link. Opt. Eng. **45**(8), 86001 (2006)
12. M. Locke, M. Czarnomski, A. Qadir, B. Setness, N. Baer, J. Meyer, W.H. Semke, High-performance two-axis gimbal system for free space laser communications onboard unmanned aircraft systems. Proc. SPIE. **7923**, 79230M-1–79230M-8 (2011)
13. K.H. Heng, N. Liu, Y. He, W.D. Zhong, T.H. Cheng, Adaptive beam divergence for inter-UAV free space optical communications. IEEE Conf. IPGC (2008)
14. S.G. Lambert, W.L. Casey, *Laser Communications in Space* (Artech House, Boston, 1995)
15. G.C. Gilbreath et al., Large-aperture multiple quantum well modulating retroreflector for free-space optical data transfer on unmanned aerial vehicles. Opt. Eng. **40**(7), 1348–1356 (2001)
16. P.G. Goetz et al., Modulating retro-reflector lasercom systems at the naval research laboratory. The IEEE Military Communications Conference- Unclassified Program- Systems Perspective Track, 1601–1606 (2010). 978-1-4244-8180-410
17. A. Carrasco-Casado, R. Vergaz, J.M. Sanchez-Pena, Design and early development of a UAV terminal and a ground station for laser communications. Proc. SPIE. **8184**, 81840E-1–81840E-9 (2011)
18. A. Carrasco-Casado, R. Vergaz, J.M. Sanchez-Pena, E. Oton, M.A. Geday, J.M. Oton, Low-impact air-to-ground free space communication system design and first results. IEEE Conference on Space Optical Systems and Applications, (2011). 978-1-4244-9685-311

19. S.S. Muhammad, T. Plank, E. Leitgeb, A. Friedl, K. Zettl, T. Javornik, N. Schmitt. Challenges in establishing free space optical communications between flying vehicle. IEEE Proceedings, CSNDSP08, 82–86, (2008). 978-1-4244-1876-308
20. L.C. Andres, R.L. Phillips, *Laser Beam Propagation through Random Media* (SPIE, Bellingham, 1998)
21. A. Ishimaru, *Wave Propagation and Scattering in Random Media* (IEEE, Piscataway, 1997)
22. A. Harris, T. Giuma, Divergence and power variations in mobile free-space optical communications. IEEE Third International Conference on Systems, 174–178 (2008). 978-0-7695-3105-208
23. K. Yoshida, T. Tsujimura, Tracking control of the mobile terminal in an active free-space optical communication system. SICE-ICASE International Joint Conference, 89-950038-5-5 98560/06, Bexco, Busan, Korea, 369–374, (Oct. 18–21, 2006)
24. V.V. Nikulin, J.E. Malowicki, R.M. Khandekar, V.A. Skomin, D.J. Legare, Experimental demonstration of a retro-reflective laser communication link on a mobile platform. Proc. SPIE. **7587**, 75870F-1–75870F-9 (2010)
25. M. Bilgi, Capacity scaling in free-space-optical mobile ad-hoc networks. A Master's Thesis, at the University of Nevada, Reno, May 2008
26. M. Yuksel, J. Akella, S. Kalyanaraman, P. Dutta, Free-space mobile ad hoc networks: Auto-configurable building blocks. Wirel. Netw. (Springer, 2007). doi:10.1007/s11276-007-0040-y
27. M. Yuksel, J. Akella, S. Kalyanaraman, P. Dutta, Optimal communication coverage for free-space-optical manet building blocks. http://www.shivkumar.org/research/papers/unycn05.pdf, Access date 2014. Also see: CiteSeer × β, Devleoped by Pennsylvania State University, 2007–2010. http://citeseerx.ist.psu.edu/viewdoc/summary?doi=10.1.1.143.5616
28. H. C. van de Hulst, *Light Scattering by Small Particles* (Dover, New York, 1981)

Chapter 7
Other Related Topics: Chaos-based and Terahertz (THz) FSO Communications

Arun K. Majumdar

7.1 Introduction

This chapter discusses two related topics: (i) chaos-based and (ii) terahertz (THz) free-space optical (FSO) communications. The first one is chaos-based FSO communication in which the application of chaos to communications can provide many promising new directions in the areas of coding, security, and ultra-wideband communications. The chapter describes generation and synchronization of optical chaotic signal where chaotic system can be applied to the encryption/decryption blocks of a digital communication system. A hybrid electronic/optical-synchronized chaos communication system is described to achieve secure communication. Chaotic modulation of data may be less sensitive to electronic nonlinearities in the FSO transceivers. The chapter points out that the use of chaotic signals may be very attractive as carriers in spread spectrum communications. A theoretical analysis demonstrating the capabilities of a secure free-space communication system using phase shift keying (PSK) modulation scheme and coherent digital receiver is presented to enhance communications security. Some recent experimental results of chaotic free-space laser communication over a turbulent channel are described.

With increasing demand, THz frequencies are being considered for short-range, high data rate applications. THz-based FSO communications is the second main topic of this chapter. It has the potential to add new capabilities for imaging, communications, sensors, and materials research. Because THz waves have a combination of optical and radio properties, they can be reflected and scattered more easily than light waves and can thus be applied to short-range FSO systems. The chapter provides information about quantum cascade laser and quantum well photo detector for THz generation and detection, modulators with THz bandwidth, and some recent results of THz FSO link.

A. K. Majumdar, *Advanced Free Space Optics (FSO),*
Springer Series in Optical Sciences 186, DOI 10.1007/978-1-4939-0918-6_7,
© Springer Science+Business Media New York 2015

7.2 Chaos-based FSO Communications

7.2.1 Basics of Chaotic Optical Communications

Mathematical way to generate chaos Chaotic behavior can be expected from any dynamic system that shows sensitivity towards initial conditions, i.e., a very high relationship with the previous values exists so that the value of the system at any point of time depends on the previous values. Small differences in initial conditions yield widely diverging outcomes for chaotic systems. Chaotic system possesses the ideal characters to be employed in crypto systems and by using chaotic methods, we can prevent all kinds of intrusions. The message can be hidden with the chaos and be sent via an FSO communication link. The message can only be retrieved at the receiver's end by generating the same chaos. Chaos can be generated mathematically. Recursive algorithms can be used to calculate the values. Any X_i^{th} value depends immediately on ${X_{i-1}}^{th}$ value so that the value can be recursively calculated. Mathematical equations can be used to calculate in simpler way. Consider the following function:

$$f(x) = p * x * (1 - x) \tag{7.1}$$

The above second-order function can be used to generate mathematical chaos. The above equation is bounded for the limits $0 < p < 4$. The equation can be written as:

$$x_{n-1} = p * x_n * (1 - x_n) \tag{7.2}$$

The starting value is x_0 and in this iterative form every nth value depends on all other previous values. The plot of such functions is also called chaotic maps. For $0 < p < 3$, the function converges to a particular value after some number of iterations. As p is increased to just greater than 3, the curve splits into two branches. This splitting is termed bifurcation. Mathematically, this tends to chaos. As the parameter "p" is further increased, the curves bifurcate again. With further increased value of "p," the bifurfaction becomes faster and beyond a certain value of "p" known as the "point of accumulation" periodicity gives way to complete chaos. This happens for $p > 3.57$ whereas for $p = 4$, chaos values are generated in the complete range of 0 to 1. This is the point we are interested in. During $3.6 < p < 4$, complete randomness and chaotic behavior is observed.

Chaotic signals generated in nonlinear electrical circuits [1–3] and lasers [4] can potentially be used as carriers for information transmission in a communication system. The advantage of a broadband information carrier is that it can enhance the robustness of communication channels to interferences with narrowband disturbances. The broadband coding signal in a chaos-based communication is generated at the hardware level where chaotic carriers offer a certain degree of privacy in the data transmission. Thus, a new type of high data rate communication system can be designed using waveforms generated by deterministic chaotic system to carry

information in a robust manner. Chaotic communication systems are based on chaos synchronization where synchronized chaotic emitters and receiver lasers are employed to encode and decode information at the hardware level. The generated chaotic signal at the emitter hides the message which can be recovered when using the appropriate receiver. Messages (information) are embedded within a chaotic carrier in the emitter, and recovered after transmission by a receiver which is synchronized with the emitter. A nonlinear filtering process is performed at the receiver where a message-free chaotic signal is generated locally which is then subtracted from the encoded transmitted signal to recover the message (information). Chaotic optical communication is possible when the broadband chaotic emissions from two spatially separated emitters (lasers) are synchronized to each other. In order to satisfy the requirement for synchronization of the two lasers, the irregular time evolution of the emitter laser optical power must be perfectly reproduced at the receiver laser. Decoding the message from the chaotic carrier is based on the nonlinear phenomenon of chaos synchronization between the emitter and the receiver so that the message can be extracted by subtracting the chaotic carrier from the input (chaotic carrier + message).

7.2.2 Chaotic FSO Communication over Atmospheric Turbulent Channel

Feasibility of chaos-based communications using fiber-optic links have been already proposed and demonstrated in the past [5, 6]. Chaotic communication in several optical systems are discussed where an erbium-doped fiber ring laser (EDFRL) produces chaotic fluctuations of light intensity onto which is modulated a message consisting of a sequence of pseudorandom digital bits [5]. Chaos and message together propagates through a standard single-mode optical fiber from the transmitter to a receiver. Message from the chaos is recovered at the receiver. The fiber link is 35 km and the data rate up to 250 Mbps is achieved by the researchers. High-speed long-distance chaos-based communications over a commercial fiber-optic channel is presented [6] for a transmission over 120 km of optical fiber at data rates of Gbps ranges achieving bit-error rates (BER) below 10^{-7}. The results provide a convincing proof-of-practical concept for optical chaos communications technology.

Although much research have been done for chaotic optical communications using fiber channels, FSO chaotic communication over a real-life highly random channel such as turbulence has not been investigated as much. This subsection discusses the concept for developing and designing FSO communication systems based on encoding and decoding of chaotic signals for recovering messages in presence of atmospheric turbulence media.

a. Double-pass Chaotic FSO Communication Link

One of the first chaotic free-space laser communications over a turbulent channel is reported [7] where a chaotic self-synchronizing free-space laser communication in

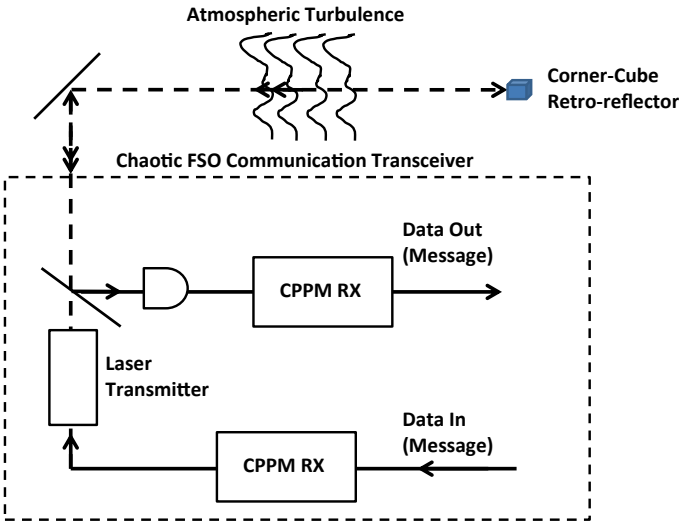

Fig. 7.1 Block diagram of a double-pass chaotic *FSO* (free-space optical)communication through atmospheric turbulence

presence of severe communication signal distortions caused by atmospheric turbulence is studied experimentally. A double-pass propagation link (~ 5 km round-trip path) using a corner cube reflector is used in their demonstration. Figure 7.1 shows a block diagram of a double-pass chaotic FSO communication. A 10 mW semiconductor laser beam ($\lambda = 690$ nm) coupled to a single-mode fiber is transmitted towards a corner-cube retroreflector 2.5 km away. The reflected beam is received by the same telescope (used by the transmitter) and is detected by a photodetector. The scintillation index for the turbulence is about 0.8–0.9, indicating a strong turbulence regime. A chaotic laser communication transceiver consists of a laser generating a chaotic sequence short-term (~ 1.0 μs) on-off pulse, triggered by transistor-transistor logic (TTL) pulse signal from a chaotic transceiver controller where the chaotic sequence of the time intervals corresponds to iterations of a chaotic process with the binary information signal added to the chaotic signal. This way a chaotic pulse position modulation (PPM) is used. The interpulse interval fluctuates chaotically ranging from 10 to 25 μsec at a ~60 kbps bit rate. A chaotic pulse position modulation receiver receives the distorted chaotic pulses detected by the photodetector, and the information signal is finally recovered from chaotic iterations. This method of chaos communication is referred to as chaotic pulse position modulation (CPPM). The BER from the real-time transmission of binary pseudorandom code data is measured to be 1.92×10^{-2}. This research thus proves the concept of chaos communication in presence of atmospheric turbulence using self-synchronizing method.

b. One-way Chaotic FSO Communication Link

Figure 7.2 shows a block diagram of a chaotic FSO communication system in presence of atmospheric turbulence channel. At the transmitter end, there is a master

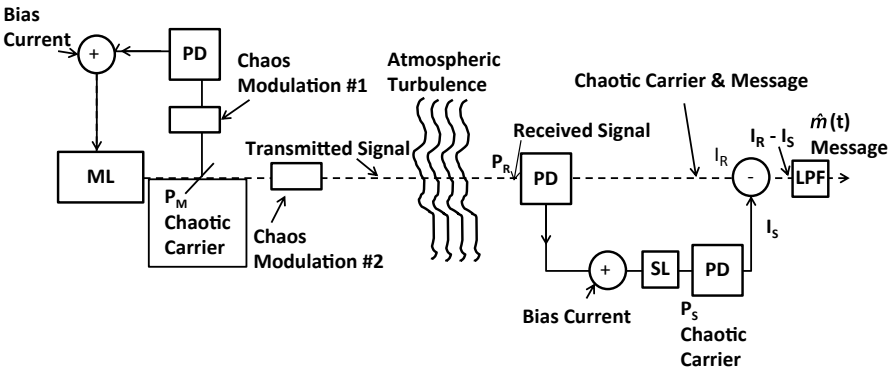

Fig. 7.2 Block diagram of a chaotic free-space optical communication system in atmospheric turbulence. The encoded message *m(t)* can be modulated either by *CIM* (chaotic intensity modulation) or *ACM* (additive chaos modulation method)

laser which is routed to chaos through a delayed optoelectronic feedback and then a message is embedded in the generated chaotic carrier. At the receiver end, a twin semiconductor laser (the slave laser) is required to synchronize to the chaotic master laser so that the message can be recovered by operating a difference between chaos and received signal and by low-pass filtering. The system described here allows for effectively masking the message at the transmitter so that an eaves-dropper is not able to recover the hidden message. The encoded message *m(t)* can be modulated either by a chaotic intensity modulation (CIM) or the additive chaos modulation (ACM) method. In the first method (CIM), the message is superposed just before the transmitter output by an intensity modulation so that the transmitted power, $P_T(t) = [1 + m(t)]\ P_M(t)$ *where* $P_M(t)$ is the chaotic carrier power. In the second method (ACM), the message can be summed inside the feedback loop to influence the chaos generation and create a symmetric scheme (the message is sent to both master and slave lasers).The signal power at the receiver P_R is converted into the photocurrent I_R. A bias current is added to the slave laser and the chaotic carrier P_S is generated through the synchronization process. If synchronization is perfect, the two carriers are equal, i.e., $P_S = P_M$. The message now can be recovered by the difference I_R-I_S. The low-pass filter eliminates the high-frequency noise and chaos components with a bandwidth B_{LPF} equal to that of the PPM pulse: $B_{LPF} = R_b M(d \log_2 M)^{-1}$ where R_b is the data (bit) rate, M is the PPM order, and d is the slot duty cycle. Note that here the message is encoded through a PPM method.

Recently numerical evaluation of the performance of an indoor free-space chaotic communication system operating at 1550 nm in presence of multipath reflections and ambient light noise is presented [8]. The Q-factor versus bit rate for two modulation schemes CIM and ACM are reported. The details are discussed in the reference [8].

A hybrid electronic/optical-synchronized chaos communication system is presented [9]. The authors reported free-space propagation demonstration. The chaotic

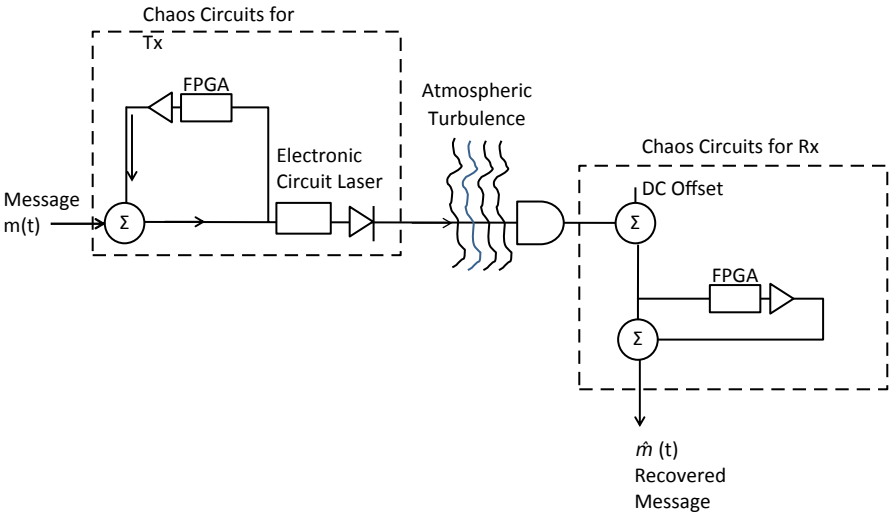

Fig. 7.3 Hybrid electronic/optical-synchronized chaos *FSO* (free-space optical) communication system

source is an electronic circuit and the transmitter is a laser. The chaotic signal is electronically injected onto an optical carrier for transmission by adding the current-boosted chaotic signal to the direct current (DC) injection current of a semiconductor laser. An optical chaotic carrier (to which a message can be added) is generated that can be transmitted in the free space. The received signal is generated by a photodetector and is applied to a matched receiver electronic circuit. Chaos synchronization and successful message recovery is thus possible with the system. The chaotic carrier plus message can be transmitted by line-of-sight, point-to-point, and free-space propagation of a laser beam. The chaotic electronic circuit [9] is a delay differential feedback (DDF) chaotic system that uses a field programmable gate array (FPGA). A concept block diagram for this hybrid electronic/optical synchronized FSO chaos communication system is shown in Fig. 7.3. The system can be operated in presence of atmospheric turbulence. The DDF can produce a high-dimensional chaos which can also improve communication security. When a message is added, the matched receiver DDF circuit only synchronizes with the chaotic transmitter and the message recovery is achieved by subtraction of the output from the input to the receiver circuit. The principle of hybrid electronic/optical chaos communication system is clearly demonstrated [9].

A new scheme for chaotic cryptography of an optical signal transmitted in a FSO link is shown in Fig. 7.4. Chaotic dynamics and synchronization are obtained by current injection into a laser pair of a common, chaotic driving signal.

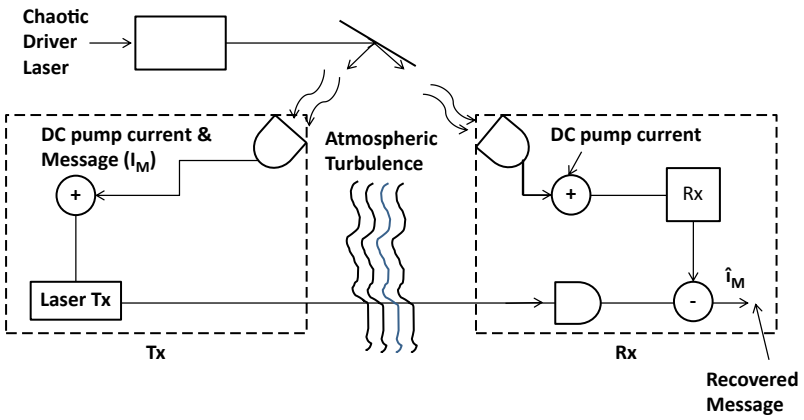

Fig. 7.4 Secure data transmission with semiconductor lasers as *Tx* and *Rx*, which are routed into the chaotic regime and synchronized by current injection of a common, chaotic-driving signal

7.2.3 Acousto-optic (AO) Chaos-based Secure FSO Communication Links

Chaos generated by acousto-optic (AO) system with feedback to encrypt a laser beam carrying data is reported [10]. Preliminary results on using such an encryption and decryption technology in building FSO communication system is discussed. Chaos encryption of data using external signal modulation of the diffracted light from a hybrid AO cell is reported. Numerical simulation shows that decryption of the encoded data is possible by using an identical AO system in the receiver. Encryption of optical signals using external modulation of the diffracted light in AO modulators and retrieval and de-encryption of the encoded signal using parametrically synchronized chaotic demodulation with another AO cell are shown to be possible [11, 12].

Most of the chaotic encryption and decryption reported were performed using nonlinear dynamics of external cavity feedback in semiconductor lasers. Researchers also generated the chaos using the nonlinearities in Er-doped fiber lasers. The researchers presented [11, 12] some results to show the possibility of (a) encryption of optical signals using external modulation of the diffracted light in AO modulators and (b) retrieval and decryption of encoded signal using parametrically synchronized chaotic demodulation with another AO cell.

A laser beam diffracted by an AO Bragg cell-based chaos encryption system is reported [11]. A diffracted laser beam is detected by a photodiode (PD) whose output is fed back electronically to the Bragg cell. In an AO cell-based FSO communication links, the data beam is made secure through chaos encryption. Chaotic modulation of the diffracted and un-diffracted beams at the output of the AO cell is achieved with suitable values of the feedback and gain parameters of the optoelectronic system. The modulation may be achieved by adjusting the bias voltage via

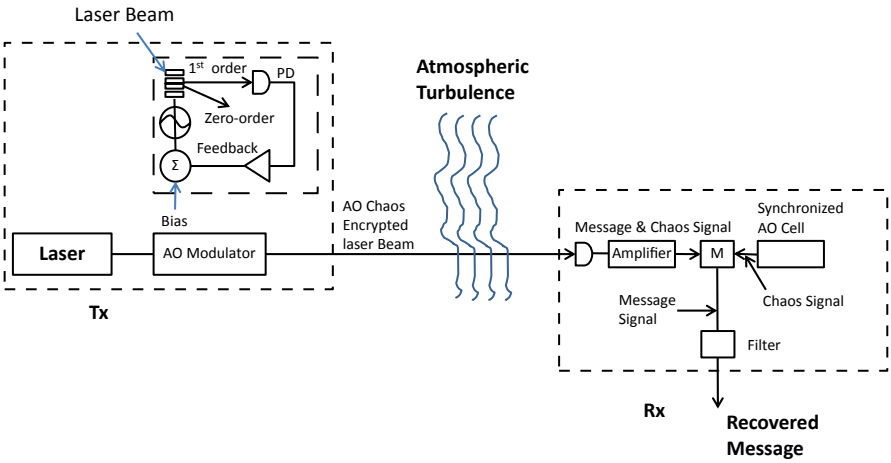

Fig. 7.5 A schematic block diagram of the chaos encryption and decryption with acousto-optic (AO) modulator

adding a modulation signal to the DC-bias level [10]. It may also be achieved by external modulation of the chaotic laser beam enabling of the chaotic signal. The chaos-encrypted beam can be detected by a PD at the receiver. Figure 7.5 shows a schematic block diagram of the chaos encryption and decryption with AO systems which shows that the current from the PD is mixed with a chaotic signal generated by an AO system identical to the one in the transmitter. It is possible to scale the chaos and the modulation bandwidth up to MHz range [10] or higher by adjusting such parameters as the delay time in the AO feedback loop.

7.3 THz FSO Communications

Edholm's law of bandwidth [13] predicts that the demand for point-to-point bandwidth in wireless short-range communications has doubled every 18 months over 25 years, and the need of data rates around 5–10 Gbps in 10–15 years from now. The carrier frequencies need to be increased beyond 100 GHz to achieve 10 Gbps data rate. Such systems will soon push towards the low THz frequency range. It is predicted [14] that wireless local area network (LAN) systems will be replaced or supplemented by the THz-based communication systems in 2017–2020. TheTHz region of the electromagnetic spectrum is typically defined as the frequency range of 0.1–10 THz corresponding to the free-space wavelength from 2 mm to 30 μm ("THz gap"). Figure 7.6 shows electromagnetic spectrum where THz region is labeled to cover 0.1–10 THz. THz wireless communication link offers some advantages compared to microwave or millimeter waves: ultra-high bandwidth, unregulated frequencies (above 300 GHz, unregulated by Federal Frequency Allocation

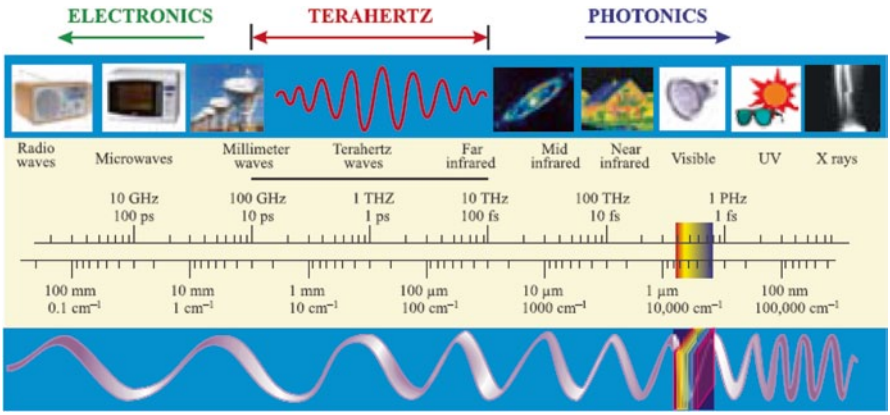

Fig. 7.6 Electromagnetic spectrum showing *THz* (terahertz) region. (Reprinted with kind permission from Springer Science+Business Media B.V., 2011, Fig. 1 [15])

Commission, FCC), less free-space diffraction than MMW links, high security. Compared to infrared (IR) links, THz has also some advantages: lower attenuation loss compared to IR attenuation under certain weather conditions (fog and dust), less scintillation effects, more eye safe than IR with available commercial source power. THz communication systems with gigabit or higher data rates have many high bandwidth potential applications such as wireless extension of broadband access fiber optical networks and of high-speed wired local networks, a wireless bridge between lower data rate wireless LANs and high-speed fiber-optical networks, high-definition television (HDTV), and broadband indoor wireless communications using portable handheld devices.

7.3.1 Atmospheric Effects Relevant to thz FSO Communication Links

For outdoor THz FSO communication links, the adverse atmospheric conditions, such as fog, rain, dust, snow, and turbulence will affect the performance of transmission links to limit the available signal to noise ratio (SNR) at the receiver and achievable BER. Figure 7.7 compares the atmospheric attenuation of millimeter waves, THz, and IR waves. The THz absorption under fog conditions at ~625 GHz is around 20 dB/km which is much less than the 200 dB/km that the IR at 1.5 µm wavelength suffers. Therefore, THz-based communication systems can serve as a back-up for foggy weather when IR connection is completely lost. Above 200 GHz and below 10 THz, the attenuation is dominated by atmospheric water vapor compared to much less attenuation due to rain and fog. Fog and smoke will cause significant attenuation in the IR to make a FSO communication system practical. Figure 7.8 shows the transmission of THz radiation in air. With current THz

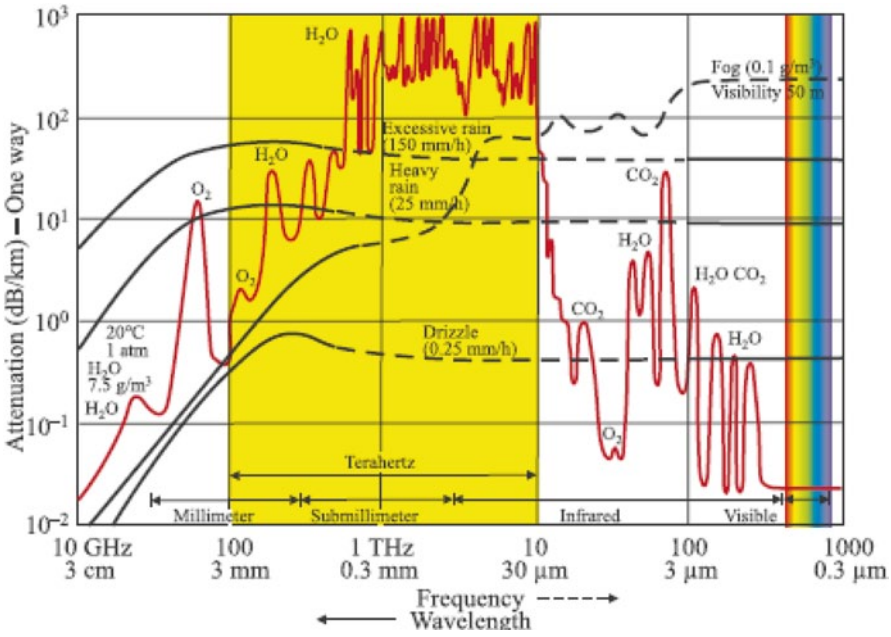

Fig. 7.7 Atmospheric attenuation of millimeter waves, *THz* (terahertz) and *IR* (infrared) waves. (Reprinted with kind permission from Springer Science+Business Media B.V., 2011, Fig. 1 [15])

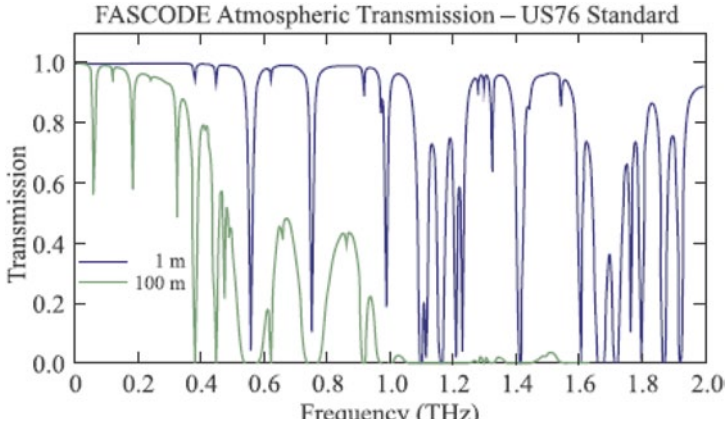

Fig. 7.8 Transmission of *THz* (terahertz) radiation in air. (Reprinted with kind permission from Springer Science+Business Media B.V., 2011, Fig. 1 [15])

detectors and sources, the measurements over distances 20 m are very difficult [15]. Due to considerable attenuation, THz waves are not very useful for long-range FSO communications.

Fog Attenuation Fog attenuation is the result of various scattering mechanisms at THz region. A dimensionless size parameter α is defined in the scattering calculation: $\alpha = \frac{2\pi r}{\lambda}$, where r is the radius of the particle involved in the THz scattering process, and λ is the operating wavelength. Depending on the value of the size parameter, α, the different scattering processes are defined as: $\alpha < 1$ (Rayleigh scattering), $\alpha \approx 1$ (Mie scattering), and $\alpha \gg 1$ (geometric scattering). The size parameter for typical fog droplets with radius 1~20 μm is $\alpha = 0.013 - 0.261$ at 625 GHz frequency. For 625 GHz, the Rayleigh scattering occurs primarily because of the fog particles in the atmosphere. The radiation from Rayleigh scattering is equally divided between forward and backward scattering. Some portion of the THz scattering (for larger value of Mie scattering) can also play some role in the overall scattering process.

Scintillation Effects on the thz Communication Link Scintillation is a result of random intensity and phase fluctuations of an optical wave as it propagates through a turbulent atmosphere. Random temporal and spatial variations of refractive index of the air blobs with thorough mixing cause scintillation. Random deflection and interference between different portions of the wave front can destroy the transmitting phase front of an optical wave when it passes through a few kilometers of propagation path. THz beams are much less to scintillation compared to IR beams used for FSO communication. Although scintillation effects limit the FSO communication performance, the effects are much smaller in THZ band compared to IR region.

Dust and smoke attenuation Due to the relatively small size of atmospheric particles such as dust and smoke compared to THz wavelength, there should be minimal THz attenuation due to airborne particulates. It is predicted that smoke has little or no effect up to 1 THz [16]. Under similar atmospheric conditions, IR wavelengths are strongly attenuated while THz wavelength shows almost no impact. Thus, THz communications are better option than IR wireless links in a situation such as battlefield or wildfire environments in which airborne particulates are extremely high in the atmospheric communication links. Reliable THz communications are possible to establish even in these adverse atmospheric conditions in presence of dust and smoke.

7.3.2 Indoor THz Communication

Because of high attenuation of THz beams, indoor communication seems to be a very viable approach. Indoor communication systems have to rely on non-line-of-sight (NLOS) paths (in addition to line-of-sight, LOS) paths including reflection

from walls. Using Friis equation for establishing a reliable indoor THz link, 31 dB gain antenna is needed to compensate for free-space damping [17]. A link budget analysis shows that a 10% bandwidth for a 350 GHz THz link would require antenna gains of 22 dB, 27 dB, 30 dB, and 33 dB for link distances of 1 m, 3 m, 5 m, and 10 m, respectively [18]. The designs of such antennas are difficult at THz range. Another factor for implementing indoor THz communications is reflective "wall paper" that increases THz reflection from walls in the event of a NLOS path in a room. In addition, for a high data rate, there would be intersymbol interference (ISI) between multiple paths and therefore the data rate must be chosen to eliminate ISI.

7.3.3 THz Wireless Communications Concepts and Hardware Development

THz Transmitter/Source THz time-domain systems can be used for establishing THz communication links. The structures have the following characteristics: (i) photoconductive antenna (PDA) structures are used for both THz transmitter and receiver, (ii) transmits around a center frequency of 0.3 THz, (iii) transmits at the maximum data rate which is limited by the repetition rate of the Ti:Saphire laser (~80 MHz) and electronic bandwidth of the PDA (~1 MHz), and (iv) needs to adjust the transmitter to receiver distance and timing of the gating pulsed for maximum THz signal.

Some of the Recent THz Communication Links Include Transmission of an audio signal through THz communication link utilizing a modified THz time-domain system and external modulator based on the depletion of a two-dimensional electron gas, transmitting the audio signals up to 25 kHz through a 0.48 m distance [19].

Analog THz link modulating the audio signals upon the THz carrier by direct modulation of the bias voltage of the THz receiver, achieving the transmission distance of 100 cm at 20 kHz [20].

Bipolar and on/off keying of THz pulses with maximum modulation index by direct signal data encoding of photoconductive emitter antenna bias voltage enabling high data rates [21].

Error-free operation at BER $<10^{-8}$ is achieved where the data rate dependent ISI are caused by limited receiver bandwidth.

Photonic MMW/Uni-traveling Carrier Photodetector (UTC-PD) Optoelectronics Systems THz communication links are developed for the last few years by Nippon Telegraph and Telephone Corporation (NTT) group in Japan. Some of the THz communication systems developed are: photonic MMW/UTC-PD THz source and Schottky diode detector [22], photonic MMW/UTC-PD THz sources and MMIC receivers [23], and an integrated MMIC transmitter and receiver [24].

Integrated Circuit Systems A coplanar waveguide MMIC chipset is presented which includes amplifiers, modulators, and demodulators as the THz transmitter and receiver in a 10 Gbps wireless link which achieved a BER of 10^{-12} over a distance of 800 m [24]. A 120 GHz transmitter with implementation of forward error-correcting codes has extended the THz communication link distance to 5.5 km with an error-free transmission of 10 Gbps [25].

Multiplied Microwave System An analog and digital video signal transmission at 300 GHz using a microwave multiplier system transmits a color video baseband signal with 6 MHz bandwidth which is modulated on an ultrahigh frequency (UHF) carrier (855.25 MHz) acting as the signal generator to be transmitted over THz link [26].

Quantum Cascade Laser (QCL) Systems A QCL THz free-space communication system consists of a 3.8 THz laser in conjunction with a cryogenically cooled (12 K) quantum well photodetector. The system can transmit analog audio data over 2 m path length. An 8-ns pulse at a repetition frequency of 455 kHz along with an audio frequency modulation then electronically modulates the QCL. After amplification of the electronic output of the photodetector and passing through a 10 kHz low pass filter, the signal is finally passed to the antenna input of an AM radio to recover the audio signal [27].

Some of the recent developments of ultra-speed wireless communication link measurements and hardware developments for carrier frequencies over 100 GHz are summarized in Table 7.1.

For detailed information on THz wireless communications, the interested readers can review the reference [32] and the other references mentioned in this section.

Table 7.1 Some of recent THz hardware and communication link parameters. *MZM* Mach-Zender modulator, *PDA* photoconductive antenna, *UTC-PD* uni-traveling carrier photodetector, *MMIC* millimeter wave integrated circuits, *NEP* noise equivalent power, τ: relaxation time for the modulator, *BER* bet error rate, *QCL* quantum cascade laser

Frequency (GHz)	THz system	THz hardware	Maxi-mum link (m)	Modulation rate/ bandwidth	BER	Reference
300	THz time-domain	a. External modulator (analog) b. PDA(analog) c. Digital	a. 0.48 b. 1 c. 1	a. 6 kHz b. 5 Kb/s c. 1 MHz	c. 10^{-8}	a. [19] b. [20] c. [21]
120	Optoelectronic/UTC-PD	Optical MZM modulator	250 (digital) 450 (ASK)	3 Gb/s	10^{-10}	[23]
120	Millimeter wave integrated circuit	MMIC MMIC	a. 800 b. 5800	a. 10 Gb/s b. 10 Gb/s	a. 10^{-12} b. 10^{-12}	a. [24] b. [25]
300	Microwave multiplication	Sub-harmonic mixer	22	6 MHz		[26]
3800	Quantum cascade laser (QCL)	Electronic modulation of QCL	2	QCL	10 KHz	[27]
a. 300,00 (i.e., 30 THz) b. 10,000 (i.e., 10 THz) c. 30–1500	THz *detector* (uncooled)	a. Piezoelectric (NEP=(1–3)×10^{-9} (W/$Hz^{1/2}$) b. Schottky diodes (NEP = 10^{-10}) c. HgCdTe HEB (NEP~4×10^{-10})		a. 100 Hz b. 10^{10} Hz c. <10^{8} Hz		[28]
a. 1400 b. 750 c. 460	THz *modulators*	a. Silicon b. Meta/ErAs/GaAs c. Meta/HEMT		a. τ = 5 ns b. τ = 20 ps c. 10 MHz		a. [29] b. [30] c. [31]

References

1. K.M. Cuomo, A.V. Oppenheim, Phys. Rev. Lett. **71**, 65 (1993)
2. L. Kocarev et al., Int. J. Bifurcation Chaos. Appl. Sci. Eng. **2**, 709 (1992)
3. T.L. Carroll, L.M. Pecora, IEEE Trans. Circuits Syst. **40**, 646 (1993)
4. P. Colet, R. Roy, Opt. Lett. **19**, 2056 (1994)
5. G.D. Vanwiggeren, R. Roy, Chaotic communication using time-delayed optical systems. Int. J. Bifurcation Chaos. **9**(11), 2129–2156 (1999)
6. A. Argyris, D. Syvridis, L. Larger, V. Annovazzi-Lodi, P. Colet, I. Fischer, J. Garcia-Ojalvo, C.R. Mirasso, L. Pesquera, K.A. Shore, Chaos-based communications at high bit rates using commercial fibre-optic links. Nature. **438**(17), 343–346 (2005)
7. N.F. Rulkov, M.A. Vorontsov, L. Illing, Chaotic free-space laser communication over a turbulent channel. Phys. Rev. Lett. **89**(27), 277905-1–27705-4 (2002)
8. L.U. Fabrizio Chiarello, M. Santagiustina, Securing wireless infrared communications through optical chaos. IEEE Photonics Technol. Lett. **23**(9), 564–566 (2011)
9. J.P. Toomey, D.M. Kane, A. Davidovic, E.H. Huntington, Hybrid electronic/optical synchronized chaos communication system. Opt. Express. **17**(9), 7556–7561 (2009)
10. A.K. Ghosh, P. Verma, S. Cheng, R.C. Huck, M.R. Chatterjee, M. Al-Saedi, Design of acousto-optic chaos based secure free-space optical communication links. Proc. SPIE 7464, 7464OL (2009)
11. M.R. Chatterjee, J.J. Hunag, Demonstartionof acousto-optic bistability andchaos by direct nonlinear circuit modeling. Appl. Opt. **31**(14), 2506–2517 (1992)
12. M.R. Chatterjee, M. AlSaedi, Examinationof chaotic signal encryption, synchronizationand retrieval using hybrid acousto-optic feedback. Proc. OSA FiO/LS/META/OF & T, paper no. FWC3 (2008)
13. S. Cherry, Edholm's law of bandwidth. Spectrum, IEEE. **41**, 58–60 (2004)
14. M. Koch, Terahertz Communications: A 2020 Vision, in *Terahertz Frequency Detection and Identification of Materials and Objects*, ed. by R.E. Miles, X.-C. Zhang, H. Eisele, A. Krotkus (Springer Science and Business Media, Dordrecht, 2007), pp. 325–338
15. A. Rogalski, F. Sizov, Terahertz detectors and focalplane arrays. Opto-Electron Rev. **19**(3), 346–404 (2011) (Springer)
16. C.M. Mann, Towards Terahertz Communication Systems, in *Terahertz Source and Systems*, ed. by R.E. Miles, P. Harrison, D. Lippens (Kluwer, Norwell, 2001)
17. M. Koch, *Terahertz Frequency Detection and Identification of Materials and Objects, Nato Science for Peace and Security Series-B: Physics and Biophysics*, ed. by R.E. Miles, X.C. Zhang, H. Eisele, A. Krotkus (Springer Science and Business Media, Dordrecht, 2007), pp. 325–338
18. R. Piesiewicz, T. Kleine-Ostmann, N. Krumbholz, D. Mittleman, M. Koch, J. Shoebel, T. Kurner, pp. 24-39, IEEE Antennas Propag. Mag. **49**(24) (2007)
19. T. Kleine-Ostmann, K. Pierz, G. Hein, P. Dawson, M. Koch, Audio signal transmission over THz communication channel using semiconductor modulators. Electron. Lett. **40**, 124–126 (2004)
20. T.-A. Liu, G.-R. Lin, Y.-C. Chang, C.-L. Pan, Aireless audio and burst cpmmmuniccation link with directly modulated THz photoconductive antenna. Opt. Express. **13**, 10416–10423 (2005)
21. L. Moller, J. Federici, A. Sinyukov, C. Xie, H.C. Lim, R.C. Giles, Data encoding on terahertz isgnals for communication and sensing. Opt. Lett. **33**, 393–395 (2008)
22. A. Hirata, T. Kosugi, N. Meisl, T. Shibata, T. Nagatsuma, High-direcetivity photonic emitter using photodiode module integrated with HEMT amplifier for a 10-Gbit/s wireless link. IEEE Trans. Microw. Theory Tech. **52**, 1843–1850 (2004)
23. A. Hirata, H. Takahashi, R. Yamaguchi, T. Kosugi, K. Murata, T. Nagatsuma, N. Kukutsu, Y. Kado, Transmission characteristics of a 120-GHz-band wireless link using radio-on-fiber technologies. J. Lightwave Technol. **26**, 2338–2344 (2008)

24. R. Yamaguchi, A. Hirata, T. Kosugi, H. Takahashi, N. Kukutsu, T. Nagatsuma, Y. Kado, H. Ikegawa, H. Nishikawa, T. Nakayama, 10-Gbit/s MMIC wireless link exceeding 800 meters. IEEE Radio and Wireless Symposium 695–698 (2008)
25. A. Hirata, T. Kosugi, H. Takahashi, J. Takeuchi, K. Murata, N. Kukutsu, Y. Kado, S. Okabe, T. Ikeda, F. Suginosita, K. Shogen, H. Nishikawa, A. Irino, T. Nakayama, N. Sudo, 5.8-km 10-Gbps data transmission over a 120-GHz-band wireless link, IEEE International Conference on Wireless Information Technology and Systems (ICWITS), 1–4 (2010)
26. C. Jastrow, K. Munter, R. Piesiewicz, T. Kurner, M. Koch, T. Kleine-Ostmann, 300 GHz channel measurement and transmission system. IRMMW-THz 33rd International Conference on Infrared, Millimeter and Terahertz Waves, 1–2 (2008)
27. P.D. Grant, S.R. Laframboise, R. Dudek, M. Graf, A. Bezinger, H.C. Liu, Terahertz free space communications demonstration with quantum cascade laser and quantum well photodetector. Electron. Lett. **45**, 952–954 (2009)
28. F.F. Sizov, V.P. Reva, A.G. Golenkov, V.V. Zabudsky, Uncooled detector challenges for THz/sub-THz arrays imaging. J. Infrared Millim. Te. doi:10.1007/s10762-011-9789-2 (2011)
29. T. Nozokido, H. Minamide, K. Mizuno, Modulationof submillimeter wave radiation by laser-produced free carriers in semiconductors. Electron. Comm. Jpn. **80**, 1–9 (1997) (Pt. II)
30. H.T. Chen, W.J. Padilla, J.M.O. Zide, S.R. Bank, A.C. Gossard, A.J. Taylor, R.D. Averitt, Ultrafast optical switching of terahertz metamaterials fabricated on ErAs/GaAs nanoisland superlattices. Opt. Lett. **32**, 1620 (2007)
31. D. Shrekenhamer, A.C. Strikwerda, C. Bingham, E.D. Averitt, S. Sonkusale, W.J. Padilla, High speed terahertz modulation from metamaterials with embedded high electron mobility transistors. Opt. Express. **19**, 9968 (2011)
32. J. Federci, L. Moeller, Review of terahertz and sub-terahertz wireless communications. J. Appl. Phys. **107**, 111101-1–111101-22 (2010)

Chapter 8
Modulating Retroreflector-based Free-space Optical (FSO) Communications

Arun K. Majumdar

8.1 Introduction

In this chapter, the niche area of free-space laser communications and data links which use modulating retroreflectors, or retro-modulators, will be discussed. This is a growing area of interest since technology can now support "shutters" that can achieve usable communications rates. Retro-modulators require very little power draw and offer extremely small form factors and mass. The chapter would be structured as follows:

1. Introduction and Background
2. Description of Modulating Retroreflector Free-Space Optical Communications System
3. Modulating Retroreflector Technologies
4. Modulated retroreflector (MRR)-based FSO Communications Systems Performance Analysis
5. Applications

8.2 Introduction and Background

Novel photonics components and devices provide new opportunities for free-space optical (FSO) communications for various applications offering flexibility and mobility. At the same time, there is an increasing demand for high data-transfer rate, light weight, power, and size for communication terminals, establishing multiple communications nodes and mobility. Some of these nodes may be located in remote areas operating in harsh environment without electric power. New sensors capable of generating large amounts of data are needed for fast information transfer. Retrocommunication, i.e., communications with retro-modulation is attractive in these cases where semi-passive optical nodes operating by retro-modulation are more suitable than conventional transceivers implementations. Conventional FSO communications requires each terminal to have a relatively complex point-and-track

A. K. Majumdar, *Advanced Free Space Optics (FSO),*
Springer Series in Optical Sciences 186, DOI 10.1007/978-1-4939-0918-6_8,
© Springer Science+Business Media New York 2015

system, leading to high cost. While conventional FSO uses similar terminals on both ends of the link, links to MRR are asymmetric links. The MRR makes the bidirectional nature of a typical communication link into a one sided alignment problem. A retroreflective communications system comprises a laser transmitter/receiver station and a remote retroreflector that can be switched "on" and "off" states. A retro-modulator is potentially less complex and more reliable than a traditional FSO system offering the advantage of significantly reducing the size, power, and weight of hardware required at the remote site for FSO communications while maintaining some of the advantages.

Retrocommunication is based on the principle that an interrogating laser is used to extract information from a remote retroreflector that can be switched "on" and "off" states. The interrogating laser illuminates the remote station where the laser light is modulated and reflected (in the same direction) back to the transmitting unit equipped with an associated detector (receiver) recovering the data signal originated from the remote retro-modulator. Note that one of the terminals can have a relatively complex and expensive laser transmitter and receiver coupled to a point-and-track system. The other terminal can have a retroreflector located behind an optical modulator. The remote terminal can only communicate when it is interrogated by a laser transmitter. The incoming light is first modulated in accordance with the input data stream, and then retroreflected directly back to the remote receiver (located at the interrogating laser site). The modulated reflected light can then be interpreted as a stream of bits recovering the data information. The MRR system can be very compact, light and very cheap as it has no laser and no tracking unit. The concept also opens up the possibility of designing a point-to-multiple-point communications with the local hub comprising the laser interrogator and many distributed MRR modules.

Like the conventional FSO communication system, the FSO communications by MRR also suffer similar optical signal propagation problems due to atmospheric effects in different weather conditions. The clear understanding of atmospheric effects due to absorption, scattering, and turbulence for different geographical locations is necessary in order to deploy these MRR systems for successful FSO communications. Furthermore, it is important to understand the two-way (double-folded) propagation path characteristics for MRR propagation compared to one-way path in conventional communication link. The signal loss, fluctuations or distortion due to the dynamic atmospheric channel will be also dominant factors for MRR FSO communications.

Modulating retroreflective FSO communications has several desirable features which make it an interesting technique for use in many future applications. Some of the advantages are: potential for achieving high-capacity secure communications with low weight (~10–100 g) and small volume, low energy/power consumption (less than 100 mW), a large field-of-view (FOV) resulting in reduced pointing requirements for the interrogating laser transceiver, and no active laser transmitter required by the MRR.

8.3 Description of MRR FSO Communications System

A FSO system using a modulating retroreflector typically consists of a transmitter and receiver (transceiver) and an MRR. The transceiver usually contains a laser source (interrogator), a photodetector, optics, and a module that performs acquisition and tracking (it points the laser towards the MRR unit). The MRR consists of a retroreflector (e.g., a corner cube) and a modulator. Depending on the type of the retro-modulator, the characteristics (such as intensity or polarization) of the reflected beam back to the interrogator is changed when the input voltage applied to the modulator is changed (according to the input data stream). FSO links to MRRs operate differently from conventional point-to-point links, see Fig. 8.1a. Typical point-to-point links use similar terminals on both ends of the link (i.e., a transceiver at both ends) and the communications can be two-way, simultaneously as needed. Links to modulated retroreflectors are asymmetric links which are composed of two different terminals: one end of the link there is the MRR and the opposing terminal is a laser interrogator, see Fig. 8.1b. The interrogator illuminates with a continuous waveform (CW) beam out to retroreflector thus providing the forward link. The purpose of the interrogation beam is thus to supply the necessary optical power for the return signal. The MRR modulates the CW beam with the input data stream, and the beam is retroreflected back in the exact same direction of the interrogator laser. The interrogator receiver then collects the return beam and reconstructs the data stream. This operation of optical retroreflector link is basically in half-duplex (HDX) mode. If bidirectional or full-duplex (FDX) data transfer is desired, a photodetector can be added to the MRR terminal to receive HDX data from the interrogator. For bidirectional data transfer, the MRR modulates the beam with data stream only when the interrogator beam is CW (no data present). Thus both the terminals share interrogator beam as the communication terminal, each as a HDX mode. The FDX operation using MRR (see Fig. 8.1c) will be discussed in details in a later section of this chapter.

8.4 MRR Technologies

In MRR communications various researchers have presented retroreflector designs using either electro-optic phase modulators, acousto-optic modulators, or micro-electromechanical modulators (MEMs). The acousto-optic and electro-optic phase modulators are undesirable for FSO communications links due to their sensitivity to atmospheric phase errors. Another type of modulators based on electro absorption in semiconductor multiple quantum well (MQW) structure is also described recently. The MEMs modulators have low reflectivity. The various types of retro-modulation technologies and their basic principles of operation are discussed in this section.

FSO communications modulators are different from the optical fiber communication modulators. Typical fiber communication modulators are waveguide based

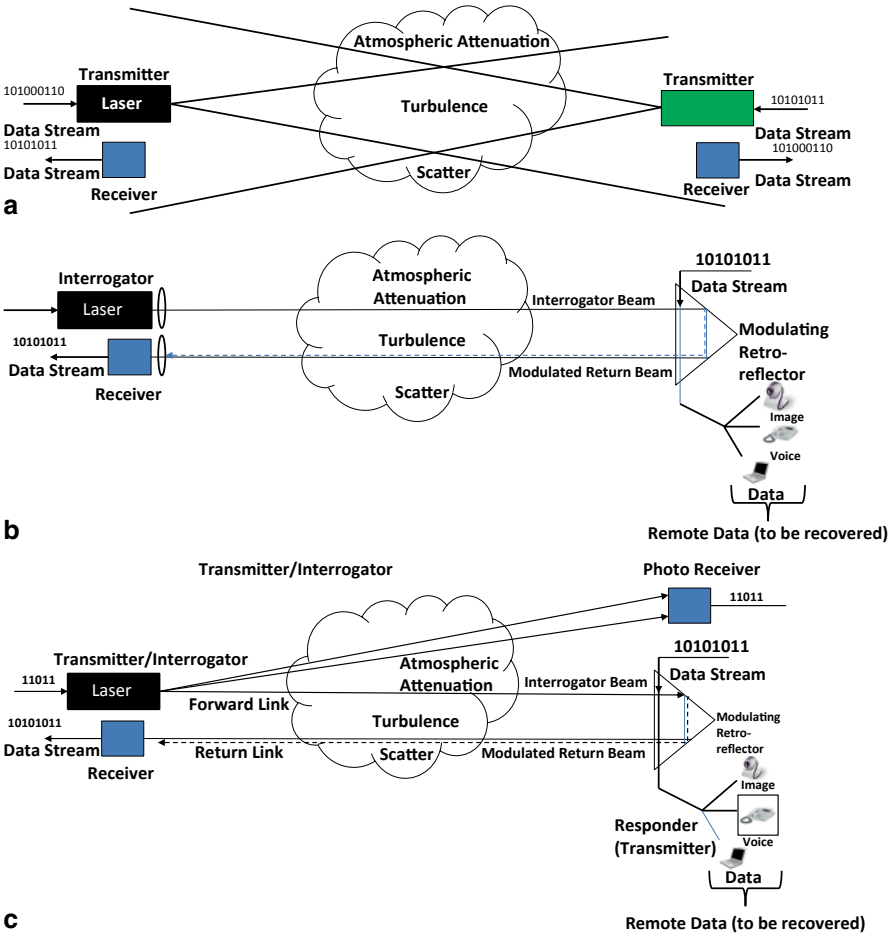

Fig. 8.1 FSO communication system. **a** Conventional FSO communication system. **b** MRR-based FSO communication system (half-duplex, HDX mode). **c** MRR-based FSO communication system concept (full-duplex, FDX mode). *FSO* free-space optical, *MRR* modulated retroreflector

with signals propagating parallel to the modulator surface with physical cross sections are in the order of a few micrometers so that the performance of gigabit speed can be achieved. In an FSO communication modulator, optical signals propagate normal to the modulator surface with cross section in the order of a few milimeter. The modulation speed therefore depends on the fabrication and integration, and is limited by these factors. To achieve multi-gigabit speeds and higher is a challenge for designing a modulator for free space optical communications. Other factors for FSO modulators will include power consumption, size and weight, robustness, and the adaptability with the modulation formats appropriate for communications through dynamic atmosphere. This section will describe below some of the optical

modulator technologies which are applicable to FSO communications. A number of technologies have been proposed, investigated, and developed for the modulation component which include electro-optic modulators (EOMs), acousto-optic modulators (AOMs), and micro-electromechanical modulators system (MEMS).

8.4.1 EOMs

EOM is an optical device in which the optical properties such as power, phase, or polarization of a laser beam change with an electrical signal. Basically the optical properties of the material of the electro-optic devices are altered with an applied voltage in a controlled way. The changes in the optical properties of a material, particularly the permittivity tensor translates into a modification of some parameter of a light wave carrier, for example, phase, amplitude, frequency, polarization, or position, as it propagates through the device. A few materials commonly used for EOM modulators are lithium niobotae ($LiNbO_3$), potassium dihydrogen phosphate (KDP), and gallium arsenide (GaAs).

The operation and application of electro-optic devices rely on the phenomenon of birefringence that is induced by application of voltage to a crystal. In a birefringent crystal an incident light ray will separate into two rays that may travel in different directions depending on its polarization. The material thus has two different indices of refraction, one for each of the two perpendicular components of polarization. Modulator devices for FSO applications can be designed using the following properties of the light wave varied in a controlled way: phase, polarization, amplitude, and frequency, and typically exhibits optimum performance at a single wavelength with some degradation in performance with wideband lasers. For communications purpose, the devices can be used in analog or digital modulation formats and the choice is dictated by the system requirements. Modulation bandwidths extending into the gigahertz range are possible. While analog modulation requires large signal to noise ratio (SNR) limiting its use to narrow-bandwidth, short-distance applications, digital modulation is more applicable to large-bandwidth and longer distance systems.

Basic Principles of Electro-Optics

a. Pockels and Kerr effects

When an electric field E is applied, the refractive index of an electro-optic medium *n(E)* is a function of E which can be expanded in a Taylor's series [1] about $E=0$,

$$n(E) = n + a_1 E + \frac{1}{2} a_2 E^2 + \ldots, \tag{8.1}$$

where the coefficients of expansion are $n = n(0)$,

$$a_1 = (dn/dE)\big|_{E=0} \text{ and } a_2 = (d^2 n/dE^2)\big|_{E=0}$$

Writing the Eq. (8.1) in terms of electro-optic coefficients $\mathrm{r} = -2a_1/n^3$ and $\mathrm{s} = -a_2/n^3$

$$n(E) = n - \frac{1}{2}\mathrm{r}\, n^3 E - \frac{1}{2}\mathrm{s}\, n^3 E^2 + \ldots, \tag{8.2}$$

The second and higher-order terms of the Eq. (8.2) are typically many orders of magnitude smaller than the n. The terms higher than the third can be neglected. The values of r and s depend on the direction of the applied electric field and the polarization of the light.

Pockels Effect In some of the materials when the third term in the Eq. (8.2) is negligible in comparison with the second which varies linearly with E as follows,

$$n(E) \approx n - \frac{1}{2}\mathrm{r}\, n^3 E \tag{8.3}$$

The medium is then known as a Pockels medium and the coefficient r is called the Pockels coefficient. Changes in the refractive index induced by electric fields are very small. Some of the common crystals used as Pockels cell include $NH_4H_2PO_4$ (ADP), KH_2PO_4 (KDP), and $LiNbO_3$ [1].

Kerr Effect In some materials which are centrosymmetric, *n(E)* is an even symmetric function (invariant to the reversal of *E,* and the coefficient r in Eq. (8.2) is zero), so that the Eq. (8.2) can be written as

$$n(E) = n - \frac{1}{2}\mathrm{s}\, n^3 E^2 \tag{8.4}$$

If the material shows this property, it is then called a Kerrr medium.

Phase Modulation

The principle behind the phase modulation is to use a crystal, such as Lithium niobate, whose refractive index is a function of the strength of the local electric field and therefore the light will travel more slowly through the crystal when exposed to an electric field. By changing the electric field in the crystal, the phase of the laser light exiting the EOM can therefore be controlled by changing the electric field in the crystal. A light wave can be phase modulated using an electro-optic crystal and an input polarizer in the proper configuration. The phase of the light leaving the crystal is directly proportional to the length of time for the light to pass through it. Figure 8.2 describes the concept of Phase Modulation process. An applied voltage V will rotate the principal axes in the crystal cross section with the light polarized along the new axis x′ principal axis when the modulation voltage V is applied. The input polarizer is aligned parallel to one of the principal axes when the voltage is on or off.

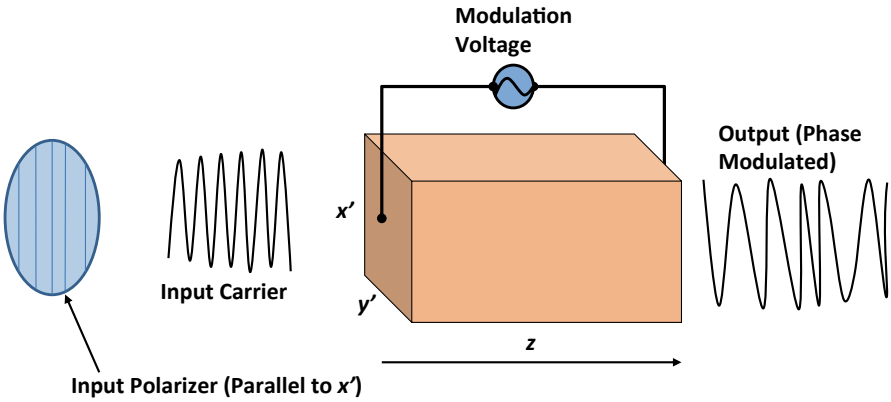

Fig. 8.2 A phase modulator (longitudinal): the light polarized along the new x′ principal axis, V is the modulation voltage applied, output light is phase modulated

Figure 8.2 indicates a polarizer along x′ axes with an input optical electric field $E_{ix'}(t) = E_i \cos \omega t$. The output electric field at the output of the crystal at $z = L$ is then [2]

$$E_o(t) = E_i \cos(\omega t - \varphi) \tag{8.5}$$

where the total phase shift,

$$\varphi = \frac{2\pi}{\lambda}(n_{x'} + \Delta n_{x'})L = \varphi_0 + \Delta\varphi_{x'} \tag{8.6}$$

In the above equation, the natural phase term $\varphi_0 = \frac{2\pi}{\lambda} L n_{x'}$ ($n_{x'}$ is the unperturbed index in the x' direction), and the electrically induced phase term, $\Delta\varphi_{x'} = \frac{2\pi}{\lambda} L \Delta n_{x'}$ for a polarization in the x' direction. $\Delta n_{x'}$ is the change in the index is $\Delta n_{x'} \approx \frac{1}{2} n_{x'}^3 . rE$ (r is the electro-optic coefficient of the EOM). Substituting the value of the change in index, the induced phase shift can be written as $\Delta\varphi_{x'} = \frac{\pi}{\lambda} n_{x'}^3 r\ V$, where the modulation voltage V is related to the applied electric field E by $E = V/L$. Note that $\Delta\varphi_{x'}$ is independent of L and is linearly dependent on L. For a transverse modulator (where the voltage is applied in a direction perpendicular to the direction of light propagation) $E = V/d$ (d is the transverse dimension), and the induced phase shift is then given by $\Delta\varphi_{x'} = \frac{\pi}{\lambda} n_{x'}^3 r\ V \left(\frac{L}{d}\right)$ (a function of the aspect ratio $\frac{L}{d}$ and the voltage V).

The applied voltage at which the induced phase shift changes by π is known as the *half-wave voltage*. This is obtained when $\Delta\varphi_{x'} = \pi$ which for longitudinal modulator is $V_\pi = \lambda / n_{x'}^3 \cdot r$ and for a transverse modulator is $V_\pi = (\lambda / n_{x'}^3 r)\ (d/L)$.

If a direct current (DC) voltage is used, a crystal and the orientation can have two possibilities: (i) the crystal having principal axes which will not rotate with applied voltage *V,* and (ii) the crystal having a characteristic plane perpendicular to the direction of propagation. If a field is applied such that the axes rotate in this plane, the input wave must be polarized along one of the new principal axes. In that case, it will always be polarized along a principal axes, whether the voltage is on or off. By turning the voltage on or off, phase modulation can be achieved.

When a sinusoidal modulation voltage is applied ($V = V_m \sin\omega_m t$), the corresponding electric field is ($E = E_m \sin\omega_m t$). The total phase shift in this case is

$$\varphi = \frac{2\pi}{\lambda}\left(n_{x'} - \frac{1}{2}n_{x'}^3 \cdot rE_m \sin\omega_m t\right)L = \frac{2\pi}{\lambda}n_{x'}L - \delta\sin\omega_m t \tag{8.7}$$

The parameter δ is known as the phase modulation index or depth-of-phase modulation, and is given by $\delta = \left(\frac{\pi}{\lambda}\right)n_{x'}^3 \cdot rE_m L = \pi V_m / V_\pi$. If we neglect the constant phase term, φ_0 and using the Bessel function identity

$$\cos(\delta\sin\omega_m t) + j\sin(\delta\sin\omega_m t) = \exp[j\delta\sin\omega_m t] = \sum_{l=-\infty}^{\infty} J_l(\delta)\exp[jl\omega t], \tag{8.8}$$

the output light wave is then given by [2]

$$\begin{aligned} E_0(t) = E_i[&J_0(\delta)\cos\omega t + J_1(\delta)\cos(\omega+\omega_m)t - J_1(\delta)\cos(\omega-\omega_m)t \\ &+ J_2(\delta)\cos(\omega+2\omega_m)t + J_2(\delta)\cos(\omega-2\omega_m)t + \ldots.] \end{aligned} \tag{8.9}$$

The output therefore consists of components at frequencies ω and $(\omega + n\omega_m)$, $n = \pm 1, \pm 2, \ldots$.

If there is no modulation, $\delta = 0$ *and* $J_0(0) = 1, J_n(0) = 0$ *for* $n \neq 0$, *and* $E_0(t) = E_i\cos\omega t = E_{i_{x'}(t)}$. For $\delta = 2.4048$, $J_0(\delta) = 0$ which means all the power is transferred to harmonic frequencies.

Polarization Modulation

The type and orientation of the nonlinear crystal, and the direction of the applied electric field can determine the phase delay which depends on polarization direction. A Pockels cell can be used for modulating the polarization state. For a linear input polarization (often oriented at 45° to the crystal axes), the output polarization will in general be elliptical, rather than simply a linear polarization state with a rotated direction. Change of the input polarization state at the output occurs by coherent addition of two orthogonal waves which can be termed as polarization modulation. For example, for a longitudinal polarization modulator, the input polarizer can be oriented along the x′ principal axis at 45° with respect to the perturbed x' and y' axes. The input light wave is decomposed equally into the two orthogonal linear

eigen polarizations along these axes. If the light is polarized along the x axis and propagates along the z principal axis (representing the fast and slow axes x' and y'), the propagating fields can be written as

$$E_{x'} = E_0 \cos\left[\omega t - \left(\frac{2\pi}{\lambda}\right) n_{x'} z\right]$$
$$E_{y'} = E_0 \cos\left[\omega t - \left(\frac{2\pi}{\lambda}\right) n_{y'} z\right] \tag{8.10}$$

The refractive indices along these two fast and slow axes are

$$n_{x'} \approx n_x - \frac{1}{2} r_x n_x^3 E = n_x - \Delta n_x$$
$$n_{y'} \approx n_y - \frac{1}{2} r_y n_y^3 E = n_y - \Delta n_y \tag{8.11}$$

In the above equation, n_x, n_y are the indices in absence of an applied field, and r_x, r_y are the electro-optic coefficient for the EOM with the orientation of the applied voltage. A phase difference or retardation Γ results between the two polarizations propagating at different speeds through the crystal which is given by [2]

$$\Gamma = \frac{2\pi}{\lambda}\left(n_{x'} - n_{y'}\right)L = \frac{2\pi}{\lambda}\left(n_x - n_y\right)L - \frac{\pi}{\lambda}\left(r_x n_x^3 - r_y n_y^3\right)EL = \Gamma_0 + \Gamma_i \tag{8.12}$$

where Γ_0 is the natural phase retardation in the absence of an applied voltage, and Γ_i is the induced retardation due to the applied voltage V. The optical fields at the output can be expressed in terms of retardation Γ is

$$E_{x'} = cos\,\omega t$$
$$E_{y'} = \cos(\omega t - \Gamma)$$

By applying the appropriate voltage magnitude, the output polarization can thus be controlled. In the absence of natural birefringence, $n_x - n_y = 0$, the half-wave voltage V_π is defined as the voltage that would produce a retardation of $\Gamma = \Gamma_i = \pi$. In this case, a vertical polarization input becomes a horizontal polarization output. The total retardation in terms of V_π (calculated assuming no birefringence) is

$$\Gamma = \Gamma_0 + \pi\left(\frac{V}{V_\pi}\right) \tag{8.13}$$

In order to achieve polarization modulation, a birefringence must exist in the crystal cross section. For a characteristic plane cross section, the input polarization propagates through the crystal unchanged with no applied voltage (V=0). With the applied voltage causes the axes to rotate 45° in the cross section with respect to the input polarization, and the input will decompose into two equal components and

finally change polarization state at the output. For the cross section with natural birefringence, the input polarization state will change with $V=0$ as well as with an applied voltage.

Amplitude Modulation

Combined with other optical elements, in particular with polarizers, Pockels cells can also be used for other kinds of modulation such as amplitude modulation. An amplitude modulator is based on a Pockels cell for modifying the polarization state and a polarizer for subsequently converting this into a change in transmitted optical amplitude and power. A quarter ($\lambda/4$) wave plate introduces a bias to produce linear modulation. The ratio of output to input intensity, i.e., the transmission $T=I_0/I_i$ is the relevant parameter for intensity modulator parameter. The transmission for this modulator is given by

$$T(V) = sin^2(\Gamma/2) = sin^2\left(\frac{\Gamma_0}{2} + \frac{\pi V}{2V_\pi}\right) \tag{8.14}$$

To accomplish linear modulation, a fixed bias of $\Gamma_0 = \frac{\pi}{2}$ must be introduced by placing an additional phase retarder, e.g., a quarter $(\lambda/4)$ wave plate at the output of the electro-optic crystal. For a sinusoidal modulation voltage $V = V_m \sin\omega_m t$, the retardation at the output of the crystal is

$$\Gamma = \Gamma_0 + \Gamma_i = \frac{\pi}{2} + \Gamma_m \sin\omega_m t \tag{8.15}$$

where $\Gamma_m = \frac{\pi V_m}{V_\pi}$ is the amplitude modulation index or depth-of-amplitude modulation. The transmission in this case can be written as [2]

$$T(V) = sin^2\left(\frac{\pi}{4} + \frac{1}{2}\Gamma_m \sin\omega_m t\right) = \frac{1}{2}\left[1 - \cos\left(\frac{\pi}{2} + \Gamma_m \sin\omega_m t\right)\right] \tag{8.16}$$

$\approx \frac{1}{2}\left[1 + \Gamma_m \sin\omega_m t\right]$ when $V_m \ll 1$, and $\Gamma_m \ll 1$ (i.e., small modulation voltage and modulation depth): the transmission or output intensity is linearly related to the modulating voltage.

8.4.2 AOModulation

In this case, a light field is modulated by an acoustic signal. The modulator is an acousto-optic crystal, which means that the refractive index depends on the pressure. Sound waves are simply the variation of pressure resulting in a variation of refractive index. As the sound wave travels through the crystal, there are regions

of high and of low refractive indexes due to the difference of pressure, depending on the sound. The acoustic wave creates a diffraction grating and we have a spacing created in the material. AOM introduce a periodic modulation of the refractive index in a transparent medium, of which light is scattered similar to the Bragg diffraction.

The periodic index modulation is generated by sound waves which form a periodic density grating when propagating through the medium. The sound waves are created by a Piezo electric transducer driven by a radio frequency (RF) signal. An acoustic absorber on the other end of the crystal prevents the acoustic wave from travelling back to the transducer. The laser beam changes its direction slightly due to Bragg diffraction. One has to distinguish between the "transmission" in the original beam direction and the "efficiency" which gives the fraction of the original beam diffracted into the first order beam. The intensity of the sound wave determines the efficiency of the AOM and is therefore used to modulate the light intensity. The switching speed of an AOM is limited by the time the sound wave needs to cross the beam diameter. In order to achieve high-speed modulation, the beam diameter has to be small. The light intensity and the laser induced damage threshold of the modulator will therefore have to be optimized. The light is scattered from a moving refractive index grating, which generates a slight frequency shift of the diffracted light, equal to the frequency of the sound wave. The movement of the acoustic wave is like a moving diffraction grating and the frequency of the diffracted beam is Doppler shifted by $\pm f_m$, a frequency modulation of light.

An AOM operating in the Bragg regime can be used in actual pass configuration to achieve a high-speed frequency MRR. The Bragg diffraction condition is given by

$$2\lambda_S sin\theta_B = \lambda_L \tag{8.17}$$

where λ_S is the acoustic wavelength in the AOM crystal, θ_B is the Bragg angle, and λ_L is the wavelength of the laser. The incident beam undergoes mirror-like reflection from the acoustic wave front where the diffracted beam and the incident beam are in phase over the entire acoustic wave front. Figure 8.3 illustrates the basic concept of the AOM-based retroreflector.

The interrogating laser beam is diffracted by the AOM device when a sequence of RF pulses (representing the data stream) is applied to the AOM. The diffracted beam is retroreflected through the AOM towards the laser interrogator, and the return signal can be detected by the presence or absence of frequency modulation [3]. The data transmission rate is determined by the spacing between pulses which requires that the rise time of the diffracted optical pulses from the AOM and the RF pulse width should be comparable or smaller than the spacing between pulses. A 1 MHz data transmission rate in Bragg regime was demonstrated [3] which requires an RF power of ~2 W, and the weight and volume of the modulator package are ~1 kg and ~3,000 cm^3, respectively. The researchers suggested potential rate to be ~1 GHz in the Raman-Nath regime and can be suitable for free space laser communications.

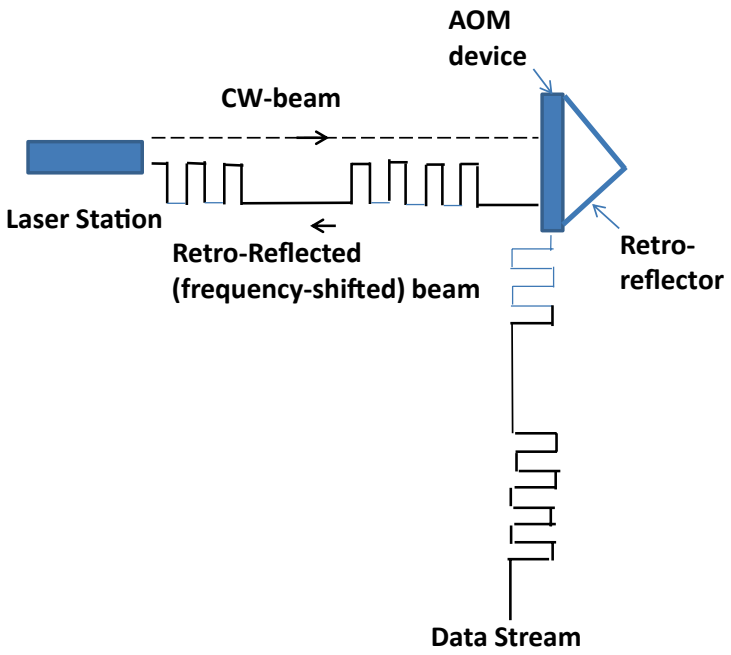

Fig. 8.3 Concept of AOM-based modulating retroreflector for FSO communication: CW-laser beam from the interrogator is incident on the AOM device and frequency-shifted beam is retroreflected towards the interrogator (*Reprinted with permission from NRC Research Press © 2003, Fig. 1, p. 627* [3]). *AOM* acousto-optic modulator, *FSO* free-space optical, *CW* continuous waveform

The AOM-based device may be suitable for certain forms of high-speed FSO communications because of its simplicity of the optical setup to establish an FSO communication link with a remote link. Devices based on electro-optic phase modulation can be used for applications involving high-speed (GHz) FSO communications where the MRR can be mounted on a moving platform such as a satellite or an unmanned aerial vehicle (UAV). The retroreflected signal can be detected with an adequate signal-to-noise-ratio using heterodyne detection technique.

8.4.3 Liquid Crystal (LC)/Ferroelectric Liquid Crystal (FLC)-based Modulators FLC Modulators

Liquid crystal (LC) materials are in a state in-between solid and liquid which under some conditions have an anisotropic order but still maintain an ability to flow. There are three phases of the LC: smectic, nematic and cholesteric. The smectic phase structure is closet to the solid state with translational and orientation order, the nematic LCs only have directional order and no long-range spatial structure, and the cholesteric comes from a nematic LC with chiral molecules (different from its

mirror image) acquiring a helical distortion. For electro-optic applications LCs with nematic phase are widely used. The nematic crystal has a useful property that the dielectric anisotropy, $\Delta\varepsilon = \varepsilon' - \varepsilon''$ (where ε' *and* ε'' are the two different dielectric constants for the dielectric tensor ε) causes the LC to interact with an external applied electric field. With positive dielectric anisotropy the average direction of the material will orient as to align with the electric field, whereas when the electric field is removed the elasticity causes the material to relax back to its initial equilibrium state. Modulation modes of nematic LCs can be described in the following way. Different modulation modes for the LC device can be realized and will depend on the alignment layers, the direction of the external electric field and the polarization of the incoming light. For the directors parallel to the alignment layers and without any twist, pure phase and combinations of phase and amplitude modulation can be achieved [4]. The complex modulation for different angles of the polarizer, α, and various delays can be calculated. Pure phase modulation can be achieved when the polarization of the incoming light is aligned with the optical axis of the LC, i.e., $\alpha = 0$, whereas for light polarized perpendicular to the optical axis, i.e., $\alpha = 90°$, the LC will not alter the polarization or the phase of the light. For all other angle, i.e., $0° < \alpha < 90°$, the polarization state will be changed resulting in an amplitude loss at the second passage of the polarizer. When the polarizer is set to $\alpha = 45°$, optimal intensity modulation can be achieved but not with totally pure amplitude modulation.

Electro-Optical Properties of FLCs Unlike nematic types FLCs exhibit a net dipole over the bulk of the material and because of their electrical polarization properties may switch very quickly under a DC field. Ferroelectrics are chiral smectic C devices, i.e., they have a layered structure with the molecules at some angle (the "cone angle") away from the layer normal. Also there is some inherent twist in the structure. The Surface Stabilized Ferroelectric Liquid Crystal (SSFLC) configuration is the most common configuration for FLC device. In this case the natural twist of the material is suppressed by the surface conditions. When a DC voltage is applied across the display substrates the molecules rotate around the cone so that in the center region the direction the molecules are pointing changes in the plane of the cell by about 45°. Thus the direction of the ferroelectric can be switched very quickly from being along the polarization direction of incident light to being 45° from the polarization direction of the light. Using a ferroelectric material retarding the light by a half wave, the state of the light on reaching the exit polarizer may be changed from 0° to 90° achieving a black and white operation.

LC operating as an Optical Shutter For MRR-based FSO communications applications, normally a laser interrogator sends the light beam towards the MRR which has LC modulator in front of a retroreflector. The MRR sends back the incoming signal towards the interrogator with the modulated information. Shutters using FLC technology offer the speed of the electronic shutters (< 100 μs) on large diameters with added advantage of having the vibration free LC shutters. Figure 8.4 illustrates the FLC-based optical switch: voltage between the electrodes switches the orientation of the FLC molecules optic axis in one of the two states, and thus the polarization of the outgoing light is changed.

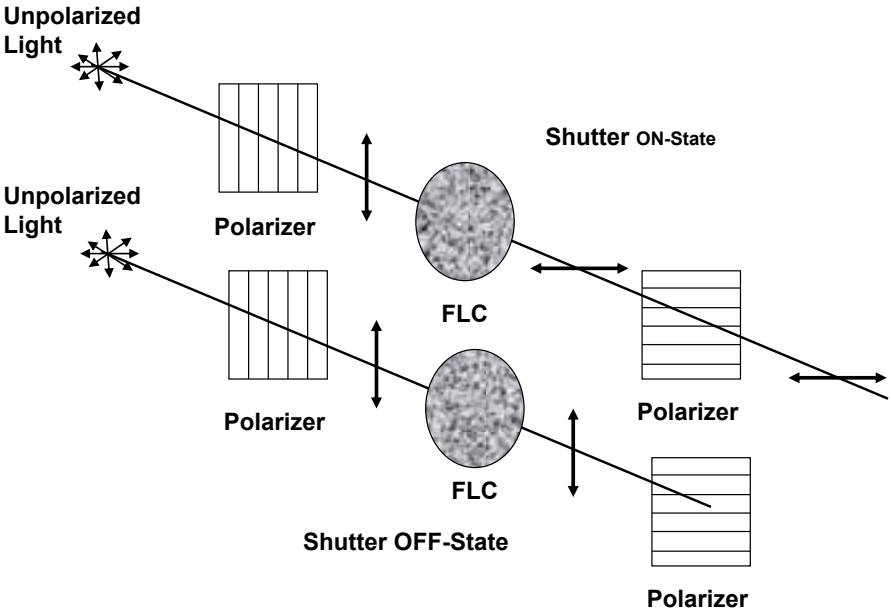

Fig. 8.4 Concept of FLC-based optical switch: voltage applied between the electrodes switches the orientation of the FLC molecules optic axis in one of the two states, changing the polarization of the outgoing light. *FLC* ferroelectric liquid crystal

FLC cells act as optical shutters when placed between linear cross polarizers or alternatively by using a polarized light source and one linear polarizer. Figure 8.5 shows how the molecular orientation is tilted by an angle θ with respect to the normal to the layers (the x-axis) exhibiting the ferroelectric properties. When placed between two closed glass plates the surface interactions permit only two stable states of molecular orientation at the angles ±θ. Applying either a + E or − E electric field in the z-direction, the molecular orientation can be switched into the stable state of either + θ or − θ and therefore the optic axis may thus be switched between two orientations. If the incident light is linearly polarized at an angle θ with the x-axis, the polarization is parallel to the optic axis for +θ state. The wave travels in this case with the extraordinary refractive index n_e without retardation. In the −θ state, the plane makes an angle 2θ with the optic axis. For 2θ = 45°, the retardation is given by [1]

$$\Gamma = 2\pi(n_e - n_0)d/\lambda_0 \tag{8.18}$$

where d = the thickness of the FLC cell, and n_0 is the ordinary refractive index. When $\Gamma = \pi$, the plane of polarization rotates 90° which means that by reversing the applied electric field, the plane of polarization can be rotated by 90°. When the FLC cell is placed between two crossed polarizers, an intensity modulator can be designed. The response time of FLC switches is typically < 20 μs at room tem-

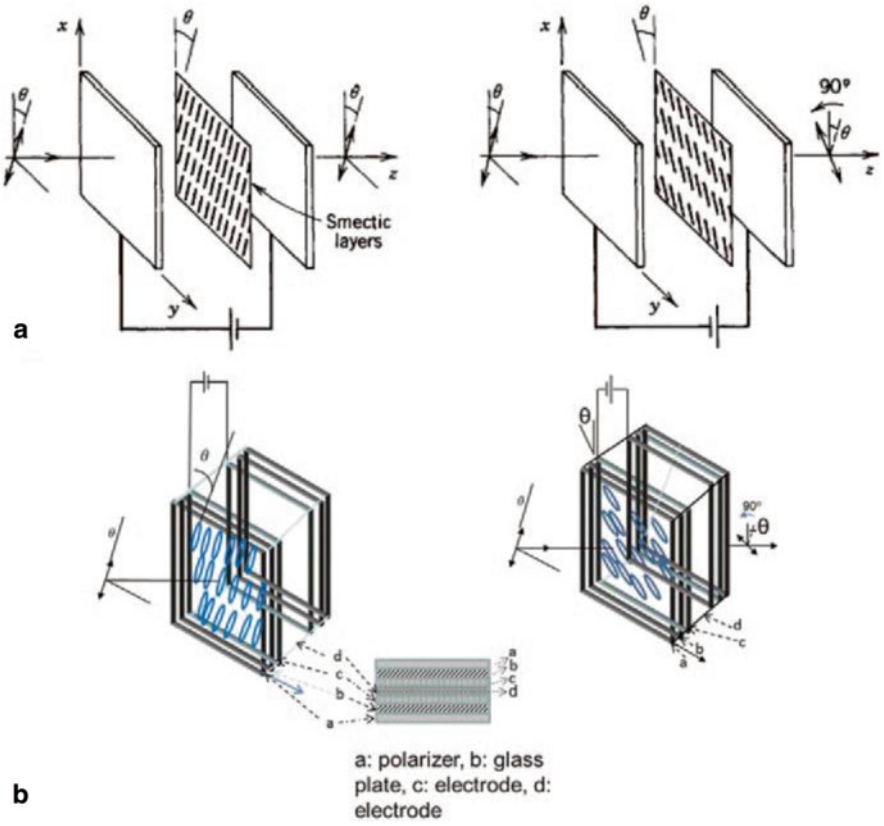

Fig. 8.5 **a** FLC molecular orientation at the angles +θ or –θ by applying electric fields +E or –E, thus showing the switching capability between two orientations (*Reprinted with permission from John Wiley & Sons, Inc. 1991* [1]. **b** The schematic of FLC when placed between two closed glass plates. *FLC* ferroelectric liquid crystal

perature which is much faster than that of nematic LCs. The switching voltage is typically ± 10 V.

8.4.4 MQW Technology for Modulation MQW Modulators

Concepts and basic principles of operating MRR devices using MQW technology offers a number of advantages compared to other types of MRR technology. Some of the advantages are: low power consumption (milliwatts, less than 1 W), low mass, compact and capable of high switching speeds (e.g., ≈ 45 Mbps in FSO communications). The working principle of MQW is based on electro absorption in semiconductor MQW and uses the stark effect to vary the absorption of a trans-

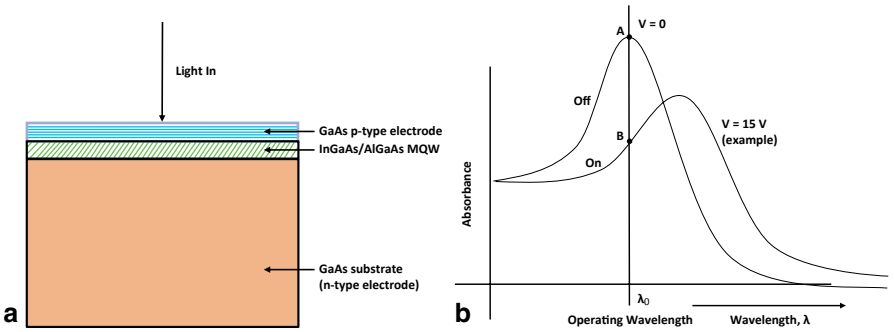

Fig. 8.6 **a** MQW schematic: GaAs material grown in alternating layers with active regions about one micron thick. **b** Typical characteristics: contrast ratio changes from no-voltage ($V=0$) to a moderate voltage (~15 V) at an operating wavelength λ_0 (interrogator laser wavelength). *MQW* multiple quantum well

missive crystal window where absorption of materials changes in response to an electric field, absorption peak remains resolved, and very fast optical modulation in semiconductors (≈40 GHz). The devices are basically p-i-n devices mode from In GaAs/AlGaAs using molecular beam epitaxial (MBE) technique [5, 6].

Figure 8.6a shows a schematic of MQW structure. When a moderate voltage (≈2–20 V) is applied across the device in reverse bias, the absorption characteristics changes causing a shift in wavelength and in magnitude. The transmission of the device near this absorption changes appreciably which then can act as a high speed on-off shutter. The modulators consist of about one hundred very thin (~10 nm) layers of several semiconductor materials, such as GaAs, AlGaAs, and In GaAs, epitaxially deposited on large (~3-in. diameter) semiconductor wafer [5]. The structure designed this way behaves like a *p-i-n* diode where the thin layers induce a sharp absorption feature at a specific wavelength. Figure 8.6b illustrates how the application of a moderate voltage shifts the transmittance at a given operating wavelength. A signal can be encoded in an On-Off-Keying (OOK) format onto the carrier interrogation beam. The contrast ratio for a MQW modulator can be defined as Imax/Imin (where Imax and Imin are the light intensities at two switching positions for two voltages, i.e., with no-voltage and for some applied voltage). The switching speed depends on the material characteristics and the area of the aperture of the device, and therefore data rates are limited by RC (Resistor Capacitor), time constant (R = sheet resistance ≈5–10 Ω, C ≈ 5nF/cm^2). The power consumption is $CV^2 f$ where f is the drive frequency. The device is a trans-missive modulator. The contrast ratio is a function of the drive voltage applied to the device, and increases with the voltage until saturated. Reference [5] describes the modulators to have contrast ratio between 1.7:1 to 4:1 for applied voltage between 15 and 25 V. For FSO communications over 1 km or higher, a large aperture size is needed for accomplishing a reasonable SNR of the received optical power. Also the speed of the MQW shutter depends inversely on the area of the modulator area. Therefore MQW modulator requires proper design for long range, high data rate FSO communications applications. However, a large power penalty may be incurred for large

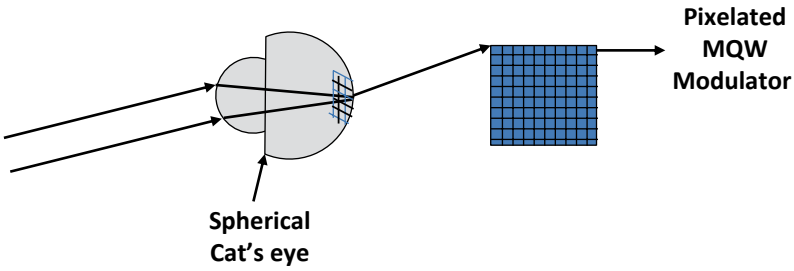

Fig. 8.7 Concept of a "Cat's eye" retro-modulator with pixelated MQW (at focal plane) (*Reprinted with permission from SPIE, 2002,* [10]). *MQW* multiple quantum well

aperture MQW shutter, since electrical power consumption scales as [5]: $D^4_{mod}.V^2 B^2 R_s$, where D_{mod} is the diameter of the modulator, V is the applied voltage, B is the maximum data rate of the device, and R_s is the sheet resistance of the device. Naval Research Laboratory (NRL) has also considered "pixelated" MQW modulator to address these problems. A trans-missive device with nine "pixels" with an overall diameter of 5 mm was achieved to support over 10 Mbps.

The two types of retro reflectors have been considered by NRL for reflecting the incoming light back to the interrogator location: (i) corner cube optical retroreflector, attached at the back of the MQW modulator, and (ii) Cat's eye retro-modulator, where an array of small shutters are placed in the focal plane of optics designed to perform as a retroreflector. In this way a small spot size (mm) allows fast data rates, and the array combined with optics effectively makes the aperture large [7]. The concept of a focal plane "Cat's eye" retro-modulator is illustrated in Fig. 8.7.

MQW-based MRR development, advances, and recent applications State of the art technology based on MQW technology for FSO communications is capable of transmitting data at tens of Mbits/s. NRL has been the pioneer in developing MQW modulators for use in MRR-based FSO communication. NRL demonstrated this technology for various space [8], airborne, and ground applications [9, 10], using 850 nm, 980 nm, and 1.55 μm infrared (IR) wavelengths. Some of the MRR using Cat's eye concept of retroreflector is also discussed here. Results for data-in-flight on a small, UAV at up to 5 Mbps was reported [9]. The device was a corner cube modulator using a 980-nm shutter, with a contrast ratio of 2:1 when driven at 12 V. MQW-MRR using a Cat's eye retroreflector with MQW in the focal plane of the Cat's eye is described [11]. A 10 Mbps free-space link over a range 1 km was demonstrated. Cat's eye MQW MRR have the potential to increase the maximum data rate of the system by more than an order of magnitude over conventional corner cube retro-modulator system. Figure 8.7 illustrates the basic concept of a focal plane "Cat's eye" retro-modulator. By using large number of pixels in the focal plane, increased data rate without decreasing optical aperture or greatly increasing power can be achieved. System field of view and speed can be traded without using a large number of pixels. Cat's eye retroreflectors are best for FSO communications

links requiring high data rates at long range, but with less restriction on space, weight and power. NRL described a Cat's eye-based MRR weighing 410 g (including electronics) for communicating at 10 Mbps in a 4 km link [12] and a new modulator for a laboratory demonstration of a 70 Mbps [11]. The performance of a 1.6 cm flat-focal-plane Cat's eye MRR for a FSO link above the Chesapeake Bay was described using a 5-W laser interrogator to achieve a 45-Mbps data rate over a range of 7 km [13]. An optical modulating retroreflector link to a small robot using an array of 6 MRRs and photodetectors with a FOV of 180 (azimuth) · 30° (elevation) was demonstrated [14] out to ranges of 1 km at 1.5 Mbps data rate. NRL also demonstrated MRR laser-com terminal for applications to small UAVs for a maximum range of 2.5 km and the data rate of 2 Mbps [15]. Live video transmission to the ground was achieved. The use of MRRs for high data-rate communication downlinks from small satellites was recently investigated [16]. In this case, a laser ground station would illuminate a retroreflector on-board the satellite while the MRR modulates the reflected signal, there by encoding a data stream on the returning beam which is received by a detector on the ground. Future possibility of using constellations of nano-satellites for a variety of missions is also pointed out.

8.4.5 MEMS Deformable Mirror Retroreflector Modulators

MEMS MRR Concepts This is a class of MRR where a modulating corner-cube retroreflector has one MEMS mirror that is based on deformable mirrors switching from flat reflecting surfaces (no voltage) to diffractive surfaces (with applied voltage) made of deformed mirror. FSO communications system performance has direct impact by the retro-modulator characteristics as follows: wave front aberration and effective optical aperture affect maximum operational range; data bandwidth is determined by modulation response time and contrast ratio; overall system utility; and robustness are determined by operational tolerances including modulator acceptance angle, wavelength range, and ability to withstand physical and thermal shock. In some practical applications, where MRR can be used for remotely data transfer, the communication range is from 0.1 to 10 km but must operate under different atmospheric turbulence conditions. The effective optical aperture must be 1 cm or larger, and the wave front distortion should be below $\lambda/10$. The system should be able to operate over a wide range of incident angles, up to about $\pm 30°$. The wavelength range for operating the communication system is also another important consideration (i.e., the MRR device also has to accommodate the interrogator (transmitting) laser wavelength ranges). The final consideration for designing MRR-based FSO communication system is the data-modulation contrast of 10:1 (desirable; 2:1 required) for an appropriate SNR and the data-modulation rate of at least 100 kHz (data rates as high as 10 s and 100 s of gigahertz will be eventually needed).

MEMS-based retro-modulators have been recently demonstrated which are suitable for low-cost, low-power compact communication over hundreds of meters to

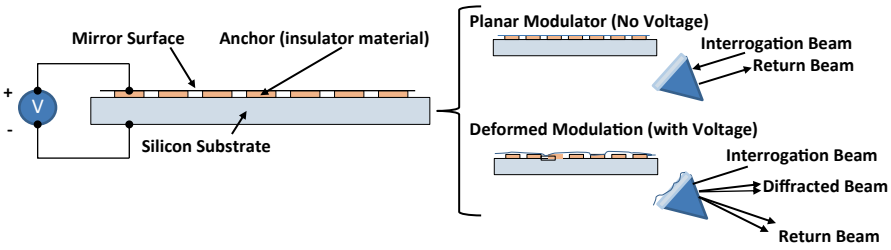

Fig. 8.8 MEMS-based modulating retroreflector (*Reprinted with permission, SPIE, 2009* [17]). *MEMS* micro-electromechanical-system

detect and modulate an incoming (interrogating) laser beam, and then to return the modulated signal to the location of the sender (i.e., towards the interrogator). This type of MRR consists of a MEMS-based electromechanical modulator combined with a passive retroreflector (e.g., a hollow retroreflector where the MEMS modulator serves as one (or more) of the three reflective facets of the retroreflector. The modulator with the MEMS technology can act as a plane mirror (with no applied voltage) maximizing the retroreflected light, or it can be made to act as a non-plane (corrugated or deformed) mirror (with applied voltage), reducing the amount of light that is retroreflected back to the sender. Modulation can be achieved by switching between these two voltages.

Modulation concept for MEMS-based Retroreflector A number of researchers have designed and developed MEMS-based MRR in recent years. For FSO communications applications, some of the concepts and basic working principles of some of these modulators are described in this section. The discussion below considers generally two types of MEMS-based MRR: (i) The first kind MEMS device [17] is based on alternating between a flat state returning most of the incident laser light to the source, and a corrugated (deformed) state acting as a diffraction grating, diverting a significant amount to higher orders (so that the most of the outgoing light does not reach the source), thus depleting the zero order return; (ii) The other kind [18] uses an MEMS deformable micromirror array switching from flat reflective surfaces (no voltage) to diffractive surfaces (with applied voltage) made of hexagonal concave mirror-lenses arrays.

The basic concept of the MEMS-based MRR is shown in Fig. 8.8. The MEMS modulator is a reflective diffraction grating with controllable groove depth. It acts as one of the three mirrors that makes up the corner-cube retroreflector and is capable of modulating a continuous laser beam by switching between an unpowered (no voltage) flat-mirror state to an energized-diffraction state (with input voltage). An electrically modulated deformable MEMS mirror is embedded in a hollow retroreflector [17] which is interrogated by a compact laser transceiver system which operates at a wavelength of 1.55 μm. The MEMS mirror modulates the interrogating laser beam and returns the modulated signal to the interrogating source, where it is decoded. The MEMS modulator uses electrostatic actuation to deform rows of edge-supported narrow plates to form a diffraction grating. The reflective gold

mirror surface supported by a tensile silicon nitride layer is maintained at a ground potential and a voltage is applied to the conductive substrate so that an electrostatic force is generated between those two surfaces resulting in deflection of the flexible mirror surface. This type of actuator can be modeled as a pair of planar electrodes of overlapping effective area A, with a spacing g (closely-spaced). A voltage V is applied between the electrodes which creates an electrostatic attractive force F_e given by [17]:

$$F_e = \frac{\varepsilon_0 A V^2}{2g^2} \tag{8.19}$$

where ε_0 is the permittivity of air (8.8×10^{-12} F/m). The above equation is modified when the electrodes deflect towards one another by an amount z:

$$F_e = \frac{\varepsilon_0 A V^2}{2(g-z)^2} \tag{8.20}$$

When one actuator electrode is kept fixed but the other movable electrode supported by a mechanically compliant spring having stiffness factor k, the mechanical restoring force F_m opposing electrode motion can be expressed by

$$F_m = -kz \tag{8.21}$$

Equating the electrical and mechanical forces at equilibrium state ($F_e = -F_m$) the applied voltage and the equilibrium deflection z are related by [17]

$$V = \sqrt{\frac{2kz(g-z)^2}{\varepsilon_0 A}} \tag{8.22}$$

The above equation shows the relationship between g, z, and V. The advantages of using electrostatic actuation to modulate the interrogating laser beam are: the actuators consume practically no power, exhibit no hysteresis, and the MEMS deformable mirrors are easy to fabricate. With no voltage applied to the MEMS modulator, the 0th order intensity of the far-field diffraction pattern contains the return beam of the interrogating illumination system which would have been received from the modulator in the field if it were mounted in a retroreflector assembly. With applied voltage, the modulator deflects and the intensity of the 0th diffraction order decreases while off-axis higher-order diffraction orders increase in intensity. The MEMS mirror can be incorporated as a facet in a hollow retroreflector to return the modulated beam to the interrogator [17].

The MEMS modulators can have various architectures. One method simply employs phase modulation by moving the retroreflector along the beam direction with MEMS actuators as described in [19]. A spherical Cat's eye retroreflector is used where the mass of the retroreflector is inversely proportional to the resonant frequency at which it can be moved (i.e., limiting the speed of modulation). One of the mirrors in a corner-cube retroreflector replacing with an MEMS actuated grat-

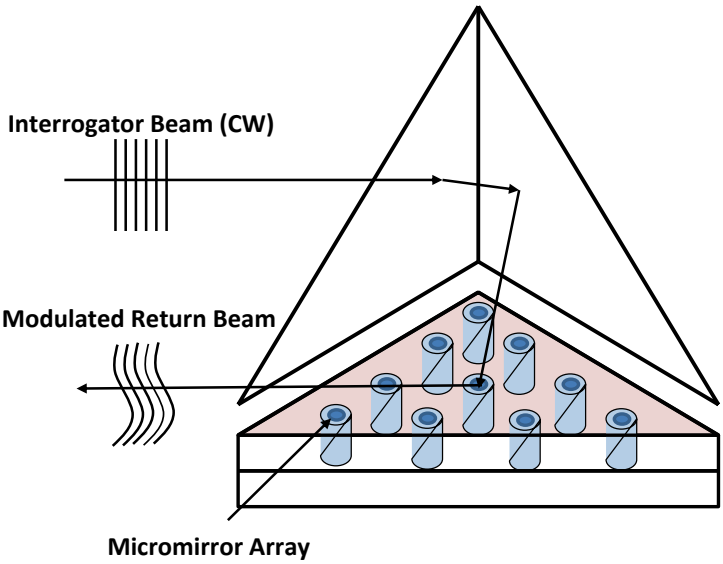

Fig. 8.9 Concept of modulating retroreflector using MEMS deformable micromirror array (*Reprinted with permission from IEEE, 2006* [18]). *MEMS* micro-electromechanical-system

ing has been considered [20] and also discussed in the earlier section. For a wide range of FSO communications applications, the existing MRR devices are unable to meet all of the requirements such as speed, wavelength, large angular field of view, lightweight, size, power consumption, modulation ratio, operational communication range, etc. Many of these issues have been mentioned in the earlier section. Furthermore for the MRR-based device for FSO communication applications, the system has to operate under varying environmental conditions e.g., turbulence, scattering and maritime atmospheres.

Large-aperture MEMS etalons modulator using a drumhead structure with a variable air gap for use with Cat's-eye retroreflector optics, is reported [21]. Concepts of modified version of similar MEMS device structure to act as a first-surface deformable mirrors rather than an etalon is described in [22, 23]. The first-surface MEMS deformable mirrors are switched from a flat to a hexagonal array of concave micro-lenses. The light distribution due to the spherical micro-lenses are determined by geometrical curvatures (geometrical regime), and interference between multiple diverging beams suppresses the zero-order reflectivity (diffraction effect). The general concept of this type of MEMS deformable mirror for retro-modulator is shown in Fig. 8.9. Note that the far-field diffraction pattern (observed at the receiver plane located near the interrogator laser beam) is the Fourier transform of the deformable-mirror surface (mirror-array). The zero-order diffraction beam determines the signal power collected by the receiver for the FSO communication, located next to the interrogator laser beam. The researchers reported in [23] that they have achieved the following performance: a10-dB contrast ratio for incident

angles upto ±68° at 1.5 μm employing three mirrors in a corner-cube retroreflector, each oriented at 54.7° to the normal of the corner-cube, for propagation distances of at least 1 km, with increased drive voltage (≈79 V) to increase the devise response to above potential 1 MHz, to be operated hot 20 C and at 100 C temperature, and extinction ratio 7:1.

Micro-Opto-Electro-Mechanical System (MOEMS) Modulator Some types of MEMS-based modulator technology utilize the concept of interference between MEMS micro-mirrors and their support substrate to modulate incident light [24, 25]. The modulating device operates over a large spectral band of wavelengths greater than 1.3 microns and a wide angular range (120°). The modulator consists of an array of silicon micro-mirrors which are parallel to the substrate and suspended by micro-beams above the substrate. The micro-mirrors move coherently and act as interference switch. The modulation is achieved by tuning a large array of Fabry-Perot cavities by applying an electrostatic force to adjust the gap between a movable mirror and the underlying silicon substrate. The basic concept of the modulating device is as follows: The modulator transmission can be modeled as a Fabry-Perot etalon where the mirror reflectivity is determined by the Fresnel reflection coefficient of silicon. The transmission of the modulator for a laser interrogator wavelength with angle of incidence, θ, and a spacing δ between the mirror and the substrate is given by [25]

$$\mathrm{T}_{\mathrm{mod}} = \frac{T^2}{(1-R)^2} \cdot \frac{1}{1 + \frac{4R}{(1-R)^2} \cdot sin^2\left(\frac{\phi}{2}\right)} \ldots\ldots\ldots\ldots\ldots \tag{8.23}$$

where

$$\phi = \frac{4\pi}{\lambda} \delta \, cos\theta$$

and

$$\mathrm{R}_{\perp} = \left\{ \frac{\left(\sqrt{n^2 - sin^2\theta} - cos\theta\right)^2}{n^2 - 1} \right\}^2$$

$$\mathrm{R}_{11} = \left\{ \frac{n^2 cos\theta - \sqrt{n^2 - sin^2\theta}}{n^2 cos\theta + \sqrt{n^2 - sin^2\theta}} \right\}^2$$

where T and R are the transmission and reflectivity of the silicon, n is the index of refraction of silicon at wavelength λ (n=3.5), and $R_{\perp}$ and R_{11} are the Fresnel reflection coefficients for the perpendicular and parallel polarizations, respectively. For a given angle of incidence, a good modulator contrast can be achieved by varying

the gap. With a high transmission, for a specific gap, the light passes through the retroreflector where the second pass returns to the interrogator. On the other hand, if the transmission is low for the specific gap, the incident light is reflected away at some random angle. The device has to be able to switch between maximum and minimum transmission by changing the spacing of the etalon to values in the range 0.1 to 1.5 microns depending on angle of incidence, θ. An electro-static force determined by the applied voltage between the substrate and the micro-mirrors pull the mirrors down to change the spacing. This type of interference-based MEMS optical modulator using as an interference switch can be used to communicate over a range of 1 km with a bit rate of 200 kbit/s.

MEMS Switchable Retroreflector Film Modulator There are some applications which require signals to be visible and obvious to naked eye. Some of the ideal requirements for these types of applications are: wide visible spectral range for a bright reflection (full width half maximum, FWHM) of > 100 nm, modulation contrast ratio > 10:1, large reflective area (e.g., > 100 cm^2), be able to accept wide input angle, switching at speeds as fast as the human eye response (< 100 ms) for obvious recognition high optical efficiency (i.e., the received retroreflected brightness is much greater than the intensity of reflections from diffusely reflecting surroundings). Low modulation power is also another important consideration. Examples of several electrically modulated retroreflector film technologies for rapid visual identification are introduced in reference [26]. This type of application will be useful for FSO visual communications where a quick response that is obvious to the naked eye is required. This section discusses the interesting switching technology based on electrowetting. The most appropriate modulation technique described here is based on electrowetting which can switch quickly, can modulate over the entire visible spectrum and into the IR, and has little angular dependence. The basic mechanism of electrowetting is the use of electromechanical force to reduce liquid contact angle on a dielectric surface. When a voltage V is applied, the contact angle θ_v can be expressed as [26, 27]:

$$\cos\theta_v = \cos\theta_y + CV^2/2\gamma_{cl} \ldots\ldots\ldots\ldots\ldots \quad (8.24)$$

Where θ_y is Young's angle (with no voltage applied), C is the capacitance per unit area of the hydrophobic surface (F/m^2), and γ_{cl} is the interfacial surface tension (N/m) between conducting fluid (e.g., water) and insulating fluid (e.g., oil). The polar fluid serves as one electrode. Electrowetting can be applied to change optical transmission with a speed as fast as a few ms for devices of < 100 μm in size applying 10–100 V voltage depending on the properties of the materials such as C and γ_{cl}.

The incident light must transmit through the modulation layer, retroreflect, and then pass back through the modulation layer a second time. Reference [27] describes switchable retroreflectors based on electrowetting lenslets that are integrated into the corner cubes. Figure 8.10 illustrates the basic principle. A corner cube retroreflector backplane is coated with electrowetting films and dosed with oil ($n > 1.4$) and water ($n \approx 1.3$). The oil and water creates a concave-shaped meniscus and acts

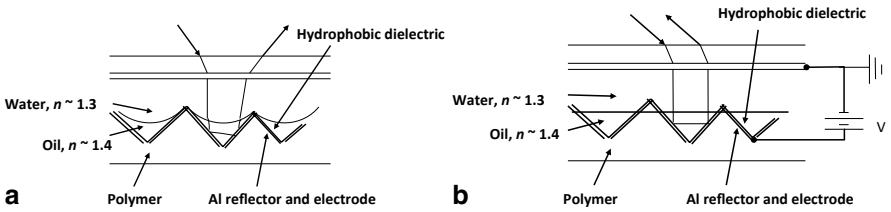

Fig. 8.10 Electrowetting lenslet retroreflector modulation. **a** Scattering state (voltage off). **b** Retroreflection (voltage on) (*Reprinted with permissionfrom the Optical Society of America (OSA), 2012* [26])

like a concave lens since the refractive index of oil is higher than that of water. The researchers have used 800 μm corner cubes when the voltage is off ($V=0$), the light incident onto the electrowetting retroreflector will be refracted passing through the concave meniscus and thus be optically scattered. The device then works like a diffuse reflector. When the voltage V is applied, electrowetting reduces the water contact angle with hydrophobic dielectric. Applying voltage ≈ 19 V, the water contact angle reaches ≈ 125°, the meniscus becomes flat and the device behaves like a conventional retro reflector. A contrast ratio of greater than 10:1 was achieved with input angle ±30°. If the corner cube is scaled to 10 μm, a very fast switching speeds of < 0.1 ms can be reached (far exceeds the response time of the human eye). Also, a large total reflective area (≈ > 100 cm^2) can be fabricated which can be thin and flexible (i.e., can be put on curved surface directly).

8.4.6 Fiber-based Amplified-Retro-Modulator (ARM): A New Concept in MRR Technology Amplified Retro-Modulator (ARM) based on single-mode optical fiber (SMF)

a. *Single channel ARM*

The performance of the laser communications return link in a MRR system is limited by the size (area) of the retro-modulator. A larger aperture retro-modulators can return more signal, but is much heavier and consume more electric power. A new concept of MRR is described in the reference [28] which uses an amplifying retro-modulator. The amplifier increases the effective area of the retro-modulator more than 300 times to make the system as effective as a larger aperture passive retro-modulator without the increased weight and power consumption of a larger retro-modulator.

How does it work? The concept is based on developing a high-efficiency FSO-SMF coupler. The conventional couplers suffer high losses. The FSO receiving element is a single-mode fiber fused to the end of a solid optic with a demonstrated increase in efficiency and achieving a very high data rate of 2.5 Gbps with this

type of retro-modulator [28]. With the conventional FSO systems for coupling into single-mode fibers, the depth-of-focus (DOF) is very small and for an ideal imaging system is given by:

$$DOF = \frac{d}{2.NA} \tag{8.25}$$

where d is the focal spot and NA is the numerical aperture of the optical fiber. For conventional single-mode fiber with a mode-field-diameter of 10.5 μm and the NA of 0.13, the DOF is 40 μm. There is therefore a severe coupling efficiency losses because of a small change in the position of the lenses due to thermal expansion or any mechanical vibrations. The new concept utilizes the pigtailed solid glass fiber collimators which are less sensitive to thermal and mechanical disturbances since the optical fiber is fused directly to the glass of the collimator. For efficient coupling of light into a SMF the light at the entrance of the receiver must have an étendue that does not exceed the étendue of the SMF and is constrained by the upper limit on the V parameter for a SMF [29]:

$$V = \frac{2\pi a_{core}}{\lambda} \cdot NA = \frac{2\pi a_{core}}{\lambda} \cdot \sin(\theta) \leq 2.405 \tag{8.26}$$

where a_{core} represents the radius of the fiber core, λ is the operating wavelength, θ is the acceptance angle of the fiber. The étendue of a single-mode fiber is given by:

$$\xi_{SMF} = \pi \cdot (a_{core} \cdot NA)^2 \leq \frac{(1.2025 \cdot \lambda)^2}{\pi} \tag{8.27}$$

where ξ_{SMF} represents the étendue of a single-mode fiber. For efficient coupling, the receiver étendue, $\xi_{receiver}$, must not exceed the étendue ξ_{SMF} of the single-mode fiber. The theoretical FOV of coupling a 2-cm diameter optical beam into an optical fiber would be 68-μradians or 14-arcsec, although in the reference [28] the experimental value of the FOV was very low, 0.8-arcsec which could be increased with the proper design of the lens system.

It was pointed out in the reference [28] that a high-efficiency optical coupling of FSO signals into a single-mode fiber was possible by combining high efficiency FSO-SMF optical couplers with high-speed modulators and very low-power consumption Erbium Doped Fiber Amplifiers (EDFAs). It was possible to develop an ARM with a return signal 2000 times the return signal from an identical aperture conventional MRR that can simultaneously be operated at several Gbps modulation rates. The total power consumption of an amplified 2.5-Gbps ARM used only 120-mW of electrical power.

The intensity incident upon a typical MRR is given by:

$$I_{inc} = \frac{P_T \cdot \eta_T \cdot \eta_{Atm}}{\Omega_T \cdot R^2} \tag{8.28}$$

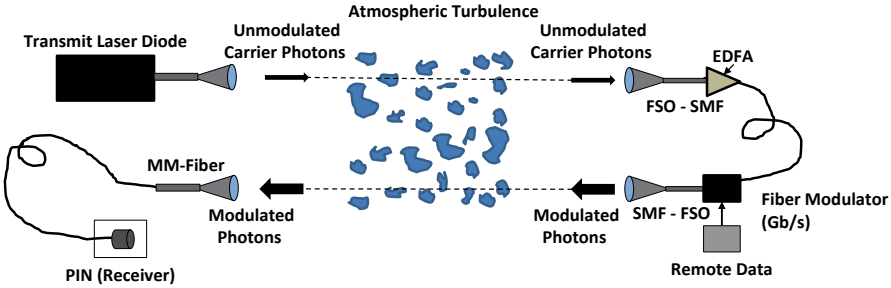

Fig. 8.11 Single-fiber-based Amplified Retro Modulator (ARM) (*Reprinted with permission from Thomas Shay/SPIE, 2004* [28])

where P_T is the transmitted power, η_T represents the efficiency of the transmit optics, η_{Atm} is the atmospheric transmission efficiency, Ω_T represents the divergence of the transmitted beam, and R represents the link range. The return signal for a conventional MRR is given by [30]:

$$P_S = I_{inc} \cdot A_{eff\_retro} \cdot \eta_{receiver} \cdot \eta_{Atm} \cdot \frac{A_{receiver}}{\Omega_r \cdot R^2} = \frac{P_T \cdot \eta_T \cdot \eta^2_{ATm} \cdot \eta_{receiver} \cdot A_{receiver}}{\Omega_T \cdot \Omega_r \cdot R^4} \cdot A_{eff\_retro} \quad (8.29)$$

where A_{eff_retro} is the effective area of the retro-modulator, $A_{receiver}$ is the receiver area, Ω_r is the divergence of the retroreflected beam, λ is the interrogator laser wavelength. If the retro-modulator has a gain of G, then the effective area of the retro-modulator is given by:

$$A_{eff\_retro} = G \cdot A_{retro} \quad (8.30)$$

where A_{retro} represents the physical area of the retro-modulator. From the above equations, the return signal from an ARM with a gain G is obtained as follows [28]:

$$P_s = \frac{P_T \cdot \eta_T \cdot \eta^2_{ATm} \cdot \eta_{receiver} \cdot A_{receiver}}{\Omega_T \cdot \Omega_r \cdot R^4} \cdot A_{retro} \cdot G \quad (8.31)$$

The above equation clearly shows that the return signal from an ARM with a gain G increases the received signal by a factor G compared with a MRR with the same aperture. With commercially available EDFA systems with a 40-dB small signal gain, it is possible to increase the effective area of the retro-modulator by nearly 4 orders of magnitude [28]. The effect of the spontaneous emission noise on the receiver SNR can be neglected. Figure 8.11 shows a schematic block diagram of the ARM system which can operate under atmospheric turbulence condition. Unmodulated photons from the interrogating diode laser beam (SMF pigtailed/collimated) are collected by the ARM's receive aperture, and coupled into a SMF (pigtailed). This method provides a robust high efficient coupling from free-space into a SMF. After amplification (using EDFA) and then subsequently the modulation, the outgoing

photons exit the smaller aperture fiber pigtailed collimator, which is co-aligned with the receive aperture at the interrogator laser location. The amplified and modulated beam thus is retroreflected back to the source and collected by a receive optics. The first retro-modulator operating at 2.5 Gbps was demonstrated in the laboratory [28].

b. *Fiber-Array-based (Multiple Channel) ARM*

The ARM described above is limited to its extremely small FOV of about ±0.004° only. In order to overcome this limitation, a recent patent by the author and his colleague [31] (Patent No. US 8, 301, 032 B2, Oct. 30, 2012) describes a wide FOV amplified Fiber-Retro system. The concept is to provide a pixellated fiber array system for both incoming and outgoing optical beams to maintaining one-to-one correlation between each set of lenslet/fiber array which can also determine the exact location of the source. The patent describes a means of achieving a wide FOV "fiber retro" system where the remote device can accept a wide angle of interrogating signal. The system consists of the receiving optics, the N×1 combiner in combination with the fiber tap, and the probe photodetector, the electronic N×1 switch, the 1×N spatial router, and the single-mode optical amplifier. Figure 8.12 shows the diagram of the "fiber retro" system. The system includes all-optical repeater without optical-to-electrical-optical (OEO) conversion process. The combined wide-angle lens and the lenslets/SMF pigtailed collimator provide the needed requirements for coupling the incident light onto the lenslets array. A wide-angle telecentric lens is incorporated with an array of the single element FSO-SMF couplers. The incident signal photons enter the telecentric lens, imaged onto the lenslet array; the output signal (after the combiner) is then optically amplified in a low-noise highly efficient EDFA. Next the signal is modulated in an electro-optical intensity modulator according to the external data. Finally the modulated and amplified photons sent out the exit port (transmit optics) back to the interrogator laser (transmitter) location. If the entrance and exit apertures are aligned to produce parallel beams, then this configuration serves as an amplified retroreflector/retro-modulator.

Effects of atmospheric turbulence on the amplified fiber retro-modulator (AFRM) The effect of atmospheric turbulence on the AFRM system using an array of fiber couplers needs to be evaluated. This can be best understood by estimating the variance of angle-of-arrival fluctuations caused by the presence of atmospheric turbulence which can be written as:

$$\sigma_a^{\,2} = 2.914 D^{-1/3} H^{-5/3} \int_0^H z^{5/3} C_n^{\,2}(z) dz \tag{8.32}$$

where D=aperture diameter, $C_n^{\,2}$ is the turbulence strength, and H is the altitude. If the communication link is along a slant path, then $C_n^{\,2}(z)$ should be replaced by sec(θ). $C_n^{\,2}(z)$ where θ is the zenith angle (away from the vertical) and the limit of integration should be taken as the slant range.

An example of link analysis for a Satellite-based system laser interrogator and low-power Gbps amplified fiber retro-modulator Figure 8.13 shows the simulation

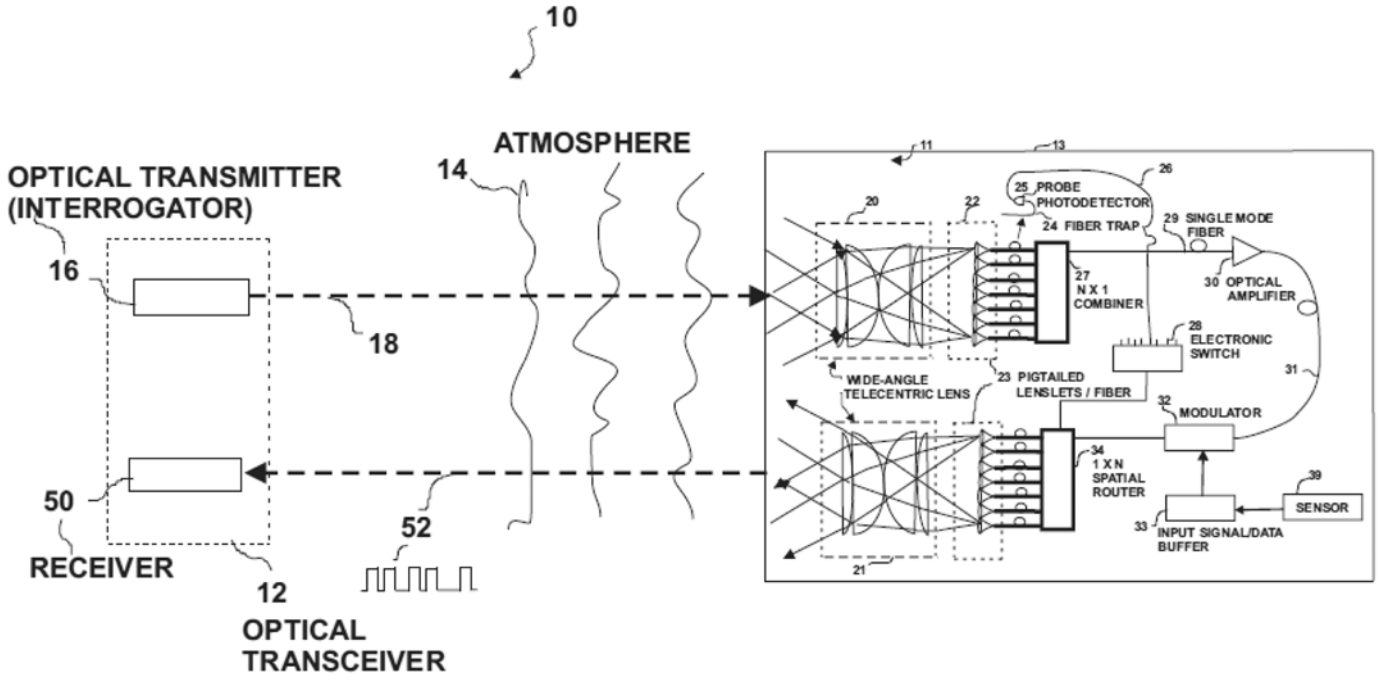

Fig. 8.12 Fiber-array-based wide-field-of-view Amplified Retro Modulator

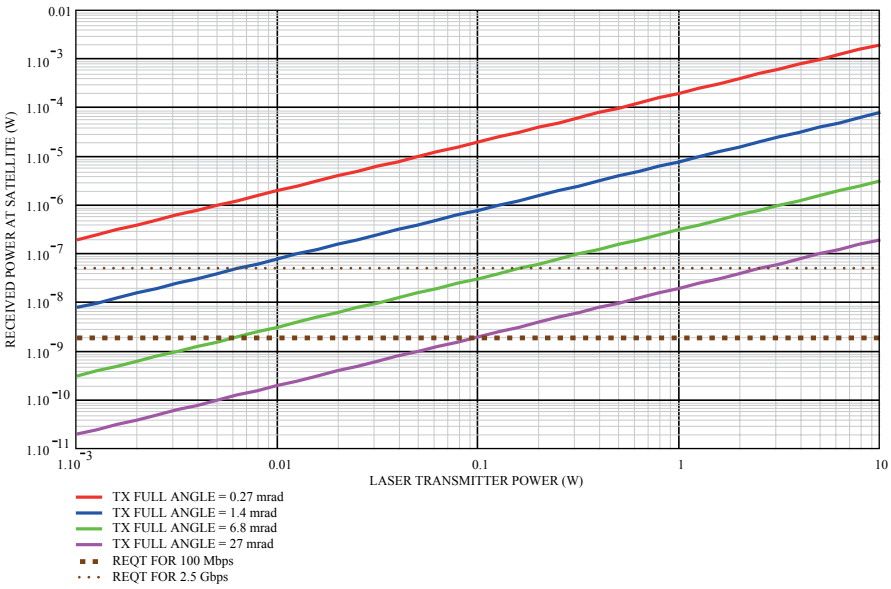

Fig. 8.13 Plot of the received power versus required laser transmitter power: an example of a Satellite-based laser interrogator and a ground-based "Fiber retro" system using fiber-array

result for a satellite-based laser interrogator and ground-based ARM. The range of the satellite was assumed to be 370 km the atmospheric transmission efficiency $=0.5$. The retroreflected beam is received by the satellite receiver of 6 in. diameter. The transmitter efficiency was assumed to be 0.5, the required bit-error-rate (BER) $=10^{-9}$, the SNR $=144$, and the gain of the retro-modulator system was taken to be 4×10^5. The simulation result shows the received power at satellite as a function of required laser transmitter power on the satellite for different values of the divergent angles of the transmitter. The two horizontal dashed lines represent the needed received power at the satellite for 100 Mbps and 2.5-Gbps data rates. To achieve a data rate of 2.5-Gbps, for a transmitter divergent beam of 6.8 mrad, it requires 160 mW of laser power whereas for transmitter divergent beam of 27 mrad, it requires about 2.5 W of laser power. These numbers are very practical and realistic.

Comparison of different MRR technologies A comparison of the features of various MRR technologies discussed in this section is summarized in Table 8.1.

8.5 MRR-based FSO Communications Systems Performance Analysis

This section will discuss the following: first, a link budget analysis for evaluating received power at the transceiver; second, determine SNR for MRR communication system; third, calculate BER for a MRR FSO communication system in presence of

Table 8.1 Performance characteristics of different MRR technology

MRR technology	Liquid crystal (LC)/Ferro-electric liquid crystal (FLC)	MQW	Electro-optics	MEMS	Amplified fiber-retro: single channel/fiber array
Modulation	Polarization and amplitude	Amplitude	Polarization and amplitude	Amplitude	Amplitude
Speed	Slow	Medium-fast	Fast	Low/medium	Very fast possible
Power consumption	Very low	Medium	High	Low	Very low
Voltage required	Low	Low	High	Low/moderate	N/A (does not require any electro-optical. acousto-optical, LC or MQW material)
MRR diameter	Large	Medium	Medium	Small	Very small for single channel to small for array device
Mass	Low	Low	High	Low	Very low
Comments		Simple and rugged, easy to array for wide FOV; response shifts with temperature Cat's eye is capable of higher bandwidth	AOM can be very compact and high-speed possible	Low cost; deformable micro-mirror array possible for higher modulation contrast, and larger FOV	Single channel has extremely small FOV; array of fiber retro provides large FOV

MRR modulated retroreflector, *MQW* multiple quantum well, *MEMS* micro-electromechanical modulators system, *AOM* acousto-optic modulators

atmospheric turbulence; finally, atmospheric scattering effects in the retroreflected received signal power will also be discussed.

8.5.1 Link Budget Analysis

MRR Link Scenario In order to establish an MRR FSO communication link, the interrogator laser would illuminate the MRR-equipped terminal. Small photodetectors or the modulator itself would be able to detect the incident beam and cue the

data transmission. If the retroreflected return beam is amplitude modulated, HDX communications are possible. This can be done simply with an OOK modulation, but more advanced modulation schemes such as pulse position modulation (PPM) can be used for higher data rates. For FDX scheme such as polarization modulation, for example, can be utilized on the interrogation uplink, and amplitude modulation (OOK) can be used for return data format in MRR down link. A receiver telescope would be co-located with the interrogator and would be equipped with the necessary optics, detectors and electronics to decode the received data stream.

Link Budget Calculations MRR system consists of three main components: MRR device, the data compressor, and the data system. The MRR makes the bidirectional nature of a typical communication link into a one-sided alignment problem. A retroreflective communication system thus comprises a laser transmitter/receiver station and a remote retroreflector that can be switched "on" or "off" states. The link budget is the computations of the optical power losses in one link and is bounded by the system dynamic range given by the transmitter output power and the receiver sensitivity. After subtracting all the optical losses across the link, any remaining dynamic range is referred to the "Link Margin", allows a link to operate under adverse atmospheric condition. There are basically three retroreflector losses: absorption loss, wave front loss (due to imperfection of the retroreflective optics), and contrast ratio (for example loss due to a certain percentage modulation depth of the quantum-well modulator).

Limitations with MRR FSO Communications All FSO communications experience limitations imposed by the atmosphere, e. g. weather-dependent attenuation. Furthermore, atmospheric turbulence causes beam spreading and wandering as well random fluctuations of the received communication signal (scintillation). While atmospheric attenuation causes large but slowly varying SNR at the receiver, turbulence causes fast SNR fluctuations (i. e., fading). In heavy fog the attenuation can be as large as 80 dB/km, or more, while in some other conditions, it may be only a few dB/km. Because of scintillation and beam wandering, turbulence reduces the received signal energy in the detector. Atmosphere therefore limits the performance of FSO communications systems, and plays an important role in the link budget analysis discussed below. In order to implement an MRR-based FSO communication, atmospheric effects such as turbulence and scattering must be considered. For example, backscatter from the interrogating beam where photons scattered by the atmosphere reflect back into the optical receiver's optical path and reduce the SNR. Mitigation techniques to reduce turbulence and scattering effects on MRR-based FSO communication system need to be employed to accomplish acceptable BER required by the FSO system.

8.5.2 Quantifying the Link Budget

The MRR acts both as a receiver and a transmitter in the optical link, the MRR optical link budget can be expressed in terms of gains and losses. To estimate the range for the MRR communication link the reflected optical power reaching the

transceiver must be estimated. In terms of gains and losses, the MRR optical link budget can be expressed as follows [12, 17]:

$$P_{rec} = P_{laser} G_{Tx} L_{Tx} L_R T_{atm} G_{MRR} L_{MRR} M L_R T_{atm} G_{Rx} L_{Rx} \tag{8.33}$$

where:

P_{rec} = received signal power
P_{laser} = interrogator laser power
G_{Tx} = transmitter antenna gain (laser collimation and pointing)
L_{Tx} = transmitter losses
L_R = range losses due to propagation path
T_{atm} = atmospheric transmission $= e^{-\alpha R}$, where α is the atmospheric coefficientof attenuation
G_{MRR} = MRR antenna gain $= \left[\frac{\pi D_{retro}}{\lambda}\right]^4 S$ (where D_{retro} = optical aperture of the retroreflector, i.e., MRR diameter, λ is the interrogator laser wavelength, and S is the MRR Strehl ratio of the optic [2]: some typical value of a MQW retro-modulator, $S = 0.4$)
L_{MRR} = MRR optical losses
M = MRR modulation efficiency
G_{Rx} = receiver antenna gain (due to interrogator receive aperture)
L_{Rx} = receiver losses

Some of the terms in the above link budgets equation can be calculated from the following formulas:

$$G_{Tx} = \frac{32}{\theta_{div}^2}, \text{ where } \theta_{div} = \text{transmitter divergence (1/e}^2 \text{ full)}$$

$$L_R = \left[\frac{\lambda}{4\pi R}\right]^2, \text{ where R = range}$$

$$G_{Rx} = \left[\frac{\pi D_{Rx}}{\lambda}\right]^2, \text{ where } D_{Rx} = \text{receiver diameter}$$

Note the strongest dependence of retroreflector links on the range which falls off as fourth power; the links fall off more strongly with range than conventional links because of their bi-directional (double-pass) nature. Due to this R^{-4} dependence, compared to the R^{-2} dependence for a one-way conventional free-space communication link, it therefore requires appreciably more to change communication performance. For example, to increase the communication range by a factor of ten, it will require four orders of magnitude in optical power. Also, the optical power received depends on the retroreflector diameter as fourth power. For MRR systems, a large aperture to minimize the transmission losses and a high modulating rate are desired at the same time. But the modulator switching time is usually RC-limited and therefore gener-

ally inversely proportional to the size of the modulator's active surface area. Thus a large retroreflector aperture will slow down the data rate and a trade-off is needed for determining the aperture size to maximize the returned optical power and the required high speed data rate while keeping the consumed electric power low. For terrestrial applications, the atmospheric losses are caused due to absorption and scattering such as Rayleigh and aerosol scattering. Propagation effects are different at different wavelengths and therefore the interrogator laser wavelength needs to be chosen accordingly. Finally, atmospheric turbulence will cause large and rapid SNR fluctuations in the received optical power (fading on a millisecond scale).

From the above link equation, the received power can be predicted for a given system architecture. For a given data rate and encoding scheme of the modulating element the number of photons received by the detector, per transmission bit can be calculated as follows:

$$n_p = \frac{Q \cdot P_{rec}}{h\nu R} \tag{8.34}$$

where:
n_p = photons per bit
Q = quantum efficiency of the detector
h = Planck's constant (6.63×10^{-34} Js)
v = frequency of light = c/λ
R = data rate

8.5.3 BER Calculation for MRR System in Presence Atmospheric Turbulence

Understanding the contribution of scintillation to the power fluctuations due to atmospheric turbulence is essential to improving the performance of FSO communication systems. BER is the standard figure-of-merit for a communication link. A BER of 10^{-6} is generally considered to be acceptable. BER is inherently limited by the contrast ratio of the modulating retroreflector device. When the signal received is very low, i.e., at the low photon levels characteristics of a communication link, the BER will be determined by the signal level, the noise in the detector and the contrast ratio of the retro-modulator device. A combination of techniques such as compression techniques, signal processed, and appropriate adaptive optics-based techniques would be necessary to improve the BER in a MRR-based FSO communication system.

Atmospheric turbulence causes the interrogator beam and the reflected beam to spread reducing the average signal level, and secondly it induces spatially and temporally varying fluctuations in intensity (scintillation). Scintillation causes the received signal to fluctuate above and below the accepted mean value, when bits of transmitted data may be lost whenever the signal is low. The signal strength

and the probability of wrongfully identifying the logic state of the signal assumes that there is an identifiable threshold signal value which separates logic state 1 (presence of signal) from logic state 0 (no signal). However, this optimal threshold value for a given bit varies with time in presence of atmospheric turbulence (due to scintillation effect). In this case, a variable threshold that is always optimal can still be implemented provided the turbulence-induced temporal fluctuations are much slower than the bit rate.

System Model for MRR-based FSO Communication in Presence of Atmospheric Turbulence

Similar to the link equation above, the signal power received by the interrogator-receiver from the MRR is given by [32]:

$$P_{rec} = \left\{ \frac{16T_{atm}^2}{\pi^2 R^4} \frac{P_{laser}}{\theta_{div}^2} \frac{A_{rec}}{f_{rec}} \frac{\sigma_{MRR}}{C_{logic}} \right\} \cdot \frac{1}{W_{EO}^2} \frac{1}{W_{ER}^2} \cdot (T_1 \cdot T_2)$$
$$= \frac{G_R G_{sys}}{R^4} \cdot \frac{1}{W_{EO}^2} \cdot \frac{1}{W_{ER}^2} \cdot (T_1 \cdot T_2) \tag{8.35}$$

The first bracketed term {..} can be written as $G_R G_{sys}/R^4$ which is the power received from the MRR with no turbulence. The other terms contribute to the received power in presence of turbulence. In the above equation, T_{atm} is the atmospheric transmission, θ_{div} is the transmitter divergence, and f_{rec} is the collection efficiency of receiver optic. The MRR is characterized by a cross-section σ_{MRR} and contrast C_{MRR}, where C_{MRR} is the "on/off" contrast ratio between logic 1 and logic 0. The power received for logic 1 from the above equation can be calculated by writing $C_{logic} = 1$, and for logic 0, the power is determined by writing $C_{logic} = C_{MRR}$. The parameter G_R was used which deviates from 1 to identify how the system performs for some deviations from a given system configuration defined by G_{sys} (e.g., due to change in orientation or angle of incidence). The term $1/(W_{EO}^2 W_{ER}^2)$ is the reduction in mean power due beam spreading on the outgoing (from interrogator to MRR) and return (from MRR to interrogator) paths. The terms T_1 and T_2 denote time-varying (due to scintillation) transmission in the outward and return paths. For a pulsed interrogator with a repetition frequency f_{rep}, the mean received energy per pulse is given by $E_{rec} = P_{rec}/f_{rep}$.

Effects of Atmospheric Turbulence on MRR-based FSO Communications

To understand the MRR-based FSO communications system which has to operate under atmospheric turbulence, the following factors need to be taken into account:

1. Received power fluctuations of the interrogator laser beam after propagating through a range, R under atmospheric turbulence characterizing by the refractive index structure constant C_n^2, an inner scale l_0, and an outer scale L_0. For horizontal path, C_n^2 is typically from 10^{-12} $m^{-2/3}$ to 10^{-16} $m^{-2/3}$, l_0 is about 2–10 mm, and L_0 is on the order of the distance between the optical path and the ground. This is usually specified as the Rytov variance, σ_1^2 which is given by [33]:

$$\sigma_1^2 = 1.23\, C_n^2 k^{7/6} R^{11/6} \tag{8.36}$$

where k is the wave number, $k=2\pi/\lambda$ for the interrogator wavelength λ.

2. The change in beam diameter term for the beam propagating from the interrogator to the MRR, denoted by W_{EO} in the earlier equation of the received power and is given by $W_{EO}=W_e/W$, where W is the beam diameter in the absence of turbulence. W_e can be calculated [33] from the equation:

$$W_e = W\left(1+1.33\,\sigma_1^2 \Lambda^{\frac{5}{6}}\right)^{1/2} \tag{8.37}$$

where $\Lambda = \dfrac{2R}{kW^2}$

3. The change in the beam diameter, W_{ER} for the beam reflected from the MRR reaching to the receiver location: In this case, the beam starts from the MRR aperture propagates towards the interrogator at which point the beam diameter is changed due to the effect of atmospheric turbulence.
4. Probability density function (PDF) of intensity fluctuations of laser beam—single and double passage:

Single passage PDF The statistics of the intensity fluctuations propagated through atmospheric turbulence is characterized by PDF, one of the recently accepted forms is given by [33] which is a Gamma-Gamma PDF:

$$p(I) = \frac{2(\alpha\beta)^{\frac{\alpha+\beta}{2}}}{\Gamma(\alpha)\Gamma(\beta)} I^{\frac{\alpha+\beta}{2}-1} K_{\alpha-\beta}\left(2\sqrt{\alpha\beta I}\right) \tag{8.38}$$

where I is the intensity normalized to the mean value, α *and* β are parameters related to scintillation, $K_\nu(x)$ is a modified Bessel function of the second kind, $\Gamma(x)$ is the gamma function. For a given scintillation index, the values of α and β can be calculated [33].

Double passage PDF The beam first originates from the interrogator laser transmitting a power P_0 producing a power P_1 at the MRR aperture, and the resultant reflection power is P_2 through the receiver aperture. The transmission parameters T_1 (from the interrogator to the MRR) and T_2 (from the MRR back to the interrogator) in the MRR received power equation discussed earlier, are time varying and fluctu-

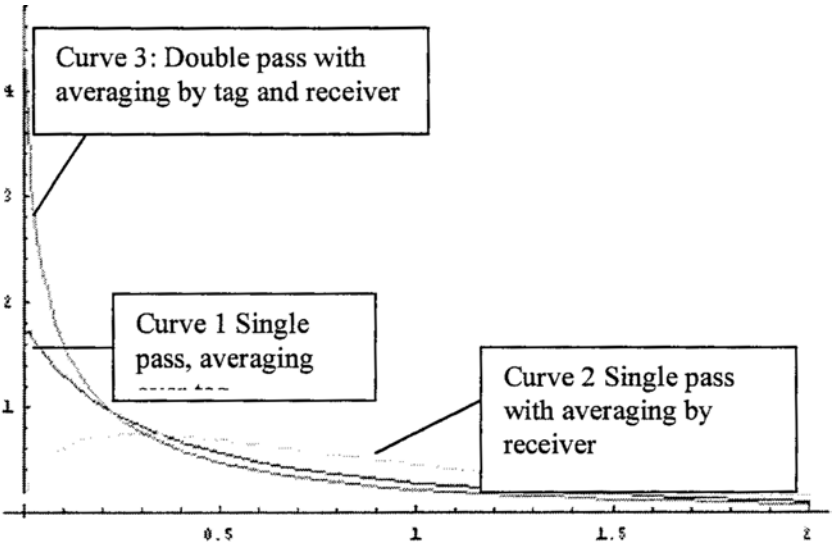

Fig. 8.14 Double-pass PDF of transmission for modulating retroreflector in presence of atmospheric turbulence: single-pass PDF's of transmission are also shown for comparison (*Reprinted with permission from SPIE, 2004* [32]). *PDF* probability density function

ates according to the turbulence characteristics of the atmosphere. The mean value of the effective transmission in each direction is 1. These transmissions in each direction can be uncorrelated so that the joint PDF can be written as the product of the individual PDFs. The double passage PDF can then be written as [32]:

$$T = T_1 T_2, \text{ and therefore } dT_2 = dT/T_1 \qquad (8.39)$$
$$P(T_1, T_2) = P_1(T_1)\, P_2(T_2)$$

One can then obtain the PDF of total round trip transmission:

$$P(T)dT = \int P_1(T_1)\, P_2\left(\frac{T}{T_1}\right)\frac{dT_1}{T_1}dT \qquad (8.40)$$

The double passage PDF can therefore be computed from the individual PDFs in each direction. Figure 8.14 shows the double pass PDF of transmission for MRR communication scenario. The single passage PDF with aperture averaging for MRR aperture and receiver telescope aperture are also shown in the figure. From the figure, it is clear that even with aperture averaging (to reduce the fluctuations due to scintillation) a double passage propagation can lead to a high level of fluctuations with a high probability of low power at the receiver. The MRR-based communication link design should take into this effect in order to determine the various system

parameters (such as aperture size for different turbulence levels, power levels of interrogator laser etc.).

BER Calculation for MRR System

In order to determine the BER of the MRR FSO communication system, one needs to know the basics of received signal, contributions of all noise sources in the system, and the relationship between the SNR to communications system performance defined by BER. A general discussion and relationship of received SNR and BER can be found in references [34, 35]. In almost every area of measurements, the ultimate limit to the detectability of a weak signal is set by noise-unwanted signals that obscure the desired signal. For laser communications systems the shot noise, background noise and thermal noise contribute to the total noise at the receiver. The goal of a lasercom system for digital communication is to transmit the maximum number of bits per second over the maximum possible range with the fewest errors. Electrical data signals are converted to optical signals via a modulator. A "1" is transmitted as a pulse of light while a "0" has no light output. The number of "1's" and "0's" transmitted per second determines the speed of the link (bit rate). At the receiving end of the link, the optical signal is detected by an optical-to-electrical converter (e.g., a photo detector). A decision circuit then identifies the "1's" and "0's" in the signal, and thus recovers the information sent. For an OOK modulation, for example, decoding is based on a decision as to whether the pulse slot time has high enough field energy or not. The selected threshold determines the best performance in decoding the correct signal with the lowest probability of making a bit decision error and thus the BER can be obtained. Thus the performance of the lasercom system can be predicted by computing the BER of the system which depends on the modulation format, and the SNR. The noise comes from all possible sources which include shot noise, dark current noise, thermal/Johnson noise in the electronics following the photodetector, and the background noise.

The calculation of BER for MRR system thus involves three steps: (i) compute the SNR for the detector (no turbulence), (ii) calculate the BER using mean signal energy and a threshold value of the signal(no turbulence), (iii) finally, calculate BER for the fluctuating signal due to turbulence (i.e., with turbulence). The procedure is discussed a follows.

1. SNR at the receiver aperture using an avalanche photodetector (APD) as an example:

The shot noise current for an APD is given by [32]:

$$I_{noise-Det} = \sqrt{2eB(I_{surf} + (I_{sig} + I_{bulk} + I_{bkgr})M^{2+\varepsilon}) + I_{amp}^2} \tag{8.41}$$

where e is the charge of the electron, B is the bandwidth of the system, and I_{surf}, I_{sig}, I_{bulk}, I_{bkgr}, I_{amp} are respectively the surface dark current, signal current (as a result of received signal power, P_s), the bulk dark current, a background

current (originating from background power, P_{bkgr}), the noise current due to the signal fed into a preamplifier, and M is the gain of APD in the operating mode. The unit of all the currents is ampere, ε is the excess noise factor for the detector. The SNR is then given by:

$$SNR_{Det} = \frac{\eta P_s}{I_{noise-Det}} \tag{8.42}$$

where the detector efficiency parameter, $\eta = MR$ and R is the detector responsivity (A/W).

2. The BER using mean signal energy and a threshold value of the signal (no turbulence):

Assuming the noise of the detector is Gaussian, the probability distribution of the received signal S, with a mean value of S_{mean} and signal variance σ_s^2 can be written as

$$P(S) = \frac{1}{\sigma_s \sqrt{2\pi}} exp\left\{-\frac{(S - S_{mean})^2}{2\sigma_s^2}\right\} \tag{8.43}$$

The distribution functions for logic 1 and logic 0 signals will be different. Consider a string of pulses where fluctuations are due to shot noise only For logic states 1 and 0, the mean signals S_1 and S_0 are given by $S_1 = RE_{mean}$ and $S_0 = \mathrm{RE_{mean}}/\mathrm{C_{MRR}}$, respectively, and the corresponding noise components $N_1 = NE_{mean}$ and $N_0 = N(RE_{mean}/C_{MRR})$, respectively. Note that E_{mean} is the mean energy per pulse received by the receiver and C_{MRR} is contrast between the mean signal for logic state 1 and that for logic state 0. Assuming the probability of false alarm equals the probability of missed detection, i.e., the probability of wrongfully detecting logic 1 is the same as the probability of wrongfully detecting 0, the threshold signal, S_{th} can be found as

$$S_{th} = \frac{(\sigma_0 S_1 + \sigma_1 S_0)}{(\sigma_0 + \sigma_1)} \tag{8.44}$$

The BER or the probability of error can then be found from

$$\text{NO TURBULENCE:} \quad BER_0 = \frac{1}{2}\left\{erfc\left(\frac{S_1 - S_{th}}{\sqrt{2}\sigma_1}\right) + erfc\left(\frac{S_{th} - S_1/C_{MRR}}{\sqrt{2}\sigma_0}\right)\right\} \tag{8.45}$$

where *erfc* is the complimentary error function.

3. The BER for the fluctuating signal due to turbulence (i.e., with turbulence):

In order to determine the BER in presence of atmospheric turbulence, the BER_0 which is considered as a conditional probability must be averaged over the PDF of the random signal to determine the unconditional mean BER [34, 36]. To perform the calculation the form of the PDF of intensity fluctuations through atmospheric

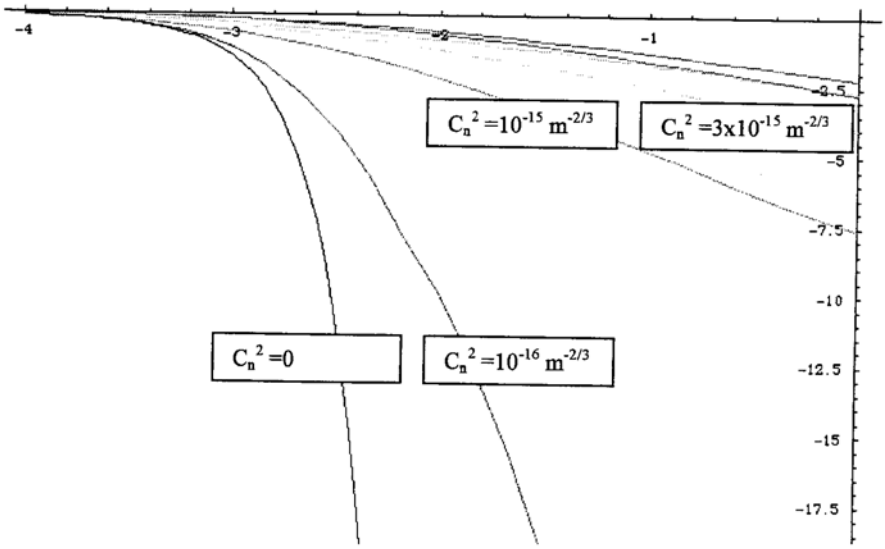

Fig. 8.15 BER (log-scale) versus system parameter G_R (log-scale) for different turbulence strength parameters, C_n^2 (*Reprinted with permission from SPIE, 2004* [32]). *BER* bit-error rate

turbulence is required. A Gamma-Gamma distribution was proposed earlier. The BER for a turbulence-induced fluctuation for a MRR FSO communication link can be written as

$$\text{IN PRESENCE OF TURBULENCE:} \quad BER_{Turb} = \int_0^\infty BER_0(E)\,p(E)\,dE \qquad (8.46)$$

where BER_0 is the BER associated with a given pulse energy with no turbulence from the earlier equation, $p(E)$ is the PDF for the incoming energy taking into account of the pulse repetition frequency of f_{rep} (note: mean received energy E_{rec} per pulse for a pulsed interrogator with a repetition frequency is related to the received power, P_{rec} by $E_{rec} = P_{rec}/f_{rep}$). A Gamma-Gamma distribution generally valid for weak to strong turbulence regime was mentioned earlier. Figure 8.15 shows a plot of system parameter relative cross-section G_R versus BER in presence of atmospheric turbulence, BER_{Turb} (for various values of turbulence strength parameter, C_n^2). A relative cross section of value of G_R of 0.3 % means the value in the log scale to be $\text{Log}_{10}(G_R) = -2.5$. From the figure, it is clear that for a given system value of G_R, the BER for the MRR system increases as the strength of turbulence becomes stronger and stronger from the no turbulence case ($C_n^2 = 0$) to $C_n^2 = 10^{-16}\ m^{-2/3}$, and then to $C_n^2 = 10^{-15}\ m^{-2/3}$. The combination of C_n^2 and the system required BER to be achieved determines the limits of retroreflective communications systems that have to operate under atmospheric turbulence. The BER can be improved by increasing the system parameter $G_R G_{sys}$ which can be accomplished by using a higher interrogator laser power, a larger aperture MRR, or a more efficient collection geometry.

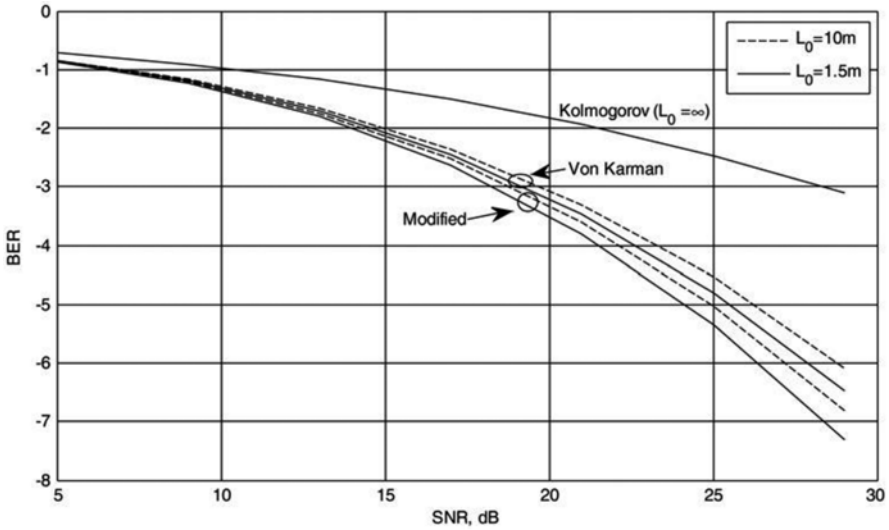

Fig. 8.16 BER (log-scale) versus SNR (dB) for different atmospheric models (spatial spectrums; *Reproduced with permission from IET, 2012* [37]). *BER* bit-error rate, *SNR* signal to noise ratio

A trade-off between all these parameters need to be performed in order determine the optimum MRR-based FSO communications system.

Recent results on the method for the evaluation of performance of free space optical communication systems utilizing MRR under weak turbulence are described in the Ref [37]. Figure 8.16 shows the BER against SNR for various spatial spectrum of atmospheric turbulence models (Kolmogorov, Von Karman, and Modified). The results are valid for weak turbulence where a log normal distribution of PDF was assumed. The results show that different spatial spectrum (i.e., different turbulence models) adopted for the calculations of BER can lead into differences in SNR required for the communications stems design. The performance model for the MRR-based FSO communications systems can be used to evaluate the system performance in terms of BER as a function of SNR, aperture diameter, MRR size, inner and outer scale sizes, C_n^2, and link distance. The model can be used for network design and for network routing with proper algorithms.

8.5.4 Atmospheric Scattering Effects on MRR-FSO Communications System

The previous section deals with the clear air turbulence (CAT) effects on the MRR FSO communications systems performance. This section will discuss the atmospheric scattering effects. There is always scattering when the photons emerging from the interrogator laser beam propagates through atmosphere. The scattering

photons can play an important role among the total photons captured by the receiver and therefore it is important to analyze the influence of atmospheric scattering on an MRR communication link.

The communication channel in this case is atmosphere which consists of air molecules and aerosol particles: the optical parameters of air molecules are the extinction coefficient k_e^{air}, the scattering coefficient k_s^{air}, and the absorption coefficient k_a^{air}, and those of aerosol particles are the extinction coefficient k_e^{aer}, the scattering coefficient k_s^{aer}, and the absorption coefficient k_a^{aer}. The extinction coefficient k_e, the scattering coefficient k_s, and the absorption coefficient k_a of the atmosphere are then given by [38]:

$$\begin{aligned} k_e &= k_e^{air} + k_e^{aer} \\ k_s &= k_s^{air} + k_s^{aer} \\ k_a &= k_a^{air} + k_a^{aer} \end{aligned} \tag{8.47}$$

The state of the MRR is controlled by the data bits of "0" or "1" which for example are corresponding to the "off" and "on" states of the amplitude modulator, respectively. The receiver captures the retroreflected modulated beam and the data is decoded.

When the state of the MRR is "on", the retroreflective power at the receiver can be written as [38]:

$$\begin{aligned} P_r &= P_t \eta_t \exp(-k_e L) \frac{A_{retro} \cos\phi}{L^2 \Omega_t} \eta_{retro} \exp(-k_e L) \frac{A_r}{L^2 \Omega_{retro}} \eta_r \\ &= P_t\, \eta_t\, \eta_{retro} \eta_r \cos\phi \exp(-2k_e L) \frac{A_{retro} A_r}{L^4 \Omega_t \Omega_{retro}} \end{aligned} \tag{8.48}$$

The parameters of the above equation are: interrogator laser power, P_t; wavelength, λ; transmitting beam divergence, θ_t; solid angle, $\Omega_t = 4\pi \sin^2\left(\frac{\theta_t}{4}\right)$. For the receiver, the parameters are: detecting area, A_r; FOV, θ_t; solid angle, $\Omega_r = 4\pi \sin^2\left(\frac{\theta_r}{4}\right)$; The range between the transmitter and the receiver is r. The parameters for the MRR: effective area, A_{retro}; incident angle on the MRR, ϕ; retroreflected beam divergence, θ_{retro}; solid angle of the MRR beam, $\Omega_{retro} = 4\pi \sin^2\left(\frac{\theta_{retro}}{4}\right)$; the optical efficiencies of the laser interrogator, the receiver, and the on-state MRR are η_t, η_r, η_{retro}, respectively. The communication range is L. Air molecules suffer Rayleigh scattering and aerosol particles show Mie scattering effect. Figure 8.17 shows the results of the individual contributions of the retroreflective and scattering powers as a function of the communication range. The retroreflective power decreases sharply with

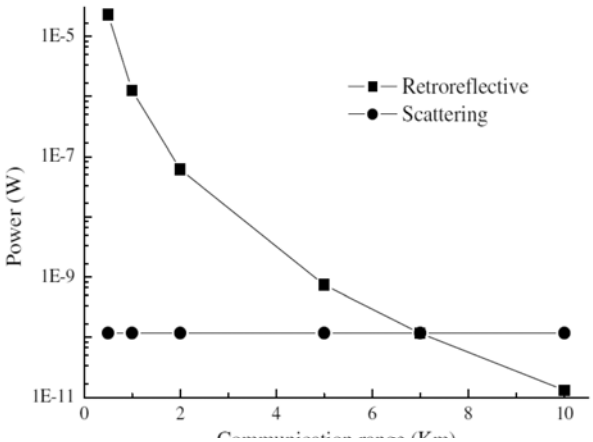

Fig. 8.17 Contributions of retroreflective and scattering signal powers as a function of the communication range (*Reprinted with permission from The Optical Society of America (OSA), 2012* [38])

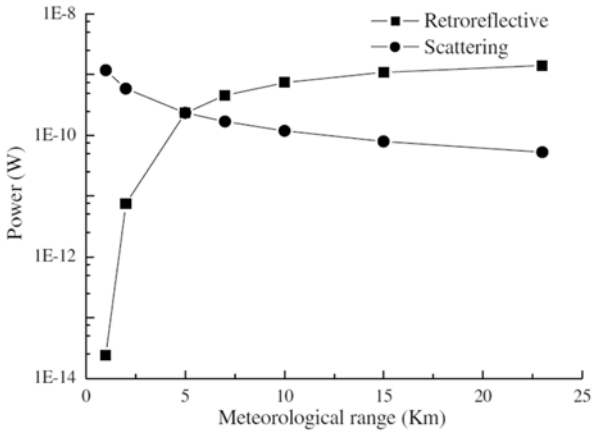

Fig. 8.18 Contributions of retroreflective and scattering signal powers as a function of the meteorological range (visibility) (*Reprinted with permission from The Optical Society of America (OSA), 2012* [38])

increased communication range, whereas the scattering power remains constant for this range.

Figure 8.18 shows the relationships between the retroreflective and scattering powers as a function of the meteorological range, sometime called "visibility." When the meteorological range decreases (i.e., visibility becomes poorer) the retroreflective power decreases correspondingly, while the scattering power increases instead, as expected for a poor visibility situation. Therefore, for a short meteorological range or poor visibility condition, the scattering power can overload a high-sensitive receiver. The MRR-based FSO communications system which has to operate under mostly scattering conditions need to be accordingly designed in terms of FOV of the receiver optics, interrogator laser power, range and other system parameters. In conclusion, in designing MRR-based FSO communications system, the scattering power, in addition to the retroreflective power, must be taken account

in the trade-off study, especially when the communication range is long or the meteorological range is short (low visibility).

8.6 Applications

MRR-based FSO communications is an exciting area with applications in many areas of commercial, biomedical, search and rescue, and industrial fields. The niche area of MRR-based free-space laser communications and data links is growing. We conclude this section by providing some examples of some recent experimental demonstrations performed by researchers and also some potential applications. Some of these applications are discussed below. The earlier sections provide the necessary backgrounds and analysis so that the readers can have full appreciations for the applications. Some of the MRR-based FSO communications applications include:

a. Ground-to-air and air-to-ground communications: real-time video transfer from UAV, Interspacecraft optical communication and navigation (guidance control for free-space platform, secure communication
b. Remote-telemetry applications: includes Mini-Rover (which was built for NASA's international space applications, it will move in the exact pattern display some data as sound and images, is an internet controlled robot
c. Locate objects of interest in a widely dispersed area, optical tagging (for tagging identification for remotely located consumables)
d. Autonomous mobile robot communication
e. Underwater optical communications
f. Car-to-infrastructure communication (telematics, car safety), communications for a vehicle, vehicle-to-vehicle optical two-way communication, FLC-based, MQW-based, fiber-retro-based
g. Optical tags (identification, sensors,)
h. High-speed wireless local area networks (WLAN)
i. Medical applications, human body transdermal optical wireless communications
j. Intra-office communications
k. Internal electronics bus interaction/communication

Retro-modulator laser communication from high altitude balloon platform The viability of retro-modulation communications was demonstrated for the first time by Swenson et al., [39] that performed the first passive retro-modulation experiment. Swenson et al. using FLC-based modulator and achieved a downlink at 12 Kbps data rate and used time division multiplexing to achieve bi-directional communications in a ground breaking experiment. A FLC-based retro-modulator is a low power 2 mW with accepted angles approaching 45° (half angle). For space applications this type of MRR satisfies the critical requirements such as large area, large acceptance angle, and low power, but speed and modulation depth at higher frequency are very low. The details of the FLC for retro-modulation were already

described in the text. The balloon reached a float altitude of 31 km and collected the modulated light reflected from the payload. A concept of a retro-modulator communications link where the remote site is a low-earth orbiting satellite was also illustrated by Swenson et al.

Data link between an UAV and ground station MQW modulating retroreflector (discussed earlier section of the text) was used by Gilbreath et al. [30] to demonstrate an IR data link between a small rotary-wing UAV and a ground based laser interrogator using the NRL's MQW retro-modulator. An Mbps optical link to a UAV in flight at a range of 100–200 ft was shown feasible, and near real-time compressed video transfer was demonstrated at the Mbps rate. Video or other forms of data can be obtained onboard the UAV and can be suitably modulated by the MRR using an appropriate format, and can retroreflect the video signal back when interrogated by a laser/receiver system. Instead of a single MQW MRR, if an array of MRR is used, the pointing requirements are considerably relaxed and the onboard FOV can be increased to accommodate the incoming beam with relaxed steering requirements. The communication package is thus very lightweight without heavy gimbaled mount and power supply and can be used for very small platforms. An InGaAs transmissive MQW modulating retro-modulator of 0.5 cm diameter was used for field tests by placing the MRR on the tail of the UAV pointing down. The six-element array of MRR was used. The UAV was flown at an altitude of 35 m. The NRL MWQ based MRR was demonstrated to support over 10 Mbps in a high signal level and captured data rates of 400 kbps and 910 kbps on a UAV in flight. Also near real-time color video using Joint Photographic Experts Group (JPEG) compression was demonstrated at a 1.2 Mbps. Results of an updated development of MQW retro-modulators for real-time video transfer using an array of devices was reported where color video using wavelet compression at 15 and 30 frames per second was achieved at 4 to 6 Mbps over 30 m in the laboratory [11]. Results at 1550 nm devices were also presented using "Cat's Eye Retromodulator." Real-time color video for a retro-modulator link of 2 m in the laboratory was also demonstrated at 3 Mbps and at 30 frames per second [40]. The device consumed about 75–100 mW and was 10 g.

Researchers have reported [41] the design of a free-space laser communication system from UAV to ground stations using MRR technology resulting in considerable reduction of power, size and weight onboard the UAV. The burden moves to the ground station but the acquisition, tracking and pointing subsystem requirements are also relaxed since the MRR acts as a pointing reference by reflecting the incoming laser beam back to the source. MEMS-based MRR was considered for achieving the data rate in the order of hundreds of Kbps and also high data rate communications with UAVs where the ground laser transmitter to be OOK-modulated at hundreds of Mbps. MEMS-based modulator is a reflective diffraction grating with controllable groove depth acting as one of the three mirrors of the retroreflector device. MEMS modulator is capable of modulating a CW laser beam by switching between an unpowered flat-mirror state to an energized-diffractive state.

The MRR technology allows transfer of information from UAVs permits communication to buoys on the water surface for information exchange and also to ve-

hicles on the ground. One single MRR can be interrogated simultaneously by many lasers. A peer-to-peer sensor network architecture using space-division multiple access (SDMA) and time division multiplexing (TDM) with optical retroreflectors is described in a report [42]. Retroreflector link in FDX mode operation is discussed.

MRR applications for Satellite Communications systems MRR devices are small and allow low powered, high data rate communications downlinks from small satellites. For space-to-space intersatellite links one satellite could be a microsatellite or smaller (Nanosat). For CubeSats, communications often dominate the power budget where MRR technology can be used. For small satellites, the ideal communication system is suggested [43] that would feature a space segment that allows high bi-directional data rates with low power consumption. A highly asymmetric system architecture using MRR devices as the transmitting element in the space segment was discussed.

Interspace laser interrogation, communication, and navigation between spacecraft platforms A novel concept utilizing MQW modulating retroreflectors to provide inter-spacecraft laser interrogation, communication, and navigation was described by Gilbreath et al. [44, 45]. An MRR enable compact, low power, and low mass optical data transfer on the order of Mbps, and relative navigation on the order of centimeters in three-axis position and arcminutes in two-axis tilt orientation was discussed. For docking missions where a close proximity operation of about 10 m are needed, the concept can work with a vision-based system.

Optical Tagging of a remotely located object An MQW retro-modulator array used as a low power, lightweight means to provide optical tagging of a remotely located object was reported by Gilbreath et al. [46]. Tagging identification was performed by demodulating the retroreflected signal using appropriate code. An array of 1/2 cm MQW devices was used at a range of about 40 m. MRR can have a potential solution for locating and identifying consumables such as food, and fuel in orbit which will be required for future long-range manned NASA missions. The MRR technology concept will also be useful as an aid for acquisition and tracking. The system can be very robust for space applications for supporting faster data rates, hence longer ranges, at lower powers than other existing devices. A MEMS-based optical tag was reported [47] in a laser communication experiment over 1 km optical range. The concept was based on employing interference to provide modulation to achieve modulation by tuning a large array of Fabry-Perot cavities via the application of an electrostatic force to adjust the gap between a movable mirror and the underlying silicon substrate. The MEMS based optical modulator was used to act as an interference switch in a modulated retroreflected tag with a bit rate of 200 Kbps.

Mobile Robot Communication MRR technology has applications for autonomous mobile robotic communication by establishing optical links to a small robot. Small robots can be used for operations in areas that may be hazardous and dangerous to humans and the robots can return video and other data from remotely located areas using high bandwidth optical communications. A single MRR will need about 1 degree pointing accuracy for operating at rates of Mbps at ranges of 1 km which

requires an active pointing and tracking. An array of 6 MRRs and photodetectors with FOV of 180° (azimuth)×30° (elevation) mounted on a small robot was described [48]. A 1.5 Mbps optical Ethernet link was established to a range of 1 km. The system worked at 1550 nm wavelength for maximum eye safety using transmits aperture of 2 in. and interrogator power of 350 mW. A transceiver board layout and its performance was described for autonomous mobile robotic application [49]. The robots were autonomous and needed to coordinate themselves without some sort of master. For robotic applications exchanging information such as position, speed, braking, turning, dimensions, and destination of the robot are essential. MRR technology can be used for this purpose. The maximum communication range achieved by the retroreflector robot was 60 ft. High data rate communication links in stationary or mobile mini-sensor suites using retro-modulator simulated on a mini-rover was demonstrated [50]. The host platform consumption of 50 mW and mass of 50 g were used for the communication subsystem. A typical example for use of this technology would be to establish communication link between a spacecraft, landed on a planet, with tens to hundreds of sensors or sensor carrying mini-rovers, distributed in the surrounding area.

FDX Communication on a Single Laser Beam The first experimental demonstration of FDX communications on a single laser beam was described by T. M. Shay et al. [51, 52]. The FDX optical communications means that a simultaneous bi-directional transmission is accomplished. The forward link beam (i.e., interrogating laser beam) simultaneously transmits the forward link data and serves as the carrier wave for the return link. MRR modulates the incident forward link beam according to the input data and is retroreflected back to the interrogator laser (receiver location). The photo-detector near the MRR serves as a receiver for the communication link from the transmitter (laser interrogator) to that receiver. The MRR is the transmitter for the receiver at the interrogator location. Thus a pair of Tx-Rx at both ends is possible which makes FDX operation. The forward data format must deliver a constant average power to the passive terminal and the return data format must be selected so that the forward data is invisible to the return link detection system. Shay et al. demonstrated with sub-carrier-FSK modulation for the forward data link, and a Circularly Polarized Keying [53] (CPK) for the return link. A diode laser interrogator transmits a linearly polarized beam which is then converted to a circularly polarized beam after passing through a quarter-wave plate, and the constant average power beam is sent to the MRR. The LC retro-modulator directs the incident beam back to the interrogator location and assigns left-handed and right-handed circular polarizations to the return beam according to binary data bit information. The LC will flip the right-handed polarized transmitter light into left-handed for a “1”, while for a “0” the incident is unchanged. A second quarter-wave plate converts the returned left and right-handed circularly polarized beams into two orthogonally polarized beams respectively. A polarizing beam splitter separates the two orthogonal linear polarizations. The return signal photons, after passing through an optical filter are incident on the receiver located at the interrogator. The LC shutter was made from phase-separated composite films LC shutter with extinction ratio falling off rapidly

with frequencies beyond 20 kHz, consumed 1/2 W of electric power for unbiased data, and an extinction ratio of less than 3.5 % at 20-Kbps. A subcarrier-FSK modulation was selected for the forward data link and the return data format can be OOK modulation. This type of MRR- FSO communication concept has an application for earth-to-low-earth-orbit (LEO) optical system which can offer lightweight, low power consumption, low data rate communications from LEO satellites.

Fiber-based 2.5-Gbps ARM for FSO Communications The concept of ARM using a high efficiency FSO-SMF coupler was described earlier in the text. The application includes the potential high data rate (~2.5 Gbps) FSO communications [51]. The optical amplifier increases the effective area of the retro-modulator by a factor of 318 and thus can provide the same return signal with a dramatic reduction in the system size and weight of the retro-modulator system.

Wide FOV Amplified Fiber-Retro for Secure High Data rate communications and Remote Data Transfer The concept of this technology was described earlier in the text. The patent [54] describes the application of the concept to an optical system for remotely communications at a high data rate between a base station and a remote station under atmospheric conditions. The remote station includes retroreflectors consists of two sets of lenslets coupled with single-mode fiber array, called "fiber retro". Amplified retro modulation is achieved requiring only one single optical amplifier and one single modulator. A transmitter located at the base station sends an interrogating optical beam to the "fiber retro" which modulates the optical beam according to the input signal/data, and redirects the modulated optical beam to the base station for detection by a receiver. This technology includes the capabilities of providing Identification of Friend-or-Foe (IFF), secure communication, and a means of achieving a wide FOV with a fiber-coupled lenslet array. The simulation result shows the application of this technology for a satellite-based laser interrogator and ground-based amplified retro-modulator. The range of the satellite in the simulation was assumed to be 370 km the atmospheric transmission efficiency of 0.5, the BER $=10^{-9}$, SNR $=144$, and the gain of the retro-modulator system was taken to be 4×10^{5}. Results show that to achieve a data rate of 2.5 Gbps, for a transmitter divergent beam of 6.8 mrad, it requires only 160 mW of laser power, whereas for transmitter divergent beam of 27 mrad, it requires about 25 W of laser power. All these numbers are very practical and realistic and show the utility of ARM system concept.

Underwater Optical Communications using a MRR Communicating with underwater sensors and vehicles is important in ocean exploration and observation. Underwater optical communication is possible at short ranges when application requires high data rates, low latency or covert operation. Optical scattering and absorption in the underwater environment limit the systems operation. Point-to-point optical links can have ranges approaching 200 m in clear water. A modulating retroreflector can be used with a laser on one interrogating platform (such as a submarine or unmanned underwater vehicle). The power-constrained platform (sensor node or small unmanned vehicle) acts as source to transmit the light beam towards a MRR.

The system can be designed to have duplex optical communication at low power. Researchers built an MRR that uses Fabry-Perot optical cavity for modulating light in the visible wavelengths for underwater communication where the intensity of the reflected or transmitted light can be modulated by electrically changing the cavity spacing [55]. Data transfer at rates of 250, 500 and 1 Mbps were demonstrated with a quadrature phase-shift keying (QPSK) modulation format. Another scenario for underwater modulating retroreflection communication link can be when one party (for example, a submarine) with more power consuming resource than another one (for example, a diver) [56]. Power requirements and the system complexity can then be put into the submarine and the diver can be equipped with a small modulating retroreflector and can collect information which can be obtained by the illuminating interrogator.

Remote Telemetry using MEMS Deformable Micromirror Array-based MRR MR concept can be used for remote telemetry application which includes remotely interrogated environmental sensors distributed over a large geographic area, and secure communications link. A laser interrogator can be mounted in an aircraft flying over the large area to interrogate the sensors remotely. The communication range for remote telemetry may extend from 0.1 to 10 km and must operate under varying environmental conditions. The system needs to operate over a wide range of incident angles, up to ±30° which is possible with a hollow corner-cube retroreflector. An MRR was described [19] with one MEMS mirror that deforms from a flat into a hexagonal array of concave reflective microlenses to disperse the retroreflected wave front. A gold-coated silicon-nitride membrane suspended over 1-mm diameter circular cavities with a 79 V applied with a modulation contrast ratio of 7:1 and achieved 100-kHz modulation over a 35° range of incident angle.

Medical Application: Retroreflective Transdermal Optical Wireless Communication MRR link is an attractive communication solution in medical applications. Transdermal high data-rate communication for use in-body devices, such as pacemakers, smart prostheses, neural signals processors at the brain interface, and cameras acting as artificial eyes as well as for collecting signals generated within the human body are just some examples. Researchers have explored the potential of retroreflected optical link as a transdermal communication modality and have examined the channel characteristics [57]. MRR is attractive solution in medical applications because of its low power consumption in the order of μW. Another biomedical application involves especially implanted brain-computer interfaces which give rise to large data sets that needs to be transmitted transcutaneous. A link at near-IR (~854 nm) can be established using an MRR in the implant, but keeping the laser and the detector on the outside [58]. The modulator and drive electronics are the only part of this system that needs to be implanted.

Some applications using MRR technology were discussed. However there are more applications to explore. Some of them include: a communication link comprised of a Helmet-mounted and vehicle-based retro modulator, vehicle-to-vehicle optical two way communications, car-to-infrastructure communication (telematics,

traffic safety), internal electronics bus interaction/communication, intra-office communications and Industrial Manufacturing. The readers might find them interesting.

Acknowledgements I would like to express my sincere thanks to Dr. Thomas M. Shay, Professor of the department of Electrical & Computer Engineering, The University of New Mexico for carefully reading this chapter and providing helpful comments in this field.

References

1. B.E.A. Saleh, M.C. Teich, *Fundamentals of Photonics*, Chap. 18, Electro-Optics (Wiley, Hoboken, NJ, 1991)
2. T.A. Maldonao, *Handbook of Optics*, Vol. II, Chap. 13 (McGraw-Hill, New York, NY, 1995)
3. G. Spirou, I. Yavin, M. Wheel, A. Vorozcovs, A. Kumarakrishnan, P.R. Battle, R.C. Swanson, A high-speed-modulated retro-reflector for laser using an acousto-optic modulator. Can. J. Phys. **81**, 625–638 (2003)
4. E. Hallstig, Nematic liquid crystal spatial light modulators for laser beam steering. Dissertation, Faculty of Science and Technology, ACTA Universitatis Upsaliensis, Uppsala, Sweden, 2004
5. G.C. Gilbreath, W.S. Rabinovich, T.J. Meehan, M.J. Vilcheck, R. Mahon, R. Barris, M. Ferraro, I. Sokolsky, J.A. Vasquez, C.S. Bovais, K. Cochrell, K.C. Goins, R. Barbehenn, D.S. Katzer, K. Ikossi-Anastasiou, M.J. Montes, Compact light weight payload for covert data link using a multiple quantum well modulations retro-reflector on a small rotary-wing unmanned airborne vehicle. Proc. SPIE **4127**, 57–67 (2000)
6. G. Charmaine Gilbreath, W.S. Rabinovich, T.J. Meehan, M.J. Velcheck, M. Stell, R. Mahon, P.G. Goetz, E. Oh, J.A. Vesquez, K. Cochrell, R.L. Lucke, S. Mozersky, Progress in development of multiple-quantum-well retro modulators for free-space data links. Opt. Eng. **42**(6), 1611–1617 (2003)
7. M.L. Bierman et al., Design and analysis of a diffraction limited Cat's eye retroreflector. Opt. Eng. **41**(7), 1665–1660 (2002)
8. G.C. Gilbreath et al., Large-aperture multiple quantum well modulating retroreflector for free-space optical data transfer on unmanned aerial vehicles. Opt. Eng. **40**(7), 1348–1356 (2001)
9. G.C. Gilbreath et al., Progress in development of multiple quantum well retro-modulators for free space data link. Opt. Eng. **42**, 1611–1617 (2003)
10. G. Charmaine Gilbreath, W.S. Rabinovich, T.J. Meehan, M.J. Vilcheck, M. Stell, R. Mahon, P.G. Goetz, E. Oh, J. Vasquez, K. Cochrell, R. Lucke, S. Mozersky, Real time video transfer using multiple quantum well retromodulators. SPIE Proc. **4821**(61), 155–162, (2002). (Gilbreath et al., Real-time 1550 nm retro-modulated video link. Proceedings of the 2003 IEEE Aerospace conference, paper No. 1560, March, 2003
11. W.S. Rabinovich, P.G. Goetz, R. Mahon, L. Swingen, J. Murphy, G.C. Gilbreath, S. Binari, E. Waluschka, Performance of Cat's eye modulating retro-reflectors for free-space optical communications. Proc. SPIE **5550**, 104–114 (2004)
12. P.G. Goetz, W.S. Rabinovich, R. Mahon, L. Swingen, G.C. Gilbreath, J.L. Murphy, H.R. Burris, M. Fa Stell, Practical considerations of retro-reflector choice in modulating retro-reflector systems. Digest of IEEE LEOS summer Topical Meetings, 2005
13. W.S. Rabinovich, P.G. Goetz, R. Mahon, L. Swingen, J. Murphy, M. Ferraro, H. Ray Burris Jr., C.I. Moore, M. Suite, G. Charmaine Gilbreath, S. Binari, D. Klotzkin, 45-Mbit/s Cat's eye modulating retro-reflectors. Opt. Eng. **46**(10), 104001 (2007)
14. W.S. Rabinovich, J.L. Murphy, M. Suite, M. Ferraro, R. Mahon, P. Goetz, K. Hacker, E. Saint Georges, S. Uecke, J. Sender, Free-space optical data link to a small robot using modulating retro-reflectors. Proc. SPIE **7464**, 746408-1 (2009)

15. P.G. Goetz et al., Modulating retro-reflector laser com systems at the Naval Research Laboratory. IEEE Military communications conference-Unclassified Program-systems Perspectives Track, 2010
16. A. Guillen Salas, J. Stupl, J. Mason, Modulating retro-reflectors: Technology, link budgets and applications. 63rd International Astro-nautical congress, Naples, Italy, IAC-12, B4, 6B, 11, 2012
17. L. Zip-Schatzberg, T. Bifano, S. Cornelissen, J. Stewart, Z. Bleir, Secure optical communication system utilizing deformable MEMS mirrors. Proc. SPIE **7209**, 72090C-1–72090C-15 (2009). (L. Zip-Schatzberg, T. Bifano, S. Cornelissen, J. Stewart, Z. Bleir, Secure optical communication system utilizing deformable MEMS mirrors. Proc. SPIE **7318**, 73180T-1–73180T-12 (2009))
18. T.K. Chan, J.E. Ford, Retroreflecting optical modulator using an MEMS deformable micromirror array. J. Lightwave Technol. **24**(1), 516–525 (2006)
19. C. Jenkins, W. Johnstone, D. Uttamchandani, V. Handerek, S. Radcriffe, MEMS actuated spherical retro reflector for free-space optical communications. Electron. Lett. **41**(23), 1278–1279 (2005)
20. D. Peterson, O. Solgaard, Free space communication link using a grating light modulator. Sensor. Actuator. **83**(1–3), 6–10 (2000)
21. C. Luo, K.W. Goossen, Optical micro electromechanical system array for free-space retro communication. IEEE Photonic. Technol. Lett. **16**(9), 2045–2047 (2004)
22. T.K. Chan, Retro-modulators and fast beam steering for free-space optical communications. Ph.D dissertation, University of California, San Diego, 2009
23. T.K. Chan, J.E. Ford, Retro-reflecting optical modulator using an MEMS deformable micro mirror array. J. Lightwave Technol. **24**(1), 516–525 (2006)
24. K.W. Goossen, Micro machined modulator and methods for fabricating the same, US Patent. 6519073, 2003
25. A.M. Scott, K.D. Ridley, D.C. Jones, M.E. MoN.e, G.W. Smith, K.M. Brunson, A. Lewin, K.L. Lewis, Retro reflectors Communications over a kilometer range using a MEMS-based optical tas. Proc. SPIE. **7480**, 74800 L-1–74800 L-10 (2009)
26. P. Schultz, B. Cumby, J. Heikenfeld, Investigation of five types of Switchable retro reflector films for enhanced visible and infrared conspicuity applications. Appl. Optics **51**(17), 3744–3754 (2012)
27. F. Mugele, J.C. Baret, Electro wetting: From basics to applications. J. Phys. Condens. Matter **17**, R705–R774 (2005)
28. T.M. Shay, R. Kumar, 2.5-Gbps amplified retro-modulator for free-space optical communications. Proc. SPIE **5550**, 122–129 (2004)
29. G. Keiser, *Optical Fiber Communications*, 2nd edn. (McGraw-Hill, New York, 1991)
30. G.C. Gilbreath, W.S. Rabinovich, T.J. Meehan, M.J. Vilcheck, R. Mahon, R. Burris, M. Ferraro, I. Sokolsky, J.A. Vasquez, C.S. Bovais, K. Cochrell, K.C. Goins, R. Barbehenn, D.S. Katzer, K. Ikossi-Anastasiou, M.J. Montes, Compact, lightweight payload for covert data link using a multiple quantum well modulating retro-reflector on a small rotary-wing unmanned airborne vehicle. Proc. SPIE **4127**, 57–67 (2000)
31. A.K. Majumdar, T.M. Shay, Wide field-of-view amplified fiber-retro for secure high data rate communications and remote data transfer, US Patent, No. US 8,301,032 B2, date of patent Oct. 30, 2012
32. A.M. Scott, K.D. Ridley, Calculations of bit error rates for retroreflective laser communications systems in the presence of atmospheric turbulence. Proc. SPIE **5614**, 31–42 (2004)
33. L.C. Andrews, R.L. Phillips, C.Y. Hopen, *Laser Beam Scintillation with applications* (SPIE, Bellingham, Washington, 2001)
34. A.K. Majumdar, Free-space laser communication performance in the atmospheric channel. J. Opt. Fiber. Commun. Rep. **2**, 345–396 (2005)
35. A.K. Majumdar, J.C. Ricklin, *Free-Space Laser Communications* (Springer, New York, 2008)
36. L.C. Andrews, R.L. Phillips, *Laser Beam Propagation through Random Media*, 2nd edn. (SPI E, Bellingham, Washington, 2005)

37. N. Avlonitis, P.B. Charlesworth, Performance of retro reflector-modulated links under weak turbulence. IET Optoelectron. **6**(6), 290–297 (2012)
38. H. Yin, T. Lan, H. Zhang, H. Jia, S. Chang, J. Yang, Theoretical evaluation of scattering effect on retroreflective free-space optical communication. J. Opt. Soc. Am. A Opt. Image Sci. Vis. **29**(12), 2608–2611 (2012)
39. C.M. Swenson, C.A. Steed, I.A. DeLaRue, R.Q. Fugate, Low power FLC-based retro modulator communications system. Proc. SPIE **2990**, 296–310
40. G. Charmaine Gilbreath, W.S. Rabinovich, R. Mahon, L. Swingen, E. Oh, T. Meehan, P.G. Goetz, Real-time 1550 nm retromodulated video link. Proceedings of the 2003 IEEE Aerospace Conference, Paper No. 1560, 2003
41. A. Carraso-Casado, R. Vergaz, J.M. Sanchez-Pena, Free-space laser communications with UAVs. Report of RT Organization, # RTO-MP-IST-099
42. J.L. Gao, Sensor network communications using space-division optical retro-reflectors for in-situ science applications. IEEE paper, 0-7803-7651-X/03, 2003
43. A.G. Salas, J. Stupl, J. Mason, Modulating retroreflectors: Technology, link budgets and applications. 63rd International Astronautical Congress, Naples, Italy, # IAC-12.B4, 6B,11, 2012
44. G. Charmaine Gilbreath, N. Glenn Creamer, W.S. Rabinovich, T.J. Meehan, M.J. Vilcheck, J.A. Vasquez, R. Mahon, E. Oh, P.G. Goetz, S. Mozersky, Modulating retroreflectors for space, tracking, acquisition and ranging using multiple quantum well technology, Proc. SPIE **4821**, 494–507 (2002)
45. N. Glenn Creamer, G. Charmaine Gilbreath, T.J. Meehan, M.J. Vilcheck, J.A. Vasquez, W.S. Rabinovich, P.G. Goetz, R. Mahon, Interspacecraft optical communication and navigation using modulating retroreflectors. J. Guid. Control Dyn. **27**(1), 100–106, (2004)
46. G.C. Gilbreath, T.J. Meehan, W.S. Rabinovich, M.J. Vilcheck, R. Mahon, M. Ferraro, J.A. Vasquez, I. Sokolsky, D. Scott Katzer, K. Ikossi-Anastasiou, P.G. Goetz, Retromodulator for optical tagging for LEO consumables. Technical Report, NRL, 2007
47. A.M. Scott, K.D. Riley, D.C.Jones, M.E. McNie, G.W. Smith, K.M. Brunson, A. Lewin, K.L. Lewis, Retroreflective communications over a kilometer range using a MEMS-based optical tag. Proc. SPIE **7480**, 2009
48. W.S. Rabinovich, J.L. Murphy, M. Suite, M. Ferraro, R. Mahon, P. Goetz, K. Hacker, W. Freeman, E. Saint Georges, S. Uecke, J. Sender, Free-space optical data link to a small robot using modulating retroreflectors. Proc. SPIE **7464**, 746408-1 - 746408-9, (2009)
49. K. Alhammadi, Applying wide field of view retroreflector technology to free space optical robotic communications. PhD dissertation in Electrical Engineering, North Carolina State University, Raleigh, North Carolina, September 2006
50. H. Hemmati, C. Esproles, W. Farr, W. Liu, P. Estabrook, Retro-modulator with a mini-rover. Proc. SPIE **5338**,50 -56, (2004)
51. T.M.Shay, J.A. MacCannell, C.D. Garrett, D.A. Hazzard, J.A. Payne, N. Dahlstrom, S. Horan, The first experimental demonstration of full-duplex communications on a single laser beam. Proc. SPIE **5160**, 265–271 (2004)
52. T.M. Shay, D. Hazzard, S. Horan, J.A. Payne, Full-duplex optical communication system, U.S. Patent. No. US 6,778,779 B1, Aug. 17, 2004
53. T.M. Shay, D.A. Hazzard, *Circular Polarization Keying*, patent pending, Serial No. 60/170,889
54. A.K. Majumdar, T.M. Shay, US Patent No. US 8,301,032 B2, Oct. 30, 2012
55. W. Cox, K. Gray, J. Muth, Underwater optical commun ication using a modulating retroreflector. http://www.sea-technology.com/features/2011/0511/retroreflector.php, 2014 Compass Publications, Inc., published in Sea Technology, Vol.52, Issue 5, p.47, May 2011.
56. S. Arnon, Underwater optical wireless communication network. Opt. Eng. **49**(1), 015001 (2010)
57. Y. Gil, N. Rotter, S. Arnon, Feasibility of retroreflective transdermal optical wireless communication. Appl. Optics **51**(18), 4232 - 4239, (2012)
58. M.Y. Abualhoul, P. Svenmarker, Q. Wang, J.Y. Anderson, A.J. Johansson, Free-space optical link for biomedical applications, 34th Annual International Conference of the IEEE EMBS, San Diego, California USA, pp. 1667–1670, 28 August–1 September, 2012

Chapter 9
Hybrid Optical/Radio Frequency (RF) Communications

L. C. Andrews, R. L. Phillips, Z.C. Bagley, N.D. Plasson and L. B. Stotts

9.1 Introduction

The concept of free-space optical communications (FSOC) has been around since the late 1960s. Lasers offered the potential for small transmitters and receivers with very high antenna gain (i.e., small transmitter spot sizes). Specifically, FSOC systems could be much more efficient and could provide orders of magnitude gains in data rate compared to a radio frequency (RF) system of the same size. Unfortunately in the 1970s and 1980s, much of the potential gain in efficiency was lost because of poor electrical-to-optical efficiency, poor optical detector efficiency, the increased transmitter spot sizes necessitated by transmitter pointing error limitations, and most importantly, link degradation from optical channel effects. The result was that the advantages of optical communications over RF communications were never realized for the past 40 years, except with one exception, fiber optical communications (FOC). This is because FOC technologies overcame the detector and efficiency problems cited above; laser light could be easily launched into fiber optic cable and FOC did not suffer the channel effects that plagued FSOC.[1] The FOC technology break-through can help move FSOC systems into a reality if the FSOC channel effects can be overcome. The realization that the latter aspect is possible came from the realization that neither FSOC nor RF communications can provide totally reliable, multi-gigabit/tetrabit per second (Gbps/Tbps) communications like a FOC system by themselves. However, they have the potential to move towards that goal by working together in a network infrastructure [1]. That is, through a hybrid optical-RF networking construct. This can be clearly seen in Table 9.1.

RF communications are generally reliable and well understood, but cannot support emerging data rate needs unless they use a large portion of the precious radio spectrum. On the other hand, FSO communications offer enormous data rates, but operate much more at the mercy of the environment. The perennial limitations of FSOC systems are directly attributable to signal fading/scintillation (optical turbulence) and path blocking (cloud obscuration) [1]. Both phenomena reduce the

[1] FOC did have its own channel effects to deal with, but their resolution is a major success story that will not be covered here.

A. K. Majumdar, *Advanced Free Space Optics (FSO),*
Springer Series in Optical Sciences 186, DOI 10.1007/978-1-4939-0918-6_9,
© Springer Science+Business Media New York 2015

availability of the optical channel to support reliable communications. Since RF paths are relatively immune to the same phenomenology, combining the attributes of a bursty high data rate FSOC link with the attributes of a low data rate (by comparison), but reliable RF link could yield attributes better than either one alone. By adding to this mix the capabilities of retransmission by, and rerouting through, a high-speed network structure, the potential to create a communication system like a FOC system with high availability and high data rates is very possible [2].

To achieve a robust high throughput backbone communications network, innovative hybrid networking and link technologies that exploit FSO/RF channel diversity and synergy must be employed to yield higher performance than either FSO or RF alone. Table 9.2 outlines the various components of a hybrid system and what negative system effect they address. This is the subject of this chapter. Specifically, we will provide an example architecture, its basic components, and performance data on how well it works. As the reader will soon see, one really needs a number of components in a hybrid system approach to ensure high link availability under all weather conditions.

9.2 Hybrid Optical/RF Communications

Recent efforts at the Defense Advanced Research Projects Agency (DARPA) and Air Force Research Laboratory (AFRL) show that the needed performance to emulate a FOC system can be achieved by a hybrid system that incorporates FSOC, directional RF, and adaptive networking. Key results are reported regarding the 2006/2007 experiments conducted under the AFRL Integrated RF/Optical Networked Tactical Targeting Networking Technologies (IRON-T2) Program [1, 3–6]. The tests for the AFRL IRON-T2 Program, culminating in IRON-T2 2008 [6], demonstrated the efficacy of a combined optical/RF communications system. Test data indicated that the FSOC technologies and hybrid approach could support reliable multi-Gigabit links under a wide range of day and night operating conditions. When atmospheric conditions, such as fog and clouds, denied optical communication, lower rate RF connectivity could sometimes be maintained if ducting and accompanying multipath interference were absent. Significant deleterious multipath effects occurred most often on low-angle RF links in the presence of temperature inversions. Varying atmospheric conditions caused one or other spectrum channel to fail, or both, or neither. The lesson learned was that no all-weather, all situation communications connectivity exists, but that a combined optical/RF communications system has greater availability than either one alone. In addition, enhanced equalization subsystems in the RF domain can alleviate some multipath interference. Moreover, operations planning can mitigate link failures by adjusting flight trajectories based on outage prediction and detection.

DARPA and AFRL have since leveraged the IRON-T2 results to further research hybrid FSO/RF system performance and design under the DARPA Optical RF Communications Adjunct (ORCA) Program and follow-on, FSO Experimental Network

Table 9.1 Complementary channel/hybrid characteristics for atmospheric networking

	RF	FSO	RF and FSO
Data rate	Low data rate	High data rate	Enables high data rate free space optical (FSO) communications with high reliability
Channel stability and QoS	Stable channel	Bursty channel	Improves network availability quality of service (QoS)
Impact of weather	*Impact of clouds*		
	Relatively immune blocking	Must have clear/haze conditions	RF operations in clouds
	Impact of Rain		
	Sometimes affected by rain	Less degradation than RF	FSO operation in rain
Ancillary benefits			Physical layer diversity improves jam resistance Size, weight, and power (SwaP) focus Leverages common power, stabilization, etc. Economical use of platform volume

Attribute	Clear	Turbulence	Clouds	Blockage	Multipath
Hybrid RF/FSO Link					
Adaptive Optics					
RF Adaptive Equalization					
Optical AGC					
Coding					
MANET					
Link Layer Retransmission					
Local Deep Queues					
Network Replay					

Table 9.2 Hybrid optical RF network reliability mechanisms. *RF* radio frequency

experiment (FOENEX) program. The intent of the ORCA/FOENEX Programs are to design, build, and test a prototype hybrid electro-optical and RF airborne backbone network. The Internet protocol (IP)-based hybrid FSO/RF network was designed to provide the capabilities and performance needed for tactical reach-back and data dissemination applications. Airborne nodes were expected to communicate between each other, up to ranges of 200 km at nominal altitudes of 25,000 ft or

higher, whereas air-to-ground links were to achieve up to a 50 km slant range. As noted in the 2009 Institute of Electrical and Electronics Engineers (IEEE) article [1], the major challenges for establishing a hybrid FSO/RF airborne communications capability are overcoming atmospheric turbulence over long ranges and low slant angles and mitigating multipath in low altitude RF.

9.2.1 ORCA Program and Objective Hybrid System Description

The overall approach for hybrid networking in ORCA was driven by the need for high-rate, long-haul tactical communications providing a high degree of availability to users [1]. A system-level approach to the ORCA design and development enabled the program to consider design trades and interactions among technologies in achieving the desired performance. The resulting design leveraged diversity, reliability, and adaptability mechanisms throughout the system in a cohesive manner—from the dual physical layer up through mobile ad hoc networking (MANET) mechanisms.

An ORCA network contains multiple air and ground platforms, each containing one or more hybrid terminals and interconnected by simultaneous hybrid FSO/RF links (each ORCA terminal head contained both FSOC and RF transceivers). Two or more independent links were required for a platform to be an "interior" node in the network that forwards data through the network. While "edge" nodes such as ground terminals could contain a single hybrid link, the presence of multiple network nodes on a platform improves overall network reliability and availability.

The ORCA network is initiated via a long-range, low-bit rate RF omnidirectional signal, providing initial telemetry information exchange among hybrid terminals as each air and ground platform comes into communications range. The telemetry signal reaches farther than the FSOC and directional RF communications channels, allowing the terminals to establish a group leader and initiate network planning. Network formation initiates once the terminals are within range to establish FSOC and/or RF links. Optical links are established using a semi-cooperative acquisition, tracking, and pointing (ATP) system consisting of a wide-field of-view (WFOV) camera, narrow-field of view (NFOV) camera, and wave front sensor (WFS) fine tracking loop with turbulence compensation. Using the initial pointing information provided by the telemetry system, node connection assignments are made and narrow optical beacon signals on each platform are pointed towards pre-selected receiving platform locations. "Receiving" WFOV on each intended connection node will then acquire and lock their beacons within respective track gates. The NFOV sensors then establish smaller track gates, where the signal is locked and the WFS on each node provides fine tracking of signals and allows the FSOC link to begin transmitting data. The RF link also uses the telemetry data to initiate link acquisition in parallel with the FSOC process. Once an end-to-end path is established between ORCA edge nodes, data begins to transit the network.

Data flows can be configured to utilize the FSO and RF links of the hybrid system in a number of ways. For example, high-throughput flows can be directed to

use the FSO links as the primary medium while lower-rate flows such as voice or chat could use the RF link as the primary medium. Alternatively, all data can use the FSOC link as the primary medium and "failover" to the RF link when outages occur and other FSOC paths are not available.

During operations, the network must adapt to changing link conditions as aircraft maneuver and atmospheric conditions change. Each terminal's field of view is limited by the location of the apertures on the platform (i.e., aircraft body), and individual links may become blocked by the relative position of each aircraft. Such outages are predictable and topology management software is able to preemptively adapt the network before blockage events occur. Also, unpredictable factors such as clouds or severe atmospheric turbulence can degrade the optical link or cause unpredicted outages that force the network to adapt.

Adaptation to link loss or quality degradation occurs in several ways within the hybrid network. At sub-second scales, heavy scintillation of the optical link can cause link disruption events (LDEs) that can result in unrecoverable packet errors. An ORCA network uses a link layer retransmission scheme, rapidly detecting the onset of scintillation events and retransmits unrecovered packets over the link via the FSO or RF as appropriate. If an LDE has a long duration or link quality degrades too severely, packets in the network may be rerouted around the affected link, resulting in a change to the network topology. Depending on network size and conditions, an end-to-end path through the hybrid network may be temporarily unavailable until the network is able to adapt through re-pointing. Currently, an ORCA network is designed to contain a 5-second cache of data to be replayed once an end-to-end path is re-established.

The primary components of the objective system are the FSOC, RF, and networking subsystems. A system block diagram is shown in Fig. 9.1. The ORCA program focused on developing key technologies for each subsystem as well as developing capabilities that allow the three components to work in a hybrid manner to maximize system performance. It is envisioned that their integrated capability will provide high reliability and the necessary performance to meet military and commercial needs. The hybrid link established by pairing FSO and RF increases the availability of each established link. Retransmission, high-speed rerouting, topology management, and replay mechanisms of the network increase the availability of an end-to-end route across the network.

9.2.2 FSOC System Overview

The ORCA FSOC subsystem is designed to accurately point the transmitter and receiver apertures for signal acquisition; couple light from free-space into a single-mode fiber and mitigate power variations in the fiber to maximize receiver sensitivity. The acquisition and pointing functions are provided by a semi-cooperative ATP system consisting of a WFOV camera, NFOV camera, and WFS fine tracking loop with turbulence compensation.

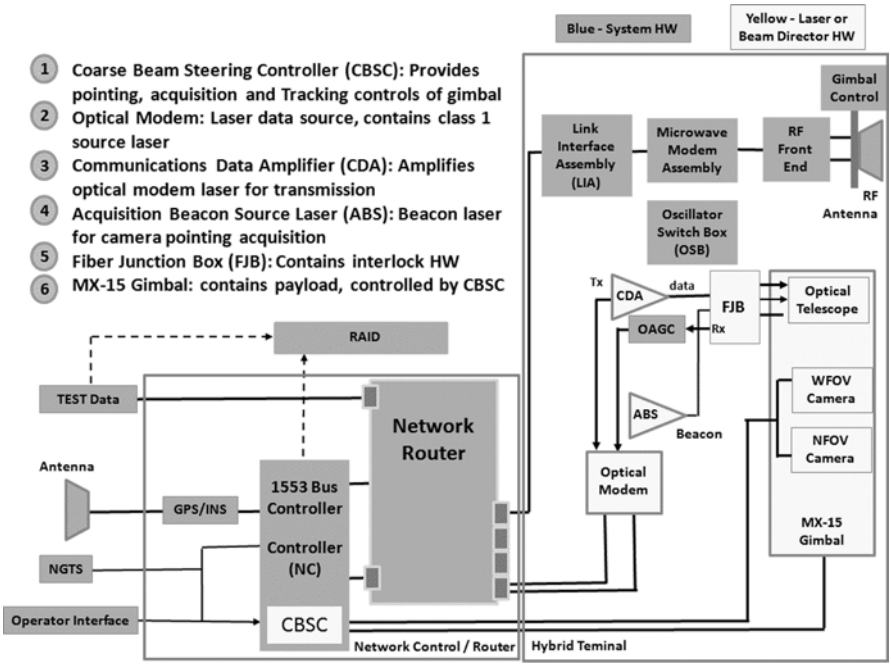

Fig. 9.1 ORCA system block diagram. *ORCA* optical radio frequency communications adjunct

While turbulence affects the acquisition process, it is more disruptive to the FSO link. A transmitted beam experiences spatial and temporal distortions due to turbulence in the form of beam wander, beam spreading (blur), and scintillation [7–10]. Airflow over the optical aperture of airborne links creates aero-optics effects that require mitigation in order to achieve reliable communication links. A key feature of the ORCA FSOC system is that the transmitter and receiver paths within the optical hardware are reciprocal, each having adaptive optics, thereby correcting both the transmitted beam and the received beam to maximize light coupling into the fiber.

The ORCA program incorporates an adaptive optics (AO) subsystem and an optical automatic gain controller (OAGC), which together are the key components for converting the highly dynamic received optical signal into a stable signal that can be processed by the optical modem. The AO subsystem uses a tip-tilt mechanism for correcting beam wander and a deformable mirror to compensate for scintillation effects. The OAGC provides low-noise optical amplification and stabilization, providing 40 dB of dynamic range while isolating optical detectors from high input power which can cause detector saturation or damage. Details of these components have been described separately in [2–6], and relevant performance characteristics are presented in this paper.

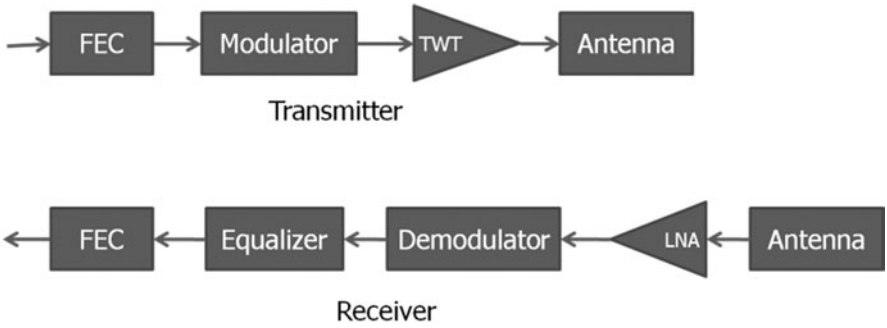

Fig. 9.2 RF subsystem diagram. *RF* radio frequency

9.2.3 RF Subsystem Overview

The ORCA RF communications subsystem components are designed to achieve efficient high rate communications over directional line-of-sight (LOS) air-to-air and air-to-ground links. Time-domain diversity is achieved through equalization and long-block length turbo codes applied as forward error control (FEC) coding. A differential feedback equalizer (DFE) reduces inter-symbol interference (ISI) caused by distortion effects such as frequency-selective fading and phase deviation and mitigates the fading caused by reflected signals (i.e., multipath interference) that arrive at the receive antenna after the LOS signal. A turbo product code (TPC) FEC is applied in order to reduce the amount of per bit energy required for reliable data reception.

Figure 9.2 illustrates the basic RF hardware configuration for the brassboard system used in the recent testing. Most of the hardware components are based on existing equipment with proven track record in other data link systems. Some modifications were made to enable unique aspects of the ORCA RF operation, particularly to accommodate air-to-air links. Principle among them is the DFE, which mitigates multipath energy resulting from ground reflections on air-to-air links that were shown in the June 2009 article [11]. The DFE estimates the reflected channel components and implements filtering with the appropriate time delay to subtract the reflected signal from the direct path signal.

9.2.4 Network Subsystem Overview

The goal of an ORCA network is to provide an IP-based transit (backbone) class network with greater than 95 % end-to-end network availability. The network is an ad hoc network in that airplanes and ground stations equipped with ORCA nodes can discover each other, form a network with a topology based on in situ conditions, and continue to adapt the topology over time. The network topology adapts to platform and environmental dynamics by re-pointing terminal apertures to establish new communications paths and by rerouting packets around degraded links. An

ORCA network hides this mobility from external networks through the use of tunneling. Incoming IP packets are encapsulated and managed internally to the ORCA network for reliable delivery to the egress point, making the ORCA network look like a single hop to external networks.

The key hardware component for the hybrid network is a high-speed router. The ORCA hybrid router is being designed to accommodate 100 Gbps aggregate throughput on a backplane to allow switching of up to four (4) duplex hybrid links and one (1) user port at 10 Gbps in each direction on a single platform. Each hybrid link uses a dedicated hybrid switching module (HSM) card containing an RF and FSO port. Each HSM corresponds to a single hybrid terminal or user port and each router (containing up to five (5) HSMs) corresponds to a single node.[2] The network manages each hybrid communications link (i.e., a paired set of FSO and RF communication links) on the same HSM as a single communications link between the two network nodes.

In addition to the hardware design challenges, a number of network technologies are being developed. LDEs are caused by mobility, atmospheric conditions, terrain, and platform blockages. Some of the LDEs—such as platform blockages —can be predicted, allowing the network to take preemptive action such as rerouting through other network paths or re-pointing apertures to create new network topologies. Other LDE causes—including atmospheric scintillation —are not always predictable and require reactive mechanisms. As discussed previously, an ORCA network uses several mechanisms to overcome phenomenology that cause LDEs of different time scales:

- Error correction coding (ECC): The FSO link uses a Reed Solomon turbo code while the RF link uses a turbo product code for bit error corrections due to sub-second LDEs.
- Retransmission: When packets cannot be recovered through ECC methods, the network provides Layer 2 retransmission to sub-second LDEs. Retransmission of packets lost on the FSO link can be resent over the FSO link or RF link.
- Integrated quality of service (QoS) and deep queues: For multi-second LDEs (less than 5 s) such as those caused by clouds, interior nodes can employ deep queuing techniques to mitigate the outage. The link is kept open and packets are held until they can be resent across the link.
- Rerouting: Alternatively, if a multi-second LDE lasts several seconds (>5 s), then the local node will reroute packets through other existing links established by the local node.
- Re-pointing: If rerouting is not possible, the network may direct the network nodes to re-point one or more apertures, adapting the network topology to improve end-to-end connectivity. The local node resumes data transmission once the new path is established.
- Replay: The network will replay up to 5 s of data from an edge node when retransmission and rerouting from the forward node are not possible. Replay may be necessary when re-pointing operations take longer than the time to fill the local node queues.

[2] Note that an air or ground platform is likely to have a single router; thus, “node” and “platform” are used interchangeably throughout this article.

9.3 FSOC Systems

FSOC has become an important application area because of the increasing need for larger bandwidths and high-data-rate transfer of information that is available at optical wavelengths. Although early interests concentrated largely on higher and higher data rates afforded by optical systems over RF systems, some of the greatest benefits of laser communication may be: (i) less mass, power, and volume as compared with RF systems, (ii) the intrinsic narrow-beam/high-gain nature of laser beams, and (iii) no regulatory restrictions for using frequencies and bandwidths.

9.3.1 Background

FSOC is a LOS technology that uses lasers to provide optical bandwidth connections without requiring fiber-optic cable. Only 5% of the major companies in the USA are connected to fiber-optic infrastructure (backbone), yet 75% are within 1 mile of fiber (known as the "Last Mile Problem"). As bandwidth demands increase and businesses turn to high-speed local area networks (LANs), it becomes more frustrating to be connected to the outside world through lower-speed connections such as digital subscriber line (DSL), cable modems, or transmission system 1 (T1s).

Typical laser wavelengths considered for FSOC systems are 850 and 1550 nanometers (nm). Low-power infrared lasers, which operate in an unlicensed electromagnetic-frequency band either are eye-safe or can be made to operate in an eye-safe manner. However, limiting the power emitted by a laser restricts the range of applicability. Depending on weather conditions, FSOC links along horizontal near-ground paths can extend from a few hundred meters up to several kilometers or more—far enough to get broadband traffic from a backbone to many end users and back. For aircraft-to-ground or aircraft-to-aircraft links, the ranges can be up to 100 km or more. Because bad weather (thick fog or clouds, mainly) can severely curtail the reach of these LOS devices, each optical transceiver node, or link head, can be set up to communicate with several nearby nodes in a network arrangement. This "mesh topology" can ensure that vast amounts of data will be relayed reliably from sensor suites to central control centers and users.

Susceptibility to fog has slowed the commercial deployment of near-ground FSOC systems. It turns out that fog (and perhaps rain and snow) considerably limits the maximum range of an FSOC link. Because fog causes significant loss of received optical power, a practical FSOC link must be designed with some specified "link margin," i.e., an excess of optical power that can be engaged to overcome foggy conditions when required. Under ideal clear-sky conditions, the absolute reliability of a laser communication link through the atmosphere is still physically limited by absorption of atmospheric constituents and the constantly present atmospheric turbulence. For a given link margin, it becomes meaningful to speak of another metric—the link availability, which is based on the fraction of the total

operating time that the link fails as a result of fog or other physical interruption. Link-availability objectives vary with the application.

FSOC technology started in the 1960s, but deleterious atmospheric effects on optical waves together with the invention of optical fibers in the early 1970s caused a decline in its immediate use. FSOC systems today can provide high-speed connections between buildings, between a building and the optical fiber network, or between ground and a satellite. Moreover, a FSOC system can often be installed in a matter of days or even hours in some cases, whereas it can take weeks or months to install an optical fiber connection. Now, because of the growing demand for access to high-data-rate connections all over the world and the inherent limitations of optical fiber networks in certain environments, there is renewed interest in FSOC.

Some additional common types of FSOC channels that are of current interest are cited below with a brief description of primary atmospheric effects:

Aircraft-ground: Laser communications to the ground from an aircraft are disrupted mostly by the atmospheric turbulence closest to the ground receiver. The primary concerns for downlink propagation paths are s*cintillation* and *angle-of-arrival fluctuations*. Also, *aircraft boundary layer effects* due to platform speed may need to be addressed.

Ground-aircraft: A transmitted laser beam from the ground to an aircraft is disrupted mostly by atmospheric turbulence near the transmitter. The primary concerns for an uplink path are *beam spreading*, *scintillation*, and *beam wander*.

Aircraft-aircraft: Although the aircraft is above much of the natural atmospheric ground-induced turbulence, atmospheric turbulence is still a concern and aircraft *boundary layer effects* due to platform speed may also need to be addressed.

9.3.2 FSOC System Performance Modeling

An FSOC link budget provides the ability to predict system performance under a wide range of conditions and enables effective operation planning. It is an extremely valuable tool but requires underlying models that accurately capture system and component performance under a wide range of environmental conditions. Perhaps the most fundamental component of a link budget is the atmospheric optical channel model. In many FSOC systems, it may also be necessary to develop an AO gain model and an OAGC model. The AO system may consist of only tip-tilt corrections or, for more sophisticated systems, include a number of higher-order AO correction modes. The atmospheric model captures the impact of the atmosphere on the power into the receiver aperture while the AO gain model addresses the various atmospheric perturbations and defines the extent to which those effects can be mitigated in order to focus light into an optical fiber. The OAGC model then defines the ability of the system to convert the light into a stable and usable optical signal to be passed along to the modem. In addition to these methods, it may still be necessary to introduce other mitigating techniques such as a FEC coding scheme or spatial diversity of transmitters and/or receivers.

Optical Channel Model The atmosphere is commonly divided into two major regimes: the atmospheric boundary layer (ABL) and the free atmosphere [12, 13]. The ABL is that region roughly 1–2 km above the Earth's surface where heating of the surface leads to convective instability, resulting in thermal plumes and strong optical turbulence (i.e., refractive-index fluctuations). The first couple of hundred meters above ground define the surface layer, roughly the first 10% of the ABL, where its properties are determined by the air-to-ground differences in atmospheric parameters. The free atmosphere refers to that portion of the atmosphere above the ABL in which the effect of the Earth's surface friction on the air motion is negligible and in which the air is usually treated (dynamically) as an ideal fluid.

Atmospheric or optical turbulence is often characterized by a single parameter C_n^2 (in units of $m^{-2/3}$), called the refractive index structure parameter. In the daytime, optical turbulence is strongest near the ground, generally characterized by C_n^2 values on the order of 10^{-14} upwards to 10^{-12} $m^{-2/3}$ or more. During this period, the air temperature gradient is negative, and, with increasing altitude, it has been observed that C_n^2 often decreases from the surface with an $h^{-4/3}$ altitude dependence, where h denotes altitude [14]. At night, the Earth's surface cools by radiation and becomes colder than the air, producing more stable conditions. This surface cooling produces a strong temperature inversion that can reach tens or hundreds of meters or more. Within the temperature inversion, C_n^2 will typically increase with increasing wind speed up to around 4 m/s, and then decrease with even stronger wind speeds. Also, the decrease in C_n^2 with altitude at nighttime does not generally follow a $h^{-4/3}$ altitude dependence; instead, similarity theory predicts the power-law relation $h^{-2/3}$ which represents more stable conditions. Morning and evening transition periods generally occur 1.5 h after sunrise and 0.5 h before sunset. During such periods of time, the air temperature and surface temperature are roughly the same and C_n^2 is minimized during any 24-hour cycle. The minimization in C_n^2 is termed the quiescent period, typically lasting on the order of a few minutes to half an hour.

Calculations of optical turbulence effects on an optical wave propagating through the atmosphere are necessary for modeling purposes and also understanding the results of experimental data involving the beam. Because such calculations rely heavily on optical turbulence models, it is important to have a good understanding of the basic behavior of C_n^2 for the geographic area of interest. In applications involving propagation across homogeneous terrain along a horizontal path, it is common to assume that the structure parameter C_n^2 remains constant along the path. This constant value can be reasonably estimated by using an instrument called a scintillometer that characterizes the average value of C_n^2 along the same path or a nearby parallel path. If propagation is along a vertical or slant path, it is necessary to use certain analytic or numerical models of optical turbulence to describe changes in C_n^2 as a function of altitude. These latter models are known as C_n^2 profile models and typically represent an average value of C_n^2 at a given altitude, based in part on various measurements made over the years.

Several C_n^2 profile models, including both day and night models, are used by the technical community for ground-to-space or space-to ground applications [12]. One

of the most widely used models for such applications is the Hufnagel-Valley (HV) model described by

$$C_n^2(h) = 0.00594\left(\frac{w}{27}\right)^2\left(\frac{h}{10^5}\right)^{10}\exp\left(-\frac{h}{1000}\right) + 2.7\times10^{-16}\exp\left(-\frac{h}{1500}\right) + A\exp\left(-\frac{h}{100}\right), \tag{9.1}$$

where h is in meters (m), w is the root-mean-square (rms) high-altitude wind speed in m/s, and A is a nominal value of C_n^2 near the ground in $\text{m}^{-2/3}$. Choosing $w = 21$ m/s and $A = 1.7\times10^{-14}$ $\text{m}^{-2/3}$ leads to what is commonly called the HV-5/7 model. This model is a modification of the original empirical model developed by Hufnagel [13, 15] for altitudes between 3 and 24 km above the surface.

One of the advantages of the HV model over other profile models is the inclusion of the two parameters w and A that can be adjusted. That is, permitting variations in high-altitude wind speed and local near-ground turbulence conditions makes the HV profile model attractive for theoretical studies over a large range of geographic locations. Also, it provides a model consistent with measurements of the Fried Parameter, r_0, and the isoplanatic angle θ_0. However, the last exponential term in (9.1) that describes near-ground turbulence conditions predicts a slow decrease in C_n^2 with altitude up to around 1 km as compared with the $h^{-4/3}$ behavior observed by Walters and Kunkel [14] and supported by a number of other early measurements. For applications that rely heavily on the behavior of C_n^2 near the ground, the HV model may therefore not be a good representation of C_n^2 behavior. Instead, another modification of the Hufnagel model that includes the $h^{-4/3}$ daytime behavior near the ground may be better suited in some cases [8–17], i.e.,

$$C_n^2(h) = M\left[0.00594\left(\frac{w}{27}\right)^2\left(\frac{h+h_s}{10^5}\right)^{10}\exp\left(-\frac{h+h_s}{1000}\right) + 2.7\times10^{-16}\exp\left(-\frac{h+h_s}{1500}\right)\right] + C_n^2(h_0)\left(\frac{h_0}{h}\right)^{4/3}, \quad h > h_0, \tag{9.2}$$

where h denotes height above ground. We will refer to (9.2) as the Hourly Analysis Program (HAP) model. In this model, the last exponential function in the HV model (9.1) has been replaced with the last term that appears in (9.2), based on the observed behavior of C_n^2 near the ground. In addition, the HAP model has introduced a reference height h_s of the ground above sea level and a scaling factor M that represents the strength of average high-altitude background turbulence.

In Fig. 9.3, we plot the profile models (1) and (2) from a reference level $h_0 = 1$ m up to an altitude of around 3 km with the same $C_n^2 = 1.7\times10^{-14}$ $\text{m}^{-2/3}$ ground value. In the plot of (2), we set $M = 1, h_s = 0,$ and $w = 21$ m/s. For the first few hundred meters, there is considerable difference between the HV and HAP models, but from

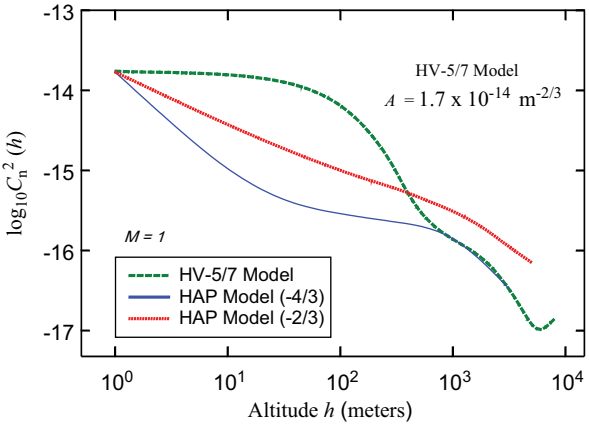

Fig. 9.3 A comparison of the HV model (*1*) with the HAP model (*2*) over altitude 1<h<3100 m. *HV* Hufnagel-Valley

roughly 1 to 20 km or more, the two models are essentially the same. For contrast, the HAP model with a −2/3 power law is also featured with the same C_n^2 ground value.

Because the power law behavior as a function of altitude changes from $h^{-4/3}$ during the day to $h^{-4/3}$ at night, it is clear that there must be a transition period between day and night. Andrews et al., [8] have recently developed a transition model that varies like h^{-p}, where p is dependent upon the temporal hour of the day. A temporal hour is defined as 1/12 the number of hours between sunrise and sunset. This more general model therefore makes use of the actual sunrise and sunset times, and particular time of day under which experiments are performed, to determine the value of p.

Atmospheric Effects on Laser Beams The three primary atmospheric phenomena that affect optical wave propagation are absorption, scattering, and refractive-index fluctuations. Absorption and scattering by the constituent gases and particles of the atmosphere are wavelength dependent and give rise primarily to attenuation of an optical wave. On the other hand, index of refraction fluctuations, also called optical turbulence, lead to random irradiance and phase fluctuations of the optical wave. These random irradiance and phase fluctuations produce a number of deleterious effects on a propagating laser beam, including the following [10]:

- *Beam spreading*—increase in beam divergence resulting in an average power decrease at the receiver
- *Beam wander*—random movement of the instantaneous center of the beam in the receiver plane
- *Loss of transverse spatial coherence*—limits the effective receiver aperture diameter in imaging and coherent detection
- *Angle-of-arrival fluctuations*—angle of arrival fluctuations in the receiver plane produce image jitter (or "dancing") in the detector plane
- *Scintillation*—irradiance fluctuations that can reduce the signal to noise ratio (SNR) and increase signal fade probability

Statistical Performance Measures The reliability of a FSOC system can be deduced from the analysis of several statistical performance measures:

- *Strehl ratio* (SR)—defined by the ratio of the long-term mean irradiance of the laser beam in atmospheric turbulence to that in free space. If the receiver is located in the far-field of the transmitter, the SR in the receiver plane (RP) can be expressed in the form [9]

$$\mathrm{SR}_{\mathrm{RP}} = \frac{1}{\left[1+\left(D_{\mathrm{Tx}} / r_{0\mathrm{T}}\right)^{5/3}\right]^{6/5}} \tag{9.3}$$

where D_{Tx} is the aperture diameter of the transmitter and $r_{0\mathrm{T}}$ is the Fried Parameter in the plane of the transmitter. The maximum value of the SR is unity in free space. In the detector plane (DP), the resulting SR is

$$\mathrm{SR}_{\mathrm{DP}} = \frac{1}{\left[1+\left(D_{\mathrm{Rx}} / r_{0\mathrm{R}}\right)^{5/3}\right]^{6/5}} \tag{9.4}$$

where D_{Rx} is the aperture diameter of the receiver and $r_{0\mathrm{R}}$ is Fried's parameter in the plane of the receiver. For a beam propagating a distance L in the positive z direction, the two Fried parameters are defined by

$$\begin{aligned} r_{0\mathrm{T}} &= \left[0.423k^2\int_0^L C_n^2(z)\left(1-\frac{z}{L}\right)^{5/3} dz\right]^{-3/5} \\ r_{0\mathrm{R}} &= \left[0.423k^2\int_0^L C_n^2(z)\left(\frac{z}{L}\right)^{5/3} dz\right]^{-3/5} \end{aligned} \tag{9.5}$$

where k is optical wave number.

- *Power in the bucket* (PIB)—the average power that enters a receiver aperture. If P_{Tx} represents the laser power at the exit aperture of the transmitter, the average PIB at the receiver is

$$\langle \mathrm{PIB} \rangle = P_{\mathrm{Tx}} \cdot \frac{D_{\mathrm{Rx}}^2}{8W^2} \cdot \tau_{\mathrm{atm}} \cdot \tau_{\mathrm{opt}} \cdot \mathrm{SR}_{\mathrm{RP}}; \quad D_{\mathrm{Rx}} \le 2\sqrt{2}W \tag{9.6}$$

where W is the free-space Gaussian beam radius of the laser beam in the receiver plane, τ_{atm} is the atmospheric transmission loss, and τ_{opt} is the receiver transmission loss. An alternative way to express the mean PIB in the far field is by

$$\langle \mathrm{PIB} \rangle = P_{\mathrm{Tx}} \cdot \frac{A_{\mathrm{Tx}} A_{\mathrm{Rx}}}{(\lambda L)^2} \cdot \tau_{\mathrm{atm}} \cdot \tau_{\mathrm{opt}} \cdot \mathrm{SR}_{\mathrm{RP}}; \quad D_{\mathrm{Rx}} \le 2\sqrt{2}W \tag{9.7}$$

where A_{Tx} and A_{Rx} denote the areas, respectively, of the transmitter aperture and receiver aperture and $\lambda = 2\pi / k$ is wavelength.

- *Power in the fiber* (PIF)—when an optical fiber is located in the detector plane, then $\langle \text{PIF} \rangle$ represents the average power that enters the fiber core. It's maximum value is

$$\langle \text{PIF} \rangle = \langle \text{PIB} \rangle \cdot \tau_{\text{fiber}} \cdot \text{SR}_{\text{DP}} \tag{9.8}$$

where τ_{fiber} represents the fiber loss due to the presence of a circulator.

For aircraft-to-aircraft or aircraft-to-ground links, the aero-optic boundary layer around the aircraft can introduce fluctuations in the beam other than those caused by atmospheric turbulence between the aircraft and the optical receiver. These aero-optic-induced fluctuations in the beam may reduce the average collected power even further than represented above. In some cases it may be possible to model the aero-optic boundary layer as a thin random phase screen from which additional beam spreading can be estimated [18].

In addition to SR, PIB, and PIF, other measures of reliability or performance capability of a FSOC system involve the fade statistics associated with the signal beam. The *fractional fade time* (also called the probability of fade) describes the percentage of time the irradiance of the received wave is below some given threshold value. Perhaps more important than knowing the probability of fade is knowing the *mean fade time*, i.e., the average length of a fade below threshold over a given time frame, and the implied packet loss per fade based on a given data rate.

The probability of fade is defined by

$$\text{Pr}_{\text{fade}} = 1 - \frac{1}{2}\int_0^{\infty} p_I(s)\text{erfc}\left(\frac{\text{TNR} - \langle \text{SNR} \rangle s}{\sqrt{2}}\right) ds \tag{9.9}$$

where TNR represents the threshold to noise ratio and <SNR> denotes the mean signal to noise ratio. The quantity $p_I(s)$ is the probability density function (PDF) of the random irradiance after passing through the receiver aperture. Commonly used models for the irradiance PDF include the lognormal model and the Gamma-Gamma distribution [10]. For sufficiently high average SNR, the probability of fade may be calculated by considering atmospheric effects alone, i.e.,

$$\text{Pr}_{\text{fade}} = \int_0^{I_T} p_I(s) ds \tag{9.10}$$

where I_T denotes the irradiance threshold. The number of negative crossings below the specified threshold level I_T characterizes the expected number of fades per unit time, $\langle n(I_T) \rangle$, and the mean fade time is then determined by the ratio $\text{Pr}_{\text{fade}} / \langle n(I_T) \rangle$ [10]. Finally, the mean packet loss per fade is determined by the product of the mean fade time and packet rate.

9.3.3 Scintillation Mitigation Techniques

Turbulence in the medium-to-saturation regime creates beam wander, spatial and angular spread, scintillation, and other negative effects on the signal beam [10]. The dominant one is scintillation that dictates system performance. To mitigate this effect, new technologies and techniques were invented. In this section, we will review some of the more popular methods for mitigating scintillation in incoherent communications systems.

Aperture Averaging Atmospheric turbulence is one of the primary phenomena that decrease the reliability of an FSOC system. For example, FSOC links can easily exhibit severe temporal short-term fading that is attributed to turbulence-induced scintillation. In some situations, this can be alleviated through increased transmitter power but this is not always practical. Increasing the receiver aperture size may also offset fading caused by scintillation. If the receiver aperture size is larger than the irradiance correlation width, the scintillation level measured by a detector begins to decrease over that of a small aperture receiver, an effect known as *aperture averaging*. However, if the receiving aperture is smaller than the correlation width of the irradiance fluctuations, the aperture behaves essentially like a "point aperture." Of course, the type of platform on which the receiver is located may limit the practical size of the receiver aperture, so the aperture averaging of a fixed size receiver may not sufficiently reduce the fading for a particular link. Another method of achieving scintillation reduction involves the notion of spatial diversity where several small aperture receivers spaced sufficiently far apart are utilized in place of one large aperture. In addition, spatial diversity at the transmitter through multiple transmit beams can also produce a scintillation reduction.

Under proper conditions, AO compensation can reduce the severity of the atmospheric effects by reducing phase aberrations induced by the turbulence. This reduction in phase fluctuations then leads to an increase in the amount of power that passes through the receiver aperture as well as that focused into the optical fiber. This is achieved by improving the SR at both the receiver plane and the detector plane. For instance, assuming the AO system only compensates for tip-tilt at both the transmitter and receiver, the SRs (9.3) and (9.4) can be improved to roughly [9]

$$\mathrm{SR}_{\mathrm{RPTT}} = \frac{1}{\left[1+0.28\left(D_{\mathrm{Tx}}/r_{0\mathrm{T}}\right)^{5/3}\right]^{6/5}};\quad \mathrm{SR}_{\mathrm{DPTT}} = \frac{1}{\left[1+0.28\left(D_{\mathrm{Rx}}/r_{0\mathrm{R}}\right)^{5/3}\right]^{6/5}} \tag{9.11}$$

The corresponding mean PIB and PIF with tip-tilt corrections are now readily obtained by replacing the SRs in (9.6) and (9.7) with the expressions in (9.11). Transmitter tip-tilt essentially removes the effects of beam wander in the receiver plane whereas receiver tip-tilt tends to remove image jitter in the detector plane caused by random angle-of-arrival fluctuations. The net result is more optical power in the optical fiber.

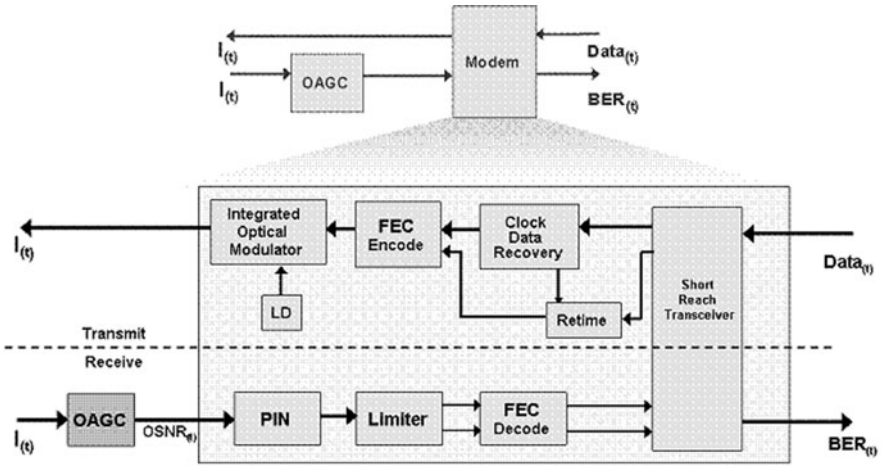

Fig. 9.4 Optical modem block diagram

In some cases, however, it has been found that aperture averaging combined with AO may still not be enough to create a reliable FSOC link. Hence, other means like the use of an OAGC combined with FEC schemes must be employed to increase the reliability and quality of service (QoS) of the FSOC network.

John Hopkins University (JHU) Applied Physics Laboratory (APL) Optical Modem This section describes the John Hopkins University (JHU) Applied Physics Laboratory (APL) optical modem that provides the significant receiver sensitivity/systems gain for mitigating turbulent effects in excess of 20+ db. It has helped the ORCA/FOENEX program provide error-free and near error-free communications for FSOC links operating in saturation regime turbulences where an additional 20–30 dB loss occurred after the AO systems, e.g., > 45–55 dB unmitigated channel fading. Figure 9.4 shows the basic architecture for the optical modem. It is composed of two stages. The first stage is called the OAGC and the second is a FEC capability [15–17]. Juarez et al., has configured these two stages to create an optical modem designed to convert the widely-varying optical signal into a stream of digital data for processing by a network router [4, 11, 19]. They can provide 25–30 dB of link performance improvement.

The OAGC must perform several functions to stabilize the highly fluctuating received signal for reliable detection. The first is protection of the photodiodes and follow-on electronics from saturation or catastrophic damage due to high optical power levels. This condition can exist in FSOC links over short distances (< 10 km an over longer ones (> 100 km during benign turbulence. Additionally, architectures employing fixed gain optical pre-amplifiers, such as erbium-doped fiber amplifiers (EDFAs), are especially susceptible because they can output power levels well above the damage thresholds of detectors in response to rapid power transients in a "Q-switch" effect. The second function the OAGC must perform is to provide low-

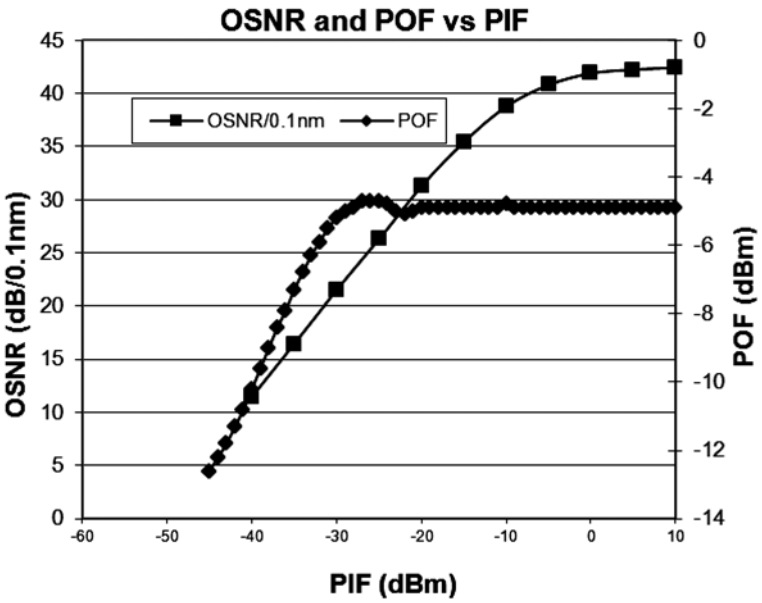

Fig. 9.5 Optical signal to noise ratio (OSNR) and power out of the fiber (POF) versus input power in the fiber (PIF)

noise optical amplification to improve receiver sensitivity. This is critical to maximize the communications link margin. Lastly, the OAGC must reduce the power transients that couple through the receiver follow-on electronics and degrade bit error rate performance. The OAGC achieves this by optically amplifying or attenuating as necessary through a series of multiple stages as discussed in [5, 11, 19] to output a constant power (POF) at a level of optimal performance for the detector. In essence, the time-variant optical input [$I(t)$] is translated into a constant output with a variable optical signal to noise ratio [OSNR(t)]. This performance is illustrated in Fig. 9.5, which presents OSNR and OAGC output power as a function of power into the OAGC (which is equivalent to PIF). The signal modulation scheme was non-return-to-zero (NRZ)-on-off keying (OOK). The maximum gain of the first generation system is shown to be between 40–45 dB. In this figure, POF stand for power out of the fiber after the OAGC.

The modem was designed to interface between the 10 Gbps Ethernet client and the 11 Gbps FSO line rate. Specifically, the modem uses a commercial off-the-shelf (COTS) Reed-Solomon [255, 239] enhanced FEC, with a 7% overhead chipset for optical links, which are designed to operate in a high received power, variable OSNR environment. Lab tests have proven that COTS FEC chips can provide the full designed 8 dB of gain, even when the power into the OAGC varies over 4 orders of magnitude. The primary penalty to outages below system sensitivity is the time the FSO side clock recovery circuitry takes to acquire clock after a fade. This

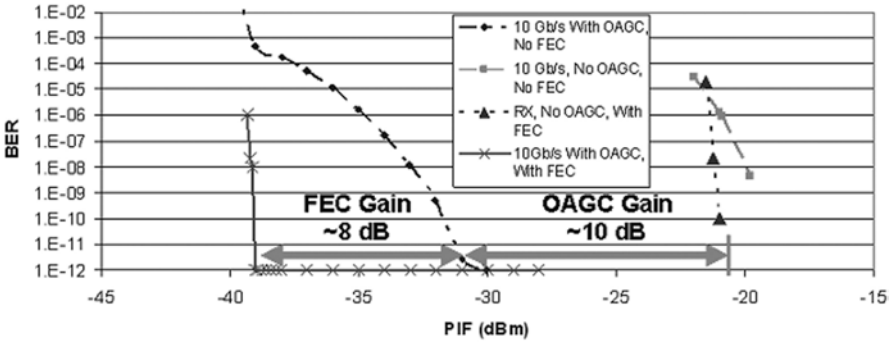

Fig. 9.6 Bit error rate versus input power in the fiber (PIF) with OAGC only, and with OAGC and FEC. *OAGC* automatic optical gain control, *FEC* forward error correction

was characterized in the lab to be on the order of 100 µs. The BER results of using the COTS FEC with the first generation OAGC are shown in Fig. 9.6. For this test, the BER performance of the back to back test was compared with and without the OAGC using InGaAs PIN/TIA receivers for both cases. For the case without the OAGC, low received optical power starves the photo-receiver and lead to decision errors by the limiting amplifier, which cannot be corrected by the FEC. For this case, the FEC provides little gain as the low receiver power quickly reduces the received signal to noise ratio. This is not surprising as the FEC chipset was designed for optical fiber communications systems with optical pre-amplification where link configurations and OSNR and power levels are carefully controlled. This type of careful OSNR and power level management is impossible to do in FSO systems due to the dynamics of the received power.

Figure 9.7 illustrates how the optical modem performed on 183 km link during late afternoon conditions [4–6 PM]. In particular, this figure shows PIF data taken on May 18, 2009 during Flight 2, with POF data taken during laboratory testing. The turbulent conditions were estimated at 5xHV 5/7. The optical modem developed for these tests utilized an NRZ-OOK modulation format, operating at a line rate of 10.3125 Gbps. The FEC used was low overhead (7%) Reed-Solomon code cited above. Combined with the OAGC originally demonstrated in 2007, the PIF noise floor (10^{-12} BER) was expected to be −39 dBmW [4], but from Fig. 9.7, we see that the OAGC was able to maintain a constant output power over a greater PIF range, thus lowering the 10^{-12} BER point to −41 dBmW. This was due to a minor system upgrade prior to Nevada field test.

Diversity The free-space optical communications airborne link (FOCAL) programs and associated research effort conducted by researchers from MIT Lincoln Laboratory have used spatial diversity, FEC, and interweaving to reduce fading loss, projected to be on the order of 20 dB [5, 20]. This section will summarize their basic approach and results [5].

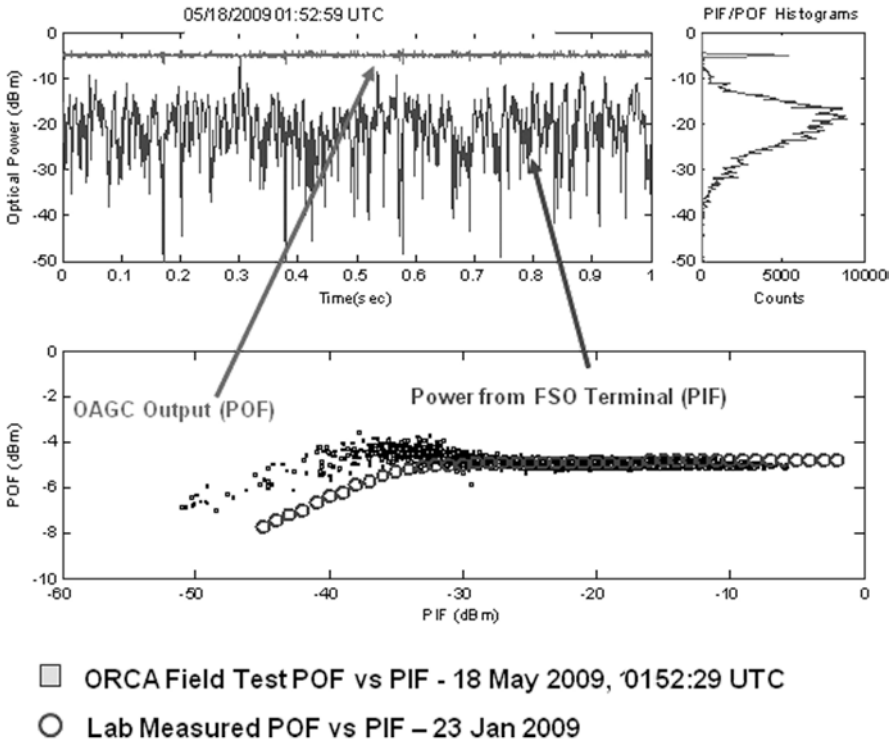

Fig. 9.7 Performance of OAGC on May 18 NTTR data, with Comparison with laboratory characterization results. *OAGC* optical automatic gain controller, *NTTR* Nevada test and training range

Optical diversity ideally reduces the log fade level by the number of apertures used if beams are statistically independent; in their experiment, four receiver apertures were employed. Achieving that independence requires separating the beams by a distance greater than the Fried Parameter [5, 20]. This is the first scintillation technique used by the FOCAL program. The researchers used an aircraft aperture of 2.54 cm with four ground 2.54 cm apertures, varying the separation from each other by 10–48 cm. The downlink signal is separately detected in each aperture chain, with signals then summed for clock recovery and bit detection. Receiver filter bandwidth is 10 GHz. A dynamic variable optical attenuator (VOA) is included in each detection circuit to stabilize signal levels at the decision circuits. A system block diagram and examples of collected data are shown in Fig. 9.8.

The second scintillation mitigation technique used by the team was FEC coding with interleaving; the basic interleaving concept is illustrated in Fig. 9.9. The FEC adds symbols to each code word allowing recovery of all symbols if some are lost to fading. The Reed-Solomon (255, 239) code used can correct 8 byte (symbol) errors per code word. For OTU1 framing with RS (255, 239) FEC, 64 code words of 255 bytes each constitute a ~50 μs frame, far shorter than a millisecond class

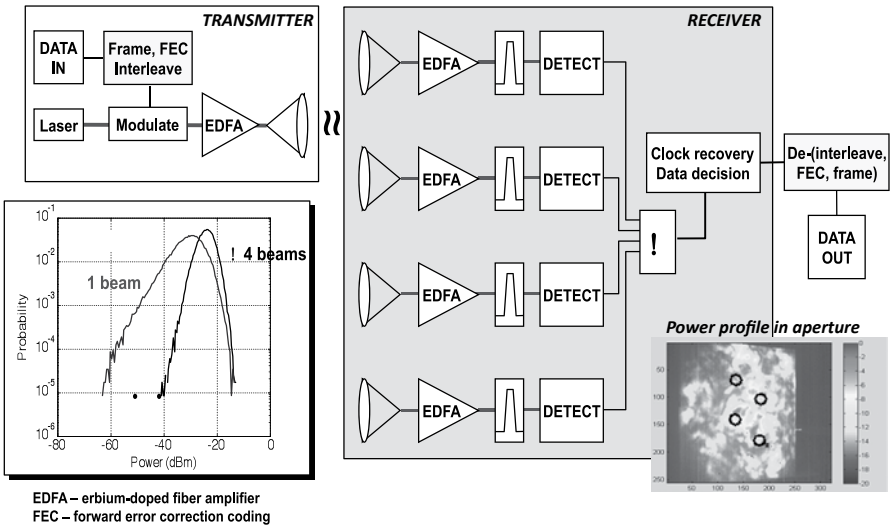

Fig. 9.8 The downlink path for the FOCAL experiment employed a single transmitter mounted in the aircraft and four independently tracked detectors in the ground-based receiver. The receiver outputs were incoherently summed, and the resulting improvement is demonstrated by the distributions shown in chart on the lower left-hand side of this figure. The detector layout and an image of the scintillation pattern is shown in the picture on the lower right-hand side of this figure [5]. *FOCAL* free-space optical communications airborne link

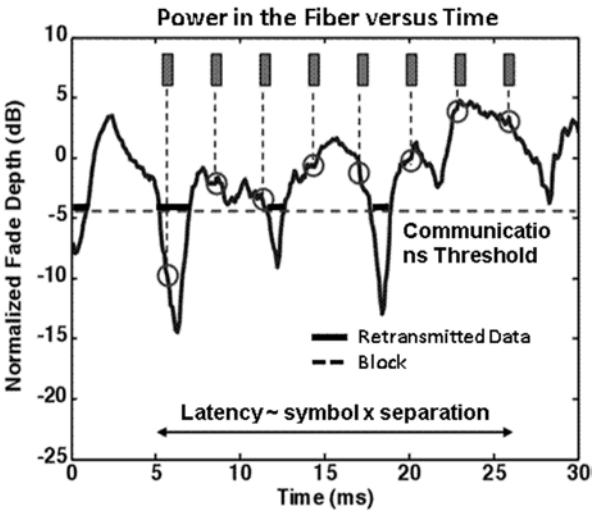

Fig. 9.9 Interleaving refers to a technique in which a code block is segmented into a string of symbols that are temporally separated in order to minimize the likelihood that an entire block will be transmitted during a channel fade. The use of encoding allows the entire code block to be recovered even if some of the symbols are decoded incorrectly [5]

atmospheric fade. If all symbols of the code word fall in the fade, the FEC is ineffective. Interleaving provides temporal diversity by spacing the code symbols by a time duration in excess of the characteristic atmospheric fade. For this work, the

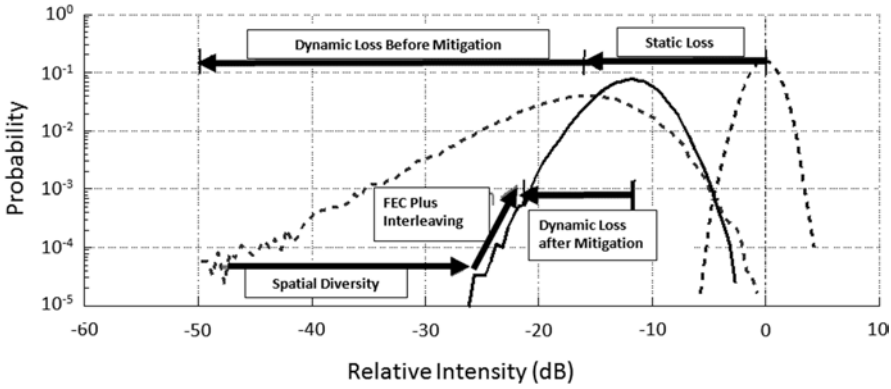

Fig. 9.10 Comparison of received signal distribution functions for a short link with low turbulence (dashed; relative humidity, Right Hand (RH), curve), a unmitigated long link with high turbulence (dashed, Left Hand (LH) curve), and the long link with scintillation mitigation (solid curve). Optimized mitigation schemes can reduce the transmitted signal power requirement by more than 20 dB. *RH* relative humidity

symbols were spaced by 5 ms, leading to a latency of 1.25s after de-interleaving. The combination of an optical mitigation scheme to reduce scintillation fading and an FEC code operating with sufficient interleaving in the data domain can make communications in the deep fading channel tractable and significantly extend the available range for air-to-ground communications.

Figure 9.10 illustrates the improvement achieved in the mean power level (referred to as the static loss) and the reduction of the signal fluctuations (referred to as the dynamic loss). Under severe turbulence conditions, the combined effect of spatial diversity, interleaving, and encoding can easily reduce the transmitted signal requirement by more than 20 dB.

9.3.4 FSOC Experimental Results

The DARPA and the AFRL have made significant progress over the last few years in the development of a FSOC link performance. This section will summarize some of those results.

ORCA Program The ORCA FSOC subsystem was designed to accurately point the transmitter and receiver apertures for signal acquisition, to couple light from free-space into a single-mode fiber, and to mitigate power variations in the fiber to maximize receiver sensitivity. The PAT functions were provided by a semi-cooperative PAT system consisting of a WFOV camera, NFOV camera, and WFS fine tracking loop with turbulence compensation.

While turbulence affects the acquisition process, it is more disruptive to the FSOC link itself. A significant feature of the ORCA FSOC system was that both the transmitter and receiver were reciprocal and each incorporated an AO subsystem,

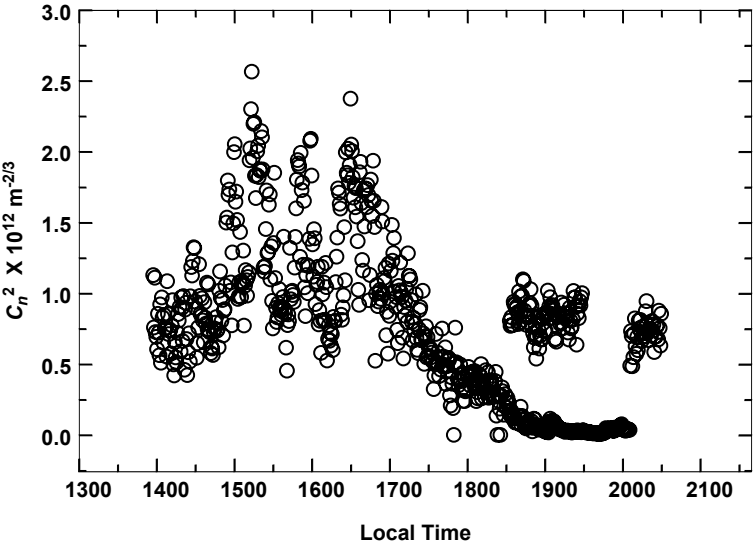

Fig. 9.11 Scintillometer measurements of C_n^2 near ground on May 16, 2009 at Antelope Peak in Nevada

thereby correcting both the transmitted beam and the received beam to maximize light coupling into the single-mode optical fiber. In addition, the ORCA system incorporated an OAGC, which together with the AO subsystem, represent the key components for converting the highly dynamic received optical signal into a stable signal that can be processed by the optical modem. The OAGC provides low-noise optical amplification and stabilization, providing 40+ dB of dynamic range while isolating optical detectors from high input power which can cause detector saturation or damage [11, 21].

Separate tests of the ORCA system were conducted over a 70-km path from ground-to-aircraft at the Patuxent River Naval Air Station (PAX) and over 80–200 km bidirectional paths between Antelope Peak at 2289 m and British Aircraft Corporation One-eleven (BAC1–11) aircraft at 8016 m altitude at the Nevada test and training range (NTTR) in 2009. The NTTR tests took place over May 16–18, 2009. Atmospheric conditions were similar all three days of testing. Typical scintillometer-measured C_n^2 data on May 16, 2009 at 1.0 m above the ground at Antelope Peak are shown in Fig. 9.11. During the middle of the day, ground level C_n^2 values were greater than 10^{-12} $m^{-2/3}$, corresponding to conditions of very strong atmospheric turbulence. Fried parameter values at the receiver on Antelope Peak typically ranged between 2 and 15 cm, whereas the same at the receiver on the BAC1–11 aircraft ranged between 20 and 70 cm.

These weighted averages were typically on the order of 10^{-17} $m^{-2/3}$, but occasionally would jump roughly an order of magnitude higher [8]. It is believed that such sudden increases were due to large updrafts that would occur as the aircraft flew

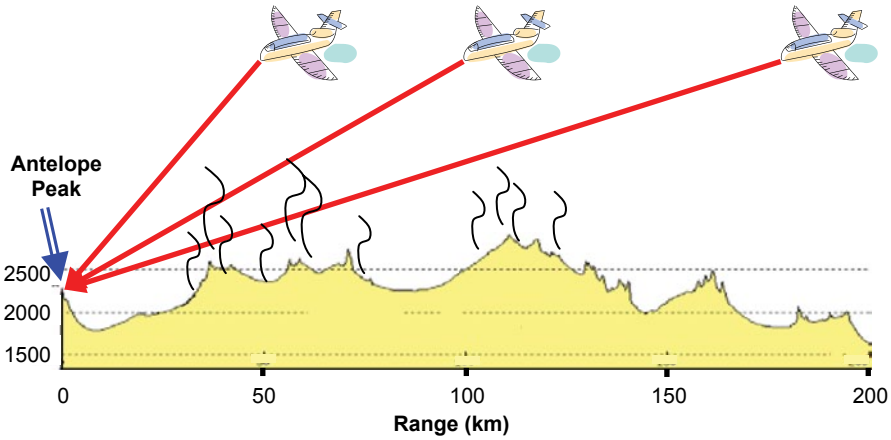

Fig. 9.12 Ground profile eastward (84°) from Antelope Peak (far left). A three-aperture scintillometer system was also used at NTTR to characterize the atmospheric channel through weighted path-averaged *Cn2* values over the path from the BAC1-11 aircraft to ground. *NTTR* Nevada test and training range, *BAC1–11* British Aircraft Corporation One-eleven

over certain high mountain peaks. A typical path that included high peaks between the aircraft and Antelope peak is illustrated in Fig. 9.12.

PIF data recorded on the downlink during Flight #1 on May 17, 2009 are shown in Fig. 9.13 versus propagation range from the aircraft. Although not discernible in Fig. 9.13, the data sometimes showed a mean PIF reading of roughly 4 dB lower when the aircraft was traveling nearly transverse (side-on) to the propagation path compared with that when the aircraft was traveling head-on towards the receiver (zero gimbal angle) [22]. This drop in mean PIF can be seen more clearly in Fig. 9.14 where the mean PIF data taken during Flight #1 on May 17, 2009 at ranges between 110 and 120 km are plotted as a function of gimbal angle. Here, the mean PIF data show a decrease of a few dB when the gimbal angle moves away from small values to either larger negative or larger positive gimbal angles. However, values of the gimbal angle were not recorded very accurately during testing so the mean gimbal angles on the abscissa in Fig. 9.14 represent only approximate values, not exact values.

The 4 dB loss in mean PIF when the aircraft was traveling nearly transverse to the propagation path was attributed to the aero-optic boundary layer effect. However, in much of the PIF data the 4 dB loss does not appear because the AO system was likely able to compensate for the aero-optic effect, but perhaps not always. An analysis of the power spectral density (PSD) associated with the beacon beam from the aircraft showed that the aero-optic boundary layer around the aircraft attained a maximum effect when the gimbal angle was near 90° to the propagation path and attained a minimum effect when the gimbal angle was near zero. This aero-optic effect is clearly revealed in the PSD plots shown below in Fig. 9.15 displaying data collected from the aircraft beacon with the 2-in aperture of the three-aperture

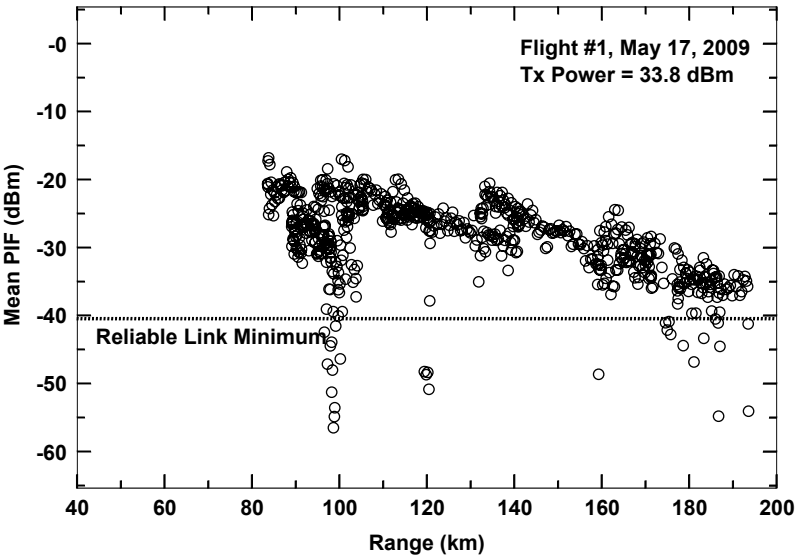

Fig. 9.13 Mean PIF data taken during Flight #1 on May 17, 2009 at NTTR as a function of range. The data represents measurements made over a 5 s timeframe with 33.8 dBmW of Transmitter (Tx) power at the exit aperture. *PIF* power in the fiber, *NTTR* Nevada test and training range

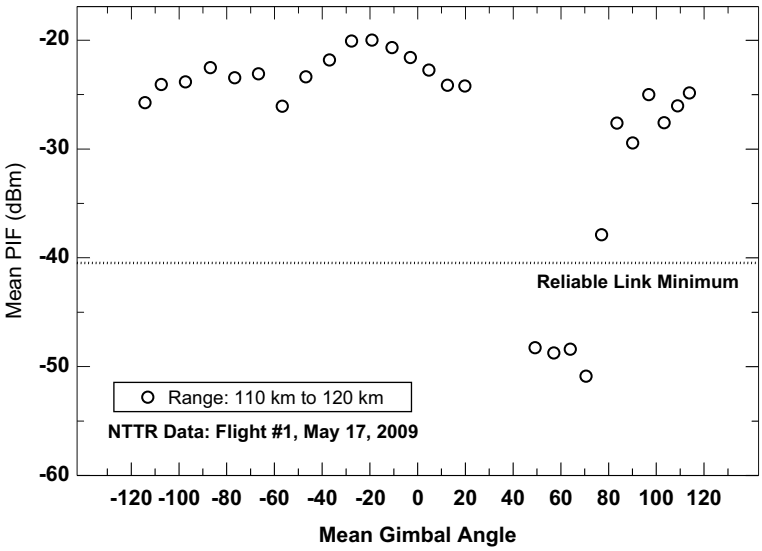

Fig. 9.14 Plot of the mean PIF at ranges of 110–120 km as a function of gimbal angle for Flight #1 on May 17, 2009 at NTTR. Mean gimbal angles on the abscissa are only approximate. *PIF* power in the fiber, *NTTR* Nevada test and training range

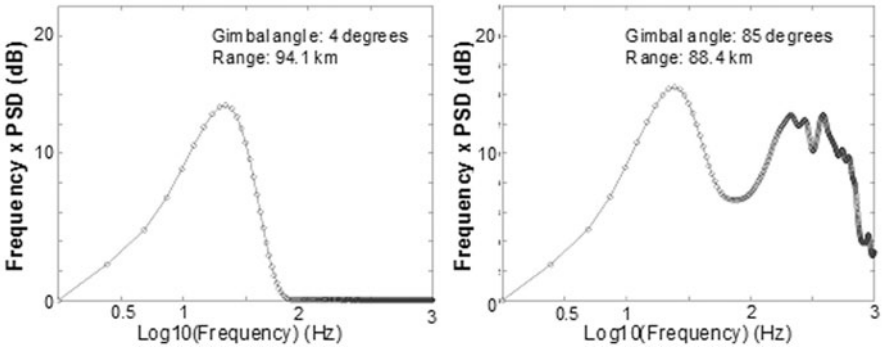

Fig. 9.15 Plot of $fS(f)$ as a function of $\log_{10}(f)$. On the left is the PSD when the gimbal angle is near zero and on the right is the PSD when the gimbal angle is near 90°. *PSD* power spectral density

scintillometer system during Flight #2 on May 16, 2009. The beacon beam was not subject to AO corrections like the data beam. These plots, which are typical of all such PSD data plots during NTTR testing, were created by plotting $fS(f)$ as a function of $\log_{10}(f)$, where f is frequency and $S(f)$ is the PSD. By plotting the data in this fashion, it can be determined which frequencies contain the most power for the irradiance variance. The PSD plot on the left in Fig. 9.7 corresponds to a gimbal angle of 4° (aircraft is nearly head-on) and the one on the right corresponds to a gimbal angle of 85° (when the aircraft presents a side view). The secondary "hump" in the PSD at higher frequencies for the plot on the right can be attributed to fluctuations in the signal caused by the aero-optic boundary layer around the aircraft. These high frequency signal fluctuations can lead to a greater number of fades per second as compared with fades from atmospheric turbulence alone, but for shorter periods of time. Mean fade times for the data beam were calculated and generally found to be 1–2 ms or less, often less than 0.5 ms.

FOENEX Program The planned Phase 2 of the ORCA program ultimately became the FOENEX program in 2010. Among other changes to the ORCA system initiated through FOENEX was the use of a new OAGC and RZ-DPSK modem with legacy FEC. System performance metrics for the FSOC subsystem on air-to-air links were initially set with information rate equal to or greater than 2.5 Gbps using a 10Gbps FSOC link, link availability equal to or greater than 95%, and packet loss rate less than or equal to 10^{-6}. For air-to-ground or ground-to-air links, these same metrics were lowered to information rate equal to or greater than 1.7 Gbps again using a 10Gbps FSOC link, 60% link availability or greater, and maximum packet loss rate of 4×10^{-6}. For the RF subsystem, the same metrics on the air-to-air links required information rate equal to or greater than 112 Mbps, link availability equal to or greater than 95%, and packet loss rate less than or equal to 4×10^{-7}. The data rate metric for air-to-ground or ground-to-air links was specified as greater than or equal to 185 Mbps, with link availability and packet loss rate the same as for air-to-

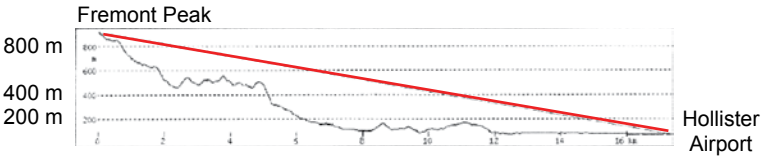

Fig. 9.16 Ground profile between Fremont Peak and Hollister Airport

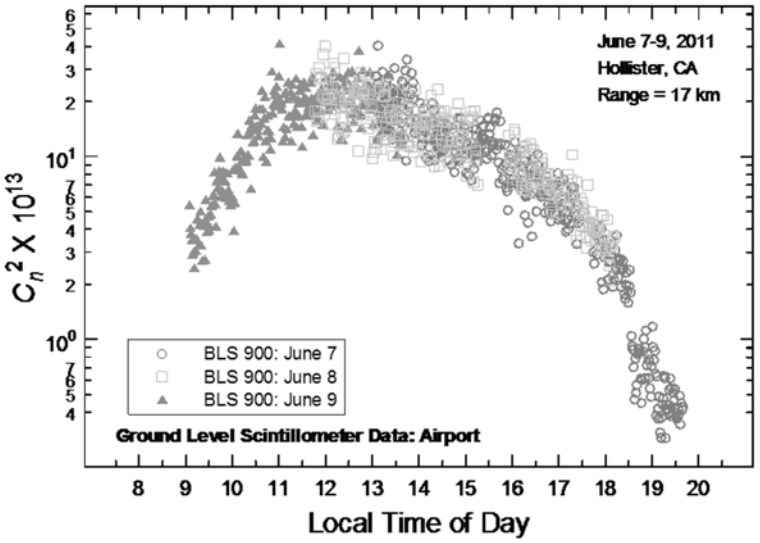

Fig. 9.17 Ground level C_n^2 values at Hollister Airport during June 7–9, 2011 measured by a BLS 900 Scintec scintillometer. *BLS* Boundary layer scintillometer

air links. The airborne platform was changed from a BAC1–11 used in the ORCA program to a Twin Otter aircraft.

Preliminary Phase 0 testing of the FOENEX system took place June 7–9, 2011 over a range of 17 km between Hollister Airport and Fremont Peak in California. The ground profile for the propagation path between Hollister Airport and Fremont Peak is shown in Fig. 9.16. Atmospheric conditions near the ground at Hollister Airport were measured with a Boundary Layer Scintillometer (BLS) 900 Scintec scintillometer instrument and results from those measurements are shown in Fig. 9.17 for the 3 days of testing. Ground conditions were fairly consistent over all 3 days for the same time of day. In addition to the BLS 900 scintillometer, a version of the three aperture scintillometer system (TASS) that was used at the ORCA NTTR testing was used to characterize the propagation channel at the Hollister site [17]. Regardless of the time of day that testing took place, the weighted path-average C_n^2 values over the path averaged around $1.9 - 2.9 \times 10^{-15}$ $m^{-2/3}$ all 3 days.

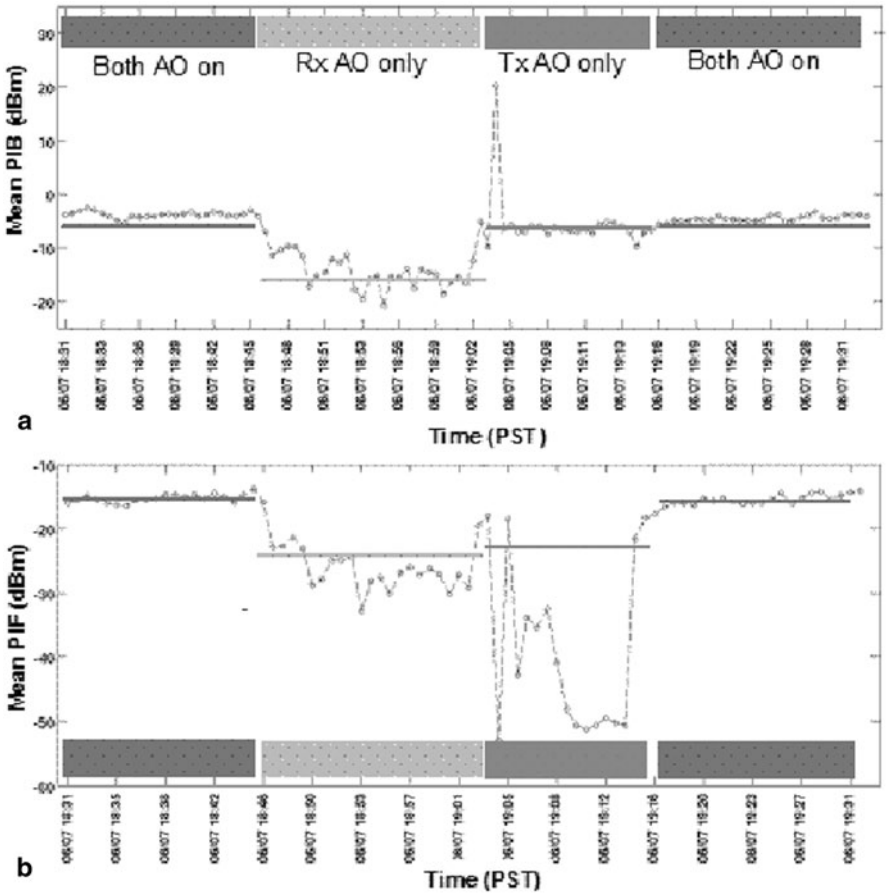

Fig. 9.18 **a** Mean PIB data collected at 6:30−7:30 pm on June 7, 2011 at the Hollister Airport end of the 17-km link. **b** Mean PIF data during the same time. PIB data is recorded at 7.68 kHz with 45 s averages, whereas PIF data is recorded at 20 kHz with 45 s averages. The blue-shaded areas represent times when the AO was turned on at both ends of the link. Red-shaded areas represent times with Tx AO on and Rx AO off, and green represents times with Rx AO on and Tx AO off. The horizontal lines represent the average theoretical values during these particular testing times. *PIF* power in the fiber, *PIB* power in the bucket, *AO* adaptive optics, *Rx* reactive extensions

Based on the weighted path-average C_n^2 values measured by TASS, the parameters M and $C_n^2(h_0)$ for the HAP model (2) were determined; this profile model was then used to calculate the Fried parameter at both ends of the path and the mean PIB and PIF as well. The Fried parameter at the Hollister Airport end of the path ranged from 1.5 to 2.5 cm during the middle part of the day and increased up to 3.0–4.5 cm in the late afternoon. At the Fremont end of the path, the Fried parameter values were roughly 1–2 cm larger.

Mean PIB and PIF values were calculated for the FOENEX 1550 nm data beam during four or the five test periods over June 7–9, 2011. The theoretical val-

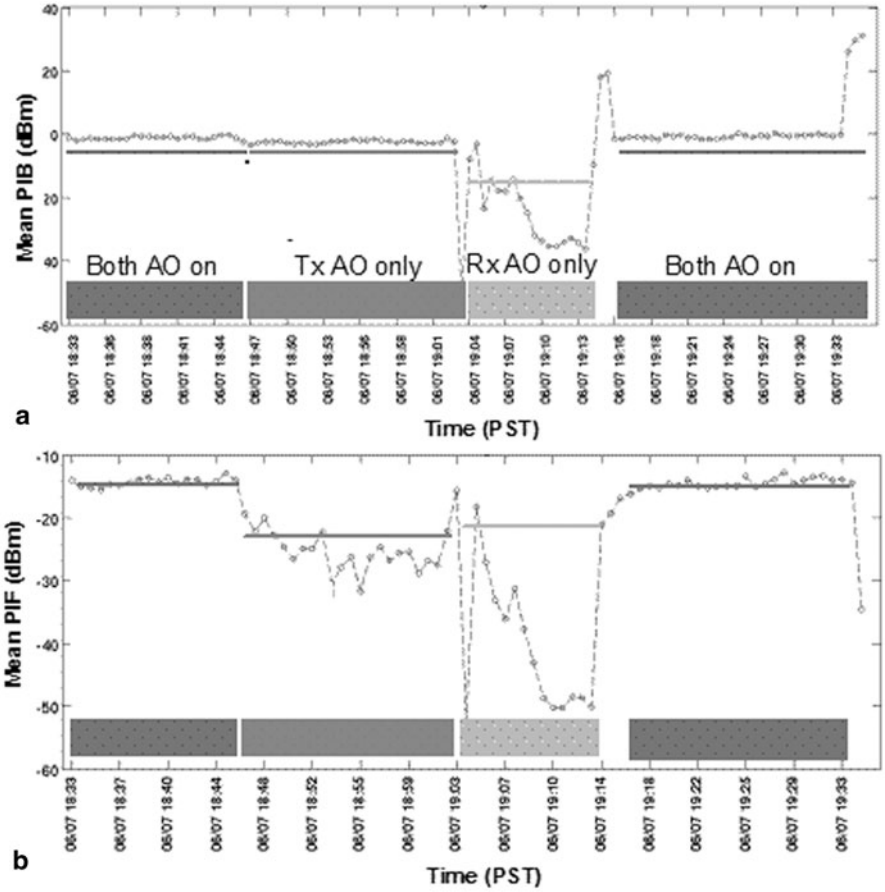

Fig. 9.19 Same as Fig. 9.18 for the Fremont Peak end of the link

ues calculated from (9.6) and (9.8) using the HAP C_n^2 profile model are shown in Fig. 9.18 for the 6:30−7:30 pm testing on June 7, 2011 at the Hollister Airport end of the link. Also shown are 45 s averaged values of the measured PIB and PIF. The blue shaded areas represent times when the AO was turned on at both ends of the link. Red shaded areas represent times with Tx AO on and Rx AO off, and green represents times with Tx AO off and Rx AO on. The colored horizontal lines represent the average theoretical values during these particular testing times. Similar results are presented in Fig. 9.19 for the Fremont Peak end of the link. The reason for the discrepancy between theory and measured mean PIF in Fig. 9.18b for Tx AO only and in Fig. 9.19b for Rx AO only is not known.

The theoretical mean PIB estimates for other testing periods from 1–2 pm and 5:10−6:15 pm on June 8, 2011 and from 12:15−1:40 pm on June 9, 2011 are similar to those in Figs. 9.18a and 9.19a. and match the measured PIB values very

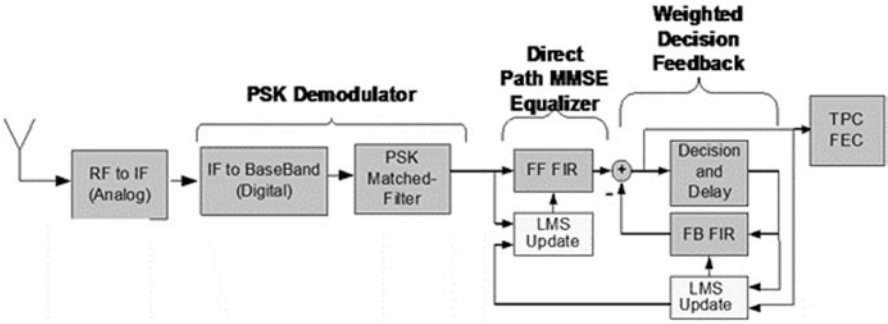

Fig. 9.20 DFE block diagram. *DFE* decision feedback equalizer

accurately (when the transmit laser power is the same). On the other hand, although the theoretical mean PIF values were also very similar to those in Figs. 9.18b and 9.19b (with the same transmit laser power), the measured PIF values dropped by around 5−10 dB from the data results shown in Figs. 9.18b and 9.19b. The reason for the losses in mean PIF during these other test times is once again not known.

9.4 RF Communications System

The challenge for the RF subsystem is to obtain a reliable RF communications link under adverse conditions to complement the performance characteristics of the FSOC channel. To accomplish this, RF communication subsystem components must be designed to achieve efficient high rate communications over directional LOS links, such as air-to-air and air-to-ground links. Time-domain diversity can be achieved through equalization and long-block length turbo codes applied as FEC coding. A DFE can reduce ISI caused by distortion effects such as frequency-selective fading and phase deviation and mitigates the fading caused by reflected signals (i.e., multipath interference) that arrive at the receive antenna after the LOS signal. A TPC FEC can also be applied in order to reduce the amount of per bit energy required for reliable data reception. Of course, the size, weight, and power (SWaP) of the overall system must be taken into account, particularly for constrained systems where limited transmit power and/or aperture size further limits communication performance.

9.4.1 RF Subsystems

Figure 9.20 depicts the RF communications system architecture for the ORCA/FOENEX program, typical of most RF systems available today. The hardware is based on existing equipment with proven track record in other data link systems. Some modifications were made to enable unique aspects of the RF operation.

Principle among these modifications is the DFE, which can mitigate multipath energy resulting from ground reflections on air-to-air links. The DFE estimates the reflected channel components and implements filtering with the appropriate time delay to subtract the reflected signal from the direct path signal.

Like the FSOC link budget, the metric for determining availability in the RFC model is the BER performance. While BER can be measured directly in an experiment, it is derived as a function of signal quality for an analytical model. Because the air-to-air RF links are susceptible to signals reflected from the Earth's surface [4], the received signal can potentially contain a non-trivial interference component due to the delayed energy of the reflected signal. For that reason, the RF model uses the signal-to-interference-plus-noise ratio (SINR) rather than the SNR as a measure of signal quality. For a given SINR, the performance of the FEC provides a statistical measure of BER.

9.4.2 RF Channel Model

In the ORCA/FOENEX systems, the transmitted RF signal is a filtered version of quadrature phase shift keyed (QPSK) modulation at Ku band. The filtered QPSK response is represented by the equivalent baseband signal

$$x(n) = \sqrt{E_b}\, d(n) e^{j\theta(n)} \tag{9.12}$$

where $E_b$is the energy per bit, $d(n)$, is the amplitude, and $\Theta(n)$ is the phase of the pulse shape filtering output at time n.

The received signal consists of two groups of channel components. The first is characterized by the direct LOS path through the troposphere and the second by the reflection path that results in some delay D. The channel response along each path is time-varying and induces variations in signal arrival time. The composite signal received at some time n can be expressed as a weighted linear combination of each symbol $x(n)$ and channel response $h_l(n)$ and $q_m(n)$ of the LOS and reflected channel, respectively:

$$y(n) = \sqrt{E_b} \sum_{i=0}^{L-1} h_i(n) \cdot x(n-l) + \sqrt{E_b} \sum_{m=0}^{M-1} q_m(n) \cdot x(n-D-l) + \eta(n) \tag{9.13}$$

The first term contains the L LOS signal components, and the second term corresponds to the M reflected signals that are delayed by D symbols. The signal at the receiver therefore contains energy from multiple symbols characterized by the $L + M$ symbols and the amplitude and phase for each channel path, resulting in ISI. The desired component is given for l=0

$$y_d(n) = \sqrt{E_b} h_0(n) \cdot x(n) \tag{9.14}$$

The other components therefore represent the unwanted signals elements producing ISI

$$l_0(n) = \sqrt{E_b}\sum_{i=0}^{L-1} h_i(n)\cdot x(n-l) + \sum_{m=0}^{M-1} q_m(n)\cdot x(n-D-l) + \eta(n) \quad (9.15)$$

The combined channel effects can be modeled as the superposition of uncorrelated flat-fading and uncorrelated frequency selective fading that can be derived from multiple propagation paths. The amplitude of each delay path is modeled as a complex Gaussian random variable with mean and standard deviation.

The energy I_0 can be characterized as zero mean and noncoherent with respect to the desired signal component, allowing the amplitude to be found as a function of the bit energy and channel responses of the LOS and reflected paths:

$$I_0 = E[|I(n)|^2] = E\left[\left|\sqrt{E_b}\sum_{i=1}^{L-1} h_i\right|^2 + \left|\sqrt{E_b}\sum_{m=1}^{M-1} q_m\right|^2\right] \quad (9.16)$$

$$I_0 = E_b \cdot E\left[\sum_{i=1}^{L-1} |h_i|^2 + \sum_{m=0}^{M-1} |q_i|^2\right] \quad (9.17)$$

The SINR can then be computed as

$$SINR = \frac{E_b}{N_0 + I_0} = \frac{E_b}{N_0}\left(1 + \frac{I_0}{N_0}\right)^{-1} \quad (9.18)$$

where the complex noise spectral density is defined as $N_0 = E[\eta(n)]$.

9.4.3 DFE Performance Model

The long delay of the reflected path relative to the LOS path results in a sparse delay spread. The large delay spread makes the optimal linear filtering approach difficult to implement. The filtering difficulties are further compounded by the time-varying delay of the reflected signal resulting from changing terrain and distances between the aircraft during flight. As a result, a DFE implemented in the form of a reduced-constraint length RAKE receiver consisting of a forward path, concatenated with linear interference cancellation. Subtracting delayed and filtered estimates of the reflected channel derived from hard-decisions from the direct path signal provides estimates of the transmitted data sequence. The receiver block diagram illustrates the concept and shows multipath power delay profiles before and after equalization, where the DFE removes the long delay path interference.

A DFE computes the signal estimate from the feed-forward and recursive feedback components:

$$\hat{x}(n) = \mathrm{w}(n)^H \mathrm{y}(n) - \mathrm{b}(n)^H sgn(\hat{\mathrm{x}}(n-D)) \quad (9.19)$$

where $(\cdot)^{\mathrm{H}}$ is the Hermitian transpose and $\mathbf{w}(n) = \left[w_0 \ldots w_{L-1}\right]^T$, $\mathbf{b}(n) = \left[b_0 \ldots b_{M-1}\right]^T$ are FIR vectors corresponding to the adaptive filter coefficients.

At time *n*, the feed forward filter output is

$$\begin{aligned} r(n) &= w(n)^H \mathrm{y} \\ &= \sum_{k=0}^{k-1} w_k(n)^H \left(\sqrt{E_b} \sum_{i=0}^{L-1} h_i(n-k)x(n-l-k) \right. \\ &\quad \left. + \sqrt{E_b} \sum_{m=0}^{M-1} q_m(n-k)x(n-m-D-k) + \eta(n-k) \right) \end{aligned} \tag{9.20}$$

Substituting (9.20) into (9.19) yields the DFE estimate of the desired symbol *x(n)* given by

$$\begin{aligned} \hat{x}(n) = &\left(\sqrt{E_b} \sum_{\mathrm{l}=0}^{\mathrm{L}-1} \sum_{\mathrm{k}=0}^{\mathrm{K}-1} w_k(n)^H h_i(n-k)x(n-l-k) \right. \\ &\left. + \sqrt{E_b} \sum_{\mathrm{m}=0}^{\mathrm{M}-1} \sum_{\mathrm{k}=0}^{\mathrm{K}-1} w_k(n)^H q_m(n-k)x(n-m-k-D) + \sum_{\mathrm{k}=0}^{\mathrm{K}-1} w_k(n)^H \eta(n-k) \right) \\ &- \sum_{\mathrm{p}=0}^{\mathrm{p}-1} b_p(n)^H \cdot sgn\left[\hat{x}(n-p-D)\right] \end{aligned} \tag{9.21}$$

Noting the double summations produce the following relationship:

$$\begin{aligned} &\sum_{\mathrm{l}=0}^{\mathrm{L}-1} \sum_{\mathrm{k}=0}^{\mathrm{K}-1} w_k(n)^H h_i(n-k)x(n-l-k) \\ &= \mathrm{w}(n)^H \mathrm{H}(n) \mathrm{x}_{\mathrm{L}}(n) \\ &= \begin{bmatrix} w_0^H & w_1^H & \ldots & w_{K-1}^H \end{bmatrix} \begin{bmatrix} \mathrm{h}(n)^T & 0\ldots & 0 \\ 0 & & \vdots \\ \vdots & \mathrm{h}(n-k)^T & 0 \\ 0 & \ldots 0 & \mathrm{h}(n-K+1)^T \end{bmatrix} \begin{bmatrix} x(n) \\ x(n-1) \\ \vdots \\ x(n-K-L+2) \end{bmatrix} \end{aligned} \tag{9.22}$$

where $\mathrm{h}(n)^T = h_o[(n) \quad h_1(n) \quad \ldots \quad h_{L-1}(n)]$ is the channel response at time *n* (in row vector form), and $\mathrm{X}_L(n)$ is a large column vector of length $L + K$. Defining *Q(n)* in the same manner allows arrangement of the terms into quadratic forms:

$$\hat{x}(n) = \sqrt{E_b} w(n)^H H(n) x_L(n) + \sqrt{E_b} w(n)^H \mathrm{Q}(n) x_M(n-D) - b(n)^H \hat{\mathrm{x}}(n-D) + \mathrm{w}(n)^H \eta(n) \tag{9.23}$$

The first term is the LOS signal; the remaining terms are the inter-symbol interference caused by the reflected multipath and filtered noise. First define the following, similar to (9.22), with the desired term of (9.15) removed,

$$\sum_{l=1}^{L-1}\sum_{k=1}^{K-1} w_k(n)^H h_l(n-k)x(n-l-k) = w_{K-1}(n)^H \mathrm{H}_{L-1}(n)x_{L-1}(n) \tag{9.24}$$

Next assume there are no propagated errors, i.e., $\hat{\mathrm{x}}(n-D)=\sqrt{E_b}\,\mathrm{x}(n-D)$, so the SINR for the DFE in terms of the filter coefficients becomes

$$SINR_{DFE} = \frac{E[|\mathrm{w}_0(n)^H h_0(n)x(n)|^2]}{E\left[\left|\mathrm{w}_{K-1}(n)^H \mathrm{H}_{L-1}(n)\mathrm{x}_{L-1}(n) + \mathrm{w}(n)^H \mathrm{Q}(n)\,\mathrm{x}_M(n-D) - \mathrm{b}(n)^H \mathrm{x}_p(n-D) + \frac{1}{\sqrt{E_b}}\mathrm{w}(n)^H \eta(n)\right|^2\right]} \tag{9.25}$$

By assuming data and noise are zero mean and the channel, data, and noise are all mutually uncorrelated with $E[\boldsymbol{x}^H\boldsymbol{x}]=1$ and with $\|v\|^2 \stackrel{\text{def}}{=} v^H v$, (9.25) reduces to

$$SINR_{DFE} = \frac{E\left[|w_0(n)^H h_0(n)|^2\right]}{E\left[\|w_{k-1}(n)^H H_{L-1}(n)\|^2\right] + E\left[\|w(n)^H Q(n)\|^2\right] + E\left[\|b(n)\|^2\right] + \frac{N_0}{E_b}E\left[\|w(n)\|^2\right]} \tag{9.26}$$

In terms of the classical linear minimum mean square error (MMSE) filter, one could define the interference vector $\mathbf{v}(n) = [h_0\ h_1\ \ldots\ h_{L-1}\ \mathbf{0}_D^{\mathbf{T}}\ q_0\ \ldots q_{M-1}]^T$, where $\mathbf{0}_D^{\mathbf{T}}$ is a zeros vector with dimensions equal to the channel delay D. In this case, the feed-back filter is not required for the assumed propagation geometries and the optimal MMSE weight vector $\boldsymbol{w}(n)^H$ is (with $\boldsymbol{V}(n)$ defined the same way as $\boldsymbol{H}(n)$ and $\boldsymbol{Q}(n)$),

$$\mathrm{w}_{opt}(n) = \mathrm{R}_{yy}^{-1}\mathrm{p}_{xy} = \mathrm{R}_{yy}^{-1}E[x(n)\,\mathrm{y}(n)] = (E_b\,\mathrm{V}(n)\,\mathrm{V}(n)^{\mathrm{H}} + N_0\mathrm{I})^{-1}\cdot \mathrm{v}(n) \tag{9.27}$$

However, this formulation would require a filter that spans the entire delay spread of D symbols with many coefficients contributing only noise. Our approach uses a modified DFE structure that assumes linear channels for both feed-forward and feed-back filters (justified by the particular geometry of the application). As a result, we assume direct LOS and reflected paths are completely separable (by virtue of delay D). This approach allows the use of smaller filter sections which simplifies the hardware implementation. In this case, the feed-forward filter equalizes only the LOS path by defining the input reference as the first L samples of $x(n)$ and the feed-back filter operates on a vector of delayed estimates of $x(n)$.

As before, we assume data and noise are zero mean and the channel, data, and noise are all mutually uncorrelated and $\hat{\mathrm{x}}(n-D)=\sqrt{E_b}\,\mathrm{x}(n-D)$. With these assumptions the mean-squared-error is

$$\begin{aligned}\mathrm{MSE} &= \mathrm{E}[|\mathrm{e}(n)|^2] = \mathrm{E}\left[|\, x(n) - (\mathrm{w}(n)^H \mathrm{y}(n) - \mathrm{b}(n)^H \hat{\mathrm{x}}(n-D))|^2\right] \\ &= \mathrm{w}(n)^H \mathrm{R}_{yy} \mathrm{w}(n) - E_b \mathrm{b}(n)^H \mathrm{R}_{xx} \mathrm{Q}(n)^H \mathrm{w}(n) - E_b \mathrm{w}(n)^H \mathrm{Q}(n) \mathrm{R}_{xx}^H \mathrm{b}(n) + E_b \mathrm{b}(n)^H \mathrm{R}_{xx} \mathrm{b}(n)\end{aligned} \tag{9.28}$$

By the orthogonality principle, it is well-known that the error sequence *e(n)* is uncorrelated with the received signal: $\mathrm{E}\left[\mathrm{e}(n)\mathrm{y}^H(n)\right]=0$, which from (9.28) implies

$$w(n)^H \mathrm{R}_{yy} = E_b \mathrm{b}(n)^{\mathrm{H}} \mathrm{R}_{xx} \mathrm{Q}(n)^{\mathrm{H}} \tag{9.29a}$$

and

$$w(n)^H = E_b \mathrm{b}(n)^{\mathrm{H}} \mathrm{R}_{xx} \mathrm{Q}(n)^{\mathrm{H}} \mathrm{R}_{yy}^{-1} \tag{9.29b}$$

Combining (9.28) and (9.29) leads to

$$MSE = E_b \mathrm{b}(n)^H (\mathrm{R}_{xx} - E_b \mathrm{R}_{xx} \mathrm{Q}(n)^{\mathrm{H}} \mathrm{R}_{yy}^{-1} \mathrm{Q}(n) \mathrm{R}_{xx}^H) b(n) \tag{9.30}$$

Substituting $\boldsymbol{R}_{yy}$ and applying the matrix inversion lemma (the Sherman-Morrison-Woodbury identity: $(A+UDV)^{-1} = A^{-1}-A^{-1}U(D^{-1}+VA^{-1}U)^{-1}VA^{-1}$) :

$$\begin{aligned}&\mathrm{R}_{xx} - E_b \mathrm{R}_{xx} \mathrm{Q}(n)^{\mathrm{H}} \mathrm{R}_{yy}^{-1} \mathrm{Q}(n) \mathrm{R}_{xx}^H \\ &= \left(\mathrm{R}_{xx}^{-1} + \mathrm{Q}(n)^{\mathrm{H}} \left(\frac{1}{E_b} \mathrm{R}_{yy} - \mathrm{Q}(n) \mathrm{R}_{xx} \mathrm{Q}(n)^{\mathrm{H}} \right)^{-1} \mathrm{Q}(n) \right)^{-1}\end{aligned} \tag{9.31}$$

(9.30) and (9.31) gives an expression for the MSE as

$$MSE = E_b \mathrm{b}(n)^H \underbrace{\left(\mathrm{I} + \mathrm{Q}(n)^{\mathrm{H}} \left(\mathrm{H}(n)\mathrm{H}(n)^{\mathrm{H}} + \frac{N_0}{E_b} \mathrm{I} \right)^{-1} \mathrm{Q}(n) \right)^{-1}}_{R_b} \mathrm{b}(n) \tag{9.32}$$

Eliminating the trivial solution $w=b=\mathbf{0}$ for minimizing (9.32) requires the use of a constraint. Typically the Lagrangian multiplier is used under the unit power constraint, $\mathrm{b}^{\mathrm{H}}\mathbf{b} = 1$. We first form the Lagrangian:

$$L(b, \lambda) = E_b \mathrm{b}(n)^H \mathrm{R}_b \mathrm{b}(n) - \lambda (b(n)^H b(n) - 1) \tag{9.33}$$

Then compute the derivative, set to 0, and solve for the optimum $\boldsymbol{b}$ that minimizes the MMSE:

$$\frac{dL(b, \lambda)}{d\mathrm{b}} = E_b \mathrm{R}_b(n) b(n) - \lambda b(n) = 0 \tag{9.34}$$

The result is the *eigenvector* relationship

$$\mathrm{R_b}(n)b_{opt}(n) = \frac{\lambda}{E_b}\mathrm{b}_{opt}(n) \tag{9.35}$$

And

$$\begin{aligned} MMSE &= E_b b_{opt}(n)^H R_b(n) b_{opt}(n) \\ &= \frac{\lambda}{E_b} b_{opt}(n)^H b_{opt}(n) = \lambda_{min} \end{aligned} \tag{9.36}$$

Therefore the optimum ***b(n)*** is the eigenvector corresponding to the minimum eigenvalue of $\boldsymbol{R}_b$ found by solving the *characteristic equation* $\det(\mathrm{A}-\lambda\mathrm{I})=0$:

$$\lambda_{min} = \arg\min_{\lambda}\left\{\det\left[\left(\mathrm{I}+\mathrm{Q}(n)^{\mathrm{H}}\left(\mathrm{H}(n)\mathrm{H}(n)^{\mathrm{H}}+\frac{N_0}{E_b}\mathrm{I}\right)^{-1}\mathrm{Q}(n)\right)^{-1}-\lambda_{min}\mathrm{I}\right]=0\right\} \tag{9.37}$$

$\mathbf{b}_{\mathrm{opt}}(n)$ is the solution to

$$\left[\left(\mathrm{I}+\mathrm{Q}(n)^{H}\left(\mathrm{H}(n)\mathrm{H}(n)^{H}+\frac{N_0}{E_b}\mathrm{I}\right)^{-1}\mathrm{Q}(n)\right)^{-1}-\lambda_{min}\mathrm{I}\right]\mathrm{b}_{opt}(n)=0 \tag{9.38}$$

where 0 is the all zeroes matrix.

Now that the Lagrangian approach has provided the optimal feed-back filter in the MMSE sense, the feed-forward filter that minimizes the MSE is determined in the usual way of finding the derivative of (9.27) with respect to ***w(n)*** given ***b(n)*** and setting the result to 0:

$$\begin{aligned} \mathrm{w}_{opt}(n)^H &= E_b b_{opt}(n)^H \mathrm{Q}(n)^{\mathrm{H}} \mathrm{R}_{yy}^{-1} \\ &= b_{opt}(n)^{\mathrm{H}}\mathrm{Q}(n)^{\mathrm{H}}\left(\mathrm{H}(n)\mathrm{H}(n)^H+\mathrm{Q}(n)\mathrm{Q}(n)^{\mathrm{H}}+\frac{N_0}{E_b}\mathrm{I}\right)^{-1} \end{aligned} \tag{9.39}$$

After substituting the optimal weights under the constraint $\boldsymbol{b}^H\boldsymbol{b}=1$ and assuming the ideal delay value is chosen ($D=D_{opt}$such that $\hat{\mathrm{x}}(n-D)=\sqrt{E_b}\,\mathrm{x}(n-D)$), the SINR is similar to the form of (9.18) and (9.26)

$$SINR_{DFE} = \frac{E_b\,|h_0|^2}{N_0\left(\lambda_{min}+\mathrm{E}\left[\left\|\mu\left(\mathrm{b}(n),\frac{E_b}{N_0}\right)\right\|^2\right]\right)} \tag{9.40}$$

The term $E[|\mu(b(n), SNR|^2]$ is the contribution due to errors in the decisions used in the feedback filtering. The analysis for this term is not treated here (in this formulation $E[|\mu(b(n), SNR|^2] = 0$ since $\hat{x}(n-D) = \sqrt{E_b}\,\mathrm{x}(n-D)$ was explicitly assumed), however empirical results for the case where $\mathbf{w}_{opt}(n)$ and $\mathbf{b}_{opt}(n)$ are determined through least-squares iterative adaptation algorithms indicate the term reduces the achievable output SINR by approximately 1dB for input SINR from (9.18) of $E_b/(I_0+N_0) \approx 4\text{dB}$.

Example Consider the channel model with input-output relationship

h(n)=[1.2 0.8−0.5], ***q(n)***=[0.2 0.5−0.2], D=10, E_b=1, and η is white noise with variance of 0.1.

$$y(n) = \sqrt{E_b}(1.2x(n) + 0.8x(n-1) - 0.5\mathrm{x}(n-2)) + \sqrt{E_b}(0.2x(n-10) + 0.5x(n-11) - 0.2x(n-12) + \eta(n)$$

The channel responses **H** and **Q** are

$$\mathrm{H} = \begin{bmatrix} 1.2 & 0.8 & -0.5 & 0 & 0 \\ 0 & 1.2 & 0.8 & -0.5 & 0 \\ 0 & 0 & 1.2 & 0.8 & -0.5 \end{bmatrix}, Q = \begin{bmatrix} 0.2 & 0.5 & -0.2 & 0 & 0 \\ 0 & 0.2 & 0.5 & -0.2 & 0 \\ 0 & 0 & 1.2 & 0.5 & -0.2 \end{bmatrix}$$

$$\mathrm{w}_{opt}(n)^{\mathrm{H}} = E_b \mathrm{b}_{opt}(n)^{\mathrm{H}} \mathrm{Q}(n)^{\mathrm{H}} \mathrm{R}_{yy}^{-1} = [-0.1948\ 0.2106\ -0.1948]$$

MMSE=$\mathrm{N}_0\lambda_{min}$= 0.08086

With the corresponding eigenvector of λ_{min} given by

$$\mathrm{b}_{opt}(n)^H = \begin{bmatrix} -0.2035 & -0.2889 & 0.5500 & -0.7289 & 0.2035 \end{bmatrix}$$

$$SINR_{DFE} = \frac{E_b \,|\, h_0 \,|^2}{N_0(\lambda_{min})} = 12.51\ dB$$

The best possible SINR (I_0=0) in this case would be

$$SINR_{DFE} = \frac{2E_b}{N_0} = 13.01\ dB$$

which means the residual interference after equalization is 0.5 dB for the particular channel realization shown, which has an input SINR of

$$SINR_{input} = \frac{E_b}{N_0 + I_0} = \frac{E_b}{N_0}\left(1 + \frac{I_0}{N_0}\right)^{-1} = -1.21 dB$$

Parameters	Units	Predicted Air-Air (25k)	Measured
Crane Rain Region	1996 Ver.	Maritime D	
Slant Range	km	200	200
Tx Altitude (above sea level)	ft	25000	25000
Rx Altitude (above sea level)	ft	25000	22000
Coded Bit Rate (Channel Rate)	Mb/s	140.8	140.8
Information rate requirement	Mb/s	112	112
Max Power Output	dBm	49.00	49.00
Transmit Antenna Gain	dBi	26.50	26.50
Net EIRP	dBm	68.39	68.39
Free Space Loss	dB	-161.98	-165.89
Low Angle Fading (95% worst case ISI < 5 symbols)	dB	-0.06	
Expected Atmospheric Attenuation @ 95%	dB	-0.56	
Receive Antenna Gain	dBi	26.50	26.50
Rx Signal Power at RFE	dBm	-71.46	-71.00
C/N at 95% Availability (Clear Air - Weather Loss)	dB	19.64	18.00
Eb/(N0+I0) at DFE output at 95% worst case	dB	15.63	12.00
Link Margin at 95% Availability	dB	10.83	7.20

Fig. 9.21 Air-to-air RF link budget predictions and measured results. *RF* radio frequency

9.4.4 RFC SNR

Figure 9.21 depicts a typical link budget for the ORCA/FOENEX RFC system with measured data for comparison. As expected, the agreement between measurement and theory is excellent. Figure 9.22 provides a view of the RF link E_b/N_0 at a range of approximately 200 km. It shows that the link maintains significant margin except when obstructed by the aircraft's wings.

9.4.5 Equalizer Performance Validation

The DFE was validated using the IRON-T2 Hawaii data played back in the laboratory. Equalizer performance can be analyzed using the metrics of SNR and SINR defined previously. Figure 9.23 below is a power delay profile computed by cross-correlating the known test data pattern with the signal before (left) and after (right) equalization. The figure on the left shows the presence of the ocean reflection arriving 53 symbols after the desired LOS signal. This waveform was captured at 12:35:10 pm on October 28, 2008.

For the example shown above, the estimated *C/I* values are 6.3 dB before equalization and 24.8 dB after equalization for a gain of 18.5 dB in *C/I* ratio. In this case, the interference is suppressed to less than 1 dB above the AWGN noise floor at the FEC input.

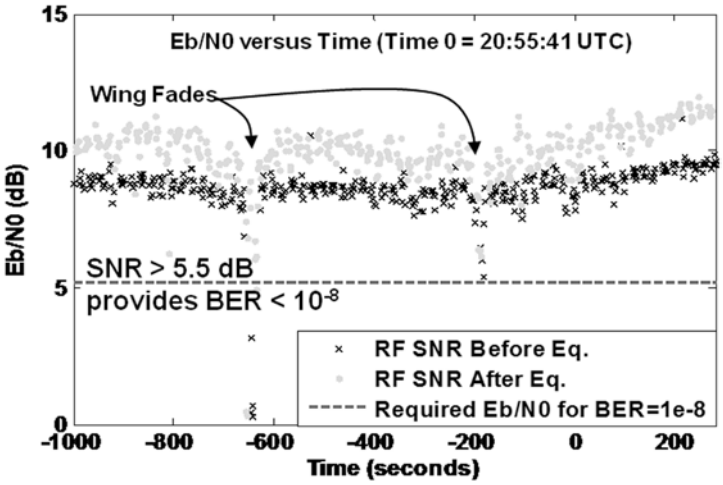

Fig. 9.22 Air-to-mountain RF link E_b/N_0 versus time at 200 km link range. *RF* radio frequency

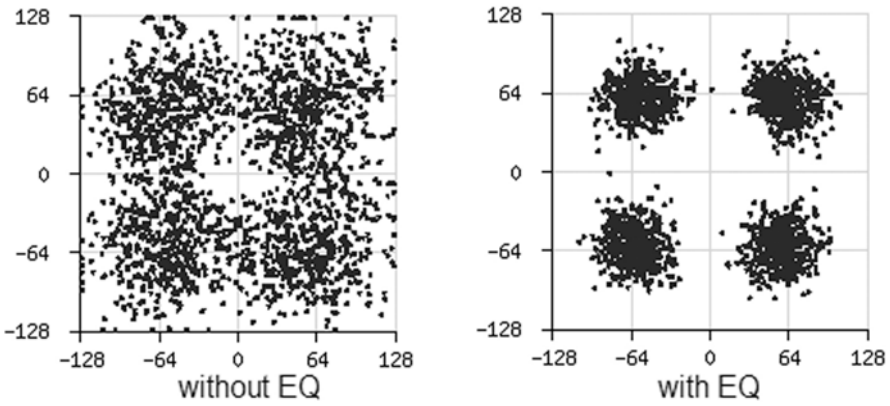

Fig. 9.23 Power delay profile of un-equalized (*left*) and equalized (*right*) symbols

The improvement in E_b/N_0 can be visualized by plotting the recovered soft-decision data with and without equalization enabled as shown in Fig. 9.24. These constellation plots correspond to the data snapshot taken at October 28, 2008 at 12:35:10 pm (i.e., 1028123510) shown in Fig. 9.25.

Although the DFE is capable of mitigating the ISI introduced by ocean reflection, it is important to obtain a good estimate of the arrival time of the ocean reflection relative to the desired signal, and tune the DFE accordingly in order for the DFE to work properly. The DFE used in this analysis has an adjustable parameter called "DFE Delay" which can be used to line up the equalizer (EQ) FIR filter temporally with the expected arrival time of the ocean reflection.

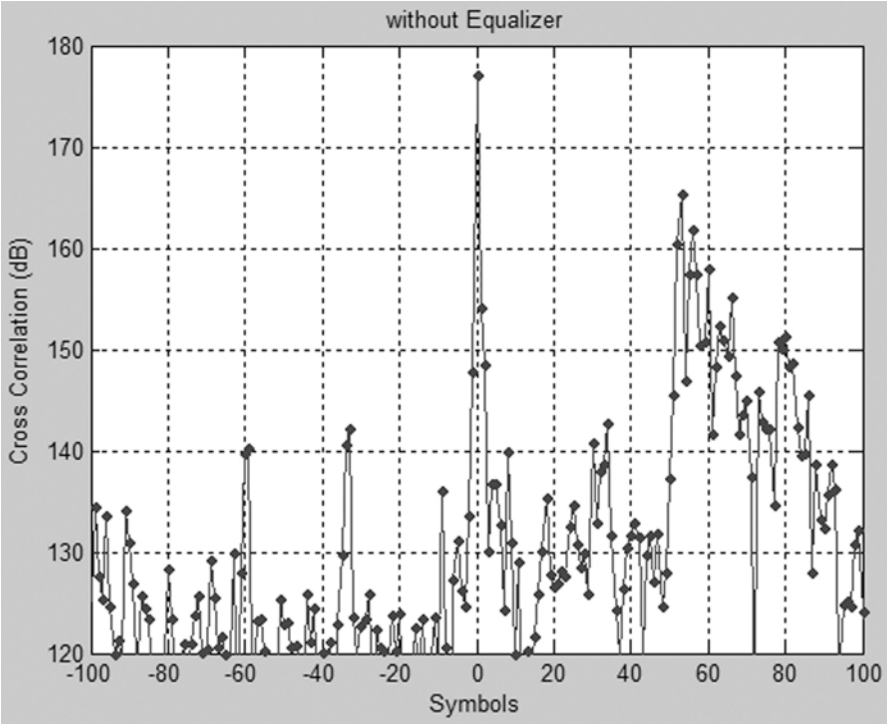

Fig. 9.24 Qualitative improvement in the SNR after applying the DFE. *SNR* signal to noise ratio, *DFE* decision feedback equalizer

Channel			Hardware Measurements				Results	
			Without Equalizer		With Equalizer			
Waveform Timestamp	C/N (dB) at RFE Output	C/I (dB)	Eb/(N0+I0) (dB)	BER	Eb/(N0+I0) (dB)	BER	Eb/(N0+I0) Gain (dB)	Residual I0/N0 (dB)
102808091137	7.4	6	0.8	0.3	2.8	0.0495	2.0	1.6
102808123310	7.4	7	2.0	0.0706	3.2	0.0439	1.2	1.2
102808122910	7.5	5	1.2	0.0755	3.1	0.0388	1.9	1.4
102808090737	8.7	6	3.8	0.0329	5.0	1.30E-03	1.2	0.7
102808123510	8.9	5	1.7	0.1	4.9	4.30E-04	3.2	1.0
102808101940	9.9	7	2.9	9.10E-03	5.8	0.00	2.9	1.1
102808090937	10	5	2.2	0.0688	6.2	0.00	4.0	0.8
102808084537	10.3	8	3.9	4.30E-03	6.5	0.00	2.6	0.8
102808122510	10.3	11	5.4	0.00	6.7	0.00	1.3	0.6
102808081807	10.7	8	5.2	1.15E-03	6.7	0.00	1.5	1.0
102108144619	12.7	5	3.7	5.16E-02	9.2	0.00	5.5	0.5
102108153206	18.8	16	14.2	0.00	15.2	0.00	1.0	0.6

Fig. 9.25 Summary of DFE validation test results.*DFE* decision feedback equalizer

The DFE was further evaluated in 12 of the 668 Hawaii RF data captures using a software modem emulator. Figure 9.15 provides the tabulated results for each of the 12 captured channel samples that were tested on ORCA/FOENEX hardware. Note *C/I* values of less than 10 dB resulted in a BER error floor of greater than 1e-3 even when *C/N0* is very high, indicating the dominance of multipath interference in those cases.

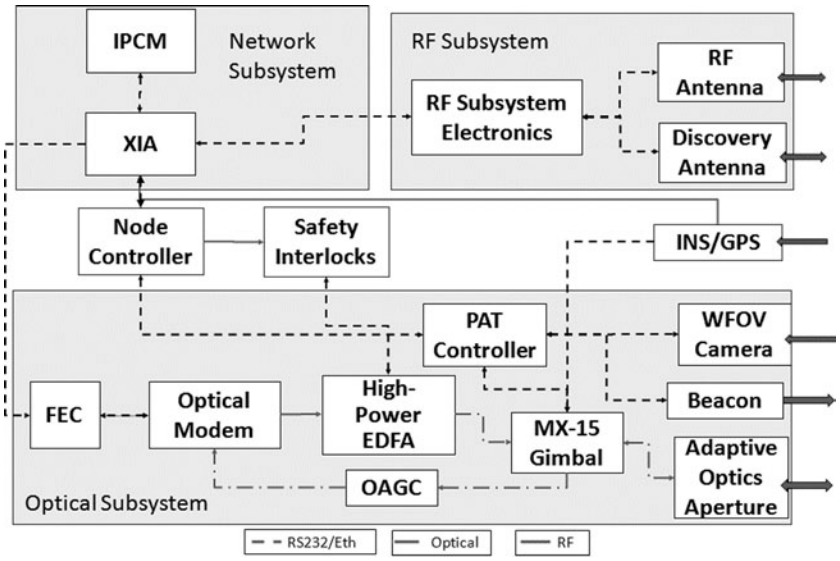

Fig. 9.26 FOENEX high-level system architecture [2]. *FOENEX* free space optical experimental network experiment

9.5 Network System

Networks are made up of nodes, which can include aircraft, ground vehicles, soldiers, sensors, and other users and producers of information. This section discusses the ORCA/Networking layout and its performance in facilitating communications and data dissemination among all those various nodes.

9.5.1 Network Architecture

Figure 9.26 shows the high level system architecture for the network [6]. Here, IPCM indicates the Inter-Platform Communications Manager (the FOENEX MANET, topology manager, and network control); and XIA refers to the XFUSION Interface Assembly (XIA is the third generation [1st generation was IRON-T2, second was ORCA Phase 1 XFUSION] hybrid-aware network router and controller developed for ORCA/FOENEX) [6]. In this configuration, the networking subsystem is realized in the XIA hybrid-aware **IP** router and provides seamless integration of the RF and FSO subsystems to form hybrid communication links utilizing the attributes and strengths of each channel to meet the network availability and QoS requirements for the FOENEX network

Figure 9.27 depicts the FOENEX Network Stack [6]. The FOENEX network system and associated network stack utilizes a layered approach to improving net-

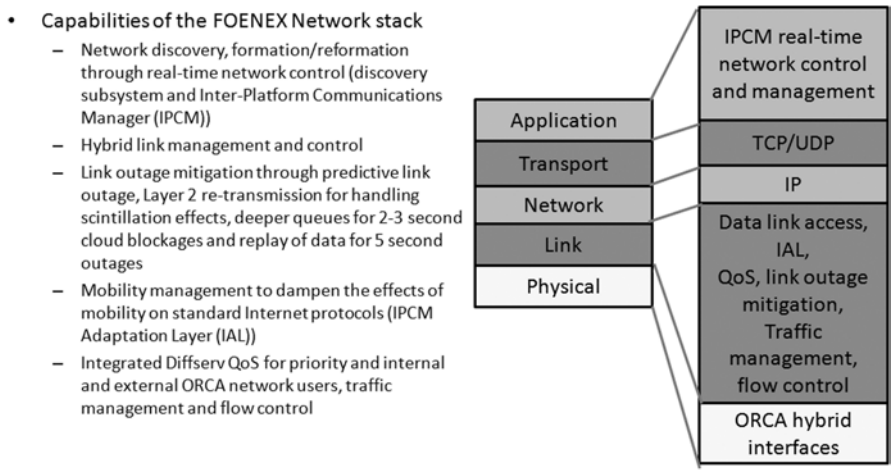

Fig. 9.27 ORCA/FOENEX network stack capabilities and breakdown [2]

work availability. At the physical layer the system utilizes the concept of hybrid links (the bonding of RF and FSO channels) for use in communications between one network node and another. These hybrid links provide reliable packet delivery techniques for link layer retransmission, prioritized failover of traffic flows from one hybrid channel to another and the ability to differentiate between atmospheric scintillation and cloud events from hybrid link outage. These link layer capabilities are tightly integrated with Diffserv quality of service (QoS) capabilities, local deep queuing techniques, and the ability to segregate network traffic flows into internal (primary mission users) and external (secondary mission users) traffic aggregates. The FOENEX MANET provides network node discovery for network formation/re-formation and reactive and proactive management of the network topology based on anticipated or incurred network outage events. Stability in the network is provided by dampening the effects of mobility on routing and higher-layer protocols and applications through the use of Layer 2 switching techniques (e.g., IPCM Adaptation Layer or IAL).

9.5.2 Network Analysis

Retransmission and failover are the key network functions that were tested in the field experiments. Retransmission is intended to increase reliable packet delivery rates across the FSO link, which experiences link disruptions due to scintillation. Failover leverages diversity in the dual physical layer, redirecting data traffic over the RF link when the FSO link is down or link quality is degraded beyond the point at which retransmission is practical.

Packet error rate (PER) data was used as a metric in evaluating the performance of the layer 2 retransmission and failover technologies. PER was evaluated by comparing

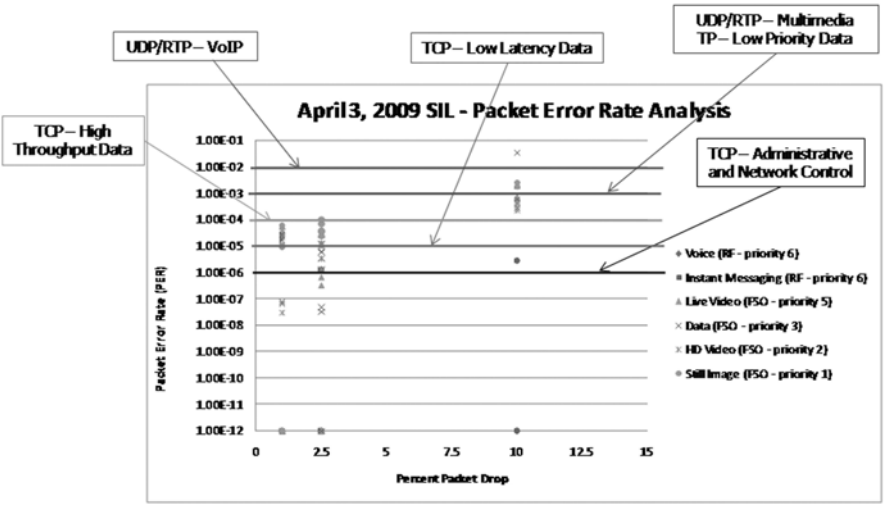

Fig. 9.28 Measured versus projected PER. *PER* packet error rate

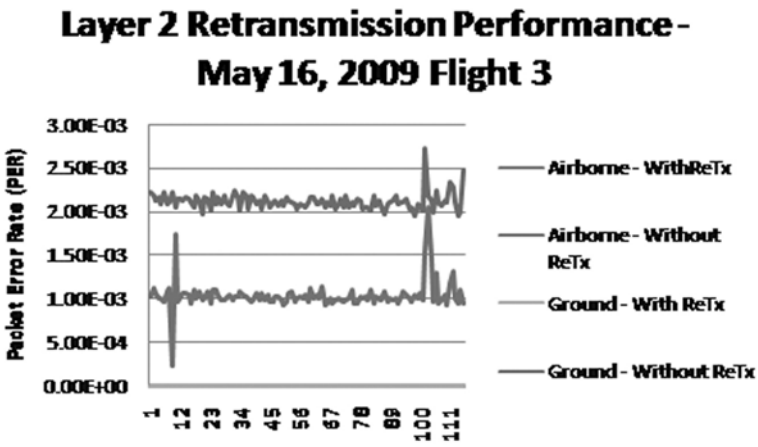

Fig. 9.29 Flight 3—Layer 2 retransmission performance given ≤1 % LDE. *LDE* link disruption event

traffic type and Internet Engineering Task Force (IETF) service class against PER requirements for wireless IP systems. Results, as shown in Fig. 9.28, indicate that the ORCA/FOENEX network provided PER performance comparable to other wireless IP systems for a point to point link with improved performance in some areas.

The experimental results shown in Figs. 9.28 and 9.29 demonstrate orders of magnitude improvement in PER utilizing layer 2 retransmission over the FSO channel using the RF channel for high priority traffic and retransmission requests. The experiments provided useful data for improving both the layer 2 retransmission and: LDE detection mechanisms for a future prototype system thus improving PER.

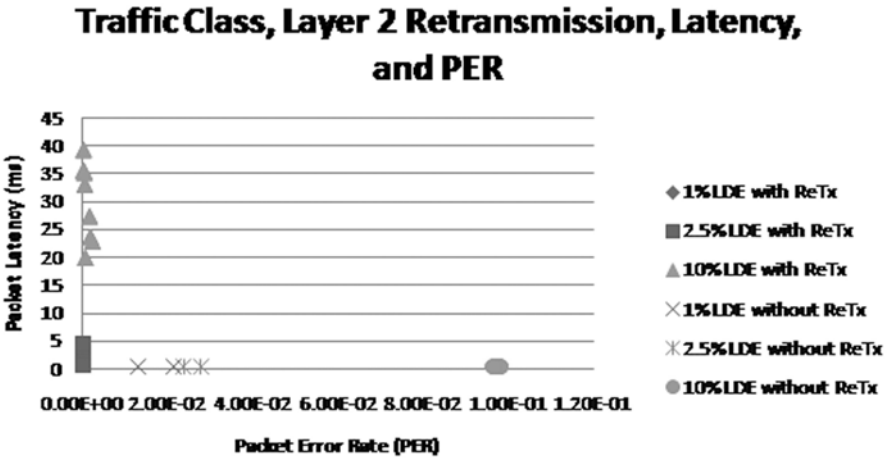

Fig. 9.30 PER versus latency trade for given LDE percentages. *PER* packet error rate, *LDE* link disruption event

Figure 9.30 shows PER as a function of latency trades for given LDE percentages. In some cases, LDE detection determined that the disruption event was a long-term outage event (e.g., cloud obstructions of the FSO link). The Phase 1 hybrid router in such cases would failover data from the FSO port of the hybrid link to the RF port of the hybrid link. Figure 9.31 highlights a portion of air-to-mountain test data showing failover events due to obstructions. As previously discussed, the RF link carried voice and chat data while a hybrid link was established. During failover events, the link was filled to its maximum capacity of 123.2 Mbps as demonstrated by the spikes in RF data rate in Fig. 9.31.

9.5.3 Packet Loss Mitigation Techniques and Effects on Packet Latency

Packet latency goals for the Phase 1 system were defined using [4]. As this was a point-to-point link experiment and the latency goals were specified for a 5 hop network, conformance with the goals must be extrapolated. Measured performance for the single hop air to ground hybrid link test indicates that end-to-end (e.g., IXIA network tester to IXIA network tester) packet latency performance is within the Phase 1 design goals for the various traffic types. This assumes the given procedures for deriving Mean IP Transfer Delay (IPTD) uses the sum of the means contributed by network Sects. (e.g., each hop). Mathematically, we use the following:

$$ORCA\,IPTD = numHops\,x\,avg\,measured\,latency$$

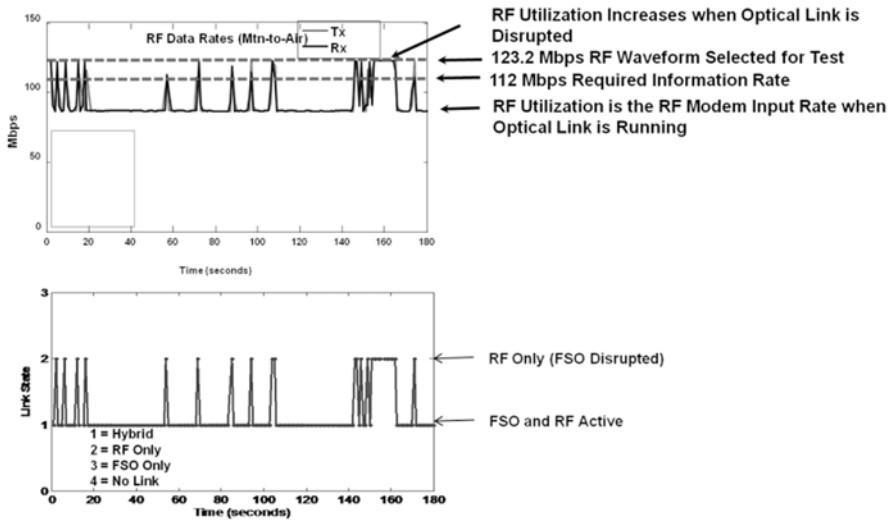

Fig. 9.31 FSO to RF failover events, May 18 air-to-mountain

Table 9.3 Latencies by traffic type, port destination, and priority for Flight 3 on May 16, 2009

IP precedence traffic type/port	DiffServ mapping	End-to-end latency goals for 5 hop network (ms)	End-to-end NTTR measured average latency (single hop) (ms)
Internet control (110)/RF	Network control (CS6)	200	0.890
Critical/ECP (101)/ FSO	Telephony (EF (CS5))	250	0.297
Flash (011)/FSO	Low latency data (AF(CS3))	200	0.350
Immediate (010)/ FSO	High throughput data (AF (CS2))	2000	0.416
Priority (001)/FSO	Low priority data (AF (CS1))	Best effort	0.326

Laboratory measurements of the Phase 1 system were performed with scintillation profiles constructed from measured data from the Hawaii IRON-T2 experiments. Specifically, laboratory measurements of PER and latency were taken for 1, 2.5, and 10% scintillation profiles both with layer 2 retransmission and without layer 2 retransmission enabled. Table 9.3 shows the measured latencies by traffic type, port destination, and priority for Flight 3 on May 16, 2009. When using retransmission, the latency requirements are achieved while improving PER by orders of magnitude (from 2 to 3 orders in most cases). The system did fall short of being able to be error free in all cases at 1% LDE, but insights gained in the experiments allowed improved retransmission in order to achieve the program goals.

Table 9.4 Test conditions for the network performance testing

Conditions of test
Protocol = IPv4/IPv6
Packet sizes = 1518 bytes
Configuration = hybrid (5 Gbps user information rate on FSO, 200 Mbps RF)
Duration = 30 min per test
Scintillation profile = 5 % Hawaii (20 min repeating segment) using hardware scintillator
L2 retransmission—disabled vs enabled
L2 retransmission timeout = 1 s

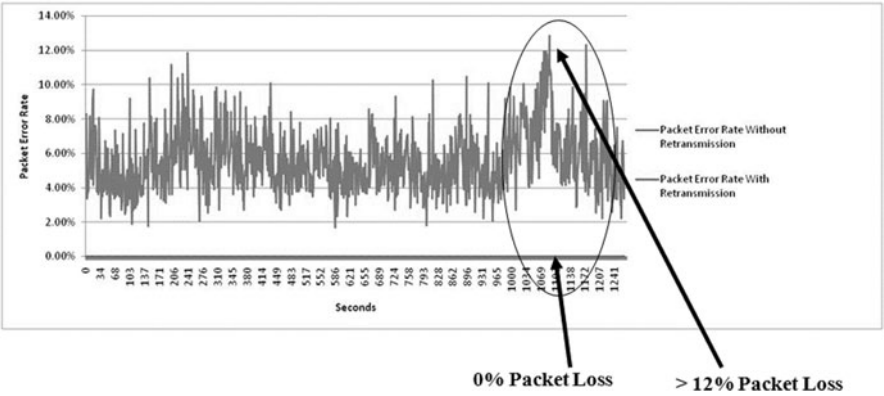

Fig. 9.32 Network packet loss results for 5 % level atmospheric turbulence, with and without Layer 2 retransmission [2]

9.5.4 Improved Retransmission Performance

To see if the network could handle 2 % or higher PER traffic, network performance was assessed using improved ORCA/FOENEX hardware and software in laboratory tests. The test data was derived from scintillation data from the AFRL IRON-T2 Hawaii experiments in October 2008. The experimental configuration consisted of two network nodes simultaneously transferring data each way, each containing a hybrid link connected to one another. The configuration tested network retransmission effectiveness. The FSO channel was 10 Gbps clock rate carrying 5 Gbps of user data sourced from an IXIA network tester. The RF channel is at a clock rate of 274 Mbps with a user information rate of 200 Mbps. Table 9.4 shows the test conditions for the network performance testing. Figure 9.32 shows the network performance for a 5 % scintillation profile, with and without Layer 2 retransmission. It is clear from this figure that the saturation-regime atmospheric turbulence occurring during the IRON-T2 Hawaii experiments created significant packet loss, > 12 % at times. The RF link was used for retransmission requests. This figure shows error free packet delivery using a hybrid link-based layer 2 retransmission packet loss mitigation technique. In other words, we do not see any degradation in data integrity errors, nor dropped packets, during the test sequence.

References

1. L.B. Stotts, J. Foshee, B. Stadler, D. Young, P. Cherry, W. McIntire, M. Northcott, P. Kolodzy, L. Andrews, R. Phillips, A. Pike, Hybrid optical RF communications. Proc. IEEE **97**(6), 1109–1127 (2009)
2. L.B. Stotts PhD, N.D. Plasson, T.W. Martin, D.W. Young, J.C. Juarez, Progress towards reliable free-space optical network. MILCOM 2011, IEEE, Baltimore, 7–10 Nov 2011
3. D. Young, J. Sluz, J. Juarez, M. Airola, R. Sova, H. Hurt, M. Northcott, J. Phillips, A. McClaren, D. Driver, D. Abelson, J. Foshee, Demonstration of high data rate wavelength division multiplexed transmission over a 150 km free space optical link, in *Proceedings of the SPIE 6578, Defense Transformation and Net-Centric Systems*, IEEE, Orlando, 2007
4. M. Northcott, A. McClaren, B. Graves, J. Phillips, D. Driver, D. Abelson, D. Young, J. Sluz, J. Juarez, M. Airola, R. Sova, H. Hurt, J. Foshee, Long distance laser communications demonstration, in *Proceedings of the SPIE 6578, Defense Transformation and Net-Centric Systems*, SPIE Orlando, 2007
5. D. Young, J. Sluz, J. Juarez, M. Airola, R. Sova, H. Hurt, M. Northcott, J. Phillips, A. McClaren, D. Driver, D. Abelson, J. Foshee, Demonstration of high data rate wavelength division multiplexed transmission over a 150 km free space optical link, MILCOM 2007, Advanced Communications Technologies 4.2, Directional Hybrid Optical/RF Networks, 2007
6. J. Latham, M. Northcott, B. Graves, J. Rozzi, IRON-T2 2008 AOptix Technologies Test Report, Contract FA8750-08-C-0185 (2009)
7. S. Karp, R.M. Gagliardi, S. E. Moran, L. B. Stotts, *Optical Channels: Fiber, Atmosphere, Water and Clouds* (Plenum Publishing Corporation, New York, 1988), pp. 5–9
8. L.C. Andrews, R.L. Phillips, *Laser Beam Propagation through Random Media*, 2nd edn. (SPIE, Bellingham, 2005), pp. 407–408
9. L.C. Andrews, *Field Guide to Atmospheric Optics* (SPIE, Bellingham, 2004), p. 50
10. W.K. Pratt, *Laser Communications Systems* (Wiley Series in Pure and Applied Optics, New York, 1969), pp. 2–9
11. L.B. Stotts, G.M. Lee, B. Stadler, Free space optical communications: Coming of age, Proceedings of the SPIE conference on atmospheric propagation V, G. Charmaine Gilbreath, Linda M. Wasiczko, Editors, 69510W, 18 April 2008
12. D. Young, J. Sluz, J. Juarez et al., Demonstration of high data rate wavelength division multiplexed transmission over a 150 km free space optical link, Military Communications Conference, 2007. MILCOM 2007. IEEE, pp. 1–6, 29–31 Oct. 2007
13. M. Northcott, A. McClaren, J. Graves, J. Phillips, et al., Long distance laser communications demonstration, Defense Transformation and Net-Centric Systems 2007. Edited by S. Raja. Proceedings of the SPIE, vol. 6578, pp. 65780S (2007)
14. F.G. Walther, G.A. Nowak, S. Michael, R. Parenti, J. Roth., J. Taylor, W. Wilcox, R. Murphy, J. Greco, J. Peters, T. Williams, S. Henion, R. Magliocco, T. Miller, A. Volpicelli, Air to ground lasercom systems demonstration, in *Proceeding of the MILCOM 2010*, IEEE, San Jose, 31 Oct–3 Nov 2010
15. Z.C. Bagley, D. Hughes, P. Kolodzy, T. Martin, T.G. Moore, H.A. Pike, N.D. Plasson, B. Stadler, L.B. Stotts, D. Young, Hybrid Optical RF Communications, Opt. Eng. 51(5), 055006 (May 25, 2012)
16. J.C. Juarez, D.W. Young, J.E. Sluz, Optical automatic gain controller for high-bandwidth free-space optical communication links. Application of lasers for sensing & free space communication (LS & C), Optical Society of America, Toronto, Ontario, Canada, 10–14 July 2011
17. J.C. Juarez, D.W. Young, J.E. Sluz, L.B. Stotts, High-sensitivity DPSK receiver for high-bandwidth free-space optical communication links. Opt. Express **19(**11) 10789–10796 (2011)
18. D.L. Walters, K.E. Kunkel, Atmospheric modulation transfer function for desert and mountain locations: The atmospheric effects on r_{0}. J. Opt. Soc. Am. **71**, 397–405 (1981)

19. R.R. Beland, Propagation through atmospheric optical turbulence, in *The Infrared and ElectroOptical Systems Handbook*, ed. by F.G. Smith, vol. 2, chap 2 (SPIE, Bellingham, 1993)
20. L.B. Stotts, B. Stadler, D. Hughes, P. Kolodzy, A. Pike, D.W. Young, J. Sluz, J. Juarez, B. Graves, D. Dougherty, J. Douglass, T. Martin, Optical communications in atmospheric turbulence, in *Proceedings of the SPIE Conference on Free-Space Laser Communications IX*, San Diego, vol. 7091, 2–6 Aug 2009, ed. by A. K. Majumdar, C. Davis
21. R.G. Walther, Diversity in Air-to-Ground Lasercom: The FOCAL Demonstration, Technical Panel, Session DoD-2: Freespace Optical Communications, 2011 Military Communications Conference (MILCOM 2011), Baltimore, MD, 7–10 Nov 2011
22. R.E. Hufnagel, Variations of atmospheric turbulence. Digest of technical papers, topical meeting on optical propagation through turbulence, OSA, Washington, D.C., 9–11 July 1974
23. R.E. Hufnagel, Propagation through atmospheric turbulence, in *The Infrared Handbook*, Chap. 6 (USGPO, Washington, 1974)
24. L.C. Andrews, R.L. Phillips, D. Wayne, T. Leclerc, P. Sauer, R. Crabbs, J. Kiriazes, Near-ground vertical profile of refractive-index fluctuations, Proc. SPIE **p. 732402** (April 30, 2009)
25. L.C. Andrews, R.L. Phillips, R. Crabbs, D. Wayne, T. Leclerc, P. Sauer, Atmospheric channel characterization for ORCA testing at NTTR, Proc. SPIE **p. 758809** (February 11, 2010)
26. L.C. Andrews, R.L. Phillips, R. Crabbs, D. Wayne, T. Leclerc, P. Sauer, Creating a Cn2 profile as a function of altitude using scintillation measurements along a slant path. Proc. SPIE **p. 82380F** (February 1, 2012)
27. D.T. Wayne, R.L. Phillips, L.C. Andrews, T Leclerc, P. Sauer, Observation and analysis of aero-optic effects on the ORCA laser communication system, Proc. SPIE **p. 80380A** (May 25, 2011)
28. L.B. Stotts, B. Sadler, D. Hughes, P. Kolodzy, A. Pike, D.W. Young, J. Sluz, J. Juarez, B. Graves, D. Dougherty, J. Douglass, T. Martin, Optical communications in atmospheric turbulence, Proc. SPIE **p. 746403** (August 21, 2009)

Chapter 10
Free-Space and Atmospheric Quantum Communications

Ronald E. Meyers, Keith S. Deacon and Arnold D. Tunick

10.1 Introduction to Free-Space and Atmospheric Quantum Communications

The *quantum internet* with free-space and atmospheric quantum channels is becoming a reality [1, 2]. Emerging from the early ideas of Feynman and his colleagues [3], quantum information science (QIS) technologies are under development around the world to construct the *quantum internet*. Destined to fulfill capabilities well beyond our current imagination, the *quantum internet* is being shaped by both the laws of quantum physics and the compelling needs for increased speed, bandwidth, and cybersecurity. Free-space and atmospheric quantum communications will play a critical role in extending the *quantum internet* to global use (Fig. 10.1). Quantum information will be teleported through mobile *information teleportation networks* that necessarily will include satellites. Recent developments in quantum physics have the potential to add to free-space and atmospheric communications, a physical layer of quantum security, increased bandwidth, and speed beyond classical communications capabilities. Achieving a quantum communications internet with distributed quantum computing capabilities will first require research involving theory, experiments, and the development of proof-of-principle physics and engineering systems. This chapter introduces the reader to free-space quantum communications by providing both a review of the fundamental foundations of quantum communications as applied to free-space and the atmosphere (Sect. 10.2) and a review of representative free-space and atmospheric quantum communications experiments (Sect. 10.3).

R. E. Meyers
US Army Research Laboratory, Adelphi, MD 20783
E-mail: ronald.e.meyers6.civ@mail.mil

A. K. Majumdar, *Advanced Free Space Optics (FSO),*
Springer Series in Optical Sciences 186, DOI 10.1007/978-1-4939-0918-6_10,
© Springer Science+Business Media New York 2015

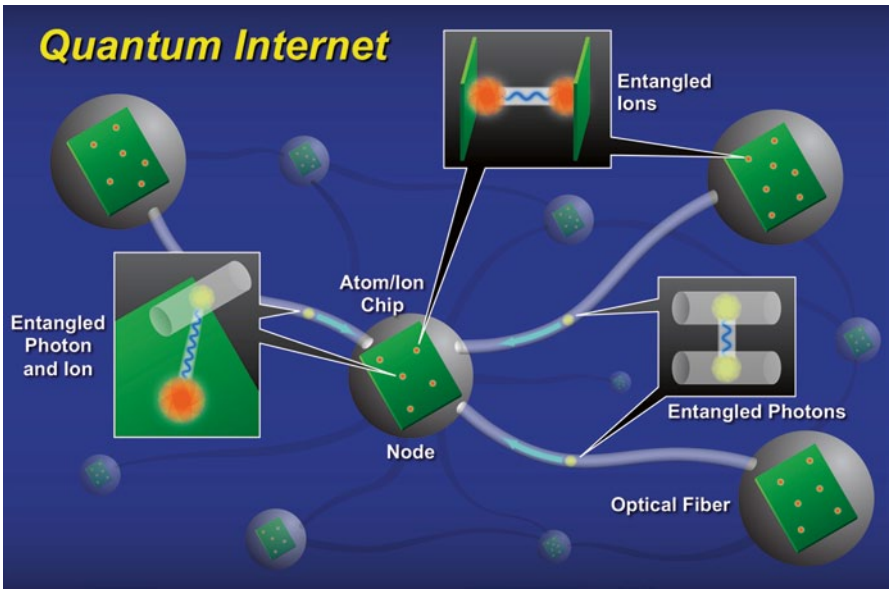

Fig. 10.1 Quantum Internet concept depiction by Ronald E. Meyers, Keith S. Deacon, and Arnold D. Tunick, US Army Research Laboratory (2011) [4]

10.2 Fundamentals for Free-Space Quantum Communications

10.2.1 Introduction

Physics strives to describe the laws that govern the evolution of the universe. A key tenet of physics is that the truth of any physical law must be tested by experiments. Proposed hypotheses are tested before a theory is formed that fairly describes the evolution in space and time of physical phenomena. Although nature is very complex, relatively few physical laws are needed to describe many of its facets. Einstein's theories of special and general relativity and quantum physics hold special places among the physical laws. Relativity has been proven on the large scale and seems to govern how stars and planets evolve while quantum physics has been the most effective in describing how particles and waves behave at the atomic and subatomic scales. The study of the full reconciliation of these theories is called quantum relativity. Nevertheless, enough is known about quantum physics and relativity to implement effective free-space atmospheric quantum communications systems. In other words, although we don't know everything, and there will be many more surprises, we know enough now to implement systems that are better in some important ways than current systems which are based on the classical understanding of physics and engineering. In 1935, Einstein in his famous EPR paper [5] raised the question of whether quantum mechanics gives a complete description of the universe. In the paper Einstein described the quantum mechanical

behavior of two quantum particles which when separated by great distances had the state of one particle respond to changes of state of the other particle. Einstein also said that such a nonlocal effect, later known as the "EPR Effect," should be tested by experiment to determine if it was correct and if it corresponded to what quantum mechanical theory had predicted. In the 1970's and since, experiments have shown that the EPR effect of entanglement does indeed exist [6, 7]. Einstein described this effect as "Spooky action at a distance." It has become clear to many scientists that quantum mechanical effects such as entanglement and teleportation can be harnessed in quantum communications to enhance the security, bandwidth, compression, movement, and storage of information. In the following sections we will provide an introduction to the fundamentals needed to begin the investigation of free-space quantum communications. While they at first may find the concepts strange and the notation unfamiliar, engineers will find that they can harness the power of quantum physics for the development of free-space and atmospheric quantum communications systems.

10.2.2 Fundamentals

The fundamentals of quantum physics describe the properties of quantum particles and quantum wavefunctions. Classical particles, such as a baseball, can be described by Newtonian physics where each particle simultaneously has a precise position and momentum. However, quantum particles such as photons and electrons have an uncertainty associated with both position and momentum such that quantum's uncertainty relationship holds, $\frac{\hbar}{2} \leq \Delta x \Delta p$, where $\hbar$ is Planck's constant over 2π [8, 9]. Experimental measurements of position and momentum always note a variability in the measured values. Thousands of careful experiments have verified this relationship. Quantum particles are said to have both particle and wave properties. When a photon detector responds with a "click" it is measuring a photon in the sense of a particle. When light passes through a double slit and interferes, the light is exhibiting its interference wave properties. When a series of single photons are passed though a double slit the same interference patterns are measured. The way to describe the evolution of quantum properties has relied upon the construct of the wavefunction, Ψ. The wavefunction is in general a complex function having both real and imaginary values. When the wavefunction is multiplied by its complex conjugate, $\Psi^* \Psi$, it forms a positive function which when normalized gives the probability of the quantum particle being found in a particular state. In the case of a photon, the probability may describe where the photon is likely to be found in space. It is a peculiar property of quantum physics that the Fourier transform of the wavefunction in configuration space gives the wavefunction in momentum space. Position and momentum are called conjugate variables. Before we go further let us discuss the quantum mathematical background and formalism.

Quantum Mathematical Background and Formalism Quantum mathematical operations may use symbols and notation that are unfamiliar to the engineer. In this

section we present notation and symbols often used in describing and developing quantum physics, quantum communications, and quantum information. Dirac developed the physics "bra" and "ket" notation. A "bra" is written as $\langle\ |$ and can be thought of as a row vector, i.e., $\langle A| = [A_1\mathbf{e}_1 + A_2\mathbf{e}_2 + A_3\mathbf{e}_3]$ and a "*ket*",$|\ \rangle$ is a column vector $|B\rangle = \begin{pmatrix} B_1\mathbf{e}_1 \\ B_2\mathbf{e}_2 \\ B_3\mathbf{e}_3 \end{pmatrix}$ where the $\mathbf{e}_1, \mathbf{e}_2, \mathbf{e}_2$ are orthogonal unit vectors [8]. An inner product operation using bra–ket notation is written as $\langle A\,|\,B\rangle = A_1B_1 + A_2B_2 + A_3B_3$. Another operator that is used when considering composite systems of more than one particle is the tensor, or direct product operator ⊗. For a two particle composite system this operation acts as shown below:

$$|A\rangle \otimes |B\rangle = \begin{pmatrix} A_1\begin{pmatrix} B_1 \\ B_2 \end{pmatrix} \\ A_2\begin{pmatrix} B_1 \\ B_2 \end{pmatrix} \end{pmatrix} = \begin{pmatrix} A_1B_1 \\ A_1B_2 \\ A_2B_1 \\ A_2B_2 \end{pmatrix}. \tag{10.1}$$

Infinite dimensional systems can also be represented in "bra–ket" notation but instead of discrete vector type components the inner, outer, and direct products are integrals over functions.

Exercise 10.1 Given that a horizontally polarized photon is $|H\rangle = \begin{pmatrix} 1 \\ 0 \end{pmatrix}$ and a vertically polarized photon is $|V\rangle = \begin{pmatrix} 0 \\ 1 \end{pmatrix}$ work out the composite states $|H\rangle \otimes |H\rangle$, $|H\rangle \otimes |V\rangle$, $|V\rangle \otimes |H\rangle$, and $|V\rangle \otimes |V\rangle$ [8].

10.1 Answer:

Using Eq. (10.1) the answers are,

$$|H\rangle \otimes |H\rangle = \left|\begin{pmatrix} 1 \\ 0 \end{pmatrix}\right\rangle \otimes \left|\begin{pmatrix} 1 \\ 0 \end{pmatrix}\right\rangle = \begin{pmatrix} 1\begin{pmatrix} 1 \\ 0 \end{pmatrix} \\ 0\begin{pmatrix} 1 \\ 0 \end{pmatrix} \end{pmatrix} = \begin{pmatrix} 1 \\ 0 \\ 0 \\ 0 \end{pmatrix}$$

$$|H\rangle \otimes |V\rangle = \left|\begin{pmatrix} 1 \\ 0 \end{pmatrix}\right\rangle \otimes \left|\begin{pmatrix} 0 \\ 1 \end{pmatrix}\right\rangle = \begin{pmatrix} 1\begin{pmatrix} 0 \\ 1 \end{pmatrix} \\ 0\begin{pmatrix} 0 \\ 1 \end{pmatrix} \end{pmatrix} = \begin{pmatrix} 0 \\ 1 \\ 0 \\ 0 \end{pmatrix}$$

$$|V\rangle\otimes|H\rangle = \left|\begin{pmatrix}0\\1\end{pmatrix}\right\rangle\otimes\left|\begin{pmatrix}1\\0\end{pmatrix}\right\rangle = \begin{pmatrix}0\begin{pmatrix}1\\0\end{pmatrix}\\1\begin{pmatrix}1\\0\end{pmatrix}\end{pmatrix} = \begin{pmatrix}0\\0\\1\\0\end{pmatrix}$$

$$|V\rangle\otimes|V\rangle = \left|\begin{pmatrix}0\\1\end{pmatrix}\right\rangle\otimes\left|\begin{pmatrix}0\\1\end{pmatrix}\right\rangle = \begin{pmatrix}0\begin{pmatrix}0\\1\end{pmatrix}\\1\begin{pmatrix}0\\1\end{pmatrix}\end{pmatrix} = \begin{pmatrix}0\\0\\0\\1\end{pmatrix}.$$

Alternately, the horizontally polarized photon can be expressed as $|H\rangle = \begin{pmatrix}H\\0\end{pmatrix}$ and the vertically polarized photon can be expressed as $|V\rangle = \begin{pmatrix}0\\V\end{pmatrix}$ so that the composite states can now be written as

$$|H\rangle\otimes|H\rangle = \left|\begin{pmatrix}H\\0\end{pmatrix}\right\rangle\otimes\left|\begin{pmatrix}H\\0\end{pmatrix}\right\rangle = \begin{pmatrix}H\begin{pmatrix}H\\0\end{pmatrix}\\0\begin{pmatrix}H\\0\end{pmatrix}\end{pmatrix} = \begin{pmatrix}HH\\0\\0\\0\end{pmatrix}$$

$$|H\rangle\otimes|V\rangle = \left|\begin{pmatrix}H\\0\end{pmatrix}\right\rangle\otimes\left|\begin{pmatrix}0\\V\end{pmatrix}\right\rangle = \begin{pmatrix}H\begin{pmatrix}0\\V\end{pmatrix}\\0\begin{pmatrix}0\\V\end{pmatrix}\end{pmatrix} = \begin{pmatrix}0\\HV\\0\\0\end{pmatrix}$$

$$|V\rangle\otimes|H\rangle = \left|\begin{pmatrix}0\\V\end{pmatrix}\right\rangle\otimes\left|\begin{pmatrix}H\\0\end{pmatrix}\right\rangle = \begin{pmatrix}0\begin{pmatrix}H\\0\end{pmatrix}\\V\begin{pmatrix}H\\0\end{pmatrix}\end{pmatrix} = \begin{pmatrix}0\\0\\VH\\0\end{pmatrix}$$

$$|V\rangle\otimes|V\rangle = \left|\begin{pmatrix}0\\V\end{pmatrix}\right\rangle\otimes\left|\begin{pmatrix}0\\V\end{pmatrix}\right\rangle = \begin{pmatrix}0\begin{pmatrix}0\\V\end{pmatrix}\\V\begin{pmatrix}0\\V\end{pmatrix}\end{pmatrix} = \begin{pmatrix}0\\0\\0\\VV\end{pmatrix}.$$

Exercise 10.2

If a photon is in an arbitrary polarization state $|A\rangle = \begin{pmatrix} \alpha \\ \beta \end{pmatrix}$

what are the composite states $|H\rangle \otimes |A\rangle$ and $|A\rangle \otimes |V\rangle$?

10.2 Answer: Again, following Eq. (10.1) the answers are

$$|H\rangle \otimes |A\rangle = \left| \begin{pmatrix} 1 \\ 0 \end{pmatrix} \right\rangle \otimes \left| \begin{pmatrix} \alpha \\ \beta \end{pmatrix} \right\rangle = \begin{pmatrix} 1\begin{pmatrix} \alpha \\ \beta \end{pmatrix} \\ 0\begin{pmatrix} \alpha \\ \beta \end{pmatrix} \end{pmatrix} = \begin{pmatrix} \alpha \\ \beta \\ 0 \\ 0 \end{pmatrix} = \begin{pmatrix} H\alpha \\ H\beta \\ 0 \\ 0 \end{pmatrix}$$

and

$$|A\rangle \otimes |V\rangle = \left| \begin{pmatrix} \alpha \\ \beta \end{pmatrix} \right\rangle \otimes \left| \begin{pmatrix} 0 \\ 1 \end{pmatrix} \right\rangle = \begin{pmatrix} \alpha\begin{pmatrix} 0 \\ 1 \end{pmatrix} \\ \beta\begin{pmatrix} 0 \\ 1 \end{pmatrix} \end{pmatrix} = \begin{pmatrix} 0 \\ \alpha \\ 0 \\ \beta \end{pmatrix} = \begin{pmatrix} 0 \\ \alpha V \\ 0 \\ \beta V \end{pmatrix}.$$

Quantum Wavefunctions Wavefunctions represent the probability amplitudes used to describe the state of a quantum particle. Quantum particles are physical entities such as photons, electrons, protons, and neutrons. They are often expressed using Dirac's bra–ket notation where the state of a particle can be written as

$$|\Psi\rangle = \sum_{i=1}^{N} c_i |\phi_i\rangle$$

where the c_i and ϕ_i are the amplitude and quantum state respectively. The c_i can be complex valued and ϕ_i can be a measurable state such as a horizontal or vertical polarization for a photon or spin up/spin down for an electron spin. The probability that a quantum particle will be measured in particular states is given by

$$P = \Psi^* \Psi.$$

Wavefunction evolution can be described by a Schrodinger equation such as the one below

$$i\hbar \frac{\partial}{\partial t} \Psi(\mathbf{r}, t) = -\frac{\hbar^2}{2m} \nabla^2 \Psi(\mathbf{r}, t), \tag{10.2}$$

where $\hbar$ is Planck's constant over 2π, m is mass, t is time and $\mathbf{r}$ is the position in space. A more accurate wavefunction propagation or evolution equation for free-

space quantum communications would have to include terms added to Eq. (10.2) to incorporate the effects of absorption, scattering, and index of refraction fluctuations as functions of space and time. It must be kept in mind that turbulence is not stationary, is inhomogeneous, and is a dynamic function of space and time.

Exercise 10.3 The Schrodinger equation describes the evolution of the quantum wavefunction in space and time. How many space boundary conditions and time initial conditions are needed to solve this equation?

Exercise 10.4 Assume that the Schrodinger equation solution is a product of space only and time only factors. For a periodic time solution to the Schrodinger equation write the differential equation for the space dependent solution in one space dimension.

Exercise 10.5 Solve for the space dependent wavefunction solutions given a finite bounded domain. What are the consequences for bounded versus unbounded domains?

Quantum Particles There are two primary classifications of quantum particles. Bosons are spin-1 particles and fermions are spin-1/2 particles. The spin numbers are measures of the quantized angular momentum. Multiple fermions cannot occupy the same quantum state while there can be any number of bosons in a particular quantum state.

Modes A mode is best described as a fundamental solution of a wave equation. The frequency and momentum of a travelling electromagnetic plane wave in two space dimensions and time is given by

$$\vec{E}(k_x, k_y, \omega) = e^{i\omega t}\left(e^{ik_x x + ik_y y}\right) \tag{10.3}$$

and with $k = \frac{\omega}{c}$, we can say that $k_x = k\cos\theta$ and $k_y = k\sin\theta$ provided that $k^2 = k_x^2 + k_y^2$ [9]. In general, electromagnetic waves undergo spherical radiation from an atom but after travelling a long distance may be approximated by a plane wave over a small sector.

Conjugate Variables Quantum variables have certain properties that are conjugate to each other such that the more information and accuracy that is known about one of the properties the less is known about the conjugate property. The relationship between these conjugate properties is governed by the Heisenberg uncertainty principle $\frac{\hbar}{2} \leq \Delta x \Delta p$. Other conjugate variable pairs include energy-time and particle number-phase [10].

Operators Quantum operators are mathematical functions that act on quantum wavefunctions to describe properties such as position and momentum [11]. Operators in quantum physics are often noted as $\hat{A}$ where $\hat{A}$ is associated with an

observable, i.e., a measurable quality of a quantum system. Examples of operators include $\hat{\mathbf{p}} = -i\hbar\nabla$ for momentum and $\hat{L} = -i\hbar\mathbf{r}\times\nabla$ for angular momentum. Another notable pair of operators in quantum mechanics are the creation operator $a^{\dagger}$ and the annihilation operator a that are often used to describe the addition or subtraction of a fixed quanta of energy to a system.

10.2.3 The Concepts of Information Content and Quantum Information

The fundamental unit of quantum information is the qubit [12, 13]

$$|\Psi\rangle = \alpha|0\rangle + \beta|1\rangle$$

with $|\alpha|^2 + |\beta|^2 = 1$. Unlike a classical bit, a qubit has the property of being both 0 and 1 at the same time. This property allows qubits to be operated on over both amplitude values of the $\alpha|0\rangle + \beta|1\rangle$ superposition at the same time. Qubits may also be combined to allow for the representation of large quantities of information. A single qubit can hold 2 bits of classical information in superposition, 2 qubits 4 bits of classical information and n qubits can represent 2^n bits of classical information. However, when the qubit is measured the outcome will be a single bit value of either 0 or 1.

10.2.4 Quantum Optics

The nature of light having particle and wave properties is still somewhat mysterious. Viewed as a wave, engineers often characterize light as electromagnetic waves that propagate and scatter after being emitted. However, quantum optics uses operators that are distinctly different from the usual terms in the conservation equations of classical physics. Quantum optics also deals with measurements made at separated time and space points which show that light has a property of coherence and distant entanglement. Glauber received the 2005 Nobel prize for his work on quantum optical coherence which elucidated the space and time quantum effects of light in which he recognized and expounded the important role of measurements in the quantum process [14]. The recent textbook by Shih [15] provides an important reference for the current state of quantum optics. In the following, we outline a few representative features of quantum optics that are relevant to free-space atmospheric quantum communications. However, this exciting field is growing quickly and we must expect many more contributions in the years to come.

Table 10.1 Hanbury-Brown Twiss experiment results

Light source	HBT result
Coherent (Laser)	No Correlation [11]
Incoherent (Thermal)	Positive Correlation (Peak) [15]
Non-classical (Entangled)	Negative Correlation (Dip) [15]

10.2.5 Quantum Sources

All light is quantum all of the time but not all measurements and analysis readily reveal distinctly quantum properties of light. There are various sources of light including incoherent radiation, coherent radiation, and nonclassical sources of radiation. Incoherent sources of radiation are sources of light that are most familiar to us. Light bulbs, lamps, and the sun are all sources of incoherent thermal light. These incoherent light sources typically have broad spectral characteristics. We note that pseudo-thermal light [16, 17] produced by the transmission of laser light through a scattering media such as a rotating ground glass plate has a much narrower spectral bandwidth than the more commonly experienced sources of thermal radiation. Coherent sources such as lasers, are available in a variety of wavelengths and can be used for many quantum applications. Nonclassical sources of light include entangled photons, produced by nonlinear processes such as spontaneous parametric down conversion (SPDC) and four wave mixing, and squeezed light where there is a trade-off between phase information and photon number information. To highlight the differences between coherent, thermal, and nonclassical light, Hanbury-Brown and Twiss (HBT) two-photon interferometry is often used [11, 14, 18]. An HBT experiment is performed when light is split by a beam splitter toward two detectors. The detectors measure incident photons and the times that the measurements took place. The measurements at the two detectors are then correlated with each other, with results shown in Table 10.1.

The coincident deviations of the intensities from the mean of each detector tend to be positively correlated for incoherent light and negatively correlated (anticorrelated) for nonclassical light [15]. The coincident deviations of the intensities for coherent light tend to be uncorrelated. Variations from standard experimental conditions may produce results that vary from these.

10.2.6 Quantum Measurement Processes

There are several important aspects with regard to quantum measurement processes. The probabilities for measuring a quantum state can be given by

$$P(n) = \sum_{n} |c_n|^2 \left|\psi_n\right\rangle\left\langle\psi_n\right|$$

where the ψ_n correspond to the quantum state to be measured, such as the horizontal or vertical polarization of a photon, and the c_n are the wavefunction amplitudes for that quantum state. As an example if one prepares a photon in a diagonal polarization $(\nearrow)$ and then performs a measurement for horizontal or vertical in the perpendicular basis $(\perp)$, the c_n are equal to $\frac{1}{\sqrt{2}}$ and there is a 50% probability that the photon will be measured as as either an H or a V photon. When measuring a composite quantum system made up of two states the Bell basis measurement is often used [8, 13]. The four possible Bell basis states using polarization are

$$\begin{aligned}
\psi^+ &= \frac{1}{\sqrt{2}}\left(\left|H_A\right\rangle\left|V_B\right\rangle + \left|V_A\right\rangle\left|H_B\right\rangle\right) \\
\psi^- &= \frac{1}{\sqrt{2}}\left(\left|H_A\right\rangle\left|V_B\right\rangle - \left|V_A\right\rangle\left|H_B\right\rangle\right) \\
\phi^+ &= \frac{1}{\sqrt{2}}\left(\left|H_A\right\rangle\left|H_B\right\rangle + \left|V_A\right\rangle\left|V_B\right\rangle\right) \\
\phi^- &= \frac{1}{\sqrt{2}}\left(\left|H_A\right\rangle\left|H_B\right\rangle - \left|V_A\right\rangle\left|V_B\right\rangle\right).
\end{aligned} \tag{10.4}$$

The following identities also hold for the Bell states:

$$\begin{aligned}
\left|H_A\right\rangle\left|H_B\right\rangle &= \frac{1}{\sqrt{2}}\left(\left|\phi^+\right\rangle + \left|\phi^-\right\rangle\right) \\
\left|H_A\right\rangle\left|V_B\right\rangle &= \frac{1}{\sqrt{2}}\left(\left|\psi^+\right\rangle + \left|\psi^-\right\rangle\right) \\
\left|V_A\right\rangle\left|H_B\right\rangle &= \frac{1}{\sqrt{2}}\left(\left|\psi^+\right\rangle - \left|\psi^-\right\rangle\right) \\
\left|V_A\right\rangle\left|V_B\right\rangle &= \frac{1}{\sqrt{2}}\left(\left|\phi^+\right\rangle - \left|\phi^-\right\rangle\right).
\end{aligned} \tag{10.5}$$

A Bell measurement is a coincidence measurement that discriminates the actual state of an unknown two-photon polarization system. A primary distinction between entangled states and nonentangled states is that an entangled state is not factorizeable into the product of two states:

$$\frac{1}{\sqrt{2}}\left(\left|H_A\right\rangle\left|V_B\right\rangle - \left|V_A\right\rangle\left|H_B\right\rangle\right) \neq \left(\left|H_A\right\rangle \pm \left|V_A\right\rangle\right) \otimes \left(\left|H_B\right\rangle \pm \left|V_B\right\rangle\right).$$

This nonfactorizeability makes the entangled states quite powerful for quantum communications, quantum computing, and quantum imaging [15, 19]. In this case we are talking about photons that have polarization entangled states. The quality of a quantum measurement is often reported in terms of "fidelity." A quantum state is said to be "faithful" if the function $F(p,q)=\sqrt{pq}$ is sufficiently close to 1, where p indicates the probability that quantum state $|\Psi\rangle$ has been prepared and q is the probability that state $|\Phi\rangle$ was measured. This idea may also be reversed to say if state $|\Phi\rangle$ was measured then the "fidelity" of how well $|\Psi\rangle$ was prepared can be assessed [13].

Another measurement technique is that of the positive operator valued measurement (POVM) in distinction to projective measurements [13, 20, 21]. POVMs reduce the probability of inconclusive measurements with the use of ancilla modes. For instance, if photons that are polarized either horizontally (H) or $+45^{\circ}$ in equal amounts are passed through a V polarizer or a -45° polarizer, then the one that passes through the V polarizer must have been a $+45^{\circ}$ photon and if the photon passes through the -45° polarizer it must have been a H polarized photon. This would yield a 25% chance to determine the polarization state of the transmitted photon. With the addition of certain "ancilla" modes of the optical fields a POVM can determine the polarization state of the transmitted photon for this example with a probability of 29.3% [13].

10.2.7 Quantum Squeezing

Quantum squeezing occurs when a process is applied to the quantum system that adjusts the relative values of a conjugate variable pair. Quantum squeezed light has been demonstrated using laser and nonlinear materials to alter the uncertainty between photon number and phase $\frac{\hbar}{2}\le\Delta n\Delta\phi$ where the uncertainty in the photon number is decreased while the uncertainty of the phase is increased. Quantum squeezed states are often used for applications in quantum metrology as well as for continuous variable QKD implementation [22].

10.2.8 Measurement Bases Used in Quantum Protocols

This section discusses the measurement bases used in quantum protocols. Measurement bases for quantum communications protocols include linear polarizations $|\Psi\rangle=\alpha|H\rangle+\beta|V\rangle$, circular polarizations $|\Psi\rangle=\alpha|R\rangle+\beta|L\rangle$, orbital angular momentum $|\Psi\rangle=\alpha|L_0\rangle+\beta|L_1\rangle$ (L_n in this superposition indicate the Laguerre mode), and time-bin superpositions $|\Psi\rangle=\alpha|L\rangle+\beta|S\rangle$ where L and S and refer to a superposition of long and short paths propagated by a quantum particle through an unbalanced Mach–Zehnder interferometer. Any quantum basis that has a measurable superposition with at least two possible results may be used in a quantum protocol.

Table 10.2 Polarization transmission

Polarization Filter Orientation	Transmission Probability
H	0%
V	100%
+45	50%
−45	50%

Coherence and Incoherence Coherence and incoherence can be defined in the following manner. Light may be said to be temporally coherent if the distance $c\tau_c$ is much greater than all of the optical path-length differences encountered in an optical system. The coherence time τ_c is defined as

$$\tau_c = \int_{-\infty}^{\infty} |g(\tau)|^2 d\tau$$

where the degree of temporal coherence is

$$g(\tau) = \frac{G(\tau)}{G(0)} = \frac{\langle U^*(t)U(t+\tau)\rangle}{\langle U^*(t)U(t)\rangle}$$

and U is the complex wavefunction of the light.

Similarly, light may be described as being spatially coherent if the *coherence area* of the light is larger than the largest aperture of an optical system. The *coherence area* is related to the complex degree of coherence

$$g(\mathbf{r}_1.\mathbf{r}_2) = \frac{G(\mathbf{r}_1.\mathbf{r}_2)}{\sqrt{\langle I(\mathbf{r}_1)\rangle \langle I(\mathbf{r}_2)\rangle}},$$

where $G(\mathbf{r}_1.\mathbf{r}_2)$ is the mutual intensity and is equal to $\langle U^*(\mathbf{r}_1,t)U(\mathbf{r}_2,t)\rangle$ and the I values are the intensities measured at positions $\mathbf{r}_1$ and $\mathbf{r}_2$ [14, 23].

Polarization Polarization in optics is generally associated with the E_x and E_y components of an electromagnetic plane wave propagating in the z direction. In quantum communications, linear polarization is restricted to two orthogonal bases; the Horizontal-Vertical (H-V) basis or the 45° rotated basis (A-D). The properties of these linear polarizations are that a particular polarization has a 100% chance to propagate through a polarization filter aligned parallel with the polarization of the light and 0% chance to propagate through a polarization filter aligned in a direction orthogonal to the polarization of the light. The orientation of the polarizing filter may uniformly vary the transmission from 0% to 100%. For instance, a photon with vertical polarization has the transmission probabilities for a prescribed set of polarization filter orientations that are shown in Table 10.2.

Polarization is a useful property for quantum information purposes as a simple way to create and manipulate a qubit, where one polarization would (when measured) take the logical value of 0 and the other measurement a value of 1. However, unlike classical logical bits a single qubit is simultaneously both 0 and 1 in superposition until measured. For instance, an equal superposition of 0 and 1 as a polarization qubit could be

$$|\Psi\rangle = \alpha|H\rangle + \beta|V\rangle$$

where $|H\rangle = 0$, $|V\rangle = 1$ and $\alpha = \beta = \frac{1}{\sqrt{2}}$ [13, 23].

Energy-Time Entanglement Energy-time entanglement and time-bin entanglement are closely related. Two particles can be energy-time entangled. Earlier we mentioned that photons can be polarization entangled. Quantum particles may be entangled in one or more properties. Energy-time entanglement has been achieved using an unpulsed pump laser and time-bin entanglement has been achieved using a pulsed laser [24]. Time-bin entanglement is a state where photons are entangled in between long and short paths of an unbalanced interferometer. That is, in quantum systems, not only can quantum particles be entangled but also their paths can be entangled. This last quantum property gives quantum scientists and engineers a lot to work with in designing quantum communications systems that exploit entanglement.

Quantum Coherence Quantum coherence refers to a property associated with photons or other quantum particles. Quantum coherence represents an ideal quantum state where the uncertainty between conjugate variables are a minimum and are equally distributed [14]. For example, position x has an uncertainty of Δx and momentum p has an uncertainty Δp and the uncertainties are both, minimum and equally distributed between Δx and Δp in the equation, e.g., when $\frac{\hbar}{2} = \Delta x \Delta p$. The closer a system is to this ideal uncertainty relationship the more coherent it is said to be. For example a laser is often a very coherent system. Conversely, when the product $\Delta x \Delta p$ is much greater than $\frac{\hbar}{2}$ the system is said to be more incoherent. For example, thermal light sources such as the sun or an incandescent light bulb would radiate incoherent light. Pseudo-thermal sources created by propagating a laser beam through a rapidly rotating ground glass plate also can produce light that has incoherent properties [16, 17]. Pseudo-thermal sources provide a convenient experimental source of partially coherent or incoherent radiation with relatively large coherence time and space scales.

Quantum Decoherence and Quantum Memory Quantum memories need to be able to preserve a quantum state long enough for operations to be performed on that quantum state. Quantum decoherence is the effect that occurs when quantum states interact with the environment and lose their quantum interference effects. Better quantum memories preserve a quantum state for a longer time [25, 26].

10.2.9 Spontaneous Parametric Downconversion (SPDC) and Upconversion

For quantum detection of correlated photons pairs at greater detection efficiencies, spontaneous parametric downconversion (SPDC) and upconversion methods have been developed [15, 27, 28]. Generally speaking the SPDC process employs a χ^2 nonlinearity of a material such as beta-barium borate (BBO) or lithium borate (LBO) to split a pump photon into two photons subject to the condition

$$\nu_P = \nu_s + \nu_i$$

where ν_P is the frequency of the pump photon and ν_s and ν_i are the frequencies of the two downconverted photons. The frequencies of ν_s and ν_i need not be equal to each other which has useful applications for quantum communications. The subscripts *s* and *i* represent signal and idler respectively. Historically "signal" refers to the higher frequency anti-Stokes photon and "idler" is the lower frequency Stokes photon [29]. Similarly, upconversion utilizes a nonlinear process whereby a photon, say at the telecommunications wavelengths (1300–1500 nm) where detector efficiency is low and noisy, is upconverted to the visible or near IR where silicon based photon detectors have much higher efficiencies and less noise. In this case the equation appears as

$$\nu_T + \nu_P = \nu_U$$

where ν_T is the frequency of the telecommunications wavelength photon and ν_U is the upconverted detector photon. The upconversion pump frequency at ν_P, the nonlinear media and the tuning of the phase-matching conditions must all be chosen to optimize the efficiency of the upconversion to ν_U for the particular detectors involved. We note that the relationship between the frequency ν and wavelength λ [9, 30] is given by the following:

$$\begin{aligned} \nu &= \frac{c}{\lambda} \\ \lambda &= \frac{c}{\nu}. \end{aligned} \tag{10.6}$$

There is research to develop better entangled photon sources for free-space applications [31] where the wavefunctions for the polarization entangled photons generated by this implementation are of the form

$$|\Psi(\phi)\rangle = \frac{1}{\sqrt{2}}(|V_{\lambda_s}V_{\lambda_i}\rangle + e^{i\phi(\lambda_s,\lambda_i)}|H_{\lambda_s}H_{\lambda_i}\rangle)$$

where λ_s and λ_i are the wavelengths of the downconverted photons and ϕ is a relative phase, typically caused by birefringence, between the two wavelengths in their device. In practice, the phase ϕ must be considered, however it is often left out of theory formalism to simplify the presentation.

10.2.10 Random Number Generation By Quantum Physics Versus the Pseudo-Random Number Generation of Classical Encryption

Pseudo-random number generators (PRNG) are commonly used in a computational environment. Monte-Carlo numerical methods are often used for approximating solutions to problems with very large numbers of degrees of freedom. The typical PRNG uses one or more "seed" numbers and performs various bit shift and "or" operations on the binary representation of the number to provide the next "random" number in the sequence [32]. This type of random number generator will eventually exhibit periodic behavior, i.e., repeating a sequence already generated. Furthermore, while most PRNGs can exhibit statistically valid "uniformity" up to becoming periodic, on other tests of statistics such as χ^2 they may fail. A quantum random number generator (QRNG) depends on the inherently random result of the measurement of the physical state of a quantum system as discussed in Sect. 10.2.6. QRNGs cannot be periodic and they lack the biases of the classically computed pseudo-random number.

10.2.11 No-Cloning Theorem

The *no-cloning* theorem in quantum physics describes the inability of linear processes to measure, copy and retransmit quantum information without destroying the superposed quantum state [13]. The no-cloning property uses the fundamentally important physics property of superposition to establish procedures that prevent an eavesdropper (Eve) from "listening" in on the communication between Alice and Bob without being detected. For instance, let us assume that Eve attempts to intercept polarization based quantum communications photons between Alice and Bob. Eve could attempt a so-called "measure and resend" attack on the quantum communications channel. In this instance Eve tried to act as Bob and randomly chose

Table 10.3 No Cloning Example

	Alice Transmission	Eve Measurement using Random Basis	Eve Resend	Bob Measurement using Random Basis
1	→	↗	↗	↑ (Error!)
2	↑	↘	↘	↑
3	↘	↑	↑	↑ (Error!)
4	↗	→	→	→ (Error!)

measurement bases and then retransmit to Bob a photon of the polarization that she measured. In principle, if Eve attempts to intercept photons and copy and resend with errors, then Alice and Bob would notice an increase in key errors thus indicating an eavesdropper. Unfortunately for Eve, but fortunately for Alice and Bob, she would be detected due to the consequences of the no-cloning property which prohibits an exact copy of a quantum state to be created. An example of four of the many possible outcomes for Alice, Bob, and Eve illustrating the effect of the no-cloning property is shown with the BB84 QKD [33] protocol in Table 10.3.

In each line of the table Alice is transmitting a photon with the indicated polarization. Eve attempts to eavesdrop by measuring those photons in a random basis and those measurement outcomes are indicated. Eve then retransmits a photon with the polarization she measured to Bob and his measurement in a random basis is indicated. The measurements at 1, 3, and 4 are identified as errors during the shared key generation process and alert Alice and Bob that there has been an attempt to eavesdrop on their quantum communications channel. While Bob measures in a randomly chosen basis to negotiate a key with Alice, the measurement by Eve using a random basis and resending to Bob introduces errors beyond those normally encountered by Alice and Bob when Eve is not present. While the no-cloning theorem applies to linear systems it does not necessarily apply to nonlinear cloning processes. Nevertheless, the no-cloning effect raises the bar for eavesdropper attacks.

There are other limitations for the security of quantum communications. For instance, it is possible to clone a quantum state using a non-linear process; a lossy channel between Alice and Bob can allow Eve to intercept quantum states and remain undetected; poor quantum efficiency of the detectors for Alice and Bob and interception of certain information can enable Eve to obtain the entire secret key [34, 35, 36].

10.2.12 Weak Coherence

Weak coherence has been used in the context of quantum communications to describe the condition where a laser pulse contains on average much less than one photon per pulse. These weak coherent approaches suffer from the fact that the number of photons in a pulse generally follows Poisson distribution [11, 23]

$$p(n) = \frac{\langle n \rangle^n e^{-\langle n \rangle}}{n!}. \tag{10.7}$$

The Poisson distribution describes the probability for n photons to be detected. $\langle n \rangle$ is the average number of photons in a given time interval T and is related to the optical power P as

$$\langle n \rangle = \frac{PT}{h\nu}.$$

It is fairly easy to see that for a given optical power, no matter how weak, there is a finite probability to have more than a single photon in a pulse. This means that QKD systems that use weak coherent pulses do not achieve the full level of security allowed by quantum physics.

Exercise 10.6 Estimate the probability for two photons in a pulse, given the average number of photons per pulse being $(a)\ \langle n \rangle = 10$, $(b)\ \langle n \rangle = 1$, $(c)\ \langle n \rangle = 0.1$. Discuss the ramifications for QKD when Eve might intercept one of these excess photons.

10.6 Answer: Using Eq. (10.7) with the probability to detect $n = 2$ photons per pulse we find for cases (a), (b), and (c) the following:

$$\begin{array}{lll} (a) & (b) & (c) \\ p(2) = \dfrac{(10)^2 e^{-10}}{2!} & p(2) = \dfrac{(1)^2 e^{-1}}{2!} & p(2) = \dfrac{(.1)^2 e^{-.1}}{2!} \\ = \dfrac{100e^{-10}}{2} & = \dfrac{1e^{-1}}{2} & = \dfrac{.01e^{-.1}}{2} \\ \simeq 2.27 \times 10^{-3} & \simeq 1.84 \times 10^{-1} & \simeq 4.52 \times 10^{-3} \end{array}$$

10.2.13 Entangled Photon Quantum Communications

In 1991, Ekert proposed a QKD protocol using entangled photons [37]. This has been experimentally demonstrated in 2000 [38]. However, another use of entangled photons for quantum communications is to utilize the quantum features of photons to enable quantum information over long distances in free-space or in fiber by entangling remote quantum memories [25, 26]. The quantum information stored in these two separated quantum memories can be used to teleport quantum information from one site to another. Teleportation with secure protocols is sometimes referred to as *tamper resistant* quantum communication because it is the entanglement itself that performs the transmission of the information in a quantum teleportation operation. The information that is sent over the classical channel really amounts to instructions on how to measure the receiver's quantum state to recover the teleported quantum information. Teleportation is discussed below.

Table 10.4 Example using entangled photons for QKD

Alice	1	0	1	0	0	1	…	1
Bob	0	1	0	1	1	0	…	0

10.2.14 Quantum Cryptography and Quantum Key Distribution

Quantum cryptography and quantum key distribution (QKD) are technologies that are being developed to exploit the quantum features of light and particles to send and to receive quantum information with the highest possible level of physical security. In the language of QKD, Alice, Bob, Charlie, and Eve refer to the sender, the receiver, a third participant, and the eavesdropper, respectively. As a simple example of quantum key generation, encryption and transmission, imagine that Alice and Bob each receive one part of an entangled pair of photons. For instance assume that the entangled photon is in the $|\Psi^-\rangle_{AB} = \frac{1}{\sqrt{2}}\left(|H_A\rangle|V_B\rangle - |V_A\rangle|H_B\rangle\right)$ state. When Alice and Bob make their measurements each would measure the orthogonal polarization, i.e., if Alice measures a $|H\rangle$ then Bob must measure a $|V\rangle$. We can also assign 0's and 1's to the polarizations so that $|H\rangle = 0$ and $|V\rangle = 1$. After many measurements of these entangled photons Alice and Bob would each have a sequence of random bits (Table 10.4).

Using this shared sequence of random bits Alice can encode a message using an exclusive binary "or" (XOR) operation and transmit that message to Bob who has a binary sequence that he can use to decode the encrypted message. Some interesting QKD schemes are the following: BB84 [33], B92 [39], Ekert91 [37], and Yuen–Kumar (Alpha-Eta or Y00) [40].

Protocols BB84 and B92 Two of the early QKD encryption protocols BB84 [33] and B92 [39] are reviewed in the following paragraphs.

The B92 QKD [39] protocol consists of the following steps:

1. Alice randomly chooses a polarization orientation for the photon she transmits as either Horizontal, $|H\rangle = |0\rangle$, or the 45° rotated basis $|D\rangle = |1\rangle$. Alice keeps track of the 0's and 1's she has sent to Bob.
2. Bob randomly chooses to measure the photon in either the V basis or the -45° basis and announces over a public channel if a measurement or a "no-measurement" result occurs.
3. When the key transmission is completed key sifting, a key reconciliation process, and tests of eavesdropping take place. The probabilities to make a measurement are indicated in Table 10.5.

Exercise 10.7 Using the B92 protocol Alice transmits to Bob a random bit sequence and Bob makes measurements in the bases indicated in Table 10.6.

The sifted key of 011 in this example assumed that all of the basis choices made by Bob produced a measurement. There is a 50% chance that any measurement attempted between the nonorthogonal bases could cause Bob to announce that a no-measurement (N) outcome occurred. Work out the sifted key by filling in the

Table 10.5 B92 Example

Alice	Bit Value	0	0	1	1	0	0	1	1
	State	H	H	45°	45°	H	H	45°	45°
Bob	Basis	V	−45°	V	−45°	V	−45°	V	−45°
	Measurement								
	Probability	0	50%	50%	0	0	50%	50%	0

Table 10.6 B92 Example

Alice	Bit Value	1	0	1	0	1	0	0	1
	State	H	45°	H	45°	H	45°	45°	H
Bob	Basis	V	−45°	V	V	−45°	−45°	−45°	−45°
	Measurement	N	N	N	Y/N	Y/N	N	N	Y/N
Shared	Key				0	1			1

Table 10.7 B92 Example

Alice	Bit value	1	1	0	1	0	0	1	1
	State	H	H	45°	H	45°	45°	H	H
Bob	Basis	V	− 45°	− 45°	V	V	− 45°	− 45°	V
	Measurement	?	?	?	?	?	?	?	?
Shared	Key	?	?	?	?	?	?	?	?

blocks marked with "?" if Alice and Bob use the transmitted bits and basis shown in Table 10.7 under the assumption that all of Bob's basis choices produced a measurement. It should be noted that the B92 protocol has been shown to be insecure.

The BB84 QKD [33] protocol consists of the following steps:

1. Alice randomly chooses a bit value 0 or 1 and a polarization basis, rectilinear or diagonal, to transmit to Bob. Alice keeps track of the 0's and 1's and the basis she has sent to Bob.
2. Bob randomly chooses a basis to measure in and records the result of the measurement as a 0 or 1.
3. A process known as key sifting then occurs where Bob announces over a public channel the measurement bases used and Alice sends back a list of the valid bases chosen by Bob. No public announcement of the outcome of a measurement or the value sent by Alice is made.
4. When the key transmission is completed a key reconciliation process and tests of eavesdropping take place. The probabilities to make a measurement are indicated below in Table 10.8.

   In the above tables + indicates a measurement done in the H–V basis, × indicates a measurement performed in the rotated 45° basis, → indicates a horizontally polarized photon, ↑ a vertical photon, ↗ a horizontal photon in a rotated 45° basis, and ↘ is a vertical photon in a 45° basis. When the symbols are combined, as in ↗↘ or →↑, this indicates that the photon state transmitted by Alice

Table 10.8 BB84 Example

Alice	Bit value	0	0	1	1	0	0	1	1
	State	→	→	↑	↑	↗	↗	↘	↘
Bob	Basis	+	×	+	×	+	×	+	×
	Measurement	→	↗↘	↑	↗↘	→↑	↗	→↑	↘
	Probability	100%	50%	100%	50%	50%	100%	50%	100%

Table 10.9 BB84 Example

Alice	Bit value	0	1	0	0	0	0	1	1
	Basis	+	+	×	+	×	×	×	×
Bob	Basis	×	×	×	×	+	+	×	×
	Measurement	0/1	0/1	0	0/1	0/1	0/1	1	1
Valid	Basis	*N*	*N*	*Y*	*N*	*N*	*N*	*Y*	*Y*
Sifted	Key			0				1	1

Table 10.10 BB84 Exercise

Alice	Bit value	0	1	0	0	1	0	0	1
	Basis	+	+	×	×	×	+	+	+
Bob	Basis	×	+	+	+	×	×	×	+
Valid	Basis	?	?	?	?	?	?	?	?
Sifted	Key	?	?	?	?	?	?	?	?

has two possible measurement outcomes in Bob's selected measurement basis. For example,

Exercise 10.8 Alice and Bob chose bases and transmitted bits as indicated in Table 10.9, which for this example yields a shared key of 011. Work out the sifted key by filling in the blocks marked with "?" if Alice and Bob use the bases and transmitted bits in Table 10.10.

Answer:

Alice	Bit value	0	1	0	0	1	0	0	1
	Basis	+	+	×	×	×	+	+	+
Bob	Basis	×	+	+	+	×	×	×	+
Valid	Basis	*N*	*Y*	*N*	*N*	*Y*	*N*	*N*	*Y*
Sifted	Key		1			1			1

QKD New Trends Research to develop tamper resistant quantum communications has led to the development of new methods and trends. One view of tamper resistant quantum communications involves the use of distant quantum memories that are entangled. These entangled quantum memories are used to perform a quantum tele-

portation of message bits from Alice to Bob. Notably, the 2 bits Alice sends to Bob to complete the teleportation operation contains no information about the bit value being teleported. Efforts are also underway to develop "reference frame free" quantum cryptography [41, 42]. Sciarrino et al. [42] experimentally demonstrated quantum information cryptography by using a liquid crystal device (named *q-plate*) that maps polarization encoded qubits into qubits with hybrid polarization-OAM states, which are shown to be invariant under arbitrary rotations around the propagation direction. Another new idea for QKD called "counterfactual QKD" was proposed by Noh [43] that would employ a "nontransmission" of information protocol to allow Alice and Bob to generate a shared quantum key. An experimental demonstration of counterfactual QKD was performed and published in 2012 by the Genovese [44] group and they concluded that there is a possibility to exploit this concept for practical QKD systems. Another new trend is for "alignment-free" quantum communications [42]. By using rotationally invariant quantum states Alice and Bob would not have to spend much effort with ensuring that they have a "shared reference frame." This would be very useful for satellite-to-ground, satellite-to-air, and air-to-satellite quantum communications.

Concept of Provable Security Provable security simply means that under a given set of assumptions that no "adversary" exists who can break a security scheme that operates under the stated set of assumptions. For quantum security, the assumptions typically include the "No-Cloning" theorem, that only a single photon or less exists per time-interval and that the adversary "Eve" has not physically taken over Alice's and/or Bob's station.

Quantum Encryption Advantages Over Classical Encryption There are several important advantages of quantum encryption over classical encryption. These advantages include secure re-keying, eavesdropper detection, and a basis in the laws of quantum physics for randomness. Another key advantage of quantum encryption is that when a quantum computer becomes available, quantum encryption methods will offer an important means for secure information transmission.

The Quantum Yuen–Kumar (Alpha-Eta) Scheme The quantum Alpha-Eta scheme [40, 45] is a means to ensure a quantum level of security at the physical communications transport layer. Alpha-Eta involves using orthogonal quantum states in a large number of bases to enable security. Free-space quantum communications using the Yuen–Kumar Alpha-Eta scheme [45] has been implemented and demonstrated using polarization [40]. The scheme was implemented as follows:
A random basis using preshared keys between sender and receiver is used to chose a randomly rotated basis to transmit and measure the photons. This basis choice encoding amounts to

$$Alice = \begin{vmatrix} \cos\theta & -\sin\theta \\ \sin\theta & \cos\theta \end{vmatrix} \begin{vmatrix} 0 \\ 1 \end{vmatrix} \Rightarrow Bob = \begin{vmatrix} \cos\theta & -\sin\theta \\ \sin\theta & \cos\theta \end{vmatrix}^{-1} \begin{vmatrix} \cos\theta & -\sin\theta \\ \sin\theta & \cos\theta \end{vmatrix} \begin{vmatrix} 0 \\ 1 \end{vmatrix}$$

to encode and recover the bit transmitted. In the example above Alice is sending the message $\left|\begin{matrix}0\\1\end{matrix}\right|$ to Bob and encodes that message in a randomly preshared rotation basis θ. Bob would receive the randomly encoded message and decode the message with the inverse rotation. The value of θ is chosen randomly using preshared keys that are possessed by Alice and Bob. The method has high security because of the extremely large basis space that can be chosen and the method has similar eavesdropping recognition capabilities as other QKD methods. One of the advantages of the Alpha-Eta scheme is that it can function well over existing fiber optic infrastructure.

Prospects for Non-line-of-sight Atmospheric Quantum Communications Meyers in 2005 proposed using polarization in the ultraviolet as a means to implement non-line-of-sight (NLOS) free-space quantum communications [46, 47]. Polarization is very robust in atmospheric propagation and the large scattering of UV light is well documented. There have been many NLOS free-space optical communications efforts that demonstrated the ability of UV light to scatter around various obstacles [48, 49]. Combining that scattering capability with polarization encoding as in the Yuen–Kumar scheme [40] would add a further layer of physical security to free-space NLOS optical communications.

Free-Space Microwave Quantum Communications Microwaves have been used for many decades for classical communications in free-space [50]. Microwave photons are very low in energy due to their long millimeter to centimeter wavelengths. Nevertheless, microwave photon detectors are sensitive enough to measure microwave photons in free-space. However, there are two key problems. The first problem is that there is a low level cosmic microwave background in the universe [51]. Second is that surrounding the earth there is an additional microwave radiation due to the large amount of microwave communication transmissions worldwide. At the same time, we know that microwave photons will exhibit quantum interference properties like photons at other wavelengths. In addition, it is possible to observe entangled photons at microwave frequencies. Thus, demonstrations of multi-photon microwave interference may provide a pathway to free-space quantum communications with microwaves [52, 53].

Teleportation Teleportation is a quantum process whereby quantum information can be transmitted over long distances [54, 55]. As an example of the process of quantum teleportation let us assume that Alice and Bob share half of an entangled photon pair that is in the state $|\Psi\rangle_{AB} = \frac{1}{\sqrt{2}}\left(|H_A\rangle|V_B\rangle - |V_A\rangle|H_B\rangle\right)$ and that Alice wants teleport to Bob a photon with a defined polarization $|\Omega_C\rangle = \frac{1}{\sqrt{\alpha^2+\beta^2}}\left[\alpha|H_C\rangle + \beta|V_C\rangle\right]$. Alice would perform a joint Bell measurement on her half of the entangled photon pair with the photon she wants to teleport. Prior to the joint-measurement, the state of the three photons is $|\Psi\rangle_{AB} \otimes |\Omega_C\rangle =$

$\frac{1}{\sqrt{2}}\left(|H_A\rangle|V_B\rangle - |V_A\rangle|H_B\rangle\right) \otimes \frac{1}{\sqrt{\alpha^2+\beta^2}}\left(\alpha|H_C\rangle + \beta|V_C\rangle\right)$. The physics of teleportation describes how the photons of Alice and Bob's entangled pair and the photon to be teleported are changed in Alice's basis to appear as if Alice's photon $|\Psi\rangle_A$ is in an entangled state with $|\Omega_C\rangle$. Using Eq. 10.4 and Eq. 10.5 the three photon state

$$\frac{1}{\sqrt{2\left(\alpha^2+\beta^2\right)}}\{\alpha\left(|H_A\rangle|V_B\rangle|H_C\rangle - |V_A\rangle|H_B\rangle|H_C\rangle\right) + \beta\left(|H_A\rangle|V_B\rangle|V_C\rangle - |V_A\rangle|H_B\rangle|V_C\rangle\right)\}$$

can be rewritten as

$$\frac{1}{2}\frac{1}{\sqrt{\alpha^2+\beta^2}}\{|\phi^+\rangle_{AC}\otimes\left(\alpha|V_B\rangle - \beta|H_B\rangle\right) + |\phi^-\rangle_{AC}\otimes\left(\alpha|V_B\rangle + \beta|H_B\rangle\right) + |\psi^+\rangle_{AC}\otimes\left(-\alpha|H_B\rangle + \beta|V_B\rangle\right) + |\psi^-\rangle_{AC}\otimes\left(\alpha|H_B\rangle + \beta|V_B\rangle\right)\}.$$

Alice has four possible outcomes for her joint measurement of the state $|\Psi\rangle_{AC}$

$$\begin{aligned}
|\Psi^1\rangle &= \frac{1}{\sqrt{2}}\left(|H_A\rangle|V_c\rangle - |V_A\rangle|H_c\rangle\right)\\
|\Psi^2\rangle &= \frac{1}{\sqrt{2}}\left(|H_A\rangle|V_c\rangle + |V_A\rangle|H_c\rangle\right)\\
|\Psi^3\rangle &= \frac{1}{\sqrt{2}}\left(|H_A\rangle|H_c\rangle - |V_A\rangle|V_c\rangle\right)\\
|\Psi^4\rangle &= \frac{1}{\sqrt{2}}\left(|H_A\rangle|H_c\rangle + |V_A\rangle|V_c\rangle\right)
\end{aligned}$$

and she would transmit 2-bits to Bob that would instruct him on what transform T to use to operate on his remaining photon of the entangled pair to complete the teleportation. The four cases and operations are 1) $T_1 = \begin{bmatrix} 1 & 0 \\ 0 & 1 \end{bmatrix}$, 2) $T_2 = \begin{bmatrix} 1 & 0 \\ 0 & -1 \end{bmatrix}$, 3) $T_3 = \begin{bmatrix} 0 & 1 \\ 1 & 0 \end{bmatrix}$ and 4) $T_4 = \begin{bmatrix} 0 & -1 \\ 1 & 0 \end{bmatrix}$. Case 1 is the identity operation and indicates that Bob's photon is in the state of the photon that Alice teleported to him. Case 2 applies a π phase shift to the $|V\rangle$ component of Bob's photon to complete the teleportation. Case 3 rotates the polarizations from $\alpha|H_B\rangle + \beta|V_B\rangle$ to $\alpha|V_B\rangle + \beta|H_B\rangle$, and Case 4 performs an operation similar to Case 3 with a π phase applied shift to the $|H\rangle$ component of Bob's photon.

Future Teleportation The US Army has a new basic research focus area developing the underpinning science for mobile quantum information teleportation networks. Initial efforts include the development of an entangled photon and atom teleportation testbed network entitled "A Quantum Network with Atoms and Photons (QNET-AP)" [56]. This research is directed toward developing quantum communications between remote sites that have quantum memories. One of the goals of the US Army demonstration plan is to entangle distant atomic memories between the US Army Research Laboratory (ARL) and the Joint Quantum Institute (JQI) of NIST that are separated by kilometers in free-space and along a fiber optical path. This distance will further allow for a locality loop-hole free test of the Bell inequalities [57, 58]. Another key goal is to develop secure quantum teleportation architectures, schemes, and protocols. This research will lead to the teleportation of quantum information between remote locations and a demonstration of "tamper resistant" quantum communications.

Recently there have been experimental demonstrations of the teleportation of quantum information using free-space optical quantum communications channels. These experiments were performed as precursors to teleportation of quantum information between the ground and satellites. The first took place in China [59] over a 97 km optical path and utilized pointing and tracking systems using lasers at 532 and 671 nm coupled to the entangled photon that is at ~788 nm. GPS was used to enable 1 ns timing accuracy between the remote stations. A wireless classical communications channel was used by Alice and Bob to complete the teleportation protocol. Fidelities from 76 % to 89 % were reported for the teleportation states that were tested. The article also reports that their acquisition, pointing and tracking (APT) system can be applied to any moving object with high accuracy. The second long distance free-space teleportation experimental demonstration took place between the Canary Islands of Tenerife and La Palma with a distance of 143 km [60]. A similar pointing to the one above was used and a 1064 nm free-space optical communications link was employed to instruct Bob on how to complete the teleportation protocol. Timing between the islands was coarsely set using GPS and then fine tuned using an entanglement assisted clock synchronization [61] to achieve 1 ns time accuracy between the locations and a 3 ns coincidence window was used for the measurements. Entanglement fidelities exceeding the classical limit of 67 % were reported. Also noted were conditions of extremely bad weather that prevented some experiments from being conducted.

Impact of Atmosphere on Quantum Communications Free-space quantum communications may be negatively influenced due to various atmospheric effects such as turbulence or environmental obscurants like fog or smoke. However, it has been recently demonstrated when using certain entangled photon states that there is a cancellation of turbulence caused angle-of-arrival fluctuations [62]. These angle of arrival fluctuations are a major contributor [63] to the degradation of quantum free-space communication quality. The atmosphere can affect photon absorption,

decoherence and/or cause phase distortions. These effects typically lead to a loss of photons that might otherwise be measured at a distant receiver. The atmospheric phase distortions can also modify the quantum state of the transmitted photon. This effect could be interpreted as a potential eavesdropping event in many QKD protocols. The fidelity of quantum communications is a measure of how well the quantum channel preserves quantum information. This is directly tied to the idea of the fidelity of quantum states.

Atmosphere's Turbulence Effects on Photon Count Fluctuations, Orbital Angular Momentum, Entanglement, Synchronization Accuracy, and Quantum Bit Error Rates Practical free-space applications of quantum communications and teleportation can be severely limited by atmospheric turbulence that brings about phase distortions, decoherence, and misalignment of transmitters and receivers. Several laboratory and outdoor experiments (see Table 10.15) have addressed how sensitive properties like entanglement and optical angular momentum are to atmospheric fluctuations in temperature and air flow. As an example, Pors et al. [64] determined that the shape of their photon detection coincidence curves were quite robust despite the turbulent conditions they generated in the laboratory. In addition they found that the OAM superposition states could be designed to have an optimal robustness against atmospheric perturbations. Heim et al. [65] showed that the theoretically predicted [66] log-normal transmission probability statistics for entangled photon pairs propagating over a 1.3 km free-space path could be enhanced by defocusing the beam of entangled photons in low atmospheric turbulence and with a highly focused beam of entangled photons in high turbulence. Earlier, researchers at Los Alamos National Laboratory [67] compared calculations of photon count distributions with measurements taken for horizontal propagation paths in weak to moderate atmospheric turbulence conditions and also found that a log-normal distribution best characterizes the probability statistics for single photons. Wu et al. [68] investigated how the atmosphere effects the synchronization accuracy in free-space quantum key distribution (QKD). Their experimental results and calculations showed that synchronization errors come mainly from the intensity fluctuation of synchronized light. By using the constant fraction discrimination method, they found that the synchronization error of a 10 km free-space QKD channel passing through a turbulent atmosphere may be limited within 300 ps which they suggest provides a sufficient synchronization accuracy for long distance free-space QKD, especially satellite-to-ground QKD.

Coupling the Atmosphere to Propagating Quantum Particles To properly represent the turbulence physics for the propagation of quantum states in the atmosphere one would need equations of motion for the atmosphere. Typically one would use the Navier–Stokes equations (NSE) with appropriate boundary and initial conditions to represent terrain, urban areas, ambient absorbers and scatterers (i.e., dust, pollution) and the weather conditions. In principle one could use generalized Schrodinger equations to represent the dynamics of the atmosphere as a composite of all

the quantum particles making up the atmosphere. In practice currently, the NSE are used to model the atmosphere and Schrodinger like equations are used to govern the motion of the photons that propagate through the atmosphere. This NSE simulated environment would of course have to be coupled to a quantum wavefunction propagator that includes quantum operators representing scattering, absorption, and index of refraction variability.

Free-space quantum communications may involve horizontal or slant path optical propagation. Several investigators have considered the important problem of quantum communications modeling along slant paths through realistic atmospheres, e.g., see Refs. [69, 70]. Some researchers are developing methods that use Wigner functions [71], Maxwell-like equations [72], new types of wavefunctions to represent photons [73, 74], or are describing photon loss at the receiver by proposing annihilation operators that describe losses related to absorption and scattering [65, 75] to model the effects of turbulence and real atmospheric conditions on the free-space propagation of quantum information. Most of these models tend to use Gaussian and Kolmogorov type statistics with a few theoretical investigations into non-Kolmogorov turbulence [69, 70]. Of course, since the atmosphere is nonstationary, inhomogeneous, and anisotropic, models will have to improve beyond the Kolmogorov models to reasonably represent the impact of turbulence on free-space quantum communications in general diurnal and seasonal varying conditions. In the following section we present experiments for free-space atmospheric quantum communications that are the beginning database for verifying free-space quantum communications models.

10.3 Free-Space and Atmospheric Quantum Communications Experiments

10.3.1 Introduction

Quantum communications (QC) is a field growing in importance. QC applications are expected to play a vital role in both the domestic and defense sectors. While fiber optic implementations of quantum communications technologies are being tested for communications infrastructure it is important to also consider free-space quantum communications that will play an important role in applications such as earth-to-satellite, end-of-line connections, and defense implementations. Quantum communications has the potential to provide enhanced security, bandwidth, and speed for free-space communications. Today's free-space quantum communications technologies accomplish transmission and detection of photons over long distances. Earlier ground-to-space laser communications experiments were important because they showed that such measurements were feasible. For example, Alley et al. [76] reported on the initial measurements retrieved from the 1969 Apollo 11 Lunar Laser Ranging Experiment conducted between a lunar retroreflector and the McDonald Obser-

vatory. Subsequently, more elaborate laser optic communications experiments were conducted, for example, in the USA and Japan, to demonstrate the capability to establish optical communication links to low earth orbiting satellites from the ground [77–81]. These later experiments also provided a platform from which to measure the effects of atmospheric turbulence on long distance laser propagation. To survey QC technological trends this section will highlight representative free-space quantum communications field experiments conducted over the past decade, to include experiments along horizontal propagation paths of varying distances, communication paths from ground-to-aircraft, ground-to-space, and in the laboratory.

10.3.2 Ground-to-ground, Ground-to-aircraft and Ground-to-satellite Experiments

Table 10.11 provides a summary of representative quantum communications field experiments along free-space propagation paths of varying distances. (A list of abbreviations used in Table 10.11 is provided in Table 10.12) Most of these experiments were conducted to implement and test various methods for quantum key distribution (QKD) in real-world atmospheric conditions. Several free-space QKD experiments were performed over horizontal distances from 0.7–1.6 km, such as those reported in [65, 82–89]. Much longer distance experiments were also conducted, most notably the quantum communications experiments across a 144 km path in the Canary Islands [90–93] and the QKD experiments over 20-, 40- and 96 km paths in China [94, 95]. One of the first practical free-space QKD experiments was conducted in daylight and nighttime conditions over a 10 km path by the Los Alamos National Laboratory (LANL) as reported by Hughes et al. [96, 97]. LANL provided in [98] a tabular summary of primary groups investigating QKD through free-space at that time. More recent QKD experiments have also demonstrated the capability to operate in daylight conditions, e.g., Refs. [99, 100]. Another free-space quantum key distribution system that was designed for daylight high-speed quantum key transmission (1 Mbps) in urban areas was reported by Garcia-Martinez et al. in [89]. Furthermore, a U.S. government sponsored project in 2009 reported a free-space quantum encryption (QE) experiment over distances up to 20 km from the ground to a flying aircraft at 10,000 feet [101]. Here, the Alpha-Eta encryption method [40, 45] was implemented and combined with advanced free-space optical terminals to send information (preshared keys) by quantum means and produce a Gbit/s air-to-ground optical link. The German Aerospace Center and their university collaborators also reported on a free-space experiment over a 20 km distance from the ground-to-aircraft conducted in March 2011 [102, 103]. In this QKD experiment, Nauerth et al. [102, 103] used attenuated laser pulses and polarization encoding to establish a 10 min. stable link producing a sifted quantum key rate of 145 bits/s with a quantum bit error rate (QBER) of 4.8%. In contrast, Temporao et al. [104] reported on a 1.5 km QKD study operating at a mid-infrared wavelengths to mitigate adverse foggy conditions (Figs. 10.2 and 10.3).

Table 10.11 Summary of Representative Free-Space Quantum Communications Field Experiments

Date	L(km)	Speed	Tech	λ(nm)	LPR	KP	QBER	Reference
2013	0.3	0.93 Mbps	QKD	850	1.5 GHz	B92	2.17%	García-Martínez [89]
2013	9.3, 12.3	–	QC	850	50 MHz	BC	1%	Liu [107]
2013	7.8	0.42 b/s	QKD	811	–	BB84	–	Cao [113]
2012	20, 40	268, 159.4	QKD	850	100 MHz	BB84	2.35, 2.73	Wang [94, 95]
	96	48 b/s					4.04%	
2012	143	–	QTel	808(404)	–	–	–	Ma [112]
2012	97	–	QTel	788(394)	–	–	–	Yin [59]
2011	20	145 b/s	QKD	1550	–	BB84	4.8%	Nauerth [102, 103]
2011	1.6	–	QKD	809	–	–	–	Heim [88]
2011	1.3	–	QKD	815	–	B92	–	Heim [65]
2010	16	–	QTel	810	–	–	–	Jin [111]
2010	1.2	–	QKD	670	–	BB84	–	Benton [99]
2010	1.305	2.7 kb/s	QKD	808	–	B92	2.48%	Erven [114]
2010	1.0	–	QKD	809	–	–	–	Heim [116]
2009	1.065	240 kb/s	QKD	1500	–	B92	0.57%	Toyoshima [87]
2009	20	2.5 Gb/s	QE	–	–	A–E	–	NuCrypt [101]
2009	1.5	2.2 Mb/s	QKD	850	1.25 GHz	BB84	3.1%	Bienfang [86]
2009	0.350	385 b/s	QKD	813	–	B92	–	Peloso [100]
2009	144	–	QKD	810	–	–	3.85%	Fedrizzi [90]
2009	0.08	17 kb/s	QKD	850	–	BB84	2.3%	Peev [117]
2009	0.1	3.2 kb/s	QKD	809	100 kHz	C–V	–	Elser [118]
								Heim [119]
2008	1.5	–	QKD	4600	750 kHz	BB84	2.3%	Temporao [104]

Table 10.11 (Continued)

Date	L(km)	Speed	Tech	λ(nm)	LPR	KP	QBER	Reference
2007	1.525	85 b/s	QKD	815	–	B92	4.92%	Erven [82] Erven [83] Weihs [120]
2006	0.48	50 kb/s	QKD	850	–	BB84	3.0–5.0%	Weier [121]
2006	1.5	200 b/s	QKD	810	–	E91	4.0%	Marcikic [84] Ling [122] Ling [123]
2006	144	12.8 b/s 42 b/s	QKD	710	249 MHz 10 MHz	BB84	6.48%	Ursin [91] Schmitt [92] Zeilinger [124]
2005	6.5	–	QKD	830	1 MHz	–	6.5%	Panthong [125]
2004	7.8	–	PE	810	–	–	9.9%	Resch [109]
2004	13	10 b/s	QKD	702	–	BB84	5.83%	Peng [126]
2004	.730	1 Mb/s	QKD	845	10 GHz	B92	1.1%	Bienfang [85]
2003	0.6	–	PE QTel	810	–	–	8.4%	Aspelmeyer [108] Ursin [110]
2002	23.4	–	QKD	–	–	–	–	Kurtsiefer [127]
2002	9.81	–	QKD	772	–	BB84	5.0% (d) 2.1% (n)	Hughes [96,97]
2002	4.0	–	QKD	835	–	–	–	Edwards [128]

Table 10.12 List of Abbreviations

Abbreviation	Definition
L (km)	Distance (in kilometers)
Tech	Technology of interest
λ (nm)	Wavelength (in nanometers)
LPR	Laser pulse rate
QKD	Quantum key distribution
CQKD	Counterfactual QKD
KP	QKD protocol
QTel	Quantum teleportation
QBER	Quantum bit error rate
PE	Polarization entanglement
NS	No-switching
SKE	Secret key encryption
C-V	Continuous variable
(d)/(n)	daytime/nighttime
BC	Bit commitment
QE	Quantum encryption
A-E	Alpha-Eta
–	No data

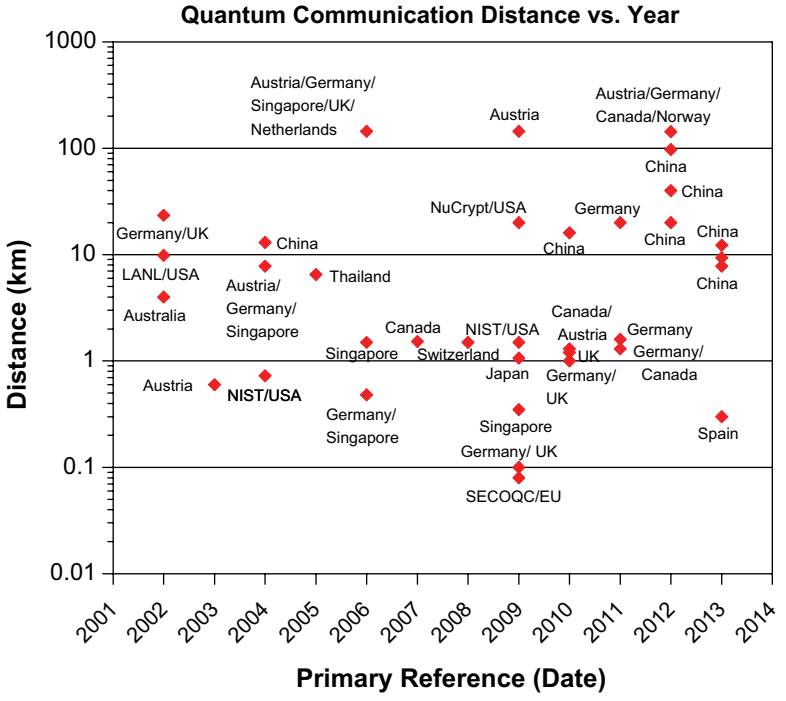

Fig. 10.2 Quantitative relationship between the propagation distance and the year the free-space quantum communication experiment was executed.

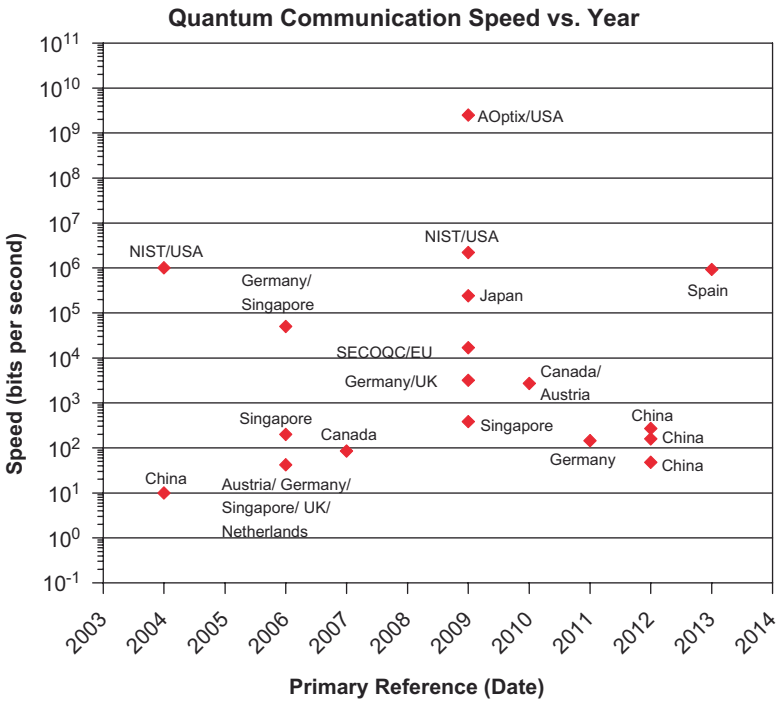

Fig. 10.3 Quantitative relationship between the transmission speed achieved and the year the free-space quantum communication experiment was executed.

Figure 10.2 shows a graph of the quantitative relationship between the propagation distances of the field experiments and the year the experiments were executed, which includes information on the country/sponsor. In Table 10.11 we also show that the field experiments implemented varying quantum protocols (e.g., BB84, B92, E91, C-V, Alpha-Eta) and varying light source wavelengths ($\lambda = 394\text{-}404$ nm, $\lambda =$ 670-850 nm, $\lambda = 1.5\ \mu m$ and $\lambda = 4.6\ \mu m$). The available data also show that achieved transmission speeds ranged from 10 bits/s to 2.5 Gbits/s (see Fig. 10.3).

Regarding QKD new trends, Liu et al. [105] reported on a measurement-device-independent QKD protocol that generated more than a 25 kbit secure key over a 50 km fiber link. This was a proof-of-principle experimental demonstration of secure quantum communications with implications for both fiber and free-space quantum channels. At the same time, Gisin et al. [106] reported on experimental demonstration of secure "bit commitment" between their locations in Geneva and Singapore based on quantum communications and special relativity. With the bit commitment (BC) protocol, Bob commits a secret bit to Alice at a given instant which he can choose to reveal some time later. Here, Bob's bit is perfectly concealed from Alice until he decides to open the commitment and reveal his bit to Alice. A free-space experimental demonstration of quantum communications (QC) using bit commitment (BC) protocols between two stations separated by more than 20 km was reported in [107].

Table 10.13 Quantum Communications Experiments to Satellites

Date	L(km)	Speed	TECH	λ(nm)	LPR	KP	QBER	Reference
2013	400	–	Single photon Exchange	702	76 MHz	–	–	Yin [131]
2009	1000	–	Photon beam Polarization	808-847	–	–	–	Toyoshima [81]
2008	1485	–	Single photon Exchange	532	17 kHz	–	–	Villoresi [129] Bonato [130]
2006	610	–	Photon beam APD, CCD	808-847	–	–	–	Toyoshima [79]

The remaining free-space experiments listed in Table 10.11 relate to long distance polarization entanglement experiments and demonstrations of quantum teleportation, such as those reported in [59, 108–113]. In addition, Erven reported on a QKD practical application using an improved entangled photon source [114] and Franson [115] presented a paper on quantum communications using entangled photon holes (EPH), which have the unique property of being relatively insensitive to photon loss and amplification. Franson [115] suggested that these features of EPH may be beneficial for QKD applications.

Table 10.13 above describes demonstration experiments related to single photon and photon beam exchanges from ground to space as reported in [79, 81, 129, 130, 131]. In these ground-to-satellite experiments, photon measurements were able to detect returns from a low earth orbiting satellite whose orbit's heights were 610 km, 1485 km, 1000 km, and 400 km respectively. Using high accuracy timing, high repetition rate pulses and narrow field of view receiver optics Yin et al. [131] reported achieving high signal-to-noise ratio (SNR) of 16:1. In contrast, high transmission losses in a 2008 single photon exchange experiment [129] prevented the successful implementation of a QKD protocol. Note that future ground-to-space QKD experiments, e.g., SEcure COmmunication based on Quantum Cryptography (SECOQC) and Space-QUEST: Quantum Entanglement for Space Experiments, have been proposed by the European Space Agency (ESA) and its collaborators from Austria, Belgium, Germany, UK, Canada, Switzerland, Czech Republic, France, Russia, Sweden, and Italy [132, 133]. Similarly, Scheidl et al. [134] reported on a proposal to perform quantum communication experiments over a distance of 400 km from the ground-to-space using the International Space Station.

Single Photon Detectors The performance of quantum communications systems significantly depends on detection efficiency and noise reduction. Development of many new products is ongoing in various locations for use in QKD and other quantum technology applications. For example, Ma et al. [135] reported that the National Institute of Standards and Technology (NIST) had developed a low noise up-conversion detector for 1310 nm using a LiNbO3 (PPLN) waveguide. In their setup, the 1310 nm signal photon is upconverted to 710 nm in the PPLN waveguide pumped by a 1550 nm laser, which is then detected by a low noise Si-APD single photon detector. NIST has integrated the upconversion Si-APD detector into various QKD systems and have performed both single photon and entangled photon pair measurements. In [135], NIST shows a comparison of performance speeds and

other characteristics of the main single photon detectors (i.e., those currently available) and the Si-APD upconversion detector that they developed at NIST. Their comparison also includes information related to two types of superconducting single photon detectors, i.e., the transition edge sensor (TES) and the superconducting single-photon detector (SSPD), which can work in the near-infrared range. More recently, Fejer et al. [136] report on upconverson and single photon detection near 2 microns.

10.3.2.1 Representative Quantum Communications Experiments (QKD and Polarization Entanglement) in the Laboratory

Table 10.14 provides information on representative quantum communications experiments (QKD and polarization entanglement) in the laboratory across varying table top propagation paths ranging from 0.5–4.0 meters in distance. Several experiments reported transmission speeds varying from 3.5 kb/s to 25 Mb/s [137–142]. The experiments implemented varying light source wavelengths from visible ($\lambda =$ 632 nm) to near-infrared ($\lambda = 1550$ nm). Most of these laboratory experiments implemented the BB84 QKD encryption protocol. An exception was the continuous-variable (C-V) QKD experiment reported in Ref. [143]. Ralph and Lam [22] suggested that C-V methods for QKD can offer distinct advantages over single photon approaches, such as implementation of deterministic teleportation protocols. Finally, Genovese et al. [44] reported on a experimental demonstration of counterfactual quantum cryptography (CQKD) in the laboratory, wherein information is transferred securely between Alice and Bob even when no photons or other quantum particles carrying the information are in fact transmitted between them. Additional discussion on counterfactual quantum communications can be found in Refs. [43, 144].

Representative Studies Related to Atmospheric Turbulence Effects on Quantum Communications Experiments Table 10.15 presents representative studies related to atmospheric turbulence effects on QC experiments to include effects on QKD and single photon statistics. Some of the key interests in recently published papers relate to photon count fluctuations, orbital angular momentum entanglement, optical vortex beams, synchronization accuracy, and quantum bit error rates. In certain quantum processes the adverse effects of turbulence can be mitigated and we expect that these features can be moved to quantum communications [19, 146, 147].

Quantum Repeaters and Quantum Memory Table 10.16 presents a representative list of recent efforts related to quantum repeaters and quantum memory to include information on the research groups, investigators, experimentally demonstrated coherence times and distance of entanglement of atoms/ions. As an example, Rolston and his colleagues at the Joint Quantum Institute (UMD/NIST) are using atomic ensembles to investigate problems in quantum communications and quantum memory. [152, 153]. Similarly, Kuzmich et al. at the Georgia Institute of Technology are conducting quantum communications experiments related to atom-photon entanglement with quantum memories reported on the time scale of one

Table 10.14 Quantum Communications Experiments in the Laboratory

Date	L(m)	Speed	TECH	λ(nm)	Sponsor	KP	QBER	Reference
2012	–	–	CQKD	812	INRIM/Italy	N09	12.0%	Genovese [44]
2010	4.0	–	QKD	670	UK	BB84	4.0%	Benton [99]
2009	0.6	–	PE	702	ORNL/USA LANL/USA	–	–	Humble [145]
2008	3.4	8.13 kb/s	QKD	860	Japan	BB84	5.5%	Toyoshima [138]
2006	0.5	3.5 kb/s	QKD	632	UK	BB84	–	Godfrey [139]
2006	0.5	–	QKD	1550	Japan	C-V	–	Hirano [143]
2006	0.7	3.8 kb/s	QKD	830	Russia	BB84	–	Kurochkin [142]
2005	–	25 Mb/s	QKD	1064	Australia	NS	–	Lance [140] Sharma [141]
2002	–	200 kb/s	QKD	670	Northwestern Univ/USA	SKE	–	Barbosa [137]

Table 10.15 Atmospheric Turbulence Effects on Quantum Communications Experiments

Date	Purpose	Key interest	Reference
2012	Single photon propagation through turbulence, beam scintillation, angle of arrival statistics	Impact of atmosphere on long-range quantum communications	Capraro [93]
2011	Entangled photon propagation through turbulence	Atmospheric effects on entanglement properties	Heim [65]
2009	Quantum light propagation through turbulence	Nonclassical photon-statistics	Semenov [65, 75]
2009	Photon propagation through turbulence	Orbital-angular-momentum entanglement	Pors [64]
2009	Photon propagation through turbulence	Optical vortex beams	Tyler [148] Boyd [149]
2007	Single photon statistics, propagation through turbulence	Reduce photon count fluctuations	Berman [150]
2007	QKD through atmosphere, 650 nm	Synchronization accuracy	Wu [68]
2007	QKD through turbulence	Turbulence effects on QBER	Yan [151]
2004	Single photon statistics, Propagation through turbulence	Experimental validation of theory	Milonni [67]

minute [154, 155]. Note that the longest reported distance entanglement for atoms and photons is 300 m in an optical fiber-based quantum communication channel [156].

10.3.3 Summary

A review of representative free-space quantum communications field experiments was presented and discussed relating to the trends in quantum technology development, so vital for future enhanced security communications in both the domestic and defense sectors. The highlighted free-space quantum communications field experi-

Table 10.16 Recent efforts related to Quantum Repeaters and Quantum Memory

Research group	Investigators	References	Coherence Time
Univ. of Michigan, Ann Arbor, MI Joint Quantum Institute (JQI), UMD/NIST College Park, MD	L. Duan, C. Monroe, D. Moehring, P. Maunz, S. Olmschenk, K. Younge, D. Matsukevich	Moehring [57] Duan [157, 158]	–
Joint Quantum Institute (JQI), UMD/NIST College Park, MD	R. Willis, F. Becerra, L. Orozco, S. Rolston	Willis [152] Rolston [153]	–
Georgia Institute of Technology Atlanta, GA	A. Radnaev, Y. Dudin, R. Zhao, H. Jen, S. Jenkins, A. Kuzmich, T. Kennedy, A Radnaer, J. Blumoff, L. Li	Radnaev [159] Dudin [160] Dudin, Kuzmich [155] Li [154]	0.1 s 10 ms 16 s
California Institute of Technology (CIT) Pasadena, CA	H. Kimble, K. Choi, H. Deng, J. Laurat	Kimble [2] Choi [161]	8 μs
Institut fur Quantenoptik, Leibniz Universitat, Hannover, Germany; Asrhus U., Denmark; CNRS, France	G. Buning, J. Will, W. Ertmer, E. Rasel, C. Klempt, J. Arlt, F. Martinez, F. Piechon	Buning [162] (^{87}Rb)	21 s
Massachusetts Institute of Technology (MIT), Harvard U., CIT, Max Planck Institute	T. Peyronel, O. Firstenberg, Q-Y Liang, S. Hofferberth, A. Gorshkov, T. Pohl, M. Lukin, V. Vuletic	Lukin [163]	–
CNRS, France	C. Deutsch, F. Ramirez, C. Lacroute, F. Reinhard, T. Schneider, J. Fuchs, F. Piechon, F. Laloe	Deutsch [164] (^{87}Rb)	58 s
CNRS, France; U. Geneva, Switz.; ICFO, Spain;	N.Sangouard, C.Simon, H. Riedmatten, N. Gisin,	Sangouard [26] Yuan [156]	300 m distance entanglement
Hefei Nat'l Lab & USTC, China;	B. Zhao, Y-A Chen,	Sangouard [25]	of Rb atoms
Inst. Theor. Phys., Heidelberg, Germany; U. Innsbruck, Austria; U. Vienna, Austria U. Calgary, Canada; U. Geneva, Switz.	J.-W. Pan, Z-S Yuan, S. Chen, J. Schmiedmayer, F. Yang, M. Torston, C. Lutz	Jin [165] Yang [166]	200 ns 28 ms
Laboratory Quantum Communication & Computation, Hefei, China;	L.-M. Duan, M.D. Lukin, J. I. Cirac, P. Zoller B. Zhao, M. Müller,	Duan [167] Zhao [168]	DLCZ scheme

Table 10.16 (Continued)

Research group	Investigators	References	Coherence
Harvard Univ,Cambridge, MA; Inst. Theor. Phys., Innsbruck, Austria	K. Hammerer, P. Zoller		
Niels Bohr Institute, Denmark;	H. Specht, C. Nolleke,	Specht [169]	180 μs
Max Planck Institute, Germany;	A. Reiserer, M. Uphoff,	Julsgaard [170]	4 ms
U. Brussels, Belgium; Palacky U., Czech Republic	E. Figueroa, S. Ritter, G. Rempe, B. Julsgaard, J. Sherson, I. Cirac, J. Flurasek, E. Polzik		
Inst. Exper. Phys., U. Innsbruck, Austria	L. Slodička, G. Hétet, N. Röck, P. Schindler, M. Hennrich, R. Blatt	Slodička [171]	1 m distance entanglement of trapped atomic ions

ments have also demonstrated the feasibility and practical use of free-space QKD systems, quantum teleportation and single photon exchange over extremely long distances. Progress has been achieved to operate high-speed free-space QKD systems during both daylight and nighttime hours, wherein previously communication links were difficult to establish during the day with high background light. Future ground-to-aircraft and ground-to-space quantum experiments will provide additional progress toward achieving highly secured worldwide communication networks. Continued development of improved entangled photon sources, photon detection systems, and improved encryption algorithms will make such free-space quantum communication technologies as quantum teleportation and QKD more efficient, more practical and more secure. For example, the US Army Research Laboratory (ARL) has been developing quantum communication technologies (see Refs. [56, 172, 173, 174]) and is expected to perform additional experiments and develop advanced technologies supporting free-space quantum communications applications.

Recently two notable free space and atmospheric quantum communications experiments have been performed. A quantum nonlocality experiment by Jennewein et al. [175] connected three quantum communications nodes. The nodes shared entanglement that was distributed from one node to two distant nodes that were 772 m and 686 m through a free space link. This experiment was a precursor to other applications such as multi-party quantum secret sharing and multi-party teleportation. Another experiment was performed by Vallone et al. [176] that simulated quantum key distribution from satellites using retro-reflectors mounted on five low earth orbit satellites. Their experiments concluded that their QBER rates were in a range suitable for QKD. They further proposed an alternative QKD scheme that would have a small impact on satellite payload. Also see Jennewein et al. [177] regarding advances towards a quantum communications satellite.

10.3.4 Exercises

Quantum Teleportation *Exercise 10.9* Let us assume that Alice and Bob share half of an entangled photon pair and that Alice wants to teleport to Bob a horizontal photon $|H\rangle$. The teleportation operation takes place when Alice performs a joint Bell measurement on her half of the entangled photon pair with the photon that she wants to teleport. Please explain.

Impact of Atmosphere on Quantum Communications *Exercise 10.10* Several methods have been experimentally demonstrated to help mitigate (a) single photon transmission loss and (b) entangled photon decoherence due to the negative impacts of atmospheric turbulence or environmental obscurants like fog or smoke. Give at least five examples.

Exercise 10.11 Has the impact of the atmosphere been the most important consideration in determining the laser light wavelength(s) for free-space quantum communications field experiments? Please explain.

Acknowledgment The authors thank the US Army Research Laboratory (ARL) for support. The authors also thank Dr. Sanjit Karmakar, a post-doc fellow at ARL, for his helpful comments on the manuscript.

References

1. P. Hemmer, Closer to a quantum internet. Physics **6**, 6–2 (2013)
2. H.J. Kimble, The quantum internet. Nature **453**, 1023–1030 (2008)
3. R.P. Feynman, Quantum mechanical computers. Found. Phys. **17**(6), 507–531 (1986)
4. R.E. Meyers, K.S. Deacon, A.D. Tunick, Quantum internet concept depiction. US Army Research Laboratory (2011)
5. A. Einstein, B. Podolsky, N. Rosen, Can quantum-mechanical description of physical reality be considered complete? Phys. Rev. **47**, 77–7 (1935)
6. J. Bell, On the Einstein Podolsky Rosen paradox. Physics **1**(3), 195–200 (1964)
7. A. Aspect, P. Grangier, G. Roger, Experimental realization of Einstein–Podolsky–Rosen–Bohm Gedanken-experiment: A new violation of Bell's inequalities. Phys. Rev. Lett. **49** (1982)
8. V. Scarani, C. Lynn, L.S. Yang, *Six quantum pieces: A first course in quantum physics*. (World Scientific, 2010)
9. R.P. Feynman, R.B. Leighton, M. Sands, *The Feynman Lectures on Physics vol. I–III* (Addison Wesley, 1997)
10. A. Lindner, D. Reisz, G. Wassiliadis, H. Freese, The uncertainty relation between particle number and phase. Phys. Lett. A **218**, 1–4 (1996)
11. M.O. Scully, M.S. Zubairy, *Quantum Optics*, 1 ed. (Cambridge University Press, Cambridge, 1997)
12. C.P. Williams, *Explorations in Quantum Computing* [AQ1](Springer, 2011)
13. M.A. Nielsen, I.L. Chuang, *Quantum Computation and Quantum Information* (Cambridge University Press, 2000)
14. R.J. Glauber, Coherent and incoherent sates of the radiation field. Phys. Rev. **131**, 2766–2788 (1963)

15. Y.H. Shih, *An Introduction to Quantum Optics: Photon and Biphoton Physics*, 1, ed. (CRC press, Taylor & Francis, 2011)
16. W. Martienssen, E. Spiller, Coherence and fluctuations in light beams. Am. J. Phys. **32**, 91–9 (1964)
17. L. Estes, L. Narducci, R. Tuft, Scattering of light from a rotating ground glass. J. Opt. Soc. Am. **61**, 130–1 (1971)
18. R. Hanbury Brown, *Intensity Interferometer* (Taylor & Francis, London, 1974)
19. R.E. Meyers, K.S. Deacon, Y.H. Shih, Turbulence-free ghost imaging. Appl. Phys. Lett. **98**, 11111–5 (2011)
20. T. Amri, J. Laurat, C. Fabre, Characterizing quantum properties of a measurement apparatus: Insights from the retrodictive approach. Phys. Rev. Lett. **106**, 02050–2 (2011)
21. T. Amri, Quantum behavior of measurement apparatus. arXiv:1001.3032 (2010)
22. T.C. Ralph, P.K. Lam, A bright future for quantum communications. Nat. Photonics **3**, 671–673 (2009)
23. B.E.A. Saleh, M.C. Teich, *Fundamentals of Photonics* (Wiley, 1991)
24. A. Cabello, A. Rossi, G. Vallone, F. De Martini, P. Mataloni, Proposed Bell experiment with genuine energy-time entanglement. Phys. Rev. Lett. **102**, 04040–1 (2009)
25. N. Sangouard, C. Simon, B Zhao, Y-A Chen, H. de Riedmatten, J-W Pan, N. Gisin, Robust and efficient quantum repeaters with atomic ensembles and linear optics. Phys. Rev. A **77**, 06230–1 (2008)
26. N. Sangouard, C. Simon, H. de Riedmatten, N. Gisin, Quantum repeaters based on atomic ensembles and linear optics. Rev. Mod. Phys. **83**, 33–80 (2011)
27. D.N. Klyshko, *Photons and Nonlinear Optics* (CRC press, Gordon & Breach, New York, 1998)
28. P. Kuo, J. Pelc, O. Slattery, M. Fejer, X. Tang, Dual-channel, single-photon upconversion detector near 1300 nm Proc. SPIE **8518**, 8518–8528 (2012)
29. H. Tu, Z. Jiang, D. Marks, S. Boppart, Intermodal four-wave mixing from femtosecond pulse-pumped photonic crystal fiber. Appl. Phys. Lett. **94**, 10110–9 (2009)
30. D. Halliday, R. Resnick, J. Walker, *Fundamentals of Physics Extended*, 10 ed. (Wiley, 2013)
31. F. Steinlechner, S. Ramelow, M. Jofre, M. Gilaberte, T. Jennewein, J.P. Torres, M.W. Mitchell, V. Pruneri, Phase-stable source of polarization-entangled photons in a linear double-pass configuration. Opt. Express **21**, 11943–11951 (2013)/P. Kwiat, K. Mattle, H. Weinfurter, A. Zeilinger, A. Sergienko, Y. Shih, High Intensity Source of Polarization Entangled Photon Pairs. Phys. Rev. Lett. **75**(24), 4337–4340 (1995)
32. D. Knuth, *The Art of Computer Programming, Volume 2: Seminumerical Algorithms*, 3 ed. (Addison-Wesley, 1997)
33. C. Bennett, G. Brassard, Quantum Cryptography: Public key distribution and coin tossing, Proceedings IEEE International Conference on Computers, Systems and Signal Processing (Institute of Electrical and Electronics Engineers, Bangalore, India, 175 1984)
34. A.L. Linares, C. Kurtsiefer, Breaking a quantum key distribution system through a timing side channel. Opt. Express **15**, 9388–9392 (2007)
35. V. Scarani, C. Kurtsiefer, The black paper of quantum cryptography: real implementation problems. [quant-ph] arXiv:0906.4547v2 (2012)
36. I. Gerhardt, Q. Liu, A.L. Linares, J. Skaar, C. Kurtsiefer, V. Makarov, Full-field implementation of a perfect eavesdropper on a quantum cryptography system. [quant-ph] arXiv:1011.0105v2 (2012)
37. A. Ekert, Quantum cryptography based on Bell's theorem. Phys. Rev. Lett. **67**, 661–663 (1991)
38. W. Tittel, J. Brendel, H. Zbinden, N. Gisin, Quantum cryptography using entangled photons in energy-time Bell states. Phys. Rev. Lett. **84**, 4737–4740 (2000)
39. C. Bennet, Quantum cryptography using any two nonorthogonal states. Phys. Rev. Lett. **68**, 3121–3124 (1992)
40. G. Barbosa, E. Corndorf, P. Kumar, H. Yuen, Quantum cryptography in free space with coherent-state light. Proc. SPIE **4821**, 409–420 (2002)

41. G. Tabia, B.G. Englert, Efficient quantum key distribution with trines of reference-frame-free qubits. [quant-ph] arXiv:0910.5375v1 (2009)
42. V. D'Ambrosio, E. Nagali, S.P. Walborn, L. Aolita, S. Slussarenko, L. Marrucci, F. Sciarrino, Complete experimental toolbox for alignment-free quantum communication. Nat. Commun. **3**, 96–1 (2012)
43. T. Noh, Counterfactual quantum cryptography. Phys. Rev. Lett. **103**, 23050–1 (2009)
44. G. Brida, A. Cavanna, I.P. Degiovanni, M. Genovese, P. Traina, Experimental realization of counterfactual quantum cryptography. Laser Phys. Lett. **9**, 247–252 (2012)
45. H.P. Yuen in *Quantum Communications and Measurements II*, ed. by P. Kumar et al. Quantum versus classical noise cryptography (Plenum Press, 2000), p. 399–404
46. R. Meyers, K. Deacon, Entangled and non-line-of-sight (NLOS) free-space photon quantum communication [Invited]. J. Opt. Netw. **5** (2005)
47. R.E. Meyers, K.S. Deacon, Free-space quantum communications system and process operative absent line of sight, US Patent 7,945,168 (17 May 11)
48. J. Yen, P. Poirier, M. O'Brien, Intentionally short-range communications (ISRC) 1993 Report. Tech. Rep. **1649**, SPAWAR, U.S. Navy, February (1994)
49. DARPA SUVOS Semiconductor Ultraviolet Optical Sources
50. W.C. Brown, The history of power transmission by radio waves. IEEE Trans. Microw. Theory Tech. **32**(9), 1230–1242 (1984)
51. P.D. Naselsky, D.I. Novikov, I.D. Novikov, *The Physics of the Cosmic Microwave Background* (Cambridge University Press, 2006)
52. C. Weedbrook, S. Pirandola, T.C. Ralph, Continuous-variable quantum key distribution using thermal states. Phys. Rev. A **86**, 02231–8 (2012)
53. C. Lang, C. Eichler, L. Steffen, J.M. Fink, M.J. Woolley, A. Blais, A. Wallraff, Correlations, indistinguishability and entanglement in Hong-Ou-Mandel experiments at microwave frequencies. Nat. Phys. **9**, 345–348 (2013)
54. C.H. Bennett, G. Brassard, C. Crepeau, R. Jozsa, A. Peres, W.K. Wooters, Teleporting an unknown quantum state via dual classical and Einstein–Podolsky–Rosen channels. Phys. Rev. Lett. **70**, 1895–1899 (1993)
55. D. Bouwmeester, J.-W. Pan, K. Mattle, M. Eibl, H. Weinfurter, A. Zeilinger, Experimental quantum teleportation. Nature **390**, 575–579 (1997)
56. R.E. Meyers, P. Lee, K.S. Deacon, A. Tunick, Q. Quraishi, D. Stack, A quantum network with atoms and photons. Proc. SPIE **8518**, 8518–8514 (2012)
57. D.L. Moehring, P. Maunz, S. Olmschenk, K.C. Younge, D.N. Matsukevich, L.-M. Duan, C. Monroe, Entanglement of single-atom quantum bits at a distance. Nature **449**, 68–71 (2007)
58. D.N. Matsukevich, P. Maunz, D.L. Moehring, S. Olmschenk, C. Monroe, Bell inequality violation with two remote atomic qubits. Phys. Rev. Lett. **100**, 15040–4 (2008)
59. J. Yin, J.-G. Ren, H. Lu, Y. Cao, H.-L. Yong, Y.-P. Wu, C. Liu, S.-K. Liao, F. Zhou, Y. Jiang, X.-D. Cai, P. Xu, G.-S. Pan, J.-J. Jia, Y.-M. Huang, H. Yin, J.-Y. Wang, Y.-A. Chen, C.-Z. Peng, J.-W. Pan, Quantum teleportation and entanglement distribution over 100-kilometre free-space channels. Nature **488**, 185–188 (2012)
60. X. Ma, T. Herbst, T. Scheidl, D. Wang, S. Kropatschek, W. Naylor, A. Mech, B. Wittmann, J. Kofler, E. Anisimova, V. Makarov, T. Jennewein, R. Ursin, A. Zeilinger, Quantum teleportation using active feed-forward between two Canary Islands. Nature 489, 269 (2012)/T. Herbst, T. Scheidl, M. Fink, J. Handsteiner, B. Wittmann, R. Ursin, A. Zeilinger, Teleportation of entanglement over 143 km. arXiv: 1403.0009v3 (2014)
61. T. Scheidl, R. Ursin, A. Fedrizzi1, S. Ramelow, X. Ma, T. Herbst, R. Prevedel, L. Ratschbacher, J. Kofler, T. Jennewein, A. Zeilinger Feasibility of 300 km quantum key distribution with entangled states. New J. Phys. **11**, 08500–2 (2009)
62. M. Pereira, L. Filpi, C. Monken, Cancellation of atmospheric turbulence angle-of-arrival fluctuations. arXiv:1202.3195v1 [quant-ph] (2012)
63. D. Fried, Statistics of a geometric representation of wavefront distortion. J. Opt. Soc. Am. **55**, 142–7 (1965)

64. B.-J. Pors, C.H. Monken, E.R. Eliel, J.P. Woerdman, Transport of orbital-angular-momentum entanglement through a turbulent atmosphere. Opt. Express **19**, 6671–6683 (2011)
65. B. Heim, C. Erven, R. Laflamme, G. Weihs, T. Jennewein, Improving entangled free-space quantum key distribution in the turbulent atmosphere, 12th European Quantum Electronics Conference (May 2011)
66. A.A. Semenov, W. Vogel, Quantum light in the turbulent atmosphere. Phys. Rev. A **80**, 021802(R) (2009)
67. P.W. Milonni, J.H. Carter, C.G. Peterson, R.J. Hughes, Effects of propagation through atmospheric turbulence on photon statistics. J. Opt. B Quantum Semiclassical Opt. **6**, S742–S745 (2004)
68. Q.-L. Wu, Z.-F. Han, E.-L. Miao, Y. Liu, Y.-M. Dai, G.C. Guo, Synchronization of free-space quantum key distribution. Opt. Commun. **275**, 486–490 (2007)
69. A. Zilberman, E. Golbraikh, N.S. Kopeika, Some limitations on optical communication reliability through Kolmogorov and non-Kolmogorov turbulence. Opt. Commun. **283**, 1229–1235 (2010)
70. Y.-X. Zhang, Y.-G. Wang, J.-C. Xu, J.-Y. Wang, J.-J. Jia, Orbital angular momentum crosstalk of single photons propagation in a slant non-Kolmogorov turbulence channel. Opt. Commun. **284**, 1132–1138 (2011)
71. M.G. Raymer, C.C. Cheng, Propagation of the optical Wigner function in random multiple-scattering media. Proc. SPIE **3927**, 156–164 (2000)
72. M.G. Raymer, B.J. Smith, The Maxwell wave function of the photon. Proc. SPIE **5866**, 29–3 (2005)
73. M. Hawton, Photon position measure. Phys. Rev. A **82**, 01211–7 (2010)
74. M. Hawton, Photon location in spacetime. Phys. Scr. **2012**, 01401–4 (2012)
75. A.A. Semenov, W. Vogel, Entanglement transfer through the turbulent atmosphere. Phys. Rev. A **81**, 02383–5 (2010); A.A. Semenov, W. Vogel, Erratum: entanglement transfer through the turbulent atmosphere. Phys. Rev. A **85**, 019908(E) (2012)
76. C.O. Alley, R.F. Chang, D.G. Curri, J. Mullendore, S.K. Poultney, J.D. Rayner, E.C. Silverberg, C.A. Steggerda, H.H. Plotkin, W. Williams, B. Warner, H. Richardson, B. Bopp, Apollo 11 laser ranging retro-reflector: initial measurements from the McDonald observatory. Science **167**, 368–370 (1970)
77. K.E. Wilson, An overview of the GOLD experiment between the ETS-VI satellite and the table mountain facility. TDA Progress Report 42–124, February 15 (1996)
78. K.E. Wilson, J.R. Lesh, K. Araki, Y. Arimoto, Overview of the ground-to-orbit lasercom demonstration (GOLD). Proc. SPIE **2990**, 2–3 (1997)
79. M. Toyoshima, Y. Takayama, T. Takahashi, K. Suzuki, S. Kimura, K. Takizawa, T. Kuri, W. Klaus, M. Toyoda, H. Kunimori, T. Jono, K. Arai, Ground-to-satellite laser communication experiments. IEEE A&E Systems Magazine (August 2008)
80. Y. Arimoto, M. Toyoshima, M. Toyoda, T. Takahashi, M. Shikalani, K. Araki, Preliminary result on laser communication experiment using Engineering Test Satellite-VI (ETS-VI). Proc. SPIE **2381**, 151–158 (1995)
81. M. Toyoshima, H. Takenaka, Y. Shoji, Y. Takayama, Y. Koyama, H. Kunimori, Polarization measurements through space-to-ground atmospheric propagation paths by using a highly polarized laser source in space. Opt. Express **17**, 22333–22340 (2009)
82. C. Erven, C. Couteau, R. Laflamme, G. Weihs, Entangled quantum key distribution over two free-space optical links. Opt. Express **16**, 16840–16853 (2008)
83. C. Erven, C. Couteau, R. Laflamme, G. Weihs, Entanglement based free-space quantum key distribution. Proc. SPIE **7099**, 70991–6 (2008)
84. I. Marcikic, A. Lamas-Linares, C. Kurtsiefer, Free-space quantum key distribution with entangled photons. Appl. Phys. Lett. **89**, 10112–2 (2006)
85. J.C. Bienfang, A.J. Gross, A. Mink, B.J. Hershman, A. Nakassis, X. Tang, R. Lu, D.H. Su, C.W. Clark, C.J. Williams, E.W. Hagley, J. Wen, Quantum key distribution with 1.25 Gbps clock synchronization. Opt. Express **12**, 2011–2016 (2004)

86. A. Restellia, J.C. Bienfang, A. Mink, C.W. Clark, Quantum key distribution at GHz transmission rates. Proc. SPIE **7236**, 72360–L (2009)
87. M. Toyoshima, H. Takenaka, Y. Shoji, Y. Takayama, M. Takeoka, M. Fujiwara, M. Sasaki, Polarization-basis tracking scheme in satellite quantum key distribution. Int. J. Opt. 25415–4 (2011)
88. B. Heim, C. Peuntinger, C. Wittmann, C. Marquardt, G. Leuchs, Free Space Quantum Communication using Continuous Polarization Variables in Applications of Lasers for Sensing and Free Space Communications, paper LWD3, Optical Society of America (2011)
89. M.J. Garcia-Martinez, N. Denisenko, D. Soto, D. Arroyo, A.B. Orue, V. Fernandez, High-speed free-space quantum key distribution system for urban daylight applications. Appl. Opt. **52**(14), 3311–3317 (2013)
90. A. Fedrizzi, R. Ursin, T. Herbst, M. Nespoli, R. Prevedel, T. Scheidl, F. Tiefenbacher, T. Jennewein, A. Zeilinger, High-fidelity transmission of entanglement over a high-loss freespace channel. Nat. Phys. **5**, 389–392 (2009)
91. R. Ursin, F. Tiefenbacher, T. Schmitt-Manderbach, H. Weier, T. Scheidl, M. Lindenthal, B. Blauensteiner, T. Jennewein, J. Perdigues, P. Trojek, B. Ömer, M. Fürst, M. Meyenburg, J. Rarity, Z. Sodnik, C. Barbieri, H. Weinfurter, A. Zeilinger, Entanglement based quantum communication over 144 km. Nat. Phys. **3**, 481–486 (2007)
92. T. Schmitt-Manderbach, H. Weier, M. Fürst, R. Ursin, F. Tiefenbacher, T. Scheidl, J. Perdigues, Z. Sodnik, J.G. Rarity, A. Zeilinger, H. Weinfurter, Experimental demonstration of free-space decoy-state quantum key distribution over 144 km. Phys. Rev. Lett. **98**, 01050–4 (2007)
93. I. Capraro, A. Tomaello, A. Dall'Arche, F. Gerlin, R. Ursin, G. Vallone, P. Villoresi, Impact of turbulence in long range quantum and classical communications. Phys. Rev. Lett. **109**, 20050–2 (2012)
94. J.-Y. Wang, B. Yang, S.-K. Liao, L. Zhang, Q. Shen, X.-F. Hu, J.-C. Wu, S.-J. Yang, Y.-L. Tang, B. Zhong, H. Liang, W.-Y. Liu, Y.-H. Hu, Y.-M. Huang, J.-G. Ren, G.-S. Pan, J. Yin, J.-J. Jia, K. Chen, C-Z Peng, J-W Pan, Direct and full-scale experimental verifications towards ground-satellite quantum key distribution. arXiv:1210.7556 [quant-ph] (29 October 2012)
95. J.-Y. Wang, B. Yang, S.-K. Liao, L. Zhang, Q. Shen, X.-F. Hu, J.-C. Wu, S.-J. Yang, H. Jiang, Y.-L. Tang, B. Zhong, H. Liang, W.-Y. Liu, Y.-H. Hu, Y.-M. Huang, B. Qi, J.-G. Ren, G.-S. Pan, J. Yin, J.-J. Jia, Y.-A. Chen, K. Chen, C-Z Peng, J-W Pan, Direct and full-scale experimental verifications towards ground-satellite quantum key distribution. Nat. Photonics **7**, 387–393 (2013)/M. Zhang, L. Zhang, J. Wu, S. Yang, X. Wan, Z. He, J. Jia, D.S. Citrin, J. Wang, Detection and compensation of basis deviation in satellite-to-ground quantum communications. Optics Express 22(8), 9871–9886 (2014)
96. R.J. Hughes, J.E. Nordholt, D. Derkacs, G.C. Peterson, Free-space Quantum Key Distribution over 10km in Daylight and at Night. Los Alamos Report LA-UR-02-449. [arXiv:quant-ph/0206092v1] (2002)
97. R.J. Hughes, J.E. Nordholt, D. Derkacs, C.G. Peterson, Practical free-space quantum key distribution over 10 km in daylight and at night. New J. Phys. **4**, 43.1–43.14 (2002)
98. R. Hughes, J. Nordholt, J. Rarity, Summary of Implementation Schemes for Quantum Key Distribution and Quantum Cryptography—A Quantum Information Science and Technology Roadmap; Part 2: Quantum Cryptography; Section 6.2: Weak Laser Pulses through Free Space (2004)
99. D.M. Benton, P.M. Gorman, P.R. Tapster, D.M. Taylor, A compact free space quantum key distribution system capable of daylight operation. Opt. Commun. **283**, 2465–2471 (2010)
100. M.P. Peloso, I. Gerhardt, C. Ho, A. Lamas-Linares, C. Kurtsiefer, Daylight operation of a free space, entanglement-based quantum key distribution system. New J. Phys. **11**, 04500–7 (2009)
101. NuCrypt, AOptix, Press Release: AOptix Technologies and NuCrypt Demonstrate Physical-Layer Quantum Encryption for the Air Force Research Laboratory. (AOptix Technologies, Campbell, 2009)

102. S. Nauerth, F. Moll, M. Rau, C. Fuchs, J. Horwath, H. Weinfurter, Air to ground quantum key distribution. 2nd Annual Conference on Quantum Cryptography (QCRYPT), Singapore, 2012/S. Nauerth, F. Moll, M. Rau, C. Fuchs, J. Horwath, S. Frick, H. Weinfurter, Air-to-ground quantum communication. Nature Photonics 7, 382–386 (2013)
103. S. Nauerth, F. Moll, M. Rau, J. Horwath, C. Fuchs, H. Weinfurter, Experimental aircraft to ground BB84 quantum key distribution. [AQ2]Proc SPIE. **8518**, (2012)
104. G. Temporao, H. Zbinden, S. Tanzilli, N. Gisin, T. Aellen, M. Giovannini, J. Faist, J.P. Von Der Weid, Feasibility study of free-space quantum key distribution in the mid-infrared. Quantum Inf. Comput. **8**, 1–11 (2008)
105. Y. Liu, T.-Y. Chen, L.-J. Wang, H. Liang, G.-L. Shentu, J. Wang, K. Cui, H.-L. Yin, N.-L. Liu, L. Li, X. Ma, J.S. Pelc, M.M. Fejer, C.-Z. Peng, Q. Zhang, J.-W. Pan, Experimental measurement-device-independent quantum key distribution. Phys. Rev. Lett. **111**, 13050–2 (2013)
106. T. Lunghi, J. Kaniewski, F. Bussières, R. Houlmann, M. Tomamichel, A. Kent, N. Gisin, S. Wehner, H. Zbinden, Experimental bit commitment based on quantum communication and special relativity. Phys. Rev. Lett. **111**, 18050–4 (2013)
107. Y. Liu, Y. Cao, M. Curty, S.-K. Liao, J. Wang, K. Cui, Y.-H. Li, Z.-H. Lin, Q.-C. Sun, D.-D. Li, H.-F. Zhang, Y. Zhao, T.-Y. Chen, C.-Z. Peng, Q. Zhang, A. Cabello, J.-W. Pan, Experimental unconditionally secure bit commitment. arXiv:1306.4413v2 [quant-ph] (25 June 2013)
108. M. Aspelmeyer, H.R. Bohm, T. Gyatso, T. Jennewein, R. Kaltenbaek, M. Lindenthal, G. Molina-Terriza, A. Poppe, K. Resch, M. Taraba, R. Ursin, P. Walther, A. Zeilinger, Long-distance free-space distribution of quantum entanglement. Science **301**, 621–623 (2003)
109. K.J. Resch, M. Lindenthal, B. Blauensteiner, H.R. Böhm, A. Fedrizzi, C. Kurtsiefer, A. Poppe1, T. Schmitt-Manderbach, M. Taraba, R. Ursin, P. Walther, H. Weier, H. Weinfurter, A. Zeilinger, Distributing entanglement and single photons through an intra-city, free-space quantum channel. Opt. Express **13**, 20–2 (2005)
110. R. Ursin, T. Jennewein, M. Aspelmeyer, R. Kaltenbaek, M. Lindenthal, P. Walther, A. Zeilinger, Quantum teleportation across the Danube. Nature **430**, 849–849 (2004)
111. X-M Jin, J-G Ren, B. Yang, Z-H Yi, F. Xhou, X-F Xu, S-K Wang, D. Yang, Y.F. Hu, S. Jiang, T. Yang, H. Yin, K. Chen, C-Z Peng, J-W Pan, Experimental free-space quantum teleportation. Nat. Photonics **4**, 376–381 (2010)
112. X.-S. Ma, T. Herbst, T. Scheidl, D. Wang, S. Kropatschek, W. Naylor, A. Mech, B. Wittmann, J. Kofler, E. Anisimova, V. Makarov, T. Jennewein, R. Ursin, A. Zeilinger, Quantum teleportation using active feed-forward between two Canary Islands. arXiv 1205.3909v1 [quant-ph] (17 May 2012)
113. Y. Cao, H. Liang, J. Yin, H.-L. Yong, F. Zhou, Y.-P. Wu, J.-G. Ren, Y.-H. Li, G.-S. Pan, T. Yang, X. Ma, C.-Z. Peng, J.-W. Pan, Entanglement-based quantum key distribution with biased basis choice via free space. Opt. Express **21**, 27260–27268 (2013)
114. C. Erven, D. Hamel, K. Resch, R. Laflamme, G. Weihs, Entanglement Based Quantum Key Distribution Using a Bright Sagnac Entangled Photon Source. First International Conference, QuantumComm 2009, Naples, Italy (2010)
115. J.D. Franson, Quantum communication using entangled photon holes. Conference-Frontiers in Optics, Rochester, NY, October 14–18 (2012)
116. B. Heim, D. Elser, T. Bartley, M. Sabuncu, C. Wittmann, D. Sych, C. Marquardt, G. Leuchs, Atmospheric channel characteristics for quantum communication with continuous polarization variables. Appl. Phys. B **98**, 635–640 (2010)
117. M. Peev et al., The SECOQC quantum key distribution network in Vienna. New J. Phys. **11**, 07500–1 (2009)
118. D. Elser, T. Bartley, B. Heim, C. Wittmann, D. Sych, G. Leuchs, Feasibility of free space quantum key distribution with coherent polarization states. New J. Phys. **11**, 04501–4 (2009)

119. B. Heim, D. Elser, T. Bartley, M. Sabuncu, C. Wittmann, D. Sych, C. Marquardt, G. Leuchs, Atmospheric channel characteristics for quantum communication with continuous polarization variables. Appl. Phys. B **98**, 635–640 (2010)
120. G. Weihs, C. Erven, Entangled free-space quantum key distribution. Proc. SPIE **6780**, 67801–3 (2007)
121. H. Weier, T. Schmitt-Manderbach, N. Regner, C. Kurtsiefer, H. Weinfurter, Free space quantum key distribution: towards a real life application. Prog. Phys. 54, 840–845 (2006)
122. A. Ling, M.P. Peloso, I. Marcikic, V. Scarani, A. Lamas-Linares, C. Kurtsiefer, Experimental quantum key distribution based on a Bell test. Phys. Rev. A **78**, 020301(R) (2008)
123. A. Ling, M. Peloso, I. Marcikic, A. Lamas-Linares, C. Kurtsiefer, Experimental E91 quantum key distribution. Proc. SPIE **6903**, 69030–U (2008)
124. A. Zeilinger, Long-distance quantum cryptography with entangled photons. Proc. SPIE **6780**, 67800–B (2007)
125. P. Panthong, S. Chiangga, K. Sripimanwat, T. Sanguankotchakorn, C. Li, L. Liang, Experimental free space quantum key distribution. Fourth International Conference on Optical Communications and Networks (ICOCN 2005), 159–162 (2005)
126. C.-Z. Peng, T. Yang, X.-H. Bao, J. Zhang, X.-M. Jin, F.-Y. Feng, B. Yang, J. Yang, J. Yin, Q. Zhang, N. Li, B.L. Tian, J.-W Pan, Experimental free-space distribution of entangled photon pairs over 13 km: towards satellite-based global quantum communication. Phys. Rev. Lett. **94**, 15050–1 (2005)
127. C. Kurtsiefer, P. Zarda, M. Halder, H. Weinfurter, P.M. Gorman, P.R. Tapster, J.G. Rarity,Quantum cryptography: a step towards global key distribution. Nature **419**, (2002)
128. P.J. Edwards, P. Lynam, The University of Canberra–Telstra Tower Free-Space Quantum Key Distribution Testbed. ITEE Society Monitor (March 2002)
129. P. Villoresi, T. Jennewein, F. Tamburini, M. Aspelmeyer, C. Bonato, R. Ursin, C. Pernechele, V. Luceri, G. Bianco, A. Zeilinger, C. Barbieri, Single-photon exchange advances Earth-to-space quantum link. New J. Phys. **10**, 03303–8 (2008)
130. C. Bonato, A. Tomaello, V. Da Deppo, G. Naletto, P. Villoresi, Study of the Quantum Channel between Earth and Space for Satellite Quantum Communications, ed. by K. Sithamparanathan. Psats 2009, LNICST 15, 37–40 (2009)
131. J. Yin, Y. Cao, S.-B. Liu, G.-S. Pan, J.-H. Wang, T. Yang, Z.-P. Zhang, F.-M. Yang, Y.-A. Chen, C.-Z. Peng, J.-W Pan, Experimental quasi-single-photon transmission from satellite to earth. Opt. Express **21**, 20032–20040 (2013)
132. J.M. Perdigues Armengol, B. Furch, C. J. de Matos, O. Minster, L. Cacciapuoti, M. Pfennigbauer, M. Aspelmeyer, T. Jennewein, R. Ursin, T. Schmitt-Manderbach, G. Baister, J. Rarity, W. Leeb, C. Barbieri, H. Weinfurter, A. Zeilinger, Quantum communications at ESA: towards a space experiment on the ISS. Acta Astronaut. **63**, 165–178 (2008)
133. R. Ursin, T. Jennewein, A. Zeilinger, Space-QUEST: quantum physics and quantum communication in space. Proc. SPIE **7236**, 72360–9 (2009)
134. T. Scheidl, E. Wille, R. Ursin, Quantum optics experiments using the international space station: a proposal. New J. Phys. **15**, 04300–8 (2013)
135. L. Ma, O. Slattery, A. Mink, X. Tang, Low noise up-conversion single photon detector and its applications in quantum information systems. Proc. SPIE **7465**, 74650–W (2009)
136. G.-L. Shentu, X.-X. Xia, Q.-C. Sun, J.S. Pelc, M.M. Fejer, Q. Zhang, J.-W. Pan, Upconversion single photon detection near 2 um. Opt. Lett. **38**, 498–5 (2013)
137. G.A. Barbosa, E. Corndorf, P. Kumar, H.P Yuen, Quantum cryptography in free space with coherent-state light. Proc. SPIE **4821**, 40–9 (2002)
138. M. Toyoshima, Y. Takayama, W. Klaus, H. Kunimori, M. Fujiwara, M. Sasaki, Free-space quantum cryptography with quantum and telecom communication channels. Acta Astronaut. **63**, 1–4 (2008)
139. M.S. Godfrey, A.M. Lynch, J.L. Duligall, W.J. Munro, K.J. Harrison, J.G. Rarity, Free-space secure key exchange from 1 m to 1000 km. Proc. SPIE **6399**, 63990–E (2006)

140. A.M. Lance, T. Symul, V. Sharma, C. Weedbrook, T.C. Ralph, P.K. Lam, No-switching quantum key distribution using broadband modulated coherent light. Phys. Rev. Lett. **95**, 18050–3 (2005)
141. V. Sharma, A.M. Lance, T. Symul, C. Weedbrook, T.C. Ralph, P.K. Lam, A complete quantum cryptographic system using a continuous wave laser. Proc. SPIE **6038**, 60380–3 (2005)
142. V.L. Kurochkin, I.I. Ryabtsev, I.G. Neizvestny, Quantum cryptography and quantum-key distribution with single photons. Russ. Microlectron. **35**, 31–36 (2006)
143. T. Hirano, A. Shimoguchi, K. Shirasaki, S. Tokunaga, A. Furuki, Y. Kawamoto, R. Namiki, Practical implementation of continuous-variable quantum key distribution. Proc. SPIE **6244**, 62440–O (2006)
144. H. Salih, Z.-H. Li, M. Al-Amri, M.S. Zubairy, Protocol for direct counterfactual quantum communication. Phys. Rev. Lett. **110**, 17050–2 (2013)
145. T.S. Humble, R.S. Bennink, W.P. Grice, I.J. Owens, Sensing intruders using entanglement: a photonic quantum fence. Proc. SPIE **7342**, 73420–H (2009)
146. R.E. Meyers, K.S. Deacon, Y.H. Shih, Ghost-imaging experiment by measuring reflected photons. Phys. Rev. A **77**, 041801(R) (2008)
147. R.E. Meyers, K.S. Deacon, Y.H. Shih, Positive-negative turbulence-free ghost imaging. Appl. Phys. Lett. **100**, 13111–4 (2012)
148. G.A. Tyler, R.W. Boyd, Influence of atmospheric turbulence on the propagation of quantum states of light carrying orbital angular momentum. Opt. Lett. **34**, 142–144 (2009)
149. R.W. Boyd, B. Rodenberg, M. Mirhosseini, S. Barnett, Influence of atmospheric turbulence on the propagation of quantum states of light using plane-wave encoding. Opt. Express **19**, 18310–18317 (2011)
150. G.P. Berman, A.A. Chumak, Quantum effects of a partially coherent beam propagating through the atmosphere. Proc. SPIE **6710**, 67100–M (2007)
151. C. Yan, H. Yu, Effect of turbulent atmosphere on quantum key distribution systems. Acta Optica. Sinica **27**, 21–25 (2007)
152. R.T. Willis, F.E. Becerra, L.A. Orozco, S.L. Rolston, Correlated photon pairs generated from a warm atomic ensemble. Phys. Rev. A **82**, 05384–2 (2010)
153. J. Lee, D.H. Park, S. Mittal, M. Dagenais, S.L. Rolston, Integrated optical dipole trap for cold neutral atoms with an optical waveguide coupler. New J. Phys. **15**, 04301–0 (2013)
154. L. Li, Y.O. Dudin, A. Kuzmich, Entanglement between light and an optical atomic excitation. Nature **498**, 466–469 (2013)
155. Y.O. Dudin, L. Li, A. Kuzmich, Light storage on the minute scale. Phys. Rev. A **87**, 031801(R) (2013)
156. Z.-S. Yuan, Y.-A. Chen, B. Zhao, S. Chen, J. Schmiedmayer, J.-W. Pan, Experimental demonstration of a BDCZ quantum repeater node. Nature 454, 1098–1101 (Aug 2008)
157. L.-M. Duan, C. Monroe, Robust quantum information processing with atoms, photons and atomic ensembles. Adv. At. Mol. Opt. Phys. **55**, 419–464 (2008)
158. L.-M. Duan, C. Monroe, Colloquium: quantum networks with trapped ions. Rev. Mod. Phys. **82**, 1209–1224 (2010)
159. A.G. Radnaev, Y.O. Dudin, R. Zhao, H.H. Jen, S.D. Jenkins, A. Kuzmich, T.A.B. Kennedy, A quantum memory with telecom-wavelength conversion. Nat. Phys. **6**, 894–899 (2010)
160. Y.O. Dudin, A.G. Radnaev, R. Zhao, J.Z. Blumoff, T.A.B. Kennedy, A. Kuzmich, Entanglement of light-shift compensated atomic spin waves with telecom light, arXiv:1009.4180v1 [quant-ph] (21 Sept 2010)
161. S. Choi, H. Deng, J. Laurat, H.J. Kimble, Mapping photonic entanglement into and out of a quantum memory. Nature **452**, 67–72 (2008)
162. G. Kleine Buning, J. Will, W. Ertmer, E. Rasel, J. Arlt, C. Klempt, F. Ramirez-Martinez, F. Piechon, P. Rosenbusch, Extended coherence time on the clock transition of optically trapped rubidium. Phys. Rev. Lett. **106**, 24080–1 (2011)
163. T. Peyronel, O. Firstenberg, Q.-Y. Liang, S. Hofferberth, A.V. Gorshkov, T. Pohl, M.D. Lukin, V. Vuletic, Quantum nonlinear optics with single photons enabled by strongly interacting atoms. Nature **488**, 57–60 (2012)

164. C. Deutsch, F. Ramirez-Martinez, C. Lacroute, F. Reinhard, T. Schneider, J.N. Fuchs, F. Piechon, F. Laloe, J. Reichel, P. Rosenbusch, Spin self-rephasing and very long coherence times in a trapped atomic ensemble. Phys. Rev. Lett. **105**, 02040–1 (2010)
165. X.-M. Jin, J. Yang, H. Zhang, H.-N. Dai, S.-J. Yang, T.-M. Zhao, J. Rui, Y. He, X. Jiang, F. Yang, G.-S. Pan, Z.-S. Yuan, Y. Deng, Z.-B. Chen, X.-H. Bao, B. Zhao, S. Chen, J.-W. Pan, Quantum interface between frequency-uncorrelated down-converted entanglement and atomic-ensemble quantum memory. arXiv:1004.4691v1 [quant-ph] (April 2010)
166. F. Yang, T. Mandel, C. Lutz, Z-S Yuan, J-W Pan, Transverse Mode Revival of a Light-Compensated Quantum Memory. arXiv:1012.2361v2 [quant-ph] (December 2010)
167. L.-M. Duan, M.D. Lukin, J.I. Cirac, P. Zoller, Long-distance quantum communication with atomic ensembles and linear optics. Nature **414**, 413–418 (November 2001)
168. B. Zhao, M. Muller, K. Hammerer, P. Zoller, Efficient quantum repeater based on deterministic Rydberg gates. Phys. Rev. A **81**, 05232–9 (2010)
169. H.P. Specht, C. Nolleke, A. Reiserer, M. Uphoff, E. Figueroa, S. Ritter, G. Rempe, A single-atom quantum memory. Nature **473**, 190–193 (2011)
170. B. Julsgaard, J. Sherson, J.I. Cirac, J. Fiuraek, E.S. Polzik, Experimental demonstration of quantum memory for light. Nature **432**, 482–486 (2004)
171. L. Slodicka, G. Hetet, N. Rock, P. Schindler, M. Hennrich, R. Blatt, Atom-atom entanglement by single-photon detection. arXiv:1207.5468v1 [quant-ph] (2012)
172. R.E. Meyers, K.S. Deacon, Entangled quantum communications and quantum imaging. Proc. SPIE **5161**, 28–0 (2004)
173. R.E. Meyers, K.S. Deacon, D.L. Rosen, Entangled Quantum Communications and Quantum Imaging, US Patent 7,536,012 (May 19, 2009)
174. R.E. Meyers, K.S. Deacon, Quantum Fourier Transform Based Information Transmission System and Method, US Patent 7,660,553 (February 9, 2010)
175. C. Erven, E. Meyer-Scott, K. Fisher, J. Lavoie, B. Higgins, Z. Yan, C. Pugh, J. Bourgoin, R. Prevedel, L. Shalm, L. Richards, N. Gigov, R. LaFlamme, G. Weighs, T. Jennewein, K. Resch, Experimental three-photon quantum nonlocality under strict locality conditions, Nat. Photonics 8, 292–296 (2014)
176. G. Vallone, D. Bacco, D. Dequall, S. Gaiarin, V. Luceri, G. Biano, P. Valloresi, Experimental Satellite Quantum Communications, arXiv:1406.4051v1 [quant-ph] (2014)
177. T. Jennewein, B. Higgins, E. Choi, Progress toward a quantum communication satellite. SPIE Newsroom, 10.1117/2.1201404.005453 (01 May 2014)

Index

A. K. Majumdar, *Advanced Free Space Optics (FSO),*
Springer Series in Optical Sciences 186, DOI 10.1007/978-1-4939-0918-6,
© Springer Science+Business Media New York 2015